The Eurasia Proceedings of Science, Technology, Engineering & Mathematics

EPSTEM

VOLUME 34 ICBASET CONFERENCE

ISSN: 2602-3199
ISBN: 978-625-6959-71-2

ICBASET 2025: 5th International Conference on Basic Sciences, Engineering and Technology (ICBASET)
May 01- 04, 2025 Trabzon, Türkiye
Edited by: Prof.Dr. Mehmet Ozaslan - Gaziantep University, Türkiye

The Eurasia Proceedings of Science, Technology, Engineering & Mathematics (EPSTEM)
ISSN: 2602-3199

ICBASET 2025

International Conference on Basic Sciences, Engineering and Technology (ICBASET)

Proceedings Book

Editor

Mehmet Ozaslan
Gaziantep University, Türkiye

ISBN: 978-625-6959-71-2

Published by the ISRES Publishing

Address: Askan Mah. Akinbey Sok. No: 5-A/Konya/TÜRKİYE

Web: www.isres.org

Contact: isrespublishing@gmail.com

Dates: May 01- 04, 2025

Location: Trabzon, Türkiye

https://2025.icbaset.net

About Editor

Prof Dr. Mehmet Ozaslan
Department of Biology, Gaziantep University, Türkiye
Website: mehmetozaslan.com
E-mail: ozaslanmd@gantep.edu.tr

Language Editor

Lecturer Ceren Dogan
School of Foreign Languages, Necmettin Erbakan University, Türkiye
Email: cerendogan@erbakan.edu.tr

Editorial Policies

ISRES Publishing follows the steps below in the procedings book publishing process.
In the first stage, the papers sent to the conferences organized by ISRES are subject to editorial oversight. In the second stage, the papers that pass the first step are reviewed by at least two international field experts in the conference committee in terms of suitability for the content and subject area. In the third stage, it is reviewed by at least one member of the organizing committee for the suitability of references. In the fourth step, the language editor reviews the language for clarity.

Review Process

Abstracts and full-text reports uploaded to the conference system undergo a review procedure. Abstracts will be evaluated on the basis of abstracts/proposals. The conference system allows the full text to be sent if the abstract is accepted. Participants must wait for the evaluation results after uploading their article abstracts to the conference system. If their abstracts are accepted, they can upload their full texts to the conference system. The full texts are then sent to at least two reviewers for review. The conference has a double-blind peer-review process. Any paper submitted for the conference is reviewed by at least two international reviewers with expertise in the relevant subject area. Based on the reviewers' comments, papers are accepted, rejected or accepted with revision. If the comments are not addressed well in the improved paper, then the paper is sent back to the authors to make further revisions. The accepted papers are formatted by the conference for publication in the proceedings.

Aims & Scope

Engineering, technology and basic sciences are closely related fields. Developments and innovations in one of them affect the others. Therefore, the focus of the conference is on studies related to these three fields. Studies in the fields of engineering, technology and basic science are accepted to the conference even if they are not associated with other fields. The conference committee thinks that a study in only one field (for example, mathematics, physics, etc.) will contribute to other fields (for example, engineering, technology, etc.) in future studies, even if it is not associated with the presentation at the conference. In line with this perspective, studies in the following fields are accepted to the conference: Biology, Chemistry, Engineering, Mathematics, Physics and Technology.

The aim of the conference is to bring together researchers and administrators from different countries, and to discuss theoretical and practical issues in all fields of Engineering, Technology and Basic Sciences.

The Eurasia Proceedings of Science, Technology, Engineering & Mathematics (EPSTEM)
ISSN: 2602-3199

Articles: 1- 46

CONTENTS

The Eurasia Proceedings of Science, Technology, Engineering & Mathematics (EPSTEM)
ISSN: 2602-3199

The Eurasia Proceedings of Science, Technology, Engineering and Mathematics (EPSTEM), 2025

Volume 34, Pages 1-7

ICBASET 2025: International Conference on Basic Sciences, Engineering and Technology

A Novel Technique for Estimation the Coefficients of ARMA Model Using Higher Order Moments

Adnan Al-Smadi
Zarqa University
Yarmouk University

Abstract: Time series data is observed in many different areas such as communication systems, signal processing, climate data and earthquake data. Statistical modeling and analysis of time series data includes transformation of the data into stationary times series and fit the time series model to the transformed data. Autoregressive Moving Average (ARMA) model is one of the most often used to fit the time series data. The proper estimation of the coefficients in the time series model is one of the important steps of modeling. In this study, a novel technique for estimating the coefficients of non-Gaussian ARMA model using higher order moments of the observed data. The proposed ARMA coefficients estimator is based on building a special matrix with entries of higher order moments of the observed output only. The observed output data may be corrupted with additive white Gaussian noise. Simulation results promise that the proposed method achieves performance comparable to existing well-known methods even when the available output signal is heavily corrupted with additive white Gaussian noise.

Keywords: Time series data, Coefficients estimation, ARMA model, Higher order moments

Introduction

Time series data is observed in many different areas such as communication systems, signal processing, climate data and earthquake data. Statistical modeling and analysis of time series data includes transformation the data into stationary times series and fit the times series model to the transformed data. Autoregressive Moving Average (ARMA) model is one of the most often used to fit the time series data (Al-Smadi & Wilkes, 2002; Wang et al. 2017). ARMA model is important and extremely useful in modeling predicting future values of a time series. The proper estimation of the coefficients in time series model is one of the important steps of modeling. The literature has a lot of papers that deals with the estimating of the coefficients of a general ARMA model using second order and third order moments (or cumulants) (Giannakis & Mendel, 1989; Swami & Mendel,1990; Wang et al. 2017).

The second order statistics work fine if the analyzed signal has Gaussian probability density function since all of its properties determined by the first and second order moments (Al-Smadi & Smadi, 2003). However, there are many real-life situations where the signal is non-Gaussian. Even though Gaussian random process still plays a significant role when processing data, non-Gaussian random processes and higher order moments are of increasing interest. Giannakis and Mendel (1989) proposed a Residual Time Series (RTS) procedure for the identification of linear time invariant (LTI) nonminimum phase systems using second and third order moments when only output data are available. They assumed that the order is given in modeling an autoregressive moving-average process. The basic idea of the algorithms in literature is to estimate the AR coefficient. Then, a residual MA time series is formed. Finally, the MA coefficients are estimated.

In system identification, the use of the Cholesky decomposition in the prediction and estimation of ARMA time series was used by Ansley (1976). He applied the Cholesky decomposition to the problem of estimating the

likelihood function of the MA and the ARMA models. Parzen and Pagano (1979) used Cholesky decomposition for obtaining predictors. Lee et. al. (2017) proposed linear models with a covariance matrix that is modeled using the coefficients of an ARMA Cholesky decomposition (ARMACD). These models allow for non-stationary processes.

In this paper, a novel technique for estimating the coefficients of non-Gaussian ARMA model using higher order moments of the observed data. The proposed ARMA coefficients estimator is based on building a special matrix with entries of higher order moments of the observed output time series data only. The observed output time series data may be corrupted with additive white Gaussian noise (Vinothkumar & Manoj, 2024). Simulation results promise that the proposed method is based on the Cholesky decomposition and achieves good performance comparable to existing well-known methods even when the available output signal is heavily corrupted with additive white Gaussian noise. Section 2 presents the problem formulation.

Problem Formulation

A general model for Autoregressive Moving Average (ARMA) model can be represented as follows:

$$A(z^{-1})x(n) = C(z^{-1})w(n) \tag{1}$$

where $x(n)$ is the observed noiseless output data. The input signal $w(n)$ is zero-mean, white noise, and non-Gaussian random process. The z^{-1} is the backward shift operator, that is,

$$z^{-1}x(n) = x(n\text{-}1) \tag{2}$$

$$A(z^{-1}) = 1 + a_1 z^{-1} + a_2 z^{-2} + \dots a_p z^{-p} \tag{3}$$

$$C(z^{-1}) = b_0 + b_1 z^{-1} + b_2 z^{-2} + \dots b_q z^{-q} \tag{4}$$

In this system, the a_i and b_i are the coefficients of the ARMA model, while p and q are the orders of the denominator and numerator polynomials, respectively. In this study, it is assumed that the orders p and q are known. The output signal $x(n)$ is observed in additive white Gaussian noise $e(n)$ as follows:

$$y(n) = x(n) + e(n) \tag{5}$$

The relationship of (1) can be rewritten in matrix form as follows, assuming the length of the sequence is N.

$$[Y_p W_q]\underline{\theta}_{pq} = \underline{e} \tag{6}$$

Or

$$R_{pq}\underline{\theta}_{pq} = \underline{e} \tag{7}$$

where R_{pq} is a composite data matrix such that

$$R_{pq} = [Y_p W_q] \tag{8}$$

$$Y_p = \begin{bmatrix} y(0) & 0 & \cdots & 0 \\ y(1) & y(0) & \cdots & 0 \\ \vdots & \vdots & \ddots & \vdots \\ y(N-1) & y(N-2) & \cdots & y(N-p) \end{bmatrix} \tag{9}$$

$$W_q = \begin{bmatrix} w(0) & 0 & \cdots & 0 \\ w(1) & w(0) & \cdots & 0 \\ \vdots & \vdots & \ddots & \vdots \\ w(N-1) & w(N-2) & \cdots & w(N-q) \end{bmatrix} \tag{10}$$

$$\underline{\theta} = [1\ a_1 \ldots a_p\ -b_0 \ldots -b_q]^T \tag{11}$$

$\underline{\theta}$ is the coefficients vector, and $\underline{e}$ is an $N \times 1$ observation and/or modeling error vector.

Proposed Algorithm

Let $y(k)$ be a zero-mean k^{th}-order stationary random process, then the k^{th}-order cumulant of this process is defined as the joint kth-order cumulant of the random variables $y(k)$, $y(k+t_1)$, $y(k+t_2)$, $\cdots$,$y(k+t_{N-1})$. That is (Mendel, 1991)

$$c_k^y(t_1, t_2, \cdots, t_{N-1}) = Cum(y(k), y(k+t_1), \cdots, y(k+t_{N-1})) \tag{12}$$

which depends only on the time difference t_1, t_2, t_{N-1}, because of the stationarity assumption. Now, if $y(k)$ is stationary random process and its moments up to order N exist, then the following relationships between moment and cumulant sequences of $y(k)$ exist (Nikias & Mendel, 1993). The first order cumulant (mean value):

$$c_1^y = m_1^y = E\{y(k)\} \tag{13}$$

The second order cumulant (covariance sequence):

$$c_2^y(t_1) = m_2^y(t_1) - (m_1^y)^2 \tag{14}$$

where $m_2^y(t_1)$ is the autocorrelation.

The third order cumulant:

$$c_3^y(t_1, t_2) = m_3^y(t_1, t_2) - m_1^y[m_2^y(t_1) + m_2^y(t_2) + m_2^y(t_1 - t_2)] + 2(m_1^y)^3 \tag{15}$$

If the process $y(k)$ is zero-mean, $m_1^y = 0$, then the second order and third order cumulants are identical to the second and third order moments. Hence, from Equation (12),

$$Cum\{y(n)\} = C_y = E[y(n)y(n+m)y(n+k)] \tag{16}$$

where the operator $E[.]$ represents the average value. The third order cross-cumulant between the signal $y(k)$ and the signal $w(k)$ is given by

$$C_{yww}(m,k) = E[y(n)w(n+m)w(n+k)] \tag{17}$$

Multiplying both sides of (5) by $y(n+m)y(n+k)$, we obtain

$$y(n)\ y(n+m)y(n+k) = x(n)\ y(n+m)y(n+k) + e(n)y(n+m)y(n+k) \tag{18}$$

Substituting Equation (5) into the first part of the right side of Equation (18),

$$y(n)\ y(n+m)y(n+k) = x(n)[x(n+m) + e(n+m)][\ x(n+k) + e(n+k)] + e(n)y(n+m)y(n+k) \tag{19}$$

Simplifying (19) and taking the expected value will result in

$$E[y(n)\,y(n+m)y(n+k)] = E[x(n)\,x(n+m)x(n+k)] + E[x(n)\,x(n+m)e(n+k)] + E[x(n)\,e(n+m)x(n+k)] + E[x(n)\,e(n+m)e(n+k)] + E[e(n)\,y(n+m)y(n+k)] \quad (20)$$

Since the additive Gaussian noise, $e(n)$, is independent of both signals $x(n)$ and $y(n)$, then the second, third, fourth, and fifth terms on the right-hand side of Equation (20) go to zeros. Hence, the cumulants of the corrupted sequence $y(n)$ and the noiseless sequence $x(n)$ are theoretically are equal; i.e.,

$$R_y(m,k) = R_x(m,k) \quad (21)$$

Now, multiplying both sides of Equation (1) by $x(n+m)x(n+k)$ and taking expected value gives

$$R_x(m,k) = -a_1\,R_x(m+1,k+1) - \ldots - a_p\,R_x(m+p,k+p) + b_0\,R_{wxx}(m,k) + \ldots + b_q\,R_{wxx}(m+q,k+q) \quad (22)$$

By arranging Equation (22) for several values of m and k, the system in (22) can be as follows.

$$\underline{r} = -(R_X)\,\underline{a} + (R_{WXX})\,\underline{b} \quad (23)$$

where $\underline{r}$ is a vector containing third order cumulants at $m = k = 0$, R_X is a matrix containing the third order cumulants of the output data and R_{WXX} is a matrix containing the third order cross cumulants of the input and output signals. Equation (23) can be written as

$$\underline{r} = R_{pq}\,\underline{\theta} \quad (24)$$

where R_{pq} is a composite data matrix

$$R_{pq} = [R_X\ R_{WXX}] \quad (25)$$

The vector $\underline{\theta}$ contains the ARMA coefficients

$$\underline{\theta} = [-\underline{a} \quad \underline{b}]^T \quad (26)$$

Multiplying both sides of (24) by $(R_{pq})^{\mathrm{T}}$

$$(R_{pq})^T R_{pq}\,\underline{\theta} = (R_{pq})^T \underline{r} \quad (27)$$

Let

$$G = (R_{pq})^T R_{pq} \quad (28)$$

Then

$$G\,\underline{\theta} = (R_{pq})^T \underline{r} \quad (29)$$

Now, let the right hand side of Equation (29) be

$$\underline{\alpha} = (R_{pq})^T \underline{r} \quad (30)$$

Hence, Equation (29) becomes

$$G\,\underline{\theta} = \underline{\alpha} \quad (31)$$

The matrix G can be decomposed Cholesky decomposition (Higham, 2009).

$$G = LL^T \quad (32)$$

Now, substitute (32) into (31) yields

$$LL^T \underline{\theta} = \underline{\alpha} \tag{33}$$

Now, let

$$\underline{d} = L^T \underline{\theta} \tag{34}$$

We first solve the following using forward substitution,

$$L\underline{d} = \underline{\alpha} \tag{35}$$

The, we solve the second part for $\underline{\theta}$ using back substitution

$$L^T \underline{\theta} = \underline{d} \tag{36}$$

The vector $\underline{\theta}$ contains the desired parameters.

Results and Discussion

The proposed technique for estimating the coefficients of non-Gaussian ARMA model using higher order moments of the observed data has been examined for several cases. A comparison of the performance of the Cholesky decomposition-based (CHDB) algorithm with the Residual Time Series (RTS) algorithm has been made for different SNRs on the output signal. The command *armarts* commands were used from was used from the *Higher-Order Spectral Analysis Toolbox User's Guide* (Swami et al. 1998) to estimate the ARMA coefficients using the RTS method. All the results were taken as the mathematical average of 100 Monte Carlo runs. The computations were performed in MATLAB.

Example 1. The data was generated according to the model

$$x(n) + 0.3x(n-1) + 0.25x(n-2) = w(n) + 0.95\, w(n\text{-}1) + 0.65w(n\text{-}2) \tag{37}$$

This is an ARMA (2,2) which has two poles and two zero. The poles are located at $0.5\, e^{\pm j107}$. The zeros are located at $0.81\, e^{\pm j126}$. The input time series data was drawn from a zero-mean non-Gaussian distribution. The exponential distribution was used. The next step was to the input time series through the system in (37). Then, the output of the system was corrupted with additive white Gaussian noise at signal to noise ratio of 20 dB on the output sequence. To estimate the ARMA coefficients, the composite higher order statistics (or cumulants) matrix R_{pq} in Equation (25) must be built. The matrix R_X consists of third order cumulants of the observed output time series data.

The matrix R_{WXX} consists of third order cross-cumulants of the unseen input time series and the observed output time series data. To estimate the input time series data, the method in Al-Smadi (2003) was used. Simulation with noise realizations based on different seed values was performed 100 times. The ARMA coefficients were estimated using the RTS and the proposed Cholesky decomposition-based (CHDB) algorithms at SNR of 20 dB on the output time series sequence. The average results of 100 Monte Carlo simulations for the RTS and the proposed CHDB algorithms at SNR of 20 dB on the output sequence are displayed in Table 1.

Table 1. True and estimated ARMA (2,2) model coefficients in Example 1

	True	CHDB Method	RTS Method
a(1)	0.3	0.2646	0.1865
a(2)	0.25	0.2511	0.2377
b(1)	0.95	0.9152	0.8517
b(2)	0.65	0.6288	0.5677

Conclusion

This paper presented a technique to estimate the coefficients of a general ARMA process. The proposed method uses the Cholesky decomposition of a special matrix with entries of higher order cumulants (HOC) of the available output data. The available output data may be contaminated by additive white Gaussian noise of unknown power spectral density. The simulation results prove the effectiveness of the proposed technique compared to the RTS, a well-known method in higher order spectral analysis.

Scientific Ethics Declaration

* The author declares that the scientific ethical and legal responsibility of this article published in EPSTEM journal belongs to the author.

Conflict of Interest

* The author declares no conflict of interest.

Funding

* This research is funded (fully/partially) by Zarqa University-Jordan

Acknowledgements or Notes

* This article was presented as an oral presentation at the International Conference on Basic Sciences, Engineering and Technology (www.icbaset.net) held in Trabzon/Türkiye on May 01-04, 2025.

References

Al-Smadi, A. (2003). Cumulant-based inverse filters for blind deconvolution. *International Journal of General Systems*, *32*(5), 503-515.

Al-Smadi, A., & Smadi, M. (2003). Study of the reliability of a binary symmetric channel under non-Gaussian disturbances. *International Journal of Communication Systems*,*16*(10), 865-973.

Al-Smadi, A., & Wilkes, D.M. (2002). Robust and accurate ARX and ARMA model order estimation of non-Gaussian processes. *IEEE Transactions on Signal Processing, 50*(3), 759-763.

Ansley, C. (1976). An algorithm for the exact likelihood of a mixed autoregressive-moving average process. *Biometrika*, *66*, 59-65.

Giannakis, G.B., & Mendel, J.M. (1989). Identification of nonminimum phase systems using higher order statistics. *IEEE Transactions on Acoustics, Speech, Signal Processing*, *37*(3), 360-377.

Higham, N.J. (2009). Cholesky factorization. *WIRE's Computational Statistics*, *1*(2), 251-254.

Lee, K., Baek, C., & Danial, M. (2017). ARMA Cholesky factor models for the covariance matrix of linear models. *Computational Statistics and Data Analysis*, *115*(11), 267-280.

Mendel, M. (1991). Tutorial on higher-order statistics (spectra) in signal processing and system theory: theoretical results and some applications. *Proceedings of the IEEE*, 79, 278-305.

Nikias, C.L., & Mendel, J.M. (1993). Signal processing with higher order spectra," *IEEE Signal Processing Magazine,* 10(3), 10-37.

Parzen, E., & Pagsano, M. (1979). An approach to modeling seasonally stationary time series. *Journal of Econometrics*, *9*(1), 137-153.

Swami, A, Mendel, J.M., & Nikias, C. (1998). *Higher order spectral an analysis Toolbox-user's guide*. Natrick, MA: The MathWorks, Inc.

Swami, A., & Mendel, J. (1990). ARMA parameters estimation using only output cumulants. *IEEE Transactions on Signal Processing*, *38*(7), 1257-1265.

Vinothkumar, G., & Manoj -Kumar, D. (2024). A novel adaptive ANC algorithm for removal of background noise in speech applications. *The International Arab Journal of Information Technology (IAJIT)*, *21*(4), 589 - 600.

Wang, K., Wu, Y., & Gao, Y., & Li, Y. (2017). New methods to estimate the observed noise variance for an ARMA model. *Measurement*, *99*, 164-170.

Author(s) Information

Adnan Al-Smadi
Zarqa University
Department of Computer Science
Zarqa-Jordan
Contact e-mail: a.alsmadi@zu.edu.jo
Yarmouk University
Department of Electronics Engineering
Irbid-Jordan

To cite this article:

Al-Smadi, A. (2025). A novel technique for estimation the coefficients of ARMA model using higher order moments. *The Eurasia Proceedings of Science, Technology, Engineering and Mathematics (EPSTEM), 34,* 1-7.

The Eurasia Proceedings of Science, Technology, Engineering & Mathematics (EPSTEM)
ISSN: 2602-3199

The Eurasia Proceedings of Science, Technology, Engineering and Mathematics (EPSTEM), 2025

Volume 34, Pages 8-14

ICBASET 2025: International Conference on Basic Sciences, Engineering and Technology

Features of a New Method for Solving Practical Problems of Continuum Mechanics Under Conditions of Complex Loading

Valery Chigirinsky
Rudny Industrial University

Sergey Kuzmin
Rudny Industrial University

Sergey Lezhnev
Rudny Industrial University

Abstract: This work, carried out within the framework of grant № AP23488953, funded by the Science Committee of the Ministry of Science and Higher Education of the Republic of Kazakhstan, considers an applied problem of continuum mechanics associated with solving a new closed problem of plasticity theory with respect to an asymmetric deformation focus during loading. The analytical solution of this problem is based on the method of argument of functions of a complex variable. The proposed approach is invariant to various areas of continuum mechanics, including not only the theory of plasticity, but also the theory of elasticity, the theory of dynamic processes. In particular, using the example of the rolling process, a closed planar problem of the theory of plasticity in an analytical form was posed and solved. The formulated system of equations includes: differential equations of equilibrium, the Huber-Mises plasticity condition, coupling equations, the equation of continuity of strain rates, the condition of constancy of volume, the equation of thermal conductivity, boundary conditions for stresses and strain rates. The solution uses approaches of limited nonlinearity, fundamental and trigonometric substitution. Under the conditions of new variables through the function argument, it was possible to simplify the intermediate result and determine not the solutions themselves, but the conditions of their existence under given boundary conditions. The solution of the asymmetric problem contributed to the identification of the effects of shape change in the processing center, which make it possible to control the processes of plastic deformation. The fundamental approach considered in this paper makes it possible to determine not only the stress-strain state of the plastic medium, but also the mathematical model of the deformed space and further possibilities for finding generalized solutions to problems of continuum mechanics.

Keywords: Continuum mechanics, Rolling, Closed problem, Asymmetric problem, Plasticity theory

Introduction

At the present stage of production development, technological processes are becoming more complicated, modern computer systems are being introduced, boundary and edge conditions are becoming more complicated, and their number is increasing, which indicates the increasing demands on technical and scientific developments of modern science. Theoretical solutions are overloaded with all kinds of assumptions and limitations, which reduces their effectiveness. There is an urgent need to generalize solutions to various processes and applied theoretical, practical and fundamental problems. One of the ways to increase the effectiveness of scientific approaches in continuum mechanics is to use invariant generalizing variables, which contribute not to obtaining the result itself, but to finding conditions for the existence of solutions. Then it becomes possible to find not just one analytical solution, but an indefinite set. At the same time, the question of how the solution is determined - by analytical, approximate or numerical methods - becomes unimportant. Such defining fundamental methods

of finding conditions for the existence of solutions include the method of function argument of a complex variable (Chigirinsky et al., 2021).

Method

This approach is based on a modern method of solving continuum mechanics problems, the method of function argument of a complex variable. The proposed method is invariant to various fields of mechanics, including not only the plasticity theory, but also the elasticity theory and the theory of dynamic processes. In particular, using the example of the rolling process, a closed problem of the theory of plasticity was posed and solved in an analytical form, in which this approach is demonstrated. The formulated system of equations of the theory of plasticity includes: differential equations of equilibrium, the Huber-Mises plasticity condition, the coupling equation, the equation of continuity of deformation rates, the condition of constancy of volume, the equation of thermal conductivity, boundary conditions. For the completeness of the presentation of this problem, the formulation and elements of solving the planar problem of the theory of plasticity in a closed form are considered:

$$\frac{\partial \sigma_x}{\partial x}+\frac{\partial \tau_{xy}}{\partial y}=0;\ \frac{\partial \tau_{yx}}{\partial x}+\frac{\partial \sigma_y}{\partial y}=0;$$
$$\left(\sigma_x-\sigma_y\right)^2+4\tau_{xy}^2=4k^2;$$
$$\frac{\sigma_x-\sigma_y}{2\cdot\tau_{xy}}=\frac{\xi_x-\xi_y}{\gamma'_{xy}}=F_1; \quad (1)$$
$$\xi_x+\xi_y=0;$$
$$\frac{\partial^2\xi_x}{\partial y^2}+\frac{\partial^2\xi_y}{\partial x^2}=\frac{\partial^2\dot{\gamma}_{xy}}{\partial y\partial x};$$
$$\frac{\partial^2 T}{\partial y^2}+\frac{\partial^2 T}{\partial x^2}=0,$$

where σ_x – normal stress; τ_{xy} – tangential stress; k – plastic shear resistance (variable); $\dot{\xi}_x$, $\dot{\gamma}_{xy}$ – linear and shear strain rate; T – temperature of the metal.

The boundary conditions are set in stresses and in terms of the strain rate:

$$\tau_n=-\left[\frac{\sigma_x-\sigma_y}{2}\cdot sin(2\varphi)-\tau_{xy}\,cos(2\varphi)\right],$$
$$\dot{\gamma}_n=-2\left[\frac{\xi_x-\xi_y}{2}\cdot sin(2\varphi)-\dot{\gamma}_{xy}\,cos(2\varphi)\right]. \quad (2)$$

where $\dot{\gamma}_n$ – the shear strain rate characterizing the boundary condition; τ_n – tangential stress characterizing the boundary condition.

Based on the system of equations (1) and (2), a simpler problem is solved to determine the stress state of the plastic medium. The statement has the form:
- differential equations of equilibrium:

$$\frac{\partial \sigma_x}{\partial x}+\frac{\partial \tau_{xy}}{\partial y}=0;\ \frac{\partial \tau_{yx}}{\partial x}+\frac{\partial \sigma_y}{\partial y}=0; \quad (3)$$

- Huber-Mises plasticity equation:

$$\left(\sigma_x - \sigma_y\right)^2 + 4\tau_{xy}^2 = 4k^2; \tag{4}$$

- differential equation of continuity of stress deformations:

$$\Delta^2 n\sigma_0 = \frac{\partial^2 n\sigma_0}{\partial x^2} + \frac{\partial^2 n\sigma_0}{\partial y^2} = 0, \tag{5}$$

- boundary conditions:

$$\tau_n = -\left[\frac{\sigma_x - \sigma_y}{2} \cdot sin(2\varphi) - \tau_{xy}\, cos(2\varphi)\right]. \tag{6}$$

Taking into account (3) and (4), a generalized differential equation of equilibrium for tangential stresses is defined in the form (Arkulis & Dorogobid, 1987):

$$\frac{\partial^2 \tau_{xy}}{\partial x^2} - \frac{\partial^2 \tau_{xy}}{\partial y^2} = \pm 2 \frac{\partial^2}{\partial x \partial y} T_i \cdot \sqrt{1 - \left(\frac{\tau_{xy}}{T_i}\right)^2}. \tag{7}$$

Ratio τ_{xy}/T_i using the trigonometric function, the boundary conditions and equation (7) are simplified.

Tangential stresses can then be represented as:

$$\tau_{xy} = H_\sigma \cdot exp\,\theta \cdot sin\, A\Phi, \tag{8}$$

where $T_i -$ intensity of tangential stresses; $A\Phi$ and $\theta -$ unknown function arguments to be defined.

If we use the function of a complex variable and reformat expression (8), after substitution in (7):

$$\begin{aligned}
&\frac{1}{2i} exp(\theta + i \cdot A\Phi) \cdot \left\{\left[(H_\sigma)_{xx} - (H_\sigma)_{yy} - 2i(H_\sigma)_{xy}\right] + 2(H_\sigma)_x \left[\left(\theta_x + A\Phi_y\right) - \right.\right. \\
&- i\left(\theta_y - A\Phi_x\right)\left.\right] - 2(H_\sigma)_y \left[i\left(\theta_x + A\Phi_y\right) - \left(\theta_y - A\Phi_x\right)\right] + H_\sigma \left[\left(\theta_{xx} - \theta_{yy} + 2A\Phi_{xy}\right) + \right. \\
&\left. + i\left(A\Phi_{xx} - A\Phi_{yy} - 2\theta_{xy}\right)\right] + H_\sigma \left[\left(\theta_x + A\Phi_y\right) - i\left(\theta_y - A\Phi_x\right)\right]^2 \Big\} - \\
&- \frac{1}{2i} exp(\theta - i \cdot A\Phi) \cdot \left\{\left[(H_\sigma)_{xx} - (H_\sigma)_{yy} + 2i(H_\sigma)_{xy}\right] + 2(H_\sigma)_x \left[\left(\theta_x + A\Phi_y\right) + \right.\right. \\
&+ i\left(\theta_y - A\Phi_x\right)\left.\right] - 2\left(H_\sigma\right)_y \left[\left(\theta_y - A\Phi_x\right) - i\left(\theta_x + A\Phi_y\right)\right] + H_\sigma \left[\left(\theta_{xx} - \theta_{yy} + 2A\Phi_{xy}\right) - \right. \\
&\left. - i\left(A\Phi_{xx} - A\Phi_{yy} - 2\theta_{xy}\right)\right] + H_\sigma \left[\left(\theta_x + A\Phi_y\right) + i\left(\theta_y - A\Phi_x\right)\right]^2 \Big\} = 0.
\end{aligned} \tag{9}$$

The differential equation (9) is a function of three variables $A\Phi$, θ and H, and it turns into an identity if the conditions are met:

$$\begin{aligned}
&\theta_x = -A\Phi_x,\ \theta_y = A\Phi_x. \\
&\theta_{xx} + \theta_{yy} = 0,\ A\Phi_{xx} + A\Phi_{yy} = 0.
\end{aligned} \tag{10}$$

Using the relations (10), the problem of identifying the argument of functions is eliminated. It should be added that the differential relations (10) are generalized invariant characteristics that make it possible to close equations (9). Thus, taking into account formulas (10), the solution of equation (9) is the expression:

$$\tau_{xy} = H_\sigma \cdot \exp\theta \cdot \sin \mathrm{A}\Phi. \tag{11}$$

Substituting solution (11) into the equilibrium equations (3), taking into account the complex variable, boundary conditions, and the equation of continuity of strain rates, we have expressions for normal stresses:

$$\begin{gathered}\sigma_x = -H_\sigma \cdot exp\theta \cdot cos A\Phi + C, \\ \sigma_y = -3H_\sigma \cdot exp\theta \cdot cos A\Phi + C, \\ \theta_x = -A\Phi_y, \theta_y = A\Phi_x, \quad \theta_{xx} + \theta_{yy} = 0, \quad A\Phi_{xx} + A\Phi_{yy} = 0.\end{gathered} \tag{12}$$

A special feature of the new method for solving continuum mechanics problems is the relations (10). They have a number of useful qualities, simplify the process of solving problems. They can be interpreted as fundamental variables of continuum mechanics. One of the notable properties of these ratios is the ability to switch from one variable to another. This is important when solving multicomponent problems, and the integration of differential equations is simplified.

The next feature is analytical solutions of different types of differential equations. For example, equation (7) is an equation of the hyperbolic type, and the equation of continuity of deformations (5) of the elliptical type is quite acceptable for solving equations of the parabolic type. This combination is explained by the use of fundamental variables in different tasks. In relation to these studies, variables close the solution of the problem, i.e. they limit the functions θ and $A\Phi$ thus, the differential equations of equilibrium, the generalized equation of equilibrium, and the continuity of deformation are identically satisfied. Such relations are known as the Cauchy-Riemann relations and the Laplace equations. Therefore, the function argument is represented as harmonic functions.

Results and Discussion

According to expressions (12), the stress states were calculated during a simple rolling process, with different technological parameters. Figures 1 and 2 show the distribution of contact normal and tangential stresses along the length of the deformation zone at different coefficients of friction and shape factor (Chigirinsky et al., 2024).

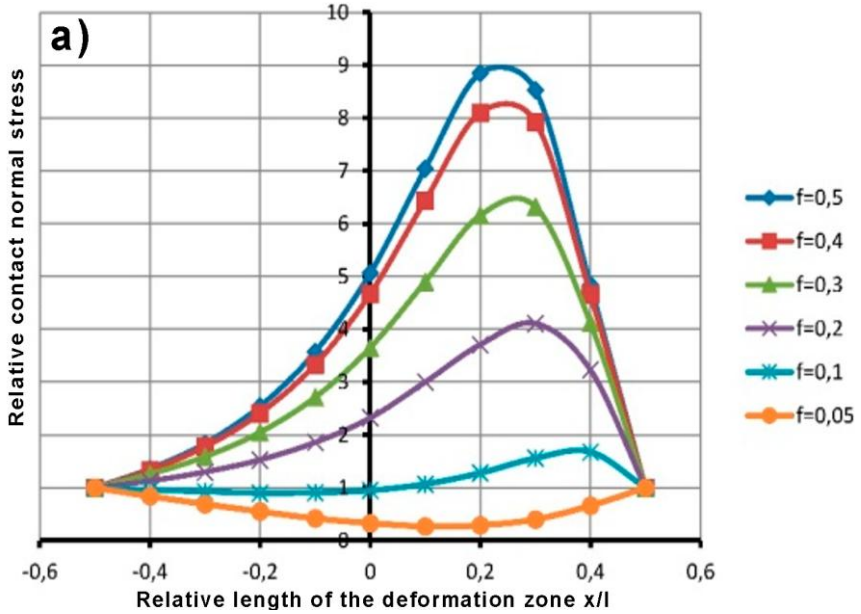

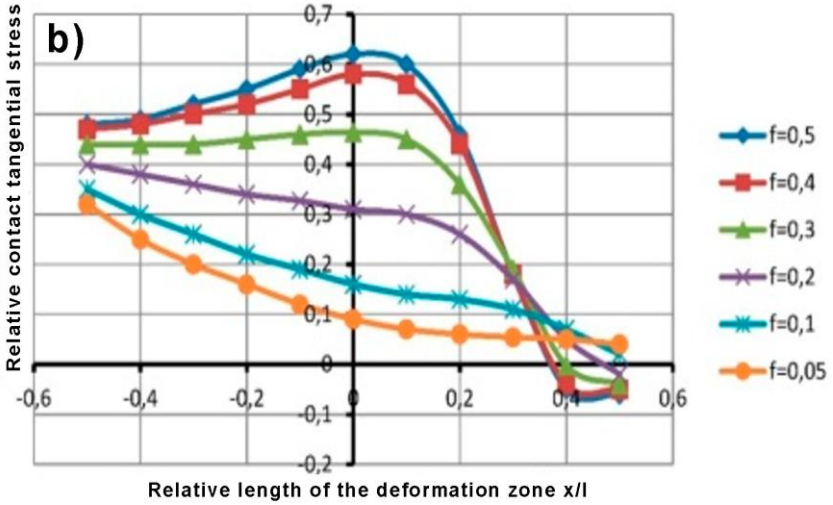

Figure 1. Distribution of contact stresses along the length of the deformation zone, depending on contact friction, at l/h=11.04, α=0.129, f=0.05-0.5: a – distribution of normal stresses; b – distribution of tangential stresses

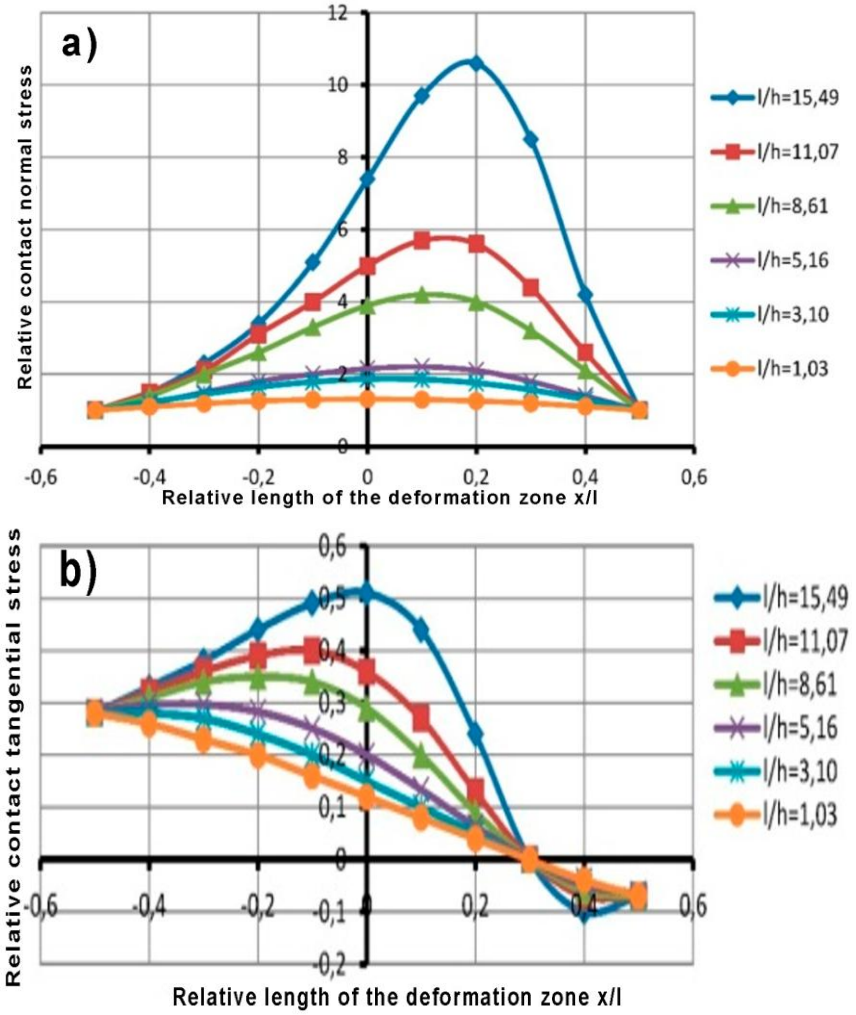

Figure 2. Distribution of contact stresses along the length of the deformation zone depending on the shape factor at l/h=1.03-15.49; α=0.077; f=0.3: a – distribution of normal stresses; b – distribution of tangential stresses

Figure 3 shows diagrams of contact stresses under different process conditions and different combinations of deformation and force loading, as well as the process of loss of stability.

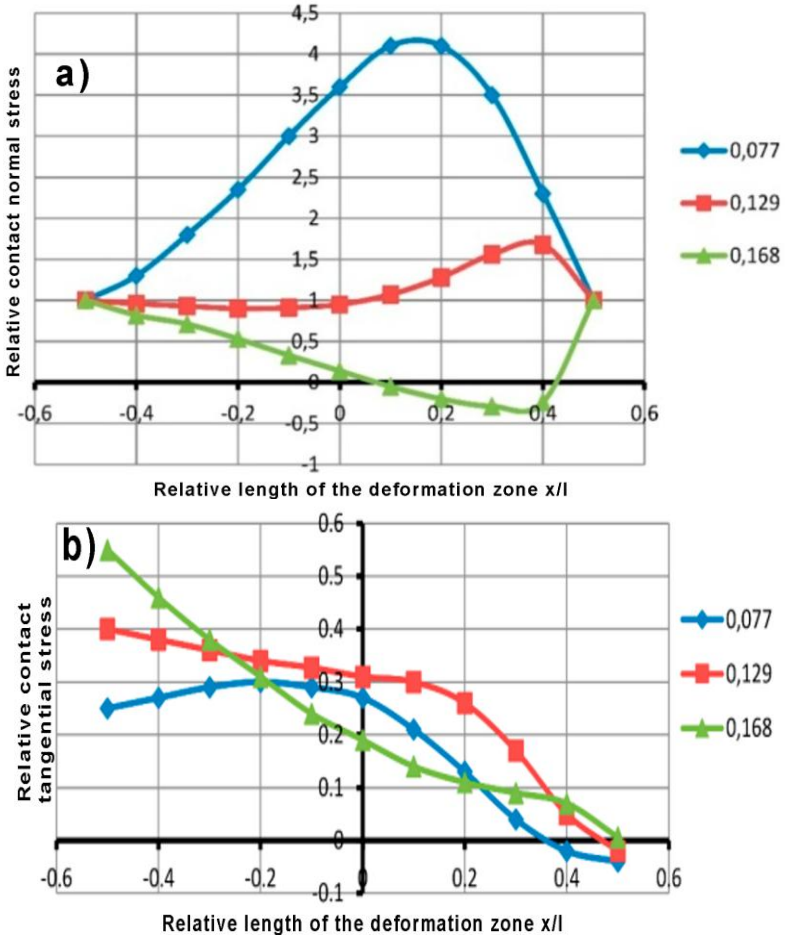

Figure 3. Distribution of contact stresses along the length of the deformation zone depending on the capture angle at: l/h=11.04; α=0.077;0.129;0.168; f=0.2: a – distribution of normal stresses; b – distribution of tangential stresses

Figure 3 shows an interesting process of loss of stability of the process with the designation of options for reducing power characteristics with an increase in deformation. The features of the function argument method make it possible to eliminate some incorrect limitations of problem solving using the analytical approach. It becomes possible to obtain results under complex and diverse boundary conditions due to the multiplicity of solutions. This is postulated by the fact that the function argument method does not show the solutions themselves, but the conditions of their existence.

Conclusion

The method of argument of functions of a complex variable was used as the basis for solving the applied problem of continuum mechanics related to solving the closed problem of plasticity theory in relation to an asymmetric deformation zone during complex loading. The formulated system of equations includes: differential equations of equilibrium, the Huber-Mises plasticity condition, coupling equations, the equation of continuity of strain rates, the condition of volume constancy, the equation of thermal conductivity, boundary conditions for stresses and strain rates. In addition, the approaches of limited nonlinearity, fundamental and trigonometric substitution were used to solve the problem. Under the conditions of new variables through the function argument, it was possible to simplify the intermediate result and determine not the solutions themselves, but the conditions of their existence under the given boundary conditions. The invariant variables in this solution are the Cauchy-Riemann relations and the Laplace differential equations. The solution of the closed problem of the theory of plasticity given in this paper, applied to an asymmetric deformation focus, showed the presence of the effect of plastic shaping. This solution makes it possible to successfully implement the necessary control of plastic deformation processes under difficult loading conditions. At the same time, the fundamental approach considered in this paper makes it possible to determine not only the stress-strain state of the plastic

medium, but also the mathematical model of the deformed space and further possibilities for finding generalized solutions to problems of continuum mechanics.

Scientific Ethics Declaration

* The authors declare that the scientific ethical and legal responsibility of this article published in EPSTEM Journal belongs to the authors.

Conflict of Interest

* The authors declare that they have no conflicts of interest

Funding

* This work was funded by the Science Committee of the Ministry of Science and Higher Education of the Republic of Kazakhstan. (Grant № AP23488953).

Acknowledgements or Notes

* This article was presented as a poster presentation at the International Conference on Basic Sciences, Engineering and Technology (www.icbaset.net) held in Trabzon/Türkiye on May 01-04, 2025.

References

Arkulis, G. E., & Dorogobid, V. G. (1987). *Plasticity theory*. Moscow: Metallurgiya.

Chigirinsky, V., Naizabekov, A., & Lezhnev, S. (2021). Closed problem of plasticity theory. *Journal of Chemical Technology and Metallurgy*, *56*(4), 867-876.

Chigirinsky, V., Naizabekov, A., Lezhnev, S., Naumenko, O., & Kuzmin S. (2024). Determining the patterns of asymmetric Interaction of plastic medium with counterdirectional metal flow. *Eastern-European Journal of Technologies. Applied mechanics*, *127*(7), 66-82.

Author(s) Information

Valery Chigirinsky
Rudny Industrial University
38, 50 let Oktyabrya str., Rudny, Kazakhstan

Sergey Kuzmin
Rudny Industrial University
38, 50 let Oktyabrya str., Rudny, Kazakhstan

Sergey Lezhnev
Rudny Industrial University
38, 50 let Oktyabrya str., Rudny, Kazakhstan
Contact e-mail: *sergey_legnev@mail.ru*

To cite this article:

Chigirinsky, V., Kuzmin, S., & Lezhnev, S. (2025). Features of a new method for solving practical problems of continuum mechanics under conditions of complex loading. *The Eurasia Proceedings of Science, Technology, Engineering and Mathematics (EPSTEM), 34,* 8-14.

The Eurasia Proceedings of Science, Technology, Engineering & Mathematics (EPSTEM)
ISSN: 2602-3199

The Eurasia Proceedings of Science, Technology, Engineering and Mathematics (EPSTEM), 2025

Volume 34, Pages 15-22

ICBASET 2025: International Conference on Basic Sciences, Engineering and Technology

Transmission Line Fault Isolation Using Artificial Intelligence via Neural Networks

Othman Alsmadi
The University of Jordan

Mohammad Alshawabkeh
Electrical Department Axiom for Metal Works

Aram Bani-Ata
The University of Jordan

Abstract: Transmitting a bulk amount of power from one place into another is normally performed using transmission lines. The increase of these transmission lines in different areas with different conditions usually leads to developing faults in these lines. Hence, it becomes of high interest in locating the line faults to maintain system stability and resume normal power flow operation. Knowing the current and voltage data is mainly the key point in locating the network faults. In this paper, a transmission line fault isolation technique using Artificial Intelligence (AI) via Artificial Neural Networks (ANNs) is presented. The current and voltage values of faults in different areas of transmission lines are studied and identified. The identification of the fault location is performed utilizing the ANN backpropagation algorithm. Based on the data provided by the ANN, a designated circuit breaker is used to isolate the fault and avoid system instability. The proposed technique is investigated by performing a comparison with recently related published work while clearly seeing the advantages of the new approach.

Keywords: Power transmission line, Fault detection and isolation, Bus systems, Artificial intelligence

Introduction

One of the most important procedures and operations that must be carried out to protect an electrical network equipment and affect its stability safety is the prompt and accurate detection of faults and isolating them from the network (Barik, et al., 2018). In a network, there are multiple types of faults that may occur in transmission lines. Faults may be characterized as a Short Circuit Fault: (AG (phase A to Ground), BG (phase B to Ground), CG, ABG, BCG, CAG, AB, BC, CA, ABC, and ABCG) or an Open Circuit Fault (Silva et al., 2006). One of the most commonly used methods is using a relay that reads the current value on the transmission line and then gives a command to the circuit breaker to trip if the current exceeds a predetermined threshold value (Piesciorovsky & Schulz, 2017; Costa, Monti, & Paiva, 2017). Accordingly, the most important relay used in the protection of transmission lines is the distance relay.

The relay is designed to trip the circuit breaker in the event of a fault which is divided into multiple zones, each with its specific impedance. Its operation principle relies on measuring the impedance of the transmission line, which is read when a fault occurs (Lotfifard et al., 2010). A non-unit protection distance relay (a global short-circuit protection scheme) is also used for long transmission systems. In this relay, supplementary currents and relay terminals receive current values from the current transformers (CTs) and voltage values from the voltage transformers (VTs).

- Selection and peer-review under responsibility of the Organizing Committee of the Conference

This aids in monitoring the apparent impedance, which serves as a practical indicator of the physical boundary settings for the several stepped zones, including the first, second, and third zones (Venkatanagaraju et al., 2021). The work in this paper is divided into different sections. Section II illustrates some of the previous studies for fault identification using neural networks, as will be the focus of this paper. Then, Section III explains the proposed methodology while outlining the process of building the neural network, training it, and testing its performance using MATLAB simulations. Section IV presents results and analysis of the proposed method performance as compared with some of the other related techniques. As a final section, Section V presents the conclusion of this paper.

Literature Overview

Power system protection has been recently considered as an imprtatnt research subject area (Ali et al., 2024). Different AI methods have been used in system modeling and optimizaton (Alsmadi et al., 2024). Many research studies have used neural networks to identify and classify faults in transmission lines. A group of researchers, in 2015, used a neural network in two stages.

In the first stage, the ANN was used to determine the presence or absence of a fault, with a single output representing "1" for fault presence and "0" for no fault. In the second stage, the neural network was used to identify the type of fault. The outputs represent each phase that experience some faults. For example, if a fault occurred in phase A to ground, then the output would be represented as 1001 (Leh, at al., 2020).

Recently, Kumari et al. used a neural network technique to identify faults in a transmission line that was 100 km long with a specific load at its end (Kumari, et al., 2023). There was one output for the neural network, which means there would be 1 output in the presence of a fault and 0 output in the absence of a fault. In 2021, Bishal et al. used neural networks to study faults in a transmission line, in which their neural network was used to trip a circuit breaker in the event of a fault. The system used in this study consisted of 1 circuit breaker, 1 load, and 1 transmission line (Bishal, et al., 2021). Khoa et al. (2022) also recently presented a paper with performance comparison of impedance-based fault location methods for transmission lines (Khoa, et al., 2022).

As a matter of fact, many researchers presented different methodologies in developing improved power system protection techniques for transmission lines fault elimination. As so, Mukherjee et al. recently published an exhaustive review presenting several methodologies while mentioning the highlights and shortcoming of each method (Mukherjee et al., 2021). However, in spite of the many algorithms developed, no method can provide acceptable results for all kinds of networks, as proved by the many different methods presented early. In this paper, we will present a different ANN technique for transmission line fault isolation and elimination with some advantages over the existed methodologies investigated in this paper.

Methodology

Artificial Neural Networks technology is a modern technique that excels in dealing with linear and mainly nonlinear problems and effectively handles massive amounts of information. In power systems, ANNs can be extensively and efficiently used in fault detection due to the infinite number of transmission lines and their various types, which results in a vast amount of information within the system. ANNs are characterized by their speed, high responsiveness, and high reliability based on their training (Jamil, Sharma, & Singh, 2015). The work in this paper is proposed as laid in Figure 1. In this section, we will present the main methodology parts as to where and how the ANN has been employed.

Back Propagation (BP)

The Back Propagation Neural Network (BPNN) is a technique that calculates weight adjustments by propagating errors from the output layer back to the input layer. Unlike two-layer artificial neural networks, the BPNN overcomes the limitation of producing similar outputs for similar inputs. The algorithm iteratively selects random weights, feeds input pairs, computes the output, updates the weights, and repeats this process for the entire training dataset until the network converges within a predefined error tolerance (Saeed, et al., 2020).

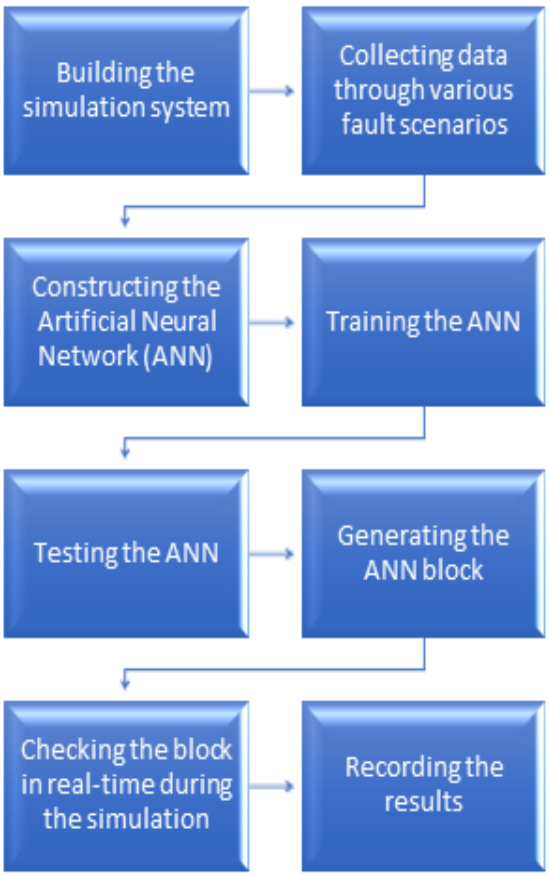

Figure 1. Proposed methodology

The widely-known iterative BP algorithm, used in this research, can handle various error functions. In each iteration, the proposed algorithm utilizes the Mean Square Error (MSE) following a reverse process through each layer in the network (Saeed et al., 2020). The total number of iterations required for the algorithm converging and the time taken for training to reach a predefined error level depend on some factors such as; structure and size of neural network, complexity of the problem being addressed, learning method, and size of the input and output datasets. These factors collectively influence the convergence and training time of the algorithm.

The effectiveness and optimal performance of a trained artificial neural network and the most suitable learning method can be evaluated by testing the final network using a designated testing dataset. This testing dataset, which is typically provided by the developer, forms an integral part of the network development process.

System Modelling of Transmission Lines

A 3-phase system consisting of transmission lines, with different lengths and various loads at the end of each line, was constructed using MATLAB software. Figure 2 illustrates the system configuration used in this research. The system includes a generator with a capacity of 20 MVA and a voltage of 3.3 KV. Table 1 provides the details of the system transmission lines (TL) and corresponding loads. The transmission line system was constructed using the MATLAB software, and the values for the transmission lines were adapted. Considered faults were assumed at different locations along the transmission lines, with 10 different locations for each transmission line. The current and voltage values were recorded only at the generator side.

Table 2 represents a sample of the current and voltage values recorded during phase-to-ground faults on different transmission lines. The voltage and current values were utilized by the RMS block in MATLAB as a training data set for the neural network. The circuit breaker that should trip, in case of a fault, is the output of the neural network. For example, if a fault occurs on line 1, this line should be isolated from the network at the feeding side. This means that the circuit breaker CB1 should be opened.

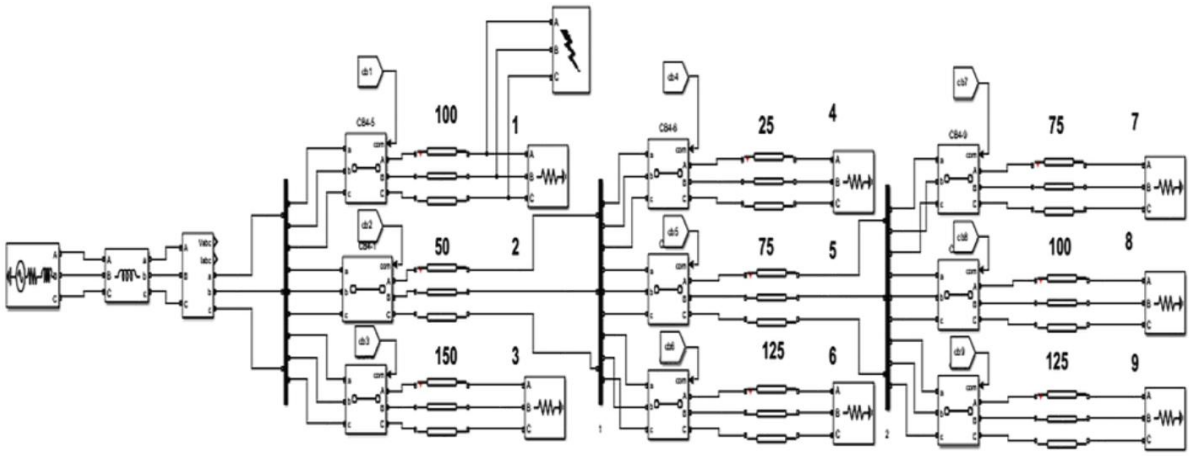

Figure 2. System configuration with a generator of a capacity of 20 MVA and a voltage of 3.3 KV.

Table 1. Considered transmission line with its corressponding loads

Transmission Line	Distance [km]	load	Power [kw]
1	100	1	50
2	50	2	----
3	150	3	50
4	25	4	100
5	75	5	----
6	125	6	100
7	75	7	500
8	100	8	500
9	125	9	500

Table 2. Current and voltage samples during phase-to-ground faults

TL	V_{AG}	V_{BG}	V_{CG}	I_A	I_B	I_C
1	0.6	0.6	0.6	37	37	37
2	0.5	0.5	0.5	71	71	71
3	0.65	0.65	0.65	23	23	23
4	0.5	0.5	0.5	50	50	50
5	0.6	0.6	0.6	33	33	33
6	0.64	0.64	0.64	21	21	21
7	0.65	0.65	0.65	19	19	19
8	0.67	0.67	0.67	13	13	13
9	0.68	0.68	0.68	10	10	10

Training and Testing

In this part, and after having prepared the necessary data for training the neural network off-line, we obtained 12800 samples that were fed into the network. In this set of data, each sample contained 6 inputs representing voltage and current values, and 9 outputs representing the circuit breaker numbers that should open in case of a fault. Figure 3 shows the neural network used in the training operation where 2 hidden layers have been employed. Training with the considered data, a mean square error of 0.003098 was achieved as shown in Figure 4.

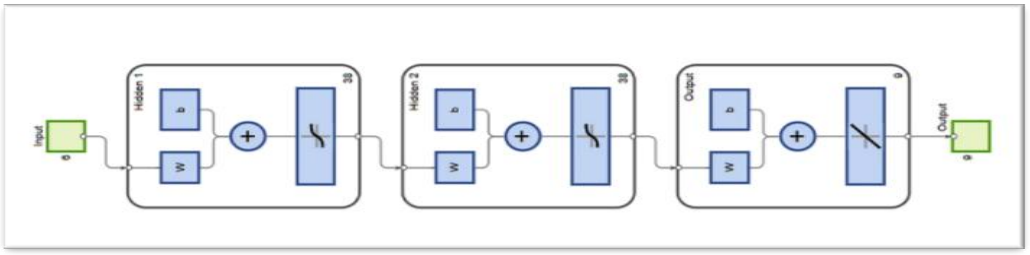

Figure 3. Training process of the ANN with two hidden layes

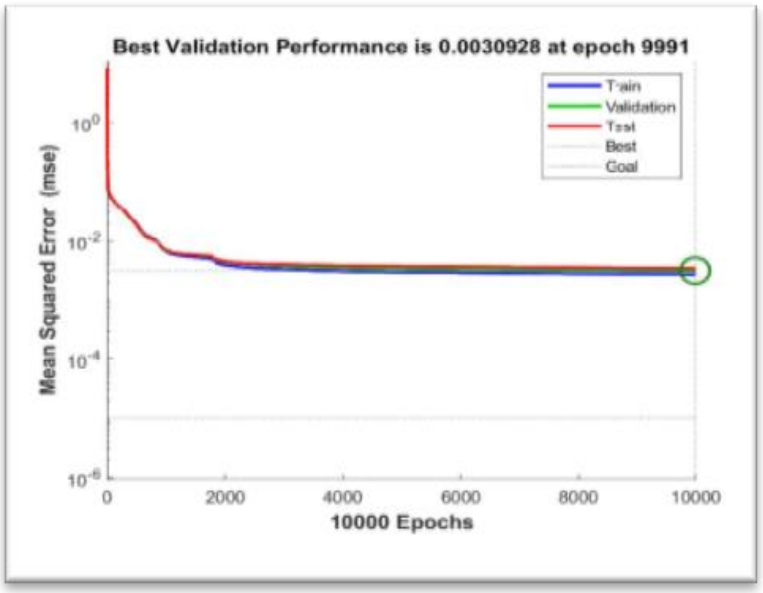

Figure 4. Mean square error convrgence.

Results and Discussion

Now that the training process was completed, a real-time application within the simulation was performed for this network. This was done by using a certain command to create a new block that contains inputs for current and voltage values, and an output for the circuit breaker number that should open during a fault. In this block, the incoming current and voltage values were processed according to the training that had been conducted previously.

A signal was taken from the block output to each circuit breaker, and the trip command was to be issued to the circuit breaker in case of a fault occurrence. Accordingly, Figure 5 represents the current curves at the generator side in the absence of the ANN assistance for all three phases, A, B, and C. As observed, a significant increase in the current values during a fault on Line 1. Figure 6 on the other hand, shows the current curves when the ANN is used and the circuit breaker is activated.

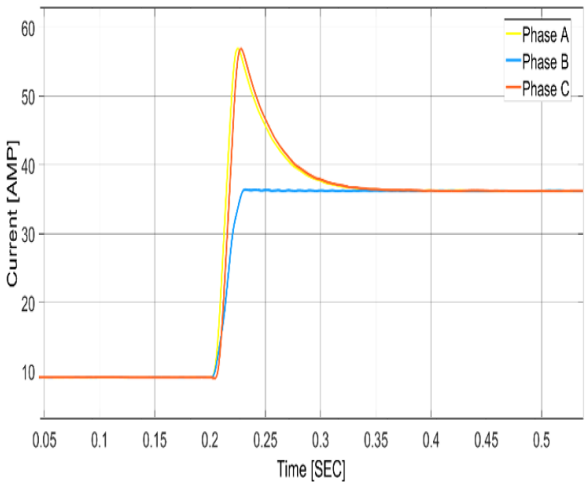

Figure 5. Generator 3-phase currents without using ANN for Line 1.

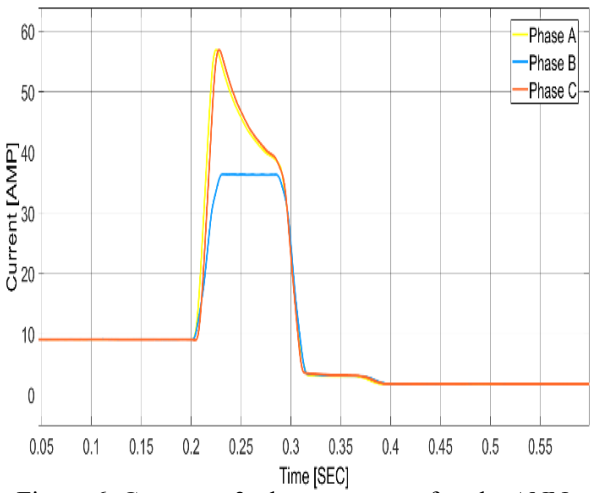

Figure 6. Generator 3-phase currents after the ANN implementation for Line 1.

Figures 7 and 8 represent respectively the current values in the absence and presence of the neural network during another fault on Line 8. Using a delay of 0.1 second, we can observe the isolation of the faulted area and the network returning to its normal state

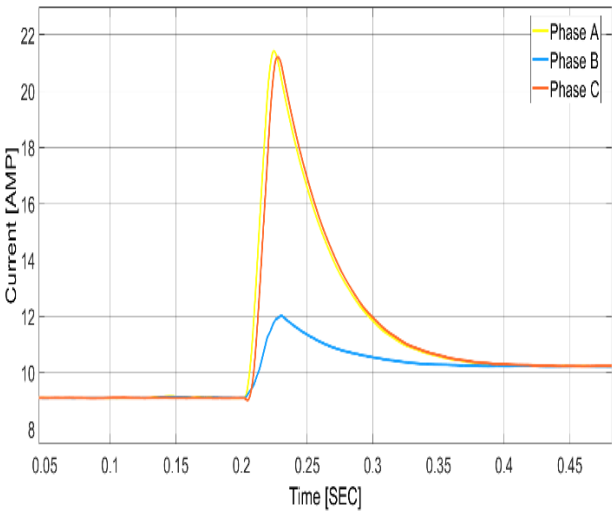

Figure 7. Generator 3-phase currents without using ANN for Line 8.

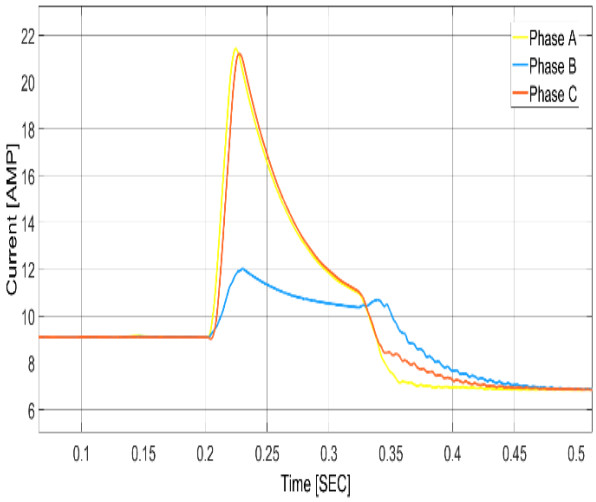

Figure 8. Generator 3-phase currents after the ANN implementation for Line 8.

To investigate the potentiality of the proposed method, a comparison of performance with different approaches published recently was made as shown in Table 3.

Table 3. Proposed approach performance comparison with different approaches

Proposed method	**No of inputs**	**Description**	**No of outputs**	**Descripton**	**Utilization of output ports**	**Number of devices used in the Network**
	6	3- phase voltage 3- phase current	9	Fault location	Signal for tripping the circuit breaker responsible for isolating the line based on the fault location.	7 loads 1 generator 9 transmission line 9 CB
[8]	6	3- phase voltage 3- phase current	1	Fault detection	-----	1 load 1 transmission line 1 generator 1 transformer
[9]	6	3- phase voltage 3- phase current	1	Fault detection	Signal to the circuit breaker present in the system.	2 loads 1 transmission line 1 generator 1 transformer 1 CB
[7]	6	3- phase voltage 3- phase current	1 4 classification #	Fault detection and classification	------	2 generators 1 transmission line

Conclusion

In this research, a transmission line fault isolation was investigated utilizing ANN. The methodology was based on the current and voltage values from a single line location in the network, which could potentially reduce the need for the use of current and voltage transformers for protection purposes in the future, which in this case, the issue becomes a centralized fault control. The current and voltage values' locations were read and fed into the ANN, which used the back-propagation algorithm. The data was analyzed and accordingly a command was The data the circuit breaker to open and isolate the fault from the network. Even though the three-phase system fault was the focus in this research, however, the same method can be applied to other types of faults as well. In comparison, it was found that the proposed method provides relatively superior results with larger databases.

Scientific Ethics Declaration

* The authors declare that the scientific ethical and legal responsibility of this article published in EPSTEM journal belongs to the authors.

Conflict of Interest

* The authors declare that they have no conflicts of interest

Funding

* This research received no specific grant from any funding agency in the public, commercial, or not-for-profit sectors.

Acknowledgements or Notes

* This article was presented as an oral presentation at the International Conference on Basic Sciences, Engineering and Technology (www.icbaset.net) held in Trabzon/Türkiye on May 01-04, 2025.

* The corresponding author would like to thank the Deanship of scinetific research, The University of Jordan, for supprting this research.

References

Ali, MN., Alsmadi, OM., & Baniyounes, A. M. (2024). Improving the protection system in the distribution networks integrated with photovoltaic cells by changing the ratio of X/R. *International Journal of Power Electronics and Drive Systems, 15*(2), 835-844.

Alsmadi, OM., Abu-Hammour, Z., Mahafzah, K. (2024). Digital systems model order reduction with substructure preservation and fuzzy logic control. *The Eurasia Proceedings of Science, Technology, Engineering & Mathematics, 28,* 14-22.

Barik, Md., Gargoom, A.,… & Mahmud, Md. (2018). A decentralized fault detection technique for detecting single phase to ground faults in power distribution systems with resonant grounding. *IEEE Transactions on Power Delivery, 33*(5), 2462-2473.

Bishal, M. R., Ahmed, S., Molla, N. M., Mamun, K. M., Rahman, A., & Al Hysam, M. A. (2021). ANN based fault detection & classification in power system transmission line. *International Conference on Science & Contemporary Technologies (ICSCT)* (pp. 1-4). IEEE.

Costa, F., Monti, A. and Paiva, S. (2017). Overcurrent protection in distribution systems with distributed generation based on the real-time boundary wavelet transform. *IEEE Trans. Power Del, 32*(1), 462–473.

Jamil, M., Sharma, S., & Singh, R. (2015). Fault detection and classification in electrical power transmission system using artificial neural network. *SpringerPlus, 4*(334), 1-13.

Khoa, N., Cuong, M. M. V., Cuong, H. Q., and Hieu, N. T.T. (2022). performance comparison of ımpedance-based fault location methods for transmission line. *International Journal of Electrical and Electronic Engineering & Telecommunications, 11*(3), 234–241.

Kumari, S., Mishra, A., Singhal, A., Dahiya, V., Gupta, M., & Gawre, S. K. (2023). Fault detection in transmission line using ann. *IEEE International Students' Conference on Electrical, Electronics and Computer Science (SCEECS)* (pp. 1-5). IEEE.

Leh, N. A. M., Zain, F. M., Muhammad, Z., Abd Hamid, S., & Rosli, A. D. (2020, August). Fault detection method using ANN for power transmission line. *International Conference on Control System, Computing and Engineering (ICCSCE)* (pp. 79-84). IEEE.

Lotfifard, S., Faiz, J., & Kezunovic, M. (2010). Detection of Symmetrical Faults by Distance Relays During Power Swings. *IEEE Transactions on Power Delivery, 5*(1), 81-87.

Mukherjee, A., Kundu, P., & Das, A. (2021). M transmission line faults in power system and the different algorithms for ıdentification, classification and localization: A brief review of method. *Journal of The Institution of Engineers, 102*, 855–877.

Piesciorovsky, E., & Schulz, N. (2017). Fuse relay adaptive overcurrent protection scheme for microgrid with distributed generators. *IET Generation Transmission Distribution, 11*(2), 540–549.

Silva, K., Souza, B., & Brito, N. (2006). Fault detection and classification in transmission lines based on wavelet transform and ANN. *IEEE Transactions on Power Delivery, 21*(4), 2058-2063.

Saeed, U., Jan, S. U., Lee, Y. D., & Koo, I. (2020). Machine learning-based real-time sensor drift fault detection using Raspberry PI. *International Conference on Electronics, Information, and Communication (ICEIC)* (pp. 1-7). IEEE.

Venkatanagaraju, K., Biswal, M., & Murty, K. (2021). Operations of distance relay third zone protection during power system critical conditions: A case study on Indian Eastern regional grid. *Springer*, *102*, 595–603.

Author(s) Information

Othman Alsmadi
The University of Jordan
Amman-Jordan
Contact e-mail: 10474*@ammanu.edu.jo*

Mohammad Alshawabkeh
Electrical Department Axiom for Metal Works
Amman-Jordan

Aram Bani-Ata
The University of Jordan
Amman-Jordan

To cite this article:

Alsmadi, O., Alshawabkeh, M., & Bani-Ata, A. (2025). Transmission line fault isolation using artificial intelligence via neural networks. *The Eurasia Proceedings of Science, Technology, Engineering and Mathematics (EPSTEM), 34,* 15-22.

The Eurasia Proceedings of Science, Technology, Engineering & Mathematics (EPSTEM)
ISSN: 2602-3199

The Eurasia Proceedings of Science, Technology, Engineering and Mathematics (EPSTEM), 2025

Volume 34, Pages 23-30

ICBASET 2025: International Conference on Basic Sciences, Engineering and Technology

New Copper(II) and Nickel(II) Complexes with Dimethylglyoxime and Amino-acids: Synthesis, Characterization and Electrochemical Properties

Hadda Bougherra
Mouloud Mammeri University of Tizi-Ouzou

Omar Berradj
Mouloud Mammeri University of Tizi-Ouzou

Abstract: Four new Cu(II) and Ni(II) ion complexes were created from the interaction of dimethylglyoxime as primary ligand and methionine or alanine as a secondary ligand, has been investigated using molar conductivity, infrared, UV/vis. The electrochemical behavior of these complexes was determined by cyclic voltammetry.The compounds prepared are solids, insoluble in water, ethanol and methanol, but soluble in dimethylsulfoxide (DMSO) and dimethylformamide (DMF). The molar conductance data confirm that two complexes are not electrolytic. The IR study shows that dimethylglyoxime ligand is coordinated to the metal ion in a bidentate manner with NN donor sites of the oxime function, where the secondary ligand is coordinated by the carboxylate oxygen and the N atom of the amino acid. The electronic spectral data indicated that the synthesized complexes have octahedral or square-planar geometries. An electrochemical application was carried out on these mixed complexes in order to study their redox properties, which indicated an irreversible oxidation corresponding of M to M(I) and of M(I) to M(II).

Keywords: Complexes, Dimethylglyoxime, Amino acids, Spectroscopic analysis, Electrochemical application

Introduction

The chemistry for oxime metal complexes has been investigated actively since the first synthesis of nickel (II) dimethylglyoximate and recognition of the chelate. Copper (II) complexes with dimethylglyoxime are known for their high stability, but their biological activity has been very scarcely studied (Bougherra et al, 2018). Amino acids are classified as promising biomolecules that can be complexed with metals to form stable and active catalysts. Therefore, Amino acid-metal complexes and their derivatives have attracted many researchers in the fields of pharmaceuticals and petrochemical industries (Alrufaydi et al., 2020).

Copper (II) and nickel (II) complexes with amino acids are of significant pharmacological interest because several of them exhibit a broad spectrum of effects, in particular anti-inflammatory, antiulcer, anticonvulsant and even anti-tumor. It has also been established that these complexes often exhibit higher pharmacological activity than that of their free ligands (Adkhis et al., 2022; Wagner et al.,2008; Baran et al. ,2009). In this work, we describe the synthesis, spectral characterization and electrochemical application of the new Ni(II) and Cu(II) complexes of dimethylglyoxime as the primary ligand and alanine or methionine as secondary one.

Experimental

Materials and Methods

All the chemical reagents and solvents used in the synthesis of the complexes were (Fluka products) used without further purification. Melting points were determined on a Stuart scientific SPM3 apparatus fitted with a microscope and are uncorrected. The infrared spectra were recorded in the region 4000–400 cm^{-1} on a BRUKER TENSOR 27 IR spectrophotometer. Electronic spectra were measured on a thermo Scientific EVOLUTION 220 ultraviolet-visible spectrophotometers (in DMSO solution); measurements were made from 200 to 800 nm. The molar Conductance values were obtained for 10^{-3} M in DMSO solution at 25 °C determined using melting point meter MPM-H2. All electrochemical experiments were carried out using a potentiostat-galvanostat EGG-273 A controlled with Power-suite software. The electrochemical cell was equipped with a modified carbon past disk as the working electrode, a platinum electrode as counter electrode and silver/silver chloride (Ag/AgCl) electrode as the reference electrode. The electrolytic bath consisted of the complexes in DMSO solution (10^{-3} M) and sodium perchlorate ($NaClO_4$ 10^{-1} M) was used as a supporting electrolyte to increase the conductivity of the bath. The electrochemical characterization was performed using the cyclic voltammetry (CV) with a scan rate of 50 mV/s.

Synthesis of Complexes

To an aqueous solution of metal salt (5 mmol) and KI or KSCN (10 mmol) was added dropwise an ethanolic solution of amino acid (5mmol). After stirring and refluxing a hot ethanolic solution of dimethylglyoxime (5 mmol) was added. Then a few drops of NaOH solution were added to keep the pH at 8. The resulting mixture is left stirring under reflux at 70 ° C for 3 hours. The precipitate obtained was isolated by filtration and washed with ethanol and diethylether. The solid was dried at room temperature.

Results and Discussion

The physical properties of the prepared complexes are summarized in Table 1**.** All the complexes are soluble in DMSO and DMF but insoluble in water, methanol and ethanol. The electrolyte or non-electrolyte nature of the complexes was confirmed by low or high values of molar conductance measured at 25°C (10^{-3} M) in a DMSO solution.

Table 1. Physical properties of the complexes

Compound formula	Yield (%)	Melting point(°C)	Color	$\Lambda(\Omega^{1}Cm^{2}mol\,mol^{-1})$	Metal (%) Cal	Found
$[Cu(H_2dmg)(Meth)(SCN)_2]$ **1**	65	260	Blue	15.2	14.35	13.98
$[Ni\ (H_2dmg)(Meth)](SCN)_2$ **2**	87	302	Red	170	13.4	13.58
$[Cu(H_2dmg)(Ala)]I_2$**3**	56	310	Gray	64.5	12.2	12
$[Ni\ (H_2dmg)(Ala)I_2]$**4**	47	312	pinck	11.2	11.38	11.2

Infrared Spectra

The assignments of the more significant IR absorption bands of the free ligands and their metal complexes are shown in Table 2 and Table 3, respectively, and the FT-IR spectrum of $[Cu(H_2dmg)(Meth)(SCN_2)]$ and $[Ni(H_2dmg)(Ala)(I_2)]$ are shown in figure 1 and figure 2, respectively. The IR spectrum of dimethylgloxime shows a band with medium intensity at 1447 cm^{-1}, which is attributed to (C=N) of the oxime. This band is shifted to higher frequency (1450-1503 cm^{-1}) in all the mixed-ligand complexes (Jadhav et al, 2013; Salih, et al, 2009; Chandar et al, 2011).

The strong absorption at 1143 cm^{-1} due to υ(N-O) of the oxime group in the free H_2dmg is shifted towards higher frequency in all the complexes (Osunlaja et al, 2009; Berradj et al, 2021). While the appearance of a band in all the complexes in the region 752- 772 cm^{-1} is due to the C=N-O deformation vibration of the oxime group, this band is shifted in free ligand at 750 cm^{-1}(Abane et al, 2019). All these features indicate that the H_2dmg is coordinated to the metal ion through the nitrogen of the oxime.

The $\upsilon(NH_3^+)$ of methionine and alanine is observed in 3146 and 3072 cm^{-1} respectively. In the complexes, NH_3^+ gets deprotonated and binds to metal through the neutral NH_2 group. The IR spectra of complexes show characteristic bands of $\upsilon(NH_2)$ in the region 3100- 3309 cm^{-1} (Mamun, et al, 2010; Wagner et al, 2004). Whereas the deformation frequency $\delta(NH_3^+)$, which is characteristic for the zwitterions, appear

at about 1615 cm^{-1} in amino acids, in the metal complexes with methionine, $\delta(NH_2)$ is shifted to higher wave numbers, while that of alanine is displaced to the lower wave numbers (Rosu et al., 2005). Hence, it can be concluded that the nitrogen of the amino group is involved in coordination.

The spectra of amino acids display $\upsilon_{as}(coo^-)$ and $\upsilon_s(coo^-)$ frequency in the 1583cm^{-1} and 1409 cm^{-1} range, respectively. In the metal complexes, $\upsilon_{as}(coo^-)$ and $\upsilon_s(coo^-)$ stretching bands are located in the region 1520-1616 cm^{-1} and 1373-1429 cm^{-1}, respectively (Tidjani-Rahmouni et al., 2014; Adkhis et al., 2000). The infrared spectra of the prepared complexes show weak bands in the range of 519-572 cm^{-1} and 426-441 cm^{-1}. They are attributed to the u(M-O) and u(M-N) vibration, respectively (Bougherra et al., 2018).

Table 2. Characteristic IR absorption bands (cm^{-1}) of the ligands

Compound	$\nu(NH_3^+)$	$\delta(NH_3^+)$	$\nu_{as}(COO^-)$	$\nu_s(COO^-)$	ν(CN)	ν(NO)	δ(NO)
Dimethylgloxime					1447	1143	750
Methionine	3146	1615	1583	14109			
Alanine	3072	1618	1583	1409			

Table 3. Characteristic IR absorption bands (cm^{-1}) of the complexes

Complex	$\nu(NH_2)$coord	$\delta(NH_2)$	$\nu_{as}(COO^-)$	$\nu_s(COO^-)$	ν(CN)	ν(NO)	δ(NO)	ν(M-O)	ν(M-N)
Complex 1	3117-3300	1661	1616	1404	1454	1205	772	572	441
Complex 2	3100-3200	1627	1558	1400	1503	1238	760	544	428
Complex 3	3309	1581	1520	1373	1450	1200	752	548	426
Complex 4	3165-3306	1603	1568	1429	1483	1238	752	519	430

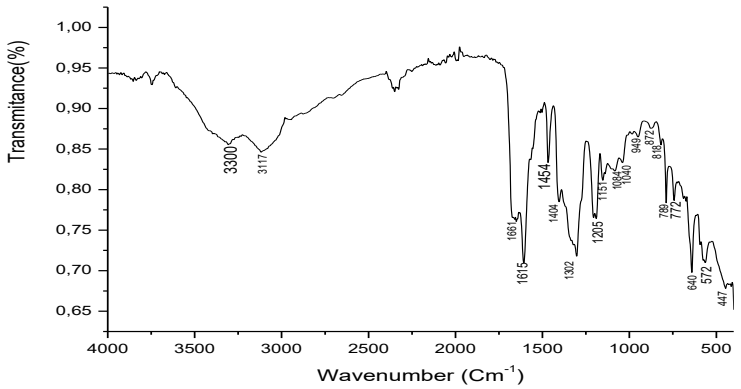

Figure 1. Infrared spectrum of [Cu(H_2dmg)(Meth)(SCN_2)]

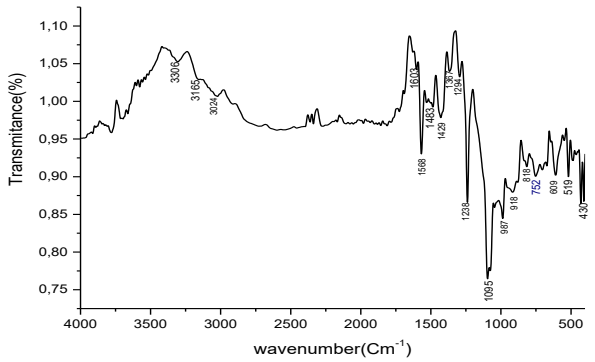

Figure 2. Infrared spectrum of [Ni(H_2dmg)(Ala)(I_2)]

Electronic Spectra

The electronic spectral data of the ligands and complexes are presented in Table 4 and Table 5 respectively, and the electronic absorption spectrum of [Ni(H_2dmg)(Meth)]($SCN)_2$ is given in Figure 3.

In the UV spectra of the ligands, the bands in the range 250-290 nm can be associated to $\pi \longrightarrow \pi^*$ intra-ligand transition. In the spectra of the complexes, these bands are shifted toward higher wavelengths, confirming the coordination of the ligands in the metal center. The spectra of complexes show a band at 430 nm for complexes with Copper(II) and at 375 nm for complexes with nickel(II) , which is assigned to charge transfer transition.

The electronic spectra of complexes 1 and 3 (complexes with Cu) show one band in the visible domain, respectively at 711 and 520 nm, this band is attributed to the d-d transition characteristic octahedral and square-planar geometry respectively (Solans-Monfort et al., 2011). In the visible range, the spectra of complex 2 exhibit two bands. These transitions are in agreement with a square-planar geometry around the Ni(II) ion (JieShen et al., 2005). Furthermore, the complex 4 shows three bands in the visible. These transitions are in agreement with an octahedral geometry around the Ni(II) ion (Randhır et al., 2000).

Table 4. Electronic spectral data of the ligands

Compound	λ (nm)	υ (cm^{-1})	Ɛ ($lmol^{-1}cm^{-1}$)	Electronic transitions
Dimethylglyoxime	290	34483	100	$\pi \longrightarrow \pi^*$
	270	37037	1300	$\pi \longrightarrow \pi^*$
Methionine	283	35336	20	$\pi \longrightarrow \pi^*$
	259	38610	30	$\pi \longrightarrow \pi^*$
Alanine	276	36232	50	$\pi \longrightarrow \pi^*$
	261	38314	43	$\pi \longrightarrow \pi^*$

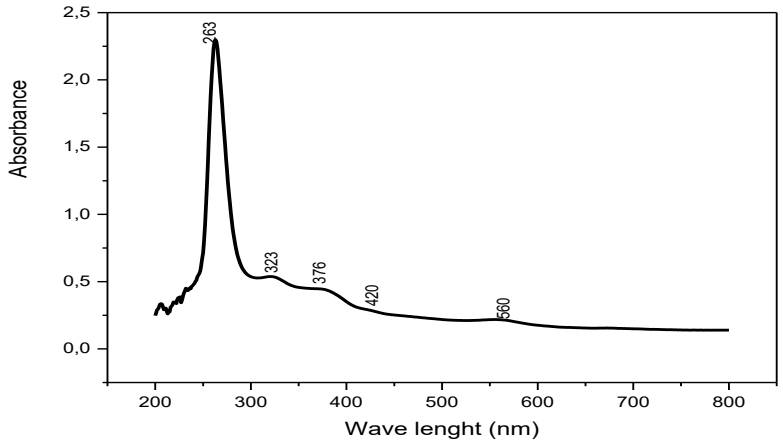

Figure 3. Electronic absorption spectrum of $[Ni(H_2dmg)(Meth)](SCN)_2$

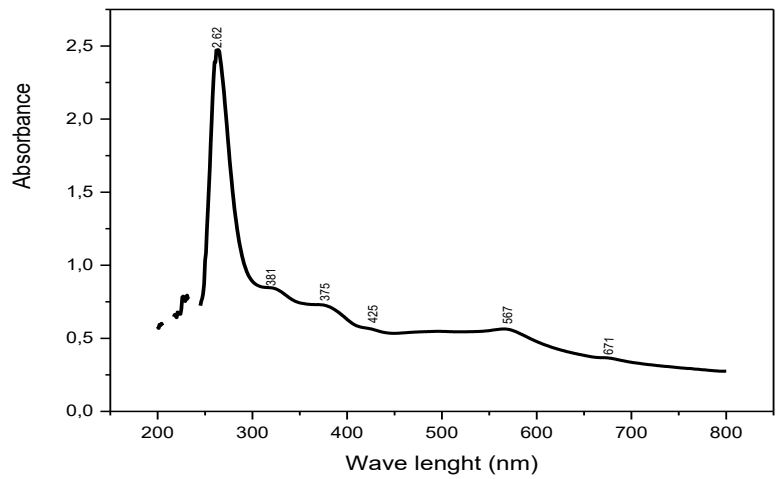

Figure 4. Electronic absorption spectrum of $[Ni(H_2dmg)(Ala)(I)_2]$

Table 5. Electronic spectral data of the complexes.

Complex	λ (nm)	υ (cm^{-1})	Ɛ ($lmol^{-1}cm^{-1}$)	Electronic Transitions
Complex 1	711	14065	711	d - d
	430	23256	300	charge transfer
	289	34602	343	π - π*
	275	36364	2810	π - π*
	268	37313	1850	π - π*
Complex 2	560	17857	200	d - d
	420	23809	300	d - d
	376	26596	400	charge transfer
	323	30960	500	π - π*
	263	38023	2300	π - π*
Complex 3	520	19231	1030	d - d
	430	23256	800	charge transfer
	316	31646	400	π - π*
	296	33784	4180	π - π*
	273	36630	4100	π - π*
Complex 4	671	14903	360	d - d
	567	17637	570	d - d
	425	23529	570	d - d
	375	26666	740	charge transfer
	321	31153	860	π - π*
	264	37879	2560	π - π*

Electrochemical Studies

The electrochemical properties of the ligands and their complexes were investigated by cyclic voltammetry in DMSO solution containing 0.1 M $NaClO_4$ as supporting electrolyte. All the measurements were carried out in 10^{-3} M solution at room temperature in the potential range +1.6 to -1.6 V with a scan rate of 50 mVs^{-1}. Electrochemical data of the ligands and the complexes are presented in Table 6 and Table 7, respectively. Typical cyclic voltammogram of [Ni (H_2dmg)(Ala)I_2] and $Ni(NO_3)_2$. $6H_2O$ are shown in Figure 5. Cyclic voltammogram of $Cu(NO_3)_2.3H_2O$ shows an irreversible oxidation process at +0.26 V assigned to the oxidation of Cu^+ to Cu^{2+} (Bougherra et al., 2018; Tidjani-Rahmouni et al., 2014).

The cyclic voltammogram of $Ni(NO_3)_2.6H_2O$ shows a quasi-reversible process characterized by the potentials Epa = -1.04, Epc = -0.92 V, which can be attributed to the reduction of Ni(II) to Ni(0), furthermore, this voltammogram also shows three anodic peaks without cathodic responses. The first and the second peaks observed at Epa1 = 0.05 and Epa2 = 0.2 V could be attributed to the successive oxidation of Ni(0) to Ni(I) and the third peak observed at Epa3 = 0.84 V can be attributed to the oxidation of Ni(I) to Ni(II) (El-Gahami et al., 2004; Ben Mansour, 2014).

By comparing the cyclic voltammograms of complexes to those of the ligands and that of metal salt taken as reference, it is easy to confirm the presence of the metal cation and ligands in the complexes. The cyclic voltammogram of the complexes 1 and 3 (complexes with copper) shows a cathodic peak, without any anodic response, observed at -0.98 V and -1.07V respectively, this peak could be assigned to the reduction of Cu(II) to Cu(0). In addition, these complexes show four peaks anodic without any cathodic response. The first peak located at 0.01 V for complex 1 and at -0.1 V for complex 3 can be attributed to the oxidation of Cu(0) to Cu(I). the second peak at 0.23 V for complex 1 and at 0.13 V for complex 3 could be assigned to the oxidation of Cu(I) to Cu(II).

The peaks anodic at -0.47 V and 1.03 V for complex 1 and at -0.6 V and 0.94 V for complex 3. All these peaks can be attributed to the oxidation of the ligands. The cyclic voltammogram of the complexes 2 and 4 (complexes with nickel) shows a cathodic peak, without any anodic response, observed at -0.66 V and -1.30 V respectively, this peak could be assigned to the reduction of Ni(II) to Ni(0)

In addition, these complexes show three peaks anodic without any cathodic response. The first peak located at -0.24 V for complex 2 and at 0.06 V for complex 4 can be attributed to the oxidation of Ni(0) to Ni(I). the second peak at 0.7 V for complex 2 and at 0.62 V for complex 4 could be assigned to the oxidation of Ni(I) to Ni(II).

However, the peaks anodic at -0.5 V for complex 2 and 1.24 V for complex 4 can be attributed to the oxidation of the ligands.

Table 6. Electrochemical data of the ligands

Compound	Epa (V)	Epc (V)	ΔE(Mv)
$Cu(NO_3)_2 .3H_20$	-	0.26	-
	-1.04	-0.92	120
$Ni(NO_3)_2 .6H_20$	0.05	-	-
	0.2	-	-
	0.84	-	-
Dimethylglyoxime	-0.7	-0.56	140
Methionine	-	1.24	-
	-0.82	-	-
Alanine	-0.38	-0.66	280

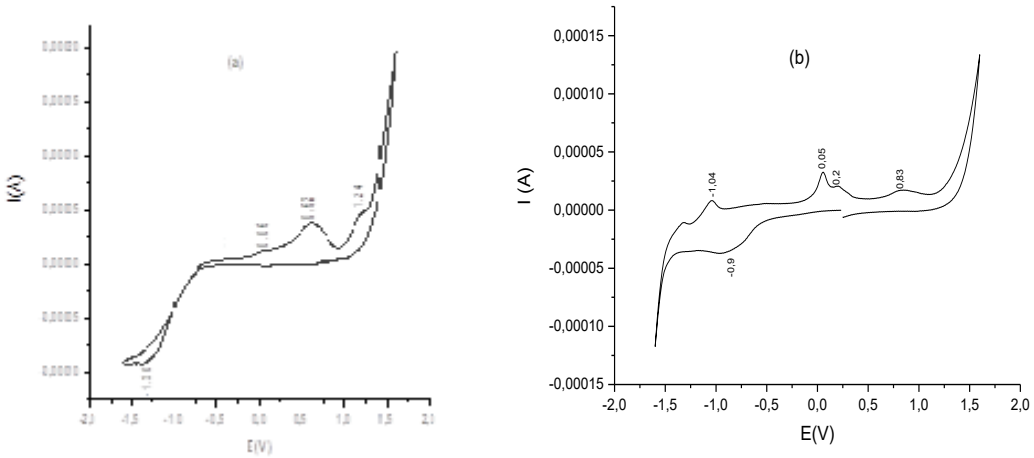

Figure 5. (a) Cyclic voltammogram of $[Ni(H_2dmg)(Ala)_2 I_2]$ and (b) of $Ni(NO_3)_2.6H_2O$

Table 7. Electrochemical data of the complexes

Complex	Epa (V)	Epc (V)
Complex 1	-	-0.98
	-0.47	-
	0.01	-
	0.23	-
	1.03	-
Complex 3	-	-1.07
	-0.6	-
	-0.1	-
	0.13	-
	0.94	-
Complex 2	-	-0.66
	-0.50	-
	-0.24	-
	0.70	-
Complex 4	-	-1.30
	0.06	-
	0.62	-
	1.24	-

Conclusion

Four complexes of (Cu or Ni) with dimethylglyoxime and amino acids (methionine or alanine) were synthesized and characterized by different physico-chemical and spectroscopic techniques. Conductimetric analysis shows

that two complexes are non-electrolytes. The IR study reveals that all the ligands are bidentate. The electron absorption spectra can be concluded that the investigated mixed-ligand complexes have an octahedral or square-planar geometries. The electrochemical behavior of complexes was determined by cyclic voltammetry, which shows an irreversible redox process corresponding of M(II) to M(0) and irreversible oxidation of M(0) to M(I) and M(I) to M(II).

Scientific Ethics Declaration

* The authors declare that the scientific ethical and legal responsibility of this article published in EPSTEM Journal belongs to the authors.

Conflict of Interest

* The authors declare that they have no conflicts of interest

Acknowledgements or Notes

* This article was presented as a poster presentation at the International Conference on Basic Sciences, Engineering and Technology (www.icbaset.net) held in Trabzon/Türkiye on May 01-04, 2025.

References

Abane, L, Adkhis, A, Terrachet,S., & Makhloufi, M. (2019). Synthesis, DFT/TD-DFT theoretical studies, experimental characterization, electrochemical and antioxidant activity of fe (III) complexes of bis(dimethylglyoximato)guanine. *Journal of Molecular Structure, 1186*, 413-422.

Adkhis, A., Benali-Baitich, O., Khan, M. A., & Bouet, G. (2000). Synthesis, characterization and the thermal behavior of mixed ligand complexes of cobalt (III) with dimethylglyoxime and some amino acids. *Synthesis and Reactions in Inorganic Metals Organometallic and Nanomaterial Chemistry, 30,* 1849-1858.

Adkhis, A., Belhocine, F., Makhloufi, M., Amrouche, T., & Terrachet, S. (2022). New copper (II) complexes with ethylenediamine, bipyridine and amino acids: Synthesis, characterization, optimization of geometry by theoretical DFT studies, electrochemical properties and biological activities. *Journal of Chemical and*,*Pharmaceutical Research, 14*(6), 1-23

Alrufaydi, Z. A., Ahmed, S. M., & Mubarak -Mater, A.T. (2020). Synthesis andcharacterization of novel transition metal complexes with L-proline and their catalytic activity evaluation towards cyclohexane oxidation. *Materials Research Express,7,* 045103

Baran, E.J., & Torre, M.H. (2009), Colegio de farmacéuticos de la provincia de buenos aires. *Latin American Journal of Pharmacy*, 28(5), 89-792.

Ben Mansour, Y (2014). *Synthèse etude physico-chimique et activité biologique des complexes de cuivre et nickel dérivés d'hydrazone et thiadiazole.* (Doctoral dissertation, Université de Tlemcen).

Berradj,O., Bougherra,H., Adkhis, A., Amrouche, T., Amraoui, N.E., & Hammoutène, D, (2021). Synthesis, spectroscopic, thermal decomposition, DFT studies and antibacterial activity of uracil cobalt (III) dimethylglyoximato complexes. *Journal of Molecular Structure 1232,* 130040.

Bougherra, H., Berradj, O., Adkhis, A., & Amrouche, T. (2018). Synthesis, characterization, electrochemical and biological activities of mixed ligand copper (II) complexes with dimethylglyoxime and amino acids. *Journal of Molecular Structure 1173,* 280-290.

Bougherra,' H., Berradj, O., & Adkhis, A. (2018). Synthesis, characterization, electrochemical studies and antioxidant activity of some new dimethylglyoxime copper (II) complexes with purine bases and ortho-phenylenediamine**.** *Journal of Chemical and Pharmaceutical Research,10*(4), 93-103.

Caleb Noble Chandar, S., Sangeetha, D., & Arumugham, M. N. (2011), Synthesis, structure, CMC values, thermodynamics of micellization, steady-state photolysis and biological activities of hexadecylamine cobalt(III) dimethyl glyoximato complexes. *Transition Metal Chemistry, 36, 211-216*.

El-Gahami, M.A., Khafagy, Z.A., Azza, M.M.A., & Ismail, N.M. (2004), Thermal, spectroscopic, cyclic voltammetric and biological activity studies of cobalt (II), nickel (II), and copper (II) complexes of dicarboxylic amino acids and 8hHydroxyquinolin. *Journal of Inorganic and Organometallic*

Polymers, 14, 117-129

Jadhav, S.S., Kolhe, N.H., & Athare, A.E. (2013) Synthesis, and characterization of mixed ligans complexes of salicyladoxime, dimethylglyoxime and benzoin with mn (II) and their biological activity. *International Journal of Pharmacy and Biological Sciences, 4,* 45-54.

JieShen, X., Xiao, L., & RenXu., R. (2005), *N*-(4-ferrocenylphenyl)-4-piperidino-1,8-naphthalimide, the ferrocene redox centre is linked to the naphthalimide fluorophore by a benzene bridge. *Acta Cryst.E61.*1185-1187.

Mamun, MA, Ahmed, P.K. Bakshi, Ehsan, MQ (2010) Synthesis and spectroscopic, magnetic and cyclic voltammetric characterization of some metal complexes of methionine: $[(c_5h_{10}no_2s)_2m^{ii}]$; m^{ii} = mn(II), co(II), ni(II), cu(II), zn(II), cd(II) and hg(II). *Journal of Saudi Chemistry Society, 14* (2010), 23-31.

Osunlaja, A.A., Ndahi, N.P., & Ameh, J.A. (2009). Synthesis, physico-chemical and antimicrobial properties of co(ıı), ni(ıı) and cu(II) mixed-ligand complexes of dimethylglyoxime - part I. *African Journal of Biotechnology, 8*(1)*,* 4-11.

Randhır, S., Suresh, K., & Amarendra, B. (2000). Synthesis and electrochemical studies of phenylazo substituted tetraaza macrocyclic complexes of ni(II). *Procee Indian Acad. Sci. (Chem. Sci.), 112*(6), 601–605.

Rosu, T., Negoiu, M., Pasculescu, S., Pahontu, E., Poirier, D., & Gulea, A. (2010) Metal-based biologically active agents: Synthesis, characterization, antibacterial and antileukemia activity evaluation of cu(II), V(IV) and ni(II) complexes with antipyrine-derived compounds. *European Journal of Medicinal Chemistry, 45*(2), 774-781.

Salih, B.M.M., & Satyanarayana, S. (2009). Vitamin b12 models: Synthesis and characterization of cyano bridged dicobaloximes and antimicrobial activity. *African Journal of Pure Application Chemistry, 3, 170-176.*

Solans-Monfort, X., Fierro, J.L.G., Hermosilla, L., Sieiro, C., Sodupe, M., and MasBalleste, R, (2011), O-o bond activation in h_2o_2 and $(ch_3)_3c$-ooh mediated by $[ni(cyclam)(ch_3cn)_2](clo_4)_2$: different mechanisms to form the same ni(III) product?. *Dalton Transactions*, 40, 6868 – 6876.

Tidjani-Rahmouni, N., Bensiradj, N.H., Djebbar, S., & Benali-Baitich, O. (2014). Synthesis, characterization, electrochemical studies and DFT calculations of amino acids ternary complexes of copper (II) with isonitrosoacetophenone biological activities. *Journal of Molecular. Structures, 1075*, 254-263.

Wagner, C. C., & Baran, E. J. (2004). Spectroscopic and magnetic behaviour of the copper (II) complex of L-tryptophan. *Acta Farm. Bonaerense 23, 339-342*.

Wagner, C.C., Torre,M.H., & Bara, E. J. (2008). Vibrational spectra of copper(II) complexes of L-proline. *Latin American Journal of Pharmacy, 27*(2), 195-197.

Author(s) Information

Hadda Bougherra
Mouloud. Mammeri University of Tizi Ouzou
Nouvelle vile BP 17 RP Tizi Ouzou, Algeria
Contact e-mail : *hadda.bougherra@ummto.dz*

Omar Berradj
Mouloud. Mammeri University of Tizi Ouzou
Nouvelle vile BP 17 RP Tizi Ouzou, Algeria

To cite this article:

Bougherra, H., & Berradj, O, (2025). New copper (II) and nickel (II) complexes with dimethylglyoxime and amino -acids: Synthesis, characterization and electrochemical properties. *The Eurasia Proceedings of Science, Technology, Engineering and Mathematics (EPSTEM), 34,* 23-30.

The Eurasia Proceedings of Science, Technology, Engineering & Mathematics (EPSTEM)
ISSN: 2602-3199

The Eurasia Proceedings of Science, Technology, Engineering and Mathematics (EPSTEM), 2025

Volume 34, Pages 31-42

ICBASET 2025: International Conference on Basic Sciences, Engineering and Technology

High-Performance of Catalyst Synthesized from Waste Can Aluminum and Rice Husk Silica for Conversion Coconut Oil into Biodiesel

Ganjar Andhulangi
Universitas Gadjah Mada

Wega Trisunaryanti
Universitas Gadjah Mada

Wasinton Simanjuntak
Universitas Lampung

Kamisah Delilawati Pandiangan
Universitas Lampung

I Ilim
Universitas Lampung

H Herliana
Universitas Lampung

K Khasandra
Universitas Lampung

Abstract: The development of biodiesel is one of the extensive research projects that have been undertaken in response to the diminishing fossil energy reserves, air pollution, and climate change. This work introduces catalysts synthesized from waste can aluminum and rice husk silica (AS) with Si/Al molar ratios of 10, 20, and 30. The catalysts were synthesized by the hydrothermal process in an autoclave at 100 ºC for 24 h, followed by calcined at 550 °C for 5 h, and evaluated as catalysts for biodiesel (fatty acid methyl esters, FAMEs) production from coconut oil. The AS-10 catalyst demonstrates highly performance, with 99.57% yield under operational conditions (10 wt.% catalyst, 1:2 oil-to-methanol ratio, 60 °C, 6 h). In addition, the catalyst has 99.69% FAME selective, with biodiesel that most closely matched the fatty acid composition of coconut oil. For the characteristic, this catalyst exhibits amorphous phase and a small average crystal size, as demonstrated by the XRD patterns and SEM images. The FTIR spectra after pyridine absorption qualitatively shows the presence of Brønsted (1546 cm^{-1}) and Lewis (1457 cm^{-1}) acid sites on this catalyst. High-performance catalytic activity is usually attributed to these characteristics, which may be able to enhance the adsorptivity towards triglycerides of coconut oil. Hence, these findings suggest the prospective use of the catalyst in the biodiesel production derived from coconut oil.

Keywords: Biodiesel, Coconut oil, Catalyst, Waste can aluminum (WCA), Rice husk silica (RHS)

Introduction

Indonesia's plentiful natural resources offer significant prospects for sustainable biodiesel development practices. The advancement of biodiesel is conducted in response to the depletion of fossil fuel reserves,

climate change, and air pollution, as well as aims to diminish import reliance on fossil fuels, which are experiencing substantial price increases (Wirawan et al., 2024). Indonesia has around 40 varieties of oil-producing plants recognized as feedstocks for biodiesel synthesis, including coconut oil (*Cocos nucifera*) (Rachmaditasari et al., 2024). The potential of coconut oil for biodiesel production is substantial, providing extensive feedstock diversity to enhance energy security and safety, improve environmental quality, and achieve energy independence (Rahman et al., 2021). The use of this local natural resource also contributes to regional development and aligns with global sustainability goals (SDGs).

In practice, the production of biodiesel is inextricably linked to the utilization of catalysts to facilitate the transesterification and esterification of coconut oil into fatty acid methyl esters (FAMEs) (Sakti La Ore et al., 2020). Nevertheless, the development of heterogeneous catalysts is fraught with a challenge in the acquisition of active, selective (Mulyatun et al., 2022), and stable catalysts (Gardy et al., 2019). Furthermore, the dependence on synthetic compounds as precursors for the synthesis of heterogeneous catalysts remains substantial. For instance, certain researchers have reported that raw materials from sodium metasilicate, sodium silicate, sodium aluminate, and α- and γ-alumina are used to produce heterogeneous catalysts, including aluminosilicate (Simanjuntak et al., 2013), alumina, silica, and zeolite (Simanjuntak et al., 2021). Despite the fact that these synthetic heterogeneous catalysts exhibit high activity, selectivity, and stability in certain instances, it is imperative to investigate catalyst development by utilizing sustainable and environmentally friendly raw materials, such as waste can aluminum (WCA) and rice husk silica (RHS), while simultaneously addressing these limitations. Combining WCA with RHS processed using hydrothermal methods (Pratika et al., 2021) is an intriguing approach. The development of sustainable catalysts by utilizing refuse and waste has contributed to advancements in materials science and is a prominent initiative for the development of next-generation catalysts (Nayak et al., 2024). Thus, the synthesis of heterogeneous catalysts (e.g., alumina and silica (AS) from the combination of WCA and RHS) provides a customizable solution for specific catalyst requirements, such as those for the production of biodiesel from coconut oil.

In this current investigation, we synthesized catalysts from waste can aluminum (WCA) and rice husk silica (RHS) with varying Si/Al ratios of 10, 20, and 30 for one-step conversion of coconut oil to biodiesel. While RHS has been frequently employed as a matrix/support in a variety of applications, as far as our literature is concerned, the use of WCA as an alumina source is limited. These catalysts are currently in the early stages of development and has the potential to be further developed to achieve the desired characteristics for specific applications. Furthermore, a sustainable solution for the development of biodiesel and heterogeneous catalysts is appealing due to the fact that it employs natural resources, refuse, and waste as raw materials. Therefore, these catalysts were experimentally tested for their performance to produce biodiesel from coconut oil.

Materials and Methods

Materials

Waste can aluminum and rice husk were used as the primary catalyst materials, obtained from the adjacent environment of Bandar Lampung City and the local rice milling industry in Pringsewu Regency, Lampung, Indonesia, respectively. Coconut oil in this study was procured from PT Barco Indonesia. Methanol (CH_3OH, Merck) was used for transesterification-esterification reagent. Nitric acid (HNO_3, Merck) was utilized for the neutralization of rice husk silica sol-gel. Reagent-grade tetrapropylammonium hydroxide (TPAOH) and sodium hydroxide (NaOH 98%) were acquired from Sigma-Aldrich.

Catalyst Preparation

The fabrication process flow of catalysts synthesized from waste can aluminum (WCA) and rice husk silica (RHS), with Si/Al ratios of 10, 20, and 30 is illustrated in Figure 1. With some modification of procedure adopted from López-Juárez et al., (2018), the aluminum was prepared from WCA. The WCA were initially sanded to remove the paint, rinsed with detergent water until impurities free, dried, and randomly cut into small sizes (± 0.5 cm) for dissolution in the subsequent stage.

The sol-gel method was employed to extract RHS (Setyawan et al., 2021). The rice husk was cleansed, washed repeatedly with hot water, and filtered, then collected, immersed in a 10% HNO_3 solution overnight, rinsed with clean water, and dried. After that, 200 g of dried rice husk was immersed in 2000 mL of 1.5% NaOH solution, heated to simmering for 30 min, chilled overnight, and filtered to produce silica-containing

filtrate (silica sol). The filtrate was progressively added with a 10% HNO_3 solution until the silica sol transformed into silica gel at a neutral pH (7.0), as determined by a universal indicator. The silica gel was aged at room temperature for 24 h before being rinsed with hot water until spotless and white. RHS was obtained by sieving it through a 200-micron sieve after 8 h of dehydrating in an oven at 80 ºC. This RHS was utilized in the subsequent procedure. After the precursor preparation process (aluminum and silica), the hydrothermal method was employed to synthesize the catalysts, namely AS-10, AS-20, and AS-30 catalysts. To prepare solution A, 11.2 g of NaOH was dissolved in 450 mL of distilled water, then 2.5 mL of TPAOH solution was added, and the mixture was stirred steadily until it was homogeneous. Solutions A were divided into two portions: 200 mL and 250 mL, respectively. After that, 2.7 g of WCA was dissolved in 200 mL of solution A (called solution B). Meanwhile, 60 g of RHS was dissolved in 250 mL of solution A (called solution C). Solutions B and C were combined until formed a homogeneous paste. The paste was then placed in an autoclave at 100 ºC for 24 h. Ultimately, the catalyst material was rinsed with distilled water, dried at 80 ºC for overnight, pulverized, and filtered through a 200-micron sieve, followed by calcination at 550 ºC for 5 h in a muffle furnace (Heraeus MR 260E).

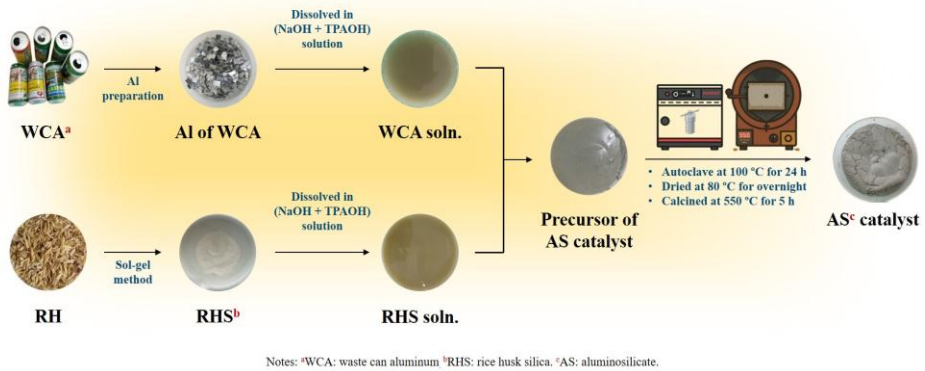

Figure 1. Fabrication of AS-10, AS-20, and AS-30 catalysts.

Catalyst Characterization

The crystal phase, crystallinity, and average crystal size (calculated by Debye Scherrer equation) of the catalysts were determined using X-ray diffraction (XRD, PANalytical type Empyrean) with Cu Kα radiation (1.54060 Å) in the 2θ range of 5 - 80º. The surface morphology and elemental composition of the catalysts were analyzed using scanning electron microscope-energy dispersive x-ray (SEM-EDX, Zeiss EVO MA 10). The acid sites before and after pyridine absorption, chemical bonds, and functional groups of the catalysts were characterized using Fourier Transform Infrared Spectroscopy (FTIR, Nicolet Avatar 360) with a wave number range of 400 - 4000 cm^{-1}.

Catalytic Performance of Catalysts in Biodiesel Production

The catalytic performance was evaluated for biodiesel production using coconut oil as the feedstock in one-pot conversion (Pandiangan et al., 2021). The experiment was conducted using reflux with 2.5 g catalyst (10 wt.% of the feed), 1:2 oil-to-methanol ratio at 60 ºC under a stirring speed of 600 rpm for 6 h. The reflux product was separated by separating the funnel. The biodiesel (FAMEs) was taken and washed with warm distilled water. The composition of biodiesel was analyzed using gas chromatography-mass spectrometry (GC-MS, QP2010 SE Shimadzu). The yield (%) and selectivity (%) were calculated to determine the catalytic performance according to the following equations (1) and (2):

$$\text{Yield (\%)} = \frac{W_{\text{biodiesel product}}}{W_{\text{feed}}} \text{ x \%FAME area} \quad (1)$$

$$\text{Selectivity (\%)} = \frac{\text{Peak area of each FAME}}{\text{Total area of GC}} \text{ x } 100 \quad (2)$$

where W_{feed} is the initial weight of feed (g), $W_{biodiesel\ product}$ is the weight of biodiesel (g), and %FAME area is GC-MS area of FAMEs.

Results and Discussion

XRD Analysis of the Catalysts

X-ray diffraction (XRD) patterns in the 2θ range between 5 and 80º, as illustrated in Figure 2, indicate that the AS-10, AS-20, and AS-30 catalysts have characteristic of kyanite (JCPDS PDF#83-1569), cristobalite (JCPDS PDF#82-1235), and aluminum oxide (JCPDS PDF#77-0396), which comprise the aluminosilicate framework. Sodium aluminum oxide (002) phase is presented in AS-10 catalyst, as indicate by the typical peak at 2θ = 7.84º (JCPDS PDF#72-1406). The typical peaks at 2θ = 31.93º (JCPDS PDF#87-1259) and 2θ = 7.84º (JCPDS PDF#72-1406) on AS-20 and AS-30 catalysts, respectively, indicate the presence of calcium silicate (020) and sodium aluminum oxide (002) phases. To ascertain the catalyst's crystallinity percentage, the area of the crystal peak is compared to the total area of the diffractogram. Overall, the crystallinity may be enhanced by an increase in the Si/Al ratio of the catalyst (Okada et al., 2025). The Debye-Scherrer equation can be employed to determine the average crystal size and the results are summarized in Table 1. Compared to AS-10 and AS-30 catalysts, the average crystal size of the AS-20 catalyst is elevated. These findings suggest that the AS-20 catalyst may have agglomerated crystalline particles. The average crystal size of the catalysts can be increased by increasing the Si/Al ratio, as explained by Wang et al. (2023).

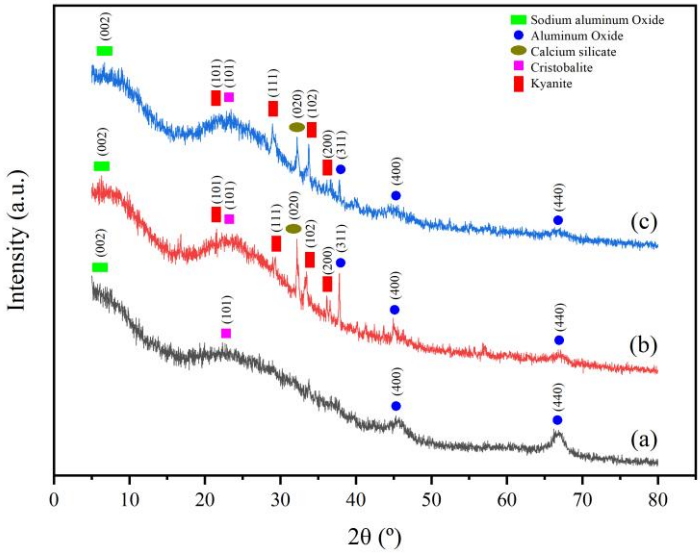

Figure 2. XRD patterns of (a) AS-10, (b) AS-20, and (c) AS-30 catalysts.

Morphological and Elemental Composition Analysis of the Catalysts

The scanning electron microscopy (SEM) was employed to characterize the morphology of AS-10, AS-20, and AS-30 catalysts at a magnification of 20,000 times. Figure 3, which displays the SEM images, demonstrates the distinct structural and surface shape differences between the AS-10 catalyst and the AS-20 and AS-30 catalysts. The AS-10 catalyst exhibits an irregular structure and a variety of particle morphologies, with an average particle diameter in the micrometer range. The AS-20 and AS-30 catalysts exhibit a porous structure and a smoother surface, with the particles' shapes dispersed randomly on the surface. In general, the XRD pattern (refer to Figure 2) confirmed that the particles of these catalysts exhibited amorphous dominance. The catalytic activity of the one-step conversion of coconut oil to biodiesel is significantly enhanced by the catalytic surface characteristics, as reported by Kwon et al. (2014).

Energy dispersive X-ray spectroscopy (EDS) provides the elemental composition for AS-10, AS-20, and AS-30 catalysts, as summarized in Table 1. Overall, these catalysts are composed of high concentrations of silicon (Si), aluminum (Al), and oxygen (O) atoms, which supports the existence of an aluminosilicate framework on the catalysts. The existence of active sites on the catalyst surface is further strengthened by the presence of other elements, including sodium (Na) and calcium (Ca). These components represent the catalyst's framework and active sites, which are crucial in the catalytic reactions of transesterification and esterification of coconut oil into biodiesel, as reported by Al-Ani et al. (2020). Furthermore, the XRD patterns confirm the existence of phases that are derived from these elements. The catalysts synthesized from WCA and RHS possess amorphous characteristics, with the aluminosilicate phase consisting of Si, Al, O, Na, and Ca.

Therefore, these characteristics are usually attributed to catalytic activity, which may be able to lead the adsorptivity towards triglycerides of coconut oil.

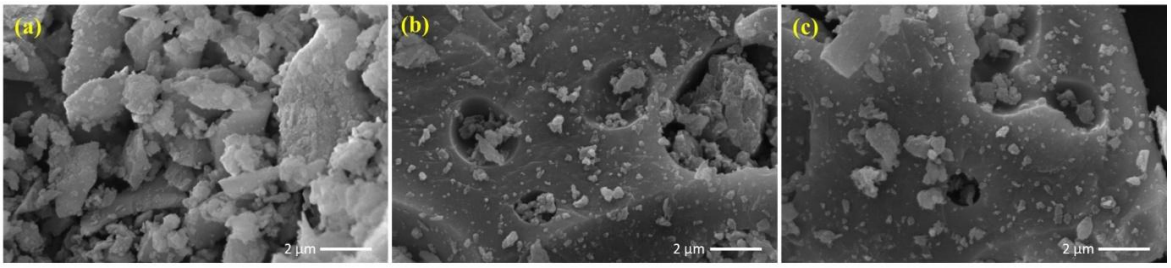

Figure 3. SEM images of (a) AS-10, (b) AS-20, and (c) AS-30 catalysts at 20,000 times magnifications.

Table 1. Elemental composition, crystallinity, and average crystal size of catalysts.

Catalysts	Elemental composition (wt.%)[a]						Crystallinity	Average crystal size[b]
	Si	Al	Na	O	Ca	C	(%)	(nm)
AS-10	29.65	16.05	9.72	39.12	nd	5.43	31.25	5.86
AS-20	30.32	14.73	4.97	28.76	16.90	4.29	36.33	17.18
AS-30	55.15	3.78	3.20	31.33	0.83	5.68	48.89	14.45

Notes: nd = not detected. [a]Analyzed by EDS. [b]Calculated by Debye Scherrer equation and XRD analysis.

FTIR and Active Sites Analysis of the Catalysts

Figure 4 illustrates the FTIR spectra of the catalysts before (1) and after (2) pyridine absorption. The characteristics of the aluminosilicate framework on the catalysts are confirmed by the Si-O-Al absorption bands of SiO_4^{4-} and AlO_4^- in the range of 466 - 599 cm^{-1}. The symmetrical stretching vibrations of the Si-O-Si bond are indicated by the absorption band at 788 cm^{-1}, whereas the asymmetrical stretching vibrations of the Si-O-Si bond are represented by the widened area at 1037 cm^{-1}. These patterns suggest the formation of Si-O-Si tetrahedral bonds in silica (Simanjuntak et al., 2013). The bending vibrations of the O-H bond of water, which is chemically bound in the silanol (Si-OH) structure of the catalyst, are indicated by the absorption band at 1654 cm^{-1}. The O-H stretch vibrations of water that are physically adsorbed on the catalyst surface are represented by the broad peaks in the 3301 - 3510 cm^{-1} areas. In addition to the identification of functional groups and bonds on the catalyst, the Brønsted and Lewis acid sites (BAS and LAS) were qualitatively determined through the FTIR spectra after the pyridine absorption (Gould & Xu, 2018). The interaction between the pyridine base and the BAS (N-H stretching vibration) of the catalyst is demonstrated by the absorption band at 1546 cm^{-1} (area 1515-1565 cm^{-1}). This band is formed by the proton contribution from the BAS. The pyridine base's N-H bending is indicated by a peak at 1457 cm^{-1} in the absorption area of 1435 - 1470 cm^{-1}, which is the result of a coordinate bond with the LAS on the catalyst (Emeis, 1993).

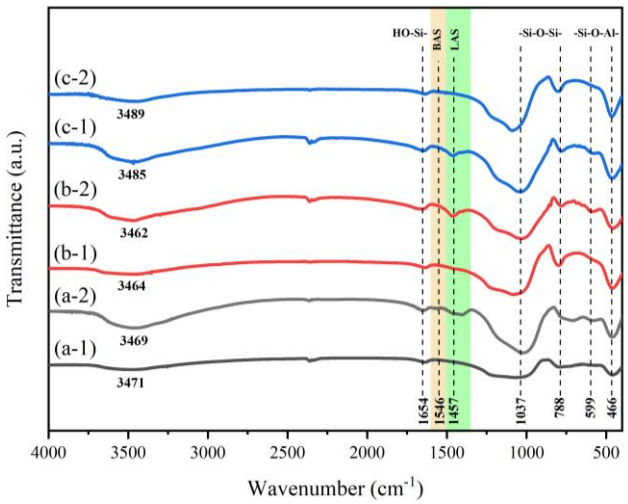

Figure 4. FTIR spectra of before (1) and after (2) pyridine absorption (a-1 and a-2) AS-10, (b-1 and b-2) AS-20, and (c-1 and c-2) AS-30 catalysts. BAS: Brønsted acid sites, LAS: Lewis acid sites.

The Brønsted acid sites on these catalysts are derived from silanol groups (Si-OH) that are present on the surface of the aluminosilicate framework. These groups provide H^+ ions that will be donated to other species. Meanwhile, Lewis acid sites are formed by the coordination of Al^{3+}, Na^+, or Ca^{2+} ions to the aluminosilicate on its surface. This process alters the electron distribution and creates empty orbitals on the Al and Si atoms of the catalyst, which facilitate the acceptance of electron pairs (Katada, 2018).

Catalytic Performance of the Catalysts in Biodiesel Production

After ensuring the characteristics of each catalyst, the catalyst's activity was systematically evaluated for the one-step transesterification and esterification reaction and compared with those of other catalysts. The GC-MS chromatogram presented in Figure 5 shows the relative quantity of FAMEs produced from coconut oil using various catalysts (AS-10, AS-20, and AS-30). The highest FAME yield can be observed by setting the operational condition of one-step conversion at 60 °C for 6 h with a stirring speed of 600 rpm, a 10 wt.% catalyst, and a 1:2 oil-to-methanol ratio. Temperature and reaction time generally influence reaction rates. The catalyst dosage, which is selective and possesses the number of active sites available, can accommodate to achieve an effective conversion. The oil-to-methanol ratio usually enhances the yield of FAME and reduces the deactivation of the catalyst due to an excess of methanol (Trisunaryanti et al., 2025). The correlation between these variables can determine the catalyst's performance and the conversion effectiveness. Thus, our investigation focuses on the catalytic performance and selectivity towards coconut oil rather than catalyst stability.

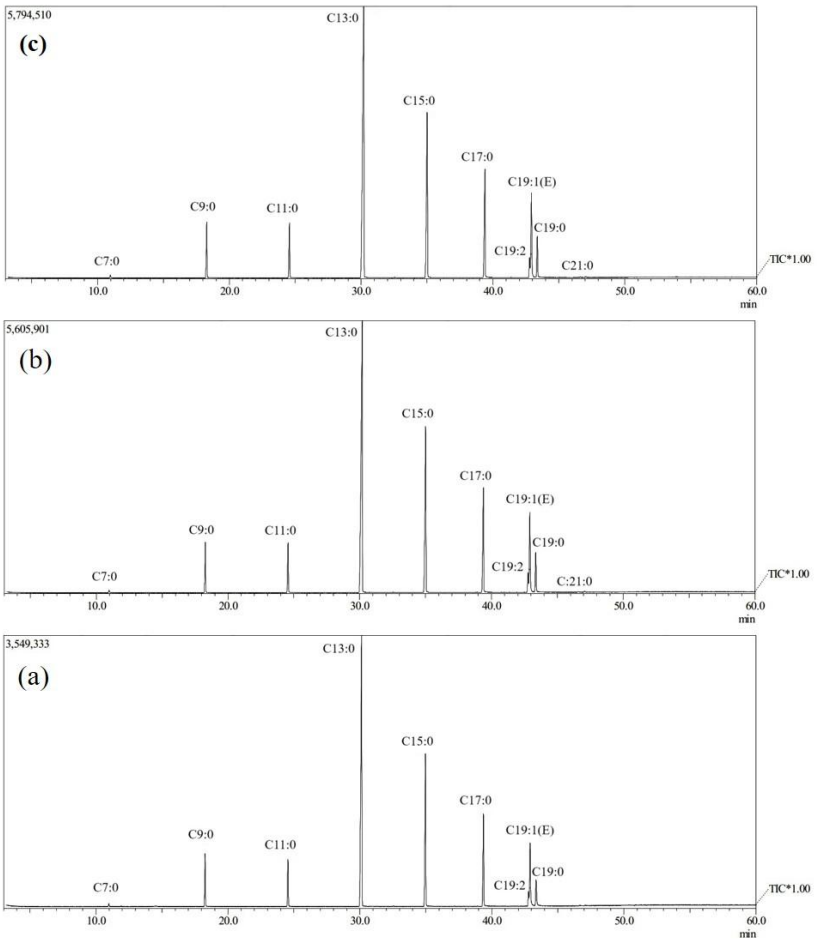

Figure 5. GC-MS chromatogram of FAMEs produced using catalysts of (a) AS-10, (b) AS-20, and (c) AS-30.

In Table 2, the biodiesel contains 100% FAMEs, with methyl palmitate, methyl myristate, and methyl laurate being the most prevalent components. The biodiesel also contains methyl caproate, which has a composition of less than 1%. This composition is consistent with the fatty acid content of coconut oil. These findings indicate that the one-step transesterification and esterification of coconut oil were entirely converted to FAMEs.

Table 2. Fatty acids of coconut oil and FAMEs in biodiesel.

Reference[a]		This work			
		Catalyst	AS-10	AS-20	AS-30
FA of coconut oil	Area (%)	FAMEs	Area (%)		
-	-	Methyl Caproate (C7:0)	0.31	0.29	0.21
Caprylic acid (C8:0)	3.35	Methyl Caprylate (C9:0)	5.41	4.58	4.79
Capric acid (C10:0)	3.21	Methyl Caprate (C11:0)	4.97	4.62	4.67
Lauric acid (C12:0)	32.72	Methyl Laurate (C13:0)	43.97	43.77	43.81
Myristic acid (C14:0)	18.38	Methyl Myristate (C15:0)	20.14	20.67	20.48
Palmitic acid (C16:0)	13.13	Methyl Palmitate (C17:0)	11.21	11.61	11.36
Linoleic acid (C18:2)	3.60	Methyl Linoleic (C19:2)	1.80	2.02	1.98
Oleic acid (C18:1)	12.88	Methyl Elaidate (C19:1(E))	8.59	9.11	8.69
Stearic acid (C18:0)	4.35	Methyl Stearate (C19:0)	3.60	3.20	3.91
-	-	Methyl Eicosanoate (C21:0)	-	0.13	0.11

Notes: FA = fatty acids. FAMEs = fatty acid methyl esters. [a]Cited from Nakpong et al., (2010) and Lugo-Méndez et al., (2021).

The results of the biodiesel yield were determined by employing Equation (1), as shown in Figure 6a. Here, the AS-10 catalyst demonstrated the highest yield of 99.57%, suggesting that the catalyst is highly effective in the conversion of coconut oil into FAMEs. The biodiesel yields using AS-20 and AS-30 catalysts under the same conditions were slightly lower at 98.06 % and 94.70 %, respectively. This decrease in yield may be influenced by the large average crystal size of the catalyst, high crystallinity, and the availability of the number of Brønsted and Lewis acid sites (BAS and LAS). Consequently, the adsorption of triglycerides on the catalyst surface and the catalytic process are decreased.

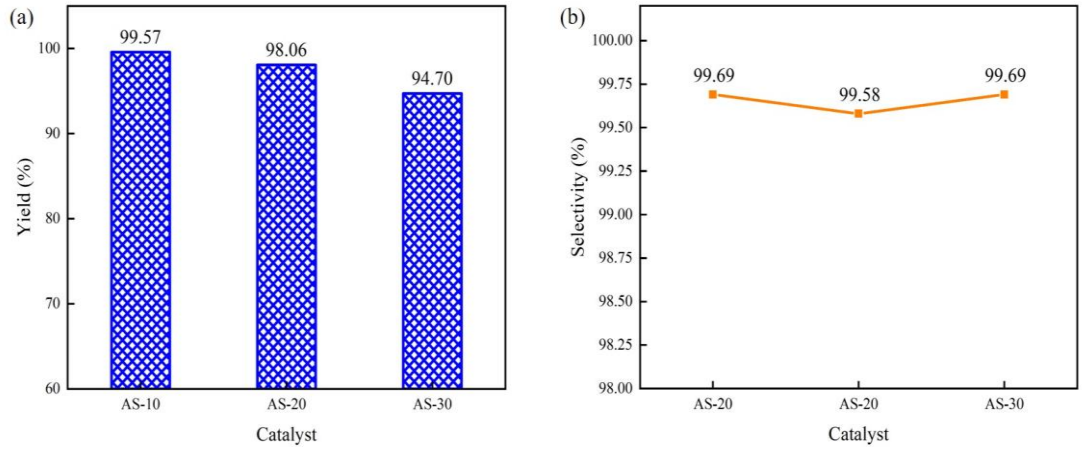

Figure 6. Graph of (a) biodiesel yield and (b) selectivity of various catalysts.

This phenomenon of yield reduction is crucial for comprehending the catalytic performance of the transesterification-esterification process, particularly in the context of the catalyst with a Si/Al ratio of 10 (AS-10), which exhibits superior performance in comparison to the catalysts with higher Si/Al ratios (AS-20 and AS-30). The catalyst surface that generates BAS and LAS may be capable of enhancing its interaction with carbonyl groups on triglycerides, thereby facilitating the adsorption and catalytic processes necessary to produce FAMEs, as explained by Cao et al. (2016).

To evaluate their catalytic selectivity, the composition of FAMEs was also compared to the fatty acid composition of coconut oil based on the secondary data from Nakpong et al. (2010) and Lugo-Méndez et al. (2021). Coconut oil is primarily composed of Caprylic acid (C8:0), Capric acid (C10:0), Lauric acid (C12:0), Myristic acid (C14:0), Palmitic acid (C16:0), Linoleic acid (C18:2), Oleic acid (C18:1), and Stearic acid (C18:0). The fatty acids of coconut oil were consistent with the FAMEs that were produced through the catalytic process using AS-10, AS-20, and AS-30 catalysts. AS-10 and AS-30 catalysts were employed to achieve the highest selectivity, which was 99.69%, as presented in Figure 6b. Nevertheless, catalyst AS-20 exhibited a selectivity value of 99.58 %, which was slightly decreasing. Despite the fact that all catalysts exhibited impressive selectivity trends, the catalytic activity varied based on the specific catalyst used. The AS-10 catalyst, which exhibits high selectivity and yield, exhibited consistent results. Nevertheless, the AS-20 catalyst showed a relatively high yield and lower selectivity, whereas the AS-30 catalyst exhibited vice versa.

This distinctive phenomenon serves as confirmation that the yield and selectivity of the catalyst are influenced by the correlation between its average crystal size, crystallinity, and active site characteristics, as explained by Barkhuizen et al. (2006).

The catalyst employed in this study has an aluminosilicate framework, according to the results of XRD, EDS, and FTIR analyses. In general, aluminosilicate is an amorphous and porous material. This characteristic is due to the aluminosilicate framework, where the tetrahedral bonding of aluminum atoms with several silicon (silanol) atoms forms Brønsted and Lewis acid sites. These active sites are typically balanced by cations like Na^+ and Ca^{2+}, which can be exchanged within the porous structure (Muraoka et al., 2016). The high catalytic performance of the one-step conversion of coconut oil to biodiesel is usually attributed to these catalyst characteristics.

Evaluation of Proposed Catalytic Mechanisms

In Figure 7, adsorption of triglycerides (TGs) and coconut oil free fatty acids (FFAs) on catalyst active sites and their activation are the primary factors governing the catalytic process of the one-step transesterification-esterification reaction for biodiesel production. The aluminosilicate (AS) catalyst's integrated Brønsted and Lewis acid sites play a critical role in the adsorption and catalytic processes. The TGs adsorbed and activated on the active sites of these catalysts are progressively converted into diacylglycerol and monoacylglycerol through a nucleophilic reaction with methanol during the transesterification process. This process results in the production of FAMEs (biodiesel), with glycerol serving as a by-product. For the esterification process, the adsorbed and activated FFAs react with methanol, resulting in the production of FAMEs and water as a by-product. Thus, these two processes are the most likely plausible mechanisms for the production of biodiesel through adsorption and catalysis.

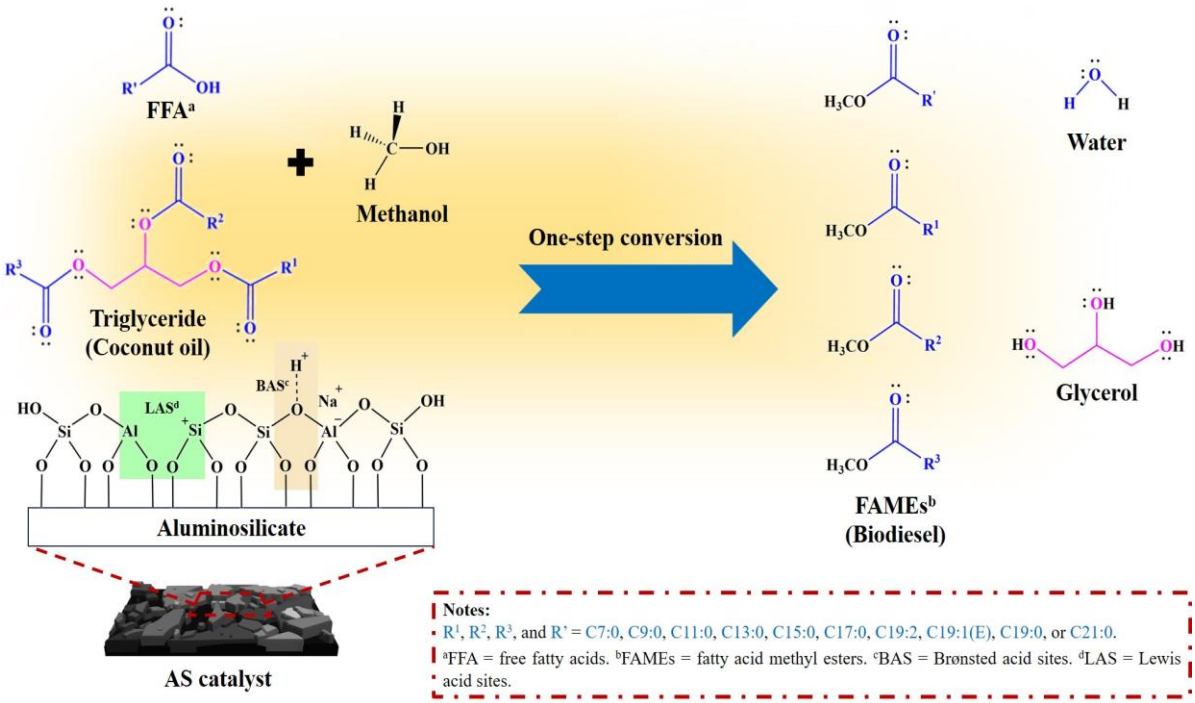

Figure 7. Proposed catalytic mechanism for biodiesel production derived from coconut oil.

In the transesterification reaction mechanism, three reversible reaction stages may occur sequentially. These phases involve the protonation (H^+) of the active site (BAS) on the AS catalyst towards one of the carbonyl groups on the coconut oil triglyceride. After the nucleophilic attack of methanol on the carbocation leading to the carbonyl group, a tetrahedral intermediate is generated. The first FAMEs and diacylglycerols are produced by the displacement of H^+ and the cleavage of these tetrahedral intermediates. The H^+ migration in each stage is bound back to the active site of the catalyst so that the catalytic process occurs continuously and repetitively (Savaliya et al., 2023). Therefore, the final products of this reaction, mixed FAMEs and glycerol, are obtained as a whole.Meanwhile, the FFA esterification reaction mechanism is purported to facilitate its interaction with the active site (LAS) on the catalyst. This reaction process involves the same stages as the transesterification

reaction in one catalytic process FAMEs and water are obtained as the final products (Guo et al., 2022). In this process, there are by-products of glycerol and water that need to be separated through washing using heated distilled water to obtain pure biodiesel products. Hence, the catalyst's characteristics, including the average crystal size, which affects the catalyst's surface area, the crystallinity, which has the potential to enhance adsorptivity, and the catalyst active sites, play an important pathways of the one-step transesterification-esterification catalytic reaction for biodiesel production.

Although the reaction mechanisms of transesterification and esterification are distinct processes, these reactions are likely to occur simultaneously and be incorporated into a one-step process. These findings highlight the importance of studying molecular interactions and catalyst characteristics in designing these reaction mechanism systems. By comprehending these factors, it may be possible to enhance of the selectivity and performance of catalysts for biodiesel production, thereby providing a promising opportunity for technological advancement in the design of catalyst materials for energy independence. Again, the experimental results obtained indicate that this catalyst has the potential to be one of the sustainable solutions for the production of biodiesel from coconut oil by offering a number of important advantages.

First, this catalyst contributes to environmental management and making it more environmentally friendly by reducing the necessity for predominantly synthetic chemicals by utilizing waste can aluminum (WCA) and rice husk silica (RHS). Second, this catalyst is capable of operating at a high efficiency with a catalyst dosage of 10 wt.% and an oil-to-methanol ratio of 1:2, thereby reducing the overall consumption of excess methanol. Third, the utilization of locally sourced WCA, RHS, and coconut oil in Indonesia not only reduces material costs but also promotes the use of sustainable, eco-friendly feedstocks. This catalyst is a practicable and environmentally favourable option in biodiesel production technology due to the combination of these features.

Comparison of the Result in This Study with Others Research

The AS-10 catalyst that was developed in this study demonstrated the highest biodiesel yield of 99.57% and a selectivity of 99.69%, indicating high-performance catalytic activity under moderate operational conditions. The AS-10 catalyst was more efficient in both yield and selectivity when compared to NiO/CaO/MgO-P (Widiarti et al., 2021) and Fe-TiO_2 (Maulidiyah et al., 2024) catalysts, as shown in Table 3. Methanol consumption can be substantially diminished by a decrease in the oil-to-methanol ratio. In summary, this minimises the total material consumption necessary for biodiesel production.

Table 3. Comparison of biodiesel production from coconut oil using various catalysts.

Catalyst	Feed : MeOH ratio	Operational conditions	Yield (%)	Selectivity (%)	Reference
AS-10	1:2	60 ºC, 6 h	99.57	99.69	This work
NiO/CaO/MgO-P	1:9	125 ºC, 3 h	89.77	99.68	Widiarti et al., 2021
NaOH	1:1	60 ºC, 6 h	80.10	-	Lugo-Méndez et al., 2021
Fe-TiO_2	5:3	UV, 3 h	30.80	-	Maulidiyah et al., 2024

This catalyst's primary advantage is its utilization of environmentally favourable raw materials, which are derived from waste can aluminum (WCA) and rice husk silica (RHS). These materials have the potential to address environmental issues, while ensuring economic feasibility. In addition, the production of sustainable and environmentally beneficial biodiesel is becoming more feasible due to the availability of local feedstock, coconut oil. The feedstock can also foster the development of local resources, contribute to the diversification of feedstocks for energy security, and align with the objectives of the SDGs. Future research should focus on the optimisation of the biodiesel production process to meet the specifications set forth by ASTM standards and pertinent regulations. Furthermore, it is imperative to conduct additional techno-economic evaluations to examine the viability and efficiency of this biodiesel production method, biodiesel, and catalyst applications in the real-world industrial sector.

Conclusion

Aluminosilicate (AS) catalysts were synthesized from waste can aluminum (WCA) and rice husk silica (RHS) with Si/Al ratios of 10, 20, and 30 using the hydrothermal method, resulting in AS-10, AS-20, and AS-30 catalysts. These catalysts have proven to be highly effective in the production of biodiesel from coconut oil,

showing outstanding performance. In particular, the performance of the AS-10 catalyst reached the highest of 99.57% with a selectivity of 99.69% compared to the other catalysts which slightly decreased in yield. This difference in catalytic performance can be attributed mainly to the catalyst characteristics. The AS-10 catalyst has an average crystal size of 5.86 nm, low crystallinity of 31.25%, and Brønsted and Lewis acid sites, all of which plausible contribute to the high catalytic performance and selectivity for biodiesel production. These characteristics are also likely to provide effectiveness in adsorption and activation towards coconut oil in the catalytic process. These findings highlight that the performance and selectivity of AS-10 catalyst for biodiesel production from coconut oil has the potential to be further developed.

Recommendations

Future research should focus on further characterization of AS catalysts synthesized from WCA and RHS in order to understand the catalyst characteristics and plausible catalytic mechanisms more comprehensively so that catalysts with good activity, selectivity, and stability can be obtained. In addition, testing this catalyst on non-edible oil is necessary to increase the diversification of feedstocks. Supporting biodiesel analysis (e.g. ^{13}C-NMR and ^{1}H-NMR analysis), as well as testing the physical and chemical properties of biodiesel according to ASTM standards and applicable regulations also need to be evaluated. Finally, studies on the scalability and environmental impact assessment of catalysts and biodiesel production processes can be conducted to ensure effectiveness, techno-economic feasibility, and sustainability for large-scale applications.

CRediT Authorship Contribution Statement

Ganjar Andhulangi: Writing – original manuscripts, Methodology, Investigation, Data curation, Software, Visualization, Project administration, Funding acquisition. *Wega Trisunaryanti:* Writing – review & editing, Supervision, Validation, Formal analysis. *Wasinton Simanjuntak & Kamisah Delilawati Pandiangan***:** Supervision, Conceptualization, Methodology, Resources, Validation, Formal analysis. *I Ilim:* Supervision, Validation, Formal analysis. *H Herliana & K Khasandra:* Investigation, Methodology, Data curation.

Scientific Ethics Declaration

* The authors declare that the scientific ethical and legal responsibility of this article published in EPSTEM Journal belongs to the authors.

Conflict of Interest

* The authors declare that they have no conflicts of interest.

Funding

* LPDP—Indonesia Endowment Fund for Education Agency supported funding for the oral presentation of this article at the International Conference on Basic Sciences, Engineering, and Technology (ICBASET) 2025.

Acknowledgements

* This article was presented as an oral presentation at the International Conference on Basic Sciences, Engineering and Technology (www.icbaset.net) held in Trabzon/Türkiye on May 01-04, 2025.

References

Al-Ani, A., Freitas, C., & Zholobenko, V. (2020). Nanostructured large-pore zeolite: The enhanced accessibility of active sites and its effect on the catalytic performance. *Microporous and Mesoporous Materials*, *293*, 109805.

Barkhuizen, D., Mabaso, I., Viljoen, E., Welker, C., Claeys, M., van Steen, E., & Fletcher, J. C. (2006). Experimental approaches to the preparation of supported metal nanoparticles. *Pure and Applied Chemistry*, *78*(9), 1759–1769.

Cao, Z., Zhang, X., Xu, C., Duan, A., Guo, R., Zhao, Z., Wu, Z., Peng, C., Li, J., Wang, X., & Meng, Q. (2016). The synthesis of al-SBA-16 materials with a novel method and their catalytic application on hydrogenation for FCC diesel. *Energy & Fuels*, *31*(1), 805–814.

Emeis, C. A. (1993). Determination of integrated molar extinction coefficients for infrared absorption bands of pyridine adsorbed on solid acid catalysts. *Journal of Catalysis*, *141*(2), 347–354.

Gardy, J., Rehan, M., Hassanpour, A., Lai, X., & Nizami, A.-S. (2019). Advances in Nano-catalysts based biodiesel production from non-food feedstocks. *Journal of Environmental Management*, *249*, 109316.

Guo, H., Cheng, J., Mao, Y., Qian, L., Shao, Y., Yang, X., & Yang, W. (2022). Acid-base bifunctional catalyst with coordinatively unsaturated cobalt-nitrogen sites for the simultaneous conversion of microalgal triglycerides and free fatty acids into biodiesel. *Bioresource Technology*, *350*, 126862.

Gould, N. S., & Xu, B. (2018). Quantification of acid site densities on zeolites in the presence of solvents via determination of extinction coefficients of adsorbed pyridine. *Journal of Catalysis*, 358, 80–88.

Katada, N. (2018). Analysis and interpretation of acidic nature of aluminosilicates. *Molecular Catalysis*, *458*, 116–126.

Kwon, E. E., Yi, H., & Jeon, Y. J. (2014). Boosting the value of biodiesel byproduct by the non-catalytic transesterification of dimethyl carbonate via a continuous flow system under ambient pressure. *Chemosphere*, *113*, 87–92.

López-Juárez, R., Razo-Perez, N., Pérez-Juache, T., Hernandez-Cristobal, O., & Reyes-López, S. Y. (2018). Synthesis of α-Al_2O_3 from aluminum cans by wet-chemical methods. *Results in Physics*, 11, 1075–1079.

Lugo-Méndez, H., Sánchez-Domínguez, M., Sales-Cruz, M., Olivares-Hernández, R., Lugo-Leyte, R., & Torres-Aldaco, A. (2021). Synthesis of biodiesel from coconut oil and characterization of its blends. *Fuel*, 295, 120595.

Maulidiyah, M., Watoni, A. H., Muzakkar, M. Z., Syawal, L. O., Irwan, I., Nurdin, M., & Umar, A. A. (2024). Fe-doped TiO_2 nanocrystals as highly efficient catalysts for heterogeneous catalytic transesterification of coconut oil. *Journal of the Taiwan Institute of Chemical Engineers*, *164*, 105705.

Mulyatun, M., Prameswari, J., Istadi, I., & Widayat, W. (2022). Production of non-food feedstock-based biodiesel using acid-base bifunctional heterogeneous catalysts: A Review. *Fuel*, *314*, 122749.

Muraoka, K., Chaikittisilp, W., & Okubo, T. (2016). Energy analysis of aluminosilicate zeolites with comprehensive ranges of framework topologies, chemical compositions, and aluminum distributions. *Journal of the American Chemical Society*, *138*(19), 6184–6193.

Nakpong, P., & Wootthikanokkhan, S. (2010). High free fatty acid coconut oil as a potential feedstock for biodiesel production in Thailand. *Renewable Energy*, *35*(8), 1682–1687.

Nayak, R. R., Khairun, H. S., Singhal, R., Bharadwaj, A. V., & Gupta, N. K. (2024). Waste-derived catalysts for sustainable biodiesel production: Current status on catalyst development and future prospectives. *Journal of the Indian Institute of Science*, 1-28.

Okada, Y., Sada, Y., Miyagi, S., Yamada, H., Ohara, K., Yanaba, Y., Yoshioka, M., Ishikawa, T., Naraki, Y., Sano, T., Okubo, T., Simancas, R., & Wakihara, T. (2025). Unraveling the relationship between aging conditions, properties of amorphous precursors and cha-type zeolite crystallization. *Microporous and Mesoporous Materials*, 381, 113099.

Pandiangan, K. D., Simanjuntak, W., Hadi, S., Ilim, I., & Amrulloh, H. (2021). Physical characteristics and utilization of ZSM-5 prepared from rice husk silica and aluminum hydroxide as catalyst for transesterification of *Ricinus communis* oil. *Materials Research Express*, 8(6), 065506.

Pratika, R. A., Wijaya, K., & Trisunaryanti, W. (2021). Hydrothermal treatment of SO_4/TiO_2 and TiO_2/CaO as heterogeneous catalysts for the conversion of jatropha oil into biodiesel. *Journal of Environmental Chemical Engineering*, 9(6), 106547.

Rahman, A., Dargusch, P., & Wadley, D. (2021). The political economy of oil supply in Indonesia and the implications for renewable energy development. *Renewable and Sustainable Energy Reviews*, *144*, 111027.

Rachmaditasari, R., Darojat, M. I., & Mahfud, M. (2024). Production of biodiesel (isopropyl ester) from coconut oil by microwave assisted transesterification: Parametric Study and Optimization. *International Journal of Renewable Energy Development*, 13(4), 662–672,

Savaliya, M. L., Tank, R. S., & Dholakiya, B. Z. (2023). Rational design of hierarchically porous sulfonic acid and silica hybrids with highly active sites for efficient catalytic biodiesel synthesis. *Chemistry of Inorganic Materials*, *1*, 100005,

Sakti La Ore, M., Wijaya, K., Trisunaryanti, W., Saputri, W. D., Heraldy, E., Yuwana, N. W., Hariani, P. L., Budiman, A., & Sudiono, S. (2020). The synthesis of SO_4/ZrO_2 and Zr/CaO catalysts via

hydrothermal treatment and their application for conversion of low-grade coconut oil into biodiesel. *Journal of Environmental Chemical Engineering*, *8*(5), 104205.

Setyawan, N., Hoerudin, & Yuliani, S. (2021). Synthesis of silica from rice husk by sol-gel method. *IOP Conference Series: Earth and Environmental Science*, *733*(1), 012149.

Simanjuntak, W., Sembiring, S., Manurung, P., Situmeang, R., & Low, I. M. (2013). Characteristics of aluminosilicates prepared from rice husk silica and aluminum metal. *Ceramics International*, *39*(8), 9369–9375.

Simanjuntak, W., Pandiangan, K. D., Sembiring, Z., Simanjuntak, A., & Hadi, S. (2021). The effect of crystallization time on structure, microstructure, and catalytic activity of zeolite-a synthesized from rice husk silica and food-grade aluminum foil. *Biomass and Bioenergy*, *148*, 106050.

Trisunaryanti, W., Triyono, Pradipta, M. F., Purbonegoro, J., & Pratiwi, A. E. (2025). Preparation and performance of 3-APTMS-modified NiO/γ-Al_2O_3 for high-efficiency biodiesel production from used palm oil. *Journal of Environmental Chemical Engineering*, *13*(3), 116149.

Wang, T., Jiao, S., Hu, W., Ishida, T., Wang, Z., Ye, J., Zheng, Y., Shi, Z., & Medepalli, S. (2023). Effects of Al/Si ratio and crystallite size on the dissolution rate of aluminosilicate glass and low-calcium scms under alkaline condition. *Materials Today Chemistry*, *33*, 101673.

Wirawan, S. S., Solikhah, M. D., Setiapraja, H., & Sugiyono, A. (2024). Biodiesel implementation in Indonesia: Experiences and future perspectives. *Renewable and Sustainable Energy Reviews*, *189*, 113911.

Widiarti, N., Bahruji, H., Holilah, H., Ni'mah, Y. L., Ediati, R., Santoso, E., Jalil, A. A., Hamid, A., & Prasetyoko, D. (2021). Upgrading catalytic activity of NiO/CaO/MgO from natural limestone as catalysts for transesterification of coconut oil to biodiesel. *Biomass Conversion and Biorefinery*, *13*(4), 3001–3015.

Author(s) Information

Ganjar Andhulangi
Universitas Gadjah Mada
Department of Chemistry, Faculty of Mathematics and Natural Sciences, Universitas Gadjah Mada, Yogyakarta, 55281, Indonesia
Contact e-mail: *ganjarandhulangi1996@mail.ugm.ac.id*

Wega Trisunaryanti
Universitas Gadjah Mada
Department of Chemistry, Faculty of Mathematics and Natural Sciences, Universitas Gadjah Mada, Yogyakarta, 55281, Indonesia

Wasinton Simanjuntak
Universitas Lampung
Department of Chemistry, Faculty of Mathematics and Natural Sciences, Universitas Lampung, Bandar Lampung, 35141, Indonesia

Kamisah Delilawati Pandiangan
Universitas Lampung
Department of Chemistry, Faculty of Mathematics and Natural Sciences, Universitas Lampung, Bandar Lampung, 35141, Indonesia

I Ilim
Universitas Lampung
Department of Chemistry, Faculty of Mathematics and Natural Sciences, Universitas Lampung, Bandar Lampung, 35141, Indonesia

H Herliana
Universitas Lampung
Department of Chemistry, Faculty of Mathematics and Natural Sciences, Universitas Lampung, Bandar Lampung, 35141, Indonesia

K Khasandra
Universitas Lampung
Department of Chemistry, Faculty of Mathematics and Natural Sciences, Universitas Lampung, Bandar Lampung, 35141, Indonesia

To cite this article:

Andhulangi, G., Trisunaryanti, W., Simanjuntak, W., Pandiangan, K.D., Ilim, I., Herliana, H., & Khasandra, K. (2025). High-performance of catalyst synthesized from waste can aluminum and rice husk silica for conversion coconut oil into biodiesel. *The Eurasia Proceedings of Science, Technology, Engineering and Mathematics (EPSTEM), 34,* 31-42.

The Eurasia Proceedings of Science, Technology, Engineering & Mathematics (EPSTEM)
ISSN: 2602-3199

The Eurasia Proceedings of Science, Technology, Engineering and Mathematics (EPSTEM), 2025

Volume 34, Pages 43-48

ICBASET 2025: International Conference on Basic Sciences, Engineering and Technology

Evaluation of the Antioxidant Activity of the Aqueous Extract of *Rosa Sempervirens* Leaves in Association with Saliva

Idir Moualek
Mouloud Mammeri University of Tizi-Ouzou

Karima Benarab
University Hospital Center of Tizi-Ouzou

Si Ammar Kadi
Mouloud Mammeri University of Tizi-Ouzou

Azeddine Mouhous
Mouloud Mammeri University of Tizi-Ouzou

Rabia Cherfouh
Mouloud Mammeri University of Tizi-Ouzou

Farid Djellal
Ferhat Abbas University of Setif

Ali Bouzourene
Mouloud Mammeri University of Tizi-Ouzou

Karim Houali
Mouloud Mammeri University of Tizi-Ouzou

Abstract: *Rosa sempervirens*, a perennial climbing shrub, is renowned for its significant antioxidant properties, primarily due to its rich polyphenolic content. The interaction between plant extracts and biological fluids such as saliva is a relatively unexplored area that could have substantial implications for the bioavailability and effectiveness of bioactive compounds. Saliva, as the first biological medium encountered during oral intake, may influence the structure and functionality of these compounds.This study aims to evaluate the impact of the association between the aqueous extract of *Rosa sempervirens* and human saliva on the plant's antioxidant potential. By examining this interaction, the research seeks to understand whether the salivary environment affects the absorption, structural integrity, or bioactivity of the extract's polyphenols. The antioxidant capacity of the extract, both before and after exposure to saliva, was assessed through various in vitro assays.Results revealed that the association between *Rosa sempervirens* extract and saliva demonstrated a potent DPPH radical scavenging activity with an IC50 value of 3.808 ± 0.126 µg/ml. The hydroxyl radical (OH) scavenging and hydrogen peroxide (H_2O_2) scavenging activities were measured, yielding IC50 values of 459.2 ± 0.126 µg/ml and 41.68 ± 0.126 µg/ml, respectively. The ferrous ion chelating activity presented an IC50 of 1064.159 ± 0.126 µg/ml, indicating moderate chelation capability. The ferric reducing antioxidant power (FRAP) and total antioxidant capacity (TAC) assays further validated the antioxidant efficacy of the association, with IC50 values of 47.5 ± 0.126 µg/ml and 358.2 ± 0.126 µg/ml, respectively.These results underscore the potential influence of saliva on the antioxidant properties of *Rosa sempervirens* extract, highlighting the need to consider the oral phase in the evaluation of polyphenol-rich plant extracts. Further

- Selection and peer-review under responsibility of the Organizing Committee of the Conference

investigation into the biochemical pathways of these interactions could provide new insights into optimizing the therapeutic applications of *Rosa sempervirens* in antioxidant therapies.

Keywords: *Rosa sempervirens*, Saliva Interaction, Antioxidant Activity, Polyphenols, Radical Scavenging, Traditional Medicine.

Introduction

Medicinal plants are a valuable source of bioactive molecules with well-documented therapeutic properties, particularly in the prevention of oxidative stress. Among them, *Rosa sempervirens*, a species of the Rosaceae family, is known for its high polyphenol content, bioactive compounds involved in various biological processes, including the neutralization of reactive oxygen species (ROS). The growing interest in these compounds stems from their ability to mitigate oxidative and inflammatory damage, providing a promising alternative to synthetic antioxidants, whose safety has raised concerns (Velioglu et al., 1998).

While the antioxidant properties of plant extracts have been extensively studied in vitro, their behavior in complex biological environments, such as saliva, remains poorly understood. Saliva is the first biological fluid that polyphenols encounter upon ingestion, potentially influencing their stability, bioavailability, and biological activity. Recent studies suggest that interactions between polyphenols and salivary proteins may alter their antioxidant properties, either by stabilizing them or modifying their chemical reactivity (Zhang et al., 2021).

In this context, the present study aims to evaluate the impact of the association between the aqueous extract of *Rosa sempervirens* and human saliva on the plant's antioxidant potential. The objective is to determine whether the salivary environment influences the absorption, structural integrity, and biochemical activity of the polyphenols present in the extract. To achieve this, several in vitro assays were conducted to analyze the radical-scavenging activity and metal-chelating capacities of this association.

Materials and Methods

Plant Collection

Rosa sempervirens leaves were collected in October 2023 from Larbaa Nath Irathen, Algeria. The plant was identified by Doctor Mahmoud Laribi, botanist at Mouloud Mammeri University of Tizi-Ouzou, department of vegetal biology, where a voucher specimen was deposited (FSBSA/MK/30oct8423). The sample was dried and then ground to obtain a powder that was stored at room temperature and in the dark until extraction.

Extract Preparation

20g of powder are dissolved in 200ml of distilled water. After 24 hours of maceration at room temperature, the filtrate was lyophilized.

Determination of DPPH Radicals Scavenging Activity

The free radical scavenging activity of the extract was measured using the stable free radical DPPH test according to the method described by (Sharma & Bhat, 2009; Santos et al., 2010). 250 µl of 0.8 mM DPPH in ethanol was mixed with 3.65 ml of extract and 100µl of Saliva. The reaction was carried out in triplicate and the absorbance was measured at 517nm after 30 minutes in dark. L-Ascorbic acid was used as reference standard.

Hydroxyl Radical Scavenging Assay

Scavenging activity of hydroxyl radical of the extract was measured according to the method of (Rajamanikandan et al., 2011) Three millilitres of the final reaction solution consisted of aliquots (500 µl) of various concentrations of the extract,100µl of Saliva, 1ml FeSO4 (1.5 mM), 0.7 ml hydrogen peroxide (6 mM) and 0.3 ml sodium salicylate (20 mM). The reaction mixture was incubated for 1 h at 37°C. L-Ascorbic acid was used as the standard. The colour development was measured at 560 nm against a blank.

Hydrogen Peroxide Radical Scavenging Activity

The scavenging ability of water extract of *Rosa sempervirens* on hydrogen peroxide was determined according to the method of (Serteser et al., 2009). A solution of hydrogen peroxide (40 mM) was prepared in phosphate buffer (pH 7.4). Saliva (100µl) and extract in distilled water (3.4 ml) was added to a hydrogen peroxide solution (0.6 ml, 40mM). Absorbance of hydrogen peroxide at 230 nm was measured 10 minutes later against a blank solution containing the phosphate buffer without hydrogen peroxide.

Ferrous Ion Chelating Activity

Ferrous ion chelating activity was determined by inhibition of the formation of iron (II)–ferrozine complex, following the method of (Dinis et al., 1994; Nabavi et al., 2012). Briefly, 100 µl of 0.6 mM $FeCl_2$ was added to 500µl of different concentrations of the extract mixed with 100µl of Saliva or EDTA (positive control). The reaction mixture was adjusted to a final volume of 1.5ml with methanol, and then 100µl of 5 mM ferrozine solution were added. The mixture was shaken vigorously and left to stand at room temperature for 5 min. Absorbance was determined at 562nm.

Ferric Reducing Power Assay

Reducing power was determined by the method described by (Oyaizu, 1986; Hazra et al., 2008). Different concentrations of extract and Saliva were mixed with 1.25 ml of 0.2 M, pH 6.6 sodium phosphate buffer and 1.25 ml of potassium ferricyanide (1%). The mixture was incubated at 50°C for 20 min. After incubation, the reaction mixture was acidified with 1.25 ml of trichloroacetic acid (10%) and centrifuged at 3000 rpm for 10 min. Finally, 0.5 ml of freshly prepared FeCl3 (0.1%) was added to this solution, and the absorbance was measured at 700nm. Aascorbic acid at various concentrations was used as standard.

Total Antioxidant Capacity

Total antioxidant capacity was estimated by phosphomolybdenum assay (Prieto et al., 1999; Rao et al., 2010) The tubes containing extract and Saliva and reagent solution (0.6 M sulfuric acid, 28 mM sodium phosphate and 4 mM ammonium molybdate) were incubated at 95°C for 90 min. Then the solution was cooled to room temperature and absorbance was read at 695 nm. Ascorbic acid was used as standard.

Results and Discussion

Table 1 presents the percentage inhibition of DPPH radical scavenging activity by the samples tested. The IC50 value, representing the concentration required to scavenge 50% of DPPH radicals, was used to compare the antioxidant potential of different samples. The IC50 of the standard (ascorbic acid) was 2.359 ± 0.091 µg/ml, significantly lower than that of *Rosa sempervirens* (IC50 = 6.201 ± 0.126 µg/ml). However, when associated, the antioxidant activity improved notably, with an IC50 value of 3.808 ± 0.126 µg/ml, indicating enhanced scavenging capacity.

Table 1. IC50 values for antioxidant activities of rosa sempervirens, its association, and standard compounds

IC50 Test	**Standard**	***Rosa sempervirens***	***Association***
DPPH radicals scavenging activity	2.359 ±0.091 µg/ml	6.201 ± 0.126 µg/ml	3.808 ± 0.126 µg/ml
Hydroxyl radical scavenging assay	758.83 ±7.40 µg/ml	894.57 ± 21.18 µg/ml	459.2± 0.126 µg/ml
Hydrogen peroxide radical scavenging activity	49.19 ± 2.70 µg/ml	107 ± 9.58 µg/ml	41.68± 0.126 µg/ml
Ferrous ion chelating activity	57.21 ± 0.44 µg/ml	2499.086±28.267 µg/ml	1064.159±0.126 µg/ml
Ferric reducing power assay	56.72±2.79 µg/ml	141.33±2.34 µg/ml	47.5± 0.126 µg/ml
Total antioxidant capacity	292 ± 7.54 µg/ml	465.65 ± 9.71 µg/ml	358.2± 0.126 µg/ml

DPPH Scavenging Activity

Hydroxyl Radical Scavenging Assay

The ability of *Rosa sempervirens* to scavenge hydroxyl radicals was assessed, with salicylic acid as a reference. As shown in Table 1, ascorbic acid demonstrated the most effective scavenging ability (IC50 = 758.83 ± 7.40 µg/ml), whereas *Rosa sempervirens* exhibited an IC50 of 894.57 ± 21.18 µg/ml. The association resulted in a significant improvement, achieving an IC50 of 459.2 ± 0.126 µg/ml, which is considerably more effective than *Rosa sempervirens* alone and ascorbic acid.

Hydrogen Peroxide Radical Scavenging Activity

The scavenging activity against hydrogen peroxide varied among the samples. Ascorbic acid showed the strongest activity (IC50 = 49.19 ± 2.70 µg/ml), while *Rosa sempervirens* alone had a higher IC50 (107 ± 9.58 µg/ml), indicating less scavenging potential. The association further enhanced the activity, reducing the IC50 to 41.68 ± 0.126 µg/ml.

Ferrous Ion Chelating Activity

The ferrous ion chelating activity was measured, with EDTA serving as the reference (IC50 = 57.21 ± 0.44 µg/ml). *Rosa sempervirens* displayed a higher IC50 of 2499.086 ± 28.267 µg/ml, suggesting lower chelating activity. The association improved the chelating effect, with an IC50 of 1064.159 ± 0.126 µg/ml, indicating better efficacy than Rosa sempervirens alone.

Ferric Reducing Power Assay

The ferric reducing power of the samples was assessed. The IC50 of Rosa sempervirens was 141.33 ± 2.34 µg/ml, indicating lower reducing capacity compared to the standard (56.72 ± 2.79 µg/ml). The association demonstrated an enhanced reducing power, with an IC50 of 47.5 ± 0.126 µg/ml.

Total Antioxidant Capacity

The total antioxidant capacity, determined by the reduction of Mo (VI) to Mo (V), showed ascorbic acid with the strongest capacity (IC50 = 292 ± 7.54 µg/ml). Rosa sempervirens alone presented an IC50 of 465.65 ± 9.71 µg/ml, while the association improved this to 358.2 ± 0.126 µg/ml, indicating a synergistic effect on the antioxidant potential. The combination of *Rosa sempervirens* with Saliva demonstrated a remarkable synergy in the inhibition of free radicals, notably DPPH● and OH●. This improvement in free radical scavenging capacity can be attributed to several factors:

The polyphenols present in *Rosa sempervirens* probably interact with the thiol residues (Cys-34) of Saliva. These residues play a crucial role in the scavenging of reactive oxygen species (ROS), thereby increasing the overall efficiency of radical scavenging (Colombo et al., 2012).

Saliva can act as a redox buffer, stabilizing polyphenols in biological environments and extending their half-life under physiological conditions (Zhang et al., 2021). This stabilization could explain the observed increase in antioxidant activity.

The hydroxyl radical, considered the most reactive of the free radicals, is particularly well neutralized by this combination. This is significant given its ability to interact with intracellular targets such as DNA, causing significant damage (Lushchak, 2014).

In contrast to the synergistic effect observed for free radical scavenging, the combination with Saliva showed a negative impact on metal ion chelation capacity and iron reduction. This phenomenon can be explained by :

Saliva, as a carrier protein, has metal-binding sites that can compete with *Rosa sempervirens* polyphenols for the chelation of metal ions, particularly Fe2+ (Sugio et al., 1999).

This competition may limit the availability of metal ions to be sequestered by the extract's polyphenols, thus reducing the overall efficiency of iron chelation and reduction.This result highlights the importance of considering the relative concentration of proteins and polyphenols in optimizing the overall antioxidant effect.

Conclusion

This preliminary study highlights the promising potential of the combination of *Rosa sempervirens* aqueous extract and Saliva. The results show a significant improvement in certain antioxidant activities, notably free radical scavenging and cell membrane protection, although a moderate impact was observed on metal chelation and iron reduction capacities.

The synergy observed in membrane stabilization and anti-inflammatory activity underlines the protective role of this combination against oxidative damage and inflammatory processes. The interactions between *Rosa sempervirens* polyphenols and Saliva appear to enhance the bioactivity of the plant extracts, making this combination promising for future therapeutic applications, particularly in the fight against oxidative stress and inflammation.

However, the complexity of the interactions observed, with variable effects depending on the tests carried out, highlights the need for further research. It would be pertinent to explore in greater detail the molecular mechanisms underlying these interactions, to optimize the relative concentrations of extract and Saliva, and to conduct *in vivo* studies to confirm these beneficial effects under physiological conditions.In conclusion, this study opens up interesting prospects for the combined use of *Rosa sempervirens* and Saliva in the development of new antioxidant and anti-inflammatory strategies, while underlining the importance of a nuanced approach to the interpretation of interactions between natural compounds and proteins.

Scientific Ethics Declaration

* The authors declare that the scientific ethical and legal responsibility of this article published in EPSTEM Journal belongs to the authors.

Conflict of Interest

* The authors declare that they have no conflicts of interest

Funding

* This research received no specific grant from any funding agency in the public, commercial, or not-for-profit sectors.

Acknowledgements

* This article was presented as an oral presentation at the International Conference on Basic Sciences, Engineering and Technology (www.icbaset.net) held in Trabzon/Türkiye on May 01-04, 2025.

References

Colombo, G., Clerici, M., Giustarini, D., Rossi, R., Milzani, A., & Dalle-Donne, I. (2012). Redox albuminomics: oxidized albumin in human diseases. *Antioxidants & Redox Signaling*. *17*(11), 1515-1527.

Dinis, T. C., Madeira, V. M., & Almeida, L. M. (1994). Action of phenolic derivatives (acetaminophen, salicylate, and 5-aminosalicylate) as inhibitors of membrane lipid peroxidation and as peroxyl radical scavengers. *Archives of Biochemistry and Biophysics, 315*(1), 161-169.

Hazra, B., Biswas, S., & Mandal, N. (2008). Antioxidant and free radical scavenging activity of Spondias pinnata. *BMC complementary and Alternative Medicine, 8*(1), 63.

Lushchak, V. I. (2014). Free radicals, reactive oxygen species, oxidative stress and its classification. *Chemico-Biological Interactions, 224*, 164-175.

Nabavi, S., Hellio, C., Alinezhad, H., Zare, M., Azimi, R., & Baharfar, R. (2012). Antioxidant and Antioxidant and of methanol extract of Hyssopus angustifolius. *Journal of Applied Botany and Food Quality, 85*, 1-4.

Oyaizu, M. (1986). Studies on products of browning reaction. *The Japanese Journal of Nutrition and Dietetics, 44*(6), 307-315.

Prieto, P., Pineda, M., & Aguilar, M. (1999). Spectrophotometric quantitation of antioxidant capacity through the formation of a phosphomolybdenum complex: Specific application to the determination a phosphomolybdenum E. *Analytical Biochemistry, 269*(2), 337-341.

Rajamanikandan, S., Sindhu, T., Durgapriya, D., Sophia, D., Ragavendran, P., & Gopalakrishnan, V. K. (2011). Radical scavenging and antioxidant activity of ethanolic extract of Mollugo nudicaulis by invitro assays. *Indian Journal of Pharmaceutical Education and Research, 45*(4), 310-316.

Rao, A. S., Reddy, S. G., Babu, P. P., & Reddy, A. R. (2010). The antioxidant and antiproliferative activities of methanolic extracts from Njavara rice bran. *BMC Complementary and Alternative Medicine, 10*(1), 4.

Santos, S. A., Pinto, P. C., Silvestre, A. J., & Neto, C. P. (2010). Chemical composition and antioxidant activity of phenolic extracts of cork from Quercus suber L. *Industrial Crops and Products, 31*(3), 521-526.

Serteser, A., Kargıoglu, M., Gok, V., Bagci, Y., Ozcan, M. M., & Arslan, D. (2009). Antioxidant properties of some plants growing wild in Turkey. *Grasas Y Aceites, 60*(2), 147-154.

Sharma, O. P., & Bhat, T. K. (2009). DPPH antioxidant assay revisited. Food chemistry, 113(4), 1202-1205.

Sugio, S., Kashima, A., Mochizuki, S., Noda, M., & Kobayashi, K. (1999). Crystal structure of human serum albumin at 2.5 a resolution. *Protein Engineering, 12*(6), 439-446.

Velioglu, Y. S., Mazza, G., Gao, L., & Oomah, B. D. (1998). Antioxidant activity and total phenolics in selected fruits, vegetables, and grain products. *Journal of Agricultural and Food Chemistry, 46*(10), 4113-4117.

Zhang, C., Guan, J., Zhang, J., Yang, J., Wang, X., & Peng, X. (2021). Protective effects of three structurally similar polyphenolic compounds against oxidative damage and their binding properties to human serum albumin. *Food Chemistry, 349*, 129118.

Author(s) Information

Idir Moualek
Mouloud Mammeri University of Tizi-Ouzou,
Algeria
Contact e-mail: *moualek_idir@yahoo.fr*

Karima Benarab
University Hospital Center of Tizi-Ouzou,
Algeria

Si Ammar Kadi
Mouloud Mammeri University of Tizi-Ouzou,
Algeria

Azeddine Mouhous
Mouloud Mammeri University of Tizi-Ouzou,
Algeria

Rabia Cherfouh
Mouloud Mammeri University of Tizi-Ouzou,
Algeria

Farid Djellal
Ferhat Abbas University of Setif
Algeria

Ali Bouzourene
Mouloud Mammeri University of Tizi-Ouzou,
Algeria

Karim Houali
Mouloud Mammeri University of Tizi-Ouzou,
Algeria

To cite this article:

Moualek, I., Benarab, K., Kadi, S.A., Mouhous, A., Cherfouh, R., Djellal, F., Bouzourene, A., & Houali, K. (2025). Evaluation of the antioxidant activity of the aqueous extract of *rosa sempervirens* leaves in association with saliva. *The Eurasia Proceedings of Science, Technology, Engineering and Mathematics (EPSTEM), 34,* 43-48.

The Eurasia Proceedings of Science, Technology, Engineering & Mathematics (EPSTEM)
ISSN: 2602-3199

The Eurasia Proceedings of Science, Technology, Engineering and Mathematics (EPSTEM), 2025

Volume 34, Pages 49-57

ICBASET 2025: International Conference on Basic Sciences, Engineering and Technology

Synthesis, Molecular Docking and in Silico ADME Prediction of 2-Benzoylamino-*N*-Phenyl-Benzamide Derivatives

Karima Ighilahriz
Mouloud Mammerie University of Tizi-Ouzou

Amina Benazzouz –Touami
Mouloud Mammerie University of Tizi-Ouzou

Malika Makhloufi-Chebli
Mouloud Mammerie University of Tizi-Ouzou

Noura Kichou
Mouloud Mammerie University of Tizi-Ouzou

Abstract: 2-Benzoylamino-*N*-phenyl-benzamide derivatives (3a–h) were synthesized starting from 2-phenyl-3,1-(4*H*)-benzoxazin-4-one and substituted anilines in the presence of acid as catalysts. The reaction were conducted without under solvent-free condition and microwave irradiation, offering an efficient and environmentally friendly synthetic approache. The compound structures were established by NMR (including extensive 2D NMR analysis). Additionally, structure–activity relationship study was performed to establish correlation between the chemical structures and their potential biological activities. Physicochemical properties of the compounds were analized, and their pharmacokinetic profiles ADME were predicted using in silico tools. these assessment included predictions of bioavailability drug-likeness levels, showing that several of the derivatives exhibited acceptable and favorable properties for pharmaceutical application. The drug-likness further supported suitability as drug candidates. Finally, molecular docking was studies were carried out to investigate the interactions of these compounds with biological targets. The docking results highlighted promising binding for certain derivatives, suggesting their potential as effective therapeutic agents. Overall, this study demonstates the successful design and synthesis of novel benzamide derivatives with encouraging pharmacological profiles for future drug development.

Keywords: Benzoylamino-*N*-phenyl-benzamides, ADME, Molecular docking

Introduction

In December 2019, the SARS-CoV-2-caused coronavirus illness 2019 (COVID-19) outbreak sparked a global health concern. It is a member of the coronavirus family of single-stranded positive-sense RNAs (Lo et al., 2020). Its genome consists of different regions including a spike protein (S) gene, an envelope protein (E) gene, a membrane protein (M) gene, and a nucleocapsid protein (N) gene (Zhu et al., 2020). ,e sequence of SARS-CoV-2 showed more than 50% identity to SARS-CoV and MERS-CoVandcloserrelationto bat-SL-CoVZC45 (Chan et al., 2020).

SARS-CoV produces several functional proteins while its main protease is emerging as a promising therapeutic target as it is responsible for the processing of translated polyprotein. ,us, inhibition of the main protease was confirmed to affect the viral replication (Yamamoto et al., 2020). Its high sequence conservation with SARS-CoV main protease suggests the effectiveness of HIV-1 protease in hibitors such as nelfinavir against it (Wu &

- Selection and peer-review under responsibility of the Organizing Committee of the Conference

McGoogan, 2020). SARS-CoV-2 shares the mode of transmission with SARS-CoV and MERS-CoV, after which it binds to ACE2 on the surface of host cells via the receptor-binding domain (RBD) in its spike proteins (Li, 2016). Blocking the ACE2 and RBD interaction by antibodies and inhibitors would be an effective way to stop the virus infection (Chung et al., 2004).

Symptoms of COVID-19 greatly resembled viral pneumonia ranging from mild to more severe eventually ending in several organ malfunction (Wu & McGoogan, 2020). Discovery of effi cacious drugs for this deadly disease could be achieved by one of the three options: testing the existing antiviral drugs which are already used to treat viral infections, secondly, screening of different existing drugs, and finally, discovery of new specific drugs based on the individual coronavirus genome (Lu et al., 2020). Chloroquine, HIV protease inhibitors, ACE-2 inhibitors, and many other drugs were predicted to be COVID-19 drug candidates (Maxmen et al., 2020).

Benzamides and their derivatives have garnered considerable attention due to their significant biological activities. A wide array of benzamide derivatives, often incorporated into clinically relevant drug candidates, exhibit notable pharmacological properties. These include anticonvulsant (Foster et al., 1999), Anti-inflammatory (Caliendo et al., 2001), Analgesic (Carnson et al., 2004), Antitumor (Xu et al., 2006) Antimicrobial (Sener et al., 2002) and antiviral activity (Chen et al., 2013). Particularly, *N*-phenylbenzamide derivatives have demonstrated a variety of applications, with several showing promising antiviral properties (Ji, X.Y., et al., 2013). It is therefore imperative to test their effectiveness in COVID-19.

Computational methods are commonly used for structure-based drug discovery (SBDD) and ligand-based drug discovery (LBDD) (Wakui et al., 2018). Since they accelerate the lengthy drug discovery and development process, recently, they have been extensively used for lead discovery against COVID-19 by virtually screening compounds with potential biological activity (Elmezayen et al., 2020). However, few studies were directed towards the discovery of multitarget drugs (Joshi et al., 2020). The present study computationally assesses the inhibitory effects of Benzoylamino-*N*-phenyl-benzamides on two potential SARS-CoV-2 drug targets and predicts their pharmacokinetics identifying promising candidates against COVID-19.

Method

Experimental Method

The melting points were take ninan open capillary tube using an Electrothermal melting point apparatus (Electrotermal, Rochford, GreatBritain). Thevaluesare reportedin Candareuncorrected. 1H and 13C NMR spectra were recorded in DMSO-d6 solutions on Bruker Avance 300 (300.13 MHz for 1H and 75.47 MHz for 13C) spectrometer. Chemical shifts are reported in parts per million (d, ppm) using TMS as internal reference and coupling constants (J) are given in hertz (Hz). 13C assignments were made using NOESY, HSQC, and HMBC (delays for one bond and long-range JC/H couplings were optimized for 145 and 7 Hz, respectively) experiments.

Computational Method

The crystal structure of the target protein for the COVID-19 study (PDB ID: 6LU7) was retrieved from the Protein Data Bank (PDB) in its 3D format. Protein structure refinement was carried out using Discovery Studio software. Prior to molecular docking, both the target proteins and the synthesized ligands were prepared using AutoDock Tools. This preparation process included energy minimization, addition of charges, incorporation of polar hydrogens, and the generation of a grid box. A grid-based docking approach was employed, with carefully defined dimensions and spacing to accurately model the active sites. The docking grid was centered at the coordinates X = -10.712, Y = 12.411, and Z = 68.831, with a grid spacing of 0.375 Å, enabling detailed exploration of the binding domain.

In Silico ADME Prediction

In silico predictive models play a crucial role in modern drug discovery by providing early estimations of the ADME (Absorption, Distribution, Metabolism and Excretion) profiles of compounds. These predictions help researchers evaluate the potential safety and efficacy of new drugs before they enter costly and time-consuming

in vitro or in vivo testing phases. Thus, SwissADME server was used to predict the ADME profile of the tested compounds.

Synthesis

A mixture of the appropriate 2-phenyl-1,3-(*4H)*-benzoxazin-4-one 1 and amines (10 mmol) was added the catalyst heteropolyacid (1.2 mol %). This mixture was heated by microwave, initially set to 300 W for 3 min and then it was increased to 450 W for 10 min. The obtained solid was washed by the water to eliminate acid.

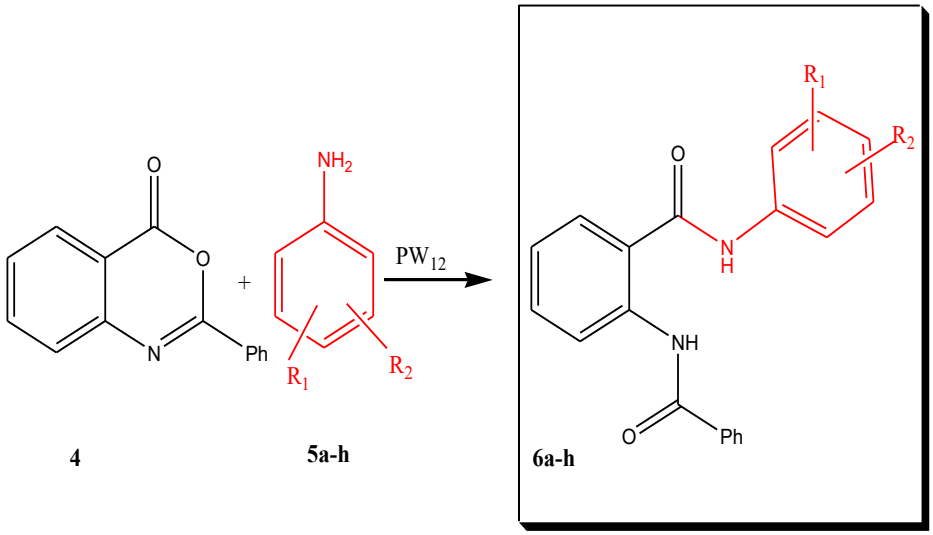

Scheme 1. Synthesis of 2-Benzoylamino-*N*-phenyl-benzamide derivatives

Results and Discussion

Caracterization

The 2-Benzoylamino-*N*-phenyl-benzamide derivatives 3a-h were prepared in good yields (65-92 %) (Ighilahriz et al., 2017). It was found that yields of products 3 depend on the nature substituent groupe aniline. the presence of electron donating groups led to a yield increase. se. With methyl and hydroxy groups in C_6H_4, the yields are 85% and 92%, respectively, against 80% for the phenyl. These groups are beneficial because of their high electron density, induced by the aromatic system unlike, the electron chloro, which led to a yield decrease from 80% to 78%. The presence of a second chlorine atom in the aniline also led to a yield decrease from 78% to 65%. Among dichloroanilines, 2,4-dichloro-C_6H_3 gave the better yield (73% against 65–70%). This decrease is attributed to the group steric effect (Table 1).

Table 1. Melting points Mp and yields of compounds 3a-h.

Compounds	ArNH	Yields (%)	Melting points (^{0}C)
3a	C_6H_5	80	281
3b	4-CH_3-C_6H_4	85	123
3c	4-OH-C_6H_4	92	160
3d	4-Cl-C_6H_4	80	161
3e	2,4-Cl_2- C_6H_3	75	140
3f	2,5-Cl_2- C_6H_3	70	167
3g	2,6-Cl_2- C_6H_3	65	162
3h	3,4-Cl_2- C_6H_3	70	192

Structures of all prepared compounds were confirmed by, IR, NMR (including extensive 2D NMR analysis, such as HSQC, HMBC, and NOESY) and elemental analysis analysis. The IR spectrum also confirms the structure of compounds 3a-h by the appearance of two characteristic bands at 1647-1674 cm-1 and 2925-3393 cm-1 corresponding to the carbonyl and imine functions, respectively (Table 2).

Table 2. IR bands for the compounds 3a-h as KBr pellets.

Compounds \ Fonction	ν C=O	υC=N
3a	1647	3280
3b	1650	2935
3c	1698	3010
3d	1660	2925
3e	1667	3293
3f	1647	3286
3g	1674	3300
3h	1647	3273

In order to clarify the structures of the synthesised compounds, 2D NMR (HMBC) analyses of compound (3d) have been selected as examples. The HMBC (heteronuclear multiple bond correlation) spectrum identifies long-range couplings between protons and carbons via two or three chemical bonds. HMBC analysis of compound 3d shows correlations between H-8 and the amide C7, confirming condensation. Additionally, correlations between H-6 and C1, C2, and C7, as well as H-2' and C1', support the proposed structure of compound 3d.

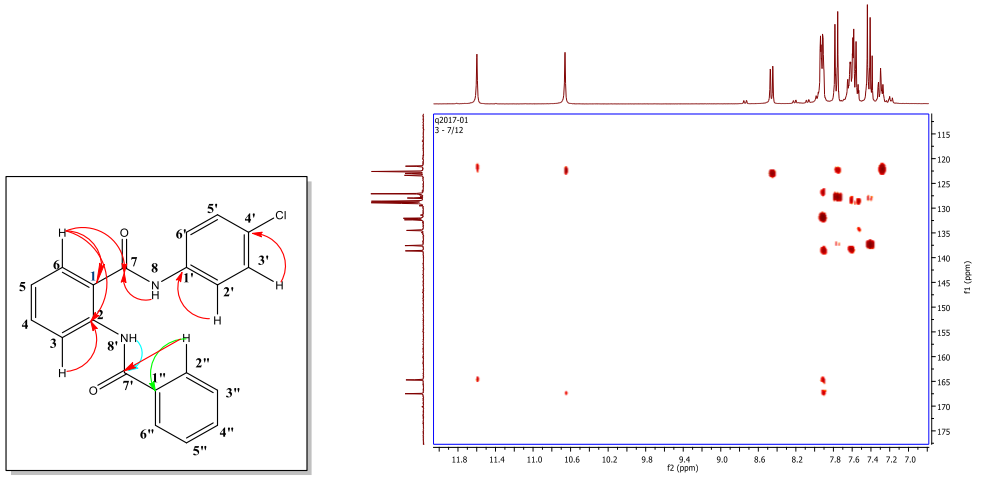

Figure 1. The HMBC spectra and connectivities of 3d

The structures of the synthesised compounds 3a-d were further confirmed by and elemental analysis (Table 3).

Table 3. Elemental analysis data for the compounds 3a-h.

Compounds	Chemical formula	Elemental analysis Calcd. %	Elemental analysis Found%
3a	$C_{20}H_{16}N_2O_2$	C 76.13, H 5.25, N 8.98, O 9.63	C 75.93, H 5.10, N 8.86, O 10.11
3b	$C_{21}H_{18}N_2O_2$	C 76.55, H 5.60, N 8.53, O 9.31	C 76.43, H 5.49, N 8.48, O 9.69
3c	$C_{20}H_{16}N_2O_3$	C 72.50, H 4.96, N 8.49, O 14.04	C 72.28, H 4.85, N 8.43, O 14.44
3d	$C_{20}H_{15}ClN_2O_2$	C 68.55, H 4.36, Cl 10.13, N 7.39, O 9.57	C 68.48; H 4.31, Cl 10.11, N 7.99, O 9.12
3e	$C_{20}H_{14}Cl_2N_2O_2$	C 62.50, H 3.71, Cl 18.48, N 7.37, O 7.94	C 62.34, H 3.66, Cl 18.41, N 7.27, O 8.31
3f	$C_{20}H_{14}Cl_2N_2O_2$	C 62.50, H 3.71, Cl 18.48, N 7.37, O 7.94	C 62.34, H 3.66, Cl 18.41, N 7.27, O 8.31
3g	$C_{20}H_{14}Cl_2N_2O_2$	C 62.50, H 3.71, Cl 18.48, N 7.37, O 7.94	C 62.34, H 3.66, Cl 18.41, N 7.27, O 8.31
3h	$C_{20}H_{14}Cl_2N_2O_2$	C 62.50, H 3.71, Cl 18.48, N 7.37, O 7.94	C 62.34, H 3.66, Cl 18.41, N 7.27, O 8.31

Binding Mode of Studied Compounds

The active site of the enzyme is formed by His41, Met49, Phe140, Leu141, Asn142, Gly143, His163, His164, Met165, Glu166, Leu167, Pro168, His172, Gln189, Thr190, and Ala191. The amino acid residues His41 and

Cys145 constitute a catalytic dyad within the active site, located between domain I and domain II (Pratama et al., 2020). The docking results demonstrate that all ligands are anchored within the catalytic site, engaging specifically with the dyad formed by His41 and Cys145, with binding energies ranging from -8.4 kcal/mol to -6.5 kcal/mol. Stabilization of the ligand–protein complexes is primarily mediated by hydrogen bonds involving Cys145, Leu4, and Ser144 for compounds 3a, 3b, 3d, 3f, and 3g; Phe140 for compound 3c; and Thr26 for compound 3h.

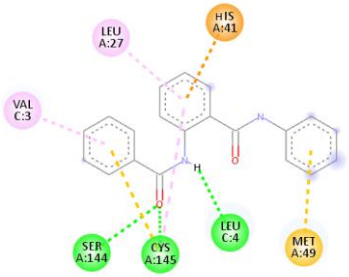

3a, *E=-8.1 Kcal/mol*

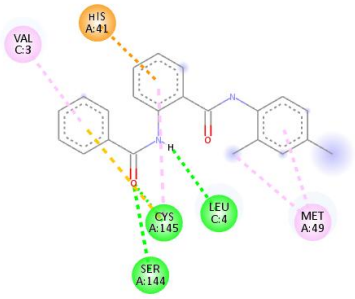

3e, *E=-8.3 Kcal/mol*

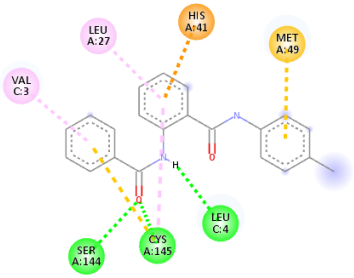

3b, *E=-8.2Kcal/mol*

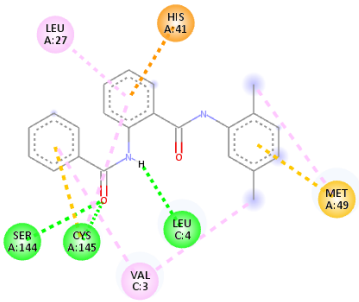

3f, *E=-8.3 Kcal/mol*

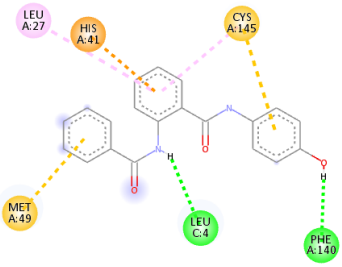

3c, *E=-7.5Kcal/mol*

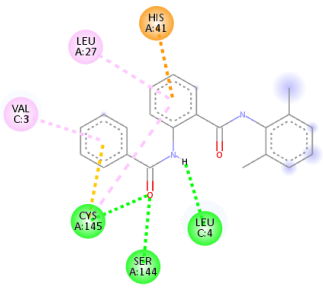

3g, *E=-7.9Kcal/mol*

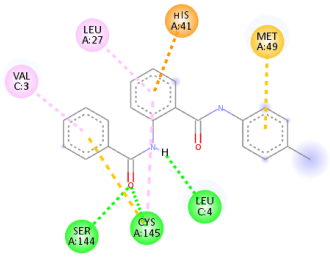

3d, *E=-8.1Kcal/mol*

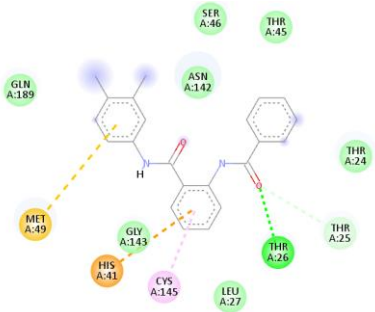

3h, *E=-6.5 Kcal/mol*

Figure 2. Promising 2-Benzoylamino-*N*-phenyl-benzamide derivatives in the active site of SARS-CoV-2 main protease (PDB ID: 6LU7).

Importantly, for all evaluated ligands, both residues of the catalytic dyad (His41 and Cys145) participate in multiples types of non-covalent interactions, including hydrophobic contacts and electrostatic interactions, underscoring their critical role in ligand binding.

In the active site of the receptor macromolecule 6LU7, the best binding conformations of compounds 3a–h were observed. The superimposition reveals that all the molecules are located within the active site cavity, indicating their direct interaction with the catalytic residues.

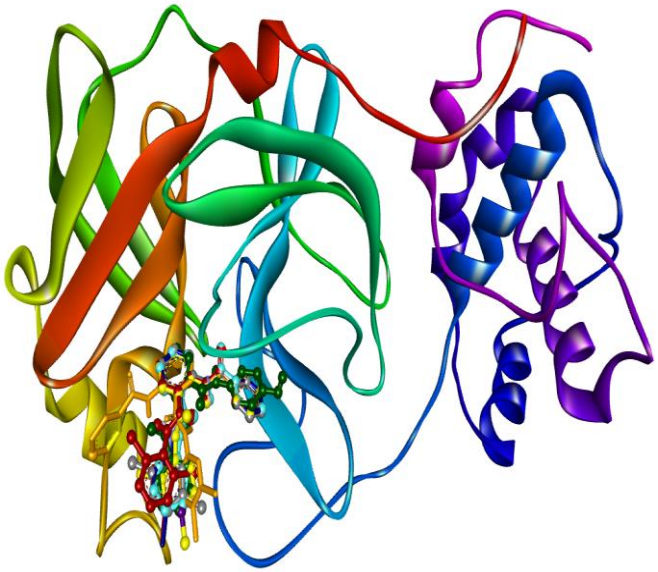

Figure 3. Superimposition of docked conformations of the compounds, **3a-h** on the crystal structure protein 6LU7.

The candidate compounds 3a–h were further evaluated for their predicted pharmacokinetic and physicochemical properties profiles using the freely accessible web-based tool SwissADME. Analyzing the ADME properties (Absorption, Distribution, Metabolism and Excretion) of the target compounds provides crucial information to guide the selection of the most promising drug candidates. The Veber and Lipinski guidelines were applied to predict the oral drug-likeness of the compounds, with all candidates complying except for a single violation of Veber's rule (TPSA > 140 Å²). The bioavailability radar plots showed that, apart from slight deviations in polarity and saturation, the evaluated 2-Benzoylamino-*N*-phenyl-benzamide derivatives (3a–h) fell within the optimal range (pink area) for key parameters including solubility, lipophilicity, flexibility, and molecular size (Fig. 4). These findings provide strong evidence supporting the potential oral bioavailability of the investigated compounds.

In Silico ADME Prediction

Table 3. Calculated physicochemical characteristics of 2-Benzoylamino-*N*-phenyl-benzamide derivatives 3a–h.

Compounds	MW g/mol	TPSA Å²	nRB	nHBA	nHBD	MlogP	Violation
Rule	≤500	≤140	≤10	≤10	≤5	≤4.15	-
3a	316.35	58.20	6	2	2	2.59	yes
3b	330.38	58.2	6	2	2	2.61	yes
3c	332.35	78.43	6	3	3	2.15	yes
3d	350.80	58.20	6	2	2	2.96	yes
3e	385.24	58.20	6	2	2	2.91	yes
3f	385.24	58.20	6	2	2	2.91	yes
3g	385.24	58.20	6	2	2	2.91	yes
3h	385.24	58.20	6	2	2	2.91	yes

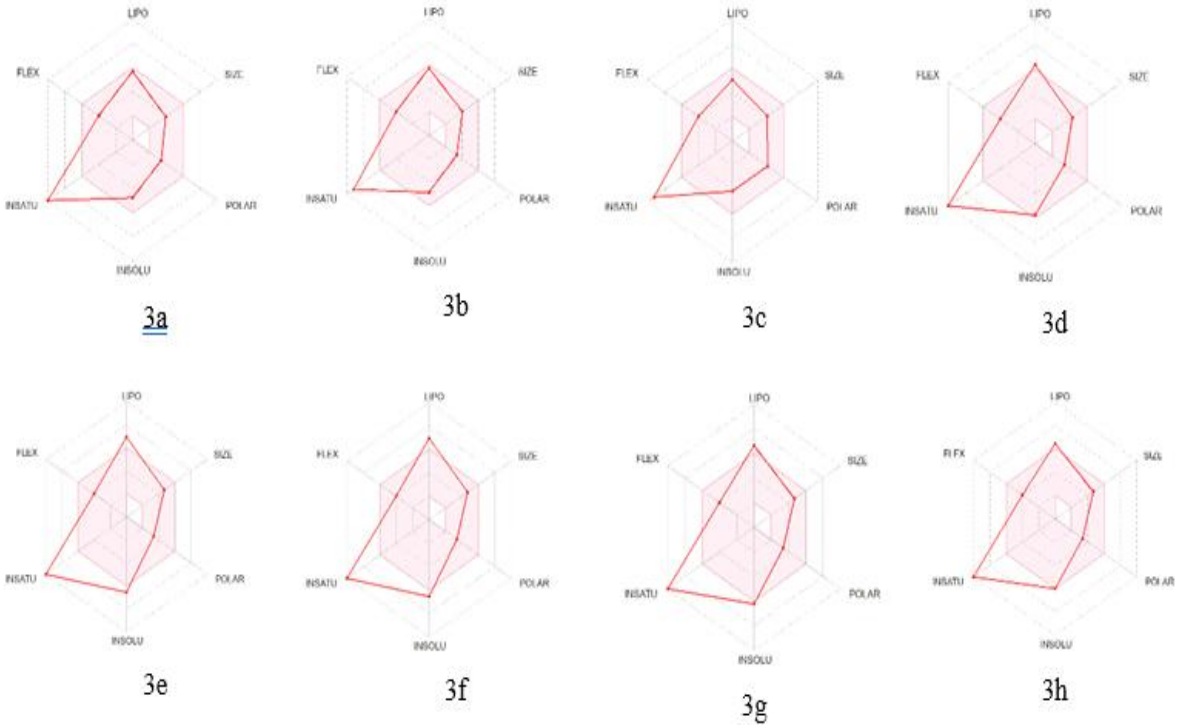

Figure 4. All the eight compounds show in colored zone are the suitable physiochemical space for oral bioavailability and show the LIPO(Lipophilicity), SIZE (Molecular Weight), POLAR (Polarity), INSOLU (Insolubility), INSATU (Instauration) and FLIX (Rotable bond flexibility) parameters

Conclusion

High yields of 2-benzoylamino-*N*-phenylbenzamide derivatives (5a–h) with short reaction times were achieved through microwave irradiation, using Keggin-type heteropolyacids as catalysts under solvent-free conditions. Moreover, all synthesized compounds demonstrated favorable values for the calculated drug similarity parameters, suggesting promising pharmacological profiles. These findings indicate that the 2-benzoylamino-N-phenylbenzamide derivatives could serve as potential candidates for further development as therapeutic agents against COVID-19.

Scientific Ethics Declaration

* The authors declare that the scientific ethical and legal responsibility of this article published in EPSTEM Journal belongs to the authors.

Conflict of Interest

* The authors declare that they have no conflicts of interest

Funding

* This research received no specific grant from any funding agency in the public, commercial, or not-for-profit sectors.

Notes

* This article was presented as a poster presentation at the International Conference on Basic Sciences, Engineering and Technology (www.icbaset.net) held in Trabzon/Türkiye on May 01-04, 2025.

References

Caliendo, G., Santagada, V., Perissutti, E., Severino, B., Fiorino, F., Warner, T. D., ... & de Nucci, G. (2001). Synthesis of substituted benzamides as anti-inflammatory agents that inhibit preferentially cyclooxygenase 1 but do not cause gastric damage. *European journal of medicinal chemistry*, *36*(6), 517-530.

Carson, J. R., Coats, S. J., Codd, E. E., Dax, S. L., Lee, J., Martinez, R. P., ... & Zhang, S. P. (2004). N-Alkyl-4-[(8-azabicyclo [3.2. 1]-oct-3-ylidene) phenylmethyl] benzamides, μ and δ opioid agonists: a μ address. *Bioorganic & Medicinal Chemistry Letters*, *14*(9), 2113-2116.

Chan, J. F. W., Yuan, S., Kok, K. H., To, K. K. W., Chu, H., Yang, J., ... & Yuen, K. Y. (2020). A familial cluster of pneumonia associated with the 2019 novel coronavirus indicating person-to-person transmission: A study of a family cluster. *The Lancet*, *395*(10223), 514-523.

Chen, L., Ao, Z., Jayappa, K.D., Kobinger, G., Liu, S., Wu, G., Wainberg, M.A., & Yao, X. (2013). Characterization of antiviral activity of benzamide derivative AH0109 against HIV-1 infection. *Antimicrob Agents Chemother*, *57,* 3547-3554.

Chen, N., Zhou, M., Dong, X., Qu, J., Gong, F., Han, Y., ... & Zhang, L.Epidemiological and clinical characteristics of 99 cases of 2019 novel coronavirus pneu monia in Wuhan, China: a descriptive study, *6e Lancet*, 395(10223), 507-513.

Chung, M. J., Zubcevic, J., Hernandez, J.,…& Prada, J. A. (2004). Structure-based discovery of a novel angiotensin-converting enzyme 2 inhibitor, *Hypertension*, *44*(6), 903-906.

Elmezayen, A. D., Al-Obaidi, A., Sahin, A. T., & Yelekci, K. (2021). Drug repurposing for coronavirus (COVID-19): In silico screening of known drugs against coronavirus 3CL hydrolase and protease enzymes. *Journal of Biomolecular Structure and Dynamics*, *39*(8), 2980-2992.

Foster, J.E., Nicholson, J.M., Butcher, R., Stables, J.P.,…& Edaf'iogho, I.O. (1999). synthesis, characterization and anticonvulsant activity of enaminones synthesis of substituted vinylic benzamides as potential anticonvulsants. *Bioorganic & Medicinal Chemistry*, *7*, 2415-2425.

Ighilahriz-Boubchir, K., Boutemeur-Kheddis, B., Rabia, C., Makhloufi-Chebli, M., Hamdi, M., & Silva, A. M. (2017). Recyclable Keggin heteropolyacids as an environmentally benign catalyst for the synthesis of new 2-benzoylamino-n-phenyl-benzamide derivatives under microwave irradiations at solvent-free conditions and the evaluation of biological activity. *Molecules*, *23*(1), 8.

Ji, X.Y.,Wang, H.Q., Hao, L.H., He, W.Y., Gao, R. M., Li, Y.P., Li, Y.H., Jiang, J.D., & Li, Z. R. (2013). Synthesis and antiviral activity of *N*-phenylbenzamide derivatives, a novel class of enterovirus 71 ınhibitors. *Molecules*, *18*, 3630-3640.

Joshi, R. S., Jagdale, S. S.,… & Bansode, S. B. (2020). Discovery of potential multi-target-directed ligands by targeting host specific SARS-CoV-2 structurally conserved main protease. *Journal of Biomolecular Structure and Dynamics, 38*, 1-16.

Lu, H. (2020). Drug treatment options for the 2019-new coronavirus (2019-nCoV), *BioScience Trends*, *14*(1), 69-71.

Maxmen, A. (2020). More than 80 clinical trials launch to test coronavirus treatments, *Nature*, *578*(7795), 347-348.

Pratama, M.R.F., Poerwono, H., & Siswodihardjo, S. (2020). Molecular docking of novel 5-O-benzoylpinostrob in derivatives as SARS-CoV-2 main protease ınhibitors. *Pharmaceutical Sciences*. *26*, 63-77.

Sener, E.A., Bingol, K.K., Arpacl, O.T., Yalcin, I.,…& Altanlar, N. (2002). Synthesis and microbiological activity of some N-(2-hydroxy-4-substituted phenylbenzamides, phenylacetamides and furamides as the possible metabolites of antimicrobial active benzoxazoles. *Il Farmaco, 57,* 45 1-456.

Wakui, N., Yoshino, R., Yasuo, N., Ohue, M., & Masakazu, M., (2018). Exploring the selectivity of inhibitor complexes with Bcl-2 and Bcl-XL: a molecular dynamics simulation approach. *Journal of Molecular Graphics and Modelling*, *79,* 166-174.

Wu, Z. McGoogan, J. M. (2020). Characteristics of and im portant lessons from the coronavirus disease 2019 (COVID 19) outbreak in China. *JAMA, 323*(13), 1239–1242.

Xu, Y. J., Miao, H. Q., Pan, W., Navarro, E. C., Tonra, J. R., Mitelman, S., ... & Liu, H. (2006). N-(4-{[4-(1H-Benzoimidazol-2-yl)-arylamino]-methyl}-phenyl)-benzamide derivatives as small molecule heparanase inhibitors. *Bioorganic & Medicinal Chemistry Letters*, *16*(2), 404-408.

Yamamoto, N., Yang, R., Yoshinaka, Y., Amari, S., Nakano, T., Cinatl, J., ... & Yamamoto, N. (2004). HIV protease inhibitor nelfinavir inhibits replication of SARS-associated coronavirus. *Biochemical and Biophysical Research Communications*, *318*(3), 719-725.

Zhu, N., Zhang, D., & Wangetal, W., (2020). A novel coronavirus from patients with pneumonia in China, 2019, *New England Journal of Medicine*, *382*(8), 727-733.

Author(s) Information

Karima Ighilahriz
Laboratory de Physic and Chemistry of Materials LPCM, Departement of Chemistry, Faculty of Sciences, University Mouloud Mammeri, TiziOuzou, 15000, Algeria
Contact e-mail: *karima.boubchir@ummto.com*

Amina Benazzouz-Touami
Laboratory de Physic and Chemistry of Materials LPCM, Departement of Chemistry, Faculty of Sciences, University Mouloud Mammeri, TiziOuzou, 15000, Algeria

Malika Makhloufi-Chebli
Laboratory de Physic and Chemistry of Materials LPCM, Departement of Chemistry, Faculty of Sciences, University Mouloud Mammeri, TiziOuzou, 15000, Algeria

Noura Kichou
Departement of Chemistry, Faculty of Sciences, University Mouloud Mammeri, TiziOuzou, 15000, Algeria

To cite this article:

Ighilahriz, K., Benazzouz-Touami A., Makhloufi-Chebli, M., & Kichou, N. (2025). Synthesis, molecular docking and in silico ADME prediction of 2-benzoylamino-*N*-phenyl-benzamide derivatives. *The Eurasia Proceedings of Science, Technology, Engineering and Mathematics (EPSTEM), 34,* 49-57.

The Eurasia Proceedings of Science, Technology, Engineering & Mathematics (EPSTEM)
ISSN: 2602-3199

The Eurasia Proceedings of Science, Technology, Engineering and Mathematics (EPSTEM), 2025

Volume 34, Pages 58-65

ICBASET 2025: International Conference on Basic Sciences, Engineering and Technology

On Mersenne GCED Matrices

Wiam Zeid
Lebanese International University

Haissam Chehade
Lebanese International University

Yahia Awad
Lebanese International University

Abstract: A Mersenne number is defined as a number of the form $M_n = 2^n - 1$, where n is a positive integer. The first five Mersenne numbers are 1, 3, 7, 15, and 31. A divisor d of a positive integer $m = p^k$, where p is a prime, is termed an exponential divisor if it satisfies $d = p^t$ with t dividing k, and it is denoted as $d|_e m$. Two integers a and b share a common exponential divisor if they have the same prime factors. The greatest common exponential divisor (*GCED*) of two integers a and b is denoted by $gced(a, b)$. A set S is called exponential factor-closed if the exponential divisor of every element of S also belongs to S. Similarly, S is *GCED*-closed if $gced(a, b)$ belongs to S for every pair a, b in S. If S is an exponential factor-closed set of distinct positive integers arranged in increasing order, the *GCED* matrix associated with S is the matrix M, where each entry M_{ij} is given by $gced(a_i, a_j)$. The Mersenne *GCED* matrix M associated with S is a square matrix where each entry M_{ij} is of the form $gced(2^{a_i} - 1, 2^{a_j} - 1)$. This paper introduces the concept of Mersenne GCED square matrices defined on a non-exponential factor-closed set. We establish a comprehensive characterization of their fundamental properties, including their structure, determinant, reciprocal, and inverse.

Keywords: Exponential divisor, Greatest common divisor, Mersenne numbers, Factor-closed set, GCED-closed set.

Introduction

Let $S = \{x_1, x_2, \ldots, x_n\}$ be a well-ordered set of distinct positive integers. The $n \times n$ matrix $A = a_{ij}$, $(\text{resp. } [A] = a_{ij})$ where $a_{ij} = (x_i, x_j)$ $(\text{resp. } a_{ij} = [x_i, x_j])$ represents the greatest common divisor of x_i and x_j (resp. the least common multiple of x_i and x_j), which is denoted by GCD (resp. LCM) matrix on the set S. The set S is a factor closed set if it includes every divisor of any $x \in S$ while S is a GCD closed set if it contains (x_i, x_j) for all x_i and x_j in S.

Mersenne numbers are a sequence of numbers of the form $M_n = 2^n - 1$, where n is a positive integer. The first five Mersenne numbers are 1, 3, 7, 15, and 31. If M_n is a prime number, it is called a Mersenne prime. It is a necessary (but not sufficient) condition: For M_n to be prime, n itself must be prime. However, not all numbers M_p (where p is prime) are Mersenne primes. For example, $M_{11} = 2047 = 23 \times 89$ is composite. Mersenne primes hold great significance in number theory, particularly due to their close relationship with perfect numbers (numbers that are equal to the sum of their proper divisors, excluding themselves), as established by the Euclid-Euler theorem. They also play a crucial role in primality testing, with the Lucas-Lehmer test being specifically designed to determine the primality of Mersenne numbers efficiently, see Awad et al. (2023a) for more details.

- Selection and peer-review under responsibility of the Organizing Committee of the Conference

Moreover, the largest known primes are often Mersenne primes, as their structure allows for more effective primality-checking algorithms. Despite their importance, an open problem in mathematics remains unresolved: it is still unknown whether there exist infinitely many Mersenne primes. Subrarao (1972) introduced the concept of exponential divisors, where $d = \prod_{i=1}^{t} p_i^{a_i}$ is an exponential divisor of $m = \prod_{i=1}^{t} p_i^{b_i}$ if a_i divides b_i for all $1 \leq i \leq t$ denoted by $d \mid_e m$. By convention, $1 \mid_e 1$ but 1 is not an exponential divisor for every $m > 1$. If two integers m and n share the same prime factors, they have a common exponential divisor. The greatest common exponential divisor (GCED) and the least common exponential multiple (LCEM) of m and n are denoted by $(m, n)_e$ and $[m, n]_e$ respectively. By convention, $(1,1)_e = [1,1]_e = 1$ and $(1, m)_e$ and $[1, m]_e$ do not exist for $m > 1$. If m and n have the same prime factorization $m = p_1^{b_1} p_2^{b_2} \dots p_k^{b_k}$ and $n = p_1^{c_1} p_2^{c_2} \dots p_k^{c_k}$, then:

$$(m, n)_e = \prod_{i=1}^{k} p_i^{gcd(b_i, c_i)}.$$

Two integers $m = p_1^{b_1} p_2^{b_2} \dots p_k^{b_k}$ and $n = p_1^{c_1} p_2^{c_2} \dots p_k^{c_k}$ are exponentially relatively prime if $(m, n)_e = 1$ or if $\gcd(b_i, c_i) = 1$ for all $1 \leq i \leq k$.

A set $S = \{x_1, x_2, \dots, x_n\}$ is exponential factor-closed (or GCED-closed) if it contains all exponential divisors of its elements (or if $\left(x_i, x_j\right)_e \in S$ for all $x_i, x_j \in S$). For example the set $\{20, 50, 100\}$ is not exponential factor closed set where as $\{10, 20, 50, 100\}$ is. The latter is also $GCED$-closed. If S is an exponential factor-closed set arranged in increasing order, the $n \times n$ matrix $(S)_e = s_{ij}$ where $s_{ij} = \left(x_i, x_j\right)_e$, is called the GCED matrix on S.

Smith (1875) showed that if $T = \{1,2, \dots, n\}$, then

$$det(T) = \prod_{i=1}^{n} \phi(i), \text{ and } det[T] = \prod_{i=1}^{n} \phi(x_i)\pi(x_i),$$

where ϕ is Euler's totient function and π is a multiplicative function such that $\pi(p^k) = -p$ for a prime p. Smith also extended these results to factor-closed sets. Beslin and Ligh (1989b), later factorized GCD matrices proving their non-singularity. In subsequent works Beslin (1989a, 1992) they further analyzed GCD matrices over GCD-closed sets, computing their determinants. Since Smith's foundational work, this field has expanded significantly, with numerous studies generalizing the structure, determinants, and inverses of GCD and LCM matrices. The study gained momentum in 1989, particularly due to Beslin and Ligh's contributions. They established that for a factor-closed set *S,* the GCD matrix S can be decomposed as AA^T, where A is upper triangular and further proved that GCD matrices are positive definite. For a well-ordered set $S = \{x_1, x_2, \dots, x_n\}$ with $x_1 < x_2 < \cdots < x_n$, the $n \times n$ power gcd matrix $(M^r) = \gcd\left(x_i, x_j\right)^r$, where r is any real number.

The set $(\mathbf{Z}^+ \backslash \{1\}, \mid_e)$ under exponential divisibility forms a poset but not a lattice, as the GCED does not always exist. Raza and Waheed (2015a, 2015b, 2012) derived structure theorems and computed determinants for GCED and LCEM matrices on ordered sets. Zeid et al. (2022) studied GCED matrices defined on both GCED-closed and non-GCED-closed sets over a unique factorization domain *D*. Additionally, they provided a comprehensive characterization of their structure, determinant, trace, and inverse. Chehade et al. (2024) investigated LCEM matrices over UFDs, providing a complete characterization of their structure, determinant, trace, and inverse. Awad et al. (2019) introduced the Fermat power GCD matrices defined on sets that were neither factor-closed nor GCD-closed. They establishedd a complete characterization for their matrix factorizations, determinants, reciprocal forms, and inverses. Awad et al. (2020) employed a generalized Jordan totient function to extend the theory of reciprocal power GCDQ and LCMQ matrices from the classical setting of natural integers to Euclidean domains. Their results included structural theorems and determinantal formulas for these matrices, which were applicable to both arbitrary and factor-closed q-ordered sets within such domains. Awad et al. (2023b) provided a complete generalization of power GCDQ and LCMQ matrices defined on q-ordered GCD-closed sets over Euclidean domains. They established structure theorems, derived formulas for determinants, reciprocals, inverses, and analyzed p-norms for these matrices. To illustrate their results, examples were presented in the Euclidean domain of Gaussian integers, $\mathbb{Z}[i]$.

In this paper, we introduce Mersenne GCED matrices of size $n \times n$ constructed over non-exponential factor-closed sets. We provide a complete structural characterization of these matrices, compute their determinants, and derive explicit formulas for their reciprocals and inverses.

Definitions and Preliminaries

Let $S = \{x_1, x_2, \ldots, x_n\}$ be an ordered set of distinct positive integers greater than 1 such that $x_1 < x_2 < \cdots < x_n$. Let $R = \{y_1, y_2, \ldots, y_m\}$ denote the minimal exponential divisor-closed set containing S (i.e., the exponential closure of S), where $y_1 < y_2 < \cdots < y_m$. The $n \times n$ greatest common exponential divisor (GCED) matrix $A_e = \left(a_{ij}\right)$ is defined by its entries:

$$a_{ij} = \left(x_i, x_j\right)_e.$$

Note that GCED matrices are symmetric.

Definition 1. The Möbius function, denoted as $\mu(n)$, is a number-theoretic function defined for positive integers n as follows:

$$\mu(n) = \begin{cases} 1, & \text{if } n = 1 \\ (-1)^k, & \text{if } n \text{ is squarefree and has } k \text{ distinct prime factors} \\ 0, & \text{if } n \text{ is not squarefree.} \end{cases}$$

Definition 2. The exponential Möbius Function, denoted as $\mu^{(e)}(n)$, is a variant of the classical Möbius function that arises in the study of exponential divisibility. It is defined as follows:

$$\mu^{(e)}(n) = \begin{cases} 1, & \text{if } n = 1 \\ (-1)^k, & \text{if } n \text{ is exponentially squarefree and has } k \text{ distinct prime factors} \\ 0, & \text{if } n \text{ is not exponentially squarefree.} \end{cases}$$

Definition 3. The arithmetic function $g(n)$ is defined as as follows:

$$g(n) = \sum_{d \mid_e n} \mu^{(e)}\left(\frac{n}{d}\right).$$

Note that if n has the prime factorization $n = p_1^{c_1} p_2^{c_2} \ldots p_r^{c_r}$, then $g(n)$ can be expanded as:

$$g(n) = \sum_{a_1 b_1 = c_1} \sum_{a_2 b_2 = c_2} \cdots \sum_{a_r b_r = c_r} p_1^{a_1} p_2^{a_2} \ldots p_r^{a_r} \mu^{(e)}\left(p_1^{b_1} p_2^{b_2} \ldots p_r^{b_r}\right).$$

The Mersenne exponential arithmetic function on S is defined as:

$$g(n) = \sum_{a_1 b_1 = c_1} \sum_{a_2 b_2 = c_2} \cdots \sum_{a_r b_r = c_r} \left(2^{p_1^{a_1} p_2^{a_2} \ldots p_r^{a_r}} - 1\right) \mu^{(e)}\left(p_1^{b_1} p_2^{b_2} \ldots p_r^{b_r}\right).$$

Using Möbius inversion, we derive the Mersenne exponential formula:

$$2^n - 1 = \sum_{d \mid_e n} g(d).$$

Matrix Definitions

The concept of the Mersenne GCED matrices is introduced in Definition 4. Mersenne matrices combine the elegance of Mersenne numbers with the utility of structured matrices, offering interesting mathematical properties and applications in computation and cryptography.

Definition 4. The Mersenne GCED matrix M defined on S is the $n \times n$ matrix whose $(ij)^{th}$ entry is given by:

$$m_{ij} = 2^{(x_i, x_j)_e} - 1,$$

where r is any real number.

Definition 5. The incidence matrix $E_{n\times n} = e_{ij}$ of S is defined as:

$$e_{ij} = \begin{cases} 1 & \text{if } x_j \mid_e x_j, \\ 0 & \text{otherwise.} \end{cases}$$

Structure of Mersenne GCED Matrices

A complete characterization of the Mersenne GCED Matrices factorizations is given in this section.

Theorem 1. (Mersenne Structure) The Mersenne GCED matrix admits the factorization

$$M = EAE^T,$$

where:

- E is the $n \times m$ incidence matrix of R relative to S, with entries

$$e_{ij} = \begin{cases} 1 & \text{if } y_j \mid_e x_i, \\ 0 & \text{otherwise.} \end{cases}$$

- A is the $m \times m$ diagonal matrix with $a_{ii} = g(y_i)$.

Proof. By construction,

$$(EAE^T)_{ij} = \sum_{k=1}^{m} e_{ik} a_{kk} e_{jk} = \sum_{y_k \mid_e (x_i, x_j)_e} g(y_k) = 2^{(x_i, x_j)_e} - 1 = m_{ij}.$$

Theorem 2. The matrix M can also be expressed as

$$M = A_r E^T,$$

where A_r is defined by

$$a_{ij} = \begin{cases} g(y_j) & \text{if } y_j \mid_e x_i, \\ 0 & \text{otherwise.} \end{cases}$$

Proof. Direct computation yields

$$(A_r E^T)_{ij} = \sum_{k=1}^{m} a_{ik} e_{jk} = \sum_{y_k \mid_e (x_i, x_j)_e} g(y_k) = m_{ij}.$$

Theorem 3. The matrix M factors as

$$M = AA^T,$$

Where

$$a_{ij} = \begin{cases} \sqrt{g(y_j)} & \text{if } y_j \mid_e x_i, \\ 0 & \text{otherwise.} \end{cases}$$

Proof. Follows immediately from Theorem 1 by taking $A = E\sqrt{A}$.

Determinant of Mersenne GCED Matrices

The determinant of the Mersenne GCED Matrices is given in the next theorem.

Theorem 4. The determinant of M is given by

$$\det(M) = \sum_{K} \left(\left(\det\left(E(K)\right)\right)^2 \prod_{i=1}^{n} g\left(y_{k_i}\right) \right),$$

where $K = (k_1, k_2, \dots, k_n)$ ranges over all multi-indices with $1 \leq k_1 < \cdots < k_n \leq m$, and $E(K)$ is the submatrix of E formed by columns $(k_1, k_2, \dots, k_n)$.

Proof. Let $C = EA^{1/2}$. Applying the Cauchy-Binet formula to $M = CC^T$:

$$\det(M) = \sum_{K} \left(\det\left(C(K)\right)\right)^2 = \sum_{K} \left(\det\left(E(K)\right) \sqrt{\prod_{i=1}^{n} g\left(y_{k_i}\right)} \right)^2 .$$

Corollary 1. If S is exponentially factor-closed, then

$$\det(M) = \prod_{i=1}^{n} g(x_i) .$$

Reciprocal of Mersenne GCED Matrices

The reciprocals of Mersenne GCED matrices defined on S and their factorizations are studied in this section.

Definition 6. The reciprocal matrix N has entries

$$n_{ij} = \frac{1}{2^{(x_i, x_j)_e} - 1}.$$

Definition 7. The reciprocal Mersenne function h is defined inductively for $1 \leq i \leq n$ as:

$$h(x_i) = \sum_{d \mid_e x_i} n_{ij} \mu^{(e)} \left(\frac{x_i}{d}\right).$$

Theorem 5. The reciprocal matrix factors as

$$N = EBE^T,$$

where $B = \operatorname{diag}\left(h(y_1), \dots, h(y_m)\right)$.

Proof. By the reciprocal Mobius inversion formula:

$$(EBE^T)_{ij} = \sum_{y_k \mid_e (x_i, x_j)_e} h(y_k) = \frac{1}{2^{(x_i, x_j)_e} - 1}.$$

Inverse of Mersenne GCED Matrices

In this section, we investigate the Inverses of Mersenne matrices defined on a set *S*.

Definition 8. The inverse of the matrix *M*, M^{-1}, satisfies $MM^{-1} = I_n$, where I_n is the $n \times n$ identity matrix.

Theorem 6. For an exponentially factor-closed set *S*, the inverse is

$$M^{-1} = FA^{-1}F^T,$$

where:

- F has entries

$$f_{ij} = \begin{cases} \mu^{(e)}\left(\frac{x_i}{x_j}\right) & \text{if } x_j \mid_e x_j, \\ 0 & \text{otherwise.} \end{cases}$$

- A is as in Theorem 1.

Proof. Since $EF^T = I_n$ (verified via Möbius inversion), the result follows from Theorem 1.

Example

Let $S = \{4, 8, 16\}$. The Mersenne GCED matrix *M* on the set *S* is

$$M = \begin{bmatrix} 15 & 3 & 15 \\ 3 & 255 & 3 \\ 15 & 3 & 65535 \end{bmatrix}.$$

Note that the set $S = \{4, 8, 16\}$ is not exponential divisor closed. $R = \{2, 4, 8, 16\}$ is it's exponential closure set.

The matrix *E* is as follows:

$$E = \begin{bmatrix} 1 & 1 & 0 & 0 \\ 1 & 0 & 1 & 0 \\ 1 & 1 & 0 & 1 \end{bmatrix}.$$

We have $g(2) = 3, g(4) = 12, g(8) = 252$, and $g(16) = 65520$.

From Theorem 1, we know that,

$$M = EAE^T = \begin{bmatrix} 1 & 1 & 0 & 0 \\ 1 & 0 & 1 & 0 \\ 1 & 1 & 0 & 1 \end{bmatrix} \begin{bmatrix} 3 & 0 & 0 & 0 \\ 0 & 12 & 0 & 0 \\ 0 & 0 & 252 & 0 \\ 0 & 0 & 0 & 65520 \end{bmatrix} \begin{bmatrix} 1 & 1 & 1 \\ 1 & 0 & 1 \\ 0 & 1 & 0 \\ 0 & 0 & 1 \end{bmatrix} = \begin{bmatrix} 15 & 3 & 15 \\ 3 & 255 & 3 \\ 15 & 3 & 65535 \end{bmatrix}.$$

And from Theorem 2,

$$M = AE^T = \begin{bmatrix} 3 & 12 & 0 & 0 \\ 3 & 0 & 252 & 0 \\ 3 & 12 & 0 & 65520 \end{bmatrix} \begin{bmatrix} 1 & 1 & 1 \\ 1 & 0 & 1 \\ 0 & 1 & 0 \\ 0 & 0 & 1 \end{bmatrix} = \begin{bmatrix} 15 & 3 & 15 \\ 3 & 255 & 3 \\ 15 & 3 & 65535 \end{bmatrix}.$$

Also, from Theorem 3,

$$M = AA^T = \begin{bmatrix} \sqrt{3} & \sqrt{12} & 0 & 0 \\ \sqrt{3} & 0 & \sqrt{252} & 0 \\ \sqrt{3} & \sqrt{12} & 0 & \sqrt{65520} \end{bmatrix} \begin{bmatrix} \sqrt{3} & \sqrt{3} & \sqrt{3} \\ \sqrt{12} & 0 & \sqrt{12} \\ 0 & \sqrt{252} & 0 \\ 0 & 0 & \sqrt{65520} \end{bmatrix} = \begin{bmatrix} 15 & 3 & 15 \\ 3 & 255 & 3 \\ 15 & 3 & 65535 \end{bmatrix}.$$

By Theorem 4, the determinant of *M* is given by

$$det(M) = \begin{vmatrix} 1 & 1 & 0 \\ 1 & 0 & 1 \\ 1 & 1 & 0 \end{vmatrix}^2 g(2)g(4)g(8) + \begin{vmatrix} 1 & 1 & 0 \\ 1 & 0 & 0 \\ 1 & 1 & 1 \end{vmatrix}^2 g(2)g(4)g(16) + \begin{vmatrix} 1 & 0 & 0 \\ 1 & 1 & 0 \\ 1 & 0 & 1 \end{vmatrix}^2 g(2)g(8)g(16)$$
$$+ \begin{vmatrix} 1 & 0 & 0 \\ 0 & 1 & 0 \\ 1 & 0 & 1 \end{vmatrix}^2 g(4)g(8)g(16)$$

$$= 250024320.$$

Conclusion

In this work, the Mersenne GCED matrices defined on defined on an exponential factor-closed and a non-exponential factor-closed set were considered. A complete characterization of their structure, determinant, trace, reciprocal and inverse was given.

Scientific Ethics Declaration

* The authors declare that the scientific ethical and legal responsibility of this article published in EPSTEM Journal belongs to the authors.

Conflict of Interest

* The authors declare that they have no conflicts of interest

Funding

* This research received no specific grant from any funding agency in the public, commercial, or not-for-profit sectors.

Acknowledgements or Notes

* This article was presented as an oral presentation at the International Conference on Basic Sciences, Engineering and Technology (www.icbaset.net) held in Trabzon/Türkiye on May 01-04, 2025.

* The authors gratefully acknowledge the invaluable contributions of the anonymous referees whose insightful comments and constructive feedback greatly enhanced the quality and clarity of this article. Their expertise and dedication have been instrumental in shaping the final version of the manuscript.

* Each author contributed equally to this article, demonstrating a collaborative effort and shared dedication to its content.

* Mathematics Subject Classification (2020): 11A25, 15A09, 15A15, 15A23.

References

Awad, Y., Mghames, R., Chehade, H., & Zeid, W. (2019). On fermat power GCD matrices defined on special sets of positive integers. *Applied Mathematical Sciences*, *13*(8), 369-379.

Awad, A., Chehade, H., & Mghames, R. (2020). Reciprocal power GCDQ matrices and power LCMQ matrices defined on factor closed sets over Euclidean domains. *Filomat*, *34*(2), 357–363.

Awad, Y., Hindi, R., & Chehade, H. (2023). Comparative study between a novel deterministic test for mersenne prımes and the well-known primality tests. *Baghdad Science Journal*, *20*(5), 50.

Awad, Y., Mghames, R., & Chehade, H. (2023). Power GCDQ and LCMQ matrices defined on GCD-closed sets over Euclidean domains. *Palestine Journal of Mathematics*, *12*(1), 30-41.

Beslin, S., & El-Kassar, N. (1989). GCD matrices and Smith's determinant for a unique factorization domain. *Bull. Number Theory Related Topics*, *13*, 17–22.

Beslin, Scott, & Ligh, S. (1989b). Greatest common divisor matrices. *Linear Algebra and Its Applications*, *118*, 69–76.

Beslin, S., & Ligh, S. (1989a). Another generalisation of Smith's determinant. *Bulletin of the Australian Mathematical Society*, *40*(3), 413–415.

Beslin, Scott, & Ligh, S. (1992). GCD-closed sets and the determinants of GCD matrices. *Fibonacci Quart*, *30*(2), 157–160.

Chehade, H. Awad, Y., & Zeid W. (2024). On lcem matrıces over unıque factorızatıon domaıns. *The Eurasia Proceedings of Science, Technology, Engineering & Mathematics (EPSTEM), 28*.

Raza, Z., & Waheed, S. A. (2015a). GCED and reciprocal GCED matrices. *Hacettepe Journal of Mathematics and Statistics*, *44*(3), 633–640.

Raza, Z., & Waheed, S. A. (2015b). GCED reciprocal LCEM matrices. *Notes on Number Theory and Discrete Mathematics*, *21*(1), 79–85.

Raza, Z., & Waheed, S. A. (2012). LCEM and reciprocal GCED matrices. *Int. J. Pure and Applied Mathematics*, *80*(5), 647–655.

Zeid, W., Chehade, H., & Rasheed, F. (2022). On GCED matrices over unique factorization domains. *Filomat*, *36*(11), 3775–3784.

Smith, H. J. S. (1875). On the value of a certain arithmetical determinant. *Proceedings of the London Mathematical Society*, *1*(1), 208–213.

Subbarao, M.V. (1972). On some arithmetic convolutions, the theory of arithmetic functions, *Lecture Notes in Mathematics, 251*(1972), 247-271.

Author(s) Information

Wiam Zeid
Lebanese International University (LIU)
Department of Mathematics and Physics
Saida, Lebanon.

Haissam Chehade
Lebanese International University (LIU)
Department of Mathematics and Physics
Saida, Lebanon.
Contact e-mail: *haissam.chehade@b-iu.edu.lb*

Yahia Awad
Lebanese International University (LIU)
Department of Mathematics and Physics
AlKhyara, West Bekaa, Lebanon.

To cite this article:

Zeid, W., Chehade, H., & Awad, Y. (2025). On mersenne GCED matrices. *The Eurasia Proceedings of Science, Technology, Engineering and Mathematics (EPSTEM), 34,* 58-65.

The Eurasia Proceedings of Science, Technology, Engineering & Mathematics (EPSTEM)
ISSN: 2602-3199

The Eurasia Proceedings of Science, Technology, Engineering and Mathematics (EPSTEM), 2025

Volume 34, 66-79

ICBASET 2025: International Conference on Basic Sciences, Engineering and Technology

Guidelines for the Development of a Green Business Model in Companies from the Raw Materials Industry

Borislava Galabova
University of Mining and Geology "St. Ivan Rilski"

Vessela Petrova
University of Mining and Geology "St. Ivan Rilski"

Abstract: The dynamics of modern economic, social, and technological conditions place the framework of a new industrial model in the paradigm of Industry 5.0. This paradigm is related to advanced digitization, big data, and artificial intelligence, while highlighting the role that technology plays in addressing the new demands of the environment. As a result, it is the acquisition and development of competencies that become the basis for adapting the individual to changes that are wide-ranging, profound, and permanent. Changes at different levels, which are also linked, also mean that skills need to be constantly improved and developed to meet the needs and expectations of technology, the economy, and society. The management of enterprises in the raw materials industry should focus on what they offer as benefits and positive effects for the external environment and stakeholders and be able to show and communicate it to the public. This can be done through changes in management strategies and models, providing the necessary resources, and developing entrepreneurial and green competences at all hierarchical levels. The goal of this study is to create a green business model that works for the raw materials industry. This model should include both entrepreneurial and green skills so that the move to Industry 5.0 and the green economy is easier and faster. The analysis of this model yields guidelines for its practical implementation. The results show that one of the most important components of the developed green business model in the Industry 5.0 paradigm remains people and their competencies. Because of this, their education and training, as well as their growth as knowledgeable people and leaders, along with the steady development of their unique skills and abilities, are the most important factors that determine how well they can handle different kinds of changes and crises.

Keywords: Business engineering, Green business model, Industry 5.0, Green competence

Introduction

The business model for the management of industrial enterprises is a new strategic model that integrates sustainability, initiative, entrepreneurship, and environmental responsibility in business processes. Its goal is not only to reduce the harmful impact on the environment but also to implement cost-effective and long-term solutions and practices that have a beneficial impact on all stakeholders. In terms of content, the green entrepreneurial model integrates various components: environmental, technological, economic, and socio-governance components. From the point of view of industrial business, the development and implementation of a green model shows the potential to achieve higher efficiency in the use of resources and cost reductions, leading to greater competitiveness. From an environmental point of view, such a model aims to reduce carbon emissions, more efficiently manage natural resources—scarce, exhaustible, and non-renewable—and protect biodiversity and the environment. Over the past few decades, extractive industries have undertaken numerous initiatives to prevent, mitigate, and minimize the adverse effects associated with extractive waste management and extraction activities (Tomova, 2023).

Consequently, this form of the model is mutually beneficial and widely useful, supporting sustainable development in the long term and supporting the transition through the green transformation and entry into Industry 5.0. The inclusion of different aspects and stakeholders makes it open and allows for greater decentralization, which increases its usefulness and applicability.

Historically, the imposition of the green business model has been associated with a growing awareness of the need for sustainable business development and the adoption of specific strategies and policies that will lead to concrete changes. The natural pursuit of business development and profit has been upgraded by adding a new component—sustainability in its various dimensions, including environmental, social, and economic sustainability. Global environmental challenges, including climate change, air and water pollution, drought, and depletion of natural resources, force industrial businesses to adapt to new realities and production to reorient themselves on a fundamentally new basis. Many of the traditional production approaches based on the objective of maximizing profits at the expense of the environment are no longer acceptable and relevant to modern requirements and strategic objectives at the national and European levels. Consequently, it became evident that we should not pursue economic development at the cost of adverse effects on the environmental and social landscape. The development of industry and society is oriented towards a new paradigm—economic activity is planned and developed not against nature, the living environment, and the health of people, but for and in relation to them. The transformation necessary to achieve this goal leads to the development of new business strategies and policies in which sustainable practices and standards are a key element and are reported and communicated to the public.

More and more industrial enterprises in various industries are developing and implementing their own green business models today as they continue to establish and improve them. In this way, they adapt, manage change, and take responsibility for the impact of their activities and their results on the environmental, social, and economic environment. Through the green model, they aim for a greater and wider positive impact, opening up the processes and including new components and stakeholders in them. In the new context, more and more complex and interdisciplinary solutions are being sought and implemented to reduce carbon emissions and waste and to orient processes and results towards people and society in search of greater usefulness and added value. Technologies related to renewable energy, biodegradable products, sustainable agriculture, and circular and green economy offer new untapped opportunities for business and entrepreneurial initiatives. Such initiatives also imply the use of green business models at their launch. Given its pronounced advantages, the green model is establishing itself as a leading trend for the industrial business, in particular in the raw materials industry. This is because the industry consciously strives for competitiveness at the global level and finds adequate responses to the changing requirements of consumers and regulators.

The existence of new business and economic realities poses challenges but also opens up new opportunities for potential and current entrepreneurs who are ready to adapt their strategies to changes and benefit from them. Given that the transition to a green economy is a fact, seizing new opportunities for entrepreneurial initiatives and developing responsible and sustainable innovations also require the "greening" of models. As a result, businesses that adapt in a timely manner have the potential to be more competitive and overcome challenges faster.

Background Theory and Literature Review

In this section, a systematic literature review was conducted to comprehensively evaluate and interpret all available research relevant to a specific research question and topic area. Contemporary business trends underscore that sustainability and resilience have become pivotal pillars for organizational survival and long-term growth. In the contemporary global economy, entrepreneurship serves not only as a catalyst for productivity, employment, and innovation (Korkmaz & Oral, 2023) but also as a driving force for societal advancement by addressing pressing environmental and social challenges. A green business model presents a versatile framework applicable across enterprises of varying scales and sectors, offering a pragmatic pathway for seamlessly integrating sustainability into business operations (Aini, 2025).

One of the critical strategies identified in the literature for achieving sustainable corporate entrepreneurship is the adoption of a green entrepreneurship orientation. This orientation adapts the traditional entrepreneurial orientation—marked by innovativeness, proactiveness, and risk-taking (Covin & Lumpkin, 2011; Makhloufi et al., 2022)—to pursue sustainable actions. In parallel, organizational resilience capacity is recognized as essential; it represents the ability of organizations to plan, monitor changes, and respond effectively during crises (Hillmann et al., 2022). The synergistic combination of green entrepreneurship orientation and

organizational resilience capacity is seen as a strategic enabler that not only helps companies respond to stakeholder pressures but also drives green innovation (Do et al., 2022).

Research has increasingly pointed out that the successful implementation of sustainable and resilient strategies requires a blend of technological knowledge and environmental problem-solving skills (Makhloufi et al., 2022). Moreover, the literature highlights a significant gap in understanding how established firms, particularly in industries with high environmental impacts such as the raw materials sector, can integrate these capabilities to foster green innovation (Mondal et al., 2023). The importance of green entrepreneurship is further reinforced by its positive economic implications. By producing environmentally friendly goods and services, firms not only sell and make a profit, they also contribute to the common good. This inherent adaptability enables organizations to sustain their competitiveness amid rapidly evolving market dynamics (Silajdzic et al., 2014; Zhang et al., 2024).

Moreover, bibliometric evaluations indicate a significant increase in academic research concerning green innovation, sustainable business practices, and ecological entrepreneurship, especially following the year 2020 (Albort-Morant et al., 2017; Arora et al., 2023). The main topics of these studies are the growth of intellectual capital, multidisciplinary approaches to green economics, and the theoretical foundations of long-term business models (Jiang et al., 2024; York & Venkataraman, 2010). These findings highlight a significant paradigm change, in which conventional financial goals are being replaced by comprehensive plans that incorporate social and environmental factors (Teran-Yepez et al., 2019) to augment their market demand and profitability while also fostering innovation in business structures.

Furthermore, green entrepreneurship is seen as instrumental in addressing global challenges like resource depletion and climate change, and the green model is the means to achieve this goal. The adherence to sustainable practices— encompassing the utilization of renewable resources and the minimization of waste— constitutes a fundamental pillar in fostering a balanced and symbiotic relationship with the natural environment (Tuncer & Korchagina, 2024; Kuzmenko et al., 2024). Therefore, green entrepreneurship transcends the mere promotion of industrial and technological progress (Dima, 2021); it also corresponds with the overarching aims of the United Nations Sustainable Development Goals by redefining traditional concepts of commercial success and endorsing enduring sustainable development (Sreenivasan & Suresh, 2023).

Taken together, the studies on the green models suggest that the Fifth Industrial Revolution did not automate physical labor so much as the way of thinking and conceptualizing. Enterprises are rapidly developing and implementing systems based on artificial intelligence, automation, and algorithms. The amount of data that accumulates is large, exceeding the capabilities of a person to process and understand it and make management decisions based on it. The need for data analysis and accelerated scientific and technological progress led to the permanent imposition of a trend for the inclusion of machines and artificial intelligence in many activities and operations. As a result, people begin to change their place in the labor process and orient themselves toward acquiring a set of new competencies in order to remain active and adequate to the needs of the labor market and the positions they occupy. It becomes clear that only investments in the knowledge economy lead to a sustainable increase in incomes. The accelerated penetration of technology leads to the need to increase people's competences, which thus creates real growth for the economy.

Therefore, investments in enterprises should be directed not only to the automation and digitalization of processes but also, in parallel, to the development of skills, knowledge, and new attitudes toward the evolution of paradigms. Industrial development has so far been based on the principle that labor is the main source of added value. In the framework of Industry 5.0, however, the added value shifts to competences, talent, and skills, which become a necessary condition for the imposition of the new industrial paradigm. What requires careful study is the creation of a specific green model in the mineral industry, since the issue has not yet been thoroughly considered in the scientific literature and is relatively poorly represented in practice. This is due to the novelty of the paradigm, the varying stages of industry development in different countries, the introduction of Industry 5.0, and the "greening" of the economy.

This study is based on the premise that the implementation of new technologies has a significant impact on people during their work activities and leads to significant changes. By incorporating digitization and Industry 4.0, concepts in mineral mining and processing industries are becoming increasingly essential (Culchesk, A. et al., 2017, Dimov et al., 2020).

In addition, digital technology can enhance the efficiency, safety, and sustainability of mining and processing (Beloglazov et al., 2020). By leveraging data analytics, real-time monitoring, and automation, mining

processing plants can achieve higher productivity and reduce environmental impact (Beloglazov et al., 2020). However, in the light of the rapid change of technology, smart manufacturing is undergoing transformation driven by two distinct paradigms: Industry 4.0 advocates for the shift towards digitization and automation, while the emerging Industry 5.0 prioritizes human-centric approaches (Argilovski et al., 2024). People are the first to discover and encounter specific problems in practice and then look for a solution to overcome them with the help of new technologies.

Industry 5.0 is predominantly characterized by customization, human-centricity, high-tech products, and high social and environmental impact, leading to more expressed support for the need for sustainability (Argilovski et al., 2024). According to the new production model, based on the concept of Industry 5.0 and the green economy, the future of industry is not only related to the development of machines and technologies but also to the evolution of man, human potential and capacity, and the logical change of his role in the processes. In the new conceptual framework for the development of industry, man is not displaced by the machine and artificial intelligence (AI) but is repositioned and retrained, and his role is changed. The reasons for this are objective—automation, digitalization, and digitization will change job positions, their duties, and their responsibilities. As a result, the requirements for the qualification of workers in industrial enterprises will also change so as to achieve symbiosis between man and machine in the work process.

In this changed context, entrepreneurial competence becomes critically important not only for developing one's own business initiatives but also for finding employment, retaining one's job, and career development. The ability to recognize, create, and use opportunities, as well as manage processes that create added value and utility, is the primary expression of entrepreneurial competence. As a multifaceted and wide-ranging competence, it implies and requires in-depth analysis and knowledge of the context, environment, opportunities, and one's own potential, which can be further developed over time. In turn, entrepreneurial competence and initiative become a necessary condition for acquiring green competence, because they imply a desire for adaptability, activity, development, and accumulation of new knowledge in the field of green and circular economy.

Sustainable living and business organizations require a change in thinking and behavior, with an emphasis on equality and justice for current and future generations in terms of consumption opportunities. Our relationship with the environment must be based on an awareness of our connection with nature. People who are keen to learn green skills need to be able to think about things in a more complete way and question the way economic systems work now. They need to be able to change these systems to fit new social, environmental, and governance (ESG) factors, which means they need to change their plans and strategies. To be effective, this knowledge acquisition must be accompanied by the accumulation of experience in green practices and initiatives. It is important to encourage both individual and collective efforts to transform society and create a sustainable future in the context of Industry 5.0 and the green economy. The implementation of the green business model is a way to ensure adequacy to the requirements and relevance to the development prospects of the industry, in particular the raw materials industry. The model helps enterprises adapt to global trends and achieve greater sustainability in their activities. This not only creates prerequisites for innovation but also creates value for society by supporting social responsibility and sustainable development.

In summary, the integration of green entrepreneurial orientation and organizational resilience capacity within a green business model offers a promising avenue for sustainable corporate entrepreneurship and business. This approach enables firms—especially those in environmentally sensitive sectors—to achieve competitive advantages while addressing critical global issues. Future research should further explore the interplay between technological capabilities, environmental problem-solving skills, and strategic initiatives in green entrepreneurship. This will provide deeper insights into the evolving dynamics of green innovation and help establish a more robust theoretical foundation for sustainable business practices, ultimately driving both economic growth and environmental stewardship.

The literature analysis developed in this section shows a notable lack of examples of how to use the green model in industrial practice. We can identify a gap between the real need to implement relevant transformations and the existing theoretical framework that serves as the foundation for these transformations. As a result of an analysis of theory and good practices, it is useful to derive specific guidelines to facilitate the implementation of such models. Based on these statements, the scientific apparatus of the study was formulated, and a specific research question was derived.

We then formulate the following research question: how can we construct an exemplary green business model that is applicable to the raw materials industry? Our aim is to address these challenges and provide guidelines

that would facilitate and accelerate its implementation. The contributions of our study are sought in offering a model that is practically oriented and actually applicable and synthesizing specific recommendations through which the model will have greater applicability and value.

Methodology

In order to reach the main goal of the research, we based it on the background theory and literature review and on surveying the opinions of employers through surveys. The purpose of this study is to derive a green business model and guidelines for its implementation. The model should work in the raw materials industry and include both entrepreneurial and green skills because of the new tendencies in economy and industry. This will make the move to Industry 5.0 and a green economy easier and faster.

The methodology for developing the model and guidelines for it includes research of scientific literature, analysis, synthesis, conducting a survey among business representatives, summary, systematic, heuristic, and graphical approaches. Through looking at how entrepreneurs work and think in the raw materials industry and figuring out what skills they need, the chances of putting Industry 5.0 into practice in both new businesses and old ones are also evaluated. We examine the opportunities and challenges that the introduction of Industry 5.0 technologies presents for entrepreneurial development in the raw materials industry.

The hypothesis is tested that the creation of a green business model supports the development of business and activities related to innovation and the greening of the economy, which in turn create new business ideas and opportunities for innovation and the development of new entrepreneurial initiatives. At the heart of the hypothesis testing is the verification and understanding of the importance of entrepreneurial and green competence, because the model should also reflect the competence framework. However, this analysis requires a review and rethinking of the models and the introduction of new elements and concepts to them. In order to verify the hypothesis, the search for opinions based on a survey and the determination of employers' attitudes are the main tasks of the study, through which to fulfill the goal. On this methodological basis, a green model is derived and proposed, and generalizations are formulated—guidelines for the applicability and increasing its usefulness and effectiveness in the raw materials industry. The study's limitations are defined by the lack of active participation from business representatives in survey studies and the challenges associated with gaining access to them. The results become the basis for drawing conclusions—guidelines for practice. The sought contribution from the study is of a theoretical and applied nature.

Analysis and Results

A Questionnaire Survey

We conducted a survey of employers in Bulgaria's raw materials industry over several months in 2024. The aim of the survey was to determine the necessary competencies of human resources currently employed or with future employment in their companies. By carrying out this task, an attempt is made to derive a certain competency profile of personnel in the raw materials industry. The survey involved 11 large and medium-sized companies in the raw materials industry with a total number of over 5,000 employees. Their distribution according to company size is as follows: 71% of the surveyed enterprises have over 250 employees, and the remaining 29% have over 50 employees. The distribution according to company size is presented graphically in Figure 1.

The questions that were asked of the business representatives concern the knowledge, skills, experience, and attitudes possessed by the employees, which are implicitly included in the content of entrepreneurial and green competence. The questions were made to find out if the business agrees with the idea that entrepreneurial and green skills are crucial for building the skills of human resources in the raw materials industry in the context of Industry 5.0 and the green economy.

The field in which the respondent works is, as expected, predominantly in the field of human resources, training, and development of personnel—57.1% of respondents. The rest of the respondents are engaged in production activities, exploration, and extraction (14.3%); are responsible for ESG (14.3%); or hold a managerial position (14.3%) (Figure 2).

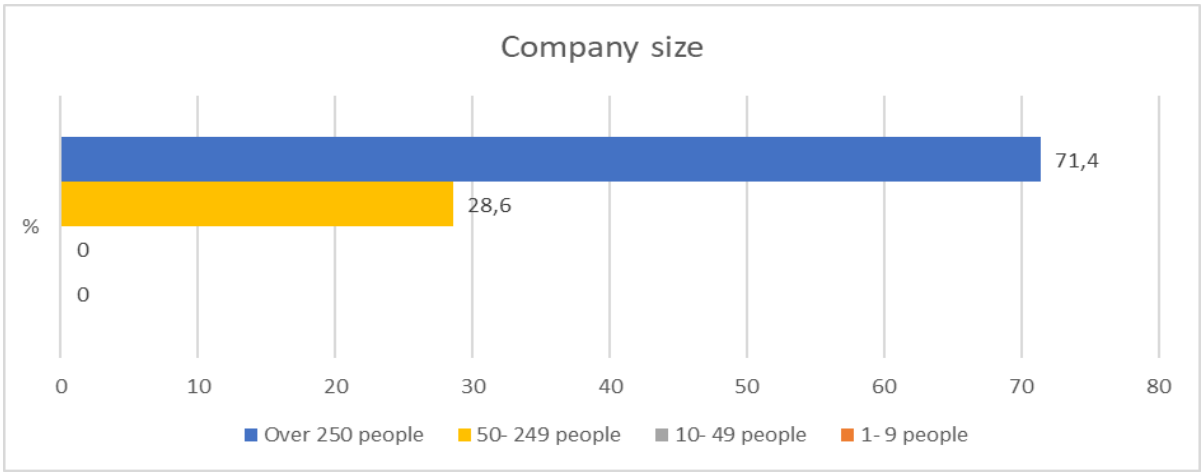

Figure. 1. Company size
Source: Own survey among business representatives, 2024

Figure 2. Field of work of the respondents
Source: Own survey among business representatives, 2024

Employers' opinions on the importance of skills related to entrepreneurial and green competence for the career development of employees in their companies are presented in Figure 3 and Figure 4.

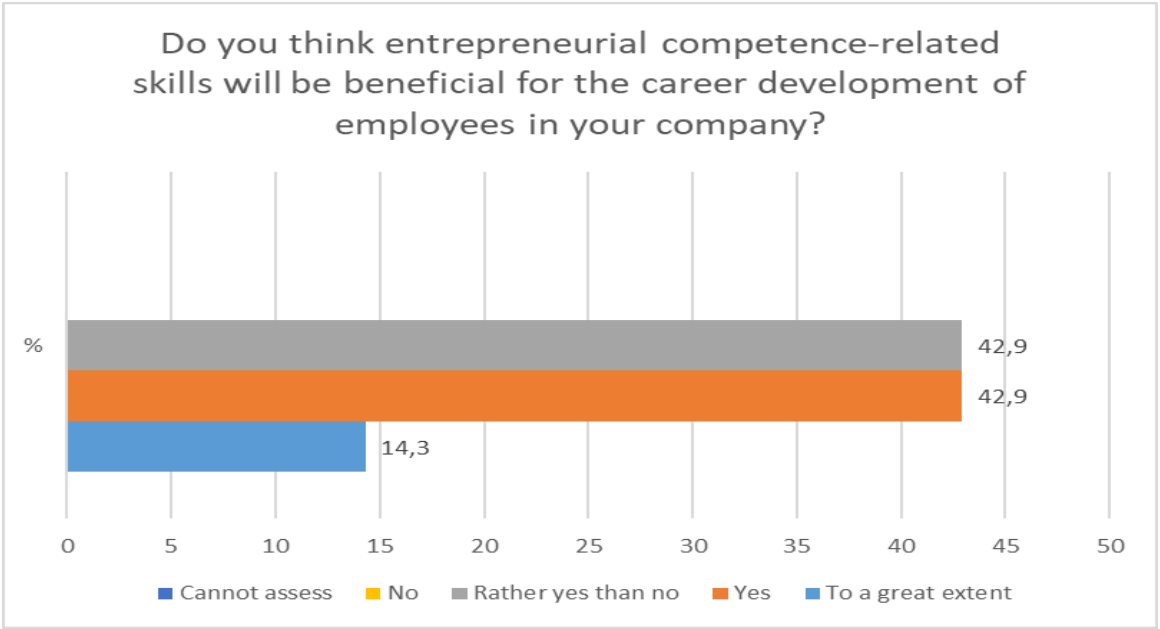

Figure 3. Employers' opinions on the importance of entrepreneurial skills for career development
Source: Own survey among business representatives, 2024

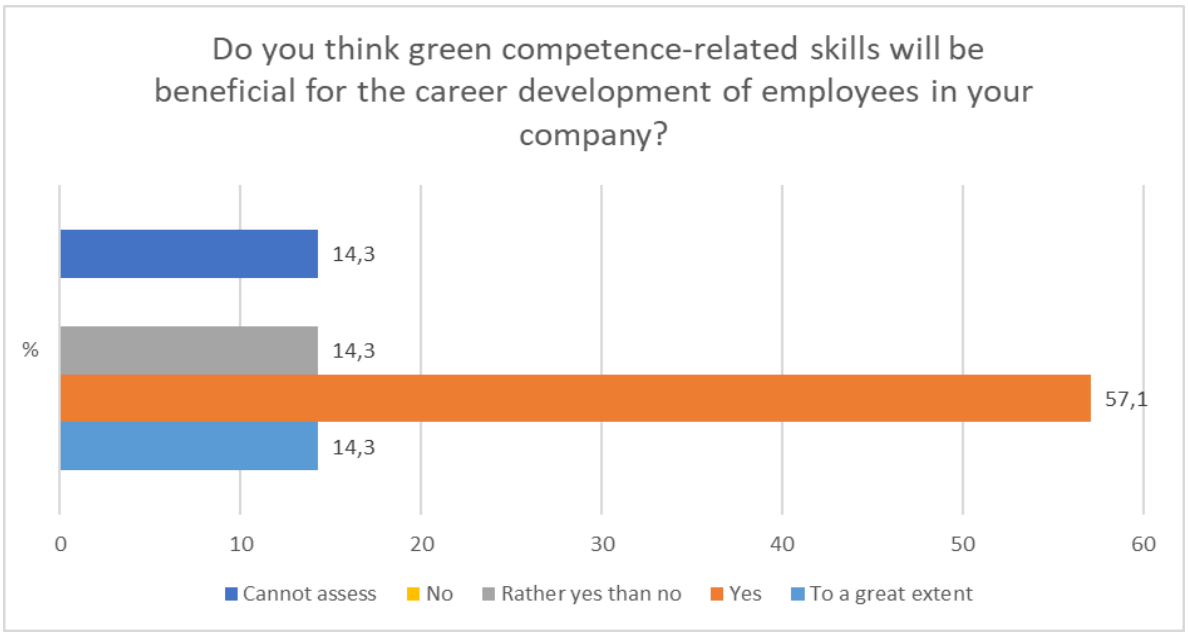

Figure 4. Employers' opinions on the importance of green competence skills for career development
Source: Own survey among business representatives, 2024

The respondents believe that skills related to entrepreneurial competence are useful for the career development of their staff. The distribution of responses is as follows: "To a large extent" represents 14.3%, "Yes" represents 42.9%, and "Rather yes than no" represents 42.9%. Managers also believe that skills related to green competence (Figure 4) can help in the career development of workers and employees in their companies: "To a large extent"—14.3%; "Yes"—57.1%; "Rather yes than no"—14.3%; and "I cannot assess"—14.3%. It is evident that in enterprises from the raw materials industry, these skills are assessed as necessary, and accordingly, requirements are set for their possession and acquisition. This can be explained by the clear need to change models, strategies, and practices, and hence the change in the competence profile in the context of Industry 5.0 and the green economy. Employers' willingness to organize formal and/or informal training to develop entrepreneurial and green competence is the focus of the next question. This is a logical question, since the previous questions prove that they recognize it as important for the activity and career development of the personnel (Figure 5 and Figure 6).

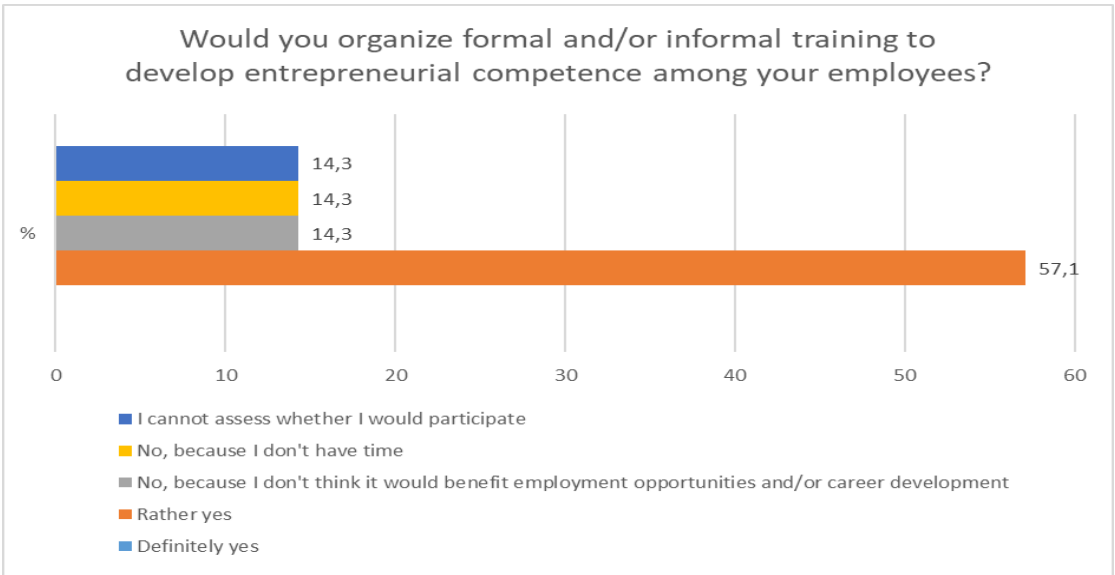

Figure 5. Employers' willingness to organize formal and/or informal training for the development of entrepreneurial competence
Source: Own survey among business representatives, 2024

Figure 6. Employers' willingness to organize formal and/or informal training for the development of green competence
Source: Own survey among business representatives, 2024

Representatives of companies in the raw materials industry largely believe that it is useful to organize formal and/or informal training for the development of entrepreneurial competence. The distribution of answers is as follows: "Rather yes" – 57.1%, "No, because I do not think it will be beneficial for the company" – 14.3%, "No, because I will need a lot of resources—financial and educational" – 14.3%, and "I cannot assess" – 14.3%.

The distribution of responses to the question of green competence is similar. The answers are as follows: "Categorically yes"—14.3%; "Rather yes"—42.9%; "No, because I don't think it will be beneficial for the company"—28.6%; and "I can't judge"—14.3%. The prevailing opinion is that employers should organize such training, because the future importance of the skills related to these two types of competences is recognized. It is striking that there is also a significant share of those who answered no, with the negative answer being justified by the lack of resources (financial and educational) and a share of those who answered that they could not judge. The lack of resources is often a factor in not undertaking or postponing training initiatives, seminars, and workshops that develop skills and lead to the accumulation of experience.

The lack of judgment is also explained by the great dynamics, rapid changes, and many new concepts that the business is not always familiar with in detail. As a result, prioritization becomes difficult, and assessing what is important, what is a priority for the company, and what changes need to be made requires in-depth management training and significant analytical capacity. Based on the study of attitudes about the importance and role of entrepreneurial and green competence among employers, it can be concluded that the need to upgrade competencies through training is recognized and justified. Employers categorically state that the acquired skills related to entrepreneurial and green competence are important for finding employment and for developing the careers of their workers and employees.

Over the past decade, it has become clear that companies that deliver value to society—to their customers, employees, and stakeholders—ultimately turn out to be the most profitable and competitive. The existence and development of enterprises in modern society is characterized by a new value orientation, the widespread use of digital technologies, the improvement of management methods, an orientation towards high-quality performance of tasks, and the achievement of long-term goals. All this is impossible without building a cohesive team of inspired and committed individuals dedicated to the goals of the organization (Trifonova, B., 2022, p. 186). Therefore, it is necessary to look for management models that create value and are more open, which would meet the need for stakeholder involvement.

The value proposition HR model was created by Ulrich and Brockbank (2005) under the name Human Resource Management that Creates Value. Ulrich and Brockbank believe that "human resource management that adds value creates a sense of benefit and value in the minds of specific groups of people—users, employees,

managers, and shareholders of the company's business—thereby helping them to achieve their specific goals (Ulrich & Brockbank, 2005, p. 26)". Their model includes five interrelated elements, depicted in Figure 7. The main idea of the model is that human resource management activities generate value in the broad sense of the word, including benefits for staff, managers, customers, investors, owners, and stakeholders.

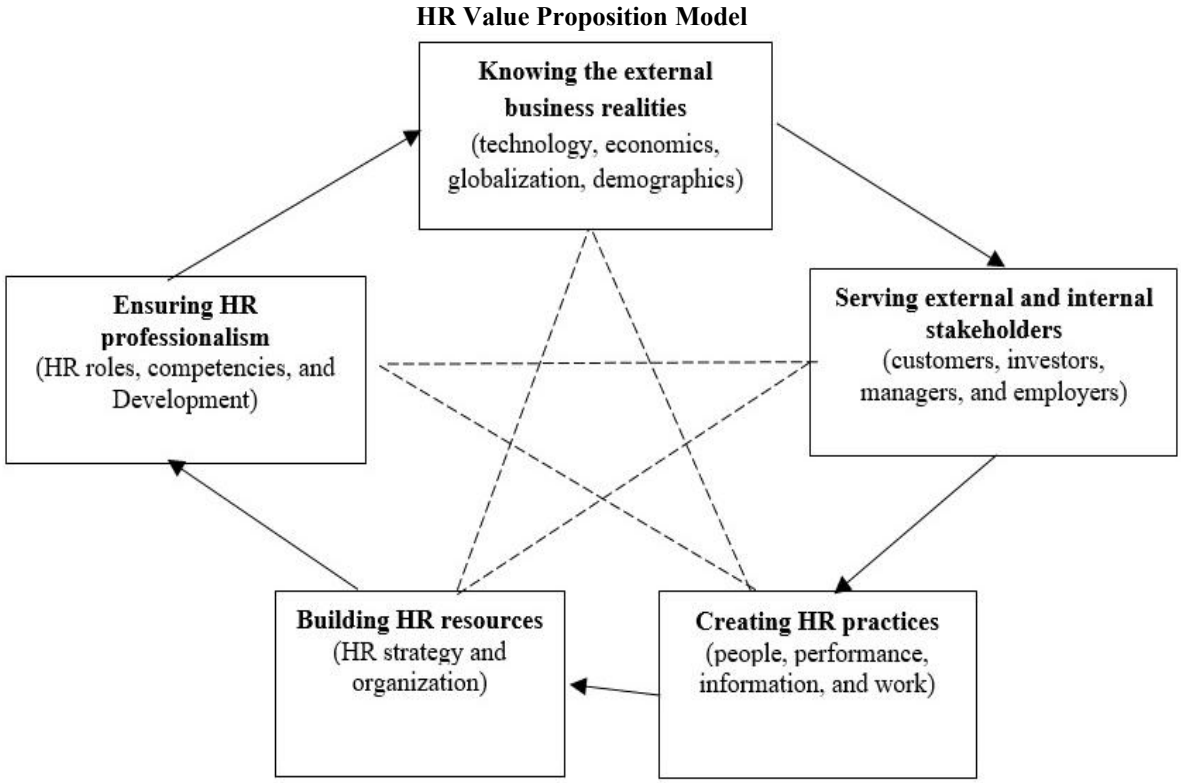

Figure 7. The Ulrich and Brockbank HR value proposition

Ulrich and Brockbank say that to make the changes that are needed from using this model, the five elements shown in Figure 7 must be consistently put into action. These elements should start with studying the outside business environment and move along the solid, continuous lines. Another approach is also possible—to follow the dotted lines or to start with an assessment of the competence of the staff, investment in resources, or another element. However, a mandatory condition for applying the model is the integrated implementation of all five elements, regardless of the choice of where to start.

The elements contain (Trifonova, 2019, p. 170):

- Excellent knowledge of the external business environment, which includes knowledge of new technologies, the economic environment, legal regulations, the demographic crisis, and imposed globalization;
- Excellent knowledge of the needs of stakeholders—staff, managers, clients, investors, and owners;
- Implementation of effective management practices in human resources management in the following areas: related to the movement of people and talent retention, related to the performance of tasks, performance assessment and remuneration received, related to the analysis of positions, and related to building the communication strategy in the organization;
- Providing the necessary resources to achieve the desired results—the organization is given the opportunity to link management practices in human resources management with the implementation of the business strategy;
- Ensuring high professionalism in enterprise management requires constant improvement in the competence of all managers within the organization.
- Ensuring high professionalism in work, which requires constant improvement of the competencies of employees in the organization, especially entrepreneurial and green competencies.

Businesses in the raw materials industry use good human resource management models because they want to create safe jobs with fair pay and long-term growth in areas where the extractive industry is strong (Trifonova, 2019, p. 171). Monitoring good practices and taking into account the attitudes of representatives becomes the

foundation for preparing and offering a green business model that is effective and applicable in an industrial environment.

Green Business Model

After looking at the study's results and the human resources management model, it is possible to come up with a model and make specific suggestions for the creation and use of similar models that include green competence in order for Industry 5.0 to enter the raw materials industry. In order to develop and justify such a model, Table 1 traces the stage sequence of mining operations and highlights the main actions of companies toward building their own green entrepreneurial model.

Table 1. Green entrepreneurial model of a raw material industry enterprise—sequence and stages

Stage of mining activities	**Stage scope**	**Actions to build the model**
Geological exploration	From the discovery of a deposit with a certain type of mineralization to a certain stage of exploration of the deposit: reconnaissance, prospecting, preliminary exploration, or detailed exploration.	Training the workforce in acquiring entrepreneurial and green competencies and opening up creative professions related to new technologies; Discovering new jobs in the virtual environment. Through the use of virtual manufacturing, the manufacturing process can be defined and verified at the beginning of the design process;
Mine site design	Feasibility study and preparation of the technical or working design for the deposit's development.	Informing local communities;
Construction	Construction of capital works, production and auxiliary buildings, purchase and delivery of machinery and equipment, and construction of infrastructure on the site.	Technological innovation, which leads to optimization of production processes, reduction of waste products, and improvement of resource utilization;
Mine commissioning and ramp-up	It covers the period from the start of production until the mine reaches full or near full production capacity.	Limiting workplaces where monotonous and health-hazardous activities are practiced;
Steady-state mine operation	This is the period during which the mine operates at full capacity and extracts reserves from the deposit.	Achieving sustainability, which includes workers having the skills to manage resources effectively, emphasizing recycling, renewable energy sources, and the sustainable use of natural resources;
Production decline phase	Decline in activity due to depletion of inventories and partial liquidation of no longer needed fixed and short-lived tangible assets.	Building effective partnerships with the community; Limiting the potential for job losses through training to acquire new digital and entrepreneurial skills and start their own business;
Mine closure or conservation	It mainly covers the period of liquidation or conservation of production facilities and completion of environmental restoration activities from the consequences of mining activities.	Prioritizing the well-being and prosperity of the community by financing new businesses in the region and working on projects and programs funded by the EU; Informing local communities about the sequence of actions to restore the environment, achieving visibility and transparency.

Based on these formulated and described stages and their sequence, a green business model applicable to enterprises in the raw materials industry is developed and proposed. The model is presented graphically in Figure 8.

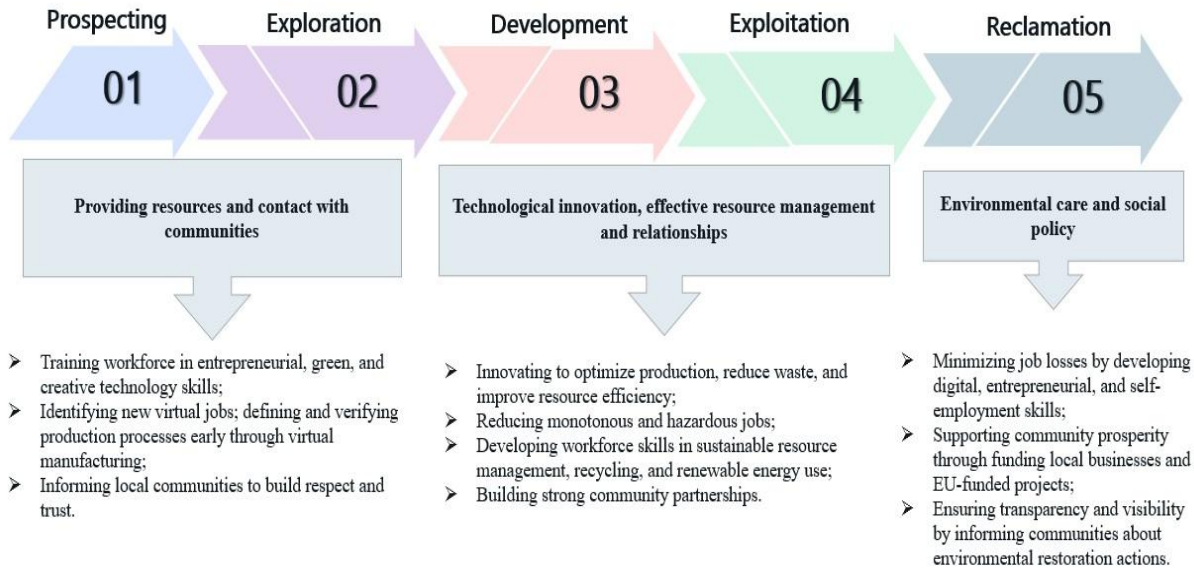

Figure 8. A green entrepreneurial model in raw materials industry enterprises

The relevant actions for building the model are as follows:

1. Providing resources and reaching out to communities
- Training the workforce in acquiring entrepreneurial and green competencies and engaging in creative and innovative professions related to new technologies.
- Discovering new jobs in the virtual environment. By using virtual manufacturing, the production process should be defined and verified at the beginning of the planning process.
- Informing local communities. Building respect and trust. Ensuring a transparent environment.

2. Technological innovation, efficient resource management, and relationships
- Technological innovation, which leads to the optimization of production processes, the reduction of waste products, and the improvement of resource use (efficiency) (Terziyski, 2024);
- Limiting the number of workplaces where monotonous and hazardous activities are practiced;
- Achieving sustainability, which includes the acquisition of knowledge and the development of skills for the efficient management of resources, with a main focus on recycling, renewable energy sources, and the sustainable use of natural resources (Hristova, et al., 2024);
- Using knowledge and skills in various initiatives to gain experience;
- Building effective, mutually beneficial partnerships with the community.

3. Environmental care and social policy:
- Limiting the potential for job losses through training to acquire new digital, green, and entrepreneurial skills and start your own business;
- Prioritizing the well-being and prosperity of the community by financing new businesses in the region and working on projects and programs financed by the EU and international funds;
- Informing local communities about the sequence of actions to restore the environment, achieving visibility and transparency.

The relevant actions are also guidelines for the possible sequence of steps that are complementary and through which the various components of sustainability can be ensured. The model is based on the principle of openness, seeking mutual benefit and involving a wide range of stakeholders in various processes. The main recommendations for its implementation are the use of a broader and integrated approach, reflecting feedback, seeking cooperation and coordination of strategies and goals, and seeking utility and added value beyond the economic aspect. The raw materials industry finds the model useful and applicable, but with adaptation, it can also discover its application in other industries.

Conclusions

The results of the study show that one of the most important components of the developed green entrepreneurial model in the Industry 5.0 paradigm is people, because the Fifth Industrial Revolution does not automate physical labor as much as thinking and conceptualization. People are the first to discover and encounter specific

problems in their practical activities and then seek a solution to overcome them with the help of new technologies. Therefore, their training and education, their development as informed individuals and leaders, as well as the consistent development of their specific skills and talents, are decisive factors for their suitability for serious transformations and crises of any nature.

The management of enterprises in the raw materials industry should focus on offering benefits to staff and stakeholders, seeking broad utility, and adequately presenting the results to the community. This can be done through internal changes in management practices, providing the necessary resources, including resource sharing, open models, and developing management capacity within the organization. It is recommended to create a relevant green entrepreneurial model, which includes both the acquisition of entrepreneurial and green competencies and management focused on value creation, stakeholder engagement, and open and decentralized approaches to creating and implementing innovations.

Technological renewal, imposed by Industry 5.0, is also needed, leading to the optimization of production processes, the reduction of waste products, improved resource use, and circular models. However, achieving sustainability is possible when workers have real practical skills for effective resource management and for working in a new work environment in which recycling, renewable energy sources, and the sustainable use of natural resources are emphasized. We have taken the first step in recognizing and accepting the importance of these skills. Further steps should be taken to change the strategies, policies, and models in the raw material industry enterprises, which should be consistently implemented, including focusing on training and actively involving employees in green initiatives. Such a strategic transformation also requires the development of competence in a wide range of specialists and managers who will plan, implement, and manage the process so that they can properly form and implement policies and strategies. This is possible by placing emphasis on education and training, formal and informal initiatives, and the search for the usefulness and applicability of new knowledge and skills in practice to achieve added value. Future research should explore the implementation of such steps and their impact, considering the study's limited scope. Furthermore, the study sparked pertinent academic discussions about future research directions and pinpointed knowledge gaps that require attention.

Scientific Ethics Declaration

* The authors declare that the scientific ethical and legal responsibility of this article published in EPSTEM Journal belongs to the authors.

Conflict of Interest

* The authors declare that they have no conflicts of interest. The authors declare that they have no known competing financial interests or personal relationships that could have appeared to influence the work reported in this paper.

Funding

* This research received no specific grant from any funding agency in the public, commercial, or not-for-profit sectors.

Acknowledgements or Notes

* This article was presented as an oral presentation at the International Conference on Basic Sciences, Engineering and Technology (www.icbaset.net) held in Trabzon/Türkiye on May 01-04, 2025.

References

Aini, N. (2025). Green business model canvas: A framework for sustainable business practice. *IOP Conference Series: Earth and Environmental Science,1441,* 012029.

Albort-Morant, G., Henseler, J., Leal-Millán, A., & Cepeda-Carrión, G. (2017). Mapping the field: A bibliometric analysis of green innovation. *Sustainability, 9*(6), 1011.

Argilovski, A., Vasileska, E., Tuteski, O., Kusigerski, B., Jovanoski, B., & Tomov, M. (2024). Bringing the gap: qualitative comparative analysis of industry 4.0 and industry 5.0. *Mechanical Engineering – Scientific Journal, 42*(1), 61–66.

Arora, N., Dhiman, N., & Shrivastava, R. (2023). How green entrepreneurship evolved over the past two decades? A glance through bibliometric analysis. *Vision: The Journal of Business Perspective*, 1217593.

Beloglazov, I, Petrov, A., & Bazhin, V. (2020). The concept of digital twins for tech operator training simulator design for mining and processing industry, *Eurasian Mining*, *2*, 50–54.

Bhatnagar, M., Taneja, S., & Ozen, E. (2022). A wave of green start-ups in India—The study of green finance as a support system for sustainable entrepreneurship. *Green Finance, 4*(2), 253–273.

Culchesk, A. M., Gava, V. L., Facin, A. L. F., Goncalves, R. F., Da Silva, J. F., & de Mesquita Spinola, M. (2025). Exploring the context of ındustry 4.0, continuous processes, and mining ındustry: A systematic literature review and research directions. *IEEE Access, 13,*43666-43697.

de Lange, D. (2017). Start-up sustainability: an insurmountable cost or a life-giving investment? *Journal of Cleaner Production, 156*, 838–854.

Dima, A. (2021). The importance of innovation in entrepreneurship for economic growth and development: A bibliometric analysis. *Review of International Comparative Management, 22*(1),120-131.

Dimov, E., Bakyrdjieva, R., & Stratiev, N. (2020). The mining industry and the recycling of raw materials as an important element of the Bulgarian economy. *Journal of Mining and Geological Sciences, 63*, 289-292.

Ebrahimi, P., & Mirbargkar, S.M. (2017). Green entrepreneurship and green innovation for SME development in market turbulence. *Eurasian Business Review 7*(2), 203–228.

Hillmann, J., A. Bergmann & E. Guenther (2022). Benefits of building organizational resilience: The case of climate change. *Highlights of Sustainability, 1*(4), 233-252.

Hristova, T., B. Evstatiev, B., Stoyanov, I., & Hristov, P. (2024). Industry 4.0−based solid waste management and future prospects in circular economy, In *Woodhead advances in pollution research, advances in energy from waste* (pp.457-502). Woodhead Publishing.

Jiang, Z., Xu, Y., Zhu, X., Liu, W., & Liu, Y. (2024). Intellectual capital and green entrepreneurship: A systematic literature review. *Journal of Intellectual Capital*, *25*(4), 801-821.

Korkmaz, M., & Oral, M. A. (2023). Entrepreneurship. International Refereed *Journal of Humanities and Academic Sciences*, (30), 20–33.

Kuzmenko, O., Serhieieva, O., & Orlova, V. (2024). Environmental entrepreneurship: State of the art and prospects. *Scientific Notes of the UniversityKROK, 2*(74), 56–61.

Makhloufi, L., Laghouag, A.A., Meirun, T., Belaid, F. (2022). Impact of green entrepreneurship orientation on environmental performance: the natural resourcebased view and environmental policy perspective. *Business Strategy and Environment, 31*(1), 425–444.

Pacheco, D., Dean, T., Payne, D. (2010). Escaping the green prison: entrepreneurship and the creation of opportunities for sustainable development. *Journal of BusinessVenture Insights, 25*(5), 464-480.

Silajdžić, I., Kurtagić, S. M., & Vučijak, B. (2014). Green entrepreneurship in transition economies: A case study of Bosnia and Herzegovina. *Journal of Cleaner Production, 88*, 376–384.

Sreenivasan, A., & Suresh, M. (2023). Exploring the contribution of sustainable entrepreneurship toward sustainable development goals: A bibliometric analysis. *Green Technologies and Sustainability, 1*(3), 100038.

Terán-Yépez, E., Marín-Carrillo, G. M., Del Pilar Casado-Belmonte, M., & De Las Mercedes Capobianco-Uriarte, M. (2019). Sustainable entrepreneurship: Review of its evolution and new trends. *Journal of Cleaner Production, 252*, 119742.

Tomova, M. (2023). Geophysical techniques for monitoring of integrated mine waste storage facility: Case study of Southeastern Bulgaria. *The Eurasia Proceedings of Science, Technology, Engineering & Mathematics (EPSTEM), 26,* 341-347

Trifonova B. (2022). The company culture in support of the enterprises from the mineral and raw material industry during a crisis. *Annual of the University of Mining and Geology "St. Ivan Rilski", 65*, 186-189.

Trifonova, B (2019). Model for HR management in mining companies. *Izvestia Journal of the Union of Scientists - Varna. Economic Sciences Series, 8*(1), 166-173.

Tuncer, B., E. Korchagina (2024). A systematic literature review and conceptual framework on green entrepreneurial orientation. *Administrative Sciences, 14*(6), 109.

Ulrich, D., & Brockbank, W. (2005), *The HR value proposition* (1st ed., p.26). Harvard Business Press.

York, J. G., & Venkataraman, S. (2010). The entrepreneur–environment nexus: Uncertainty, innovation, and allocation. *Journal of Business Venturing, 25*(5), 449–463.

Zhang, X., Li, Y., & Teng, X. (2024). How does green entrepreneurial orientation improve enterprises' sustainable performance? Evidence from the agricultural sector in China. *Business Ethics, the Environment & Responsibility*, 12706.

Author(s) Information

Borislava Galabova
University of Mining and Geology "St. Ivan Rilski"
Prof. Boyan Kamenov Str., Sofia, Bulgaria
Contact e-mail: *borislava.galabova@mgu.bg*

Vessela Petrova
University of Mining and Geology "St. Ivan Rilski"
Prof. Boyan Kamenov Str., Sofia, Bulgaria

To cite this article:

Galabova, B., & Petrova, V. (2025). Guidelines for the development of a green business model in companies from the raw materials industry. *The Eurasia Proceedings of Science, Technology, Engineering and Mathematics (EPSTEM), 34,* 66-79.

The Eurasia Proceedings of Science, Technology, Engineering & Mathematics (EPSTEM)
ISSN: 2602-3199

The Eurasia Proceedings of Science, Technology, Engineering and Mathematics (EPSTEM), 2025

Volume 34, Pages 80-86

ICBASET 2025: International Conference on Basic Sciences, Engineering and Technology

Biochemical and Blood Lipid Parameters of Broiler Chickens Fed Sagebrush (Artemisia Herba-Alba Asso)

Si Ammar Kadi
Mouloud Mammeri University of Tizi-Ouzou

Azeddine Mouhous
Mouloud Mammeri University of Tizi-Ouzou

Zahia Dorbane
Mouloud Mammeri University of Tizi-Ouzou

Nacima Zirmi-Zembri
Mouloud Mammeri University of Tizi-Ouzou

Nadia Belaid-Gater
Specialised Technological Institute for Agricultural Training – ITSFA

Farid Djellal
Ferhat Abbas University

Hocine Guermah
University of Msila

Ali Bouzourene
Mouloud Mammeri University of Tizi-Ouzou

Idir Moualek
Mouloud Mammeri University of Tizi-Ouzou

Rabia Cherfouh
Mouloud Mammeri University of Tizi-Ouzou

Dahia Saidj
Saad Dahlab University

Abstract: The use of medicinal plants in animal feed has gained attention due to their pharmacological properties, cost-effectiveness, and availability. This study evaluated the effects of an infusion from Artemisia herba-alba (white wormwood) on biochemical and lipid parameters in broiler chickens. Two hundred one-day-old Cobb 500 chicks were divided into a control group (plain water) and an experimental group (Artemisia infusion) over 31 days. The infusion was prepared by steeping 60 g of Artemisia powder in 1 liter of water for 8 hours, then diluting it in 40 liters. Weekly measurements included live weight, feed intake, water consumption, feed conversion ratio (FCR), and mortality. Blood samples were analyzed for glucose, urea, creatinine, total proteins, cholesterol (total, HDL, LDL), and triglycerides. Results showed significant increases in blood glucose (2.37 g/L vs. 1.61 g/L) and triglycerides (0.65 g/L vs. 0.29 g/L) in the treated group, indicating effects on carbohydrate and lipid metabolism. Total cholesterol also increased (1.17 g/L vs. 1.04 g/L), while HDL

cholesterol slightly decreased (0.55 g/L vs. 0.59 g/L). LDL cholesterol rose (0.49 g/L vs. 0.39 g/L), suggesting modulation of lipoprotein metabolism. Renal function (urea, creatinine) and total protein levels remained stable, indicating no adverse effects on kidney function or protein synthesis. These effects are attributed to bioactive compounds in Artemisia herba-alba, such as flavonoids and terpenoids, known to influence energy and lipid metabolism. The study highlights its potential as a natural feed additive to improve broiler metabolic health. However, further research is needed to fully understand its mechanisms and long-term implications. This work supports the use of medicinal plants as sustainable alternatives to synthetic additives in poultry production.

Keywords: Broiler, Blood parameters, Sagebrush

Introduction

The use of medicinal plants in animal feed has been of increasing interest over the last few decades due to their pharmacological properties, their cost effectiveness and their availability (Acamovic & Brooker, 2005). In the poultry sector, optimising broiler growth performance and health is a major challenge, especially in the face of metabolic diseases, infections and oxidative stress (Diaz-Sanchez et al., 2015). Natural feed additives, such as plant extracts, are increasingly being used to replace antibiotics and chemical additives to promote sustainable and environmentally friendly animal production (Windisch et al., 2008).

Among these medicinal herbs, Artemisia herba-alba, commonly known as sagebrush or wormwood, occupies an important place in traditional medicine and modern scientific research. It is known for its multiple therapeutic properties, including antioxidant, anti-inflammatory, antimicrobial, hypoglycaemic and hypolipidemic effects (Bora & Sharma, 2011). These properties are mainly attributed to the presence of bioactive compounds like flavonoids, terpenoids and polyphenols, which have a synergistic effect in modulating different physiological processes (Tariq et al., 2009). This plant is native to the arid and semi-arid regions of the Mediterranean basin and the Middle East.

The species of the genus Artemisia have been the subject of extensive research for their pharmacological properties. In particular, Artemisia herba-alba has been widely studied for its beneficial effects on animal and human health. According to Boudjelal et al. (2013), extracts of this plant exhibit antidiabetic properties in diabetic rats through regulation of blood glucose levels and improvement of lipid profiles. Also, these studies indicate that A. herba-alba may have a beneficial effect on energy and fat metabolism. Thus, Artemisia herba-alba, with its rich phytochemical profile, represents a promising option for improving biochemical and lipid parameters in broilers while minimising the risks associated with using synthetic substances (Abdel-Wahhab et al., 2011).

However, in spite of these advances, only a few studies have focused on the effects of A. herba-alba on the biochemical and lipid parameters of broiler chickens, especially when it is administered as an infusion. Existing research has mainly focused on the effects of this plant in rodents or *in vitro* models, leaving a gap in the literature regarding its use in poultry nutrition (Abdel-Wahhab et al., 2011). For example, Abdel-Wahhab et al. (2011) showed that extracts of A. herba-alba can protect against aflatoxin-induced toxicity in rats, but there is limited data on its effects in poultry.

Biochemical and lipid parameters in the blood are important indicators of the health and metabolism of animals. Blood glucose levels, for example, reflect the energy balance and the ability of the body to regulate glucose (Dibner et al., 2007). Cholesterol and triglyceride levels are important markers of lipid metabolism, while total protein, urea and creatinine provide insight into renal function and nutritional status (Kaneko et al., 2008). In poultry production, perturbations in these parameters can lead to health problems including metabolic dysfunction, reduced growth and increased mortality (Diaz-Sanchez et al., 2015).

The use of medicinal plants, such as A. herba-alba, could help to maintain the balance of these parameters, in particular under conditions of stress or disease. For example, Zeggwagh et al., (2007) demonstrated that A. herba-alba extract ameliorated lipid profiles in hypertensive rats, while El-Haskoury et al. (2018) showed that the plant has antioxidant properties and protects against kidney toxicity. These findings suggest that A. herba-alba may have a similar effect in broiler chickens, improving the metabolic health of the birds and reducing the risk of disease.

This study evaluated the effect of an infusion of Artemisia herba-alba aerial parts on biochemical (blood glucose, urea, creatinine and total protein) and lipid (total cholesterol, HDL cholesterol, LDL cholesterol and

triglycerides) parameters in broiler chickens. The aim was to determine whether this infusion could have a positive effect on the energy and lipid metabolism of the animals, while maintaining the health of the kidneys and the liver. The results obtained could contribute to a better understanding of the mechanisms of action of A. herba-alba. They could also open up new perspectives for its use in animal nutrition.

This study is part of a broader effort to explore natural alternatives to synthetic feed additives aimed at promoting more sustainable and humane poultry production (Windisch et al., 2008). By investigating the effects of A. herba-alba on the biochemical and lipid parameters of broiler chickens, we hope to provide robust scientific data to support its use in animal nutrition, while helping to reduce the risks associated with using chemical substances.

Material and Method

200 day-old Cobb 500 broiler chicks of mean initial weight of 33.68g were obtained from a local hatchery in the same area. The rearing period was divided into three phases. Three commercial diets were used during the experiment: starter (crumbled), grower (pelleted) and finisher (pelleted). All chicks were reared together during the first 11 days of the starter phase. At 11 days of age, the chicks were individually weighed, marked and randomly divided into three equal groups to ensure uniformity in the number of chicks (100 chicks per group) and the total weight of the group, with four replicates of 25 chicks per group.

The experimental design comprised:

- A control group (T) that was provided with plain drinking water.
- An experimental group (A) given an infusion prepared from the aerial parts of Artemisia herba-alba (sagebrush or white wormwood). The infusion was renewed every 24 hours for 31 consecutive days (from 11 to 42 days of age).

The preparation of the infusion was in accordance with the method described by Leila (1977). Aerial parts of Artemisia herba-alba were purchased from a local herbalist. The infusion was prepared according to the same protocol every night for the experimental group throughout the study: 60 g Artemisia powder was mixed with 1 litre water in a bottle and infused for 8 hours at room temperature. The next morning, the aqueous solution was filtered. It was then diluted in a container with 40 litres of water. During the six weeks of the experiment, the following parameters were monitored: Weekly individual live weight, Feed intake per day, Daily water consumption, Weekly feed conversion ratio (FCR) and Mortality rate.

For comparison of biochemical profiles and lipid metabolism between the two groups, blood samples were taken from one randomly selected chicken per replicate at the end of the experiment. The blood samples were then sent to a specialised laboratory for analysis. The following parameters were determined: Blood glucose, Blood urea, Blood creatinine, Total proteins, Total cholesterol, HDL cholesterol, LDL cholesterol and Triglycerides.

Results and Discussion

The results of this study show that the infusion prepared from the aerial parts of Artemisia herba-alba powder has a significant effect on the biochemical and lipid parameters of broiler chickens. These effects can be attributed to the bioactive compounds present in Artemisia herba-alba, such as flavonoids, terpenoids, polyphenols and sesquiterpenes, which are known for their pharmacological properties on energy and lipid metabolism.

Biochemical Parameters (Table 1)

Table 1. Biochemical parameters in the blood of chickens from both lots

	Control lot	Artemisia Lot
Blood glucose (mg/ml)	1.61	2.37
Blood urea (mg/ml)	<0.04	<0.04
Blood creatinine (mg/ml)	3	4
Total protein (mg/ml)	31	30

Blood Glucose

Blood glucose levels increased significantly in the group treated with Artemisia herba-alba infusion (2.37 g/L) compared with the control group (1.61 g/L). This increase may be related to the effect of the bioactive compounds in Artemisia herba-alba on carbohydrate metabolism. According to Boudjelal et al. (2013), Artemisia herba-alba extracts exhibit hypoglycaemic properties in diabetic animals; however, in our case, the increase in blood glucose may reflect a transient stimulation of energy metabolism. A recent study by Benbott et al. (2020) showed that Artemisia herba-alba extracts can influence blood glucose regulation by modulating hepatic and pancreatic enzyme activity. In addition, El-Masry et al. (2022) reported that flavonoids in Artemisia herba-alba may stimulate hepatic glucose release, which may explain the increase observed in this study.

Blood Urea and Creatinine

Blood urea levels remained below 0.04 g/L in both groups, indicating that renal function was not affected by the administration of Artemisia herba-alba infusion. Similarly, creatinine levels, although slightly higher in the treated group (4 mg/L versus 3 mg/L in the control group), remained within normal physiological limits. These findings are consistent with those of Zeggwagh et al. (2007), who demonstrated that Artemisia herba-alba does not exhibit renal toxicity at moderate doses. A more recent study by El-Haskoury et al. (2018) confirmed that Artemisia herba-alba extracts do not impair renal function in treated animals. Ait-Ouazzou et al. (2021) also showed that phenolic compounds in Artemisia herba-alba have a protective effect on the kidneys, supporting our findings.

Total Protein

The level of total protein remained relatively stable between the two groups (31 g of protein/l for the control group and 30 g of protein/l for the treated group). This suggests that the Artemisia herba-alba infusion did not significantly affect protein synthesis or the nutritional status of the chickens. These results are in agreement with those of Abdel-Wahhab et al. (2011), who observed that the extracts of Artemisia herba-alba did not have any effect on the total protein content of the treated animals. Bouhrim et al. (2020) also reported that Artemisia herba-alba extracts did not significantly alter total protein levels in healthy animals.

Triglycerides

A significant increase in triglycerides was observed in the Artemisia herba-alba infusion group (0.65 g/L) compared with the control group (0.29 g/L). This increase may be related to the effect of bioactive compounds in Artemisia herba-alba on lipid metabolism. According to Tilaoui et al. (2015), Artemisia herba-alba extracts may affect lipid metabolism by modulating hepatic enzyme activity. A recent study by Boukhris et al. (2019) showed that Artemisia herba-alba extracts can stimulate lipolysis, which may explain the observed increase in triglycerides in this study. El Abbouyi et al. (2021) also reported that Artemisia herba-alba extracts may increase triglyceride levels by stimulating the mobilisation of lipid reserves.

Lipid Parameters (Table 2):

Table 2. Lipid parameters in the blood of chickens from both lots of chickens

	Control lot	Artemisia Lot
Total cholesterol (mg/ml)	1.04	1.17
HDL cholesterol (mg/ml)	0.59	0.55
LDL cholesterol (mg/ml)	0.39	0.49
Triglycerides (mg/ml)	0.29	0.65

Total Cholesterol

The level of total cholesterol increased in the group treated with the Artemisia herba-alba infusion (1.17 g per litre) compared with the control group (1.04 g per litre). This increase may be related to the effect of the bioactive compounds contained in Artemisia herba-alba on the metabolism of lipids. Artemisia herba-alba

extracts may affect cholesterol synthesis and degradation, according to Tilaoui et al. (2015). A recent study by El Abbouyi et al. (2021) showed that extracts of Artemisia herba-alba can modulate the expression of genes that are involved in the metabolism of cholesterol. Khadir et al. (2020) also reported that Artemisia herba-alba extracts were able to increase the level of total cholesterol in the treated animals.

HDL Cholesterol

There was a slight decrease in HDL cholesterol levels in the treated group (0.55 g/L) compared with the control group (0.59 g/L). Although this decrease is small, it may be an indication of a slight effect of the Artemisia herba-alba infusion on reverse cholesterol transport. Nevertheless, the change remains within normal physiological limits. According to Eddouks et al. (2005), Artemisia herba-alba extracts have variable effects on HDL cholesterol depending on the dose and duration of treatment. Artemisia herba-alba extracts were also found to slightly reduce HDL levels in treated animals by Bouhrim et al. (2020).

LDL Cholesterol

The level of LDL cholesterol was increased in the treated group (0.49 g/L) in comparison with the control group (0.39 g/L). The effect of the bioactive compounds in Artemisia herba-alba on lipoprotein metabolism may explain this increase. According to Boudjelal et al. (2013), extracts of Artemisia herba-alba may have an effect on the synthesis and degradation of lipoproteins. A recent study by Khadir et al. (2020) showed that Artemisia herba-alba extracts can increase LDL levels in treated animals. This is in agreement with our results. El Abbouyi et al. (2021) also reported that Artemisia herba-alba extracts may increase LDL levels through modulation of hepatic enzyme activity.

Triglycerides

Consistent with the biochemical results discussed above, there was a significant increase in triglycerides in the treated group (0.65 g/L) compared with the control group (0.29 g/L). According to Zeggwagh et al. (2007), extracts of Artemisia herba-alba are able to stimulate the mobilisation of lipid reserves in order to meet the increased demand for energy. The ability of Artemisia herba-alba extracts to influence triglyceride metabolism by modulating hepatic enzyme activity was confirmed by Boukhris et al. (2019). El Abbouyi et al. (2021) also reported that Artemisia herba-alba extracts may increase triglyceride levels through stimulation of lipolysis.

Conclusion

The results of this study showed a significant effect of Artemisia herba on biochemical and lipid parameters in broilers. The bioactive compounds of Artemisia herba-alba seem to have an effect on energy and lipid metabolism, based on the observed effects on blood glucose, triglycerides, total cholesterol and LDL cholesterol. However, these effects vary depending on the parameters studied. Further research is needed to better understand the mechanisms of action and long-term implications.

Scientific Ethics Declaration

* The authors declare that the scientific ethical and legal responsibility of this article published in EPSTEM Journal belongs to the authors.

Conflict of Interest

* The authors declare that they have no conflicts of interest

Funding

* This research received no specific grant from any funding agency in the public, commercial, or not-for-profit sectors.

Acknowledgements or Notes

* This article was presented as a poster presentation at the International Conference on Basic Sciences, Engineering and Technology (www.icbaset.net) held in Trabzon/Türkiye on May 01-04, 2025.

References

Abdel-Wahhab, M. A., Ahmed, H. H., & Hagazi, M. M. (2011). Prevention of aflatoxin-induced toxicity in rats by Artemisia herba-alba extract. *Journal of Applied Sciences Research*, *7*(12), 2223-2232.

Acamovic, T., & Brooker, J. D. (2005). Biochemistry of plant secondary metabolites and their effects in animals. *Proceedings of the Nutrition Society*, *64*(3), 403-412.

Ait-Ouazzou, A., Lorán, S., Arakrak, A., & Laglaoui, A. (2021). Protective effects of Artemisia herba-alba extracts against renal toxicity induced by heavy metals in rats. *Toxicology Reports*, *8*, 1-7.

Benbott, A., Bahri, L., Boubekri, N., & Zama, D. (2020). Effects of Artemisia herba-alba on glucose metabolism in diabetic rats: Role of liver and pancreatic enzymes. *Journal of Ethnopharmacology*, *253*, 112634.

Bora, K. S., & Sharma, A. (2011). The genus Artemisia: a comprehensive review. *Pharmaceutical Biology*, *49*(1), 101-109.

Boudjelal, A., Henchiri, C., Sari, M., Sarri, D., Hendel, N., Benkhaled, A., & Ruberto, G. (2013). Antidiabetic effects of Artemisia herba-alba in streptozotocin-induced diabetic rats. *Journal of Medicinal Plants Research*, *7*(13), 791-800.

Bouhrim, M., Ouassou, H., Choukri, M., & Ziyyat, A. (2020). Effects of Artemisia herba-alba on lipid profile and oxidative stress in hyperlipidemic rats. *Journal of Medicinal Food*, *23*(5), 543-550.

Boukhris, M., Hadrich, F., Chtourou, H., Dhouib, A., & Sayadi, S. (2019). Hypolipidemic and antioxidant effects of Artemisia herba-alba in high-fat diet-induced hyperlipidemic rats. *Journal of Food Biochemistry*, *43*(7), e12888.

Diaz-Sanchez, S., D'Souza, D., Biswas, D., & Hanning, I. (2015). Botanical alternatives to antibiotics for use in organic poultry production. *Poultry Science*, *94*(6), 1419-1430.

Dibner, J. J., Richards, J. D., Knight, C. D., & Downs, J. E. (2007). Metabolic challenges and the role of feed additives in poultry nutrition. *Journal of Applied Poultry Research*, *16*(1), 150-159.

Eddouks, M., Maghrani, M., Lemhadri, A., Ouahidi, M. L., & Jouad, H. (2005). Ethnopharmacological survey of medicinal plants used for the treatment of diabetes mellitus, hypertension and cardiac diseases in the south-east region of Morocco (Tafilalet). *Journal of Ethnopharmacology*, *82*(2-3), 97-103.

El Abbouyi, A., El Khyari, S., & Filali-Ansari, N. (2021). Modulation of cholesterol metabolism by Artemisia herba-alba in hypercholesterolemic rats. *Journal of Ethnopharmacology*, *265*, 113-120.

El-Haskoury, R., Al-Waili, N., Kamoun, Z., & Lyoussi, B. (2018). Antioxidant activity and protective effect of Artemisia herba-alba against renal toxicity induced by carbon tetrachloride in rats. *Biomedicine & Pharmacotherapy*, *97*, 1-7.

El-Masry, T. A., El-Ghorab, A. H., & El-Sayed, M. M. (2022). Effects of Artemisia herba-alba on glucose metabolism and liver function in diabetic rats. *Journal of Ethnopharmacology*, 285, 114-120.

Kaneko, J. J., Harvey, J. W., & Bruss, M. L. (2008). *Clinical biochemistry of domestic animals* (6th ed.). Academic Press.

Khadir, F., Bendahmane, M., & Benabadji, N. (2020). Effects of Artemisia herba-alba on lipid profile and oxidative stress in hyperlipidemic rats. *Journal of Medicinal Plants Research*, *14*(4), 123-130.

Leila, S. F. M. (1977). A manual on some Philippine medicinal plants (preparation of drug materials). *Botanical Society UP*, 20, 78-82.

Tariq, K. A., Chishti, M. Z., Ahmad, F., & Shawl, A. S. (2009). Anthelmintic activity of extracts of Artemisia absinthium against ovine nematodes. *Veterinary Parasitology*, *160*(1-2), 83-88.

Tilaoui, M., Mouse, H. A., Jaafari, A., & Zyad, A. (2015). Comparative phytochemical analysis of essential oils from different biological parts of Artemisia herba-alba and their cytotoxic effect on cancer cells. *PLoS ONE*, *10*(7), e0131799.

Windisch, W., Schedle, K., Plitzner, C., & Kroismayr, A. (2008). Use of phytogenic products as feed additives for swine and poultry. *Journal of Animal Science*, *86*(14), E140-E148.

Zeggwagh, N. A., Farid, O., Michel, J. B., & Eddouks, M. (2007). Cardiovascular effect of Artemisia herba-alba aqueous extract in spontaneously hypertensive rats. *Methods and Findings in Experimental and Clinical Pharmacology*, *29*(5), 331-336.

Author(s) Information

Si Ammar Kadi
Department of Agronomical Sciences, Faculty of Biological Sciences and Agronomical Sciences, Mouloud Mammeri University of Tizi-Ouzou, Algeria
Contact email: siammar.kadi@ummto.dz

Azeddine Mouhous
Department of Agronomical Sciences, Faculty of Biological Sciences and Agronomical Sciences, Mouloud Mammeri University of Tizi-Ouzou, Algeria

Zahia Dorbane
Department of Agronomical Sciences, Faculty of Biological Sciences and Agronomical Sciences, Mouloud Mammeri University of Tizi-Ouzou, Algeria

Nacima Zirmi-Zembri
Department of Agronomical Sciences, Faculty of Biological Sciences and Agronomical Sciences, Mouloud Mammeri University of Tizi-Ouzou, Algeria

Nadia Belaid-Gater
Specialised Technological Institute for Agricultural Training – ITSFA, Tizi-Ouzou, Algeria

Farid Djellal
Department of Agronomical Sciences, Faculty of Natural and Life Sciences. University F. Abbas, Sétif -1- Algeria.

Hocine Guermah
Department of Agronomical Sciences, Faculty of Natural Sciences, M. Boudiaf University, M'Sila, Algeria

Ali Bouzourene
Department of Agronomical Sciences, Faculty of Biological Sciences and Agronomical Sciences, Mouloud Mammeri University of Tizi-Ouzou, Algeria

Idir Moualek
Department of Biochemical and microbiological science, Faculty of Biological Sciences and Agronomical Sciences, Mouloud Mammeri University of Tizi-Ouzou, Algeria

Rabia Cherfouh
Department of Agronomical Sciences, Faculty of Biological Sciences and Agronomical Sciences, Mouloud Mammeri University of Tizi-Ouzou, Algeria

Dahia Saidj
Veterinary Sciences Institute, Saad Dahlab University, Blida, Algeria

To cite this article:

Kadi, S. A., Mouhous, A., Dorbane, Z., Zirmi-Zembri, N., Belaid-Gater, N., Djellal, F., Guermah, H., Bouzourene, A., Moualek, I., Cherfouh, R., & Saidj, D. (2025). Biochemical and blood lipid parameters of broiler chickens fed sagebrush (Artemisia herba-alba asso). *The Eurasia Proceedings of Science, Technology, Engineering & Mathematics (EPSTEM), 34,* 80-86.

The Eurasia Proceedings of Science, Technology, Engineering & Mathematics (EPSTEM)
ISSN: 2602-3199

The Eurasia Proceedings of Science, Technology, Engineering and Mathematics (EPSTEM), 2025

Volume 34, Pages 87-92

ICBASET 2025: International Conference on Basic Sciences, Engineering and Technology

Development and Experimental Testing of a New Technology for Producing Screw Fittings from Bar Scrap of Ferrous Metals

Sergey Lezhnev
Rudny Industrial University

Dmitry Goldabin
Rudny Industrial University

Elena Shiriaeva
Nosov Magnitogorsk State Technical University

Dmitry Kuis
Belarusian State Technological University

Abstract: One of the simplest and most frequently used methods of recycling ferrous scrap is its remelting and further reuse. But at the same time, in some countries of the world, another method of processing ferrous scrap has entered into practice, namely, recycling of some metal products that have served their service life by various methods of hot pressure treatment to obtain a finished commercial product. In our opinion, this method of processing ferrous scrap and alloys can be attributed to "green" technologies, as it allows you to make a small contribution to improving the environmental situation in the world. This work, carried out within the framework of grant № AP14869135, funded by the Science Committee of the Ministry of Science and Higher Education of the Republic of Kazakhstan, is devoted to the development and research of a new technology for processing scrap in the form of pieces of reinforcement made of 25G2S steel to obtain high-quality finished metal products in the form of screw fittings. The developed technology included two stages. At the first stage, the reinforcement pieces are performed on a radial-shear rolling mill to obtain conventional rods of the desired diameter and create initial conditions for the formation of a gradient ultrafine-grained structure in the resulting screw profile. The second stage is the direct production of screw fittings with a gradient ultra-fine-grained structure on a combined installation. Metallographic studies have shown that after the implementation of the second stage of obtaining screw fittings, a gradient structure is observed in 25G2S steel in the longitudinal direction, with equiaxed grains (ranging in size from 11-14 μm) in the peripheral region and with elongated, directional-oriented grains in the central region of the resulting reinforcement.

Keywords: Radial-shear rolling, Combined installation, Bar scrap, Recycling, Screw reinforcement profile

Introduction

At the beginning of this work, it is necessary to note two main points that determine its relevance. Firstly, everyone knows that in the modern world, industrial and civil engineering widely uses various building materials based on reinforced concrete structures. A key trend in this area is to increase the reliability and durability of reinforced concrete products while reducing the cost of reinforcement manufacturing as one of the main construction objects. Reinforcement, including screw reinforcement, has been used for decades in the construction industry, although it is quite durable, but in conditions of increased demand for the quality of reinforced concrete structures, the requirements for the quality of reinforcement, including an increase in its life cycle, are correspondingly increasing. Therefore, the development of new or improvement of previously known

technologies for producing high-quality products in the form of reinforced reinforcement profiles for various purposes is, as noted above, currently an urgent task.

Secondly, currently in many countries of the world, a number of different technological processes have been developed for the processing of certain metal products that have served their service life using hot pressure treatment into a ready-to-sell product. The founder of this field of processing metal products that have served their service life by hot pressure treatment is the American scientist E.E. Slick, who at the beginning of the last century developed a technology for processing railway rails by hot rolling in calibers in order to obtain flange profiles (Slick, 2021). But then the technology he proposed was not widely used in practice. It was only at the end of the 20th century that the global scientific community and manufacturers of metal products became interested in this area. Here are just some works Badyuk and Leshchenko (2010) and Smirnov et al. (1995) and Bakhtinov (2000) and McGahhey (1991) devoted to the development and study of technologies for processing railway rails by hot rolling to produce various finished metal products. Another promising method of recycling some metal products that have served their service life is their rolling in radial-shear rolling mills (Galkin, 2007). However, most often this method is applicable only for recycling cylindrical metal products, for example, used railway axles (Grevtseva & Galkin, 2017) and pumping rods (Galkin & Romantsev, 2014), as well as bar scrap of ferrous metals and alloys (Lezhnev et al., 2021-1), including in the form of fittings (Lezhnev et al., 2021-2). In all cases, this method is based on the principle of hot radial shear rolling of a used so-called bar to a smaller diameter and then using the resulting bar with a smaller cross-section for its intended purpose. It should be noted that radial shear rolling makes it possible to obtain long-length products from various materials with a gradient ultrafine-grained structure, which has been proven, including in (Gamin et al., 2023; Ozhmegov et al., 2023; Dobatkin et al., 2019; Gamin et al., 2020; Karpov et al., 2018; Valeev et al., 2015), and in addition, this method is the most technologically advanced and easy to implement compared to many other methods of metal pressure treatment, which realize severe plastic deformation during the deformation process (Galkin et al., 2015).

As already mentioned above, radial-shear rolling makes it possible to obtain high-quality bars with a gradient fine-grained structure from ferrous scrap. These bars can be used as a final marketable product, or subjected to further pressure treatment to produce various metal products, for example, hardware products or a clamping screw for formwork. Continuing to develop the direction of processing ferrous bar scrap using radial-shear rolling, we proposed to use a previously developed new combined process (Lezhnev et al., 2023a) combining radial-shear rolling and pressing through a screw matrix for these purposes (processing of bar scrap) (Fig.1). The main difference in this case will be only that bar scrap of round cross-section of ferrous metals will be used as the initial blanks. The final product will still be a high-quality commercial product in the form of screw fittings with a gradient ultrafine-grained structure and with a given level of mechanical properties. That is, in this case, we are solving the two relevant tasks discussed above.

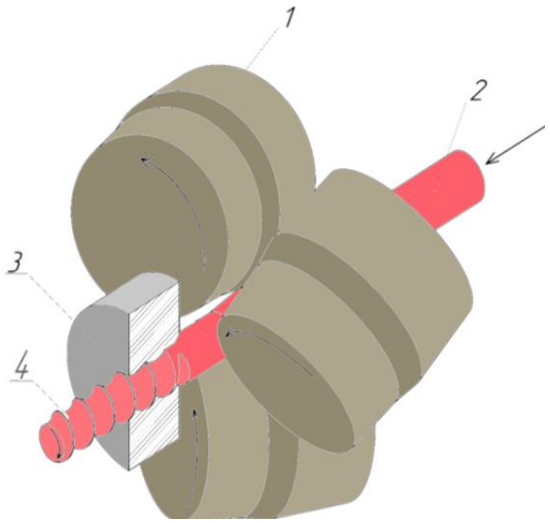

Figure 1. Combined method for producing screw fittings: 1 – rolling rolls, 2 – initial blank, 3 – die, 4 – screw profile

In the works Lezhnev et al. (2024) and Lezhnev et al. (2023b) devoted to computer modeling in the DEFORM software package of a new combined process for producing screw fittings, the possibility of its implementation has already proved. The purpose of this work is to experimentally confirm the possibility of obtaining

commercial products from bar scrap in the form of screw fittings with a gradient ultrafine-grained structure during the implementation of a new combined method, the scheme of which is shown in Figure 1.

Method

To achieve this goal, physical experiments were conducted using two radial-shear rolling mills: SVP 14-40 and RSR 10-30. At the same time, a laboratory combined installation for producing screw fittings was assembled on the basis of the RSR 10-30 mill (Fig. 2a), by installing on it a specially made die with a screw profile with maximum diameter of the working screw channel 20 mm (Fig. 2b-c).

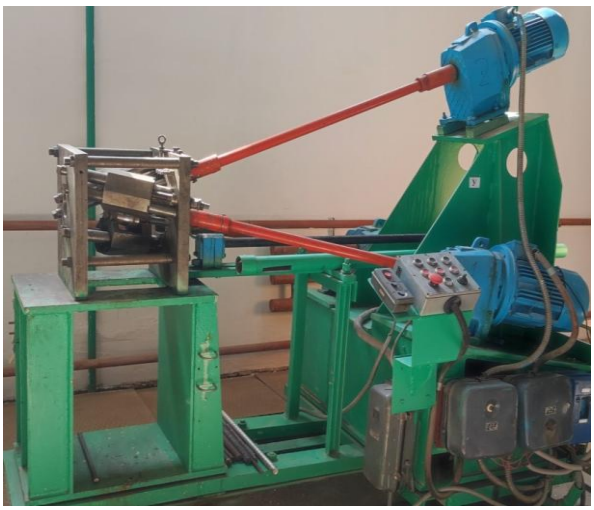

a)

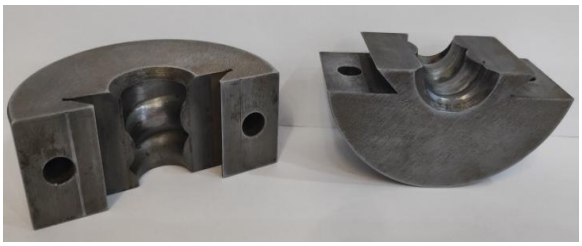

b)

c)

Figure 2. Combined installation for producing screw fittings assembled on the basis of the RSR 10-30 mill: a – radial-shear rolling mill RSR 10-30; b – die with a screw profile; c - working cage of the RSR 10-30 mill with an installed die

Ferrous scrap in the form of rebar pieces with a diameter of 32 mm and a length of 150 to 200 mm (steel grade 25G2S), which were subjected to homogenizing annealing, were used as the initial blanks for the physical

experiment. The technology of rolling scrap in the form of pieces of reinforcement (GOST 5781-82) into a ready-to-sell product in the form of screw reinforcement included two stages: the 1st stage was the production of a conventional cylindrical billet from the reinforcement, i.e. rolling out the reinforcing profile of the initial billet (reinforcement) at the radial-shear rolling mill SVP 14-40. At this stage, in addition to rolling out the reinforcement profile, initial conditions are created for the formation of a gradient ultrafine-grained structure in the future of the resulting screw reinforcement. The 2nd stage is the direct production of screw fittings with a gradient ultrafine-grained structure by deforming a cylindrical billet previously obtained at the first stage on a combined installation assembled on the basis of the RSR 10-30 mill.

During the implementation of the 1st stage, pieces of reinforcement with a diameter of 32 mm, preheated and kept at a temperature of 1000°C, were deformed on a radial-shear rolling mill SVP 14-40 to a diameter of 22 mm in 4 passes according to a reversible scheme (Galkin & Kharitonov, 2003) with an absolute compression step in diameter per pass equal to 2.5 mm. After that, the received rods were sent back to the furnace for heating (the temperature in the furnace is 1000°C). At the 2nd stage, the rods with a diameter of 22 mm obtained at the 1st stage were deformed using a combined installation assembled on the basis of the RSR 10-30 mill. In this case, the rod was first rolled in the working cage of the RSR 10-30 mill with an absolute compression of 2 mm in diameter, at the outlet of which it entered the matrix with a working screw channel (Fig. 2b) and, due to the pushing force created by the rolls, was pushed through the screw channel.

Results and Discussion

The analysis of the microstructure evolution of the resulting screw reinforcement was carried out using a metallographic complex, including a MI-1 light microscope, a Nikon Colorpix-4300 digital camera with a photo adapter. The microstructure was studied in the center and surface area of the resulting screw reinforcement. The results of metallographic studies are shown in Figure 3.

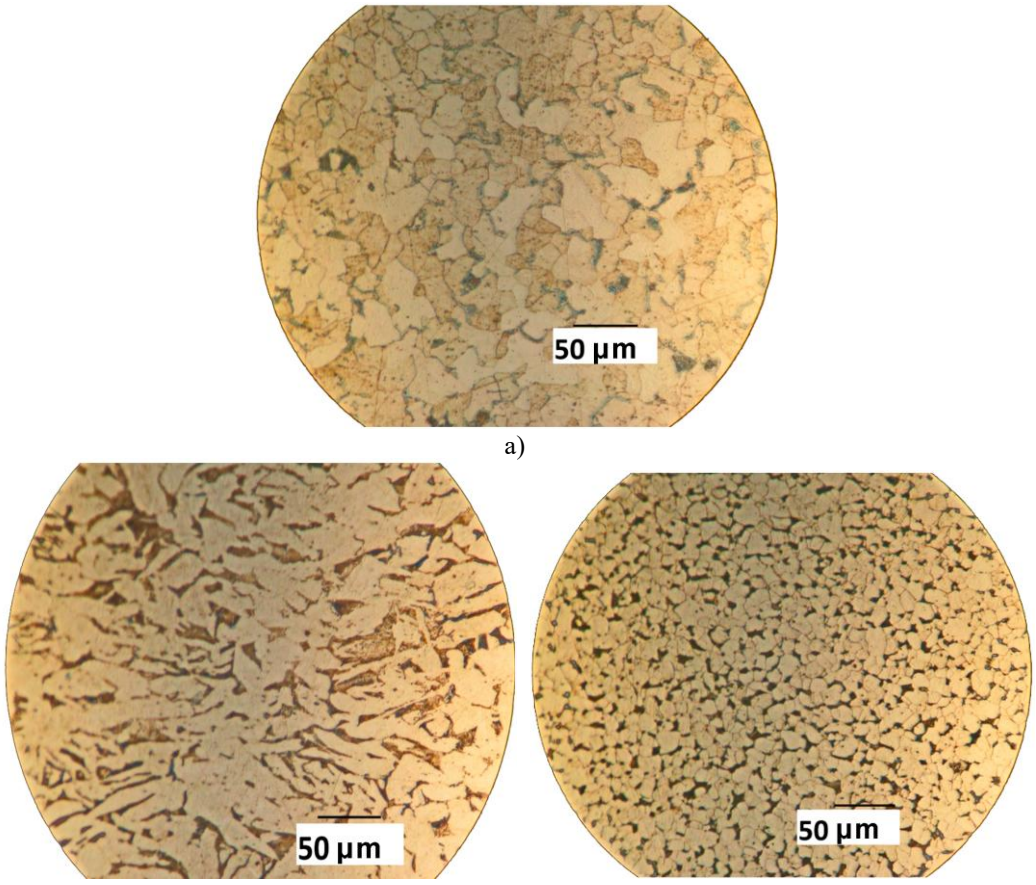

a)

b) c)

Figure 3. Microstructure of the resulting screw reinforcement of 25G2S steel (longitudinal direction): a – initial; b – central zone; c – surface zone

An analysis of the microstructure evolution of 25G2S steel after the implementation of the 2nd stage of deformation showed that during the implementation of the proposed technological process, the initial microstructure significantly decreased throughout the volume of the deformable metal. Thus, in the surface zone, the grain size decreased to 11-14 μm (Figure 3a). In this case, the microstructure in this zone of the resulting screw profile has a predominantly equiaxed ultrafine-grained character. In the central zone of the resulting screw reinforcement, grains elongated in the direction of rolling are observed to a greater extent, ranging in size from 6-10,5 x 1,1-1,7 μm (Fig. 3b), which is due to the preliminary deformation of the initial pieces of reinforcement according to the standard radial-shear rolling scheme . But at the same time, elongated grains, misoriented in directions, are also observed in the central zone, lying also in the range of 6-10,5 x 1,1-1,7 μm (Fig. 3c), which is justified by the back pressure arising from the side of the screw die and the additional twisting of the bar in this die when pushing the bar through it.

Conclusion

The research carried out in this work has proved that the proposed combined technological process for producing screw fittings from ferrous scrap is feasible in practice. Metallographic studies have shown that during the implementation of the new combined process, the goal was achieved to produce screw fittings with a gradient structure. Thus, the resulting reinforcement has an ultrafine-grained recrystallized grain structure with a grain size of 11-14 μm in the surface zone, and a structure with elongated, directional grains in the central zone of this reinforcement.

Scientific Ethics Declaration

* The authors declare that the scientific ethical and legal responsibility of this article published in EPSTEM Journal belongs to the authors.

Conflict of Interest

* The authors declare that they have no conflicts of interest

Funding

* This research was funded by the Science Committee of the Ministry of Science and Higher Education of the Republic of Kazakhstan (Grant no. AP14869135).

Acknowledgements or Notes

* This article was presented as a poster presentation at the International Conference on Basic Sciences, Engineering and Technology (www.icbaset.net) held in Trabzon/Türkiye on May 01-04, 2025.

References

Badyuk, S. I., & Leshchenko, A. I. (2010). Obtaining long-range rolled profiles from worn-out railway rails. *Pressure Treatment of Materials, 4*, 162-167.

Bakhtinov, Yu. B. (2000). On the expediency of rolling worn rails into long profiles, *Production of rolled products, 7*, 2-4.

Dobatkin, S., Galkin, S., Estrin, Y., Serebryany, V., Diez, M., Martynenko, N., Lukyanova, E., & Perezhogin, V. (2019). Grain refinement, texture, and mechanical properties of a magnesium alloy after radial-shear rolling. *Journal of Alloys and Compounds, 774*, 969-979.

Galkin, S. P., & Kharitonov, E. A. (2003). Reversible radial shear rolling. Essence, opportunities, advantages. *Titanium, 1*, 39-45.

Galkin, S. P. (2007). *Screw rolling method*. RU Patent 2293619.

Galkin, S. P., & Romantsev, B. A. (2014). Innovative technology of recycling pumping rods using technology and mini radial-shear rolling in the conditions of JSC Ochersky Machine-Building Plant. *Engineering Practice, 9*, 58-61.

Galkin, S. P., Romantsev, B. A., & Kharitonov, E. A. (2015). Realization of the innovative potential of the universal radial shear rolling method. *Ferrous Metals, 1*, 27-34.

Gamin, Y. V., Akopyan, T. K., Koshmin, A. N., Dolbachev, A. P., & Goncharuk, A. V. (2020). Microstructure evolution and property analysis of commercial pure Al alloy processed by radial-shear rolling. *Archives of Civil and Mechanical Engineering, 20*, 143.

Gamin, Y., Akopyan, T., Galkin, S., Nguyen, X., Cheverikin, V., Fortuna, A., Razinkin, A., Ovsyannikov, B., & Esakov, S. (2023). Effect of radial shear rolling on grain refinement and mechanical properties of the Al–Mg–Sc alloy. *Journal of Materials Research, 38*, 4542-4558.

Grevtseva, V. V., & Galkin, S. P. (2017). Experimental testing of the technology of reuse of railway axles using radial shear rolling. *72nd Days of Science for students of NUST MISIS* (pp. 27-30).

Karpov, B. V., Patrin, P. V., Galkin, S. P., Kharitonov, E. A., & Karpov I. B. (2018). Radial-shear rolling of titanium alloy VT-8 bars with controlled structure for small diameter ingots (≤200 mm). *Metallurgist, 61*(9-10), 884-890.

Lezhnev, S., Naizabekov, A., Panin, E., Volokitina, I., & Kuis, D. (2021-1). Recycling of stainless-steel bar scrap by radial-shear rolling to obtain a gradient ultrafine-grained structure. *Metalurgija 60*(3-4), 339-342.

Lezhnev, S., Naizabekov, A., Panin, E., Kuis, D., & Kasperovich, A. (2021-2). Modeling and experimental evaluation of the possibility of using a radial-shear rolling mill for recycling bar scrap of ferrous metals. *Machines, Technologies, Materials, 1*, 41-43.

Lezhnev, S., Naizabekov, A., Panin, E., Tolkushkin, A., Kuis, D., Kasperovich, A., & Yordanova, R. (2023a). Development and computer simulation of the new combined process for producing a rebar profile. *Modelling and Simulation in Engineering, 2023*, 7348592.

Lezhnev, S., Panin, E., Tolkushkin, A., Kuis, D., & Kasperovich, A. (2023b). Development and computer simulation of a new technology for forming and strengthening screw fittings. *Journal of Chemical Technology and Metallurgy, 58*(5), 955-960.

Lezhnev, S., Naizabekov, A., Tolkushkin, A., Panin, E., Kuis, D., Arbuz, A., Tsyba, P., & Shyraeva, E. (2024). Choosing the Design of a Radial-Shear Rolling Mill for Obtaining a Screw Profile. *Modelling, 5*, 1101-1115.

McGahhey, B. D. (1991). Rail recycle process, US Patent 4982591.

Ozhmegov, K., Kawalek, A., Naizabekov, A., Panin, E., Lutchenko, N., Sultanbekov, S., Magzhanov, M., & Arbuz, A. (2023). The Effect of Radial-Shear Rolling Deformation Processing on the Structure and Properties of Zr-2.5Nb Alloy. *Materials, 16*(10), 3873.

Slick, E. E. (1914). *Method of rolling flanged shapes*. US Patent 1086789.

Smirnov, V. K., Shilov, V. A., & Mikhailenko, A.M. (1995). Technology of processing railway rails for long-range. *Steel, 2*, 46-48.

Valeev, I. S., Valeeva, A. K., Fazlyakhmetov, R. F., & Khalikova, G. R. (2015). Effect of radial-shear rolling on structure of aluminum alloy D16 (Al-4.4Cu-1.6Mg). *Inorganic Materials: Applied Research, 6*(1), 45-48.

Author(s) Information

Sergey Lezhnev
Rudny Industrial University
38, 50 let Oktyabrya str., Rudny, Kazakhstan

Dmitry Goldabin
Rudny Industrial University
38, 50 let Oktyabrya str., Rudny, Kazakhstan

Elena Shiriaeva
Nosov Magnitogorsk State Technical University
38, Lenin str., Magnitogorsk, Russia

Dmitry Kuis
Belarusian State Technological University
13a, Sverdlova str., Minsk, Belarus
Contact e-mail: kuisdv@belstu.by

To cite this article:

Lezhnev, S., Goldabin, D., Shiriaeva, E., & Kuis, D. (2025). Development and experimental testing of a new technology for producing screw fittings from bar scrap of ferrous metals. *The Eurasia Proceedings of Science, Technology, Engineering and Mathematics (EPSTEM), 34,* 87-92.

The Eurasia Proceedings of Science, Technology, Engineering & Mathematics (EPSTEM)
ISSN: 2602-3199

The Eurasia Proceedings of Science, Technology, Engineering and Mathematics (EPSTEM), 2025

Volume 34, Pages 93-101

ICBASET 2025: International Conference on Basic Sciences, Engineering and Technology

Detection of Antimicrobial Activity of *Aspergillus terreus* Against Clinical Isolates of *Serratia marcescens*

Maryam Kamel Mohammed
University of Baghdad

Ali Muhsin Ali
University of Baghdad

Shaymaa Fadhel Abbas Albaayit
University of Baghdad

Abstract: Out of a total of fifty samples, thirty-five isolates were identified as *Serratia marcescens*. These diverse clinical samples were collected over a three-month period, from October 2023 to December 2023, from several hospitals in Baghdad, including Fatima Al-Zahraa Hospital, Al-Sader Hospital, Ibn Al-Balady Hospital, and Al-Imam Ali Hospital. The clinical samples primarily included urine from patients with urinary tract infections (UTIs). All isolates were cultured on nutrient agar, MacConkey agar, and blood agar, and their identities were confirmed through biochemical testing and the Vitek 2 compact system. Based on phenotypic virulence factors, the *S. marcescens* isolates showed varying positive patterns: 32 out of 35 (91.42%) for protease production, 35 out of 35 (100%) for motility, 27 out of 35 (77.14%) for hemolysin production, and 22 out of 35 (62.85%) for Prodigiosin pigment production. The susceptibility of the S. marcescens isolates to two carbapenem antibiotics (Imipenem and Meropenem) was evaluated using the disk diffusion method. The sensitivity tests revealed high resistance to both IPM and MEM, with resistance rates of 34.28% (12 isolates) and 42.85% (15 isolates), respectively. A bioactive compound extracted from *Aspergillus terreus*, isolated from soil, demonstrated significant activity against *S. marcescens* at varying concentrations. Many of these fungal metabolites exhibited potent anti-disease efficacy, and secondary metabolites were found to stimulate host defenses through various signal transduction mechanisms.

Keywords: Multidrug resistance, Carbapenem, Virulence factors

Introduction

Serratia is a Gram-negative, rod-shaped bacterium measuring 0.9–2 µm in length and 0.5–0.8 µm in diameter. It is facultatively anaerobic, motile, and non-spore-forming. The bacterium is catalase-positive but oxidase-negative and produces a red pigment called Prodigiosin, which gives rise to red or pink colonies on nutrient agar media. This pigment is associated with the bacterial cell membrane (Mahdi et al., 2013). *S. marcescens* produces several virulence factors, including enzymes such as phospholipases, lipases, nucleases, chitinases, and proteases. Additionally, it has the ability to form biofilms on both abiotic and biotic surfaces. This biofilm formation facilitates bacterial colonization and persistence on medical devices like prostheses and catheters, contributing to increased antibiotic resistance (Abbas & Hegazy, 2020). Studies have shown that infections caused by certain strains of *Serratia marcescens* are challenging to treat due to their high resistance to various antibiotics, including aminoglycosides, β-lactams, and fluoroquinolones (Stock et al., 2003).

This highlights the need for new treatment strategies. Microorganisms produce a diverse range of industrially significant metabolites during their growth phases, such as dyes, enzymes, pigments, and antibacterial agents.

During the stationary phase of microbial growth, organisms like fungi, actinomycetes, and bacteria synthesize chemical compounds known as antimicrobial agents through metabolic processes (Alkhulaifi et al., 2019; Albaayit, 2021). The rich chemistry of natural products primarily stems from secondary metabolites, a class of compounds with significant therapeutic potential (Albaayit et al., 2021; Albaayit, 2020). Some of the most potent secondary metabolites developed into therapeutic drugs have originated from filamentous fungi (Ahmed et al., 2019). Thus, this study aimed to isolate and identify *Serratia marcescens* from UTI patients, evaluate their antibiotic resistance profiles, and characterize their phenotypic virulence factors. Additionally, the study investigated the antimicrobial potential of an extract derived from *Aspergillus terreus*, isolated from soil, against *S. marcescens*. The research further sought to assess the capability of the extract to produce antimicrobial agents and perform chemical identification of the active purified compound.

Method

Sample Collection

Over a three-month period, from October 2023 to December 2023, fifty diverse clinical samples were collected from various hospitals in Baghdad, including Fatima Al-Zahraa Hospital, Al-Sader Hospital, Ibn Al-Balady Hospital, and Al-Imam Ali Hospital. The clinical samples primarily consisted of urine.

Isolation and Identification of *Serratia marcescens*

All clinical samples were directly cultured on blood agar plates and incubated at 37ºC for 24 hours. Colonies appearing opaque, grayish, or white on blood agar were subsequently recultured on MacConkey agar plates for further identification and incubated at 37ºC for another 24 hours. To obtain pure colonies, the selected colonies were subculture on fresh MacConkey agar plates (Mekhael & Yousif, 2009). Final identification and confirmation were carried out using the VITEK® 2 Compact system, which provided accurate species-level identification based on automated biochemical profiling

Antibiotic Sensitivity Test

The antibiotic sensitivity of the isolates towards Imipenem and Meropenem was assessed using the disc diffusion method (Kirby-Bauer method). Antibiotic discs were carefully placed on the surface of the medium, which had been inoculated with the bacterial isolates, using sterilized forceps. The plates were then incubated at 37°C for 24 hours. After incubation, the zones of inhibition surrounding the discs were measured in millimeters (mm). The results were compared with the Clinical Laboratory Standards Institute (CLSI, 2023) guidelines to classify the isolates as susceptible (S), resistant (R), or intermediate (I).

Fungal Culture and Isolation of *Aspergillus terreus*

The fungi were isolated from a soil sample using the serial dilution agar plate method under sterile conditions. For serial dilution, 9 mL of sterilized distilled water was added to each of five test tubes. The first test tube, labeled 10^{-1}, was inoculated with 1 g of the soil sample (Bizuye et al., 2013). To isolate fungi, potato dextrose agar (PDA) was used as the growth medium. To inhibit bacterial growth, the PDA plates were supplemented with 0.2 g/L of streptomycin. From each test tube, 0.1 mL of the diluted sample was spread onto the PDA plates, which were then incubated at 30°C for 6–7 days. By the fifth day, morphologically distinct fungal colonies appeared on the plates. These colonies were individually subcultured to obtain pure cultures. The pure fungal colonies were then transferred to PDA slants and stored at 4°C for future use (Sakthiselvan et al., 2015).

Extraction of Bioactive Compounds from *Aspergillus terreus*

On day 16, the natural products were extracted by harvesting the fungal cells, which were then centrifuged at 3000 RPM for 5 minutes. The resulting pellet was dissolved in ethanol at a concentration of 1g/10 mL. The mixture was sonicated at 24,000 Hz to break the cells. After sonication, the mixture was centrifuged again at 3000 RPM for 10 minutes, and the supernatant (leachate) was collected. The ethanol was removed from the supernatant using an evaporator set at a temperature below 40°C to concentrate the extract. The extract was then

dissolved in a small amount of distilled water, and bioactive compounds were precipitated by adding 70% ammonium sulfate. The mixture was cooled at 3000 RPM for 30 minutes to separate the precipitate. The ammonium sulfate was removed from the precipitate by dialysis, and the contents of the dialysis bag were transferred to a discater, a container with low pressure. This process was performed to obtain the protein-containing natural products as dry matter, as described by Siddiquee et al. (2012).

Results and Discussion

Identification of *S. marcescens* Isolates

Fifty urine specimens from UTI patients were cultured on MacConkey agar and blood agar media. Suspected late lactose- and non-lactose-fermenting isolates, as well as hemolytic and non-hemolytic isolates of *Serratia marcescens*, were further identified using catalase and oxidase tests. The isolates were then confirmed using the VITEK2 GN ID Card system. Out of the collected Serratia species, 35 isolates were identified as *S. marcescens.*

Cultural Characteristics

For the primary identification of *Serratia marcescens* obtained from urine samples, isolates were identified and characterized based on their morphology, cultural characteristics, and biochemical tests. On MacConkey agar, *S. marcescens* appeared as pale-colored colonies due to their non-lactose-fermenting nature (Slonczewski and Foster, 2009). As shown in (Figure 1), it is crucial not to confuse the red-pigmented Serratia colonies on MacConkey agar with lactose fermentation, as the pigment, prodigiosin, is a non-soluble compound (Mahlen, 2011). Microscopically, *S. marcescens* was observed as Gram-negative rods. Biochemically, all Serratia isolates were catalase-positive, as shown in (Figure 2), and oxidase-negative (Mohammed et al., 2018).

Figure 1. *S. marcescens* colonies on MacConkey agar

A **B**

Figure 2. *S. marcescens* catalase test positive on slide (A) and macConkey agar (B)

Protease Test

As shown in Figure 3, 32 (91.42%) of *S. marcescens* isolates in this study were positive for protease enzyme production, while 3 isolates were negative. Proteases are enzymes that hydrolyze peptide bonds in proteins, breaking them down into amino acid monomers (Rawlings et al., 2011). *S. marcescens* produces metalloproteases, which exhibit toxic effects on host cells. These enzymes play a critical role in breaking down proteins in the surrounding medium, providing a nutrient source for the bacteria. Proteases are considered key

virulence factors, aiding pathogenic microbes in penetrating host tissues and utilizing proteins as a nutritional source, as highlighted in research by Al-Shmgani et al. (2024).

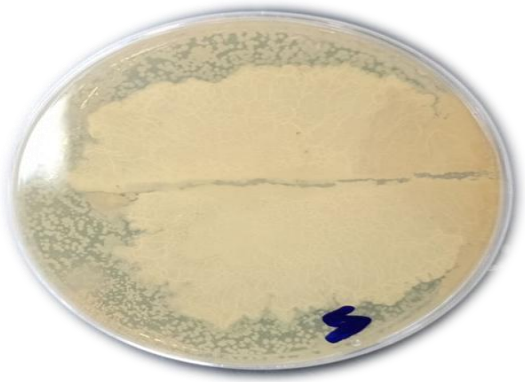

Figure 3. Positive protease test of *S. marcescens* on milk agar

Motility Test

All 35 (100%) *S. marcescens* isolates were found to be motile when tested using semi-solid motility medium. When grown in liquid medium (Figure 4), *S. marcescens* cells exhibited swimming behavior and displayed distinct morphological characteristics. Motility is considered one of the most significant virulence factors of *S. marcescens*. This bacterium employs various mechanisms for movement, including swimming facilitated by its flagellum (Mahmoud, 2015).

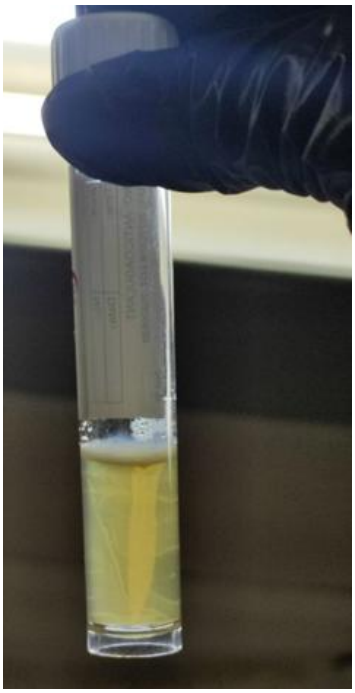

Figure 4. Positive swimming motility test of *S. marcescens*

Hemolysin Production

Out of 35 *S. marcescens* isolates cultured on blood agar, 27 (77.14%) exhibited beta hemolysis, while 8 isolates showed gamma hemolysis, as illustrated in (Figure 5). To confirm the diagnosis of *S. marcescens*, the isolates were grown on blood agar, which serves as an enrichment medium and helps distinguish between hemolytic and non-hemolytic isolates. On blood agar, *S. marcescens* colonies appeared as large, round, red, opaque, moist colonies with hemolytic activity (Ibraheem et al., 2023).

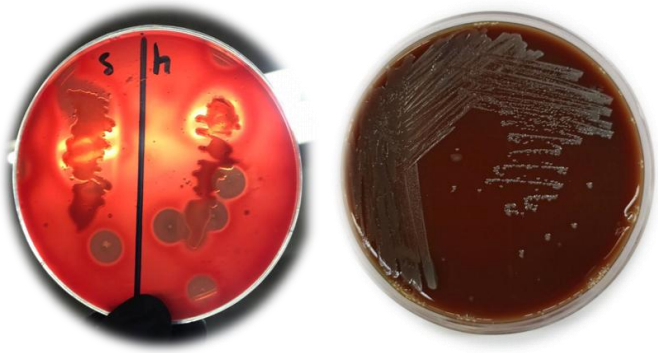

Figure 5. *S. marcescens* colonies on blood agar

Prodigiosin Production

Serratia marcescens has the ability to produce prodigiosin, a secondary metabolite commonly associated with its isolates (Mahmoud, 2015). As shown in Table 1, 22 (62.85%) of the *S. marcescens* isolates in this study were identified as prodigiosin producers when cultured on nutrient agar, as depicted in (Figure 6). The remaining 13 isolates were non-pigment producers. Pigment-producing isolates demonstrated the ability to produce prodigiosin at both 28°C and 37°C. One of the most distinctive features of Serratia colonies is their red pigmentation, attributed to prodigiosin. This pigment is produced by several Serratia species, including *S. marcescens*, *S. rubidaea*, and *S. plymuthica*, while some other Serratia species do not produce prodigiosin (Bdaiwi et al., 2019).

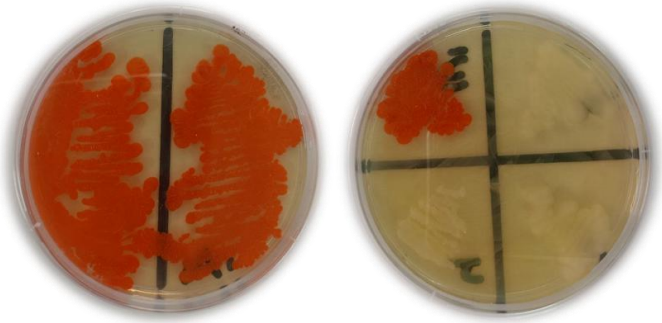

Figure 6. Pigmented and non-pigmented *S. marcescens* isolates on nutrient agar medium

Table 1. The pigmented and non-pigmented *S. Marcescens*

Description	Isolates number
Pigment produce isolates	22
Non pigment produce isolates	13
Total Isolates	35

Antibiotics Susceptibility Test

The susceptibility of *S. marcescens* isolates to two antibiotics from the carbapenem class (imipenem and meropenem) was determined using the disk diffusion method. The results were interpreted according to the recommendations of CLSI (2023). The antibiotic resistance patterns of the studied isolates are presented in Table 2 and Figure 7. The sensitivity test results revealed that S. marcescens isolates exhibited high resistance to both meropenem (MEM) and imipenem (IPM).

Table 2. Determination of diameter zone of antibiotics test of *S. marcescens* isolates

No.	R(%)	I(%)	S(%)
IPM	12 (34.28%)	6 (17.14%)	17 (48.57%)
MEM	15 (42.85%)	4 (11.42%)	19 (54.28%)
CLSI	<19 mm	20-22 mm	>23

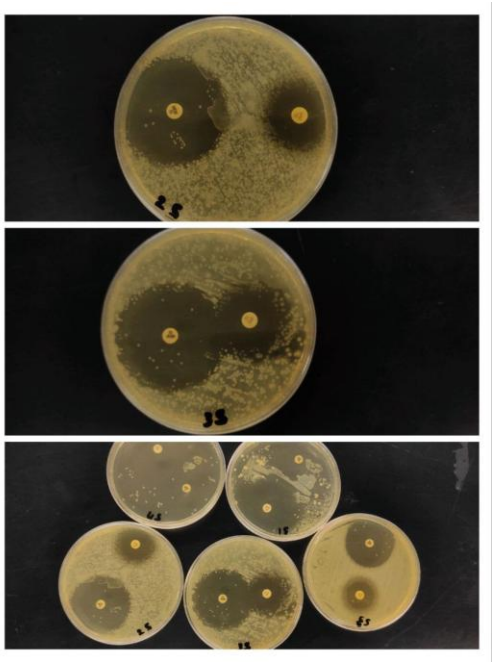

Figure 7. Antibiotic test of *S. marcescens*

One of the most remarkable scientific achievements in history is the discovery and subsequent development of antibiotics. Penicillin remains one of the most effective and safe antibiotics. Since its discovery, thousands of antibiotics have been isolated from soil microbes; however, only about 50 are still in use due to the toxicity of many others to humans (Aminov et al., 2010). The misuse and overexploitation of antibiotics have led to the development of multidrug resistance in harmful microorganisms. Consequently, there is an increasing demand for novel antimicrobial compounds effective against drug-resistant pathogens (Albaayit et al., 2021).

The emergence, selection, and spread of bacterial resistance to multiple antibiotics highlight the urgent need for innovative methods to prevent and treat bacterial infections (Albaayit et al., 2022). Notably, numerous fungal species have demonstrated efficacy against bacterial, viral, and fungal infections resistant to current treatments, making them a valuable source of natural antimicrobial compounds. Antibacterial and antifungal activities can be used to identify potential antimicrobial molecules extracted from various stages of fungal growth (Al-ani & Albaayit, 2018).

Antimicrobial of Bioactive Compound Extraction from Fungi

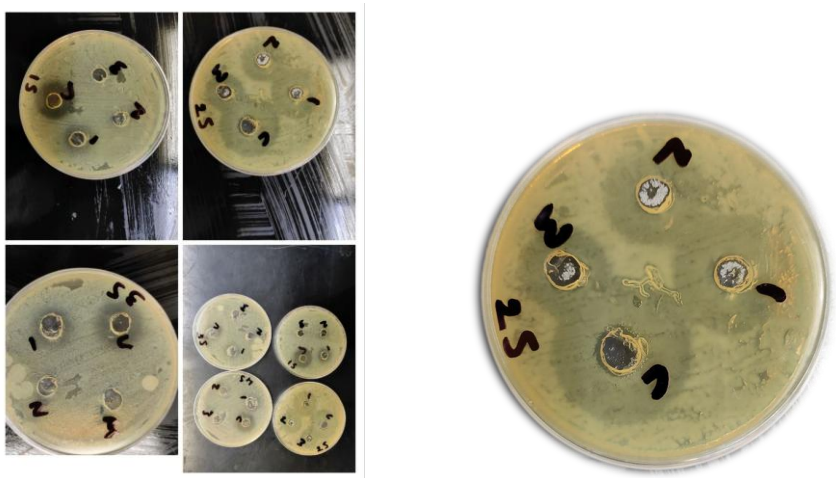

Figure 8. Bioactive extract product on *S. marcescens*

Soil is a crucial source of microorganisms that produce bioactive substances, many of which have demonstrated anti-disease efficacy. Secondary metabolites produced by these microorganisms stimulate host defenses through

various signal transduction mechanisms. The bioactive compound showed significant activity against *S. marcescens*, with inhibition zone diameters ranging from 8 to 33 mm at different concentrations, as illustrated in (Figure 8).

According to the findings of the study, chemical analysis of fungi from the Aspergillus species, obtained from soil, has significantly advanced in recent years, leading to the discovery of new molecular structures with a broad range of pharmacological properties, making them valuable sources of antimicrobial agents (Elkhayat et al., 2016). In contrast, this study highlights the enormous potential of filamentous fungi to produce a wide array of bioactive compounds, which have applications in antibiotics, anticancer treatments, and antifungal drugs (Hawar et al., 2023).

A novel metabolite, asperfumin, produced by the endophytic fungus *Aspergillus fumigatus* CY018, has been shown to inhibit *Candida albicans*, as reported in similar studies by other researchers (Cardoso et al., 2020). Members of the Aspergillus genus are well-known producers of secondary metabolites, such as polyketides (e.g., aflatoxins), non-ribosomal peptides (e.g., ferricrocin), and indole terpenes. These metabolites are considered important resources for new drug exploration (Al-Samarraie et al., 2021).

Four fungal strains—*Aspergillus flavus* (NCIM No. 524), *Aspergillus fumigatus* (NCIM No. 902), *Penicillium marneffei*, and *Trichophyton mentagrophytes* have all been reported to exhibit resistance to the antifungal properties of isochrontriazoles and thiadiazole in similar studies by other researchers. Isoquinoline derivatives from isochromen dione have been discovered to possess significant biological characteristics (Saeed & Zaman, 2006). These isoquinoline derivatives are known to exhibit a range of biological properties, including narcotic, anti-angiogenic, antiallergic, anti-inflammatory, antifungal, antimalarial, antibacterial, antiviral, and anticancer effects (Notte & Leighton, 2008).

This study's results align with previous research showing that various metabolites of isocoumarins possess bioactivities such as cytotoxicity, antimicrobial properties, algicidal effects, protease inhibition, acetylcholinesterase activity, antimalarial properties, immunostimulation, and plant growth regulation, among others (Guo et al., 2020). Additionally, similar studies suggest that dihydroisocoumarins, primarily derived from natural sources such as microbes, bacteria, and fungi (including endophytic, soil, and marine fungi), have significant biological potential (Orfali et al., 2020).

Conclusion

Serratia marcescens is an important cause of nosocomial infections in hospitals, with the highest isolation rate observed from urine samples. The incidence of infection is higher among females compared to males. The isolates demonstrated resistance to carbapenem class antibiotics, with the highest levels of resistance observed against imipenem (IPM) and meropenem (MEM). Additionally, *S. marcescens* produces various phenotypic virulence factors, including hemolysin, protease, and prodigiosin, each exhibiting different patterns. The bioactive compound extract of *Aspergillus terreus* extract, demonstrated high-level activity against *S. marcescens* isolates.

Scientific Ethics Declaration

* The authors declare that the scientific ethical and legal responsibility of this article published in EPSTEM Journal belongs to the authors.

Conflict of Interest

* The authors declare that they have no conflicts of interest

Funding

* This research received no specific grant from any funding agency in the public, commercial, or not-for-profit sectors.

Acknowledgements or Notes

* This article was presented as an oral presentation at the International Conference on Basic Sciences, Engineering and Technology (www.icbaset.net) held in Trabzon/Türkiye on May 01-04, 2025.

References

Abbas, H.A., & Hegazy, W.A.H. (2020). Repurposing anti-diabetic drug "Sitagliptin" as a novel virulence attenuating agent in *Serratia marcescens*. *PLoS One, 15*(4), e0231625.

Ahmed, R.N., Mercy, B.O. & Idris, S.O. (2019). Evaluation of secondary metabolites of some fungi isolated from beach soils of Lagos, Nigeria against some pathogens. *Iraqi Journal of Science, 60*(10), 2114-2122.

Al-ani, L. K. T., & Albaayit, S. F. A. (2018). Antagonistic of some Trichoderma against *Fusarium oxysporum* sp. f. cubense tropical race 4 (FocTR4). *The Eurasia Proceedings of Science Technology Engineering and Mathematics*, *(2),* 35-38.

Albaayit, S. F. A. (2021). Evaluation of anti-methicillin resistant *Staphylococcus aureus* property of *Clausena excavata* leaves by using atomic force microscopy and flowcytometry techniques. *Pakistan Journal of Agricultural Sciences, 58*(1), 315-320.

Albaayit, S.F.A. (2020). *In vitro* evaluation of anticancer activity of *Moringa peregrina* seeds on breast cancer cells. *The Eurasia Proceedings of Science Technology Engineering and Mathematics*, *11*, 163-166.

Albaayit, S.F.A., Khan, M., Abdullah, R., & Hezmee M.N.M. (2021). Ethyl acetate extract of *Clausena excavata* induces growth inhibition of non-small-lung cancer, NCI-H460, cell line via apoptosis. *Journal of Applied Biomedicine, 19*(1), 40–47.

Albaayit, S.F.A., Maharjan, R., Abdullah, R., & Noor M.H.M. (2021). AntiEnterococcus faecalis, cytotoxicity, phytotoxicity, and anticancer studies on *Clausena excavata* burum. f. (rutaceae) leaves. *Biomed Research International 2021*, 3123476.

Albaayit, S.F.A., Maharjan, R., Abdullah, R., & Mohd Noor, M. H. (2022). Evaluation of anti-methicillin-resistant *Staphylococcus aureus* property of zerumbone, *Journal of Applied Biomedicine*. *20*(1), 15-21.

Alkhulaifi, M.M., Awaad, A.S., Al-Mudhayyif, H.A., Alothman, M.R., Alqasoumi, S.I., & Zain, S.M. (2019). Evaluation of antimicrobial activity of secondary metabolites of fungi isolated from Sultanate Oman soil. *Saudi Pharmaceutical Journal, 27*(3), 401-405.

Al-Samarraie, M. Q., AL-Obaedi, A. I., Hamed, N. M., & AL-Azzawie, A. F. (2021). Molecular ıdentification of Aspergillus nigar using randomly amplified polymorphic deoxyribonucleic acid polymerase chain reaction Technique. *Journal of Drug Delivery Technology*, *11*(4), 1221-1224.

Al-Shmgani, H. S., Ashij, M. A., Khalil, K. A., & Mohammed, H. A. (2024). Synthesis and characterization of proteolytic enzyme loaded on silver nanoparticles. *Ibn AL-Haitham Journal for Pure and Applied Sciences, 37*(1), 43-53.

Aminov, R.I. (2010). A brief history of the antibiotic era: lessons learned and challenges for the future. *Frontiers in Microbiology, 1,*134.

Bdaiwi, Q.O., Kareem, A.A., Hussein, S.A., & Ali, A.M. (2019). Prevalence of β-lactam resistant *Klebsiella Pneumoniae* ısolates among clinical specimensin Baghdad hospitals. *Indian Journal of Public Health Research & Development, 10*(11), 4935.

Bizuye, A., Moges, F., & vndualem, B. (2013). Isolation and screening of antibiotic producing actinomycetes from soils in Gondar town, North West Ethiopia. *Asian Pacific Journal of Tropical Disease, 3*(5), 375-381.

Cardoso, R.V.C., Carocho, M., & Fernandes, A. (2020). Influence of Calcium Silicate on the Chemical Properties of Pleurotus ostreatus var. Florida (Jacq.) P. Kumm. *Journal of Fungi Basel, 6*(4), 299.

Clinical and Laboratory Standards Institute (CLSI). (2023). *Performance standard for antimicrobial susceptibility testing: Twenty-six informational supplement (35th ed.).* M100-S21 CLSM100™.

Elkhayat, E.S, Ibrahim, S.R, Mohamed, G.A, Ross, S.A., & Terrenolide S. (2016). A new antileishmanial butenolide from the endophytic fungus *Aspergillus terreus*. *Natural Product Research, 30*(7), 814-820.

Guo, H.X., Huang, C.Y., Yan, Z.Y., Chen, T., Hong, K., & Long, Y.H. (2020). New furo[3,2-h]isochroman from the mangrove endophytic fungus *Aspergillus* sp. 085242. *Chinese Journal of Natural Medicines, 18*(11), 855-859.

Hawar, S. N., Taha, Z. K., Hamied, A. S., Al-Shmgani, H. S., Sulaiman, G. M., & Elsilk, S. E. (2023). Antifungal activity of bioactive compounds produced by the endophytic fungus Paecilomyces sp.(JN227071. 1) against Rhizoctonia solani. *International Journal of Biomaterials*, *2023*(1), 2411555.

Ibraheem, D. R., Hussein, N. N., & Sulaiman, G. M. (2023). Antibacterial activity of silver nanoparticles against pathogenic bacterial ısolates from diabetic foot patients. *Iraqi Journal of Science, 64*(5), 2223-2239.

Mahdi, R., Hasan, S., & Hasan, J. (2013). The effect of *Serratia marcescens* protease on human lymphocytes transformation. (2023). *Iraqi Journal of Science, 54*(3), 531-535.

Mahmoud, S. T., Luti, K. J. K., & Yonis, R. W. (2015). Enhancement of prodigiosin production by *Serratia marcescens* S23 via introducing microbial elicitor cells into culture medium. *Iraqi Journal of Science, 56*(3),1938-1951.

Mekhael, R. & Yousif, S.Y. (2009). The role of red pigment produced by *Serratia marcescens* as antibacterial and plasmid curing agent. *Journal of Duhok University, 12*(1), 268-274.

Mohammed, N.T., Nadhom, B.N., & Mousa, S.T. (2018). Hematological variations of mice inoculated by *Serratia marcescens* whole cell sonicated antigens. *International Journal of Veterinary Science 7*(3), 159-161.

Notte, G.T., & Leighton, J.L. (2008). A new silicon lewis acid for highly enantioselective mannich reactions of aliphatic ketone-derived hydrazones. *Journal of the American Chemical Society, 130*(21), 6676-6677.

Orfali, R., Perveen, S., Al-Taweel, A. & Penipyranicins, A.C. (2020). Antibacterial methylpyran polyketides from a hydrothermal spring sediment *Penicillium* sp. *Natural Product Research; 83*(12), 3591-3597.

Rawlings, N. D., Barrett, A. J., & Bateman, A. (2011). Asparagine peptide lyases: a seventh catalytic type of proteolytic enzymes. *Journal of Biological Chemistry, 286*(44), 38321-38328.

Saeed, A., & Zaman, A. (2006). Sodium borohydride reduction of aromatic carboxylic acids via methyl esters. *Journal of Chemical Sciences*, *118*(5), 419–423.

Sakthiselvan, P., Naveena, B., & Partha, N. (2015). Molecular characterization of a xylanase-producing fungus isolated from fouled soil. *Brazilian Journal of Microbiology,45*(4), 1293-1302.

Siddiquee, S., Cheong, B.E., Taslima, K., Kausar, H., & Hasan, M.M. (2012). Separation and identification of volatile compounds from liquid cultures of *Trichoderma harzianum* by GC-MS using three different capillary columns. *Journal of Chromatographic Science 50*(4), 358- 367.

Slonczewski, J., Foster, J., & Zınser, E. (2009). *Microbiology: An evolving science* (pp.91-488). W.W. Norton and Company, Inc.

Stock, I., Grueger, T., & Wiedemann, B. (2003). Natural antibiotic susceptibility of strains of *Serratia marcescens* and the *S. liquefaciens* complex: *S. liquefaciens* sensu stricto, *S. proteamaculans* and *S. grimesii*. *International Journal of Antimicrobial agents, 22*(1), 35-47.

Author(s) Information

Maryam Kamel Mohammed
University of Baghdad
Department of Biology, College of Science
Al-Jadriya, Baghdad 10070, Iraq

Ali Muhsin Ali
University of Baghdad
Department of Biology, College of Science
Al-Jadriya, Baghdad 10070, Iraq

Shaymaa Fadhel Abbas Albaayit
University of Baghdad
Department of Biology, College of Science
Al-Jadriya, Baghdad 10070, Iraq
Contact e-mail: *Shaymaa_albaayit@yahoo.com*

To cite this article:

Mohammed, M.K., Ali, A.M., & Albaayit, S.F.A. (2025). Detection of antimicrobial activity of *Aspergillus terreus* against clinical isolates of *Serratia marcescens*. *The Eurasia Proceedings of Science, Technology, Engineering and Mathematics (EPSTEM), 34,* 93-101.

The Eurasia Proceedings of Science, Technology, Engineering & Mathematics (EPSTEM)
ISSN: 2602-3199

The Eurasia Proceedings of Science, Technology, Engineering and Mathematics (EPSTEM), 2025

Volume 34, Pages 102-106

ICBASET 2025: International Conference on Basic Sciences, Engineering and Technology

Effect of Using ß-Pentosanase Enzyme in Feed on Broilers Performance

Achour Mennani
Mohamed Boudiaf University

Sadam Houcin Lahmar
University of Batna

Abstract: The aim of this study was to determine the effect of using the ß-pentosanase enzyme on the zootechnical performance of broiler chickens. The study was carried out on 165-day-old broiler chicks, divided into 5 batches of 33 chicks each (Batch 1: control without incorporation; Batches 2, 3, 4 and 5: with enzyme incorporation (at a dose of 25g enzyme/100kg feed) during the start-up, growth, finishing and rearing phases respectively). Data analysis showed that incorporation of the ß-pentosanase enzyme had a very highly significant influence ($P<0.001$) on weight at 21 days and 42 days, highly significant ($P<0.01$) on weight at 47 days and significant on weight at 56 days of age. This incorporation had a very highly significant influence ($P<0.001$) on weight gain between (0 and 21) days, highly significant ($P<0.01$) on weight gain between (22 and 42) days, significant ($P<0.05$) on weight gain between (43 and 47) days and non-significant ($P>0.05$) on weight gain between (48 and 56) days and with a remarkable improvement in feed conversion. We conclude from this study that the incorporation of the ß-pentosanase enzyme into broiler feed had a significant positive effect on broiler zootechnical performance, notably average weights and daily weight gain in the first two growth phases, with a notable improvement in feed conversion. However, this incorporation had no effect on the above-mentioned zootechnical parameters during the last growth phase (between 48 and 56 days).

Keywords: ß-pentosanase enzyme, Broiler chicken, Zootechnical performance

Introduction

Advances in nutrition are partly responsible for the progress of the poultry industry. Today, the mastery of feeding techniques is the most important means of reducing production costs and improving the quality of products, better adapted to agricultural conditions, it also makes it possible to correct certain depressive effects caused by the environment. In farmed poultry, more than in any other animal production, well-established nutrition enables animals to externalize their production performance. Poultry feed currently covers almost all nutritional requirements. In this sector, deficiencies are rare and generally due to absorption problems, or to human errors such as feed formulation, or farmers' demands on the incorporation rates of certain raw materials in feed. Thus, the quality of the raw materials and their incorporation rates are always the most important aspect on which the quality and characteristics of the feed depend (Larbier & Leclercq, 1992)

Currently, the use of enzymes in different types of poultry feed is well established worldwide, with the aim of improving the nutritional efficiency of poultry feeds. The possibility of using exogenous enzymes in monogastric feeds, mainly for poultry, has provided nutritionists with an important tool for improving feed digestibility and reducing feed costs (Zakaria et al., 2010). This translates into better animal performance, improved litter quality and better bird health, which in turn has a positive effect on reducing production costs (Saleh et al., 2005; Cowieson & Ravindran, 2008a, 2008b).

In this context, we propose this work, which aims to test the effect of incorporating the enzyme ß-pentosanase into broiler feed, and also to assess the effect of this incorporation on broiler performance during the different growth phases.

Materials and Methods

Animal Material

A total of 165-day-old chicks of Arbor Acres strain, with a mean initial weight of 37.01 ± 3.08g, were identified and weighed to be randomly distributed over the 5 batches and reared separately for a duration of 56 days under the same breeding conditions. The distribution of the chicks was done in such a way as to have an experimental setup consisting of five groups according to the rate of incorporation of pentosanase enzyme (with a dose of 25g enzyme/100kg feed) into the food during the different growth phases (Table 1 and Table 2).

Table 1. Food formula according to the different phases of growth

Raw materials (%)	Starting (0-21 days)	Growth (22-42 days)	Finishing (0-21 days)
Corn	60.9	62 ,9	68,9
Soybean meal	29	27	21
CMV	1	1	1
Phosphate	1	1	1
Wheat bran	8	8	8
Limestone	1	1	1
Salt (NaCl)	0,1	0,1	0,1

Table 2. Incorporation rate of ß-pentosanase enzyme (with a dose of 25g enzyme/100kg feed) in the different feed

variables	Control batch	Batch I	Batch II	Batch III	Batch IV
Starting (0-21 days)	-	+	-	-	+
Growth (22-42 days)	-	-	+	-	+
Finishing (0-21 days)	-	-	-	+	+

Variables Analyzed

The variables analyzed are: Weights at 21, 42 and 56 days (W21, W42 and W56) and average daily gain: ADG (0-21) d, ADG (22-42) d, ADG (43-56) d.

Statistical Analysis

The variables were subjected to a descriptive analysis and an analysis of variance by the least squares using the general univariate linear model, this analysis was carried out with the software SPSS (26). The general linear model was used to test the effect of incorporation of ß-pentosanase enzyme on the different variables; the significance and homogeneity between different averages were achieved by the application of S.N.K test.

Results and Discussion

Effect of Incorporation of ß-pentosanase Enzyme on The Different Weights

The results shown in Table 3 indicate clearly that the incorporation of the ß-pentosanase enzyme into the concentrated broiler feed had a highly significant influence ($P < 0.01$) on hen weight at 21, 42 and 56 days. The best weights at 21 days of age were attributed to individuals from batches IV and III, with average weights of 762.68g and 730.58g respectively. These 2 batches (IV and III) received ß-pentosanase enzyme in the concentrated feed during this growth phase, which explains the positive effect of incorporating ß-pentosanase enzyme into the feed.

The control batch and batch II (not receiving the enzyme in the feed) had lower 21-day weights than the other batches in this study, at 671.68g and 699.33 respectively. Regarding the weight of chickens at 42 days, a very significant superiority was recorded in batch IV, which received the incorporation of the ß-pentosanase enzyme in the feed during the start-up and growth phases. This continuous incorporation contributed to the achievement of this very remarkable growth performance.

The weight recorded for individuals in this batch was 2440.99g. The control batch (without incorporation) recorded the lowest weight compared with the other batches, with an average of 2141.59g. A weight value at 56 days of age of 3731.14g was recorded for individuals in batch IV, which still gives this batch superiority, as it receives incorporation of the enzyme into the feed during all phases of growth (from 0 to 56 days). This superiority is explained by the energy content of the feed resulting from the direct effect of the enzyme action. This high energy value improves chicken growth (Peric et al., 2011).

Furthermore, the positive effect of incorporating the enzyme ß-pentosanase into the concentrated feed on poultry weights found in this study is strongly identical to the results found by Brene et al (1993) and mentioned that a crude enzyme preparation can be used for feed production, this enzyme complex improved the performance of the to varying degrees when added to different cereals. The response to enzyme treatment was influenced by the amount of enzyme added and by the type of cereal making up the feed. The maximum response was noted for cereal-based diets such as barley and oats, and this was the case in our study where the diet was also cereal-based, which is corn.

Table 3. Effect of incorporation of pentosanase enzyme on the different weights

Batchs	W_{21} (g)	W_{42} (g)	W_{56} (g)
Control batch	671,68^{b}	2107,37^{b}	2977,11^{b}
Batch I	722,45^{a}	2141,59^{b}	3086,59^{b}
Batch II	699,33^{b}	2218,33^{b}	3255,26^{ab}
Batch III	730 ,58^{a}	2248,63^{b}	3306,86^{ab}
Batch IV	762,68^{a}	2440,99^{a}	3731,14^{a}
Average	718,46	2234,42	3280,10
Significant	P<0,01	P<0,01	P<0,01

Means affected by different letters in the same column differ significantly at the threshold of (P<0.05).

Effect of Incorporation of ß-pentosanase Enzyme on Average Daily Gain (ADG)

Concerning the average daily gain variable and according to the results summarized in Table 4, the incorporation of the ß-pentosanase enzyme into the concentrated broiler feed had a significant influence (P <0.05) on the average daily gain ADG(0-21d) and ADG(43-56d) and had a highly significant effect on the average daily gain ADG(22-42d). The best weight gains in the 0-21 day growth phase were achieved by batch IV followed by batch I, both of which received enzyme incorporation during this phase and had average ADG(0-21d) of 34.51g/d and 32.66 g/d respectively.

During the 22–42-day phase, the best performance was achieved by batch IV and batch II, which were fed an enzyme-treated concentrate feed during the growth phase, resulting in a remarkable improvement in ADG(22-42d). Batches IV and II scored ADG (22-42d) values of 83.91 g/d and 75.95 g/d , and the lowest ADG(22-42d) performances were recorded by the control batch and batch I, with ADG(22-42d) averages of 71.78 g/d and 70.95 g/d respectively. This difference is clearly explained by the positive effect of incorporating the ß-pentosanase enzyme into the feed on ADG improvement (22-42d). The last growth phase was also characterized by a remarkable superiority of the ADG value (22-42d) of batch IV compared with the other experimental batches. This batch recorded a ADG value (22-42d) of 81.87 g/d, while the lowest value was recorded by the control batch which never received the incorporation of ß-pentosanase enzyme in the concentrated feed, i.e. an average ADG (22-42d) of 55.55 g/d.

The positive effect of incorporating ß-pentosanase enzyme into concentrated feed on improving broiler ADG found in our study is strongly similar to the results obtained by Yanti et al (2024), who reported that broiler weight gain increased with the addition of doses of multienzymes with an incorporation of 0.19 g/kg to 0.33 g/kg feed. The observed increase in chicken weight can be explained by the positive effect of enzyme supplementation in the feed.

Table 4. Effect of incorporation of pentosanase enzyme on average daily gain (ADG)

Batchs	$ADG_{0-21d)}$	$ADG_{(22-42d)}$	$ADG(_{43-56d)}$
Control batch	$30,24^{b}$	$71,78^{b}$	$55,55^{c}$
Batch I	$32,66^{a}$	$70,95^{b}$	$60,12^{c}$
Batch II	$31,55^{b}$	$75,95^{ab}$	$68,26^{b}$
Batch III	$32\ ,98^{a}$	$75,85^{ab}$	$63,46^{bc}$
Batch IV	$34,51^{a}$	$83,91^{a}$	$81,87^{a}$
Average	32,44	75,80	66,21
Significant	P<0,05	P<0,01	P<0,05

Means affected by different letters in the same column differ significantly at the threshold of (P<0.05).

Conclusion

Our results in this study show that the incorporation of "pentosanase enzyme" with a dose of 25g enzyme/100kg of feed into concentrated broiler feed has a significant effect on the average daily weight and gain of broiler chicken. So, it is advisable to incorporate "pentosanase enzyme" into the concentrated broiler feed with a dose of 25g enzyme/100kg of feed to improve its zootechnical performance including live weight and average daily gain.

Scientific Ethics Declaration

* The authors declare that the scientific ethical and legal responsibility of this article published in EPSTEM Journal belongs to the authors.

Conflict of Interest

* The authors declare that they have no conflicts of interest

Funding

* This research received no specific grant from any funding agency in the public, commercial, or not-for-profit sectors.

Acknowledgements or Notes

* This article was presented as a poster presentation at the International Conference on Basic Sciences, Engineering and Technology (www.icbaset.net) held in Trabzon/Türkiye on May 01-04, 2025.

References

Yanti, A. F., Mahfudhoh, N. L., Sajidan, & Budiharjo, A. (2024). Biotechnology application of single enzyme and multienzyme in feed, and its effect on growth performance and carcass persentage in broiler. *BIO Web of Conferences, 127*, 01006.

Brenes, A., Guenter, W., Marquardt, R. R., & Rotter, B. A. (1993). Effect of β-glucanase/pentosanase enzyme supplementation on the performance of chickens and laying hens fed wheat, barley, naked oats and rye diets. *Canadian Journal of Animal Science, 73*(4), 941–951.

Cowieson, A. J., & Ravindran, V. (2008a). Effect of exogenous enzymes in maize-based diets varying in nutrient density for young broilers: Growth performance and digestibility of energy, minerals and amino acids. *British Poultry Science, 49*(1), 37–44.

Cowieson, A. J., & Ravindran, V. (2008b). Sensitivity of broiler starters to three doses of an enzyme cocktail in maize-based diets. *British Poultry Science, 49*(3), 340–346.

Larbier, M., & Leclercq, B. (1992). *Poultry nutrition and feeding* (p.355). In Qua (Ed.).

Saleh, F., M. Tahir, A. Ohtsuka and K. Hayashi, 2005. A mixture of pure cellulase, hemicellulase and pectinase improves broiler performance. *British Poultry Science, 46*, 602-606.

Zakaria, H. A. H., A.R. Jalal, M., & Abu Ishmai, M. A. (2010). The influence of supplemental multi-enzyme feed additive on the performance, carcass characteristics and meat quality traits of broiler chickens. *International Journal of Poultry Science, 9*(2), 126–133.

Author(s) Information

Achour Mennani
Department of Agronomy, Faculty of Sciences, Mohamed Boudiaf University M'sila
M'sila28000, Algeria
Contact e-mail:*Achour.mennani@univ-msila.dz*

Sadam Houcin Lahmar
Department of Agronomy, Agronomic and Veterinary institute, University of Batna,
Batna 05000, Algeria

To cite this article:

Mennani, A., & Lahmar, S.H. (2025). Effect of using ß-pentosanase enzyme in feed on broilers performance. *The Eurasia Proceedings of Science, Technology, Engineering and Mathematics (EPSTEM), 34,* 102-106.

The Eurasia Proceedings of Science, Technology, Engineering & Mathematics (EPSTEM)
ISSN: 2602-3199

The Eurasia Proceedings of Science, Technology, Engineering and Mathematics (EPSTEM), 2025

Volume 34, Pages 107-119

ICBASET 2025: International Conference on Basic Sciences, Engineering and Technology

Enhancing the Efficiency and Security of the Rabin Public-Key Cryptosystem Using Gaussian Integers

Yahia Awad
Lebanese International University

Haissam Chehade
Lebanese International University
The International University of Beirut

Ramiz Hindi
Lebanese International University

Abstract: The Rabin public-key cryptosystem is renowned for its provable security, making it one of the most extensively studied cryptographic schemes. Initially defined over the ring of integers, it has been extended to polynomial rings over finite fields. This work introduces a novel generalization of the Rabin cryptosystem to the domain of Gaussian integers $Z[i]$, incorporating novel arithmetic operations and modifications tailored to this framework. We develop comprehensive encryption and decryption algorithms, supplemented by illustrative examples that clarify these adaptations. A comparative analysis between the classical Rabin scheme and its Gaussian integer extension reveals significant differences in security and computational complexity, demonstrating that the extended scheme significantly enhances resilience against attacks, particularly by mitigating decryption ambiguity and brute-force complexity. Empirical results, supported by computational experiments and graphical analysis, show that the time required for potential attacks increases substantially when transitioning from natural integers to Gaussian integers, a consequence of the richer algebraic structure of $Z[i]$, which imposes additional computational challenges for adversaries. By leveraging these properties, the modified Rabin cryptosystem offers a robust defense against common cryptanalytic techniques, positioning it as a promising alternative for secure communication. This work not only lays the foundation for further exploration of public-key cryptography in alternative algebraic domains but also opens new avenues for both theoretical research and practical applications.

Keywords: Rabin cryptosystem, Gaussian integers, Cryptographic security, Algebraic coding theory

Introduction

The Rabin public-key cryptosystem, introduced in 1978 by Rabin (1978), is the first asymmetric encryption scheme proven to be as secure as the factorization of a Blum integer $n = pq$. Its security hinges on the computational difficulty of the quadratic residues problem and the challenge of computing square roots modulo n. While determining these roots is straightforward when the factorization is known, it becomes significantly more complex when it is not. One of the primary advantages of the Rabin cryptosystem is its reliance on the intractability of integer factorization. The encryption process is exceptionally fast and efficient, requiring minimal computational effort, particularly when the Jacobi symbol does not need to be computed. However, the decryption process, which utilizes the Chinese Remainder Theorem (CRT), operates at a speed comparable to that of RSA decryption.

Despite these benefits, the Rabin cryptosystem has a notable drawback: the squaring operation in the encryption process results in a four-to-one mapping. Consequently, decrypting the ciphertext yields four possible solutions, necessitating an additional rule to determine the correct plaintext. This issue can be addressed by introducing pre-specified redundancy into the original message before encryption, as discussed in (Galbraith, 2012). Similar to the RSA and ElGamal cryptosystems, the classical Rabin encryption scheme is traditionally formulated in the ring of integers modulo n, denoted as Z_n. However, analogous encryption techniques can be extended to other algebraic structures, such as the domain of Gaussian integers $Z[i]$, provided that the underlying arithmetic operations are well-defined and efficiently implementable.

In this study, we propose a modification of the Rabin public-key cryptosystem by extending its computational framework from Z_n to $Z[i]$, incorporating a digital signature scheme. We begin with a concise review of the classical Rabin cryptosystem in Z_n, followed by the development of the necessary computational methods for the extended scheme using Gaussian integer arithmetic. Detailed algorithms and illustrative examples are provided to support the proposed modifications.

To address the inherent ambiguity in the decryption process, we introduce a novel approach: encoding pre-specified redundancy within the imaginary part of the plaintext while preserving the original message in the real part. This technique enables the efficient extraction of the correct plaintext by selecting the square root that contains the redundant imaginary component, thereby resolving the uniqueness issue present in the classical Rabin cryptosystem. To evaluate the effectiveness of the proposed scheme, we conduct a comparative analysis between the extended Rabin cryptosystem in $Z[i]$ and its classical counterpart in Z_n. The results, supported by empirical data and graphical illustrations, demonstrate that the extended scheme offers improved security and efficiency. Notably, our findings indicate that messages encoded in Gaussian integers exhibit greater resistance to cryptographic attacks compared to those based on traditional integers. Finally, we highlight the key advantages of the modified scheme and explore potential applications, paving the way for future research in this promising area of cryptographic security.

Related Works

In recent years, there has been a significant surge of interest in extending classical public-key cryptosystems beyond their conventional domain of integers to more complex algebraic structures, such as the rings of Gaussian integers $Z[i]$ and polynomials over finite fields $Z[x]$. These extensions aim to exploit the distinctive algebraic properties of these domains to enhance the security, efficiency, and applicability of cryptographic systems.

Extensions of the RSA Cryptosystem

El-Kassar and Awad (2005) introduced modifications to the RSA cryptosystem within the domain of Gaussian integers, establishing a foundational framework for further research in this area. Later, Fazekas (2023) developed analogues of widely used encryption schemes, including RSA, in the contexts of Eisenstein and Gaussian integers, thereby advancing the understanding of public-key cryptography in these extended domains.

Extensions of the ElGamal Cryptosystem

Awad et al. (2025) proposed an innovative approach that integrates the ElGamal and RSA algorithms to enhance the security and efficiency of public-key cryptosystems. This hybrid method leverages the strengths of both encryption schemes while mitigating the limitations associated with integer factorization and discrete logarithm problems. Earlier, El-Kassar et al. (2021) extended the classical ElGamal encryption scheme from the ring of natural integers Z to the domain of Gaussian integers $Z[i]$.

The study provides a detailed analysis of the necessary arithmetic adaptations, theoretical proofs, computational procedures, and numerical illustrations, highlighting the advantages of the modified scheme over its classical counterpart. . In addition, Kojok et al. (2002) extended the ElGamal signature scheme to the domain of Gaussian integers, demonstrating the feasibility and security implications of such adaptations. Fazekas (2023) also investigated the ElGamal encryption scheme within the settings of Eisenstein and Gaussian integers, offering comprehensive theoretical analyses and practical implementations.

Extensions of the Rabin Cryptosystem

Awad et al. (2018) extended the Rabin public-key cryptosystem from its traditional domain of natural integers n to the domain of Gaussian integers $Z[i]$ modulo n. This adaptation required the development of extended arithmetic tools, including Legendre symbols, quadratic residues, and versions of fundamental theorems such as Wilson's theorem and the Chinese Remainder Theorem. The study provides rigorous proofs, algorithmic formulations, illustrative examples, and a discussion of the modified scheme's advantages (Awad, El-Kassar & Kadri, 2018). El-Kassar et al. (2004) further advanced the Rabin cryptosystem by extending its computational procedures to arithmetic over polynomials in $Z[x]$, thereby facilitating its adaptation to other algebraic structures (El-Kassar, Haraty, & Awad, 2004).

Other Notable Extensions

Munuera-Merayo (2021) introduced an extension of Mignotte's Secret Sharing Scheme to the ring of Gaussian integers, addressing key limitations in previous constructions and demonstrating the applicability of $Z[i]$ in secure information distribution (Munuera-Merayo, 2021). Fazekas (2023) conducted an extensive study on public-key cryptography within the context of Eisenstein and Gaussian integers, incorporating adaptations of the Diffie–Hellman Key Exchange protocol. This research broadens the scope of cryptographic applications in these algebraic settings (Fazekas, 2023).

Collectively, these studies underscore the potential advantages of modifying classical cryptographic schemes for use in domains such as Gaussian and Eisenstein integers. The unique algebraic properties of these structures may contribute to enhanced security features, novel cryptographic methodologies, and expanded applications in public-key cryptography. Notably, many of these extensions do not require specialized hardware or software, making them practical for real-world implementation and further research.

The Traditional Rabin Public-Key Cryptosystem in Z_n

Similar to other asymmetric cryptographic schemes, the Rabin public-key cryptosystem employs a pair of keys: a public key, which is publicly available for encryption, and a private key, which remains confidential to the intended recipient. The operational framework of the Rabin cryptosystem can be outlined as follows:

1. Public Key Generation:
User A selects two large, random odd prime numbers p and q, ensuring they are of approximately equal size, and computes n as their product $n = pq$. For computational efficiency, particularly in determining square roots modulo p and q, primes of the form $4k + 3$ are often preferred, though the scheme remains valid for any prime numbers. The public key is n, while the private key consists of the pair (p, q).

2. Encryption of Plaintext:
To secure a message $m \in Z_n$, sender B utilizes the public key n and computes the ciphertext using the formula $c \equiv m^2 (mod\, n)$. The encrypted message is then transmitted to A.

3. Decryption of Ciphertext:
Upon receiving the ciphertext c, recipient A leverages their private key (p, q) to retrieve the original message by solving for the square roots modulo n. The decryption process follows these steps:

1. Compute $m_p \equiv c^{\frac{p+1}{4}} (mod\, p)$ and $m_q \equiv c^{\frac{q+1}{4}} (mod\, q)$.
2. Apply the Chinese Remainder Theorem (CRT) to obtain four potential values m_1, m_2, m_3, and m_4 for $m (mod\, n)$ that satisfy $m \equiv \pm m_p (mod\, p)$and $m \equiv \pm m_q (mod\, q)$.
3. A predefined redundancy mechanism is utilized to identify the correct original message from four possible options.

Illustrative Example:

Suppose we select $p = 1051$ and $q = 1031$, leading to $n = 1083581$. The public key is 1083581, while the corresponding private key is the pair $(1051,1031)$. If the message $m = 101011$ belongs to $Z_{1083581}$, encryption

yields the ciphertext $c = m^2 \equiv 223425(mod\ 1\,083581)$. To decrypt the ciphertext, A calculates $m_p = 27$ and $m_q = 936$. Applying the Chinese Remainder Theorem, four possible square roots are derived as 101011, 428923, 654658, and 982570. The redundancy criteria help A identify the correct plaintext as $m = 101011$.

Ensuring Uniqueness in Rabin Decryption with Predefined Redundancy

Since the Rabin function $f(x) \equiv x^2(mod\ n)$ is not injective, encryption results in a four-to-one mapping, leading to four potential solutions during decryption. To guarantee that the decrypted message is accurate, redundancy must be embedded within the message, or additional bits should be appended. One common approach, as suggested by Srivastava and Mathur (2013), is to impose a condition in which the least significant l bits of the binary representation of m are all set to one. An alternative approach, proposed by Galbraith (2012), involves repeating the last l bits of the message. By choosing l sufficiently large, the probability of multiple square roots satisfying the required bit pattern becomes negligibly small. The encoding process typically follows the formula:

$$x = 2^l m + (2^l - 1),$$

where the message space is defined as:

$$M_k = \{m : 1 < m < n/2^l, \text{where } gcd\ (n, 2^l m + (2^l - 1)) = 1\}$$

Alternatively, it can be written as:

$$M_k = \{0,1\}^{k-l-2}$$

If none or more than one of the computed roots satisfies the redundancy condition, decryption is considered unsuccessful. Otherwise, the original message can be recovered by computing $m = \lfloor x/2^l \rfloor$.

Arithmetic in the Gaussian Integer Domain $Z[i]$

The domain Gaussian integers, denoted by $Z[i]$ is an Euclidean domain. It is defined as $Z[i] = \{a + bi \mid a, b \in Z, and\ i^2 = -1\}$, where the associated norm function is given by $\delta(a + bi) = a^2 + b^2$. It is a well-established fact that, under this norm, $Z[i]$ forms an integral domain with unique factorization (UFD), with the units being ± 1 and $\pm i$. Consequently, the associates of any Gaussian integer α are $\pm\alpha$ and $\pm\alpha i$.

The Euclidean algorithm within $Z[i]$ is described as follows: for any Gaussian integers α and $p \neq 0$, there exist uniquely determined (up to associates) integers q and r such that the relation $\alpha = qp + r$ holds, where either $r = 0$ or $\delta(r) < \delta(p)$. Moreover, the greatest common divisor (gcd) of p and q can be uniquely expressed in the form $gcd(p, q) = px + qy$ for some $x, y \in Z[i]$.

Primes in Z[i]: The Gaussian primes up to associates are:

1. $\alpha = 1 + i$.
2. π and $\overline{\pi}$, where $\pi\overline{\pi}$ is an odd prime integer of the form $4k$ +1.
3. Any odd prime integer p of the form $4k$ + 3.

Moreover, if $\delta(z)$ is prime in Z, then z is irreducible in $Z[i]$ and hence it is prime.

Complete Residue Systems in Z[i]: Let $p \in Z[i]$, and $< p >= pZ[i]$ denote the principal ideal generated by p. A complete residue system modulo p is a set, denoted as $A(p)$, which provides a collection of unique representatives for the cosets of $< p >$ within $Z[i]$. The number of elements in this system is given by $\delta(p)$. The studies by El-Kassar [6] and Cross [5] established that:

1. $A(\gamma p) = \{s + r\gamma \mid s \in A(\gamma); r \in A(p)\}$
2. $A(\alpha^{2m}) = \{a + bi \mid 0 \leq a \leq 2^m - 1; 0 \leq b \leq 2^m - 1\}$
3. $A(\alpha^{2m+1}) = \{a + bi \mid 0 \leq a \leq 2^{m+1}; 0 \leq b \leq 2^m - 1\}$
4. $A(\pi^n) = \{a \mid 0 \leq a \leq q^n - 1; \pi\overline{\pi} = q\}$
5. $A(p^n) = \{a + bi \mid\ 0 \leq a \leq p^n - 1; 0 \leq b \leq q^n - 1\}$

Reduced Residue Systems in Z[i]: The reduced residue class modulo p refers to the set $R(p)$, which consists of all elements in $A(p)$ that are coprime with p. The cardinality of this set is denoted by $\phi(p)$, an extension of Euler's totient function ϕ within the domain of Gaussian integers $Z[i]$. Research by Cross (1983) and El-Kassar (1991) has established that the function ϕ is multiplicative.

1. $\phi(\alpha^n) = 2^n - 2^{n-1}$
2. $\phi(\pi^n) = q^{n-1}(q-1)$
3. $\phi(p^n) = p^{2n-2}(p^2-1)$

Below, we present several revised theorems and results essential for the extension of the Rabin public-key cryptosystem from Z_n to $Z[i]$. Detailed proofs of these results can be found in Awad et al. (2018).

Definition 1. Let *x* and *n* be two relatively prime Gaussian integers. Then, *x* is quadratic residue modulo *n*, denoted by $x \in Q_n$, if the congruence $r^2 \equiv x(mod\, n)$has a solution. Otherwise, *x* is a quadratic non residue modulo *n*, and it is denoted by $x \in \overline{Q}_n$.

Theorem 1. Let *x* be any Gaussian integer, and let *p* be a Gaussian prime with $p \not\approx 1+i$. If $gcd(x,p) \approx 1$, then the congruence $r^2 \equiv x(mod\, n)$ has either no solution or exactly two incongruent solutions modulo *p*.

Theorem 2. Let $p \not\approx 1+i$ be a Gaussian prime. Then,$|Q_p| = |\overline{Q}_p| = \frac{\phi(p)}{2}$.

Theorem 3. (*Wilson's Theorem in Z*[*i*]) If $p \in Z[i]$ be a Gaussian prime, then $\prod_{a \in R(p)} a \equiv -1(mod\, p)$.

Theorem 4. Let *x* be any Gaussian integer, and let *p* be a Gaussian prime such $p \nmid x$. Then, $\left(\frac{x}{p}\right) \equiv x^{\frac{\phi(p)}{2}}(mod\, p)$, where $\left(\frac{x}{p}\right)$ is the extended Legendre symbol to *Z*[*i*].

Theorem 5. If $p \in Z[i]$ is a Gaussian prime such that $p \not\approx 1+i$. Then, the congruence $r^2 \equiv -1(mod\, n)$is solvable.

Theorem 6. (*Chinese Remainder Theorem in Z*[*i*]) Let $m_1, m_2, \ldots, m_k$ be *k* pairwise relatively prime Gaussian integers and let $a_1, a_2, \ldots, a_k$be any *k* Gaussian integers. Then, the system of linear congruencies $\{x \equiv a_i(mod\, m_i) \mid 1 \le i \le k\}$ has a unique solution x_0. Moreover, any two such solutions are congruent modulo $M = m_1 m_2 \ldots m_k$.

Theorem 7. Suppose that $n = pq$ with *p* and *q* are two Gaussian primes different from $\alpha = 1+i$. If $r^2 \equiv x(mod\, n)$ is solvable, then there are exactly four incongruent solutions modulo *n*.

Theorem 8. Let $n = pq$ be a composite Gaussian integer where $p = 4k_1 + 3$and$q = 4k_2 + 3$are odd prime integers. Then, the complete residue system modulo *n* is the set of Gaussian integers such that

$$A(n) = \{\lambda + \gamma i \mid 0 \le \lambda \le n-1; 0 \le \gamma \le n-1\}.$$

From the above theorems, we deduce that the order of *A*(*n*) is $q(n) = p^2q^2 = n^2$ and that of *R*(*n*) is

$$\phi(n) = (p^2q^2 - 1)(p^2q^2 - 1) = (n^2-1)^2.$$

The proofs of the following theorems can be found in Koval (2011).

Theorem 9. Let $z = c + di$ be a Gaussian integer, then *z* has a square root $r = a + bi$ if and only if $\delta(z)$ has a square root modulo *p*, where *p* is a Gaussian prime integer of the form $4k+3$.

Theorem 10. Let $z = c + di$ be a Gaussian integer, and let p be a prime integer of the form $4k+3$. If $d = 0$, then

1. z always has a square root r.
2. If $a^2 \equiv c(mod\, p)$, then z has two square roots $r = \pm a$ modulo p.
3. If c does not have a square root, then $r = \pm bi$ are the square roots of z modulo p, and $r^2 \equiv -a(mod\, p)$.

Theorem 11. Let p be a Gaussian prime of the form $4k + 3$, and let $z = c + di$ such that $d \not\equiv 0(mod\, p)$. If r and $-r$ are two square roots of $\delta(z)$ modulo p, then there are exactly two square roots of z modulo p. They are: $\xi_1 = a + bi$ and $\xi_2 = -a - bi$, where a and b are two non-zero Gaussian integers such that $a \equiv \sqrt{2^{-1}(c + r)}$ modulo p and $b \equiv (2a)^{-1}d$ modulo p, or $b = \sqrt{-2^{-1}(c + r)}$ modulo p and $a = (2b)^{-1}d$ modulo p.

Extending the Rabin Public-Key Cryptosystem Using Gaussian Integers

The arithmetic properties within the domain of Gaussian integers can be leveraged to extend the Rabin public-key cryptosystem in the following manner:

1. Select two Gaussian prime numbers, p and q, both satisfying the condition $4k + 3$. The public key is then represented by the Blum integer $n = pq$, while the private key consists of the pair (p, q).
2. Encryption of a message $m \in R(n)$ is performed by computing the congruence $c \equiv m^2(mod\, n)$. The resulting value c serves as the ciphertext.
3. Decryption involves determining the four possible Gaussian square roots of c modulo n, followed by a selection process to retrieve the original message.

Why Choose Gaussian Primes of the Form $4k + 3$?

Gaussian primes can be classified into two distinct types. The first category includes primes that are associated with real primes of the form $4k + 1$, expressed as $p \approx \pi$, where $\pi\overline{\pi}$ corresponds to such a prime. The second type consists of Gaussian primes derived from real primes of the form $4k + 3$. Consequently, when constructing the composite Gaussian integer n, three different scenarios arise depending on the chosen prime factors.

1. If $p \approx \pi_1$ and $q \approx \pi_2$, where $\pi_1\overline{\pi}_1$ and $\pi_2\overline{\pi}_2$ are odd prime integers of the form $4k + 1$, then, due to [6], the complete residue system modulo $n = pq$ is of the form $A(n) = \{a + bp \mid a \in A(p), b \in A(q)\}$ where $A(p) = \{a \mid 1 \leq a \leq p - 1\}$ and$A(q) = \{b \mid 1 \leq b \leq q - 1\}$. Hence, the order of $A(n)$ is $(p - 1)(q - 1)$ and that of $R(n)$ is $pq - 1$. This case is similar to the classical one and it will not be taken into consideration.

2. If $p \approx \pi_1$ and $q = p$, where $\pi_1\overline{\pi}_1$ and p are odd prime integers of the form $4k + 1$ and $4k + 3$ respectivitly, then the factorization problem of the composite Gaussian integer $n = pq$, which has the form $a + bi$, could be easily solved by finding $gcd(a, b)$ which equals to p. But, the security of Rabin public-key cryptosystem relies on the intractability of factoring n so this case will be also neglected.

3. If p and q are odd prime integers of the form $4k + 3$, then the complete residue system modulo $n = pq$ is of the form $A(n) = \{r + sp | r \in A(p), s \in A(q)\}$ with order n^2, which is much larger than that in the classical one. So, in our modification of the Rabin public-key cryptosystem to the domain of Gaussian integers, we are only interested in the Gaussian primes of the form $4k + 3$.

Selection of Plaintext Messages

Plaintext messages $m \in A(n)$ can take one of two possible forms. The first form is expressed as $m = a + bi$, where a and b are integers, and $b \neq 0$. The second form simplifies to $m = a$, where $a \in Z$, resembling the structure used in the set of natural integers. In our proposed modification, we focus primarily on the first case, where m takes the form $m = a + bi$ with $b \neq 0$.

Gaussian Quadratic Residue Square Roots

Determining the Gaussian square roots of Gaussian quadratic residues $m = a + bi$ within $A(p)$ poses a significant challenge. However, this problem can be addressed by extending the existing algorithms designed for computing square roots in Z_n to the domain $Z[i]$. The algorithm outlined below presents a method for computing Gaussian square roots of Gaussian quadratic residues modulo any Gaussian prime p.

Algorithm 1. Square Roots Modulo Gaussian Primes

***Step* 1**: If $\left(\frac{c}{p}\right) = -1$, then c does not have a square root modulo p and terminate with failure.

***Step* 2**: Compute the inverse $c^{-1}(mod\ p)$ by the extended Euclidean algorithm in $Z[i]$.

***Step* 3**: Write $\phi(p) = 2^s t$, where t is an odd integer.

***Step* 4**: Select a quadratic non-residue integer $b = x' + y'i$ modulo p such that $b \in R(p)$.

***Step* 5**: Set $x \equiv b^t(mod\ p)$ and $r \equiv c^{(t+1)/2}(mod\ p)$.

***Step* 6**: For $i = 1$ to $s - 1$:

6.1 Compute $\delta \equiv (r^2 c^{-1})^{2^{s-i-1}}(mod\ p)$.
6.2 If $\delta \equiv -1(mod\ p)$, then set $r \equiv rx(mod\ p)$, and $x \equiv x^2(mod\ p)$.
6.3 If $\delta \equiv 1(mod\ p)$, then repeat with a new value of i.

***Step* 7**: Return $(r, -r)$ as the two square roots of c modulo p.
In the following, we present the modified Rabin public-key cryptosystem in $Z[i]$.

- **Public and Private keys Generation Algorithm:**

1. Generate two large random and distinct Gaussian primes p and q, each roughly the same size and of the form $4k + 3$.
2. Compute $n = pq$.
3. The public-key is n and *A*'s private-key is (p, q).

- **Messages Encryption Algorithm:**

1. Obtain *A*'s authentic public-key n, and choose the plaintext message as a Gaussian integer $m \in A(n)$.
2. Compute the ciphertext $c \equiv m^2(mod\ n)$, and send it to entity *A*.

- **Ciphertext Decryption Algorithm:**

1. Apply the Chinese Remainder Theorem in $Z[i]$ to determine the four square roots m_1, m_2, m_3, and m_4 of c modulo n.
2. Entity *A* decides which of these is the original message m by selecting the obtained square root with redundancies in its imaginary part.

Example 2. Let $p = 1051$ and $q = 1031$be two randomly chosen Gaussian integers of the form $4k + 3$, then $n = 1083581$. The public-key is 1083581 and *A*'s private-key is the pair $(1051, 1031)$. The number of different choices for the message m is equal to the order of the complete residue system modulo n, which is $|A(n)| = 1174147783561$. Let $m = 101011 + 111111i$, where the pre-specified redundancy is in its imaginary part, then the ciphertext is $c \equiv m^2 \equiv 891018 + 486027i(mod\ 1\,083581)$. To decrypt the received ciphertext c, entity *A* uses the private keys p and q, the above algorithm, and the Chinese Remainder Theorem over $Z[i]$ to find the four square roots: $m_1 = 101011 + 111111i$, $m_2 = 428923 + 461094i$, $m_3 = 654658 + 622487i$, and $m_4 = 982570 + 972470i$. Entity *A* knows that the original message is m_1 by checking the redundancy of the imaginary parts of the obtained four square roots because m_1 is the one that contains a redundancy in its imaginary part.

Rabin Digital Signature Scheme in $Z[i]$

Rabin (1978) described a trapdoor hash 2 to 1 function $f: {Z_p}^* \to {Z_p}^*$ such that $f(x) = x^2$. This mapping can be utilized in digital signature system for public-key encryption. If p and q are two odd prime integers and $n = pq$, then $f: {Z_n}^* \to {Z_n}^*$ is a 4 to 1 mapping on Z_n. Each member in the image of f has exactly four distinct pre-images and the invertibility of this function is proven to be as difficult as factoring the integer n. Therefore, factorization of n serves as a trapdoor for $f(x)$. The Rabin public-key signature scheme is akin to that of RSA with an even

public exponent $e = 2$. The message space $M = Z_n^*$ and the signing space $M_s = Q_n$ and signatures are square roots. A redundancy function R from the message space M to M_s is selected and is public knowledge.

In the following section, we present a modification of the fundamental Rabin public-key signature scheme, originally introduced by Rabin. This modification extends the scheme from its traditional domain of natural integers Z_n to a new setting over the domain of Gaussian integers $Z[i]$ modulo n, utilizing the extended arithmetic in $Z[i]$.The Rabin public-key digital signature scheme in $Z[i]$ is described as follows:

Algorithm 2. (*Key Generation for the Rabin Public-key Digital Signature*) Entity *A* should do the following:

***Step* 1:** Generates two Gaussian primes p and q, then computes $n = pq$.

***Step* 2:** The public-key is n and the private-key is the pair (p, q).

Algorithm 3. (*Rabin Signature Generation)* Entity *A* signs a message m as follows:

***Step* 1**: Chooses $M \in Z_n^*[i]$, and Computes $\mu = R(m)$.

***Step* 2**: Compute $s = \sqrt{\mu}(mod\, n)$.

***Step* 3**: *A*'s signature of m is s.

Algorithm 4. (*Rabin Signature Generation*) To verify *A*'s signature s and recover the message m, entity *B* should do the following:

***Step* 1**: Obtains *A*'s authentic public key n.

***Step* 2**: Computes $\mu \equiv s^2(mod\, n)$.

***Step* 3**: Verifies that $\mu \in Z_n^*[i]$, otherwise entity *B* will reject the signature.

***Step* 4**: Recovers $m \equiv R^{-1}(\mu)(mod\, n)$.

Example 3. Let $p = 3$ and $p = 7$, then $n = 21$. The public-key is 21, and *A*'s private-key is the pair $(3, 7)$. The signing space M_s is the set of Gaussian quadratic residues $Q_{21} = \{i, 21 + i, 42 + i, 2i, 21 + 2i, 42 + 2i, 7 + 3i, 14 + 3i, 28 + 3i, 35 + 3i, 49 + 3i, 56 + 3i, 4i, 21 + 4i, 42 + 4i, 5i, 21 + 5i, 42 + 5i, 7 + 6i, 14 + 6i, 28 + 6i, 35 + 6i, 49 + 6i, 56 + 6i, 1, 8, 22, 29, 43, 50, 15 + i, 36 + i, 57 + i, 1 + 2i, 8 + 2i, 22 + 2i, 29 + 2i, 43 + 2i, 50 + 2i, 1 + 4i, 8 + 4i, 22 + 4i, 29 + 4i, 43 + 4i, 50 + 4i, 1 + 5i, 8 + 5i, 22 + 5i, 29 + 5i, 43 + 5i, 50 + 5i, 1 + 6i, 8 + 6i, 22 + 6i, 29 + 6i, 43 + 6i, 50 + 6i,\quad 2, 16, 23, 37, 44, 58, 2 + i, 16 + i, 23 + i, 37 + i, 44 + i, 58 + i, 9 + 2i, 30 + 2i, 51 + 2i, 2 + 4i, 16 + 4i, 23 + 4i, 37 + 4i, 44 + 4i, 58 + 4i, 9 + 5i, 30 + 5i, 51 + 5i, 10, 17, 31, 38, 52, 59, 10 + i, 17 + i, 31 + i, 38 + i, 52 + i, 59 + i, 10 + 2i, 17 + 2i, 31 + 2i, 38 + 2i, 52 + 2i, 59 + 2i, 10 + 3i, 17 + 3i, 31 + 3i, 38 + 3i, 52 + 3i, 59 + 3i, 3 + 4i, 24 + 4i, 45 + 4i, 10 + 5i, 17 + 5i, 31 + 5i, 38 + 5i, 52 + 5i, 59 + 5i, 4, 11, 25, 32, 46, 53, 4 + i, 11 + i, 25 + i, 32 + i, 46 + i, 53 + i, 4 + 2i, 11 + 2i, 25 + 2i, 32 + 2i, 46 + 2i, 53 + 2i, 4 + 3i, 11 + 3i, 25 + 3i, 32 + 3i, 46 + 3i, 53 + 3i, 18 + 4i, 39 + 4i, 60 + 4i, 4 + 5i, 11 + 5i, 25 + 5i, 32 + 5i, 46 + 5i, 53 + 5i, 5, 19, 26, 40, 47, 61, 5 + i, 19 + i, 26 + i, 40 + i, 47 + i, 61 + i, 12 + 2i, 33 + 2i, 54 + 2i, 5 + 4i, 19 + 4i, 26 + 4i, 40 + 4i, 47 + 4i, 61 + 4i, 12 + 5i, 33 + 5i, 54 + 5i, 13, 20, 34, 41, 55, 62, 6 + i, 27 + i, 48 + i, 13 + 2i, 20 + 2i, 34 + 2i, 41 + 2i, 55 + 2i, 62 + 2i, 13 + 4i, 20 + 4i, 34 + 4i, 41 + 4i, 55 + 4i, 62 + 4i, 13 + 5i, 20 + 5i, 34 + 5i, 41 + 5i, 55 + 5i, 62 + 5i, 13 + 6i, 20 + 6i, 34 + 6i, 41 + 6i, 55 + 6i, 62 + 6i\}$.

For simplicity, take $M = M_s$ and the redundancy function to be the identity mapping, that is, $\mu = R(m) = m$. To sign a message $m = 10 + 3i$, entity *A* computes $R(10 + 3i) = \mu = 10 + 3i$, and the Gaussian square roots of $10 + 3i$ modulo 21 are $19 + 15i, 5 + 15i, 2 + 6i$, and $16 + 6i$. If entity *A* chooses the signature of *m* to be $s = 2 + 6i$ which is any of the Gaussian square roots of $m = 10 + 3i$, then entity *B* verifies *A*'s signature by computing $\mu = s^2(mod\, 2\, 1) = 10 + 3i$. Since $\mu = 10 + 3i \in M_R$ (Image of *R*), entity *B* accepts the signature and recovers $m = R^{-1}(\mu) = 10 + 3i$.

Comparative Study between the Modified Rabin Cryptosystem in $Z_n[i]$ with the Classical Cryptosystem in Z_n

In this section, we present a comparative study of the classical Rabin public-key cryptosystem in the domain of natural numbers Z_n and its modified version in the domain of Gaussian integers $Z_n[i]$. The study is divided into two parts: The first part analyzes the hacking time (cryptanalysis time) required for square root-finding tools, while the second part examines the decryption time of the Rabin cryptosystem in both settings. This analysis aims to determine which setting offers better security and efficiency.

Hacking Time Study

In this study, we simulate the average time required to decrypt a randomly selected set of messages m of varying structures using square root finding techniques. These methods are applied to messages encrypted with randomly generated prime integers p and q, both of which are of approximately equal size.

The procedure begins with the generation of two large, distinct Gaussian prime numbers p and q, each satisfying the form $4k + 3$ and having roughly the same magnitude. The product $n = pq$ is then computed. Next, we randomly select messages m from the complete residue system

$$A(n) = \{\lambda + \gamma i | 0 \leq \lambda \leq n-1; 0 \leq \gamma \leq n-1\} \cong Z_n^*[i],$$

and compute the corresponding ciphertext using the relation

$$c \equiv m^2 (mod\, n)$$

The decryption process, or cryptanalysis, focuses on determining the average computational time required to retrieve the plaintext messages by computing

$$m \equiv \sqrt{c} (mod\, n).$$

Since the selected random messages have distinct structures - either as real integers or as Gaussian integers - we consider only the real parts of all chosen messages $m \in Z_n^*[i]$ to represent the real message space $m \in Z_n$.

To conduct the experiment, we utilized the built-in function *RandomSample* to randomly select a set of messages m from $Z_n^*[i]$. The simulation was performed for prime numbers ranging in size from 200 to 3600 digits, evaluating the time required to decrypt both real and Gaussian integer messages using square root finding methods. The results indicate that, on average, decrypting Gaussian integer messages is significantly more computationally demanding than decrypting their real counterparts.

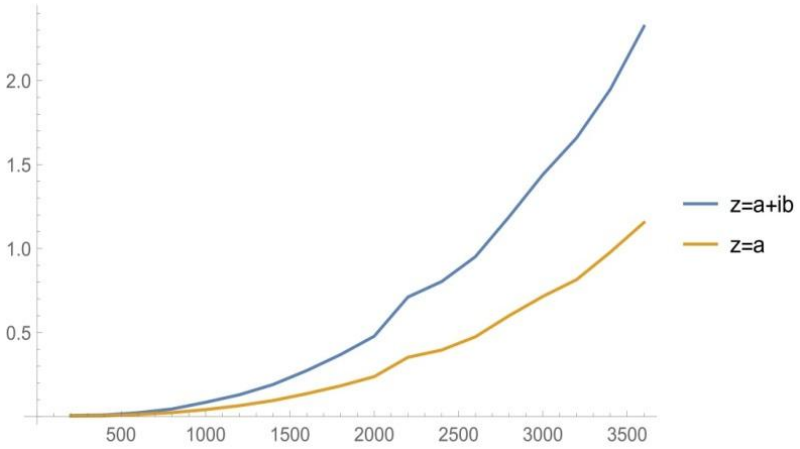

Figure1. Average hacking time for real and Gaussian messages from digit 200 to 3600 for *p* and *q* with 200 as a step size

In particular, the *RandomSample* function required approximately **5088.26 seconds** to process **15 random sample messages**, with a step size of 200. The resulting data, illustrated in Figure 1**,** clearly demonstrate that the

application of square root finding methods to Gaussian integer messages presents a greater computational challenge, thereby enhancing security when compared to their real integer counterparts.

Decryption Time Study

In this study, we maintain the same number of random messages but employ different algorithms: the Chinese Remainder Theorem (**CRT**), Mathematica's built-in **ExtendedGCD** function for Gaussian integers, the Rabin public-key decryption algorithm for the modified (**RBK**) scheme, and Mathematica's **PowerMod** function for natural numbers. The analysis is conducted for both real and Gaussian integer plaintext messages, using a step size of 2 and prime integers p and q ranging from 1 to 30 digits. The simulations required approximately 1051.28 seconds to produce the following results:

Table1. Average time needed for CRT, ExtendedGCD, RBK and PowerMod from digit 1 to 30 with step size 2

#	CRT	EGCD	RBK	PowerMod
1	0.0000936889	0.00011119	0.0000301594	0.0000150797
2	0.0000959785	0.000111479	0.0000303963	0.0000154218
4	0.000101084	0.000116111	0.0000313963	0.0000207905
6	0.000125112	0.000125638	0.0000335806	0.00033578
8	0.000120953	0.000130296	0.0000358176	0.000546396
10	0.000142191	0.000140823	0.0000397388	0.00126056
12	0.000137059	0.000167666	0.0000446601	0.00342509
14	0.000134138	0.00013248	0.0000368703	0.00692387
16	0.000143797	0.000138112	0.0000414758	0.0357867
18	0.00014956	0.000146692	0.0000411599	0.0713948
20	0.000332069	0.000310358	0.00011769	0.180183
22	0.000296988	0.000272935	0.000102137	0.335622
24	0.000312963	0.000283725	0.000104637	3.4898
26	0.000332017	0.000301383	0.000117243	6.11951
28	0.000358492	0.000337701	0.000126427	11.0364
30	0.000383756	0.00035107	0.000137902	48.7704

Based on the results presented in Table 1, it is evident that the **PowerMod** function for real numbers requires a significant amount of time to compute the square roots of $c \equiv m^2 (mod\, n)$. Consequently, after removing the **PowerMod** function from the study, the program executed more efficiently, completing in approximately 49,786.5 seconds with a step size of 50. The following figure illustrates the average time curve for decrypting fifteen randomly generated real and Gaussian integer messages, ranging from 1 to 5,000 digits.

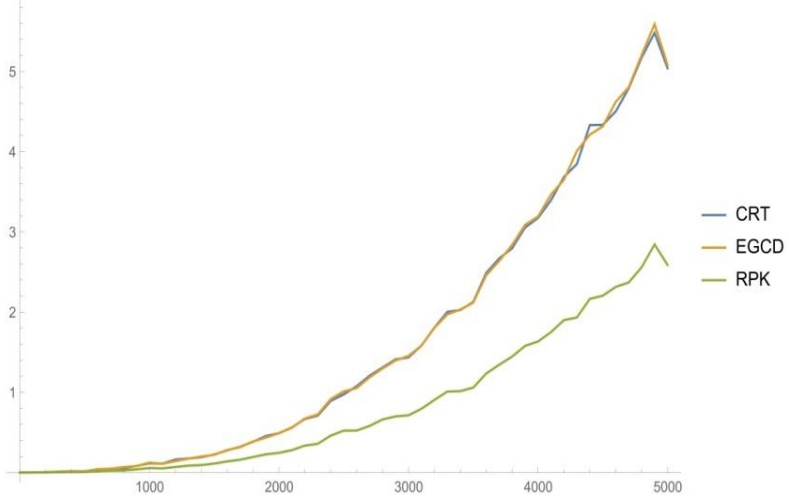

Figure 2. Decryption average time for real and Gaussian messages up to 5000 digits

It is obvious that both the **CRT** and the **ExtendedGCD** for Gaussian integers are more secure and stronger than that of the real integers. It seems that we can either use the **CRT** or the **ExtendedGCD** to obtain the unique solution for the square roots of Gaussian integers. Along these lines, we acquire that the Gaussian integer messages

devour time much more than the real messages so as to break. Consequently, Rabin cryptosystem in the new settings is more secure than Rabin cryptosystem in the classical settings.

Benefits of the Enhanced Rabin Public-Key Cryptosystem in the Gaussian Integer Domain $Z[i]$

Based on the analysis conducted in this chapter, as well as the theoretical discussions, we can summarize the key advantages of the modified Rabin cryptosystem within the Gaussian integer set $Z[i]$, compared to its classical counterpart.

1. **No Extra Effort Required:** The process of generating the odd prime numbers p and q follows the same level of complexity in both the conventional and the enhanced versions of the Rabin cryptosystem.

2. **Expanded Message Space:** When p and q are Gaussian primes of the form $4k + 3$, the total number of elements in the complete residue system $Z_n \cong Z_n/< n >$ is $n = pq$, whereas in the Gaussian integer domain, $Z_n[i] \cong Z[i]/< n >$ contains p^2q^2 elements. Consequently, the modified scheme significantly broadens the range of message choices by a factor of pq, which increases the complexity of potential attacks.

3. **No Additional Computational Complexity:** The computational steps required in the enhanced cryptosystem remain fundamentally similar to those in the classical method, without the need for additional complex operations.

4. **Comparable Performance:** The encryption process in the Rabin scheme primarily relies on a single modular squaring operation, which makes it an exceptionally fast process. Although the decryption process is relatively slower compared to encryption, its speed is comparable to decryption in cryptosystems such as RSA.

5. **Distinct Decryption Strategy (No Need for Redundancy in the Original Message):** A known drawback of the classical Rabin cryptosystem is the challenge of identifying the correct message among four potential solutions. Typically, this issue is addressed by embedding predefined redundancy in the original message before encryption, such as repeating the final digits of the message. In contrast, the proposed approach eliminates the need for such modifications. Instead, the original message remains as the real part of the Gaussian integer, and redundancy is introduced in the imaginary component (as demonstrated in Example 2). This method preserves the integrity of the original message and facilitates the correct selection of the valid solution based on the redundant imaginary part, thereby enhancing security without extra effort (illustrated in Examples 1 and 2).

6. **Enhanced Security Against Attacks:** Our findings suggest that the Rabin cryptosystem within $Z_n[i]$ offers superior security compared to both the classical Rabin and RSA schemes. Messages represented as Gaussian integers provide enhanced resistance to attacks compared to real-valued messages. Additionally, brute-force attacks become increasingly inefficient due to the substantial size of n.

Conclusion

In this work, we extended the Rabin public-key cryptosystem from its traditional setting over the natural numbers Z to a new framework within the domain of Gaussian integers $Z[i]$. The necessary arithmetic operations in this new setting were developed, and computational procedures for the modified scheme were established. Additionally, we conducted a comparative analysis between the modified cryptosystem and its classical counterpart. The results, supported by accompanying diagrams, demonstrated that the time required to compromise the modified cryptosystem is significantly longer than that of the original version.

Our modifications yield several notable advantages. Most importantly, we introduced a novel approach for determining the uniqueness of the Rabin decryption scheme and selecting the correct plaintext message from the four square roots generated during the decryption process. Ultimately, we proved that the modified cryptosystem in $Z[i]$ offers enhanced security and robustness against hacking attempts while maintaining the same computational complexity as the classical scheme.

While this study demonstrates the advantages of extending the Rabin cryptosystem to the domain of Gaussian integers, several avenues for further research remain. One potential direction is exploring the cryptosystem's adaptation to other algebraic structures, such as the Eisenstein integers or polynomial rings, to assess whether similar security enhancements can be achieved. Additionally, further optimizations in decryption efficiency and key selection strategies could be investigated to improve computational performance. Finally, a deeper security analysis, including resistance against quantum attacks, would provide valuable insights into the long-term viability of the modified scheme in post-quantum cryptographic environments.

Recommendations

Based on the findings of this study, several promising directions for future research are recommended. Expanding the implementation of modified public-key cryptosystems to broader algebraic structures - such as Euclidean domains, polynomial rings, or other unique factorization domains - could further enhance their versatility and security. Practical applications in areas like secure communication, blockchain technology, and digital signature schemes should be actively explored to assess real-world benefits. Additionally, future work should focus on optimizing performance and conducting comprehensive security analyses under diverse attack models, including those relevant to emerging quantum threats. These efforts will be essential to validate and strengthen the cryptosystem's applicability in evolving cryptographic landscapes.

Scientific Ethics Declaration

* The authors declare that the scientific ethical and legal responsibility of this article published in EPSTEM journal belongs to the authors.

Conflict of Interest

* The authors declare that they have no conflicts of interest

Funding

* This research received no specific grant from any funding agency in the public, commercial, or not-for-profit sectors.

Acknowledgements or Notes

* This article was presented as an oral presentation at the International Conference on Basic Sciences, Engineering and Technology (www.icbaset.net) held in Trabzon/Turkey on May 01-04, 2025.

* The authors gratefully acknowledge the invaluable contributions of the anonymous referees whose insightful comments and constructive feedback greatly enhanced the quality and clarity of this article. Their expertise and dedication have been instrumental in shaping the final version of the manuscript.

* Each author has contributed equally to this article, demonstrating a collaborative effort and shared dedication to its content.

* AMS Subject Classification: 11T71, 11R52, 94A60, 11A55, 68P25.

References

Awad, Y. A., El-Kassar, A. N., & Kadri, T. (2018). Rabin public-key cryptosystem in the domain of Gaussian integers. *International Conference on Computer and Applications* (ICCA18) (pp.1-340). IEEE.

Awad, Y., Hindi, R., & Chehade, H. (2023). Comparative study between a novel deterministic test for Mersenne primes and the well-known primality tests. *Baghdad Science Journal, 20*(5).

Awad, Y., Jomaa, D., Alkhezi, Y., & Hindi, R. (2025). A new approach combining RSA and ElGamal algorithms: Advancements in encryption and digital signatures using Gaussian integers. *Jordanian Journal of Computers and Information Technology (JJCIT), 11*(1), 54–72.

Buck, N. (2010). *Quadratic reciprocity for the rational integers and the Gaussian integers (*Master's thesis, University of North Carolina at Greensboro, pp.53–65).

Cross, J. T. (1983). The Euler's ϕ-function in the Gaussian integers. *The American Mathematical Monthly, 90*, 518–528.

El-Kassar, A. N. (1991*). Generalizations of Lehmer's equations, greatest common divisor matrices, and Euler's totient for a U.F.D.* (Doctoral dissertation, University of Southwestern Louisiana).

El-Kassar, A. N., Rizk, M., Mirza, N., & Awad, Y. A. (2001). El-Gamal public key cryptosystem in the domain of Gaussian integers. *International Journal of Applied Mathematics, 7*(4), 405–412.

El-Kassar, A. N., & Awad, Y. A. (2005). Modified RSA in the domain of Gaussian integers and rings of polynomials over finite fields. *18th International Conference on Computer Applications in Industry and Engineering* (pp. 298–303). ISCA.

El-Kassar, A. N., & Haraty, R. (2004). ElGamal public-key cryptosystem using reducible polynomials over a finite field. *13th International Conference on Intelligent and Adaptive Systems and Software Engineering* (pp. 189–194). ISCA.

El-Kassar, A. N., Haraty, R., & Awad, Y. A. (2004). Rabin public key cryptosystem in rings of polynomials over finite fields. *Third International Conference on Computer Science, Software Engineering, Information Technology, e-Business, and Applications*, 1-5.

ElGamal, T. (1985). A public key cryptosystem and a signature scheme based on discrete logarithms. *IEEE Transactions on Information Theory* (pp.469–472).

Fazekas, S. (2023). Public key cryptography over the Gaussian and Eisenstein integers. (Master's thesis, National University of Ireland, Maynooth).

Galbraith, S. (2012). *Mathematics of public key cryptography*. Cambridge University Press.

Kojok, B., El-Kassar, A. N., & Raad, F. (2002). ElGamal signature scheme in the domain of Gaussian integers. *International Conference on Research Trends in Science and* T*echnology (RTST),* 275–282.

Koval, A. (2011). *Security systems based on Gaussian integers: Analysis of basic operations and time complexity of secret transformations.* (Doctoral dissertation, New Jersey Institute of Technology).

Menezes, A. J., Van Oorshot, P. C., & Vanstone, S. A. (1997). *Handbook of applied cryptography*. CRC Press.

Munuera-Merayo, D. (2021). On Mignotte secret sharing schemes over Gaussian integers. *arXiv preprint arXiv:2104.06361.*

Rabin, M. (1978). *Digitalized signature as intractable as factorization (Technical report MIT/LCS/TR-212).* MIT Laboratory for Computer Science.

Rivest, R., Shamir, A., & Adleman, L. (1978). A method for obtaining digital signatures and public key cryptosystems. *Communications of the ACM, 21,* 120–126.

Srivastava, A. K., & Mathur, A. (2013). The Rabin cryptosystem & analysis in measure of Chinese remainder theorem. *International Journal of Scientific and Research Publications, 3*(6),1-4.

Author(s) Information

Yahia Awad
Lebanese International University (LIU)
Department of Mathematics and Physics
AlKhyara, West Bekaa, Lebanon.
Contact e-mail: *yehya.awad@liu.edu.lb*

Haissam Chehade
Lebanese International University (LIU)
Department of Mathematics and Physics
Saida, Lebanon.
The International University of Beirut (BIU)
Department of Mathematics and Physics
Beirut, Lebanon.

Ramiz Hindi
Lebanese International University (LIU)
Department of Mathematics and Physics
AlKhyara, West Bekaa, Lebanon.

To cite this article:

Awad, Y., Chehade, H., & Hindi. R. (2025). Enhancing the efficiency and security of the rabin public-key cryptosystem in the domain of Gaussian integers. *The Eurasia Proceedings of Science, Technology, Engineering and Mathematics (EPSTEM), 34,* 107-119.

The Eurasia Proceedings of Science, Technology, Engineering & Mathematics (EPSTEM)
ISSN: 2602-3199

The Eurasia Proceedings of Science, Technology, Engineering and Mathematics (EPSTEM), 2025

Volume 34, Pages 120-138

ICBASET 2025: International Conference on Basic Sciences, Engineering and Technology

Soft Semi # Generalized α-Connectedness in Soft Topological Spaces

Raja Mohammad Latif
Prince Mohammad Bin Fahd University

Abstract: Soft set theory is a newly emerging tool to deal with uncertain problems and has been studied by researchers in theory and practice. The concept of soft topological space is a very recently developed area having many research scopes. Soft sets have been studied in proximity spaces, multi-criteria decision-making problems, medical problems, mobile cloud computing networks, defense learning systems, and approximate reasoning, etc. The objective of this paper is to use $S_{\tilde{\tau}}S_{emi}{}^{\#}g\alpha$ –open sets and $S_{\tilde{\tau}}S_{emi}{}^{\#}g\alpha$ –closed sets to introduce the concepts of $S_{\tilde{\tau}}S_{emi}{}^{\#}g\alpha$ –separated sets, $S_{\tilde{\tau}}S_{emi}{}^{\#}g\alpha$ –connected space, $S_{\tilde{\tau}}S_{emi}{}^{\#}g\alpha$ –disconnected space, $S_{\tilde{\tau}}S_{emi}{}^{\#}g\alpha$ –component of a soft set, locally $S_{\tilde{\tau}}S_{emi}{}^{\#}g\alpha$ –connected space, and totally $S_{\tilde{\tau}}S_{emi}{}^{\#}g\alpha$ –disconnected space. We investigate and study the properties and characterizations of these spaces in soft topological spaces.

Keywords: $S_{\tilde{\tau}}S_{emi}{}^{\#}g\alpha$ –closed set, $S_{\tilde{\tau}}S_{emi}{}^{\#}g\alpha$ –separated set, $S_{\tilde{\tau}}S_{emi}{}^{\#}g\alpha$ –connected space

I. Introduction

The real world is too complex for our immediate and direct understanding. We create ‘‘models’’ of reality that are simplifications of aspects of the real world. Unfortunately, these mathematical models are too complicated, and we cannot find the exact solutions. The uncertainty of data while modeling problems in engineering, physics, computer sciences, economics, social sciences, medical sciences, and many other diverse fields makes it unsuccessful to use the traditional classical methods. These may be due to the uncertainties of natural environmental phenomena, of human knowledge about the real world, or to the limitations of the means used to measure objects. For example, vagueness or uncertainty in the boundary between states or between urban and rural areas, or the exact growth rate of population in a country’s rural area, or making decisions in a machine-based environment using database information. Thus, classical set theory, which is based on the crisp and exact case, may not be fully suitable for handling such problems of uncertainty. There are several theories, for example, the theory of fuzzy sets, theory of intuitionistic fuzzy sets, theory of vague sets, theory of interval mathematics, and the theory of rough sets. These can be considered as tools for dealing with uncertainties, but all these theories have their own difficulties. The reason for these difficulties is, possibly, the inadequacy of the parametrization tool of the theory as it was mentioned by Molodtsov. He initiated the concept of soft set theory as a new mathematical tool that is free from the problems mentioned above. He presented the fundamental results of the new theory and successfully applied it to several directions such as smoothness of functions, game theory, operations research, Riemann-integration, Perron integration, theory of probability, etc. A soft set is a collection of approximate descriptions of an object. He also showed how soft set theory is free from the parametrization inadequacy syndrome of fuzzy set theory, rough set theory, probability theory, and game theory. Soft systems provide a very general framework with the involvement of parameters. Soft set theory has been applied in several directions. The researchers introduced the concept of soft sets to deal with uncertainty and to solve complicated problems in economics, engineering, sociology, and environment because of unsuccessful use of classical methods. The well-known theories that can be considered as mathematical tools for dealing with uncertainties and imperfect knowledge are theory of fuzzy sets, theory of vague sets, theory of interval

- Selection and peer-review under responsibility of the Organizing Committee of the Conference

mathematics, theory of intuitionists fuzzy sets, theory of rough sets and theory of probability. During recent years, soft set theory emerged as a best mathematical tool to deal with uncertainties, imprecision and vagueness. Many engineering, medical science, economics, environment problems have various uncertainties, and the soft set theory came up with the reasonable solutions to these problems. A soft set is a collection of approximate descriptions of objects. Some researchers have presented a systematic survey of the literature and the developments of Topological Spaces in soft set theory. They have also provided some applications of soft set theory in software engineering, innovation, medical diagnosis, data analysis, decision making etc. All these tools require the specification of some parameter to start with. The theory of soft sets gives a vital mathematical tool for handling uncertainties and vague concepts. Recently several researchers introduced the notion of soft topology and established that every soft topology induces a collection of topologies called the parametrized family of topologies induced by the soft topology. They discussed soft set-theoretical operations and gave an application of soft set theory to a decision-making problem. Several mathematicians published papers on applications of soft sets and soft topology. Soft sets and soft topology have applications in data mining, image processing, decision-making problems, spatial modeling, and neural patterns. Research works on soft set theory and its applications in various fields are progressing rapidly. Decision-making and topology have a long joint tradition since the modern statement of the classical Weierstrass extreme value theorem. It combines two topological concepts called continuity of a real-valued function and compactness of the domain (both with respect to a given topology). They represent a necessary and sufficient condition to guarantee the existence of the maximum and minimum values of the function. The success of the Mathematical Problems in Engineering technique was amplified by its adoption in fields like engineering sciences, computer sciences, and mathematical economics. This matter can be adopted in the version of soft setting by replacing the classical notions(compactness, function, and real numbers) by their soft counterparts (soft compactness, soft function, and soft real numbers). Some practical experiments in civil engineering require classification of the materials according to their characteristics (attribute set or parameter set E), which can be expressed using the concept of soft sets. We study the separation of them concerning the group of soft sets, which are constructed from the practical experiments. In this group of soft sets, we add the absolute and null soft sets to initiate a soft weak structure. The researchers in the communication engineering endeavor to select the best protocol to solve the noisy problems in wireless networks. They evaluate the performance of these protocols according to the proposed scenarios. The researchers in Soft Theory may plan with some engineers to propose some protocols using the appropriate soft structure to select the optimal protocol to solve the interference problems in wireless networks. The objective of this paper is to use $S_{ff}S_{emi}{}^{\#}g\alpha$ –open sets and $S_{ff}S_{emi}{}^{\#}g\alpha$ –closed sets to introduce the concepts of $S_{ff}S_{emi}{}^{\#}g\alpha$ –separated sets, $S_{ff}S_{emi}{}^{\#}g\alpha$ –connected space, $S_{ff}S_{emi}{}^{\#}g\alpha$ –disconnected space, $S_{ff}S_{emi}{}^{\#}g\alpha$ –component of a soft set, locally $S_{ff}S_{emi}{}^{\#}g\alpha$ –connected space, and totally $S_{ff}S_{emi}{}^{\#}g\alpha$ –disconnected space. We investigate and study the properties and characterizations of these in soft topological spaces.

II. Preliminaries

Definition 2.1. Let X be an initial universe set and E be a collection of all possible parameters with respect to X, where parameters are the characteristics or properties of objects in X. Let $P(X)$ denote the power set of X, and let A be a non-empty subset of E. A pair (F,A) is called a soft set over X, where F is a mapping given by $F:A\to P(X)$. In other words, a soft set over X is a parameterized family of subsets of the universe X. For $e\in A$, $F(e)$ may be considered as the set e–approximate elements of the soft set (F,A). Clearly, a soft set is not a set. For two soft sets (F,A) and (G,B) over the common universe X, we say that (F,A) is a soft subset of (G,B) if (i) $A\subseteq B$ and (ii) for all $e\in A$, $F(e)$ and $G(e)$ are identical approximations. We write $(F,A)\subseteq(G,B)$. (G,B) is said to be a soft superset of (F,A), if (F,A) is a soft subset of (G,B). Two soft sets (F,A) and (G,B) over a common universe X are said to be soft equal if (F,A) is a soft subset of (G,B) and (G,B) is a soft subset of (F,A).

Definition 2.2. The union of two soft sets of (F,A) and (G,B) over the common universe X is soft set $(H,C)=(F,A)\bigcup(G,B)$, where $C=A\bigcup B$, and $H(e)=F(e)$ if $e\in A-B$, $H(e)=G(e)$ if $e\in B-A$ and $H(e)=F(e)\bigcup G(e)$ if $e\in A\bigcap B$.

Definition 2.3. The Intersection (H,C) of two soft sets (F,A) and (G,B) over a common universe X denoted $(F,A)\bigcap(G,B)$ is defined as $C=A\bigcap B$ and $H(e)=F(e)\bigcap G(e)$ for all $e\in C$.

Definition 2.4. For a soft set (F,A) over the universe U, the relative complement of (F,A) is denoted by $(F,A)^C$ and is defined by $(F,A)^C=(F^C,A)$, where $F^C:A\to P(X)$ is a mapping defined by $F^C(e)=X-F(e)$ for all $e\in A$.

Definition 2.5. A soft set (F,E) over X is said to be (i) A null soft set, denoted by $\tilde{\phi}$, if $\forall$ $e\in E$, $F(e)=\phi$. (ii) An absolute soft set, denoted by $\tilde{X}$, if $\forall$ $e\in E$, $F(e)=X$.

Definition 2.6. Let $\tilde{\tau}$ be the collection of soft sets over X. Then $\tilde{\tau}$ is said to be a soft Topology on X if
(i) $\tilde{\phi}$, $\tilde{X}$ belong to $\tilde{\tau}$
(ii) The union of any number of soft sets in $\tilde{\tau}$ belongs to $\tilde{\tau}$
(iii) The intersection of any two soft sets belongs to $\tilde{\tau}$.
The triplet $(\tilde{X},\tilde{\tau},E)$ is called a soft topological space over X. The complement of a soft open set is called soft closed set over X.

Definition 2.7. Let $(\tilde{X},\tilde{\tau},E)$ be a soft topological space over X and (F,E) be a soft set over X. Then
(i) Soft interior of a soft set (F,E) denoted by $S_{ft}Int(F,E)$ is defined as the union of all soft open sets over X contained in (F,E).
(ii) Soft closure of a soft set (F,E) denoted by $S_{ft}Cl(F,E)$ is defined as the intersection of all soft closed super sets over X containing (F,E).

Definition 2.8. A S_{ft}-subset (F,A) of a S_{ft}-Top-Space $(\tilde{X},\tilde{\tau},E)$ is called a $S_{ft}\alpha$-closed set if $S_{ft}Cl\left[S_{ft}Int\left(S_{ft}Cl(F,A)\right)\right]\subseteq(F,A)$. The complement of a $S_{ft}\alpha$-closed set is called $S_{ft}\alpha$-open set.

Definition 2.9. A S_{ft}-subset (F,A) of a S_{ft}-Top-Space $(\tilde{X},\tilde{\tau},E)$ is called a $S_{ft}g$-closed set if $S_{ft}Cl(A,E)\subseteq(U,E)$ whenever $(F,A)\subseteq(U,E)$ and (U,E) is soft open in $(\tilde{X},\tilde{\tau},E)$.

Definition 2.10. A S_{ft}-subset (F,A) of a S_{ft}-Top-Space $(\tilde{X},\tilde{\tau},E)$ is called a $S_{ft}S_{emi}$-closed set if $S_{ft}Int\left[S_{ft}Cl(F,A)\right]\subseteq(F,A)$. The complement of a $S_{ft}S_{emi}$-closed set is called a $S_{ft}S_{emi}$-open set.

Definition 2.11. A S_{ft}-subset (F,A) of a S_{ft}-Top-Space $(\tilde{X},\tilde{\tau},E)$ is called a soft $S_{ft}g^{\#}\alpha$-closed set if $S_{ft}\alpha Cl(F,A)\subseteq(U,E)$, whenever $(F,A)\subseteq(U,E)$ and (U,E) is $S_{ft}g$-open in $(\tilde{X},\tilde{\tau},E)$. The complement of a $S_{ft}g^{\#}\alpha$-closed set is called a $S_{ft}g^{\#}\alpha$-open set.

Definition 2.12. A S_{ft} –subset (F,A) of a S_{ft} –Top –Space $(\tilde{X},\tilde{\tau},E)$ is called a soft $S_{ft}{}^{\#}g\alpha$ –closed set if $S_{ft}\alpha Cl(F,A)\subseteq(U,E)$, whenever $(F,A)\subseteq(U,E)$ and (U,E) is $S_{ft}g^{\#}\alpha$ –open in (X,τ,E). The complement of a $S_{ft}{}^{\#}g\alpha$ –closed set is called a $S_{ft}{}^{\#}g\alpha$ –open set.

Definition 2.13. A S_{ft} –subset (F,A) of a S_{ft} –Top –Space $(\tilde{X},\tilde{\tau},E)$ is called a soft $S_{ft}S_{emi}{}^{\#}g\alpha$ –closed set if $S_{ft}S_{emi}Cl(F,A)\subseteq(U,E)$, whenever $(F,A)\subseteq(U,E)$ and (U,E) is $S_{ft}{}^{\#}g\alpha$ –open in (X,τ,E). The complement of a $S_{ft}S_{emi}{}^{\#}g\alpha$ –closed set is called a $S_{ft}S_{emi}{}^{\#}g\alpha$ –open set in (X,τ,E).

Definition 2.14. Let $(\tilde{X},\tilde{\tau},E)$ be a soft topological space over X and (F,A) be a soft set over X. Then

(i) $S_{ft}S_{emi}{}^{\#}g\alpha$ –interior of a soft set (F,A) denoted by $S_{ft}S_{emi}{}^{\#}g\alpha$ –$Int(F,A)$ is defined as the union of all soft $S_{ft}S_{emi}{}^{\#}g\alpha$ –open sets over X contained in (F,A).

(ii) $S_{ft}S_{emi}{}^{\#}g\alpha$ –closure of a soft set (F,A) denoted by $S_{ft}S_{emi}{}^{\#}g\alpha$ –$Cl(F,A)$ is defined as the intersection of all soft $S_{ft}S_{emi}{}^{\#}g\alpha$ –closed sets over X containing (F,A).

Theorem 2.15. (i) Every S_{ft} –closed set in a soft topological space is $S_{ft}S_{emi}{}^{\#}g\alpha$ –closed set.

(ii) Every S_{ft} –open set in a S_{ft} –Top –Space is $S_{ft}S_{emi}{}^{\#}g\alpha$ –open set.

Theorem 2.16. Let (F,A) and (G,B) be two S_{ft} –subsets of a S_{ft} –Top –Space $(\tilde{X},\tilde{\tau},E)$. Then the following statements are true.

(i) (F,A) is $S_{ft}S_{emi}{}^{\#}g\alpha$ –open if and only if $S_{ft}S_{emi}{}^{\#}g\alpha$ –$Int(F,A)=(F,A)$.

(ii) $S_{ft}S_{emi}{}^{\#}g\alpha$ –$Int(F,A)$ is $S_{ft}S_{emi}{}^{\#}g\alpha$ –open.

(iii) (F,A) is $S_{ft}S_{emi}{}^{\#}g\alpha$ –closed if and only if $S_{ft}S_{emi}{}^{\#}g\alpha$ –$Cl(F,A)=(F,A)$.

(iv) $S_{ft}S_{emi}{}^{\#}g\alpha$ –$Cl(F,A)$ is $S_{ft}S_{emi}{}^{\#}g\alpha$ –closed..

(v) $S_{ft}S_{emi}{}^{\#}g\alpha$ –$Cl[(X,E)-(F,A)]-(X,E)$ –$S_{ft}S_{emi}{}^{\#}g\alpha$ –$Int(F,A)$.

(vi) $S_{ft}S_{emi}{}^{\#}g\alpha$ –$Int[(X,E)-(F,A)]=(X,E)-S_{ft}S_{emi}{}^{\#}g\alpha$ –$Cl(F,A)$.

(vii) If (F,A) is $S_{ft}S_{emi}{}^{\#}g\alpha$ –open in $(\tilde{X},\tilde{\tau},E)$ and (G,B) is S_{ft} –open in $(\tilde{X},\tilde{\tau},E)$, then $(F,A)\bigcap(G,B)$ is $S_{ft}S_{emi}{}^{\#}g\alpha$ –open in $(\tilde{X},\tilde{\tau},E)$.

$(viii)$ A point $x_{\alpha}\in S_{ft}S_{emi}{}^{\#}g\alpha$ –$Cl(F,A)$ if and only if every $S_{ft}S_{emi}{}^{\#}g\alpha$ –open set in $(\tilde{X},\tilde{\tau},E)$ containing x intersects (F,A).

(ix) Arbitrary intersection of $S_{ft}S_{emi}{}^{\#}g\alpha$ –closed sets in $(\tilde{X},\tilde{\tau},E)$ is S_{ft} –S_{emi} –$^{\#}g\alpha$ –closed in $(\tilde{X},\tilde{\tau},E)$.

(x) An arbitrary union of $S_{ft}S_{emi}{}^{\#}g\alpha$ –open sets in $(\tilde{X},\tilde{\tau},E)$ is $S_{ft}S_{emi}{}^{\#}g\alpha$ –open in $(X,\tilde{\tau},E)$.

Definition 2.17. A S_{ft} –*Top –Space* $(\tilde{X},\tilde{T},E)$ is said to be soft connected if there does not exist a pair F_A and G_B of nonempty, disjoint soft open subsets of $(\tilde{X},\tilde{T},E)$ such that $\tilde{X}=F_A\tilde{\bigcup}G_B$.

III. Soft $S_{emi}{}^{\#}g\alpha$ –Separated Sets

In this section, we will introduce and investigate the basic properties of $S_{ft}S_{emi}{}^{\#}g\alpha$ *–separated* sets.

Definition 3.1. Two non-null soft disjoint S_{ft} *–sets* F_E and G_E in a S_{ft} *–Top –Space* $\left(\tilde{X},\tilde{T},E\right)$ are called Soft Semi$^{\#}g\alpha$ *–separated* $\left(S_{ft}S_{emi}{}^{\#}g\alpha\text{ –separated}\right)$ sets if $G_E\tilde{\cap}\left[S_{ft}S_{emi}{}^{\#}g\alpha\text{ –}Cl\left(F_E\right)\right]=\left[S_{ft}S_{emi}{}^{\#}g\alpha\text{ –}Cl\left(G_E\right)\right]\tilde{\cap}F_E=\tilde{\phi}$

Definition 3.2. A Soft Semi$^{\#}g\alpha$ *–separation* $\left(S_{ft}S_{emi}{}^{\#}g\alpha\text{ –separation}\right)$ of a S_{ft} *–Top –Space* $\left(\tilde{X},\tilde{T},E\right)$ is a pair of $S_{ft}S_{emi}{}^{\#}g\alpha$ *–separated* sets such that $F_E\tilde{\cup}G_E=\tilde{X}$.

Definition 3.3. Let $\left(\tilde{X},\tilde{T},E\right)$ be a S_{ft} *–Top –Space.* A Soft Semi$^{\#}g\alpha$ *–connected* soft connected$\left(S_{ft}S_{emi}{}^{\#}g\alpha\text{ –connected}\right)$ set over X is a S_{ft} *–set* $F_E\tilde{\in}S_{ft}S\left(X\right)_E$ which does not have a $S_{ft}S_{emi}{}^{\#}g\alpha$ *–separation* in the soft relative topology induced on the soft subset F_E.

Proposition 3.4. Every $S_{ft}S_{emi}{}^{\#}g\alpha$ *–connected* set in a S_{ft} *–Top –Space* $\left(\tilde{X},\tilde{T},E\right)$ is a S_{ft} *–connected* set.

Proof. Let F_E be a $S_{ft}S_{emi}{}^{\#}g\alpha$ *–connected* set in a S_{ft} *–Top –Space* $\left(\tilde{X},\tilde{T},E\right)$. Then there does not exist a $S_{ft}S_{emi}{}^{\#}g\alpha$ *–separation* of F_E. Since every S_{ft} *–open* set is a $S_{ft}S_{emi}{}^{\#}g\alpha$ *–open* set, there does not exist a S_{ft} *–separation* of F_E. Hence, F_E is a S_{ft} *–connected* set in the S_{ft} *–Top –Space* $\left(\tilde{X},\tilde{T},E\right)$.

Theorem 3.5. Let $\left(\tilde{X},\tilde{T},E\right)$ be a S_{ft} *–Top –Space* and F_E be a $S_{ft}S_{emi}{}^{\#}g\alpha$ *–connected* set. Let G_A and H_B be $S_{ft}S_{emi}{}^{\#}g\alpha$ *–separated* sets. If $F_E\tilde{\subseteq}G_A\tilde{\cup}H_B$. Then either $F_E\tilde{\subseteq}G_A$ or $F_E\tilde{\subseteq}H_B$.

Proof. Let $\left(\tilde{X},\tilde{T},E\right)$ be a S_{ft} *–Top –Space* and $F_E\tilde{\in}S_{ft}S\left(X\right)_E$ be a $S_{ft}S_{emi}{}^{\#}g\alpha$ *–connected* set. Let G_A and H_B be $S_{ft}S_{emi}{}^{\#}g\alpha$ *–separated* sets such that $F_E\tilde{\subseteq}G_A\tilde{\cup}H_B$. We have to prove either $F_E\tilde{\subseteq}G_A$ or $F_E\tilde{\subseteq}H_B$. Suppose not. Then $F_E\tilde{\not\subset}G_A$ and $F_E\tilde{\not\subset}H_B$. Then, $K_E=G_A\tilde{\cap}F_E\neq\phi$ and $L_E=H_B\tilde{\cap}F_E\neq\phi$ and $F_E=K_E\tilde{\cup}L_E$. Since $K_E\tilde{\subseteq}G_A$ implies that $S_{ft}S_{emi}{}^{\#}g\alpha\text{ –}Cl\left(K_E\right)\tilde{\subseteq}S_{ft}S_{emi}{}^{\#}g\alpha\text{ –}Cl\left(G_A\right)$. Since G_A and H_B are $S_{ft}S_{emi}{}^{\#}g\alpha$ *–separated* sets, we have $\left[S_{ft}S_{emi}{}^{\#}g\alpha\text{ –}Cl\left(G_A\right)\right]\tilde{\cap}H_B=\tilde{\phi}$. Therefore, $\left[S_{ft}S_{emi}{}^{\#}g\alpha\text{ –}Cl\left(G_A\right)\right]\tilde{\cap}H_B=\left[S_{ft}S_{emi}{}^{\#}g\alpha\text{ –}Cl\left(K_E\right)\right]\tilde{\cap}H_B=\left[S_{ft}S_{emi}{}^{\#}g\alpha\text{ –}Cl\left(K_E\right)\right]\tilde{\cap}L_E=\tilde{\phi}$. Again $L_E\tilde{\subseteq}H_B$ implies $S_{ft}S_{emi}{}^{\#}g\alpha\text{ –}Cl\left(L_E\right)\tilde{\subseteq}S_{ft}S_{emi}{}^{\#}g\alpha\text{ –}Cl\left(H_B\right)$. Since G_A and H_B are $S_{ft}S_{emi}{}^{\#}g\alpha$ *–separted* sets, we have $G_A\tilde{\cap}\left[S_{ft}S_{emi}{}^{\#}g\alpha\text{ –}S_{ft}\left(H_B\right)\right]=\tilde{\phi}$. Therefore, $G_A\tilde{\cap}\left[S_{ft}S_{emi}{}^{\#}g\alpha\text{ –}Cl\left(H_B\right)\right]=G_A\tilde{\cap}\left[S_{ft}S_{emi}{}^{\#}g\alpha\text{ –}Cl\left(L_E\right)\right]=K_E\tilde{\cap}\left[S_{ft}S_{emi}{}^{\#}g\alpha\text{ –}Cl\left(L_E\right)\right]=\tilde{\phi}$. But $F_E=K_E\tilde{\cup}H_E$. Therefore, there exists a $S_{ft}S_{emi}{}^{\#}g\alpha$ *–separation* of F_E. Hence, F_E is not a $S_{ft}S_{emi}{}^{\#}g\alpha$ *–connected* set. This is a contradiction. Therefore, either $F_E\tilde{\subseteq}G_A$ or $F_E\tilde{\subseteq}H_B$.

Theorem 3.6. If F_E is $S_{ft}S_{emi}{}^{\#}g\alpha$ *–connected* set, then $S_{ft}S_{emi}{}^{\#}g\alpha\text{ –}Cl\left(F_E\right)$ is $S_{ft}S_{emi}{}^{\#}g\alpha$ *–connected* set.

Proof. Let F_E be $S_{\tilde{\pi}}S_{emi}{}^{\#}g\alpha$ *–connected* set in a $S_{\tilde{\pi}}$*–Top –Space* $\left(\tilde{X},\tilde{T},E\right)$. We have to prove that $S_{\tilde{\pi}}S_{emi}{}^{\#}g\alpha$ *–*$Cl\left(F_E\right)$ is a $S_{\tilde{\pi}}S_{emi}{}^{\#}g\alpha$ *–connected* set. Suppose not. Then there exists a $S_{\tilde{\pi}}S_{emi}{}^{\#}g\alpha$ *–separation* of $S_{\tilde{\pi}}S_{emi}{}^{\#}g\alpha$ *–*$Cl\left(F_E\right)$. Therefore there exists a pair of $S_{\tilde{\pi}}S_{emi}{}^{\#}g\alpha$ *–separated* sets G_A and H_B such that $\left[S_{\tilde{\pi}}S_{emi}{}^{\#}g\alpha\text{–}Cl\left(F_E\right)\right]=G_A\tilde{\cup}H_B$. But $F_E\subseteq S_{\tilde{\pi}}S_{emi}{}^{\#}g\alpha\text{–}Cl\left(F_E\right)=G_A\tilde{\cup}H_B$. Since F_E is $S_{\tilde{\pi}}S_{emi}{}^{\#}g\alpha$ *–connected* set, then by Theorem 3.5 either $F_E\tilde{\subseteq}G_A$ or $F_E\tilde{\subseteq}H_B$. If $F_E\tilde{\subseteq}G_A$ then $S_{\tilde{\pi}}S_{emi}{}^{\#}g\alpha\text{–}Cl\left(F_E\right)\tilde{\subseteq}S_{\tilde{\pi}}S_{emi}{}^{\#}g\alpha\text{–}Cl\left(G_A\right)$. Since $H_B\tilde{\subseteq}\ S_{\tilde{\pi}}S_{emi}{}^{\#}g\alpha\text{–}Cl\left(F_E\right)$, then $H_B=\tilde{\phi}$. This is a contradiction. Similarly, if $F_E\tilde{\subseteq}H_B$, we can prove $G_A=\tilde{\phi}$ which is a contradiction. Thus, there is not any $S_{\tilde{\pi}}S_{emi}{}^{\#}g\alpha$ *–separation* of $S_{\tilde{\pi}}S_{emi}{}^{\#}g\alpha\text{–}Cl\left(F_E\right)$. Hence $S_{\tilde{\pi}}S_{emi}{}^{\#}g\alpha\text{–}Cl\left(F_E\right)$ is $S_{\tilde{\pi}}S_{emi}{}^{\#}g\alpha$ *–connected* set.

Theorem 3.7. If F_E is $S_{\tilde{\pi}}S_{emi}{}^{\#}g\alpha$ *–connected* set and $F_E\tilde{\subseteq}G_E\tilde{\subseteq}S_{\tilde{\pi}}S_{emi}{}^{\#}g\alpha\text{–}Cl\left(F_E\right)$, then G_E is $S_{\tilde{\pi}}S_{emi}{}^{\#}g\alpha$ *–connected* set.

Proof. Let $F_E\tilde{\in}S_{\tilde{\pi}}S\left(X\right)_E$ be a $S_{\tilde{\pi}}S_{emi}{}^{\#}g\alpha$ *–connected* set such that $F_E\tilde{\subseteq}G_E\tilde{\subseteq}S_{\tilde{\pi}}S_{emi}{}^{\#}g\alpha\text{–}Cl\left(F_E\right)$. We have to prove that G_E is $S_{\tilde{\pi}}S_{emi}{}^{\#}g\alpha$ *–connected* set. Suppose G_E is not a $S_{\tilde{\pi}}S_{emi}{}^{\#}g\alpha$ *–connected* set. Then there exists a pair of $S_{\tilde{\pi}}S_{emi}{}^{\#}g\alpha$ *–separated* sets K_A and L_B such that $G_E=K_A\tilde{\cup}L_B$. Since $F_E\tilde{\subseteq}G_E$ and $F_E\tilde{\subseteq}K_A\tilde{\cup}L_B$. We claim that either $F_E\tilde{\subseteq}K_A$ or $F_E\tilde{\subseteq}L_B$. For, $F_E\tilde{\cap}K_A\neq\tilde{\phi}$ and $F_E\tilde{\cap}L_B\neq\tilde{\phi}$. Then $F_E=\left(F_E\tilde{\cap}K_A\right)\tilde{\cup}\left(F_E\tilde{\cap}L_B\right)$. But $F_E\tilde{\cap}K_A$ and $F_E\tilde{\cap}L_B$ are $S_{\tilde{\pi}}S_{emi}{}^{\#}g\alpha$ *–separated* sets. This is a contradiction to that $S_{\tilde{\pi}}S_{emi}{}^{\#}g\alpha$ *–connectivity* of F_E. Hence, our claim is proved that G_E is $S_{\tilde{\pi}}S_{emi}{}^{\#}g\alpha$ *–separated* set. Suppose $F_E\tilde{\subseteq}K_A$, then $S_{\tilde{\pi}}S_{emi}{}^{\#}g\alpha\text{–}Cl\left(F_E\right)\tilde{\subseteq}\ S_{\tilde{\pi}}S_{emi}{}^{\#}g\alpha\text{–}Cl\left(K_A\right)$. Since K_A and L_B are $S_{\tilde{\pi}}S_{emi}{}^{\#}g\alpha$ *–separated* sets. $\left[S_{\tilde{\pi}}S_{emi}{}^{\#}g\alpha\text{–}Cl\left(K_A\right)\right]\tilde{\cap}L_B=\tilde{\phi}$. Therefore, $\left[S_{\tilde{\pi}}S_{emi}{}^{\#}g\alpha\text{–}Cl\left(F_E\right)\right]\tilde{\cap}L_B=\tilde{\phi}$. But $L_B\tilde{\subseteq}G_E$. Then by hypothesis $L_B\tilde{\subseteq}G_E\tilde{\subseteq}S_{\tilde{\pi}}S_{emi}{}^{\#}g\alpha\text{–}Cl\left(F_E\right)$. Therefore, $\left[S_{\tilde{\pi}}S_{emi}{}^{\#}g\alpha\text{–}Cl\left(F_E\right)\right]\tilde{\cap}L_B=L_B$. Thus, we have $\left[S_{\tilde{\pi}}S_{emi}{}^{\#}g\alpha\text{–}Cl\left(F_E\right)\right]\tilde{\cap}L_B=\tilde{\phi}$ and $\left[S_{\tilde{\pi}}S_{emi}{}^{\#}g\alpha\text{–}Cl\left(F_E\right)\right]\tilde{\cap}L_B=L_B$. Hence $L_B=\tilde{\phi}$, which is a contradiction. Similarly, if $F_E\tilde{\subseteq}L_B$, then we can prove $K_A=\tilde{\phi}$. This is a contradiction. Therefore, there does not exist a $S_{\tilde{\pi}}S_{emi}{}^{\#}g\alpha$ *–separation* of G_E. Hence, G_E is a $S_{\tilde{\pi}}S_{emi}{}^{\#}g\alpha$ *–connected* set.

Theorem 3.8. The soft union F_E of any family $\left\{F_{E_j}:j\in J\right\}$ of $S_{\tilde{\pi}}S_{emi}{}^{\#}g\alpha$ *–connected* sets having a nonempty soft intersection is $S_{\tilde{\pi}}S_{emi}{}^{\#}g\alpha$ *–connected* set.

Proof. Suppose that $F_E=G_A\tilde{\cup}H_B$ where G_A and H_B form a $S_{\tilde{\pi}}S_{emi}{}^{\#}g\alpha$ *–separation* of F_E. By hypothesis, we may choose a soft point $x_e\tilde{\in}\bigcap_{j\in J}F_{E_j}$. Then $x_e\tilde{\in}F_{E_j}$ for all $j\in J$. If $x_e\tilde{\in}F_E$, then either $x_e\tilde{\in}G_A$ or $x_e\tilde{\in}H_B$ but not both. Since G_A and H_B are disjoint soft sets, we must have $F_{E_j}\tilde{\subseteq}G_A$, since F_{E_j} is $S_{\tilde{\pi}}S_{emi}{}^{\#}g\alpha$ *–connected* and it is true for all $j\in J$, and so $F_E\tilde{\subseteq}G_A$. From this, we obtain that $H_B=\tilde{\phi}$, which is a contradiction. Thus, there does not exist a $S_{\tilde{\pi}}S_{emi}{}^{\#}g\alpha$ *–separation* of F_E. Therefore, F_E is $S_{\tilde{\pi}}S_{emi}{}^{\#}g\alpha$ *–connected*.

IV. Soft $S_{emi}{}^{\#}g\alpha$ –Connected Space

In this section, we introduce the $S_{\tilde{\tau}}S_{emi}{}^{\#}g\alpha$ *–connected* space and discuss its properties in $S_{\tilde{\tau}}$ *–Top –Space.*

Definition 4.1. Let $\left(\tilde{X},\tilde{T},E\right)$ be a $S_{\tilde{\tau}}$ *–Top –Space.* If there does not exist a $S_{\tilde{\tau}}S_{emi}{}^{\#}g\alpha$ *–separation* of $\tilde{X}$, then it is said to be $S_{\tilde{\tau}}S_{emi}{}^{\#}g\alpha$ *–connected* space.

Proposition 4.2. Every $S_{\tilde{\tau}}S_{emi}{}^{\#}g\alpha$ *–connected* space $\left(\tilde{X},\tilde{T},E\right)$ is $S_{\tilde{\tau}}S_{emi}{}^{\#}g\alpha$ *–connected* space.

Proof. Let $\left(\tilde{X},\tilde{T},E\right)$ be a $S_{\tilde{\tau}}S_{emi}{}^{\#}g\alpha$ *–connected* space. Then there does not exist a $S_{\tilde{\tau}}S_{emi}{}^{\#}g\alpha$ *–separation* of $\tilde{X}$. Since every $S_{\tilde{\tau}}$ *–open* set is a $S_{\tilde{\tau}}{}^{\#}g\alpha$ *–open* set, there does not exist a $S_{\tilde{\tau}}$ *–separation* of $\tilde{X}$. Therefore, $\left(\tilde{X},\tilde{T},E\right)$ is a $S_{\tilde{\tau}}$ *–connected* space.

Theorem 4.3. Let $\left(\tilde{X},\tilde{T},E\right)$ be a $S_{\tilde{\tau}}$ *–Top –Space.* Then the following statements are equivalent:

(i) $\tilde{\phi}$ and $\tilde{X}$ are the only $S_{\tilde{\tau}}S_{emi}{}^{\#}g\alpha$ *–clopen* sets in $\left(\tilde{X},\tilde{T},E\right)$.

(ii) $\tilde{X}$ is not the soft union of two soft disjoint non-empty $S_{\tilde{\tau}}S_{emi}{}^{\#}g\alpha$ *–open* sets.

(iii) $\tilde{X}$ is not the soft union of two soft disjoint non-empty $S_{\tilde{\tau}}S_{emi}{}^{\#}g\alpha$ *–closed* sets.

(iv) $\tilde{X}$ is not the soft union of two $S_{\tilde{\tau}}S_{emi}{}^{\#}g\alpha$ *–separated* sets.

Proof. (i) $\Rightarrow$ (ii): Assume that $\tilde{\phi}$ and $\tilde{X}$ are the only $S_{\tilde{\tau}}S_{emi}{}^{\#}g\alpha$ *–clopen* sets in $\left(\tilde{X},\tilde{T},E\right)$. Suppose (ii) is false. Then $\tilde{X}=G_A\tilde{\bigcup}H_B$, where G_A and H_B are two soft disjoint, non-empty $S_{\tilde{\tau}}S_{emi}{}^{\#}g\alpha$ *–open* sets. Clearly $H_B=G_A^C$ is $S_{\tilde{\tau}}S_{emi}{}^{\#}g\alpha$ *–closed* and non-empty. Thus H_B is a non-empty proper $S_{\tilde{\tau}}S_{emi}{}^{\#}g\alpha$ *–clopen* set in $\tilde{X}$, which shows that (i) is false.

(ii) $\Rightarrow$ (iii): Assume that, $\tilde{X}$ is not the soft union of two soft disjoint non-empty $S_{\tilde{\tau}}S_{emi}{}^{\#}g\alpha$ *–open* sets. Suppose (iii) is false. Then $\tilde{X}=G_A\tilde{\bigcup}H_B$ where G_A and H_B are two soft disjoint non-empty $S_{\tilde{\tau}}S_{emi}{}^{\#}g\alpha$ *–closed* sets. Now G_A and H_B being respectively the soft complement of H_B and G_A. Therefore G_A and H_B are $S_{\tilde{\tau}}S_{emi}{}^{\#}g\alpha$ *–open* sets. This contradicts (ii).

(iii) $\Rightarrow$ (iv): Assume that $\tilde{X}$ is not the soft union of two soft disjoint non-empty $S_{\tilde{\tau}}S_{emi}{}^{\#}g\alpha$ *–closed* sets. If (iv) is false, then $\tilde{X}=G_A\tilde{\bigcup}H_B$, where G_A and H_B are $S_{\tilde{\tau}}S_{emi}{}^{\#}g\alpha$ *–separated* sets. Then $G_A\tilde{\bigcap}\left[S_{\tilde{\tau}}S_{emi}{}^{\#}g\alpha\text{–}Cl\left(H_B\right)\right]=\tilde{\phi}$ and this implies that $S_{\tilde{\tau}}S_{emi}{}^{\#}g\alpha\text{–}Cl\left(H_B\right)\tilde{\subseteq}H_B$. But $H_B\tilde{\subseteq}S_{\tilde{\tau}}S_{emi}{}^{\#}g\alpha\text{–}Cl\left(H_B\right)$. Therefore, $S_{\tilde{\tau}}S_{emi}{}^{\#}g\alpha\text{–}Cl\left(H_B\right)=H_B$ and hence H_B is a $S_{\tilde{\tau}}S_{emi}{}^{\#}g\alpha$ *–closed* set. Similarly, G_A is a $S_{\tilde{\tau}}S_{emi}{}^{\#}g\alpha$ *–closed* set, which is a contradiction to (iii). Therefor (iv) is true.

(iv) $\Rightarrow$ (i): Assume that $\tilde{X}$ is not the soft union of two $S_{\tilde{\tau}}S_{emi}{}^{\#}g\alpha$ *–separated* sets. Suppose (i) is false. Then there exists a non-empty proper $S_{\tilde{\tau}}S_{emi}{}^{\#}g\alpha$ *–clopen* subset H_A of $\tilde{X}$. Then $H_B=H_A^C$ is a non-empty, $S_{\tilde{\tau}}S_{emi}{}^{\#}g\alpha$ *–clopen* set and $\tilde{X}=G_A\tilde{\bigcup}H_B$, where G_A and H_B are non-empty disjoint

$S_{\tilde{\pi}}S_{emi}{}^{\#}g\alpha$ *–clopen* sets. Since G_A and H_B are $S_{\tilde{\pi}}S_{emi}{}^{\#}g\alpha$ *–clopen* sets, $S_{\tilde{\pi}}S_{emi}{}^{\#}g\alpha\text{–}Cl(G_A)=G_A$ and $S_{\tilde{\pi}}S_{emi}{}^{\#}g\alpha\text{–}Cl(H_B)=H_B$. Therefore, $S_{\tilde{\pi}}S_{emi}{}^{\#}g\alpha\text{–}Cl(G_A)\tilde{\cap}H_B=G_A\tilde{\cap}H_B=\tilde{\phi}=G_A\tilde{\cap}\left[S_{\tilde{\pi}}S_{emi}{}^{\#}g\alpha\text{–}Cl(H_B)\right]$. Thus $\tilde{X}$ is a soft union of $S_{\tilde{\pi}}S_{emi}{}^{\#}g\alpha$ *–separated* sets. This is a contradiction to (iv). Therefore (i) must be true.

Theorem 4.4. Let $(\tilde{X},\tilde{T},E)$ be a $S_{\tilde{\pi}}$ *–Top –Space* such that any two soft points x_α and y_β of $\tilde{X}$ are contained in some $S_{\tilde{\pi}}S_{emi}{}^{\#}g\alpha$ *–connected* subspace $\tilde{Y}$ of $\tilde{X}$. Then $\tilde{X}$ is $S_{\tilde{\pi}}S_{emi}{}^{\#}g\alpha$ *–connected* space.

Proof. Let $(\tilde{X},\tilde{T},E)$ be a $S_{\tilde{\pi}}$ *–Top –Space* and $(\tilde{Y},\tilde{T}_Y,E)$ be a $S_{\tilde{\pi}}S_{emi}{}^{\#}g\alpha$ *–connected* subspace of $\tilde{X}$. Let x_α, y_β be two disjoint soft points in $\tilde{X}$. Suppose that x_α and y_β in $\tilde{X}$ are contained in the $S_{\tilde{\pi}}S_{emi}{}^{\#}g\alpha$ *–connected* subspace $\tilde{Y}$ of $\tilde{X}$, we have to prove, $(\tilde{X},\tilde{T},E)$ is a $S_{\tilde{\pi}}S_{emi}{}^{\#}g\alpha$ *–connected* space. Suppose $(\tilde{X},\tilde{T},E)$ is not a $S_{\tilde{\pi}}S_{emi}{}^{\#}g\alpha$ *–connected* space. Then there exists a $S_{\tilde{\pi}}S_{emi}{}^{\#}g\alpha$ *–separation* in $\tilde{X}$. Therefore, there exists a pair of non-empty, soft disjoint $S_{\tilde{\pi}}S_{emi}{}^{\#}g\alpha$ *–separated* sets G_A and H_B. Since G_A and H_B are non-empty soft sets, there exist x_α and y_β such that $x_\alpha\tilde{\in}G_A$ and $y_\beta\tilde{\in}H_\beta$. Since $(\tilde{Y},\tilde{T}_Y,E)$ is a $S_{\tilde{\pi}}S_{emi}{}^{\#}g\alpha$ *–connected* soft subspace of $(\tilde{X},\tilde{T},E)$, which contains x_α and y_β, therefore by Theorem 3.5, either $\tilde{Y}\tilde{\subseteq}G_A$ or $\tilde{Y}\tilde{\subseteq}H_B$. But $G_A\tilde{\cap}H_B=\tilde{\phi}$, which is a contradiction. Therefore $(\tilde{X},\tilde{T},E)$ is $S_{\tilde{\pi}}S_{emi}{}^{\#}g\alpha$ *–connected* space.

Corollary 4.5. If a $S_{\tilde{\pi}}$ *–Top –Space* $(\tilde{X},\tilde{T},E)$ contains a $S_{\tilde{\pi}}S_{emi}{}^{\#}g\alpha$ *–connected* subspace $(\tilde{Y},\tilde{T}_Y,E)$ such that $S_{\tilde{\pi}}S_{emi}{}^{\#}g\alpha\text{–}Cl(\tilde{Y})=\tilde{X}$, then $\tilde{X}$ is $S_{\tilde{\pi}}S_{emi}{}^{\#}g\alpha$ *–connected* space.

Proof. Let $(\tilde{Y},\tilde{T}_Y,E)$ be a $S_{\tilde{\pi}}S_{emi}{}^{\#}g\alpha$ *–connected* subspace of $(\tilde{X},\tilde{T},E)$ such that $S_{\tilde{\pi}}S_{emi}{}^{\#}g\alpha\text{–}Cl(\tilde{Y})=\tilde{X}$. Since $(\tilde{Y},\tilde{T}_Y,E)$ is a $S_{\tilde{\pi}}S_{emi}{}^{\#}g\alpha$ *–connected* subspace, $\tilde{Y}$ is a $S_{\tilde{\pi}}S_{emi}{}^{\#}g\alpha$ *–connected* set. Then by Theorem 3.6, $S_{\tilde{\pi}}S_{emi}{}^{\#}g\alpha\text{–}Cl(\tilde{Y})$ is $S_{\tilde{\pi}}S_{emi}{}^{\#}g\alpha$ *–connected* set. Therefore, $\tilde{X}=S_{\tilde{\pi}}S_{emi}{}^{\#}g\alpha\text{–}Cl(\tilde{Y})$ is a $S_{\tilde{\pi}}S_{emi}{}^{\#}g\alpha$ *–connected* set. Hence $(\tilde{X},\tilde{T},E)$ is a $S_{\tilde{\pi}}S_{emi}{}^{\#}g\alpha$ *–connected* space.

Theorem 4.6. If $(\tilde{Y},\tilde{T}_Y,E)$ and $(\tilde{Z},\tilde{T}_Z,E)$ are $S_{\tilde{\pi}}S_{emi}{}^{\#}g\alpha$ *–connected* subspaces of a $S_{\tilde{\pi}}$ *–Top –Space* $(\tilde{X},\tilde{T},E)$ are such that $\tilde{Y}\tilde{\cap}\tilde{Z}\neq\tilde{\phi}$, then $\tilde{Y}\tilde{\cup}\tilde{Z}$ is $S_{\tilde{\pi}}S_{emi}{}^{\#}g\alpha$ *–connected* subspace.

Proof. Suppose $\tilde{Y}\tilde{\cup}\tilde{Z}$ is not $S_{\tilde{\pi}}S_{emi}{}^{\#}g\alpha$ *–connected* subspace, then there exists a $S_{\tilde{\pi}}S_{emi}{}^{\#}g\alpha$ *–separation* of $\tilde{Y}\tilde{\cup}\tilde{Z}$. Thus, there exists a pair of $S_{\tilde{\pi}}S_{emi}{}^{\#}g\alpha$ *–separated* sets G_A and H_B such that $G_A\tilde{\cup}H_B=\tilde{Y}\tilde{\cup}\tilde{Z}$. Since $\tilde{Y}\tilde{\subseteq}\tilde{Y}\tilde{\cup}\tilde{Z}=G_A\tilde{\cup}H_B$ and $\tilde{Y}$ is $S_{\tilde{\pi}}S_{emi}{}^{\#}g\alpha$ *–connected*, then by Theorem 3.5, either $\tilde{Y}\tilde{\subseteq}G_A$ or $\tilde{Y}\tilde{\subseteq}H_B$. Since $\tilde{Z}\tilde{\subseteq}\tilde{Y}\tilde{\cup}\tilde{Z}=G_A\tilde{\cup}H_B$ and $\tilde{Z}$ is $S_{\tilde{\pi}}S_{emi}{}^{\#}g\alpha$ *–connected*, then either $\tilde{Z}\tilde{\subseteq}G_A$ or $\tilde{Z}\tilde{\subseteq}H_B$.

(i) If $\tilde{Y}\tilde{\subseteq}G_A$ and $\tilde{Z}\tilde{\subseteq}G_A$, then $\tilde{Y}\tilde{\cup}\tilde{Z}\tilde{\subseteq}G_A$. Hence $H_B=\tilde{\phi}$. This is a contradiction.

(ii) If $\tilde{Y} \tilde{\subseteq} G_A$ and $\tilde{Z} \tilde{\subseteq} H_B$, then $\tilde{Y} \tilde{\cap} \tilde{Z} \tilde{\subseteq} G_A \tilde{\cap} H_B = \tilde{\phi}$, which is a contradiction to our assumption. In the same way, we can get a contradiction if $\tilde{Y} \tilde{\subseteq} H_B$ and $\tilde{Z} \tilde{\subseteq} G_A$ or if $\tilde{Y} \tilde{\subseteq} H_B$ and $\tilde{Z} \tilde{\subseteq} H_B$. Therefore $\tilde{Y} \tilde{\cup} \tilde{Z}$ is $S_{\#} S_{emi}{}^{\#} g\alpha$ *–connected* subspace of $\left(\tilde{X}, \tilde{T}, E\right)$.

Corollary 4.7. Let $\left(\tilde{X}, \tilde{T}_1, E\right)$ and $\left(\tilde{X}, \tilde{T}_2, E\right)$ be $S_{\#}$ *–Top –Spaces* such that $\tilde{T}_2 \tilde{\subseteq} \tilde{T}_1$ and $\left(\tilde{X}, \tilde{T}_1, E\right)$ is $S_{\#} S_{emi}{}^{\#} g\alpha$ *–connected* space. Then $\left(\tilde{X}, \tilde{T}_2, E\right)$ is a $S_{\#} S_{emi}{}^{\#} g\alpha$ *–connected* space.

Proof. Suppose $\left(\tilde{X}, \tilde{T}_2, E\right)$ is not $S_{\#} S_{emi}{}^{\#} g\alpha$ *–connected* space. Then there exists a $SS_{\#} S_{emi}{}^{\#} g\alpha$ *–separation* G_A and H_B of $S_{\#} S_{emi}{}^{\#} g\alpha$ *–separated* sets in $\tilde{X}$ with soft topology $\tilde{T}_2$. Since $\tilde{T}_2 \tilde{\subseteq} \tilde{T}_1$, G_A and H_B are $S_{\#} S_{emi}{}^{\#} g\alpha$ *–separated* set in $\tilde{X}$ with soft topology $\tilde{T}_1$. This is a contradiction. Hence, the result follows.

Proposition 4.8. Let $\left(\tilde{X}, \tilde{T}, E\right)$ be a $S_{\#}$ *–Top –Space* over X. Then the following statements are equivalent:

(1) $\left(\tilde{X}, \tilde{T}, E\right)$ is $S_{\#} S_{emi}{}^{\#} g\alpha$ *–connected*.

(2) There exists no $F_E, G_E \tilde{\in} S_{\#} S_{emi}{}^{\#} g\alpha - C\left(\tilde{X}, \tilde{T}, E\right) - \left\{\tilde{\phi}\right\}$ such that $F_E \tilde{\cap} G_E = \tilde{\phi}$ and $F_E \tilde{\cup} G_E = \tilde{X}$, where $S_{\#} S_{emi}{}^{\#} g\alpha - C\left(\tilde{X}, \tilde{T}, E\right) = \left\{F_E^C \tilde{\in} S_{\#} S_{emi}{}^{\#} g\alpha - O\left(\tilde{X}, \tilde{T}, E\right)\right\}$.

(3) There exists no $F_E, G_E \tilde{\in} S_{\#} S\left(X\right)_E - \left\{\tilde{\phi}\right\}$ such that $\left[F_E \tilde{\cap} S_{\#} S_{emi}{}^{\#} g\alpha - Cl\left(G_E\right)\right] \tilde{\cup} \left[S_{\#} S_{emi}{}^{\#} g\alpha - Cl\left(F_E\right) \tilde{\cap} G_E\right] = \tilde{\phi}$ and $F_E \cup G_E = \tilde{X}$.

(4) There exists no $F_E \tilde{\in} S_{\#} S\left(X\right)_E - \left\{\tilde{\phi}, \tilde{X}\right\}$ such that $F_E \tilde{\in} \left[S_{\#} S_{emi}{}^{\#} g\alpha - O\left(\tilde{X}, \tilde{T}, E\right)\right] \tilde{\cap} \left[S_{\#} S_{emi}{}^{\#} g\alpha - C\left(\tilde{X}, \tilde{T}, E\right)\right]$.

Proof. $(1) \Rightarrow (2)$. Assume there exist $F_E, G_E \tilde{\in} S_{\#} S_{emi}{}^{\#} g\alpha - C\left(\tilde{X}, \tilde{T}, E\right) - \left\{\tilde{\phi}\right\}$ such that $F_E \tilde{\cap} G_E = \tilde{\phi}$ and $F_E \tilde{\cup} G_E = \tilde{X}$. Then $\forall\ e \in E,\ F_E\left(e\right) \tilde{\cap} G_E\left(e\right) = \tilde{\phi}$ and $F_E\left(e\right) \tilde{\cup} G_E\left(e\right) = \tilde{X}$. Thus $\forall\ e \in E,\ F^C\left(e\right) = X - F\left(e\right) = G\left(e\right)$ and $G^C\left(e\right) = X - G\left(e\right) = F\left(e\right)$, which implies that $F_E^C = G_E \tilde{\in} S_{\#} S_{emi}{}^{\#} g\alpha - C\left(\tilde{X}, \tilde{T}, E\right) - \left\{\tilde{\phi}\right\}$ and $G_E^C = F_E \tilde{\in} S_{\#} S_{emi}{}^{\#} g\alpha - C\left(\tilde{X}, \tilde{T}, E\right) - \left\{\tilde{\phi}\right\}$. Then there exist $F_E, G_E \tilde{\in} S_{\#} S_{emi}{}^{\#} g\alpha - O\left(\tilde{X}, \tilde{T}, E\right) - \left\{\tilde{\phi}\right\}$ such that $F_E \tilde{\cap} G_E = \tilde{\phi}$ and $F_E \tilde{\cup} G_E = \tilde{X}$. However, $\left(\tilde{X}, \tilde{T}, E\right)$ is $S_{\#} S_{emi}{}^{\#} g\alpha$ *–connected*. This is a contradiction.

$(2) \Rightarrow (3)$. Assume there exist $F_E, G_E \tilde{\in} S_{\#} S\left(X\right)_E - \left\{\tilde{\phi}\right\}$ such that $\left[F_E \tilde{\cap} S_{\#} S_{emi}{}^{\#} g\alpha - Cl\left(G_E\right)\right] \cup \left[S_{\#} S_{emi}{}^{\#} g\alpha - Cl\left(F_E\right) \cap G_E\right] = \tilde{\phi}$ and $F_E \tilde{\cup} G_E = \tilde{X}$. Obviously, $F_E \tilde{\cap} G_E = \tilde{\phi}$. Now $S_{\#} S_{emi}{}^{\#} g\alpha - Cl\left(G_E\right) = S_{\#} S_{emi}{}^{\#} g\alpha - Cl\left(G_E\right) \tilde{\cap} \tilde{X} = S_{\#} S_{emi}{}^{\#} g\alpha - Cl\left(G_E\right) \tilde{\cap} \left(F_E \tilde{\cup} G_E\right) = \left[S_{\#} S_{emi}{}^{\#} g\alpha - Cl\left(G_E\right) \tilde{\cap} F_E\right] \tilde{\cup} \left[S_{\#} S_{emi}{}^{\#} g\alpha - Cl\left(G_E\right) \tilde{\cap} G_E\right] = G_E$, which implies that G_E is a $S_{\#} S_{emi}{}^{\#} g\alpha$ *–closed* set. By using the same methods, we can show that F_E is also a $S_{\#} S_{emi}{}^{\#} g\alpha$ *–closed* set. Hence there exist $F_E, G_E \tilde{\in} S_{\#} S_{emi}{}^{\#} g\alpha - C\left(\tilde{X}, \tilde{T}, E\right) - \left\{\tilde{\phi}\right\}$ such that $F_E \tilde{\cap} G_E = \tilde{\phi}$ and $F_E \tilde{\cup} G_E = \tilde{X}$. This is a contradiction. So (3) holds.

$(3)\Rightarrow(4)$. Assume there exists $F_E \tilde{\in}\left[\mathrm{S}_{\#}\mathrm{S}_{emi}{}^{\#}\mathrm{g}\alpha\text{-}O\left(\tilde{X},\tilde{T},E\right)\right]\tilde{\cap}\left[\mathrm{S}_{\#}\mathrm{S}_{emi}{}^{\#}\mathrm{g}\alpha\text{-}C\left(\tilde{X},\tilde{T},E\right)\right]-\left\{\tilde{\phi},\tilde{X}\right\}$. If we take $G_E = F_E^C$ then $F_E, G_E \tilde{\in}\left[\mathrm{S}_{\#}\mathrm{S}_{emi}{}^{\#}\mathrm{g}\alpha\text{-}O\left(\tilde{X},\tilde{T},E\right)\right]\tilde{\cap}\left[\mathrm{S}_{\#}\mathrm{S}_{emi}{}^{\#}\mathrm{g}\alpha\text{-}C\left(\tilde{X},\tilde{T},E\right)\right]-\left\{\tilde{\phi}\right\}\left(\tilde{\subseteq}\,\mathrm{S}_{\#}S(X)_E-\left\{\tilde{\phi}\right\}\right)$. Besides, we have $\left[F_E\,\tilde{\cap}\,\mathrm{S}_{\#}\mathrm{S}_{emi}{}^{\#}\mathrm{g}\alpha\text{-}Cl\left(G_E\right)\right]\tilde{\cup}\left[G_E\,\tilde{\cap}\,\mathrm{S}_{\#}\mathrm{S}_{emi}{}^{\#}\mathrm{g}\alpha\text{-}Cl\left(F_E\right)\right]=F_E\,\tilde{\cap}\,G_E=\tilde{\phi}$ and $F_E\,\tilde{\cup}\,G_E=\tilde{X}$. This is a contradiction, so (4) holds.

$(4)\Rightarrow(1)$. Assume $\left(\tilde{X},\tilde{T}_2,E\right)$ is not $\mathrm{S}_{\#}\mathrm{S}_{emi}{}^{\#}\mathrm{g}\alpha\text{-}connected$. Then there exist $F_E, G_E \tilde{\in}\,\mathrm{S}_{\#}\mathrm{S}_{emi}{}^{\#}\mathrm{g}\alpha\text{-}O\left(\tilde{X},\tilde{T},E\right)-\left\{\tilde{\phi}\right\}$ such that $F_E\,\tilde{\cap}\,G_E=\tilde{\phi}$ and $F_E\,\tilde{\cup}\,G_E=\tilde{X}$. It is easy to see that $F_E^C=G_E$ and $G_E^C=F_E$. Thus $\mathrm{F}_E, G_E \tilde{\in}\left[\mathrm{S}_{\#}\mathrm{S}_{emi}{}^{\#}\mathrm{g}\alpha\text{-}O\left(\tilde{X},\tilde{T},E\right)\right]\tilde{\cap}\left[\mathrm{S}_{\#}\mathrm{S}_{emi}{}^{\#}\mathrm{g}\alpha\text{-}C\left(\tilde{X},\tilde{T},E\right)\right]-\left\{\tilde{\phi},\tilde{X}\right\}$. This is a contradiction.

Theorem 4.9. A non-null proper subset F_E of a $\mathrm{S}_{\#}\mathrm{S}_{emi}{}^{\#}\mathrm{g}\alpha\text{-}connected$ space $\left(\tilde{X},\tilde{T},E\right)$ has a non-null $\mathrm{S}_{\#}\mathrm{S}_{emi}{}^{\#}\mathrm{g}\alpha\text{-}boundary$ points.

Proof. Suppose, by contrary, that $\mathrm{S}_{\#}\mathrm{S}_{emi}{}^{\#}\mathrm{g}\alpha\text{-}Bd\left(F_E\right)=\tilde{\phi}$. Then $\mathrm{S}_{\#}\mathrm{S}_{emi}{}^{\#}\mathrm{g}\alpha\text{-}Cl\left(F_E\right)=\mathrm{S}_{\#}\mathrm{S}_{emi}{}^{\#}\mathrm{g}\alpha\text{-}Int\left(F_E\right)$, which means that F_E is both $\mathrm{S}_{\#}\mathrm{S}_{emi}{}^{\#}\mathrm{g}\alpha\text{-}open$ and $\mathrm{S}_{\#}\mathrm{S}_{emi}{}^{\#}\mathrm{g}\alpha\text{-}closed$. But this contradicts the $\mathrm{S}_{\#}\mathrm{S}_{emi}{}^{\#}\mathrm{g}\alpha\text{-}connectedness$ of $\left(\tilde{X},\tilde{T},E\right)$. Hence, $\mathrm{S}_{\#}\mathrm{S}_{emi}{}^{\#}\mathrm{g}\alpha\text{-}Bd\left(F_E\right)\neq\tilde{\phi}$, as required.

Definition 4.10. A soft mapping $f:\left(\tilde{X},\tilde{\tau},E\right)\to\left(\tilde{Y},\tilde{\sigma},K\right)$ is said to be $\mathrm{S}_{\#}\mathrm{S}_{emi}{}^{\#}\mathrm{g}\alpha\text{-}continuous$ $\left(\mathrm{resp.,}\mathrm{S}_{\#}\mathrm{S}_{emi}{}^{\#}\mathrm{g}\alpha\text{-}irresolute\right)$ if $f^{-1}\left(H_K\right)$ is a $\mathrm{S}_{\#}\mathrm{S}_{emi}{}^{\#}\mathrm{g}\alpha\text{-}open$ set where H_K is a soft open $\left(\mathrm{S}_{\#}\mathrm{S}_{emi}{}^{\#}\mathrm{g}\alpha\text{-}open\right)$ set.

Proposition 4.11. Let f be a $\mathrm{S}_{\#}\mathrm{S}_{emi}{}^{\#}\mathrm{g}\alpha\text{-}continuous$ mapping of a $\mathrm{S}_{\#}\mathrm{S}_{emi}{}^{\#}\mathrm{g}\alpha\text{-}connected$ space $\left(\tilde{X},\tilde{T},E\right)$ onto a $\mathrm{S}_{\#}\text{-}Top\text{-}Space$ $\left(\tilde{Y},\tilde{\sigma},K\right)$. Then $f\left(\tilde{X}\right)$ is *connected*.

Proof. Suppose that $f\left(\tilde{X}\right)=\tilde{Y}$ is *disconnected*. Then we get $\tilde{\sigma}$ contains two non-null disjoint soft open sets F_K and G_K. By hypothesis, $f^{-1}\left(F_K\right)$ and $f^{-1}\left(G_K\right)$ are disjoint $\mathrm{S}_{\#}\mathrm{S}_{emi}{}^{\#}\mathrm{g}\alpha\text{-}open$ sets in $\left(\tilde{X},\tilde{T},E\right)$. Since f is surjective, these $\mathrm{S}_{\#}\mathrm{S}_{emi}{}^{\#}\mathrm{g}\alpha\text{-}open$ sets are non-null. Thus $\left(\tilde{X},\tilde{T},E\right)$ is $\mathrm{S}_{\#}\mathrm{S}_{emi}{}^{\#}\mathrm{g}\alpha\text{-}disconnected$. But this is a contradiction. Hence, $\left(\tilde{Y},\tilde{\sigma},K\right)$ is $\mathrm{S}_{\#}\mathrm{S}_{emi}{}^{\#}\mathrm{g}\alpha\text{-}connected$.

Theorem 4.12. Let f be a $\mathrm{S}_{\#}\mathrm{S}_{emi}{}^{\#}\mathrm{g}\alpha-$ function from a $\mathrm{S}_{\#}\text{-}Top\text{-}Space$ $\left(\tilde{X},\tilde{T},E\right)$ onto a soft space $\left(\tilde{Y},\tilde{\sigma},K\right)$. Suppose $\left(\tilde{X},\tilde{T},E\right)$ is $\mathrm{S}_{\#}\mathrm{S}_{emi}{}^{\#}\mathrm{g}\alpha\text{-}connected$. Then $\left(\tilde{Y},\tilde{\sigma},K\right)$ is $\mathrm{S}_{\#}\mathrm{S}_{emi}{}^{\#}\mathrm{g}\alpha\text{-}connected$.

Proof. Our assumption is that $\left(\tilde{Y},\tilde{\sigma},K\right)$ is not $\mathrm{S}_{\#}\mathrm{S}_{emi}{}^{\#}\mathrm{g}\alpha\text{-}connected$. Therefore, there exists a non-empty proper subset H_K of $\left(\tilde{Y},\tilde{\sigma},K\right)$ which is both $\mathrm{S}_{\#}\mathrm{S}_{emi}{}^{\#}\mathrm{g}\alpha\text{-}open$ and $\mathrm{S}_{\#}\mathrm{S}_{emi}{}^{\#}\mathrm{g}\alpha\text{-}closed$. Then the

inverse image of H_K under f is both $S_{\tilde{\tau}}S_{emi}{}^{\#}g\alpha$ *–open* and $S_{\tilde{\tau}}S_{emi}{}^{\#}g\alpha$ *–closed* in $\left(\tilde{X},\tilde{T},E\right)$, which contradicts our hypothesis.

Corollary 4.13. A $S_{\tilde{\tau}}S_{emi}{}^{\#}g\alpha$ *–irresolute* function maps $S_{\tilde{\tau}}S_{emi}{}^{\#}g\alpha$ *–connected* set onto $S_{\tilde{\tau}}S_{emi}{}^{\#}g\alpha$ *–connected* set.

Theorem 4.14. Consider a $S_{\tilde{\tau}}S_{emi}{}^{\#}g\alpha$ *–continuous* function f from a $S_{\tilde{\tau}}$ *–Top –Space* $\left(\tilde{X},\tilde{T},E\right)$ onto a $S_{\tilde{\tau}}$ *–Top –Space* $\left(\tilde{Y},\tilde{\sigma},K\right)$. If $\left(\tilde{X},\tilde{T},E\right)$ is $S_{\tilde{\tau}}S_{emi}{}^{\#}g\alpha$ *–connected*, then $\left(\tilde{Y},\tilde{\sigma},K\right)$ is soft connected.

Proof. Consider $\left(\tilde{Y},\tilde{\sigma},K\right)$ is not soft connected. Then there is a nonempty proper subset of $\left(\tilde{Y},\tilde{\sigma},K\right)$ which is both soft open and soft closed. Then the inverse image of H_K under f is both $S_{\tilde{\tau}}S_{emi}{}^{\#}g\alpha$ *–open* and $S_{\tilde{\tau}}S_{emi}{}^{\#}g\alpha$ *–closed* in $\left(\tilde{X},\tilde{T},E\right)$, a contradiction. Though the concept of soft continuity, $S_{\tilde{\tau}}g^{**}$*–continuity* and $S_{\tilde{\tau}}S_{emi}{}^{\#}g\alpha$ *–irresolute* are independent of each other, but they behave similarly in the case of $S_{\tilde{\tau}}S_{emi}{}^{\#}g\alpha$ *–connectedness*, that is, these functions map a $S_{\tilde{\tau}}S_{emi}{}^{\#}g\alpha$ *–connected* set onto a soft connected set.

Definition 4.15. A soft function $f:\left(\tilde{X},\tilde{\tau},E\right)\to\left(\tilde{Y},\tilde{\sigma},K\right)$ is called $S_{\tilde{\tau}}S_{emi}{}^{\#}g\alpha$ *–homeomorphism* if f is both $S_{\tilde{\tau}}S_{emi}{}^{\#}g\alpha$ *–continuous* and $S_{\tilde{\tau}}S_{emi}{}^{\#}g\alpha$ *–open*.

Remark 4.16. A soft-homeomorphism preserves $S_{\tilde{\tau}}S_{emi}{}^{\#}g\alpha$ *–connectedness*.

Theorem 4.17. If $\left(\tilde{X},\tilde{T},E\right)$ is $S_{\tilde{\tau}}S_{emi}{}^{\#}g\alpha$ *–connected* space, then $\left(\tilde{X},\tilde{T},E\right)\times\{a\}$ is also $S_{\tilde{\tau}}S_{emi}{}^{\#}g\alpha$ *–connected*.

Proof. Obviously, $\left(\tilde{X},\tilde{T},E\right)$ is soft homeomorphic to $\left(\tilde{X},\tilde{T},E\right)\times\{a\}$. Then by the previous remark, $\left(\tilde{X},\tilde{T},E\right)\times\{a\}$ is $S_{\tilde{\tau}}S_{emi}{}^{\#}g\alpha$ *–connected*.

Theorem 4.18. If $\left(\tilde{X},\tilde{T},E\right)$ and $\left(\tilde{Y},\tilde{\sigma},K\right)$ are two $S_{\tilde{\tau}}S_{emi}{}^{\#}g\alpha$ *–connected* spaces, then $\left(\tilde{X},\tilde{T},E\right)\times\left(\tilde{Y},\tilde{\sigma},K\right)$ is also $S_{\tilde{\tau}}S_{emi}{}^{\#}g\alpha$ *–connected*.

Proof. For any soft point $\left(x_\alpha,y_\beta\right)$ in the product $\left(\tilde{X},\tilde{T},E\right)\times\left(\tilde{Y},\tilde{\sigma},K\right)$, each of the subspaces $\left(\tilde{X},\tilde{T},E\right)\times\{y_\beta\}\tilde{\cup}\left(\tilde{Y},\tilde{\sigma},K\right)\times\{x_\alpha\}$ is $S_{\tilde{\tau}}S_{emi}{}^{\#}g\alpha$ *–connected* since it is the union of two $S_{\tilde{\tau}}S_{emi}{}^{\#}g\alpha$ *–connected* subspaces with a point in common. Then by Theorem 4.6, $\left(\tilde{X},\tilde{T},E\right)\times\left(\tilde{Y},\tilde{\sigma},K\right)$ is also $S_{\tilde{\tau}}S_{emi}{}^{\#}g\alpha$ *–connected*.

V. Soft $S_{emi}{}^{\#}g\alpha$ –Disconnected Space

In this section, we present a new concept of $S_{\tilde{\tau}}S_{emi}{}^{\#}g\alpha$ *–disconnected* space and discuss some of its properties.

Definition 5.1. A $S_{\tilde{\mu}}$ *–Top –Space* $\left(\tilde{X},\tilde{T},E\right)$ is said to be a $SoftSemi^{\#}g\alpha$ *–disconnected* $\left(S_{\tilde{\mu}}S_{emi}{}^{\#}g\alpha\right.$ *–disconnected* $\left.\right)$ space if there exists a $S_{\tilde{\mu}}S_{emi}{}^{\#}g\alpha$ *–separation* of $\tilde{X}$.

Theorem 5.2. A $S_{\tilde{\mu}}$ *–Top –Space* $\left(\tilde{X},\tilde{T},E\right)$ is $S_{\tilde{\mu}}S_{emi}{}^{\#}g\alpha$ *–disconnected* if and only if there exists a non-empty proper soft subset of $\tilde{X}$ which is both $S_{\tilde{\mu}}S_{emi}{}^{\#}g\alpha$ *–open* and $S_{\tilde{\mu}}S_{emi}{}^{\#}g\alpha$ *–closed*.

Proof. Let $\left(\tilde{X},\tilde{T},E\right)$ be a $S_{\tilde{\mu}}$ *–Top –Space* and F_E be a non-empty proper soft subset which is both $S_{\tilde{\mu}}S_{emi}{}^{\#}g\alpha$ *–open* and $S_{\tilde{\mu}}S_{emi}{}^{\#}g\alpha$ *–closed* set. Since F_E is $S_{\tilde{\mu}}S_{emi}{}^{\#}g\alpha$ *–closed*, $S_{\tilde{\mu}}S_{emi}{}^{\#}g\alpha$ *–*$Cl\left(F_E\right)=F_E...(*)$. Also, F_E is $S_{\tilde{\mu}}S_{emi}{}^{\#}g\alpha$ *–open* implies $F_E^C=G_E$ (say) is $S_{\tilde{\mu}}S_{emi}{}^{\#}g\alpha$ *–closed*. Therefore, $S_{\tilde{\mu}}S_{emi}{}^{\#}g\alpha$ *–*$Cl\left(G_E\right)=G_E...(**)$. Since G_E is the soft complement of F_E in $\tilde{X}$, therefore $F_E\tilde{\bigcup}G_E=\tilde{X}$ and $F_E\tilde{\bigcap}G_E=\tilde{\phi}$. Now $F_E\tilde{\bigcap}G_E=\tilde{\phi}$ implies that $\left[S_{\tilde{\mu}}S_{emi}{}^{\#}g\alpha\text{ –}Cl\left(F_E\right)\right]\tilde{\bigcap}G_E=\tilde{\phi}$ *by* $(*)$ and $F_E\tilde{\bigcap}\left[S_{\tilde{\mu}}S_{emi}{}^{\#}g\alpha\text{ –}Cl\left(G_E\right)\right]=\tilde{\phi}$ *by* $(**)$. Since $\tilde{X}=G_E\tilde{\bigcup}G_E$ and $\left[S_{\tilde{\mu}}S_{emi}{}^{\#}g\alpha\text{ –}Cl\left(F_E\right)\right]\tilde{\bigcap}G_E=\tilde{\phi}$, $F_E\tilde{\bigcap}\left[S_{\tilde{\mu}}S_{emi}{}^{\#}g\alpha\text{ –}Cl\left(G_E\right)\right]=\tilde{\phi}$, therefore $\tilde{X}$ is $S_{\tilde{\mu}}S_{emi}{}^{\#}g\alpha$ *–disconnected*. Therefore, we conclude that $\left(\tilde{X},\tilde{T},E\right)$ is $S_{\tilde{\mu}}S_{emi}{}^{\#}g\alpha$ *–disconnected*. Conversely, suppose that $S_{\tilde{\mu}}$ *–Top –Space* $\left(\tilde{X},\tilde{T},E\right)$ is $S_{\tilde{\mu}}S_{emi}{}^{\#}g\alpha$ *–disconnected* space. Therefore, there exists a pair of non-empty proper soft subsets of $\tilde{X}$ such that $\tilde{X}=G_A\tilde{\bigcup}H_B$, $S_{\tilde{\mu}}S_{emi}{}^{\#}g\alpha$ *–*$Cl\left(G_A\right)\tilde{\bigcap}H_B=\tilde{\phi}$, $G_A\tilde{\bigcap}S_{\tilde{\mu}}S_{emi}{}^{\#}g\alpha$ *–*$Cl\left(H_B\right)=\tilde{\phi}$. Hence, we conclude that the $S_{\tilde{\mu}}$ *–Top –Space* $\left(\tilde{X},\tilde{T},E\right)$ is $S_{\tilde{\mu}}S_{emi}{}^{\#}g\alpha$ *–disconnected* space. Now $G_A\tilde{\subseteq}S_{\tilde{\mu}}S_{emi}{}^{\#}g\alpha$ *–*$Cl\left(G_A\right)$. Therefore, $\left[S_{\tilde{\mu}}S_{emi}{}^{\#}g\alpha\text{ –}Cl\left(G_A\right)\right]\tilde{\bigcap}H_B=\tilde{\phi}$ implies that $G_A\tilde{\bigcap}H_B=\tilde{\phi}$. Also $\tilde{X}=G_A\tilde{\bigcup}H_B$. Therefore, $G_A=H_B^C$. Thus, G_A is a proper soft subset of $\tilde{X}$ which is non-empty. Again, therefore $G_A\tilde{\bigcup}H_B=\tilde{X}$ implies $G_A\tilde{\bigcup}\left[S_{\tilde{\mu}}S_{emi}{}^{\#}g\alpha\text{ –}Cl\left(H_B\right)\right]=\tilde{X}$ and $H_B\tilde{\subseteq}\left[S_{\tilde{\mu}}S_{emi}{}^{\#}g\alpha\text{ –}Cl\left(H_B\right)\right]$. We have $G_A\tilde{\bigcap}H_B=\tilde{\phi}$ implies $G_A\tilde{\bigcap}\left[S_{\tilde{\mu}}S_{emi}{}^{\#}g\alpha\text{ –}Cl\left(H_B\right)\right]=\tilde{\phi}$. We conclude that $G_A=\tilde{X}-\left[S_{\tilde{\mu}}S_{emi}{}^{\#}g\alpha\text{ –}Cl\left(H_B\right)\right]$. But as H_B is $S_{\tilde{\mu}}S_{emi}{}^{\#}g\alpha$ *–closed* set. Therefore $G_A=\tilde{X}-\left[S_{\tilde{\mu}}S_{emi}{}^{\#}g\alpha\text{ –}Cl\left(H_B\right)\right]$ is $S_{\tilde{\mu}}S_{emi}{}^{\#}g\alpha$ *–open set*$...(***)$. Similarly, we can prove $H_B=\tilde{X}-\left[S_{\tilde{\mu}}S_{emi}{}^{\#}g\alpha\text{ –}Cl\left(G_A\right)\right]$ is $S_{\tilde{\mu}}S_{emi}{}^{\#}g\alpha$ *–open* set. Now $G_A=H_B^C$, where H_B is $S_{\tilde{\mu}}S_{emi}{}^{\#}g\alpha$ *–open* set. Therefore, G_A is $S_{\tilde{\mu}}S_{emi}{}^{\#}g\alpha$ *–closed* and we have already shown in $(***)$ that G_A is $S_{\tilde{\mu}}S_{emi}{}^{\#}g\alpha$ *–open*. Hence, G_A is a non-empty proper soft subset which is both $S_{\tilde{\mu}}S_{emi}{}^{\#}g\alpha$ *–open* and $S_{\tilde{\mu}}S_{emi}{}^{\#}g\alpha$ *–closed* set.

Theorem 5.3. A $S_{\tilde{\mu}}$ *–Top –Space* $\left(\tilde{X},\tilde{T},E\right)$ is $S_{\tilde{\mu}}S_{emi}{}^{\#}g\alpha$ *–disconnected* space if and only if any one of the following statements holds good.

(i) $\tilde{X}$ is the soft union of two non-empty disjoint $S_{\tilde{\mu}}S_{emi}{}^{\#}g\alpha$ *–open* sets.

(ii) $\tilde{X}$ is the soft union of two non-empty disjoint $S_{\tilde{\mu}}S_{emi}{}^{\#}g\alpha$ *–closed* sets.

Proof. Let $\left(\tilde{X},\tilde{T},E\right)$ be a $S_{\tilde{\mu}}S_{emi}{}^{\#}g\alpha$ *–disconnected* space. We have to prove $\tilde{X}$ is the soft union of two non-empty disjoint $S_{\tilde{\mu}}S_{emi}{}^{\#}g\alpha$ *–open* $\left(S_{\tilde{\mu}}S_{emi}{}^{\#}g\alpha\right.$ *–closed* $\left.\right)$ subsets of $\tilde{X}$. Since $\left(\tilde{X},\tilde{T},E\right)$ is a $S_{\tilde{\mu}}S_{emi}{}^{\#}g\alpha$ *–disconnected* space, then by Theorem 5.2, there exists a non-empty proper soft subset F_E of

$\tilde{X}$ which is both $S_{\tilde{\pi}}S_{emi}{}^{\#}g\alpha$ *–open* and $S_{\tilde{\pi}}S_{emi}{}^{\#}g\alpha$ *–closed*. Consequently, F_E^C is non-empty, which is both $S_{\tilde{\pi}}S_{emi}{}^{\#}g\alpha$ *–closed* and $S_{\tilde{\pi}}S_{emi}{}^{\#}g\alpha$ *–open*. Also, $F_E \tilde{\bigcup} F_E^C = \tilde{X}$ and $F_E \tilde{\bigcap} F_E^C = \tilde{\phi}$. From above, we conclude that $\tilde{X}$ is the soft union of two disjoint non-empty $S_{\tilde{\pi}}S_{emi}{}^{\#}g\alpha$ *–open* $\left(S_{\tilde{\pi}}S_{emi}{}^{\#}g\alpha \text{ –closed}\right)$ sets. As F_E and F_E^C are both $S_{\tilde{\pi}}S_{emi}{}^{\#}g\alpha$ *–open* as well as $S_{\tilde{\pi}}S_{emi}{}^{\#}g\alpha$ *–closed*. Conversely suppose, $\tilde{X}$ is the soft union of two non-empty disjoint $S_{\tilde{\pi}}S_{emi}{}^{\#}g\alpha$ *–open* sets. That is $\tilde{X} = G_A \tilde{\bigcup} H_B$ and $G_A \tilde{\bigcap} H_B = \tilde{\phi}$. We need to prove $\left(\tilde{X}, \tilde{T}, E\right)$ is a $S_{\tilde{\pi}}S_{emi}{}^{\#}g\alpha$ *–disconnected* space. Since $G_A = H_B^C$ is $S_{\tilde{\pi}}S_{emi}{}^{\#}g\alpha$ *–open* so that G_A is $S_{\tilde{\pi}}S_{emi}{}^{\#}g\alpha$ *–closed* set. Also, H_B is non-empty. Therefore $G_A = H_B^C$ is a proper soft subset of $\tilde{X}$ which is non-empty and is both $S_{\tilde{\pi}}S_{emi}{}^{\#}g\alpha$ *–open* and $S_{\tilde{\pi}}S_{emi}{}^{\#}g\alpha$ *–closed* set. Hence, by Theorem 5.2, the $S_{\tilde{\pi}}$ *–Top –Space* $\tilde{X}$ is $S_{\tilde{\pi}}S_{emi}{}^{\#}g\alpha$ *–disconnected* space. In the second case, if both G_A and H_B are both non-empty $S_{\tilde{\pi}}S_{emi}{}^{\#}g\alpha$ *–closed* sets, then $G_A = H_B^C$ and H_B is $S_{\tilde{\pi}}S_{emi}{}^{\#}g\alpha$ *–closed* set. Therefore, G_A is $S_{\tilde{\pi}}S_{emi}{}^{\#}g\alpha$ *–open* set. As above G_A will be a proper non-empty soft subset that is both $S_{\tilde{\pi}}S_{emi}{}^{\#}g\alpha$ *–open* and $S_{\tilde{\pi}}S_{emi}{}^{\#}g\alpha$ *–closed* set. Hence, by Theorem 5.2, the $S_{\tilde{\pi}}$ *–Top –Space* $\left(\tilde{X}, \tilde{T}, E\right)$ is $S_{\tilde{\pi}}S_{emi}{}^{\#}g\alpha$ *–disconnected* space.

VI. Soft $S_{emi}{}^{\#}g\alpha$ –Component of a Soft Set and Soft Topological Space

In this section, we introduce the concept of $S_{\tilde{\pi}}S_{emi}{}^{\#}g\alpha$ *–component* of a soft subset as well as $S_{\tilde{\pi}}S_{emi}{}^{\#}g\alpha$ *–component* of a $S_{\tilde{\pi}}$ *–Top –Space* and discuss their properties and characterizations.

Definition 6.1. Let F_E be a soft subset of a $S_{\tilde{\pi}}$ *–Top –Space* $\left(\tilde{X}, \tilde{T}, E\right)$ and x_e be any soft point of F_E, then the soft union of all $S_{\tilde{\pi}}S_{emi}{}^{\#}g\alpha$ *–connected* subsets of F_E containing x_e is defined as the $S_{\tilde{\pi}}S_{emi}{}^{\#}g\alpha$ *–component* of F_E with respect to x_e and is denoted by $S_{\tilde{\pi}}S_{emi}{}^{\#}g\alpha - C\left(F_E, x_e\right)$.

$S_{\tilde{\pi}}S_{emi}{}^{\#}g\alpha - C\left(F_E, x_e\right) = \tilde{\bigcup}\left\{P_E \tilde{\subseteq} F_E : x_e \tilde{\in} P_E, P_E \text{ is } S_{\tilde{\pi}}S_{emi}{}^{\#}g\alpha \text{ –connected set}\right\}$.

Proposition 6.2. $S_{\tilde{\pi}}S_{emi}{}^{\#}g\alpha - C\left(F_E, x_e\right)$ is a $S_{\tilde{\pi}}S_{emi}{}^{\#}g\alpha$ *–connected* set.

Proof. The $S_{\tilde{\pi}}S_{emi}{}^{\#}g\alpha$ *–component* of F_E with respect to the soft point x_e is the soft union of all $S_{\tilde{\pi}}S_{emi}{}^{\#}g\alpha$ *–connected* subsets of F_E which have a nonempty soft intersection (as each contains the soft point x_e). Then by Theorem 3.8, $S_{\tilde{\pi}}S_{emi}{}^{\#}g\alpha - C\left(F_E, x_e\right)$ is a $S_{\tilde{\pi}}S_{emi}{}^{\#}g\alpha$ *–connected* set.

Remark 6.3. $S_{\tilde{\pi}}S_{emi}{}^{\#}g\alpha - C\left(F_E, x_e\right)$ is the largest $S_{\tilde{\pi}}S_{emi}{}^{\#}g\alpha$ *–connected* subset of F_E containing x_e.

Theorem 6.4. Let $\left(\tilde{X}, \tilde{T}, E\right)$ be a $S_{\tilde{\pi}}$ *–Top –Space.* Then the following statements are true.

(i) Each soft point in $\tilde{X}$ is contained in exactly one $S_{\tilde{\pi}}S_{emi}{}^{\#}g\alpha$ *–component* of $\tilde{X}$.

(ii) The $S_{\tilde{\pi}}S_{emi}{}^{\#}g\alpha$ *–components* with respect to two different soft points of $\tilde{X}$ are either identical or soft disjoint.

Proof. (i) Let x_e be an arbitrary soft point of $\tilde{X}$ and $\{P_{E_\lambda} : \lambda \in \Lambda\}$ be the collection of all $S_{\#}S_{emi}{}^{\#}g\alpha$ *−connected* subsets of $\tilde{X}$ which contain x_e. Since the soft singleton $\{x_e\}$ is $S_{\#}S_{emi}{}^{\#}g\alpha$ *−connected*, the collection $\{P_{E_\lambda} : \lambda \in \Lambda\}$ of all soft $S_{\#}S_{emi}{}^{\#}g\alpha$ *−connected* subsets containing the soft point x_e is non-empty. Then $\bigcap\{P_{E_\lambda} : \lambda \in \Lambda\} \neq \phi$, as x_e is contained in each P_{E_λ}. Now, $S_{\#}S_{emi}{}^{\#}g\alpha - C(\tilde{X}, x_e)$ is the soft union of $\{P_{E_\lambda} : \lambda \in \Lambda\}$ having a non-empty soft intersection. Then by **Theorem 3.8,** $S_{\#}S_{emi}{}^{\#}g\alpha - C(\tilde{X}, x_e)$ is also $S_{\#}S_{emi}{}^{\#}g\alpha$ *−connected*. Again $S_{\#}S_{emi}{}^{\#}g\alpha - C(\tilde{X}, x_e)$ is the maximal $S_{\#}S_{emi}{}^{\#}g\alpha$ *−connected* subset of $\tilde{X}$ containing x_e. Therefore, $S_{\#}S_{emi}{}^{\#}g\alpha - C(\tilde{X}, x_e)$ is $S_{\#}S_{emi}{}^{\#}g\alpha$ *−component* of $\tilde{X}$ with respect to x_e. Now we have to prove that there is no other $S_{\#}S_{emi}{}^{\#}g\alpha$ *−component* of $\tilde{X}$ containing x_e. Now, suppose $S_{\#}S_{emi}{}^{\#}g\alpha - C^{*}(\tilde{X}, x_e)$ be another $S_{\#}S_{emi}{}^{\#}g\alpha$ *−component* of $\tilde{X}$ containing x_e. Then $S_{\#}S_{emi}{}^{\#}g\alpha - C^{*}(\tilde{X}, x_e)$ is a $S_{\#}S_{emi}{}^{\#}g\alpha$ *−connected* subset of $\tilde{X}$ containing x_e. But $S_{\#}S_{emi}{}^{\#}g\alpha - C(\tilde{X}, x_e)$ being a $S_{\#}S_{emi}{}^{\#}g\alpha$ *−component* is the maximal $S_{\#}S_{emi}{}^{\#}g\alpha$ *−connected* subset of $\tilde{X}$ containing x_e. Consequently $S_{\#}S_{emi}{}^{\#}g\alpha - C^{*}(\tilde{X}, x_e) \tilde{\subseteq} S_{\#}S_{emi}{}^{\#}g\alpha - C(\tilde{X}, x_e)$. Similarly $S_{\#}S_{emi}{}^{\#}g\alpha - C(\tilde{X}, x_e) \tilde{\subseteq} S_{\#}S_{emi}{}^{\#}g\alpha - C^{*}(\tilde{X}, x_e)$ and hence $S_{\#}S_{emi}{}^{\#}g\alpha - C(\tilde{X}, x_e) = S_{\#}S_{emi}{}^{\#}g\alpha - C^{*}(\tilde{X}, x_e)$. This implies x_e is contained in exactly one $S_{\#}S_{emi}{}^{\#}g\alpha$ *−component* of $\tilde{X}$.

(ii) $S_{\#}S_{emi}{}^{\#}g\alpha - C(\tilde{X}, x_\alpha)$ and $S_{\#}S_{emi}{}^{\#}g\alpha - C(\tilde{X}, y_\beta)$ be respectively the $S_{\#}S_{emi}{}^{\#}g\alpha$ *−components* of $\tilde{X}$ with respect to two different soft points x_e and y_β of $\tilde{X}$ with $x_e \neq y_\beta$. If $S_{\#}S_{emi}{}^{\#}g\alpha - C(\tilde{X}, x_\alpha) \bigcap S_{\#}S_{emi}{}^{\#}g\alpha - C(\tilde{X}, y_\beta) = \tilde{\phi}$, then the proof is over. Suppose $S_{\#}S_{emi}{}^{\#}g\alpha - C(\tilde{X}, x_\alpha) \bigcap S_{\#}S_{emi}{}^{\#}g\alpha - C(\tilde{X}, y_\beta) \neq \tilde{\phi}$. We may choose a soft point $z_\gamma \tilde{\in} S_{\#}S_{emi}{}^{\#}g\alpha - C(\tilde{X}, x_\alpha) \bigcap S_{\#}S_{emi}{}^{\#}g\alpha - C(\tilde{X}, y_\beta)$. Then $z_\gamma \tilde{\in} S_{\#}S_{emi}{}^{\#}g\alpha - C(\tilde{X}, x_\alpha)$ and $z_\gamma \tilde{\in} S_{\#}S_{emi}{}^{\#}g\alpha - C(\tilde{X}, y_\beta)$. Since $S_{\#}S_{emi}{}^{\#}g\alpha - C(\tilde{X}, z_\gamma)$ is the maximal $S_{\#}S_{emi}{}^{\#}g\alpha$ *−component* of $\tilde{X}$ with respect to z_γ. Therefore $S_{\#}S_{emi}{}^{\#}g\alpha - C(\tilde{X}, x_\alpha) \subseteq S_{\#}S_{emi}{}^{\#}g\alpha - C(\tilde{X}, z_\gamma) \ldots (1)$. Since $x_\alpha \tilde{\in} S_{\#}S_{emi}{}^{\#}g\alpha - C(\tilde{X}, x_\alpha) \subseteq S_{\#}S_{emi}{}^{\#}g\alpha - C(\tilde{X}, z_\gamma)$, we have $x_\alpha \tilde{\in} S_{\#}S_{emi}{}^{\#}g\alpha - C(\tilde{X}, z_\gamma)$. Also $S_{\#}S_{emi}{}^{\#}g\alpha - C(\tilde{X}, z_\gamma)$ is a $S_{\#}S_{emi}{}^{\#}g\alpha$ *−connected* set containing x_α. But, $S_{\#}S_{emi}{}^{\#}g\alpha - C(\tilde{X}, x_\alpha)$ is the maximal $S_{\#}S_{emi}{}^{\#}g\alpha$ *−component* set containing x_α. Therefore $S_{\#}S_{emi}{}^{\#}g\alpha - C(\tilde{X}, z_\gamma) \subseteq S_{\#}S_{emi}{}^{\#}g\alpha - C(\tilde{X}, x_\alpha) \ldots (2)$. From (1) and (2), we have $S_{\#}S_{emi}{}^{\#}g\alpha - C(\tilde{X}, x_\alpha) = S_{\#}S_{emi}{}^{\#}g\alpha - C(\tilde{X}, z_\gamma)$. Similarly $z_\gamma \tilde{\in} S_{\#}g^{**} - C(\tilde{X}, y_\beta)$ implies that $S_{\#}S_{emi}{}^{\#}g\alpha - C(\tilde{X}, y_\beta) = S_{\#}S_{emi}{}^{\#}g\alpha - C(\tilde{X}, z_\gamma)$. Thus we have $S_{\#}S_{emi}{}^{\#}g\alpha - C(\tilde{X}, x_\alpha) = S_{\#}S_{emi}{}^{\#}g\alpha - C(\tilde{X}, y_\beta)$.

Definition 6.5. The $S_{\#}S_{emi}{}^{\#}g\alpha$ *−component* of a space $\tilde{X}$ of a $S_{\#}$ *−Top −Space* $(\tilde{X}, \tilde{T}, E)$ is the maximal $S_{\#}S_{emi}{}^{\#}g\alpha$ *−connected* subspace of $(\tilde{X}, \tilde{T}, E)$. The $S_{\#}S_{emi}{}^{\#}g\alpha$ *−component* of a $S_{\#}$ *−Top −Space* $(\tilde{X}, \tilde{T}, E)$ is denoted as $S_{\#}S_{emi}{}^{\#}g\alpha - C(\tilde{X})$.

Theorem 6.6. Each $S_{\tilde{\mu}}S_{emi}{}^{\#}g\alpha$ *–component* of a $S_{\tilde{\mu}}$ *–Top –Space* $\left(\tilde{X},\tilde{T},E\right)$ is a $S_{\tilde{\mu}}S_{emi}{}^{\#}g\alpha$ *–closed* set.

Proof. Let $S_{\tilde{\mu}}S_{emi}{}^{\#}g\alpha\text{–}C\left(\tilde{X}\right)$ be a $S_{\tilde{\mu}}S_{emi}{}^{\#}g\alpha$ *–component* of $\tilde{X}$. Then, $S_{\tilde{\mu}}S_{emi}{}^{\#}g\alpha\text{–}C\left(\tilde{X}\right)$ is the maximal $S_{\tilde{\mu}}S_{emi}{}^{\#}g\alpha$ *–connected* subset of $\tilde{X}$. By Theorem 3.6, $S_{\tilde{\mu}}S_{emi}{}^{\#}g\alpha\text{–}Cl\left[S_{\tilde{\mu}}S_{emi}{}^{\#}g\alpha\text{–}C\left(\tilde{X}\right)\right]$ is also $S_{\tilde{\mu}}S_{emi}{}^{\#}g\alpha$ *–connected* and $S_{\tilde{\mu}}S_{emi}{}^{\#}g\alpha\text{–}Cl\left[S_{\tilde{\mu}}S_{emi}{}^{\#}g\alpha\text{–}C\left(\tilde{X}\right)\right]\subseteq S_{\tilde{\mu}}S_{emi}{}^{\#}g\alpha\text{–}C\left(\tilde{X}\right)$. But $S_{\tilde{\mu}}S_{emi}{}^{\#}g\alpha\text{–}C\left(\tilde{X}\right)\subseteq S_{\tilde{\mu}}S_{emi}{}^{\#}g\alpha\text{–}Cl\left[S_{\tilde{\mu}}S_{emi}{}^{\#}g\alpha\text{–}C\left(\tilde{X}\right)\right]$. Hence, $S_{\tilde{\mu}}S_{emi}{}^{\#}g\alpha\text{–}C\left(\tilde{X}\right)=$ $S_{\tilde{\mu}}S_{emi}{}^{\#}g\alpha\text{–}Cl\left[S_{\tilde{\mu}}S_{emi}{}^{\#}g\alpha\text{–}C\left(\tilde{X}\right)\right]$. Therefore, $S_{\tilde{\mu}}S_{emi}{}^{\#}g\alpha\text{–}C\left(\tilde{X}\right)$ is a $S_{\tilde{\mu}}S_{emi}{}^{\#}g\alpha$ *–closed* set.

Theorem 6.7. In a $S_{\tilde{\mu}}$ *–Top –Space* $\left(\tilde{X},\tilde{T},E\right)$, the set of all disjoint $S_{\tilde{\mu}}S_{emi}{}^{\#}g\alpha$ *–components* of soft points of $\tilde{X}$ form a partition of $\tilde{X}$.

Proof. Let $S_{\tilde{\mu}}S_{emi}{}^{\#}g\alpha\text{–}C\left(\tilde{X},x_\alpha\right)$ and $S_{\tilde{\mu}}S_{emi}{}^{\#}g\alpha\text{–}C\left(\tilde{X},y_\beta\right)$ be two $S_{\tilde{\mu}}S_{emi}{}^{\#}g\alpha$ *–components* of distinct soft points x_α and y_β in $\tilde{X}$. Now for any soft point $x_\alpha\,\tilde{\in}\,\tilde{X}$, $x_\alpha\,\tilde{\in}\,S_{\tilde{\mu}}S_{emi}{}^{\#}g\alpha\text{–}C\left(\tilde{X},x_\alpha\right)$ and hence $\tilde{X}=\tilde{\bigcup}\left\{\{x_\alpha\}:x_\alpha\in\tilde{X}\right\}\,\tilde{\subseteq}\,\tilde{\bigcup}\left\{S_{\tilde{\mu}}S_{emi}{}^{\#}g\alpha\text{–}C\left(\tilde{X},x_\alpha\right):x_\alpha\in\tilde{X}\right\}$, by considering only the disjoint $S_{\tilde{\mu}}S_{emi}{}^{\#}g\alpha$ *–components* with respect to the soft point $x_\alpha\,\tilde{\in}\,\tilde{X}$. This implies that $\tilde{X}\,\tilde{\subseteq}\,\tilde{\bigcup}\left\{S_{\tilde{\mu}}S_{emi}{}^{\#}g\alpha\text{–}C\left(\tilde{X},x_\alpha\right):x_\alpha\in\tilde{X}\right\}\,\tilde{\subseteq}\,\tilde{X}$. Therefore $\tilde{\bigcup}\left\{S_{\tilde{\mu}}S_{emi}{}^{\#}g\alpha\text{–}C\left(\tilde{X},x_\alpha\right):x_\alpha\in\tilde{X}\right\}=\tilde{X}$.

VII. Locally Soft $S_{emi}{}^{\#}g\alpha$ –Connected Space

In this section, we introduce the concept locally $S_{\tilde{\mu}}S_{emi}{}^{\#}g\alpha$ *–connected* space and discuss its properties. Also, we analyse locally $S_{\tilde{\mu}}S_{emi}{}^{\#}g\alpha$ *–connected* space with other soft connectedness like $S_{\tilde{\mu}}S_{emi}{}^{\#}g\alpha$ *–connected* space, soft connected space and locally soft connected space.

Definition 7.1. A $S_{\tilde{\mu}}$ *–Top –Space* $\left(\tilde{X},\tilde{T},E\right)$ is called locally $S_{\tilde{\mu}}S_{emi}{}^{\#}g\alpha$ *–connected* at $x_e\in\tilde{X}$ if and only if for every $S_{\tilde{\mu}}S_{emi}{}^{\#}g\alpha$ *–open* set P_E containing x_e, there exist a $S_{\tilde{\mu}}S_{emi}{}^{\#}g\alpha$ *–connected* soft open set F_E such that $x_e\,\tilde{\in}\,F_E\,\tilde{\subseteq}\,P_E$.

Definition 7.2. A $S_{\tilde{\mu}}$ *–Top –Space* $\left(\tilde{X},\tilde{T},E\right)$ is said to be locally $S_{\tilde{\mu}}S_{emi}{}^{\#}g\alpha$ *–connected* if and only if it is locally $S_{\tilde{\mu}}S_{emi}{}^{\#}g\alpha$ *–connected* at each of its soft points.

Theorem 7.3. Every $S_{\tilde{\mu}}S_{emi}{}^{\#}g\alpha$ *–component* of a locally $S_{\tilde{\mu}}S_{emi}{}^{\#}g\alpha$ *–connected* space is $S_{\tilde{\mu}}S_{emi}{}^{\#}g\alpha$ *–open* set.

Proof. Let $S_{\tilde{\mu}}S_{emi}{}^{\#}g\alpha\text{–}C\left(\tilde{X}\right)$ be a $S_{\tilde{\mu}}S_{emi}{}^{\#}g\alpha$ *–component* of a locally $S_{\tilde{\mu}}S_{emi}{}^{\#}g\alpha$ *–connected* space $\left(\tilde{X},\tilde{T},E\right)$ and let $x_e\,\tilde{\in}\,S_{\tilde{\mu}}S_{emi}{}^{\#}g\alpha\text{–}C\left(\tilde{X},x_e\right)$. Now $\tilde{X}$ is locally $S_{\tilde{\mu}}S_{emi}{}^{\#}g\alpha$ *–connected*. Therefore, it is locally $S_{\tilde{\mu}}S_{emi}{}^{\#}g\alpha$ *–connected* at each soft point $x_e\in\tilde{X}$. This implies that each $S_{\tilde{\mu}}S_{emi}{}^{\#}g\alpha$ *–open* set

containing x_e contains a $S_{\tilde{\pi}}S_{emi}{}^{\#}g\alpha$ *−connected* open set P_E containing the soft point x_e. Since the $S_{\tilde{\pi}}S_{emi}{}^{\#}g\alpha$ *−component* $S_{\tilde{\pi}}S_{emi}{}^{\#}g\alpha - C\left(\tilde{X}, x_e\right)$ is the maximal $S_{\tilde{\pi}}S_{emi}{}^{\#}g\alpha$ *−connected* set containing x_e, $x_e \tilde{\in} P_E \tilde{\subseteq} S_{\tilde{\pi}}S_{emi}{}^{\#}g\alpha - C\left(\tilde{X}, x_e\right)$, where P_E is $S_{\tilde{\pi}}S_{emi}{}^{\#}g\alpha$ *−open* set. Therefore, $S_{\tilde{\pi}}S_{emi}{}^{\#}g\alpha - C\left(\tilde{X}, x_e\right) = \tilde{\cup}\left\{P_E : x_e \tilde{\in} P_E \subseteq S_{\tilde{\pi}}S_{emi}{}^{\#}g\alpha - C\left(\tilde{X}, x_e\right)\right\}$. Thus, $S_{\tilde{\pi}}S_{emi}{}^{\#}g\alpha - C\left(\tilde{X}, x_e\right)$ is the soft union of all $S_{\tilde{\pi}}S_{emi}{}^{\#}g\alpha$ *−open* sets containing x_e. Therefore, $S_{\tilde{\pi}}S_{emi}{}^{\#}g\alpha - C\left(\tilde{X}, x_e\right)$ is $S_{\tilde{\pi}}S_{emi}{}^{\#}g\alpha$ *−open* set.

Theorem 7.4. A $S_{\tilde{\pi}}$ *−Top −Space* $\left(\tilde{X}, \tilde{T}, E\right)$ is locally $S_{\tilde{\pi}}S_{emi}{}^{\#}g\alpha$ *−connected* if and only if the $S_{\tilde{\pi}}S_{emi}{}^{\#}g\alpha$ *−components* of $S_{\tilde{\pi}}S_{emi}{}^{\#}g\alpha$ *−open* sets are soft open.

Proof. Suppose that $\left(\tilde{X}, \tilde{T}, E\right)$ is locally $S_{\tilde{\pi}}S_{emi}{}^{\#}g\alpha$ *−connected*. Let P_E be a $S_{\tilde{\pi}}S_{emi}{}^{\#}g\alpha$ *−open* set and F_E be a $S_{\tilde{\pi}}S_{emi}{}^{\#}g\alpha$ *−component* of P_E. If $x_e \tilde{\in} F_E$, then $x_e \tilde{\in} P_E$. Since $\left(\tilde{X}, \tilde{T}, E\right)$ is locally $S_{\tilde{\pi}}S_{emi}{}^{\#}g\alpha$ *−connected* space, there is a $S_{\tilde{\pi}}S_{emi}{}^{\#}g\alpha$ *−connected* open set O_E such that $x_e \tilde{\in} O_E \tilde{\subseteq} P_E$. Since F_E is the $S_{\tilde{\pi}}S_{emi}{}^{\#}g\alpha$ *−component* of x_e and O_E is $S_{\tilde{\pi}}S_{emi}{}^{\#}g\alpha$ *−connected*, we have $x_e \tilde{\in} O_E \tilde{\subseteq} F_E$. This shows that F_E is soft open.

Conversely, let $x_e \tilde{\in} \tilde{X}$ be arbitrary and let P_E be a $S_{\tilde{\pi}}S_{emi}{}^{\#}g\alpha$ *−open* set containing x_e. Let F_E be the $S_{\tilde{\pi}}S_{emi}{}^{\#}g\alpha$ *−component* of P_E such that $x_e \tilde{\in} F_E$. Now F_E is a $S_{\tilde{\pi}}S_{emi}{}^{\#}g\alpha$ *−connected* open set such that $x_e \tilde{\in} F_E \tilde{\subseteq} P_E$.

Theorem 7.5. A $S_{\tilde{\pi}}$ *−Top −Space* $\left(\tilde{X}, \tilde{T}, E\right)$ is locally $S_{\tilde{\pi}}S_{emi}{}^{\#}g\alpha$ *−connected* if and only if, given any soft point $x_e \tilde{\in} \tilde{X}$ and a $S_{\tilde{\pi}}S_{emi}{}^{\#}g\alpha$ *−open* set P_E containing x_e, there is a soft open set O_E containing x_e such that O_E is contained in a single $S_{\tilde{\pi}}S_{emi}{}^{\#}g\alpha$ *−component* of P_E.

Proof. Let $\tilde{X}$ be locally $S_{\tilde{\pi}}S_{emi}{}^{\#}g\alpha$ *−connected*, $x_e \tilde{\in} \tilde{X}$ and P_E be a $S_{\tilde{\pi}}S_{emi}{}^{\#}g\alpha$ *−open* set containing x_e. Let F_E be a $S_{\tilde{\pi}}S_{emi}{}^{\#}g\alpha$ *−component* of P_E that contains x_e. Since $\tilde{X}$ is locally $S_{\tilde{\pi}}S_{emi}{}^{\#}g\alpha$ *−connected* and P_E is $S_{\tilde{\pi}}S_{emi}{}^{\#}g\alpha$ *−open*, there is a $S_{\tilde{\pi}}S_{emi}{}^{\#}g\alpha$ *−connected* open set O_E such that $x_e \tilde{\in} O_E \tilde{\subseteq} P_E$. By Remark 6.3, F_E is the maximal $S_{\tilde{\pi}}S_{emi}{}^{\#}g\alpha$ *−connected* set containing x_e and so $x_e \tilde{\in} O_E \tilde{\subseteq} F_E \tilde{\subseteq} P_E$. Since $S_{\tilde{\pi}}S_{emi}{}^{\#}g\alpha$ *−components* are disjoint soft sets, it follows that O_E is not contained in any other soft $S_{\tilde{\pi}}S_{emi}{}^{\#}g\alpha$ *−component* of P_E. Conversely , we suppose that given any soft point $x_e \tilde{\in} \tilde{X}$ and any $S_{\tilde{\pi}}S_{emi}{}^{\#}g\alpha$ *−open* set P_E containing x_e, there is a soft open set O_E containing x_e which is contained in a soft singleton $S_{\tilde{\pi}}S_{emi}{}^{\#}g\alpha$ *−component* F_E of P_E. Then, $x_e \tilde{\in} O_E \tilde{\subseteq} F_E \tilde{\subseteq} P_E$. Let $y_\beta \tilde{\in} F_E$, then $y_\beta \tilde{\in} P_E$. Thus, there is a soft open set O_A such that $y_\beta \tilde{\in} O_A$ and O_A is contained in a single $S_{\tilde{\pi}}S_{emi}{}^{\#}g\alpha$ *−component* of P_E. Since the $S_{\tilde{\pi}}S_{emi}{}^{\#}g\alpha$ *−components* are disjoint soft sets and $y_\beta \tilde{\in} F_E$, $y_\beta \tilde{\in} G_E \tilde{\subseteq} F_E$. Thus F_E is soft open. Thus, for every $x_e \tilde{\in} \tilde{X}$ and for every $S_{\tilde{\pi}}S_{emi}{}^{\#}g\alpha$ *−open* set P_E containing x_e, there is a $S_{\tilde{\pi}}S_{emi}{}^{\#}g\alpha$ *−connected* open set F_E such that $x_e \tilde{\in} F_E \tilde{\subseteq} P_E$. Thus $\left(\tilde{X}, \tilde{T}, E\right)$

is locally $S_{\tilde{\pi}}S_{emi}{}^{\#}g\alpha$ *–connected* at x_e. Since $x_e \tilde{\in} \tilde{X}$ is arbitrary, $\left(\tilde{X},\tilde{T},E\right)$ is locally $S_{\tilde{\pi}}S_{emi}{}^{\#}g\alpha$ *–connected* space.

VIII. Totally Soft $S_{emi}{}^{\#}g\alpha$ –Disconnected Space

In this section, we introduce the concept of totally $S_{\tilde{\pi}}S_{emi}{}^{\#}g\alpha$ *–disconnected* space in a $S_{\tilde{\pi}}$ *–Top –Space* and discuss its properties and characterizations.

Definition 8.1. $S_{\tilde{\pi}}S_{emi}{}^{\#}g\alpha$ *–disconnected* means $\tilde{X}$ is the soft union of two nonempty disjoint $S_{\tilde{\pi}}S_{emi}{}^{\#}g\alpha$ *–open* sets or $S_{\tilde{\pi}}S_{emi}{}^{\#}g\alpha$ *–closed* sets in $\tilde{X}$.

Definition 8.2. A $S_{\tilde{\pi}}$ *–Top –Space* $\left(\tilde{X},\tilde{T},E\right)$ is said to be totally $S_{\tilde{\pi}}S_{emi}{}^{\#}g\alpha$ *–disconnected* space if and only if for each pair of distinct soft points $x_\alpha, y_\beta \tilde{\in} \tilde{X}$, there exists a $S_{\tilde{\pi}}S_{emi}{}^{\#}g\alpha$ *–disconnection* $F_E \tilde{\cup} G_E$ of $\tilde{X}$ such that $x_\alpha \in F_E$ and $y_\beta \in G_E$, where F_E, G_E are both either $S_{\tilde{\pi}}S_{emi}{}^{\#}g\alpha$ *–connected* open sets or $S_{\tilde{\pi}}S_{emi}{}^{\#}g\alpha$ *–connected* closed sets.

Example 8.3. Every discrete $S_{\tilde{\pi}}$ *–Top –Space* $\tilde{X}$ is totally $S_{\tilde{\pi}}S_{emi}{}^{\#}g\alpha$ *–disconnected* space. Indeed, let $x_\alpha, y_\beta \tilde{\in} \tilde{X}$ and $x_\alpha \neq y_\beta$. Then $\{x_\alpha\} \tilde{\cup} \left(\tilde{X} - \{x_\alpha\}\right)$ is $S_{\tilde{\pi}}S_{emi}{}^{\#}g\alpha$ *–disconnection* of $\tilde{X}$.

Proposition 8.4. A soft subspace of a totally $S_{\tilde{\pi}}S_{emi}{}^{\#}g\alpha$ *–disconnected* space is totally $S_{\tilde{\pi}}S_{emi}{}^{\#}g\alpha$ *–disconnected* space. Each totally soft disconnected space is a totally $S_{\tilde{\pi}}S_{emi}{}^{\#}g\alpha$ *–disconnected* space. The $S_{\tilde{\pi}}S_{emi}{}^{\#}g\alpha$ *–components* of a totally $S_{\tilde{\pi}}S_{emi}{}^{\#}g\alpha$ *–disconnected* space $\left(\tilde{X},\tilde{T},E\right)$ are soft singleton subsets of $\tilde{X}$.

Proof. Let $\left(\tilde{X},\tilde{T},E\right)$ be a totally $S_{\tilde{\pi}}S_{emi}{}^{\#}g\alpha$ *–disconnected* space and $\tilde{Y}$ be a soft subset of $\tilde{X}$ consisting of two or more than two soft points. Let x_α and y_β be two distinct soft points of $\tilde{Y}$. Then x_α and y_β are also distinct soft points of $\tilde{X}$. Now $\left(\tilde{X},\tilde{T},E\right)$ is totally $S_{\tilde{\pi}}S_{emi}{}^{\#}g\alpha$ *–disconnected*. Therefore, there exists a $S_{\tilde{\pi}}S_{emi}{}^{\#}g\alpha$ *–disconnection* $F_A \tilde{\cup} G_B$ of $\tilde{X}$ such that $x_\alpha \tilde{\in} F_A$ and $y_\beta \tilde{\in} G_B$. Let $P_C = F_A \tilde{\cap} \tilde{Y}$ and $Q_D = G_B \tilde{\cap} \tilde{Y}$. We claim that $P_C \tilde{\cup} Q_D$ is a $S_{\tilde{\pi}}S_{emi}{}^{\#}g\alpha$ *–disconnection* of $\tilde{Y}$. For, since $x_\alpha \tilde{\in} \tilde{Y}$, $x_\alpha \tilde{\in} F_A$, $y_\beta \tilde{\in} \tilde{Y}$, $y_\beta \tilde{\in} G_B$. Both P_C and Q_D are non-empty. Also, $P_C \tilde{\cap} Q_D = \left(F_A \tilde{\cap} \tilde{Y}\right) \tilde{\cap} \left(G_B \tilde{\cap} \tilde{Y}\right) = \left(F_A \tilde{\cap} G_B\right) \tilde{\cap} \tilde{Y} = \tilde{\phi} \tilde{\cap} \tilde{Y} = \tilde{\phi}$. That is P_C and Q_D are soft disjoint. Thus, $\tilde{Y}$ is $S_{\tilde{\pi}}S_{emi}{}^{\#}g\alpha$ *–disconnected* and hence $\tilde{Y}$ a soft subset containing two or more than two soft points cannot be a $S_{\tilde{\pi}}S_{emi}{}^{\#}g\alpha$ *–component* of $\tilde{X}$. Therefore, the $S_{\tilde{\pi}}S_{emi}{}^{\#}g\alpha$ *–components* of $\tilde{X}$ are soft singleton subsets of $\tilde{X}$ which are the only $S_{\tilde{\pi}}S_{emi}{}^{\#}g\alpha$ *–connected* subsets of $\tilde{X}$.

Conclusions

Connectedness is an important and major area of topology, and it can give many relationships between other scientific areas and mathematical models. The notion of connectedness captures the idea of the hanging-togetherness of image elements in an object by giving a firmness of connectedness to every feasible path

between every possible pair of image elements. It is an essential tool for designing algorithms for image segmentation. We have used the notions of $S_{ft}S_{emi}{}^{\#}g\alpha$ –open sets and $S_{ft}S_{emi}{}^{\#}g\alpha$ –closed sets to introduce $S_{ft}S_{emi}{}^{\#}g\alpha$ –separated sets, $S_{ft}S_{emi}{}^{\#}g\alpha$ –connected space, $S_{ft}S_{emi}{}^{\#}g\alpha$ –disconnected space, $S_{ft}S_{emi}{}^{\#}g\alpha$ –component of a soft set and soft topological space, locally $S_{ft}S_{emi}{}^{\#}g\alpha$ –connected space and totally $S_{ft}S_{emi}{}^{\#}g\alpha$ –disconnected space in soft topological spaces. We have investigated properties and characterizations of these new spaces in soft topological spaces. We hope that the concepts initiated herein will be beneficial for researchers and scholars to promote and progress the study of soft topology and decision-making problems with applications in many fields soon.

Recommendations

In the future, it is recommended to utilize soft semi #generalized α-open sets to initiate new kinds of soft semi #generalized α-compactness, namely soft semi #generalized α-Lindelofness, almost (approximately, mildly) soft semi #generalized α-compactness, and almost (approximately, mildly) soft semi #generalized α-Lindelofness. The equivalent conditions of each one of them can be investigated. Also, the behavior of these spaces under soft semi #generalized α-irresolute maps can be investigated. Furthermore, the enough conditions for the equivalence among the four sorts of soft semi #generalized α- compact spaces and for the equivalence among the four sorts of soft semi #generalized α-Lindelof spaces can be explored. The relationships between enriched soft topological spaces and the initiated spaces can be investigated in different cases. Some properties which connect some of these spaces with some soft topological notions, such as soft semi #generalized α-T_2-spaces and soft subspaces, can be obtained.

Scientific Ethics Declaration

* The author declares that the scientific ethical, and legal responsibility of this article published in EPSTEM journal belongs to the author.

Conflict of Interest

* The authors declare that they have no conflicts of interest

Funding

* The author is highly and greatly indebted to Prince Mohammad bin Fahd University Al Khobar, Saudi Arabia, for providing all necessary research facilities during the preparation of this research paper.

Acknowledgements or Notes

*This article was presented as an oral presentation at the International Conference on Basic Sciences, Engineering and Technology (www.icbaset.net) held in Trabzon/Türkiye on May 01-04, 2025.

References

Benchalli, S.S., Patil, P.G., & Dodamani, A. S. (2017). Some properties of soft β-connected spaces in soft topological spaces. *International Journal of Pure Mathematical Sciences, 18,* 13 – 21.

Chen, B. (2013). Soft semi-open sets & related properties in soft topological spaces. *Applied Mathematics and Informatics Sciences, 1*(7), 287–294.

Gomathi, N., & Indira, T. (2022). On soft generalized** closed sets in soft topological spaces. *Advances and Applications in Mathematical Sciences*, *21*(10), 5575–5595.

Hamko, Q. H., Ahmed, N. K., & Khalaf, A. B. (2020). On soft P_c –*Connected* spaces. *Iraqi Journal of Science, 61*(11), 3072–3081.

Hussain, S., & Ahmad, B. (2011). Some properties of soft topological spaces. *Computers & Mathematics with Applications, 62*(11), 4058–4067.

Hussain, S. (2015). A note on soft connectedness. *Journal of the Egyptian Mathematical Society, 23*(1), 6–11.

Jackson, S., & Chitra, S. (2023). Connectedness in soft topological spaces. *Journal of Pharmaceutical Negative Results, 14*(3), 115–118.

Jackson, S., & Chitra, S. (2023). New class of connectedness in soft topological spaces. *Advances and Applications in Mathematical Sciences, 22*(4), 873–882.

Karuppayal, V. R., & Malarvizhi. Soft generalized #α-closed sets in soft topological spaces. *International Journal of Advanced and Innovative Research, 3*(10), 298–305.

Al-Khafaj, M. A. K, & Mahmood, M. H. (2014). Some properties of soft connected spaces and soft locally connected spaces. *IOSR Journal of Mathematics, 10*(5), 102–107.

Kokilavani, V., & Vivek Prabu, M. (2013). Semi #generalized α closed sets and semi #generalized α-homeomorphism in topological spaces. *Proceedings of the National Conference on Recent Advances in Mathematical Analysis and Applications (NCRAMAA-2013)*, 153–161.

Kokilavani, V., & Vivek Prabu, M. (2016). Some new sets using soft semi #gα-closed sets in soft topological spaces. *International Journal of Mathematics and Soft Computing, 6*(1), 49–56.

Kokilavani, V., Sindu, D., & Vivek Prabu, M. (2014). Soft #generalized α-closed sets in soft topological spaces. *International Journal of Advanced and Innovative Research, 3*(10), 265–271.

Lin, F. (2013). Soft connected spaces and soft paracompact spaces. *International Journal of Mathematical and Computational Sciences, 7*(2), 277–283.

Molodtsov, D. A. (1999). Soft set theory—First results. *Computers & Mathematics with Applications, 37*(4–5), 19–31.

Al-Khafaj, M. A. K., & Mahmood, M. H. (2014). Some properties of soft connected spaces and soft locally connected spaces. *IOSR Journal of Mathematics, 10*(5),102–107.

Peyghan, E., Samadi, B., & Tayebi, A. (2012). On soft connectedness. *arXiv:1202.1668v1 [math.GN].*

Rajput, A. S., & Thakur, S. S. (2019). α-Connectedness between soft sets. *International Journal of Students' Research in Technology & Management*, *7*(4), 9–14.

Rathee, S., & Girdhar, R. (2021). On soft ω-connectedness in soft topological spaces. *Communications in Mathematics and Applications, 12*(3), 457–474.

Saleh, H. Y., Asaad, B. A., & Mohammed, R. A. (2023). Connectedness, local connectedness, and components on bipolar soft generalized topological spaces. *Journal of Mathematics and Computer Science, 30,* 302–321.

Al-Shami, T. M., & Abo-Tabl, E.S. A. (2021). Connectedness and local connectedness on infra soft topological spaces. *Mathematics, 9*(15), 1759.

Subhashini, J. J., & Sekar, C. (2014). Soft P-connected via soft P-open sets. *International Journal of Mathematics Trends and Technology, 6,* 203–214.

Willard, S. (1970). *General topology.* Reading, Mass.: Addison Wesley Pub. Co.

Willard, S., & Latif, R. M. (1997). Semi-open sets and regularly closed sets in compact metric spaces. *Mathematica Japonica, 46*(1), 157–161.

Yuksel, S., Ergul, Z. G., & Guven, Z. (2014). Soft connected spaces. *International Journal of Pure & Engineering Mathematics (IJPEM), 2*(3), 121 – 134.

Author Information

Raja Mohammad Latif
Department of Mathematics and Natural Sciences
Prince Mohammad Bin Fahd University
Al Khobar, Kingdom of Saudi Arabia
Contact e-mail: *rlatifl@pmu.edu.sa*

To cite this article:

Latif, R. M. (2025), Soft semi # generalized α-connectedness in soft topological spaces. *The Eurasia Proceedings of Science, Technology, Engineering and Mathematics (EPSTEM), 34,* 120-138.

The Eurasia Proceedings of Science, Technology, Engineering & Mathematics (EPSTEM)
ISSN: 2602-3199

The Eurasia Proceedings of Science, Technology, Engineering and Mathematics (EPSTEM), 2025

Volume 34, Pages 139-150

ICBASET 2025: International Conference on Basic Sciences, Engineering and Technology

Accuracy of Different Modes of Bomb Dropping from Aircraft

Milen Atanasov
Georgi Benkovski Bulgarian Air Force Academy

Abstract: The development of targeting systems is carried out under the influence of the requirements set by the conditions of combat use of aircraft, which are characterized by high speed and dynamism. The emergence of new methods for solving the targeting task in targeting systems leads to the expansion of aircraft combat capabilities, as well as to changes in tactical techniques and maneuvers. Combat tactics themselves also develop as a result of improving old ones and developing new methods of combat use. To implement the new methods, it is necessary to improve targeting systems.To solve the targeting task in bomb dropping, the non-program method is used, implemented on the various existing types of aircraft targeting systems. The non-program method, depending on the attack modes (horizontal flight, dive, pitch up) and the field of view of the sighting system, is implemented through the Constantly Computed Release Point (CCRP) and Constantly Computed Impact Point (CCIP) modes. This article proposes a method for solving the targeting problem when dropping bombs by angular velocity from horizontal flight and dive.Bomb dropping by angular velocity is a method that has not been used so far for solving the targeting problem. The moment of bomb dropping is determined by comparing the angular velocities of tracking the target with the required ones. This method also allows the use of container type targeting systems. All this expands the areas of combat use of aircraft.To study the targeting process and determine the errors of bomb dropping, mathematical modelling of the targeting process is performed using the CCRP and CCIP modes for bomb dropping as well as bomb dropping by angular velocity. The probabilistic characteristics of the dropping error are determined, and a comparative analysis of the same is performed for different methods of bomb dropping.

Keywords: Accuracy, Targeting systems, Aircraft

Introduction

Modern targeting systems (TS) are automated systems with the integration of on-board equipment and the use of on-board digital computers (ODCs) (Biliderov & Kambushev, 2019).

Characteristic features of targeting systems are:

- Full automation of the measurement of data on the state and movement of the aircraft.
- Full automation of the target tracking systems, with the initial target designation being performed manually or automatically depending on the technological level of the aircraft's equipment.
- Primary processing of data from the sensors is performed by the subsystem computers.
- The ODC performs complex processing of incoming information for controlling the subsystems and coordinates the interaction between them.
- The algorithm for determining the coordinates of the point of impact of the means of destruction is synthesized on the basis of predicting the movement of the target and solves the main task of external ballistics.
- The display of targeting and piloting information is performed using optical-electronic devices.
- Control of aircraft in targeting modes is usually carried out manually by direct marks.

Currently, work is underway to improve the combat use modes of aircraft based on solving finite variation problems for intersecting the motions.

Mathematical Model of CCIP and CCRP Modes

In the non-program method, the drop moment is determined by comparing the target coordinates determined during the flight and their calculated values. When using a vertical maneuver, in addition to determining the drop moment, the start of the vertical maneuver must be selected. The mathematical dependencies of the aiming parameters for bomb-dropping can be obtained from the vector aiming equation (Figure 1).

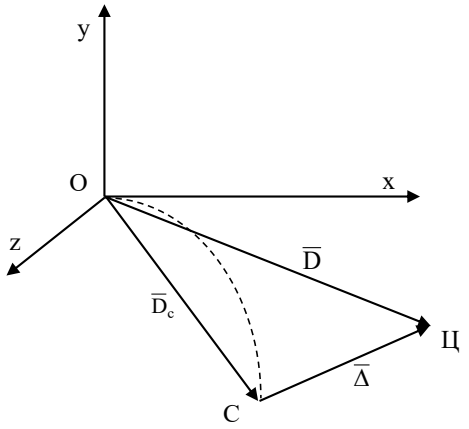

Figure 1. Bomb-dropping targeting vector scheme

$$\overline{\Delta} = \overline{D} - \overline{D}_c, \tag{1}$$

where $\overline{\Delta}$ is the aiming parameter.

In the general case, projecting equation (1) onto the axes of the coordinate system $O\eta'\zeta'\xi'$is obtained:

$$\begin{aligned} \Delta_\eta &= \eta' - \eta'_c; \\ \Delta_y &= y - Y; \\ \Delta_\xi &= \xi' - \xi'_c, \end{aligned} \tag{2}$$

where Δ_η, Δ_y, Δ_ξ ($\zeta' \equiv Y$) are projections of the aiming parameters on the corresponding axes;

η', y, ξ' – the current coordinates of the target;

$\eta'_н$, Y, $\xi'_н$ – the calculated target coordinates at the time of dropping.

The current coordinates of the target can be determined by the sighting and information navigation subsystems. The calculated coordinates of the target are calculated by the ODC. In this case, it is assumed that each point of the combat trajectory is considered as a possible drop point. This allows the current flight parameters of the aircraft to be used as initial conditions: H, V1, λ, etc. to determine the ballistic elements of the bombs. With the assumption made, the current y and calculated Y coordinates of the target coincide and are equal to the flight altitude of the aircraft, i.e. y=Y= −H. Then the parameter Δ_y will be identically equal to zero. Therefore, in the aiming process, it is necessary for Δ_η and Δ_ξ to tend to zero.

Zeroing of $\Delta_\xi = \xi' - \xi'_c$ represents the task of aiming in direction (lateral aiming), and zeroing $\Delta_\eta = \eta' - \eta'_c$ constitutes the task of aiming in distance (determination of the moment of bomb drop).

The following designations are accepted:

$$\begin{aligned} \Delta_{\xi} &= q; \\ \Delta_{\eta} &= p, \end{aligned} \tag{3}$$

където

q is the direction aiming parameter;

p – the distance aiming parameter.

Performing aiming during bomb-dropping (zeroeing the parameters q and p) can be done using two possible methods: CCIP and CCRP.

Constantly Computed Impact Point Modes

When using the CCIP method, the aiming grid is indicated, the central point of which shows the point of contact of the bomb with the ground, if the combat button is pressed at that moment. In this case, the position of the movable grid relative to the coordinate system connected to the aiming head $Ox_sy_sz_s$ is determined using the necessary angles B_s and E_s (Stoĭkov & Atanasov, 2009), which are calculated in discrete mode by the ODC based on the current flight parameters of the aircraft and the ballistic elements (A_0, T).

The target position relative to the same coordinate system is determined by the current angles β_s and ε_s.

When using this method the aiming parameters are:

$$\begin{aligned} q &= \beta_s - B_s; \\ p &= \varepsilon_s - E_s. \end{aligned} \tag{4}$$

When aiming, the pilot strives to align the moving grid with the target (q=0, p=0) and press the fire button. This method is used when the target remains in the pilot's field of vision until the bomb is released. Such conditions exist when dropping bombs from horizontal flight and from a dive. A disadvantage of using this method of bomb dropping is that the target must be constantly monitored, and the angles of deviation of the aiming grid must be within the permissible limits for the specific type of targeting system, which in turn imposes restrictions on the initial conditions for bomb dropping. As an advantage, it can be emphasized that the pilot continuously monitors the target until the moment of release and the ODC determines the necessary angles of the aiming grid.

The ballistic task for the type of aviation bomb used is solved using the current flight parameters of the aircraft, the necessary coordinates of the target X, Z in the Oxyz coordinate system are determined. The calculated target sighting angles B and E in the considered coordinate system are determined using the following expressions (Stoĭkov & Atanasov, 2009):

$$\begin{aligned} B &= \operatorname{arctg}\frac{Z}{X}; \\ E &= \operatorname{arctg}\left(\frac{H}{X}\cos B\right). \end{aligned} \tag{5}$$

Projections D_{cx1}, D_{cy1}, D_{cz1} are determined in the expression:

$$\begin{bmatrix} D_{cxl} \\ D_{cyl} \\ D_{czl} \end{bmatrix} = A_{l,st} \begin{bmatrix} X \\ H \\ Z \end{bmatrix} \tag{6}$$

expression:

$$\begin{bmatrix} D_{нx1} \\ D_{ну1} \\ D_{нz1} \end{bmatrix} = A_{1,ст} \begin{bmatrix} X \\ H \\ Z \end{bmatrix} \tag{9.51}$$

where $A_{1,st}$ is the transition matrix for going from the Oxyz stabilized coordinate system to the $Ox_1y_1z_1$ coordinate system;

$$A_{1,st} = \begin{bmatrix} \cos\vartheta & \sin\vartheta & 0 \\ -\sin\vartheta\cos\gamma & \cos\vartheta\cos\gamma & \sin\gamma \\ \sin\vartheta\sin\gamma & -\cos\vartheta\sin\gamma & \cos\gamma \end{bmatrix}. \tag{7}$$

Angles B_1 и E_1 are determined by the formulas:

$$\begin{aligned} B_1 &= \operatorname{arctg}\left(\frac{D_{czl}}{D_{cxl}}\right); \\ E_1 &= \operatorname{arctg}\left(\frac{D_{cyl}\cos B_1}{D_{cxl}}\right). \end{aligned} \tag{8}$$

To determine the calculated angles of the movable grid B_c and E_c, are used the formulas:

$$\begin{aligned} B_в &= B; \\ E_в &= E_1 - \alpha_{mount}. \end{aligned} \tag{9}$$

Constantly Computed Release Point Modes

CCRP mods is used when $E_s > \varepsilon_{lim}$, i.e. the target in the process of aiming is hidden by the front part of the aircraft body before the moment of drop. In this case, the parameters q and p are determined by the formula (9). The current coordinates of the target η' и ξ' are determined by the formulas:

$$\begin{aligned} \eta' &= \eta'_0 - \eta'_{dist}; \\ \xi' &= \xi'_0 - \xi'_{dist}, \end{aligned} \tag{10}$$

where η'_{dist} and ξ'_{dist} is the distance traveled by the aircraft for the remaining time $t_{ост}$ from the target attachment to the moment of bomb dropping.

The distance traveled is determined by integrating the ground speed W of the aircraft. The initial coordinates of the target η'_0 and ξ'_0 are determined using the onboard sighting and rangefinder system. The distance traveled is determined by integrating the ground speed W of the aircraft. The initial coordinates of the target η'_0 and ξ'_0 are determined using the onboard sighting and rangefinder system. The calculated coordinates of the target , are determined by the formula:

$$\begin{bmatrix} \eta'_c \\ 0 \\ \xi'_c \end{bmatrix} = A_{\eta'\zeta'\xi',ст} \begin{bmatrix} X \\ 0 \\ Z \end{bmatrix}, \tag{11}$$

where $A_{\eta'\zeta'\xi',st} = \begin{bmatrix} \cos\psi & 0 & -\sin\psi \\ 0 & 1 & 0 \\ \sin\psi & 0 & \cos\psi \end{bmatrix}$

The remaining time t_r is determined by the equation:

$$t_r = \frac{\eta' - \eta'_c}{W_\eta}. \tag{12}$$

Пускането на бомбите се извършва автоматично при q=0, p=0.

Mathematical Model of Bomb Drop by Angular Velocity

Modern aircraft are equipped with new generation optical-electronic systems, which have tracking systems for automatic target designation. When the target is captured by the tracking system, the angular velocity of the target tracking is measured by sensors. This enables the pilot (operator) to continuously monitor the target, both at night and during the day. The angular velocity $\overline{\omega}$ of the target sighting line is a carrier of information about both the coordinates and the speed of the target. They are necessary for solving the aiming task when dropping bombs. Bomb-dropping is carried out when the angular velocity of the target tracking $\overline{\omega}$ is equalized with the calculated angular velocity of the target tracking $\overline{\omega}_c$, i.e. $\overline{\omega} = \overline{\omega}_c$.

The calculated angular velocity $\overline{\omega}_н$ is determined by the calculated coordinates of the target X and Z and the information about the flight parameters received from the radio-electronic equipment. The target and the area around it are shown on a display or the head-up display. If a mismatch is observed between the target and the aiming grid, the pilot makes a correction to eliminate it. When aiming at a moving target, it is necessary for the pilot (operator) to hold the aiming grid on the target when locking onto the target, so that synchronous tracking can be performed by the tracking device. The bomb is released automatically after the aiming parameters are zeroed.

$$\begin{aligned} q_{\omega i} &= \omega_i - \omega_{ic} \text{ - параметър на прицелване по посока;} \\ p_{\omega j} &= \omega_j - \omega_{jc} \text{- distance aiming parameter} \end{aligned} \tag{13}$$

where ω_i is the measured angular velocity of the axis Oi of the tracking device;
ω_j – the measured angular velocity of the axis Oi of the tracking device.

From the calculated calculated target coordinates X and Z and the current aircraft flight parameters, the calculated angular velocities ω_{ic}, ω_{jc} are calculated. The calculated X and Z coordinates are determined by the formula:

$$\begin{bmatrix} X \\ Y \\ Z \end{bmatrix} = \begin{bmatrix} A_x + U_x T + V_{цх} T \\ -H \\ U_z T + V_{цz} T \end{bmatrix}. \tag{14}$$

To determine the unknown quantities V_{tx} and V_{tz} the following expression is used:

$$\overline{W}_p = \overline{W} - \overline{V}_t .$$

$$\begin{bmatrix} V_{цх} \\ 0 \\ V_{цz} \end{bmatrix} = \begin{bmatrix} W_x \\ W_y \\ W_z \end{bmatrix} - A_{ст,l} A_{l,сл} \begin{bmatrix} W_{прг} \\ W_{прi} \\ W_{прj} \end{bmatrix}, \tag{15}$$

where W_{pr}, W_{pi}, W_{pj} are the projections of $\overline{W}_p$ on the axes of the system Orij.

The projections of $\overline{W}_p$ are determined by the formulas (Atanasov, 2007):

$$\begin{aligned} W_{pr} &= -\omega_{1i} l_j + \omega_{1j} l_i - \dot{D}; \\ W_{pi} &= \omega_{1r} l_j - \omega_{1j} l_r - \omega_j D; \\ W_{pj} &= -\omega_{1r} l_i + \omega_{1i} l_r + \omega_i D; \end{aligned} \tag{16}$$

The calculated angular velocities ω_{ic} и ω_{jc} are determined by formula. (16):

$$\begin{aligned} \omega_{jc} &= -\frac{W_{ic}}{D_н}; \\ \omega_{ic} &= \frac{W_{jc}}{D_c}, \end{aligned} \tag{17}$$

$$D_c = \sqrt{X^2 + H^2 + Z^2} \ .$$

From the above it is clear that the use of the method of bomb-dropping by angular velocity allows the velocity of the target to be calculated without prior detection, which makes it easier for the pilot to aim, and it is not necessary to measure the current distance D to the target. The presence of tracking systems (TS) in the TS when using this method allows the use of guided and unguided weapons in one attack.

Determining the Areas of Initial Conditions Under Which Bomb-Dropping Carried out

As a result of the mathematical modeling, are determined the possible ranges of initial conditions V_0, H_0 and λ at which bomb dropping is performed using TS – 1 and TS – 2. When dropping bombs at angular velocity (i.e. when using TS – 2), container-type targeting systems are also used, having thermal imaging electronic-optical sighting systems with multiple image magnification (from 20 to 30 times). This allows detection and recognition from long distances (up to 60 [km]) (Atanasov, 2007). For TS – 1, the ranges of initial conditions at which the CCIP and CCRP bomb dropping methods are used have been determined. The research was carried out at bomb-dropping from horizontal flight using TS – 1 and TS – 2 at speeds V=180 – 280 [m/s] and altitudes H=400 – 1800 [m] (Figure 3.6).

From Figure 2, it is clear that the range of conditions in which the CCRP method is used for bomb-dropping is larger than the range in which the CCIP method is used. When dropping bombs at a higher angular velocity, the range of possible initial conditions increases approximately 1.8 times compared to the same range in the CCIP and CCRP methods (Figure. 2).

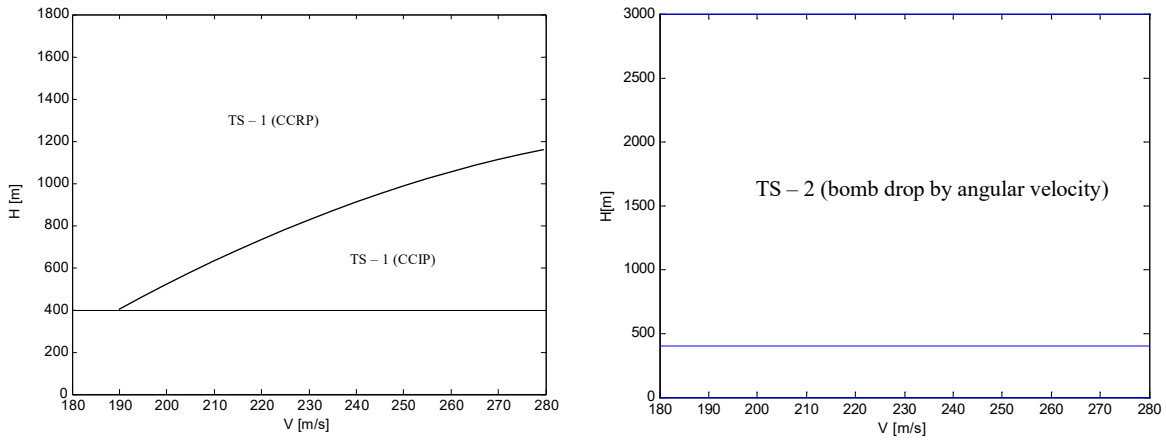

Figure 2 Areas of possible initial conditions for bomb-dropping from horizontal flight

The areas of possible initial conditions (PIC) for a dive bomb-dropping using TS – 1 and TS – 2 have been determined under the following conditions: V_0=180 – 260 [m/s]; H_0=900 – 3000 [m]; ε_0=-6^0, - 10^0, - 14^0; λ= - 20^0.

When dropping bombs with a dive angle of $\lambda = -20^0$, the area of PIC for bomb-dropping using TS – 2 increases approximately from 2.2 to 3 times compared to the same when using ATS – 1 (Figure 3). With an increase in ε_0, the area of PIC when using TS – 2 increases compared to the same when using TS – 1 (Figure 3). From Figure. 3 it is evident that for angles $\varepsilon_0 < -10^0$, bomb-dropping is performed using one of two methods - CCIP or CCRP (when using TS – 1).

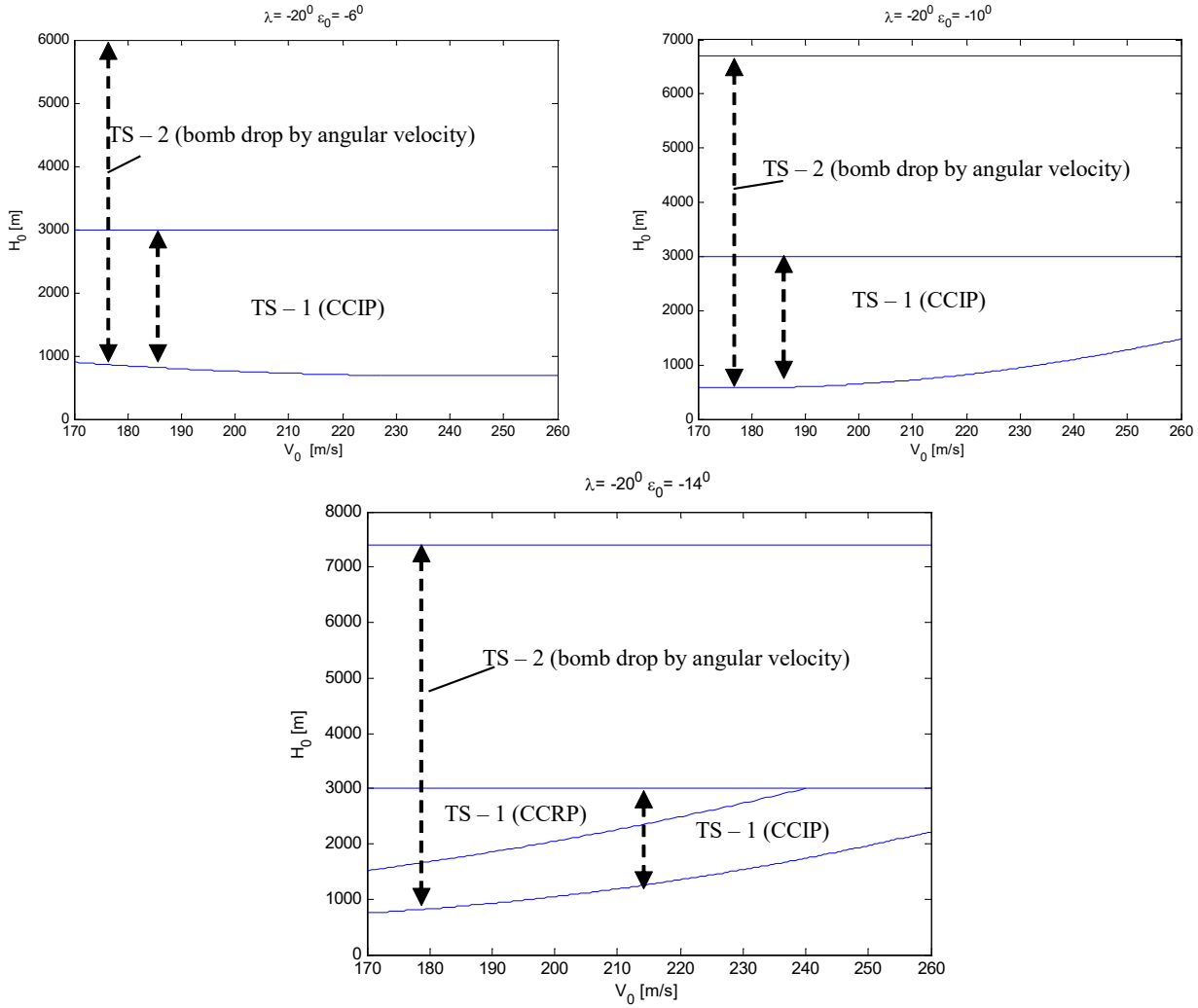

Figure 3. Range of possible initial conditions for a dive bomb drop with an angle of $\lambda = -20^0$

From Figure 2 and 3 the following conclusions can be drawn:

- The range of possible conditions for bomb-dropping from horizontal flight using TS – 2 is approximately 1.8 times larger compared to the same when using TS – 1.

The range of possible conditions for bomb-dropping from a dive using TS – 2 increases between 3.4 – 6.2 times compared to the same when using TS – 1.

- With a decrease in the target sighting angle ε_0, the range of possible initial conditions for bomb-dropping increases for TS – 1, and for TS – 2 it decreases.

- In order to expand the possible ranges of initial conditions for bomb-dropping from a dive using TS – 1, it is necessary for the initial target sighting angle ε_0 to decrease with the increasing of λ.

Determining the Probabilistic Characteristics of the Bomb-Dropping Error

Determining the Probabilistic Characteristics of the Bomb-Dropping Error When Using TS – 1.

When dropping bombs from a horizontal flight from altitudes up to 500 [m] using the CCIP and CCRP methods, the probable deviation E_x of the error Δx is determined by the dependence (Atanasov, 2007):

$$E_x=(20-30)\frac{1}{1000}H\ [m]; \tag{18}$$

When dropping a bomb from a horizontal flight from altitudes H=500 – 5000 [m], the probable deviation E_x is determined by (Atanasov, 2007):

$$E_x=(20-30)\frac{1}{1000}H\ [m]; \tag{19}$$

- during dive bombing and dive recovery bombing[16]:

$$E_x=(20-30)(1+\sin\lambda)\frac{1}{1000}H\ [m], \tag{20}$$

where

$$\sigma_{\Delta x}=E_x\ 1.4815. \tag{21}$$

From the empirical formulas (19) – (21) the limits of variation of the root mean square deviation of the bomb-dropping error are determined:

- from horizontal flight:

$$\sigma_{\Delta x\ min}=0.0296\ H\ [m];\ \sigma_{\Delta x\ max}=0.0444\ H\ [m]; \tag{22}$$

- from a dive:

$$\sigma_{\Delta x\ min}=0.0296\ (1+\sin\lambda)\ H\ [m];\ \sigma_{\Delta x\ max}=0.0444\ (1+\sin\lambda)\ H\ [m]; \tag{23}$$

As a result of the mathematical modeling, the probability characteristics of the bomb-dropping error ($\sigma_{\Delta x}$) from horizontal flight and dive using TS – 1 and TS – 2 are determined. The research is conducted for bomb-dropping from horizontal flight using TS – 1 for velocities and altitudes: V= 180 – 260 [m/s]; H=600 – 1800 [m].

As a result of the modeling, the calculated root mean square deviation $\sigma_{\Delta x}$ of the error Δx is shown in Table 1 and Figure 4. With the increase in the velocity V and the height H of the bomb-dropping, $\sigma_{\Delta x}$ changes from 21 to 57 [m]. The influence of the change in the velocity V on the value of $\sigma_{\Delta x}$ is less than the influence of the height H on $\sigma_{\Delta x}$ (Figure 4).

Table 1. Standard root mean square deviation $\sigma_{\Delta x}$ of the bomb-dropping error from horizontal flight

$\sigma_{\Delta x}$ [m] ($\lambda= 0^0$)					
	V=180 [m/s]	**200**	**220**	**240**	**260**
H=600 [m]	23.37	21.095	21.097	23.295	27.77
900	30.36	29.622	29.227	29.178	29.473
1200	38.36	38.286	37.61	36.331	34.45
1500	47.37	47.089	46.218	44.755	42.703
1800	57.39	56.03	55.05	54.45	54.23

Figure 4 shows that at H= 600 [m] and velocity V=200 – 220 [m/s]; H=900 [m] and velocity V=240 – 260 [m/s] the root mean square deviation $\sigma_{\Delta x}$ has minimal significance as the bomb-dropping method changes.

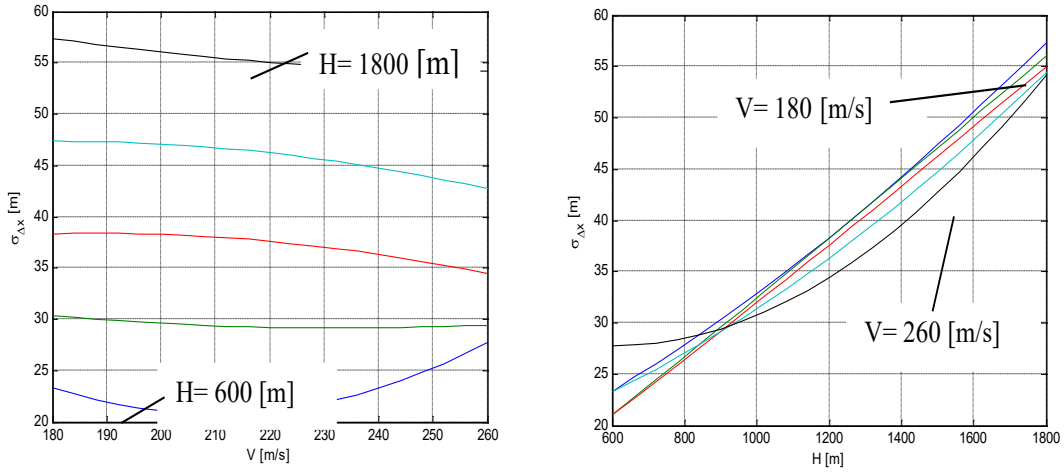

Figure 4. Dependence of $\sigma_{\Delta x}$ on V and H. when bomb-dropping from horizontal flight.

Table 2 gives values for the standard deviation of the error $\sigma_{\Delta xmin}$ and $\sigma_{\Delta xmax}$ obtained using fomula (22). Table 3 gives the standard deviations of the error $\sigma_{\Delta x}$ when bom-dropping with a dive angle of $\lambda = -20^0$ using TS – 1. At a height of H=1500 [m], V=180 – 200 [m/s] and for H=1800 [m], speeds of V=200 – 220 [m/s], the method of bomb-dropping is changed (CCRP with CCIP), as a result of which $\sigma_{\Delta x}$ becomes of minimal significance (Table 3).

Table 2. The limits of variation of $\sigma_{\Delta xmin}$ and $\sigma_{\Delta xmax}$ of the bomb-dropping error from horizontal flight

	$\sigma_{\Delta x\ min}$[m]	$\sigma_{\Delta x\ max}$[m]
H=600 [m]	17.7780	26.6670
900	26.6670	40.0005
1200	35.5560	53.3340
1500	44.4450	66.6675
1800	53.3340	80.0010

Table 3. Root mean square deviation $\sigma_{\Delta x}$ of the dive bombing error

$\sigma_{\Delta x}$ [m] ($\lambda = -20^0$)					
	V=180 [m/s]	**200**	**220**	**240**	**260**
H=600 [m]	11.57	12.184	12.8	13.419	14.04
900	14.561	15.909	17.121	18.199	19.141
1200	18.47	19.807	21.15	22.497	23.85
1500	23.296	23.88	24.886	26.315	28.166
1800	29.04	28.126	28.33	29.651	32.09

Determining the Probabilistic Characteristics of the Bomb-Dropping Error When Using TS – 2.

The probabilistic characteristics of the bomb-dropping error when using TS – 2 are determined under the same conditions under which they were determined for TS – 1. The root mean square deviation $\sigma_{\Delta x}$ of the bomb-dropping error from horizontal flight varies in the range from 18.23 to 47.31 [m], with the change in $\sigma_{\Delta x}$ having a steady character (Table 4). It is evident that $\sigma_{\Delta x}$ increases with the increase in the velocity V and the height H of the bomb-dropping, with the latter having a greater impact on the value of $\sigma_{\Delta x}$.

Table 4. Root mean square deviation $\sigma_{\Delta x}$ of the bomb drop error in angular velocity from horizontal flight

$\sigma_{\Delta x}$ [m] ($\lambda = 0^0$)					
	V=180 [m/s]	**200**	**220**	**240**	**260**
H=600 [m]	18.23	18.955	19.53	19.955	20.23
900	22.764	24.589	25.813	26.434	26.453
1200	27.02	29.537	31.38	32.547	33.04
1500	30.999	33.8	36.233	38.297	39.993
1800	34.7	37.376	40.37	43.681	47.31

The root mean square deviations $\sigma_{\Delta x}$ of the bomb-dropping error when diving with an angle $\lambda = -20^0$ obtained as a result of the modeling are given in Table 5. The values of $\sigma_{\Delta x}$ vary in the range from 8.93 to 27.49 [m], and they increase with the increasing of the velocity V and height H of bomb-dropping (Table 5). The values of $\sigma_{\Delta x}$ decrease with the increasing of the dive angle λ.

Table 5. Root mean square deviation $\sigma_{\Delta x}$ of the bomb drop error in angular velocity from dive

$\sigma_{\Delta x}$ [m] ($\lambda = -20^0$)					
	V=180 [m/s]	**200**	**220**	**240**	**260**
H=600 [m]	8.9346	9.1808	9.4705	9.8035	10.18
900	12.584	13.446	14.019	14.304	14.301
1200	16.2	17.405	18.2	18.585	18.56
1500	19.782	21.059	22.014	22.646	22.956
1800	23.33	24.407	25.46	26.488	27.49

Comparative Analysis of the Probabilistic Characteristics of the Bomb-Dropping Error from Horizontal Flight

As a result of the mathematical modeling, a comparative analysis of the accuracy of bomb-dropping from horizontal flight using TS-1 and TS-2 is carried out, and for this purpose is determined $\sigma_{\Delta x1}$:

$$\Delta\sigma_{\Delta x}=\sigma_{\Delta x1} - \sigma_{\Delta x2}; \tag{24}$$

Table 6 shows the differences $\Delta\sigma_{\Delta x}$ for the considered bomb-dropping conditions. For the entire range of bomb-dropping conditions from horizontal flight, the difference $\Delta\sigma_{\Delta x}$ is greater than zero. This shows that the root mean square deviation $\sigma_{\Delta x2}$ of the error when using TS – 2 is smaller than the same when using TS – 1. The difference $\Delta\sigma_{\Delta x}$ varies in the range from 1.41 to 22.69 [m]. For bomb-dropping speeds and heights at which the bomb-dropping method changes (when using TS – 1), $\Delta\sigma_{\Delta x}$ takes minimum values (Figure 6).

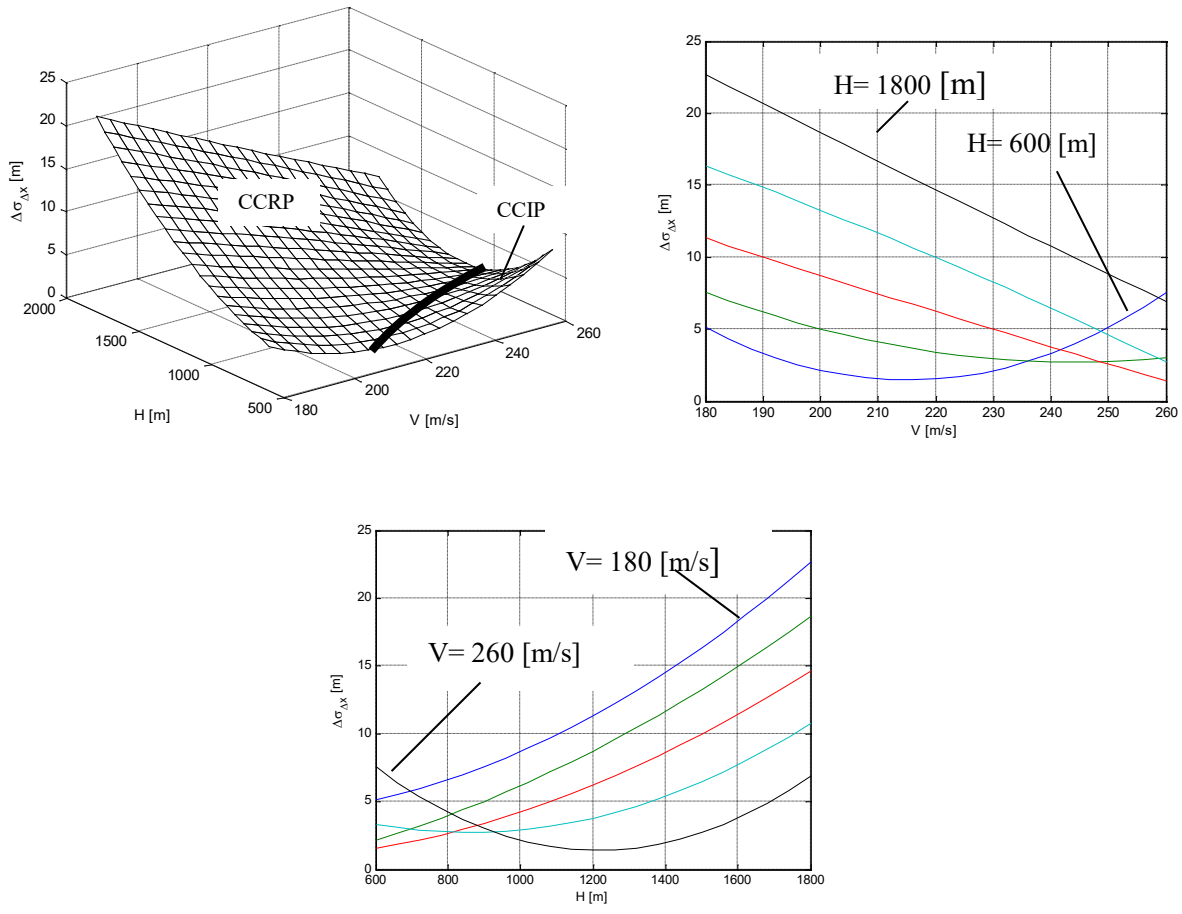

Figure 5. Dependence of $\Delta\sigma_{\Delta x}$ on V and H during bomb-dropping from horizontal flight

Table 6. Comparative analysis of bomb drop accuracy from horizontal flight

$\Delta\sigma_{\Delta x}$ [m] ($\lambda = 0^0$)					
	V=180 [m/s]	**200**	**220**	**240**	**260**
H=600 [m]	5.14	2.14	1.54	3.34	7.54
900	7.596	5.033	3.414	2.744	3.02
1200	11.34	8.749	6.23	3.784	1.41
1500	16.371	13.289	9.985	6.458	2.71
1800	22.69	18.654	14.68	10.769	6.92

A comparative analysis of the probabilistic characteristics of the bomb-dropping error from dives with angles $\lambda = -20^0$ when using TS – 1 and TS – 2 for bomb-dropping velocities and heights: V=180 – 260 [m/s]; H=600 – 1800 [m] is performed.

Table 7. Comparative analysis of dive bombing accuracy

$\Delta\sigma_{\Delta x}$ [m] ($\lambda = -20^0$)					
	V=180 [m/s]	**200**	**220**	**240**	**260**
H=600 [m]	2.64	3.00	3.33	3.62	3.86
900	1.98	2.46	3.10	3.90	4.84
1200	2.27	2.40	2.95	3.91	5.29
1500	3.51	2.82	2.87	3.67	5.21
1800	5.71	3.71	2.87	3.16	4.60

From Tables 7 it can be seen that the bomb-dropping accuracy with the use of TS – 2 is greater than when using TS – 1 with a dive angle $\lambda = -20^0$.

Conclusion

1. The results obtained from the mathematical modeling of the aiming process with the targeting system using the bomb-dropping methods of indicating the point of CCRP and indicating the moment of bomb-dropping are analogous to the results obtained from the objective control system of a fighter-bomber aircraft, the methodological manual for combat use.
2. The range of possible initial conditions for bomb-dropping by angular velocity from horizontal flight increases approximately 1.8 times, and when diving it increases between 1.4 and 6.2 times compared to the same when using existing bomb-dropping methods.
3. With an increase in the dive angle, the range of possible initial conditions decreases when using the currently employed aircraft targeting systems, and with a targeting system using the bomb-dropping by angular velocity method, the same range increases.
4. When using the bomb-dropping by angular velocity method from horizontal flight, the root mean square deviation of the bomb-dropping error decreases by 1.41 – 22.69 [m], and when diving - by 1.64 – 12.72 [m] compared to the same when using existing methods.
5. The method of bomb-dropping by angular velocity allows:

- bomb-dropping with unguided bombs from airplanes, helicopters and unmanned aerial vehicles at any time of the day and in any weather conditions;
- the use of guided and unguided weapons in one attack;
- he delivery of various cargoes to hard-to-reach areas, fire extinguishing, fighting snow

Recommendations

1. When aiming, the pilot, using the control elements of the tracking system, places the marker on the target and performs a target lock.
2. The subsequent flight should be carried out so that the predicted line of the CCRP points passes through the target.
3. When the given conditions are met, the drop will be carried out automatically on the corresponding section of the trajectory.

Scientific Ethics Declaration

* The author declare that the scientific ethical and legal responsibility of this article published in EPSTEM Journal belongs to the author.

Conflict of Interest

* The authors declare that they have no conflicts of interest

Funding

* This research received no specific grant from any funding agency in the public, commercial, or not-for-profit sectors.

Acknowledgements or Notes

* This article was presented as oral presentation at the International Conference on Basic Sciences, Engineering and Technology (www.icbaset.net) held in Trabzon/Türkiye on May 01-04, 2025.

* The research in this article was carried out in fulfilment of Task 3.1.4. "Research, development and improvement of munitions" from the National Scientific Program "Security and Defence", adopted by RMS No. 731 of 21.10.2021. and according to Agreement No. D01-74/19.05.2022.

References

Atanasov, M. (2014), *Tochnost na reshavane na zadachata na pritselvane s neupravlyaemi aviatsionni bombi*, Pleven, Bulgaria: Monografiya.

Atanasov, M. (2007). *Vŭzmozhnosti za reshavane na zadachata na pritselvane pri bombopuskane po ŭglova skorost*. (Dissertation).

Kambushev M., Biliderov S., Yovchev K., Chikurtev D., Kambushev K., Chivarov N. (2019). Influence of atmospheric turbulence on the control of flying robotics systems. *XXVIII International Scientific Conference Electronics (ET)* (pp. 1-4). IEEE.

Stoĭkov O., Atanasov M. (2009). *Aviatsionni pritselni sistemi – Pŭrva chast*. Bulgaria, Dolna Mitropoliya:VGTS.

Author Information

Milen Atanasov
Georgi Benkovski Bulgarian Air Force Academy
St. St. Ciril and Methodius 1, 5855, Dolna Mitropolia
Bulgaria
Contact e-mail: *matanasov@af-acad.bg,*

To cite this article:

Atasanov, M. (2025). Accuracy of different modes of bomb dropping from aircraft. *The Eurasia Proceedings of Science, Technology, Engineering and Mathematics (EPSTEM), 34,* 139-150.

The Eurasia Proceedings of Science, Technology, Engineering & Mathematics (EPSTEM)
ISSN: 2602-3199

The Eurasia Proceedings of Science, Technology, Engineering and Mathematics (EPSTEM), 2025

Volume 34, Pages 151-164

ICBASET 2025: International Conference on Basic Sciences, Engineering and Technology

Variational Principle for Studying the Long-Term Stability of Structural Materials Subjected to Neutron Irradiation Taking into Account Geometric Nonlinearity

Abdulla Hasanov
Nakhchivan State University

Yusif Orujov
Azerbaijan State University of Oil and Industry

Abstract: In various branches of modern engineering, including nuclear power engineering and rocket and space technology, structural elements in various forms are widely used. During operation, they can be subjected to both force and non-mechanical loads (thermal, radiation). During operation, they are subjected to radiation loads. Thus, neutron fluxes, penetrating deep into the material, radically change its mechanical properties. Moreover, when irradiated for several years and at high temperatures, as is the case in nuclear reactors, creep deformations become significant, and irradiation and temperature affect the creep of materials differently. Therefore, in those areas of technology where neutron radiation and high temperatures are present, when designing structures, it is necessary to take into account the effect of radiation and temperature on the mechanical properties of the material. The task is further complicated when taking into account geometric nonlinearity.It is practically impossible to obtain an exact solution to such problems, therefore the development of approximate methods is of particular importance. In nonlinear problems, one of the effective approximate methods of solution is the variational method. To solve long-term stability problems by the variational method, it is necessary to develop these methods to be able to take into account geometric nonlinearity and changes in mechanical characteristics. This means that it is necessary to construct a functional that would take into account changes in the mechanical characteristics of the body, taking into account creep deformation and geometric nonlinearity.The article proposes a functional for studying the stability of structural materials (the stress-strain state (SSS) of a body) under neutron irradiation, taking into account geometric nonlinearity and creep deformations. It is proven that the Euler equations of the functional take the form of an equation describing the stress-strain state of a thin shell under irradiation, taking into account geometric nonlinearity and creep deformations.

Keywords: Creep deformation, Variational principle, Neutron, Deformation components, Stress-strain state

Introduction

The development of nuclear energy, rocket, and space technology requires a particularly careful approach to the issues of strength and stability of structures under the influence of radiation. The study of the effects of neutron radiation on the strength and stability of structures is of particular importance. Neutron streams, penetrating deep into the material, sharply alter its mechanical properties. Moreover, when radiation exposure continues for several years and the temperature is high, as is the case in nuclear reactors, creep deformations become significant, with radiation and temperature affecting the creep of materials differently.

Radiation-induced changes in the mechanical properties and swelling of structural materials can significantly affect the performance of active zone elements, and these factors should be considered when determining the kinetics of stressed and deformed states (Likhachev & Pupko, 1975). Therefore, many issues related to the

calculation of the stress-strain state and the determination of performance considering the specifics of the structures require further development and improvement. In particular, it is necessary to develop mathematical methods for solving systems of equations that describe the kinetics of the stress-strain state of structures. A more detailed study of the patterns of deformation and swelling processes of dividing and structural materials is needed (Likhachev & Pupko, 1975). In connection with the widespread use of nuclear energy for peaceful purposes, many scientists began to address the issues of the impact of radiation on the mechanical properties of materials.

The first observations of measurements of elastic properties as a result of irradiation were made for graphite (Wassilew C. et al., 1987). It was found that irradiation of graphite in a reactor leads to the formation of a harder and more brittle material. The Young's modulus increases by approximately three times after irradiation with a dose. The first theoretical calculations were carried out for metals by Denis (1952).

Detailed calculations, taking into account the relaxation of the nearest neighboring atoms, led to the following conclusions: the presence of a small fraction of implanted atoms and vacancies results in a significant increase in the elastic modulus of copper—by 5–7% per 1% of implanted atoms. It was established that in the case of vacancies alone, the reduction in the modulus occurs mainly due to the influence of the entire mass of the material. Consequently, the increase in the elastic modulus is primarily associated with the presence of implanted atoms. A considerable increase in the modulus was experimentally observed by Thompson and Holmes (1956) in copper monocrystals after irradiation in a reactor. In the book by Glesston and Edlund (1954), the following formula is derived, which shows the law by which the intensity of radiation decreases with depth in the material:

$$J_z = J_0 e^{-N\sigma z} \text{ or } J(z) = J_0 \exp(-\mu z)$$

where σ -is the microscopic cross-section, $N\sigma$ -is the macroscopic cross-section, N is the number of nuclei in $1sm^3$ of the irradiated material, $\mu = const$ - is the macroscopic cross-section, $[\mu] = 1/см$, J_0 - is the irradiation intensity on the surface, J_z - is at a depth from the surface. The value of σ - depends on the energy of the bombarding neutron. The macroscopic cross-section is defined as:

$$\mu = N \cdot \sigma \text{ or } \mu = N_0 \cdot \frac{\rho}{A} \cdot \sigma,$$

where $N_0 = 6{,}02 \cdot 10^{23}$ -is Avogadro's number, ρ -is the density of the irradiated material, A -is the atomic weight of the material.

Many works are devoted to studying the effect of irradiation on the radiation creep of structural materials and fuel elements (Gulgazli& Efendiev, 2017; Gorokhovet al., 2020; Breslavsky & Tatarinova, 2023; Onimus et al., 2020). In the book by Likhachev and Pupko (1975) the creep strain rate for an irradiated body is presented in the following form:

$$\dot{\varepsilon}_{ij}^{c} = \frac{3}{2} F_c \frac{S_{ij}}{\sigma_u}$$

where - S_{ij} is the stress deviator components, σ_u - is the stress intensity, $F_c = F_c(\sigma_u, T, D)$ is determined from experience, $\dot{\varepsilon}_{ij}^{c}$ -is the creep deformation rate, T- is the temperature, D- is the radiation dose.

Formulation of the Variational Principle

Basic Ratios

Let a body of volume V be irradiated by an intense flux of neutrons: on part S_σ of the surface, surface forces are specified, and on the remaining part S_u of the surface, displacements are specified. Then the equilibrium equation, taking into account geometric nonlinearity, the relationship between the rates of the components of

deformations and stresses, and the boundary conditions in the Cartesian coordinate system have the following form (Volmir,1972; Amenzade, 1976; Aliyev et al., 2024):

$$\left[\sigma_{ij}(u_{\alpha,i}+\delta_{\alpha i})\right]_{,j}=0\,, \tag{1}$$

$$\dot{\varepsilon}_{ij}=\dot{\varepsilon}_{ij}^{e}+\dot{\varepsilon}_{ij}^{p}+\dot{\varepsilon}_{ij}^{c}+\dot{\varepsilon}_{ij}^{v}\,, \tag{2}$$

$$\dot{\varepsilon}_{ij}^{e}=\frac{1}{E}\left[\dot{\sigma}_{ij}-\nu(3\dot{\sigma}\delta_{ij}-\dot{\sigma}_{ij})\right]-\frac{1}{E}\left[\left(3\delta_{ij}\sigma-\sigma_{ij}\right)\left(\frac{\partial\nu}{\partial T}\dot{T}+\frac{\partial\nu}{\partial D}\dot{D}\right)\right]-$$

$$-\frac{1}{E^{2}}\left[\sigma_{ij}-\nu\left(3\sigma\delta_{ij}-\sigma_{ij}\right)\right]\left(\frac{\partial E}{\partial T}\dot{T}+\frac{\partial E}{\partial D}\dot{D}\right),$$

$$\dot{\varepsilon}_{ij}^{p}=\left[F_{\sigma}\dot{\sigma}_{u}+F_{T}\dot{T}+F_{D}\dot{D}\right]\cdot S_{ij}\,,$$

$$\dot{\varepsilon}_{ij}^{c}=\frac{3S_{ij}}{2\sigma_{u}}\cdot F_{c}\,,$$

$$\dot{\varepsilon}_{ij}^{v}=\frac{\partial(\alpha T)}{\partial T}\cdot\dot{T}\delta_{ij}+\frac{1}{3}\dot{S}\delta_{ij}\,,$$

$$\begin{cases}\sigma_{ij}\left(\delta_{\alpha i}+u_{\alpha,i}\right)\cdot n_{j}=\overline{N}_{\alpha} & на\ \ S_{\sigma},\\ u_{i}=\overline{u}_{i} & на\ \ S_{u},\end{cases} \tag{3}$$

where σ_{ij} -are the stress tensor components, $\dot{\varepsilon}_{ij}=\dot{\varepsilon}_{ij}^{e}+\dot{\varepsilon}_{ij}^{p}+\dot{\varepsilon}_{ij}^{c}+\dot{\varepsilon}_{ij}^{v}$ are the strain tensor components, ε_{ij}^{e} - and ε_{ij}^{p} - are, respectively, the elastic and plastic strain components, ε_{ij}^{c} -are the creep strain components, ε_{ij}^{v} - are the volume strain components that arise due to temperature and irradiation, $E(D,T)$ - is Young's modulus, $\nu(D,T)$ - is Poisson's ratio, S_{ij} - are the stress deviator components, α - is the coefficient of thermal expansion, $\overline{N}_{i}$ -are the components of the surface force vector, $\overline{u}_{i}$ - are the displacements on the surface S_{u}, a δ_{ij} -are the Kronecker symbols, $\sigma_{u}=\sqrt{\frac{3}{2}S_{ij}S_{ij}}$ -are the intensities of shear stresses, $\sigma=\frac{1}{3}\sigma_{ii}$ - is the hydrostatic pressure, $F_{\sigma}(\sigma_{u},T,D),F_{T}(\sigma_{u},T,D),F_{D}(\sigma_{u},T,D)$ do not depend on the type of stress state and are determined from experience under uniaxial tension as follows (Likhachev & Pupko, 1975):

$$F_{\sigma}=\frac{3}{2\sigma_{u}}\left(\frac{1}{E_{k}}-\frac{1}{E}\right),$$

where $E_{k}(\sigma_{u},T,D)=\frac{d\sigma_{0}}{d\varepsilon_{0}}$ is the tangent modulus, σ_{0} and ε_{0} are the stress and strain under uniaxial tension, respectively,

$$F_{T}=\frac{3}{2\sigma_{u}}\left(\beta+\frac{1}{E^{2}}\cdot\frac{dE}{dT}\cdot\sigma_{u}\right),$$

where $\beta(\sigma_{u},T,D)=\frac{d\varepsilon_{0}}{dT}$ is the coefficient of temperature compliance, $F_{D}=\frac{3}{2\sigma_{u}}\gamma$, $\gamma(\sigma_{u},T,D)=\frac{d\varepsilon_{0}}{dD}$ is the coefficient of radiation compliance, $F_{c}(\sigma_{u},T,D)$ - is determined from experience, $S(T,D)$ - is the swelling function, n_{α} - are the components of the normal to the surface of the body. The dot over the values means

differentiation with respect to time, and the comma means covariant differentiations. The summation from 1 to 3 is performed over repeating indices.

Functional of the Variational Principle

The proposed functionality for this task is as follows:

$$J=\int_V\Bigg\{\dot\sigma_{ij}\dot\varepsilon_{ij}+\frac{1}{2}\sigma_{ij}\dot u_{\alpha,j}\dot u_{\alpha,i}-\dot\sigma_{ij}\Bigg[\frac{1}{2E}\left(\dot\sigma_{ij}-\nu\left(3\dot\sigma\delta_{ij}-\dot\sigma_{ij}\right)\right)-\frac{1}{E}\left(3\sigma\delta_{ij}-\sigma_{ij}\right)\left(\frac{\partial\nu}{\partial T}\dot T+\frac{\partial\nu}{\partial D}\dot D\right)-$$

$$-\frac{1}{E^2}\left(\sigma_{ij}-\nu(3\sigma\delta_{ij}-\sigma_{ij})\right)\cdot\left(\frac{\partial E}{\partial T}\dot T+\frac{\partial E}{\partial D}\dot D\right)+\left(\frac{1}{2}F_\sigma\dot\sigma_u+F_T\dot T+E_D\dot D\right)S_{ij}+\frac{3}{2}F_c\cdot\frac{S_{ij}}{\sigma_u}+$$

$$+\frac{\partial(\alpha T)}{\partial T}\dot T\delta_{ij}+\frac{1}{3}\dot S\delta_{ij}\ \Bigg]\Bigg\}dV-\left(\int_{S_\sigma}\dot{\bar N}_i\dot u_i ds+\int_{S_u}\left(\dot u_i-\dot{\bar u}\right)\dot N_i\right)ds \tag{4}$$

Proof

Let us prove that the Euler equations of the proposed functional (4) give the system (1), (2) and (3). Let us calculate the first variation of the functional (4). Let us assume that only the speeds of displacements and stresses vary.

$$\delta J=\int_V\Bigg\{\dot\sigma_{ij}\delta\dot\varepsilon_{ij}+\dot\varepsilon_{ij}\delta\dot\sigma_{ij}+\sigma_{ij}\dot u_{\alpha,i}\delta\dot u_{\alpha,j}-\Bigg[\frac{1}{2E}\left(\dot\sigma_{ij}-\nu\left(3\dot\sigma\delta_{ij}-\dot\sigma_{ij}\right)\right)-$$

$$-\frac{1}{E}\left(3\sigma\delta_{ij}-\sigma_{ij}\right)\left(\frac{\partial\nu}{\partial T}\dot T+\frac{\partial\nu}{\partial D}\dot D\right)-\frac{1}{E^2}\left(\sigma_{ij}-\nu(3\sigma\delta_{ij}-\sigma_{ij})\right)\times$$

$$\times\left(\frac{\partial E}{\partial T}\dot T+\frac{\partial E}{\partial D}\dot D\right)+\left(\frac{1}{2}F_\sigma\dot\sigma_u+F_T\dot T+F_D\dot D\right)S_{ij}+\frac{3}{2}F_c\cdot\frac{S_{ij}}{\sigma_u}+$$

$$+\frac{\partial(\alpha T)}{\partial T}\dot T\delta_{ij}+\frac{1}{3}\dot S\delta_{ij}\ \Bigg]\delta\dot\sigma_{ij}-$$

$$-\dot\sigma_{ij}\Bigg[\frac{1}{2E}\left(\delta\dot\sigma_{ij}-\nu\left(3\delta_{ij}\delta\dot\sigma-\delta\dot\sigma_{ij}\right)\right)+\frac{1}{2}F_\sigma S_{ij}\delta\dot\sigma_u\ \Bigg]\Bigg\}dV-$$

$$-\int_{S_\sigma}\dot{\bar N}_i\delta\dot u_i ds+\int_{S_u}\left(\dot u_i-\dot{\bar u}\right)\delta\dot N_i ds\,. \tag{5}$$

Here we took into account $\delta\dot{\bar N}_i=0$ - on S_σ and $\delta\dot{\bar u}_i=0$ on S_u. We transform the integrand. It is known that

$$\varepsilon_{ij}=\frac{1}{2}\left(u_{i,j}+u_{j,i}+u_{\alpha,i}u_{\alpha,j}\right)$$

then

$$\dot\varepsilon_{ij}=\frac{1}{2}\left(\dot u_{i,j}+\dot u_{j,i}+\dot u_{\alpha,i}u_{\alpha,j}+u_{\alpha,i}\dot u_{\alpha,j}\right).$$

$$\delta\dot{\varepsilon}_{ij} = \frac{1}{2}\left(\delta\dot{u}_{i,j} + \delta\dot{u}_{j,i} + u_{\alpha,j}\delta\dot{u}_{\alpha,i} + u_{\alpha,i}\delta\dot{u}_{\alpha,j}\right) =$$

$$= \frac{1}{2}\left(\delta\dot{u}_{i,j} + u_{\alpha,i}\delta\dot{u}_{\alpha,j}\right) + \frac{1}{2}\left(\delta\dot{u}_{j,i} + u_{\alpha,j}\delta\dot{u}_{\alpha,i}\right) \tag{6}$$

In (6) taking into account $\delta\dot{u}_{i,j} = \delta_{\alpha i}\delta\dot{u}_{\alpha,j}$ and $\delta\dot{u}_{j,i} = \delta_{\alpha j}\delta\dot{u}_{\alpha,i}$, we then obtain:

$$\delta\dot{\varepsilon}_{ij} = \frac{1}{2}\left(\delta_{\alpha i} + u_{\alpha,i}\right)\delta\dot{u}_{\alpha,j} + \frac{1}{2}\left(\delta_{\alpha j} + u_{\alpha,j}\right)\delta\dot{u}_{\alpha,i} \tag{7}$$

Taking into account (7), we transform the first term (5) as follows:

$$\int_V \dot{\sigma}_{ij}\delta\dot{\varepsilon}_{ij}dV = \int_V \dot{\sigma}_{ij}\left(\delta_{\alpha i} + u_{\alpha,i}\right)\delta\dot{u}_{\alpha,j}dV =$$

$$\int_V \left[\dot{\sigma}_{ij}\left(\delta_{\alpha j} + u_{\alpha,i}\right)\delta\dot{u}_{\alpha}\right]_{,j} dV - \int_V \left[\dot{\sigma}_{ij}\left(\delta_{\alpha i} + u_{\alpha,i}\right)\right]_{,j}\delta\dot{u}_{\alpha}dV \tag{8}$$

When obtaining (8), we took into account the symmetry of the tensor σ_{ij} . Applying the Gauss-Ostrogradsky theorem, from (8) we obtain:

$$\int_V \dot{\sigma}_{ij}\delta\dot{\varepsilon}_{ij}dV = \int_{S_\sigma + S_u} \dot{\sigma}_{ij}\left(\delta_{\alpha i} + u_{\alpha,i}\right)\delta\dot{u}_{\alpha}n_j dS - \int_V \left[\dot{\sigma}_{ij}\left(\delta_{\alpha i} + u_{\alpha,i}\right)\right]_{,j}\delta\dot{u}_{\alpha}dV\,, \tag{9}$$

where n_j - are the components of the normal to the surface *S*.

We transform the third term in (5) as follows:

$$\int_V \sigma_{ij}\dot{u}_{\alpha,i}\delta\dot{u}_{\alpha,j}dV = \int_V \left[\sigma_{ij}\dot{u}_{\alpha,i}\delta\dot{u}_{\alpha}\right]_{,j} dV - \int_V \left[\sigma_{ij}\dot{u}_{\alpha,i}\delta\dot{u}_{\alpha}\right]_{,j}\delta\dot{u}_{\alpha}dV =$$

$$= \int_{S_\sigma + S_u} \sigma_{ij}\dot{u}_{\alpha,i}\delta\dot{u}_{\alpha}n_j dS - \int_V \left[\sigma_{ij}\dot{u}_{\alpha,i}\right]_{,j}\delta\dot{u}_{\alpha}dV \tag{10}$$

Let us transform the following terms into (5):

$$\int_V \left[\frac{1}{2E}\left(\dot{\sigma}_{ij} - \nu\left(3\dot{\sigma}\delta_{ij} - \dot{\sigma}_{ij}\right)\right)\delta\dot{\sigma}_{ij} + \frac{1}{2E}\left(\delta\dot{\sigma}_{ij} - \nu\left(3\delta_{ij}\delta\dot{\sigma} - \delta\dot{\sigma}_{ij}\right)\right)\dot{\sigma}_{ij}\right]dV =$$

$$= \int_V \left[\frac{1}{E}\left(\dot{\sigma}_{ij} - \nu\left(3\dot{\sigma}\delta_{ij} - \dot{\sigma}_{ij}\right)\right)\delta\dot{\sigma}_{ij}\right]dV\,. \tag{11}$$

In obtaining (11) we used the following equalities:

$$\dot{\sigma}\delta\dot{\sigma}_{ij}\delta_{ij} = 3\dot{\sigma}\delta\dot{\sigma}\,, \quad \dot{\sigma}_{ij}\delta\dot{\sigma}\delta_{ij} = 3\dot{\sigma}\delta\dot{\sigma}\,,$$

and also took into account that σ_{ij} is a symmetric tensor.

$$\int_V \left(\frac{1}{2} F_\sigma \dot{\sigma}_u S_{ij} \delta \dot{\sigma}_{ij} + F_\sigma \dot{\sigma}_{ij} S_{ij} \delta \dot{\sigma}_u \right) dV = \int_V F_\sigma \dot{\sigma}_u S_{ij} \delta \dot{\sigma}_{ij} dV \tag{12}$$

When receiving (12) we used the fact that

$$\frac{1}{2} F_\sigma \dot{\sigma}_u S_{ij} \delta \dot{\sigma}_{ij} = \frac{1}{2} F_\sigma \left(\sqrt{\frac{3}{2} S_{\alpha\beta} S_{\alpha\beta}} \right)^{\cdot} S_{ij} \cdot \delta \left(\dot{S}_{ij} + \dot{\sigma} \delta_{ij} \right) =$$

$$= \frac{3}{4} F_\sigma \cdot \frac{1}{\sigma_u} \dot{S}_{\alpha\beta} S_{\alpha\beta} S_{ij} \delta \dot{S}_{ij},$$

$$\frac{1}{2} F_\sigma \cdot \frac{3}{2} \cdot \frac{1}{\sigma_u} \cdot \dot{S}_{\alpha\beta} S_{\alpha\beta} S_{ij} \delta \dot{\sigma} \delta_{ij} = 0,$$

$$\frac{1}{2} F_\sigma \cdot \dot{\sigma}_{ij} S_{ij} \delta \dot{\sigma}_u = \frac{1}{2} F_\sigma \cdot \cdot S_{ij} \left(\dot{S} + \dot{\sigma} \delta_{ij} \right) \delta \left(\sqrt{\frac{3}{2} S_{\alpha\beta} S_{\alpha\beta}} \right)^{\bullet} =$$

$$= \frac{3}{4} F_\sigma \cdot \frac{1}{\sigma_u} \dot{S}_{\alpha\beta} S_{\alpha\beta} S_{ij} \delta \dot{S}_{ij}.$$

Thus, for the first variation, taking into account the transformations (8), (10) (11), (12) we obtain:

$$\delta J = \int_{S_\sigma} \left[\sigma_{ij} \left(u_{\alpha,i} + \delta_{\alpha i} \right) n_j - \overline{N}_\alpha \right]^{\bullet} \delta \dot{u}_\alpha dS + \int_V \left[\left(\dot{\varepsilon}_{ij} - \dot{\varepsilon}^e_{ijj} - \dot{\varepsilon}^p_{ij} - \dot{\varepsilon}^c_{ij} - \dot{\varepsilon}^Y_{ij} \right) \delta \dot{\sigma}_{ij} \right] dV -$$

$$- \int_V \left[\sigma_{ij} \left(u_{\alpha,i} + \delta_{\alpha i} \right) \right]_{,j} \delta \dot{u}_\alpha dV - \int_{Su} \left(\dot{u}_i - \dot{\overline{u}}_i \right) \delta \dot{N}_i ds.$$

Equating δJ to zero and using the fundamental lemma of the calculus of variations, we obtain (Elsholts,1969):

$$\left[\sigma_{ij} \left(u_{\alpha,i} + \delta_{\alpha i} \right) \right]^{\bullet}_{,j} = 0, \tag{13}$$

$$\dot{\varepsilon}_{ij} = \dot{\varepsilon}^e_{ijj} + \dot{\varepsilon}^p_{ij} + \dot{\varepsilon}^c_{ij} + \dot{\varepsilon}^v_{ij}, \tag{14}$$

$$\begin{aligned} &\left[\sigma_{ij} \left(u_{\alpha,i} + \delta_{\alpha i} \right) n_j \right]^{\bullet} = \dot{\overline{N}}_\alpha \qquad \text{на } S_\sigma \\ &\dot{u}_i = \dot{\overline{u}}_i \qquad\qquad\qquad\qquad \text{на } S_u \end{aligned} \tag{15}$$

Integrating (13), (14), (15) over time and taking into account that there was no irradiation at the initial moment of time, we obtain the complete system (1), (2), (3). Thus, we have shown that the stationary state of the proposed functional is achieved on functions describing the stress-strain state of a deformable solid under irradiation, taking into account geometric nonlinearity and creep deformation.

Long-Term Stability of the Rod

Statement of the Problem

A prismatic rod of constant thickness $2h$ is rigidly fixed at the ends and is irradiated with a neutron flux so that the irradiation intensity is constant along the lateral surface. It is assumed that the rod is thin, i.e. $\gamma = h/l << 1$ ($2l$ is the length of the rod), temperature $T = const$, Poisson's coefficient $\nu = const$. We assume that the irradiation is one-sided.

Let us take a right-hand Cartesian coordinate system *Oxyz* so that the *x*-axis is directed along the rod axis and passes through the center of gravity of the cross-section, and the *y*- and *z*-axes are directed along the principal axes of inertia of the cross-section (Figure 1).

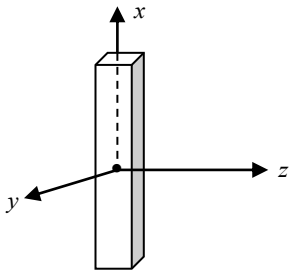

Figure 1.

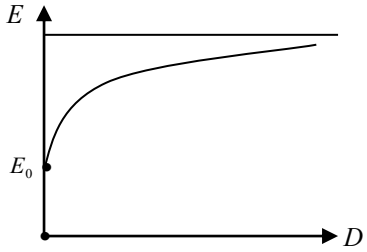

Figure 2.

We make the following assumptions: 1) The points of the middle surface do not move along the *x*-axis, and the geometric nonlinearity exists only in the normal direction *z*; 2) The Kirchhoff-Love hypothesis is satisfied, i.e., $\varepsilon_{xz} = \varepsilon_{yz} = \varepsilon_{zz} = 0$, where the *z*-coordinate is directed along the normal; 3) The points of the beam do not move along the *y*-axis, and the other quantities do not depend on *y*. Then, the components of the strain tensor of the middle surface and the components of its bending are expressed through the components of the displacement vector on the middle surface as follows:

$$\varepsilon = \frac{1}{2}\left(\frac{\partial w}{\partial x}\right)^2; \quad \theta = -\frac{\partial^2 w}{\partial r^2}, \tag{16}$$

where $w(x,t)$ - displacement of the mid-layer point in the direction of the z-axis; $\varepsilon(x,t), \theta(x,t)$ - accordingly, deformation and change of curvature on the mid-surface of the rod, *t* - time.

In solving this problem, following theoretical and experimental work, we assume that under irradiation, Young's modulus increases monotonically depending on the irradiation dose *D*, but is limited from above, and therefore Young's modulus *E* (*D*) is selected in the form (Cybulskise, 1971; Murray,1972; Onimus et al., 2020) (Fig. 2).

$$E(D) = E_0 \cdot \frac{kD + J\tau_0}{D + J\tau_0} \text{ or } E(D) = E_0 \cdot \frac{kD + J_0 e^{-\mu h}\tau_0}{D + J_0 e^{-\mu h}\tau_0} \tag{17}$$

where E_0 - is the Young's modulus of the unirradiated material, $k = const > 1$-is a dimensionless quantity, $\tau_0 = const = 1$, τ_0-is a measure of time.

It is assumed that the dose of irradiation *D* depends linearly on *t* (Glesson & Edlund, 1954; Onimus et al., 2020), i.e.,

$$D = Jt = J_0 \exp(-\mu z)\, t.$$

Expression (17) for unilateral irradiation can be rewritten as:

$$E(z,t) = E_0 \cdot \frac{ke^{\mu z} \cdot t + \tau_0}{e^{\mu z} \cdot t + \tau_0}.$$

In nuclear reactors, neutrons are fast, i.e., they have an energy of $U > 1$ Mew. Based on the above and considering that the rod is thin, we can conclude that $\mu z << 1$. Therefore, when expanding in a series $\frac{1}{E(z,t)}$ by μz we take only the linear terms and introduce the dimensionless time $\tau = \frac{t}{\tau_0}$, we get:

$$\frac{1}{E(z,t)} = \frac{1}{E_0}\left[\frac{\tau+1}{k\tau+1} - \frac{\mu\tau(k-1)}{(k\tau+1)^2}\cdot z\right]$$

In the linear stressed state, i.e., the stress components

$$\sigma_{12} = \sigma_{13} = \sigma_{23} = \sigma_{22} = \sigma_{33} = 0, \sigma_{11} = \sigma$$

and the components of the deviator and the intensity of shear stresses, respectively, have the form:

$$S_{12} = S_{13} = S_{23} = 0, S_{11} = \frac{2}{3}\sigma, S_{22} = S_{33} = -\frac{\sigma}{3}, \sigma_u = \sqrt{\frac{3}{2}S_{ij}S_{ij}} = \sigma$$

Thus, based on the above, the equation of state for this problem has the form:

$$\dot{\tilde{\varepsilon}} = \dot{\tilde{\varepsilon}}^e + \dot{\tilde{\varepsilon}}^c + \dot{\tilde{\varepsilon}}^v, \tag{18}$$

where $\tilde{\varepsilon}$ is the deformation component at an arbitrary point of the rod; $\tilde{\varepsilon}^e$ -is the elastic deformation component, $\tilde{\varepsilon}^c$ -is the creep deformation component, and $\tilde{\varepsilon}^v$ -is the volumetric deformation component.

According to the work (Amenzade,197Gulgazli, 2012), the rates of the elastic deformation component, creep deformation, and volumetric deformation are:

$$\dot{\tilde{\varepsilon}}^e = \left[\frac{\sigma}{E}\right]^{\bullet}, \quad \dot{\tilde{\varepsilon}}^c = F_c, \dot{\tilde{\varepsilon}}^v = \frac{1}{3}\dot{S},$$

where S is the volumetric swelling caused only by irradiation and determined empirically, and the function $F_c = F_c(\sigma_i, D)$ is defined empirically.

Then, the equation of state (18) will be presented in the following form (Likhachev & Pupko, 1975; Gulgazli, & Efendiev, 2017):

$$\dot{\tilde{\varepsilon}} = \left[\frac{\sigma}{E}\right]^{\bullet} + F_c + \frac{1}{3}\dot{S} \tag{19}$$

Following theoretical and experimental works, the dependence of S and F_c on D can be approximated as follows (Cybulskise, 1971; Murray,1972; Onimus et al., 2020):

$$S = KD, \quad F_c = \Omega(T, D)\cdot\sigma_u$$

where B and K are empirical constants, $\overline{U}$ - is the average neutron energy in reactors with fast neutrons, and the function $\Omega(D)$ has the following form: $\Omega = B\overline{U}J_0 e^{-\mu(h-z)}$.

In equation (19), the first term expresses the rate of elastic deformation, the second - the rate of creep deformation, and the third - the rate of volumetric swelling in the corresponding direction.

Then, the variational equation for this problem has the form (4):

$$\int_V \left[\dot{\tilde{\sigma}}\delta\dot{\tilde{\varepsilon}} + \dot{\tilde{\varepsilon}}\delta\dot{\tilde{\sigma}} + \tilde{\sigma}\frac{\partial\dot{w}}{\partial x}\delta\frac{\partial\dot{w}}{\partial x} - \left(\frac{\dot{\tilde{\sigma}}}{2E} - \frac{\tilde{\sigma}}{E^2}\frac{\partial E}{\partial D}\cdot\dot{D} + \frac{\dot{S}}{3}\right)\delta\dot{\tilde{\sigma}} - \left(F_c + \frac{\dot{\tilde{\sigma}}}{2E}\right)\delta\dot{\tilde{\sigma}}\right]dv = 0\,. \tag{20}$$

Based on the known relationships of the components of the finite deformation tensor in a layer of the rod, removed at a distance z from the central layer, we have the form (Volmir,1972):

$$\widetilde{\varepsilon} = \widetilde{\varepsilon} + z\theta \tag{21}$$

The component of the stress tensor at an arbitrary point of the rod has the form (Volmir,1972):

$$\widetilde{\sigma} = \frac{1}{2h} N(x,t) + \frac{3z}{2h^3} M(x,t) \tag{22}$$

where

$$N(x,t) = \int_{-h}^{h} \widetilde{\sigma}(x.z,t)dz; \qquad M(x,t) = \int_{-h}^{h} z\widetilde{\sigma}(x,z.t)dz\,. \tag{23}$$

Considering that the origin is at the central layer of the rod, the expression for S and F_c in reactors with fast neutrons has the form:

$$\dot{S} = K\dot{D}, \quad F_c = \left[\frac{1}{2h} N(x,t) + \frac{3z}{2h^3} M(x,t)\right]\Omega\,, \tag{24}$$

for one-sided irradiation:

$$\dot{S} = KJ_0 e^{-\mu(h-z)}\,,\ \Omega = B\overline{U}J_0 e^{-\mu(h-z)};$$

Considering (21) and (22) in (20), we get:

$$\begin{aligned}\int_V \Bigg[&\left(\frac{\dot{N}}{2h} + \frac{3z\dot{M}}{2h^3}\right)\delta(\dot{\varepsilon} + \dot{\theta}z) + (\dot{\varepsilon} + \dot{k}z)\delta\left(\frac{\dot{N}}{2h} + \frac{3z\dot{M}}{2h^3}\right) + \left(\frac{N}{2h} + \frac{3zM}{2h^3}\right)\frac{\partial\dot{w}}{\partial x}\delta\frac{\partial\dot{w}}{\partial x} - \\ &-\left(\frac{N}{2hE} + \frac{3zM}{2h^3E} + \frac{S}{3}\right)^{*}\delta\left(\frac{\dot{N}}{2h} + \frac{3z\dot{M}}{2h^3}\right) - F_c\delta\left(\frac{\dot{N}}{2h} + \frac{3z\dot{M}}{2h^3}\right)\Bigg]dv = 0.\end{aligned} \tag{25}$$

Assuming that the rod's size in the *y*-axis direction is equal to one, and by expanding the integral over *z* in (25), we get:

$$\begin{aligned}\int_{-l}^{l} \Big\{&\dot{N}\delta\dot{\varepsilon} + \dot{M}\delta\dot{\theta} + \dot{\varepsilon}\delta\dot{N} + \dot{\theta}\delta\dot{M} + \frac{\partial\dot{w}}{\partial x}\delta\frac{\partial\dot{w}}{\partial x}\cdot N - \left[\frac{Np_0}{4h^2E_0} + \frac{3Mp_1}{4h^4E_0} + S_1\right]^{\bullet}\delta\dot{N} - \left[\frac{3Np_1}{4h^4E_0} + \right. \\ &\left. + \frac{9Mp_2}{4h^4E_0} + S_2\right]^{\bullet}\delta\dot{M} - \Omega_0 N\delta\dot{N} - \Omega_1 M\delta\dot{N} - \Omega_1 N\delta\dot{M} - \Omega_2 M\delta\dot{M}\Big\}dx = 0.\end{aligned} \tag{26}$$

$$p_0 = \int_{-h}^{h}\left[\frac{\tau+1}{k\tau+1} - \frac{\mu\tau(k-1)}{(k\tau+1)^2}\cdot z\right]dz = \frac{\tau+1}{k\tau+1}\cdot 2h\,; \quad p_1 = \int_{-h}^{h} z\cdot\left[\frac{\tau+1}{k\tau+1} - \frac{\mu\tau(k-1)}{(k\tau+1)^2}\cdot z\right]dz = \frac{2h^3}{3}\cdot\frac{\mu\tau(1-k)}{(k\tau+1)^2}\,;$$

$$p_2 = \int_{-h}^{h} z^2\cdot\left[\frac{\tau+1}{k\tau+1} - \frac{\mu\tau(k-1)}{(k\tau+1)^2}\cdot z\right]dz = \frac{2h^3}{3}\cdot\frac{\tau+1}{k\tau+1}\,;$$

$$\dot{S}_1 = \int_{-h}^{h}\frac{1}{6h}\dot{S}dz = \frac{1}{6h\mu}KJ_0\left(1 - e^{-2\mu h}\right); \qquad \dot{S}_2 = \int_{-h}^{h}\frac{1}{2h^3}\dot{S}zdz = \frac{1}{2h^3\mu}KJ_0\left(h - \frac{1}{\mu} + he^{-2\mu h} + \frac{1}{\mu}e^{-2\mu h}\right);$$

$$\Omega_0 = \int_{-h}^{h} \frac{1}{4h^2}\Omega dz = \frac{B\overline{U}J_0}{4h^2\mu}\left(1-e^{-2\mu h}\right);\ \ \Omega_1 = \int_{-h}^{h} \frac{3z}{4h^4}\Omega dz = \frac{3B\overline{U}J_0}{4h^3\mu}\left(1+e^{-2\mu h}+\frac{1}{\mu h}e^{-2\mu h}-\frac{1}{\mu h}\right);$$

$$\Omega_2 = \int_{-h}^{h} \frac{9z^2}{4h^6}\Omega dz = \frac{9B\overline{U}J_0}{4h^4\mu}\left(1-e^{-2\mu h}-\frac{2}{\mu h}-\frac{2}{\mu h}e^{-2\mu h}+\frac{2}{\mu^2h^2}-\frac{2}{\mu^2h^2}e^{-2\mu h}\right).$$

By the condition, the rod is rigidly fixed at both ends, i.e., the boundary conditions can be written as:

$$w(x,\tau)\Big|_{x=-l,l}=0;\ \ \frac{\partial w}{\partial x}\Big|_{x=-l,l}=0\,. \tag{27}$$

Based on the boundary conditions (27) and physical considerations, for bending $w(x,\tau)$, we accept the following approximation:

$$w(x,\tau)=\varphi(\tau)\cos^2\frac{\pi x}{2l}, \tag{28}$$

where $\varphi(\tau)$ is the unknown function of time.

Then the components of the strain rate tensor of the middle surface have the following form:

$$\dot{\varepsilon}=\frac{1}{2}\left[\left(\frac{\partial w}{\partial x}\right)^2\right]^{\bullet}=\frac{\pi^2}{4l^2}\cdot\varphi(\tau)\cdot\dot{\varphi}(\tau)\sin^2\frac{\pi x}{l}, \tag{29}$$

$$\dot{\theta}=\left[-\frac{\partial^2 w}{\partial x^2}\right]^{\bullet}=\frac{\pi^2}{2l^2}\dot{\varphi}(\tau)\cos\frac{\pi x}{l}. \tag{30}$$

Based on the equation of state (19) for the force and moments, we obtain the following approximations:

$$N(x,\tau)=N_1(\tau)+N_2(\tau)\sin^2\frac{\pi x}{l}+N_3(\tau)\cos\frac{\pi x}{l}, \tag{31}$$

$$M(x,\tau)=M_1(\tau)+M_2(\tau)\sin^2\frac{\pi x}{l}+M_3(\tau)\cos\frac{\pi x}{l}. \tag{32}$$

By substituting the accepted approximations for the components of deformations, forces, and moments (29), (30), (31), and (32) into (26), and expanding the integrals over *x*, and equating the coefficients of the variations of $\delta\dot{\varphi},\delta\dot{N}_1,\delta\dot{N}_2,\delta\dot{N}_3,\delta\dot{M}_1,\delta\dot{M}_2,\delta\dot{M}_3$ to zero, we obtain a system of differential equations. When obtaining the system of differential equations, we introduced the following dimensionless quantities:

$$\overline{\varphi}=\frac{\varphi}{l},\ \ \overline{N}_i=\frac{N_i}{lE_0},\ \overline{M}_i=\frac{M_i}{l^2E_0},\ \ (i=1,2,3),$$

$$\overline{p}_j=\frac{p_j}{h^{j+1}},\ \ \overline{\Omega}_j=l^{j+1}E_0\Omega_j,\ \ (j=0,1,2)\ ;\ \ \dot{\overline{S}}_1=\dot{S}_1,\ \ \dot{\overline{S}}_2=l\dot{S}_2,\ \ \gamma=\frac{l}{h},\ \overline{\mu}=\mu h\,.$$

For the obtained system of differential equations, the initial conditions are taken in the following form:

$$N_1=0,\ N_2=0,\ N_3=0,\ M_1=0,\ M_2=0,\ M_3=0,\ \overline{\varphi}=\overline{\varphi}_0\ \ \text{at}\ \ \tau=0\,.$$

The resulting system was solved on a computer using the fourth-order Runge-Kutta method. In this case, Poisson's ratios were taken as $\nu = 0{,}5$, and it was assumed that Young's modulus does not depend on radiation dose, i.e., $E = E_0 = const$, and for radiation creep, experimental data obtained in reactors with fast neutrons were used. In this case, we have:

$$\overline{p}_0 = 2,\ \overline{p}_1 = 0,\ \overline{p}_2 = \frac{2}{3};\quad \dot{\overline{S}}_1 = \frac{1}{3\overline{\mu}} KJ_0\left(1 - e^{-2\overline{\mu}}\right);\quad \dot{\overline{S}}_2 = 0;\quad \overline{\Omega}_0 = \frac{B\overline{U}J_0E_0}{2\gamma\overline{\mu}}\left(1 - e^{-2\overline{\mu}}\right);\quad \overline{\Omega}_1 = 0;$$

$$\overline{\Omega}_2 = \frac{9B\overline{U}J_0E_0}{2\gamma^3\overline{\mu}}\left(1 - e^{-2\overline{\mu}} - \frac{2}{\overline{\mu}} - \frac{2}{\overline{\mu}}e^{-2\overline{\mu}} + \frac{2}{\overline{\mu}^2} - \frac{2}{\overline{\mu}^2}e^{-2\overline{\mu}}\right);\quad \overline{\theta}_1 = -\frac{4\gamma K}{3B\overline{U}E_0}\left(1 - e^{-2B\overline{U}J_0E_0e^{-\overline{\mu}}\tau}\right);\quad \overline{\theta}_2 = 0.$$

The results obtained are shown in Figures 3-5. In the numerical solution of this problem, we used experimental data obtained for SW 316 steels.

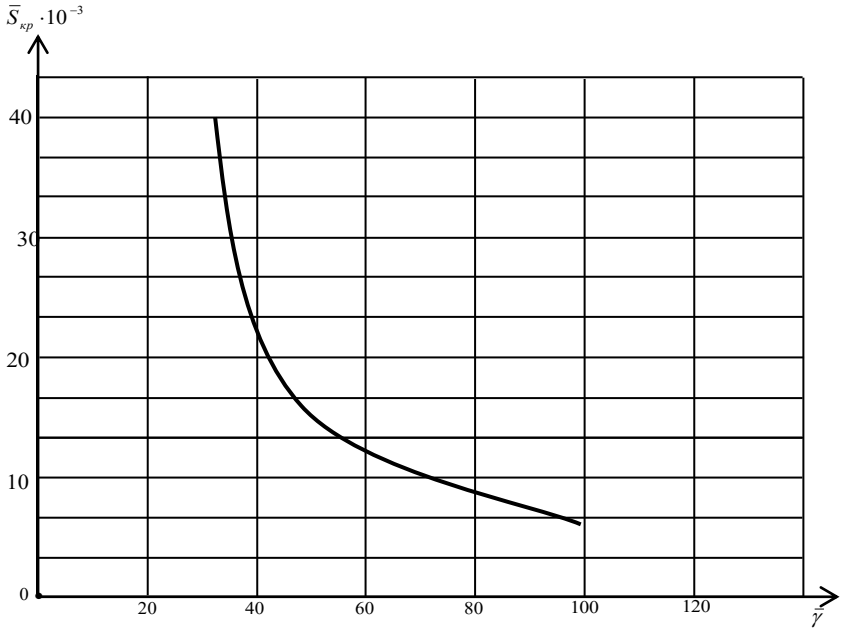

Figure 3. The dependence of the critical volumetric swelling on the relative thickness for a rod.

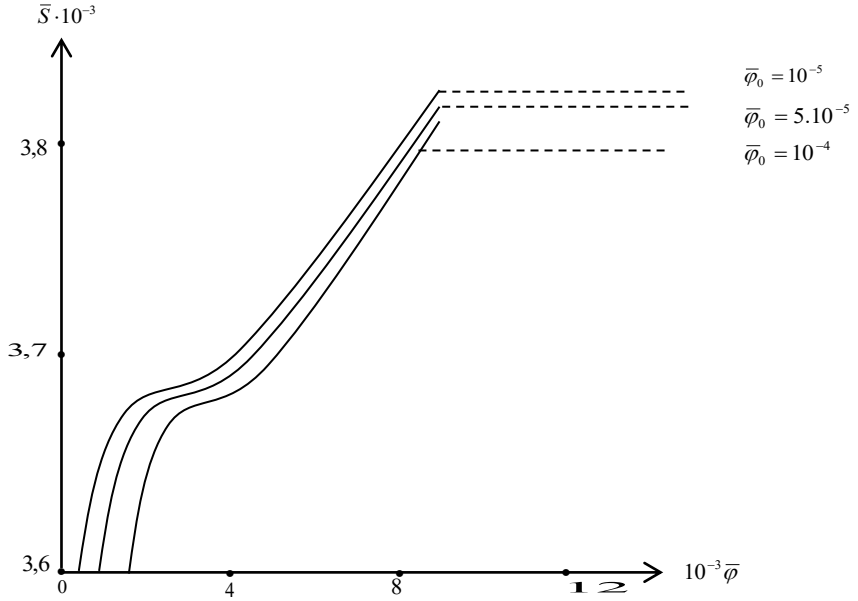

Figure 4. The dependence of $\overline{S} = \overline{S}(\overline{\varphi})$ at different values of the initial bend $\overline{\varphi}_0$ (SW 316).

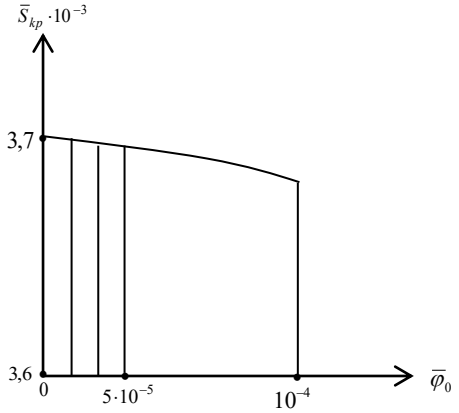

Figure 5. $\overline{S}_{кр} = \overline{S}_{кр}(\overline{\varphi}_0)$ for a straight rod made of steel SW 316 and for $\gamma = 30$

The diagrams show that the critical volumetric swelling S_{kp} and, accordingly, the critical time t_{kp} decrease with an increase in the initial deflection and relative thickness γ.

Results and Discussion

In those areas of technology where neutron radiation and high temperatures are present, it is necessary to take into account the effect of radiation and temperature on the mechanical properties of the material when designing structures. The problem is further complicated when geometric nonlinearity is taken into account. A functionality for solving such problems using the variational method is proposed.

The advantages of the proposed functional (4) are that:

1. A functionality has been developed for studying the stress-strain state of a structure subjected to neutron irradiation. This functionality takes into account geometric nonlinearity, creep, and changes in the mechanical properties of the material depending on the irradiation dose.
2. It has been proven that the Euler equations obtained on the basis of this functional are equations describing the stress-strain state (SSS) of structural elements. Using this functional, it is possible to analyze the behavior of structures subjected to neutron irradiation.
3. In practical application of this functional, we obtain not a system of nonlinear algebraic equations, as is the case when the stresses and strains themselves change independently, but a system of nonlinear ordinary differential equations.
4. The Euler equation of this functional, which gives us the equilibrium equation, explicitly includes creep and plastic deformation components, and it is taken into account that all components depend on the temperature and radiation dose. The temperature and radiation dose themselves depend on time. Therefore, using this functional, it is possible to study the behavior of structural materials both under the influence of radiation and temperature, and separately.
5. The proposed functional was used to study the long-term stability of rods. In the numerical solution of this problem, experimental data obtained for SW316 steels were used.

The results are shown in Figures 3-5.

Thus, using this functional, it is possible to study the stress-strain state of three-dimensional structural elements under the influence of radiation and temperature, both jointly and separately.

Scientific Ethics Declaration

* The authors declare that the scientific ethical and legal responsibility of this article published in EPSTEM Journal belongs to the authors.

Conflict of Interest

* The authors declare that they have no conflicts of interest

Funding

* This research received no specific grant from any funding agency in the public, commercial, or not-for-profit sectors.

Acknowledgements or Notes

* This article was presented as a poster presentation at the International Conference on Basic Sciences, Engineering and Technology (www.icbaset.net) held in Trabzon/Türkiye on May 01-04, 2025.

References

Aliyev, I. G., Latifov, F.S., Guliyeva, A.M., Seyidov, N.H., & Hasanov, A. I. (2024). Parametric vibrations of a damaged orthotropic geometrical shell stiffened with an inhomogeneous rod and rings on viscoelastic medium. *International Journal on Technical and Physical Problems of Engineering (IJTPE), 16*(3), 389-395.

Alizade, A. N., & Gulgazli, A.S. (1979). Variational principle for determining the stress-strain state of an elastic shell during irradiation with allowance for geometric nonlinearity. sciences of the Azerbaijan SSR.*The Series is Technical and Mathematical,6*, 84-87.

Amenzade, Yu.A. (1976). *Theory of elasticity* (p.272). Moscow: Higher School.

Breslavsky, D., & Tatarinova, O. (2023). Creep and irradiation effects in reactor vessel internals. *Advanced Structured Materials*, *194,* 83–104.

Breslavsky, D.,Palamarchuk, P.,Tolstolutska, G., &Altenbach, H. (2023). Stress-strain state and wear modelling for fuel rod –grid contact. *Problems of Atomic Science and Technology*, *2*(144), 8-14.

Chirkov, I. Y. (2021). Analysis of irradiation swelling and irradiation creep models with the stress effect account in the problems of inelastic strain mechanics. *Strength of Materials, 53*, 199-212.

Cybulskis, P. (1971) The technology in-pile creep measurements. *Reactor Technology, 14*(4), 315.

Dienes G.J. (1952). Effect of radiaction on the elastic constants. *Physical Review Journals, 87*, 666.

Dienes, G.J. (1952). A theoretical estimatc of the effect of radiaction on the elastic constants of simple metals. *Physical Review Journals*, *86*, 228.

Fomina, S.P., & Malovytsia, M. S. (2024). Actual problems of nuclear power engıneerıng and the search for solutıons. *XXI International Conference on Physics of Radiation Phenomena and Radiation Materials Science,* 23-25

Glesson S., & Edlund M. (1954). Fundamentals of the theory of nuclear reactors. *Physics Today, 7*(2), 20.

Gorokhov, V., Kazakov, D., Kapustin., K., & Churilov, Y. (2020). Simulation of fracture of heat-resistant alloys under creep and neutron irradiation conditions. *Procedia Structural Integrity, 28*, 1416–1425.

Gulgazli, A. S., & Efendiev, O.H. (2017). Variational principle for determining the stress-strain state of porous bodies. *International Journal of Current Research, 9*(10), 59603-59607.

Gulgazli, A.S. (2012). *Plasticity and creep under repeated loading* (p.176). Saarbrucken, German: Lambert Academic Publishing.

Iskanderov, R.A., & Tabatabaei, J.M. (2020). Vibrations of fluid-filled inhomogeneous cylindrical shells strengthened with lateral ribs. *International Journal on Technical and Physical Problems of Engineering (IJTPE*), *12*(1), 121-125.

Iskanderov, R.A., & Shafiei- Matanagh, H. (2020). Free vibrations of a conical shell with spiring associated mass and stiffened with a cross system of ribs in medium. *International Journal on Technical and Physical Problems of Engineering, (IJTPE), 12*(2), 1-5.

Kalchenko,A., & Lazarev, N. (2022).Swelling prediction of AISI 304 and 18Cr10NiTi austenitic stainless steels using various empirical functions. *Problems of Atomic Science and Technology*, *140*(4), 25- 32.

Latifov, F. S., Mammadov, S.A., Garayev, P.S., & Hasanov, A.I. (2024). Vibrations of bolstered hemispherical cushion. *International Journal on Technical and Physical Problems of Engineering, (IJTPE), 16*(3), 113-119.

Likhachev, Y. I., & Pupko, V.Y. (1975). *Strength of fuel elements of nuclear reactors*. Moscow.

Onimus, F., Jourdan, T., Xu, C., Campbell, A. A., & Griffiths, M. (2021). Irradiation creep in materials. *Comprehensive Nuclear Materials*, *1*, 310-366.

Thompson, D. O., & Holmes, D. K. (1956). Effects of neutron irradiation upon the Young's modulus and internal friction of copper single crystals. *Journal of Applied Physics*, *27*(7), 713-723.

Volmir, A.S. (1972). *Nonlinear dynamics of plates and shells*. (p.536). Maik Nauka Publishing.

Wassilew, C., Schneider, W., & Ehrlich, K. (1987). Creep and creep-rupture properties of type 1.4970 stainless steel during and after irradiation. *Radiation Effects*, *101*(1-4), 201-219.

Author(s) Information

Abdulla Hasanov
Nakhchivan State University
Nakhchivan, The Republic of Azerbaijan
Contact e-mail: *abdullahesenov@ndu.edu.az*

Yusif Orujov
Azerbaijan State University of Oil and Industry
Baku, The Republic of Azerbaijan

To cite this article:

Hasanov, A., & Orujov, Y. (2025). Variational principle for studying the long-term stability of structural materials subjected to neutron irradiation taking into account geometric nonlinearity. *The Eurasia Proceedings of Science, Technology, Engineering and Mathematics (EPSTEM), 34,* 151-164.

The Eurasia Proceedings of Science, Technology, Engineering & Mathematics (EPSTEM)
ISSN: 2602-3199

The Eurasia Proceedings of Science, Technology, Engineering and Mathematics (EPSTEM), 2025

Volume 34, Pages 165-171

ICBASET 2025: International Conference on Basic Sciences, Engineering and Technology

3D Interpretation of Gravity Anomalies in the Potentially Promising Oil and Gas Region of Ajinohur

Gunel Sadigova
Institute of Geology and Geophysics of the Ministry of Science and Education of Azerbaijan Republic

Aynur Zamanova
Institute of Geology and Geophysics of the Ministry of Science and Education of Azerbaijan Republic

Khadija Mustafayeva
Institute of Geology and Geophysics of the Ministry of Science and Education of Azerbaijan Republic

Abstract: This article presents the interpretation of Bouguer gravity anomalies using the 3D prism method in the potentially promising Ajinohur oil and gas region. According to this model, the surface depth of the crystalline basement is calculated by considering the density contrast at the bottom of the low-velocity zones in the upper part of the Earth's crust and the quadratic dependence of the density difference on depth.The study aims to conduct a numerical analysis of the gravity field of the potentially promising oil and gas region of Ajinohur and develop a digital gravity model of the sedimentary layer thickness.For the interpretation of the gravity anomalies in the potentially promising oil and gas region of Ajinohur, a sedimentary basin is viewed as a number of prisms placed in juxtaposition. The decrease of density contrast in sedimentary basins is approximated by a quadratic function. Based on the gravimetric field data of the studied area, the gravity model of the sedimentary layer thickness was constructed using the GR3DSTR computer program.From the gravity model of the sedimentary layer thickness, it was found that the maximum thickness is near Ajinohur Lake, in the Gamigaya-Ajibulag area (16 km), and the minimum is in the structural area of Aydinbulag, Chaykend, and Eastern Dashuz (6-8 km).The sedimentary layer thickness in the area where the Gojashen structures are located is 8 km. The regions of negative local gravity anomalies correspond to areas where the sedimentary layer thickness increases, such as in the Gamigaya-Ajibulag area. Conversely, a decrease in the sedimentary layer thickness is observed in the zone of local gravity maxima (Dashuz, Aydinbulag, Gojashen). The correspondence between the calculated sedimentary layer thickness with seismic sections and well data was also determined.The gravity model of the sedimentary layer thickness is of practical importance in oil and gas exploration and in selecting drilling well locations.

Keywords: Gravity anomaly, Sedimentary basin, Gravity model

Introduction

The selected research area, the potentially promising oil and gas region of Ajınohur, is located in the eastern part of the Gabirri-Ajınohur basin. It is bordered by the Alazan River to the west and the Girdiman River to the east. Extending along the southern slope of the Greater Caucasus Mountain range, it is separated from the Alazan-Ayrichay depression. Geologically, the Ajinohur area lies at the junction of the Kura depression and the Greater Caucasus. Despite the negative results of traditional exploration works conducted here, the region is considered to be potentially promising in terms of oil and gas resources.

Despite the application of geophysical research and geological exploration over many years in the Ajinohur region, many issues regarding the area's oil and gas potential remain unresolved, and the tectonics of the

- Selection and peer-review under responsibility of the Organizing Committee of the Conference

Mesozoic-aged sediments have not been sufficiently studied. The reason for this is the complex seismic conditions in most parts of the area, the limited ability to use seismic exploration methods, and the deep location of the Mesozoic-aged sediments. It is believed that the lack of Deep Seismic Profiling and well data in the region can be compensated for by gravimetric data. Analyses suggest that studying the deep structure of the Ajınohur region and discovering new oil and gas fields here requires the application of modern geophysical methods (Yusifov & Suleymanov, 2015). It is well known that gravity field anomalies play a crucial role in studying the geological-tectonic structure of the Earth's crust. When these data are analyzed alongside results from other geophysical methods, they offer valuable insights into the geological structure.

Since the end of the last century, digital methods have been increasingly applied to the interpretation of potential fields. In this regard, extensive research has been conducted by Blakely, Simpson, Straxov, Stepanova, Əmiraslanov, Kadirov, Serkerov, and others. Today, the digital analysis of gravity field data has become a significant area within the theory of potential field interpretation. The development and application of gravity field transformation methods to identify density boundaries within the geological structure of any area remains a highly relevant issue.

The main features of the crustal depth structure, based on the gravity field data of the Kura depression, where the Ajınohur region is located, have been studied. It has been found that the crustal foundation in the Gabirri-Ajınohur and Yevlakh-Agjabadi depressions of the Kura tectonic element undergoes significant bending. High-precision gravimetric surveys have led to the discovery of new local uplifts in various areas of the Kura depression, and their geological structure, as well as oil-gas potential, has been predicted by Mammadov Qadirov, Aliyev, Khanbabayev, Hasanov, and others). In these studies, gravimetric palettes and correlation formulas were primarily used.

In recent years, based on the numerical analysis of gravity field data, researchers Blakely (1996) and Kadirov (2000) and Sadygova (2020) have proposed several mathematical methods for separating regional and local gravity anomalies, estimating the depths of the anomaly-causing sources, and refining the structure of the crystalline basement and sedimentary layers.

Method

3D Modeling of Gravity Anomalies of the Study Area

A map of gravity anomalies in the Bouguer reduction of the study area was compiled to estimate the thickness of the sedimentary layer using gravity field data (Figure 1). The study area is located in the Ganikh-Ayrichay gravity minimum zone, which is characterized by negative gravity anomalies (Kadirov, 2000). Gravity anomalies below -40 mGal are observed in the Mingachevir, Sheki, and Oghuz regions. In particular, the lowest gravity anomaly values were recorded in the northwest of Sheki (-90 mGal) and the Gamigaya-Ajibulag zone (-65 mGal).

For the purpose of studying the gravity anomalies, the Bouguer anomaly map was initially divided into 3 km squared cells, and the Bouguer anomaly values were determined at the grid nodes. The origin of the coordinate system was placed at the southwestern corner of the study area, with the X-axis directed to the east and the Y-axis directed to the north. The number of cells was selected as Nx = 43 and Ny = 38, respectively.

A gravity model of the sedimentary layer thickness was constructed using the GR3DSTR computer program based on the gravimetric field data of the studied area. The density parameter of the sedimentary layer was approximated as a quadratic function, based on the known density values of the rocks, and entered into the program (Bhaskara & Ramesh, 1991).

The thickness of the sedimentary layer is investigated based on the quantitative analysis of the gravity field, considering the following conditions: a) a density contrast in the range of 0.3-0.4 g/cm³ at the bottom of the low-velocity zone, and b) a variation in density difference with depth, according to a quadratic function. In a section of the Earth's crust surrounding the crystalline basement, the density difference of rocks with depth can be approximated by the following quadratic function:

$$\Delta\rho(z)=a_0+a_1z+a_2z^2 \quad (1)$$

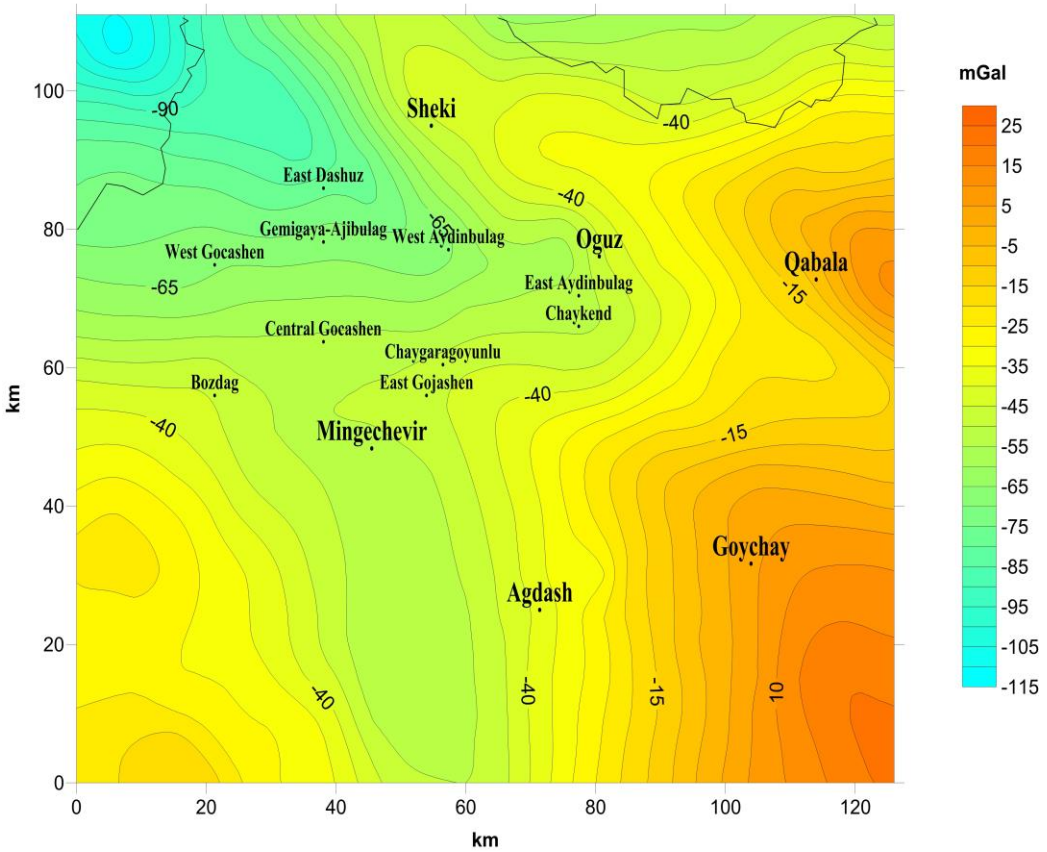

Figure 1. Bouguer gravity anomalies in the potentially promising oil and gas region of Ajinohur

Where the Z-axis is directed towards the center of the Earth, a_0 is the density value at the surface, and a_1 and a_2 are the constants of the quadratic function. For the three-dimensional modeling of gravity anomalies, the part of the Earth's crust surrounding the crystalline basement can be considered a collection of multiple adjacent prisms. The following formula expresses the equation for the gravity anomaly of a prism, where the density contrast varies with depth according to a quadratic function.

$$\Delta g(x,y) = \gamma a_0 \left| z \arctan\frac{xy}{zR} + \frac{x}{2}\ln\frac{R-y}{R+y} + \frac{y}{2}\ln\frac{R-x}{R+x} \right|_{x=X_1}^{X_2} \Bigg|_{y=Y_1}^{Y_2} \Bigg|_{z=Z_1}^{Z_2}$$

$$+ \gamma a_1 \left| \frac{z^2}{2}\arctan\frac{xy}{zR} - \frac{x^2}{2}\arctan\frac{yz}{xR} - \frac{y^2}{2}\arctan\frac{xz}{yR} \right.$$

$$+ xy\ln(2R+2z) \Big|_{x=X_1}^{X_2} \Big|_{y=Y_1}^{Y_2} \Big|_{z=Z_1}^{Z_2} + \gamma a_2 \left| \frac{z^3}{3}\arctan\frac{xy}{zR} \right.$$

$$- \frac{x^3}{3}\ln\frac{R-y}{R+y} - \frac{y^3}{6}\ln\frac{R-x}{R+x} + \frac{2}{3}xyR \Big|_{x=X_1}^{X_2} \Big|_{y=Y_1}^{Y_2} \Big|_{z=Z_1}^{Z_2} \quad (2)$$

Here, $X_1=x+T$, $X_2 = x-T$, $Y_1=y+W$, $Y_2=y-W$, $R = \sqrt{X^2 + Y^2 + Z^2}$, γ - gravity constant, T and W - the half-dimensions of the bottom of the prism.

The GR3DSTR computer program, developed by R. Bhaskara and B. Ramesh in FORTRAN-77, is used for three-dimensional modeling of gravity anomalies, accounting for the density contrast with depth (Bhaskara & Ramesh, 1991).

Results and Discussion

Application of GR3DSTR Program for Modeling Gravity Anomalies of the Study Area

The structure of the sedimentary layer in the Ajınohur prospective oil and gas region has been detailed in several monographs based on well and seismic exploration data (Kerimov, 2009; Yusifov & Aslanov, 2018). Geophysical and geological research conducted in the studied area so far has identified four seismic complexes within the sedimentary layer. These sedimentary complexes are as follows: 1) Quaternary sediments, 2) Neogene, 3) Paleogene, and 4) Cretaceous.

If we assume that the density difference at the boundary between the Cenozoic (Paleogene) and Mesozoic (Cretaceous) layers is 0.27 g/cm³ and at the boundary of the crystalline basement it is 0.15 g/cm³, we can determine the quadratic dependence of the density difference on depth. In determining the quadratic dependence of the density difference ($\Delta\rho$) on depth at the bottom of the low-velocity zone, the density difference is considered to be 0.4 g/cm³. Figure 2 illustrates the quadratic dependence of the density difference on depth. The coefficients of the quadratic function, which describe the relationship between density difference and depth, are provided below:

$$a_0 = -0.0009,\ a_1 = 0.0306,\ a_2 = -0.4026$$

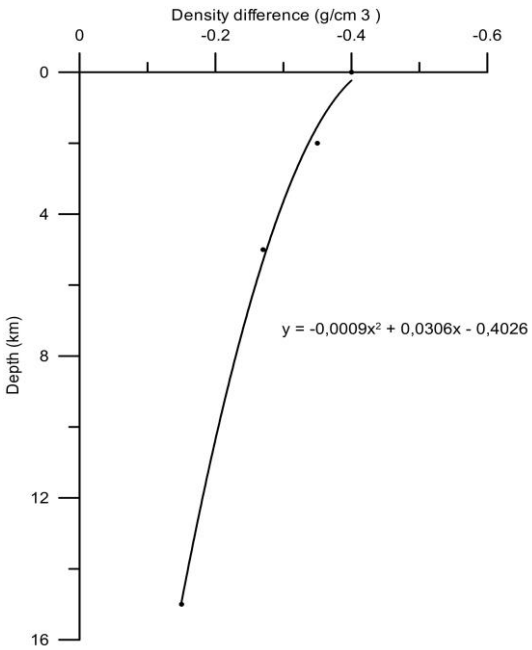

Figure 2. The dependence curve of the density difference on depth

The sedimentary layer thickness was calculated using the GR3DSTR program, based on the calculated values of the Bouguer gravity anomaly and the coefficients of the quadratic function. Figure 3 shows the gravity model of the sedimentary layer thickness obtained after 10 iterations. The sedimentary layer thickness model shows significant thickness near Ajınohur Lake and the Gamigaya-Ajibulag area, with an average thickness of 16 km. In the areas surrounding this zone to the north and south, the sedimentary layer thickness decreases. In the Aydinbulag, Chaykend, and Eastern Dashuz areas, the average thickness ranges between 6 and 8 km, while in the area of the Gojashen structures, it is 8 km. The regions where the sedimentary layer thickness increases correspond to negative local gravity anomaly areas, specifically in the Gamigaya-Ajibulag area. In the local gravity maximum zones of Dashuz, Aydinbulag, and Gojashen, a decrease in sedimentary layer thickness is observed (Kadirov et al., 2024). The correspondence of the calculated sedimentary layer thickness with seismic sections and well data was determined (Yusifov & Süleymanov, 2015).

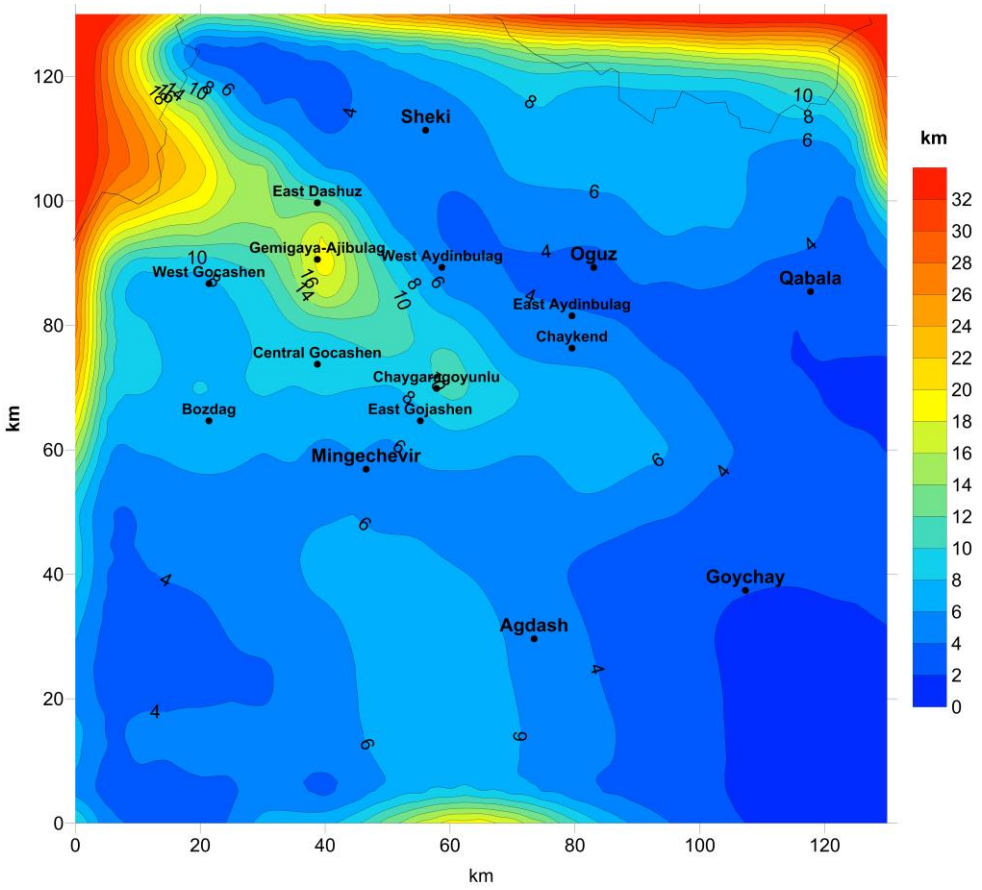

Figure 3. Gravity model of the sedimentary layer thickness in the potentially promising oil and gas region of Ajinohur

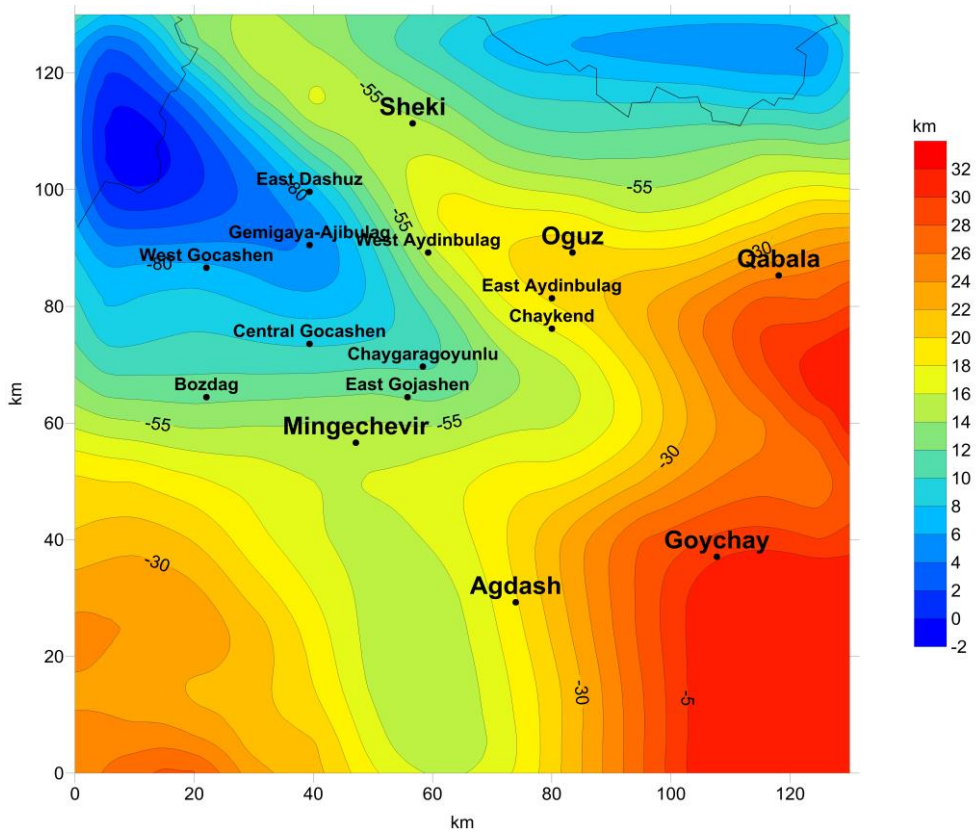

Figure 4. Gravity effect of the sedimentary layer thickness in the potentially promising oil and gas region of Ajinohur

Figure 4 illustrates the gravity effect calculated based on the obtained sedimentary layer thickness distribution in the potentially promising oil and gas region of Ajinohur. The minimum gravity effect, ranging between -55 and -80 mGal, was recorded in the northwestern part of the map, specifically in the Gamigaya-Ajibulag and Northwestern zones.

If we compare the gravity effect of the sedimentary layer with the Buge anomaly map (after a 30 mGal correction), we can observe that the values are consistent. This indicates that the selection of 10 iterations for calculating the sedimentary layer thickness distribution is correct.

Conclusion

The gravity model of the sedimentary layer thickness was developed using the GR3DSTR computer program, based on the gravimetric field data of the studied area. In the gravity model, the highest thickness values are observed in the Gamigaya-Ajibulag area (16 km), while the minimum thickness values are found in the Aydinbulaq, Chaykend, and East Dashuz structures (6-8 km).

Recommendations

The methodology developed in this study is both theoretically and practically significant and can be applied to other regions. The gravity model of sedimentary layer thickness is particularly valuable in oil and gas exploration as well as in the selection of well locations.

Scientific Ethics Declaration

* The authors declare that the scientific ethical and legal responsibility of this article published in EPSTEM Journal belongs to the authors.

Conflict of Interest

* The authors declare that they have no conflicts of interest.

Funding

* The research was carried out at the expense of budgetary financing of the Institute of Geology and Geophysics of the Ministry of Science and Education of the Azerbaijan Republic.

Acknowledgements or Notes

* This article was presented as a poster presentation at the International Conference on Basic Sciences, Engineering and Technology (www.icbaset.net) held in Trabzon/Türkiye on May 01-04, 2025.

References

Bhaskara, R. D., & Ramesh, B. N. (1991). A fortran-77 computer program for three-dimensional analysis of gravity anomalies with variable density contrast. *Computers and Geosciences*, *17*(5), 655-667.

Blakely, R. J. (1996). *Potential theory in gravity and magnetic applications*. Cambridge: Cambridge University Press.

Kadirov, F. A. (2000). *Gravity field and models of the deep structure of Azerbaijan*.Azerbaijan, Baku: Nafta-Press.

Kadirov, A. H., Zamanova, A. H., Sadigova, G. R., & Mustafayeva, K. K. (2024). The gravity field power spectrum and the deep structure of the Ajinour region (Azerbaijan). *Geophysical Research*, *25*(1), 57–68.

Karimov, M.K. (2009). *Deep structure and oil and gas potential of depression zones of Azerbaijan and the South Caspian*. Baku: CBS.

Sadygova, G. R. (2020). Gravity anomalies of the Southeast Caucasus. *Geophysical Journal*, *42*(2), 138-151.

Yusifov, Kh. M., & Aslanov, B. S. (2018). *Oil and gas basins of Azerbaijan*. Baku: Mars Print.

Yusifov, Kh. M., & Suleymanov, A. M. (2015). *Geological foundations of oil and gas exploration in Mesozoic sediments in Azerbaijan*. Baku: Mars Print.

Author(s) Information

Gunel Sadigova
Institute of Geology and Geophysics of the Ministry of Science and Education of Azerbaijan Republic AZ1073, H.Javid av., 119, Baku, Azerbaijan
Contact e-mail: *gsadigova@yahoo.com*

Aynur Zamanova
Institute of Geology and Geophysics of the Ministry of Science and Education of Azerbaijan Republic AZ1073, H.Javid av., 119, Baku, Azerbaijan

Khadija Mustafayeva
Institute of Geology and Geophysics of the Ministry of Science and Education of Azerbaijan Republic, AZ1073, H.Javid av., 119, Baku Azerbaijan

To cite this article:

Sadigova, G., Zamanova, A., & Mustafayeva, K. (2025). 3D interpretation of gravity anomalies in the potentially promising oil and gas region of Ajinohur. *The Eurasia Proceedings of Science, Technology, Engineering and Mathematics (EPSTEM), 34,* 165-171.

The Eurasia Proceedings of Science, Technology, Engineering & Mathematics (EPSTEM)
ISSN: 2602-3199

The Eurasia Proceedings of Science, Technology, Engineering and Mathematics (EPSTEM), 2025

Volume 34, Pages 172-181

ICBASET 2025: International Conference on Basic Sciences, Engineering and Technology

Performance Comparison of WebAssembly and Phaser in Procedural Maze Generation

Noa Midzic
University of Zagreb

Matija Novak
University of Zagreb

Abstract: Phaser and WebAssembly are both excellent options for web game development, each offering unique advantages. This paper specifically focuses on procedural maze generation and compares the performance of WebAssembly (using C++ and SDL) and Phaser across various levels of complexity, defined by maze dimensions. The study aims to assess execution time efficiency and identify performance trends across different scenarios. Using the Depth-First Search (DFS) algorithm, we conducted multiple test runs at increasing maze sizes to evaluate the scalability and computational efficiency of both technologies. The results indicate that WebAssembly enables near-native execution of C++ code in web browsers, leading to significant performance advantages in larger maze dimensions. Specifically, WebAssembly exhibited a more consistent, linear increase in execution time, making it a strong candidate for handling computationally intensive tasks. In contrast, Phaser performed slightly better in smaller maze dimensions but demonstrated greater variability and steeper increases in execution time as complexity grew. The findings suggest that while Phaser is an accessible and user-friendly framework for game development, its performance may not scale as efficiently as WebAssembly when dealing with complex procedural generation tasks. However, the study also acknowledges limitations, such as fewer test runs for larger mazes and potential differences in implementation efficiency between the two technologies. Overall, WebAssembly appears better suited for tasks requiring high-performance execution, whereas Phaser remains a viable option for less demanding applications where ease of use and rapid development are prioritized.

Keywords: Phaser, WebAssembly, Performance comparison, Experiment, Web game development

Introduction

Game development has emerged as a significant subfield of software engineering, driven by the widespread adoption of computer games (Wu et al., 2012). Additionally, game development has gained prominence as an effective pedagogical tool for teaching programming, as illustrated in Cagiltay (2007) or Wilson et al. (2024). A variety of frameworks exist to support this purpose, with Phaser (Faas, 2017) being a good choice for web-based game development, which is the focus of this paper. Phaser offers advantages due to its versatility, enabling the development of both basic web games and more serious games (Pavkov et al., 2017) as project requirements evolve. The selection of an appropriate framework is largely dependent on the specific requirements and genre of the game under development.

On the other hand, frameworks like Phaser, which is written in JavaScript, tend to have more overhead compared to games developed in C++. With the advent of WebAssembly, it is now possible to develop web games using C++, as demonstrated in Battagline (2019). In a previous work Midžić (2024) one of the objectives was to create a browser game using C++ with WebAssembly, which raised the question of the potential benefits of game develop- ment with WebAssembly compared to traditional frameworks used for browser games. This

- Selection and peer-review under responsibility of the Organizing Committee of the Conference

question forms the central focus of this study, which compares the performance of WebAssembly with C++ and SDL against Phaser in the procedural generation of a game world, exemplified by a dynamically generated maze.

WebAssembly is a binary instruction format that serves as a compilation target for programming languages like C, C++, and Rust. It allows these languages to be executed in web browsers at near-native speeds, enabling developers to write performance-critical parts of web applications in languages other than JavaScript. It has gained widespread support from major browsers, but compiling source code into WebAssembly requires the use of additional tools such as Emscripten to integrate C/C++ into web applications. On the other hand, Phaser is an open-source JavaScript framework for building HTML5 games, widely adopted due to its simplicity and extensive documentation. Because of its popularity and rapid development capabilities, Phaser was chosen as a suitable framework for browser game development to compare against a WebAssembly-based game.

The procedural generation of game worlds refers to using algorithms to create game environments dynamically, rather than designing them manually. This approach is often used in game development to both reduce storage requirements for game assets and offer non-repeating or limitless variations in level design. Since the complexity of procedural generation algorithms and the computational resources required for real-time generation can impact performance, particularly on less powerful devices, optimisation is necessary to ensure smooth performance in games across different platforms.

A review of the literature shows that several studies have compared the performance of JavaScript and WebAssembly. A 2022 study by Macedo et al. (2022) on the runtime and energy efficiency performance between WebAssembly and JavaScript demonstrates gains in favour of WebAssembly. Similarly, other studies like Herrera et al. (2018) or Reiser et al. (2017) also show the advantage of WebAssembly compared to JavaScript.

In the context of gaming performance, there are some experiments that highlighted WebAssembly's benefits over JavaScript. In (Ylenius, 2020) three versions of the same game were implemented: one in pure JavaScript, one using a combination of JavaScript and WebAssembly, and one entirely in WebAssembly. The WebAssembly version not only demonstrated the best execution performance but also the most stable memory usage. However, no studies were found that directly compare WebAssembly's performance to Phaser or other game frameworks. Only mention of Phaser and Webssembly was in a master thesis (Mustonen, 2023) that compared web based engine design.

The motivation behind this article is to research whether WebAssembly can be used to optimise the performance in procedural generation of game worlds, compared to a JavaScript framework such as Phaser. In the context of a procedurally generated game world, a maze generation algorithm implemented with Depth-First Search (DFS) was chosen due to its sufficient time complexity for performance testing. Section 2 describes the structure of the projects created for performance comparison, the methods used for performance evaluation and measurement, as well as the specifications of the device used to conduct testing. In Section 3 the results of the measurements are presented, analysed and discussed while Section 4 presents the conclusion.

Method

The code used for testing implements a maze generator utilizing a Depth-First Search (DFS) algorithm with backtracking, written in C++ for the WebAssembly version and in JavaScript for the Phaser version. It creates a grid of cells, each initially surrounded by walls. The algorithm starts at a random cell, marks it as visited, selects an unvisited neighbouring cell, removes the wall between them, and moves to the next cell. This process repeats until all cells are visited, resulting in a complete maze with a single path from start to finish. If the algorithm encounters a cell with no unvisited neighbours, it backtracks to the previous cell and continues. The final output is a randomly generated maze with a path from upper left corner to lower right corner.

In terms of code, Phaser not only manages the maze generation but also the rendering, making it a higher-level solution for building browser games. In contrast, the WebAssembly version is implemented in C++ using SDL2 for rendering, which involves directly manipulating the pixel buffer and provides a lower-level control over the rendering process. Both implementations employ the same DFS with backtracking algorithm, ensuring equivalence in logic used for maze generation. However, their performance may vary due to differences in the environment and tools. As a high-level JavaScript framework, Phaser carries the overhead of JavaScript's garbage collection and additional processing related to its game engine features. In contrast, WebAssembly

benefits from direct memory access, allowing it to bypass garbage collection. The code, along with the measurements and the R script used for result analysis, is available at *https://github.com/nmidzic20/phaser-wasm-maze-generator*.

The measurements were conducted by running tests on mazes of increasing size: 10x10, 30x30, 60x60, 90x90 (with 100 test runs each), 110x110 (50 runs), and 130x130 and 150x150 (20 runs each). The goal was to compare performance both for small mazes, which require only a few minutes to generate, and large mazes, which can take several hours. Tests were carried out in order from smaller to larger dimensions, with each dimension repeated either 100, 50, or 20 times to obtain an average for that size. To avoid bias, test were conducted alternately – one run for Phaser, followed by one for WebAssembly, and so on. Since larger mazes take significantly longer to generate, the number of runs for these mazes was reduced due to time constraints.

During the analysis of the results, a descriptive statistical analysis was performed, which included visualizing the data with boxplots and calculating measures such as quantiles, mean, median, standard deviation, and variance. The Shapiro-Wilk test was applied to assess the normality of the data distributions. Based on the Shapiro-Wilk test, if the p-value was greater than 0.05, indicating that the data followed a normal distribution, parametric tests were conducted. Conversely, if the p-value was less than 0.05, indicating that the data did not meet the normality assumption, non-parametric tests were performed.

These tests were employed to determine whether there was a statistically significant difference in performance times between the Phaser and WebAssembly technologies across the generation of different maze dimensions.
The technologies employed in this study were WebAssembly and Phaser, with C++ and JavaScript as the respective programming languages for the test code. Additionally, an R script and R Studio were used for analysing the measurements. The testing device was equipped with an Intel Core i7-10750H CPU running at 2.60 GHz and 16 GB of RAM, with Google Chrome serving as the browser for testing. The measurements were collected over the course of one week, with no significant breaks between the test runs for a particular maze dimension category.

Results and Discussion

The analysis involves performance measurements of two technologies, Phaser and WebAssembly, across various maze dimensions used in the testing. Average execution times for each technology were collected, and the results are presented in Table 1.

Table 1. Average time for maze generation comparison between WebAssembly and Phaser

Dimension	Number of test runs	WebAssembly (miliseconds)	Phaser (miliseconds)
10x10	100	3.359,14	3.278,96
30x30	100	30.017,28	29.942,66
60x60	100	119.993,50	119.925,40
90x90	100	269.948,00	270.331,50
110x110	50	403.215,90	405.354,80
130x130	50	563.200,80	723.647,30
150x150	20	749.787,20	1.127.674,00

Figure 1 illustrates the average performance times across all maze dimensions, recorded in milliseconds. Both Phaser and WebAssembly show a gradual increase in mean execution times as the maze dimensions expand, but the increase is more pronounced for Phaser, especially from dimension 130x130 onward, where Phaser's mean execution time becomes significantly higher than that of WebAssembly.

At smaller dimensions, Phaser has a slight speed advantage over WebAssembly on average, though this advantage diminishes as the maze increases. Specifically, Phaser is approximately 2,39% faster for 10x10 mazes, 0,25% faster for 30x30, and 0,06% faster for 60x60 mazes. However, starting at 90x90 dimension, Phaser's execution time increases more rapidly than that of WebAssembly, leading to WebAssembly consistently outperforming Phaser at larger dimensions. WebAssembly is 0,14% faster at 90x90 and 0,53% faster at 110x110. The performance gap becomes significantly more pronounced for larger mazes, with WebAssembly being 22,17% faster at 130x130 and 33,51% faster at 150x150 dimensions.

This trend is more clearly illustrated in Figure 2, which shows the difference in median execution time between the two technologies. After a minimal increase at smaller maze sizes, a sharp jump occurs at the 110x110 dimension, followed by rapid linear growth.

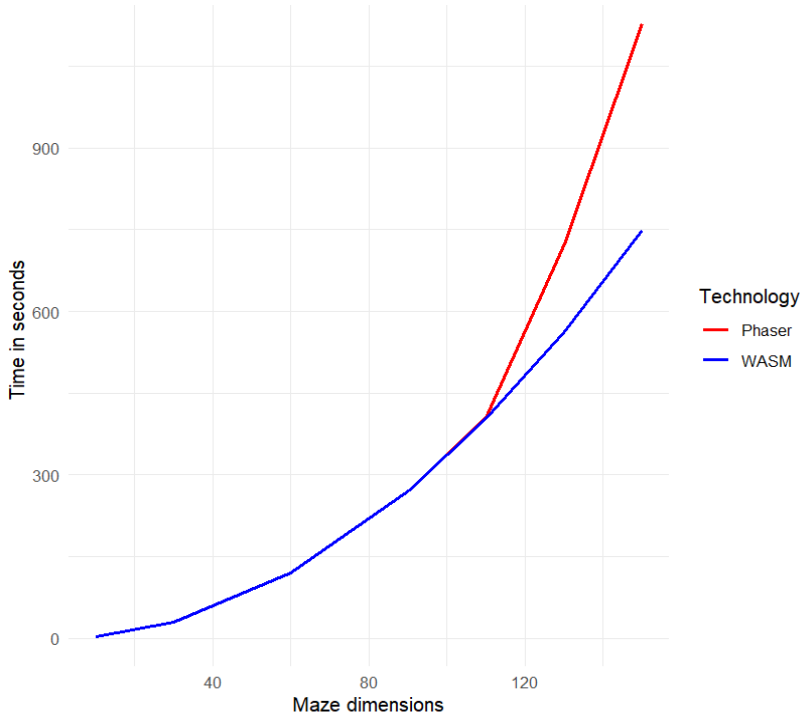

Figure 1. Comparison graph for Phaser and WebAssembly by means in seconds for each dimension

The distribution of execution times in milliseconds for each maze dimension can be evaluated by comparing the mean and median values. When the mean and median are the same or nearly identical, it suggests a normal distribution, while a significant difference between them indicates skewness, either to the left (negative skew) or to the right (positive skew). Table 2 outlines the distributions for each dimension and technology category.

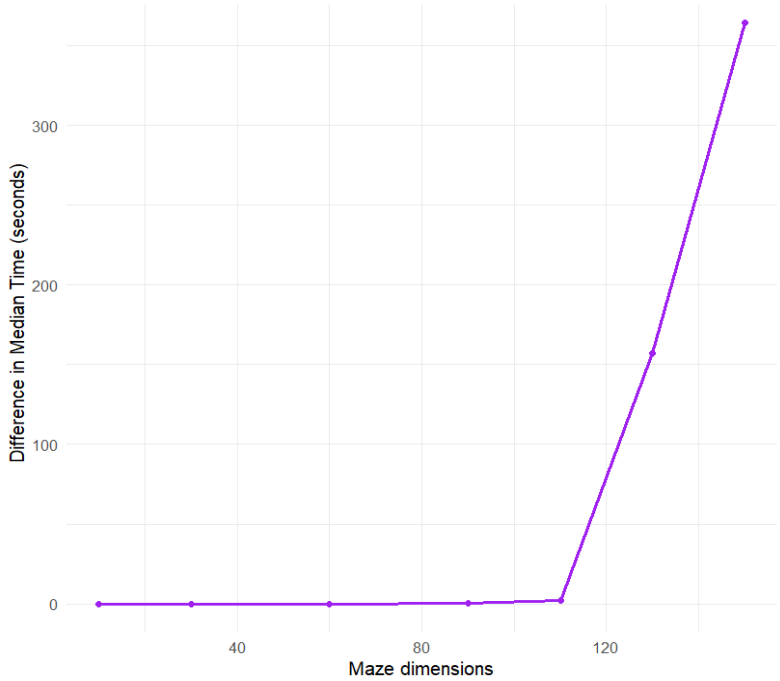

Figure 2. Graph of the median time difference in seconds for Phaser and WebAssembly for each dimension

Phaser tends to show slight to significant positive skew for larger maze dimensions (90, 110, 130, 150), with the skew becoming more pronounced as the dimensions increase. In contrast, WebAssembly generally displays a normal distribution for most dimensions. Boxplot analysis indicates that Phaser has more outliers than WebAssembly, particularly as the maze dimension increases. For example, dimension 110x110 as shown in Figure 3 or dimension 150x150 as shown in Figure 4.

Table 2. Data distribution by dimension and technology

Dimension	Phaser Distribution	WASM Distribution
10x10	Normal	Slight positive skew
30x30	Normal	Normal
60x60	Normal	Normal
90x90	Slight positive skew	Normal
110x110	Slight positive skew	Normal
130x130	Positive skew	Normal
150x150	Strong positive skew	Normal

We can analyse whether the spread (variability) of performance times increases more rapidly for Phaser or WebAssembly by using the standard deviation or interquartile range (IQR) as measures of spread, and plotting how these values change across the dimensions. Figure 5 shows the comparison using standard deviation, which measures the overall variability of the data. Figure 6 displays the comparison using interquartile range, which indicates the range within which the middle 50% of the data falls (between the 1st and 3rd quartiles), thereby reducing the impact of outliers on the comparison.

As maze dimensions increase, the spread in performance times grows more rapidly for Phaser than for WebAssembly, particularly from the 60x60 dimension onwards, where outliers begin to emerge, with the greatest spike occurring at the 110x110 dimension. This indicates that larger mazes lead to more variability in performance, particularly for Phaser, where execution times are more inconsistent. In many cases, Phaser struggles to maintain stable performance, resulting in a greater number of outliers.

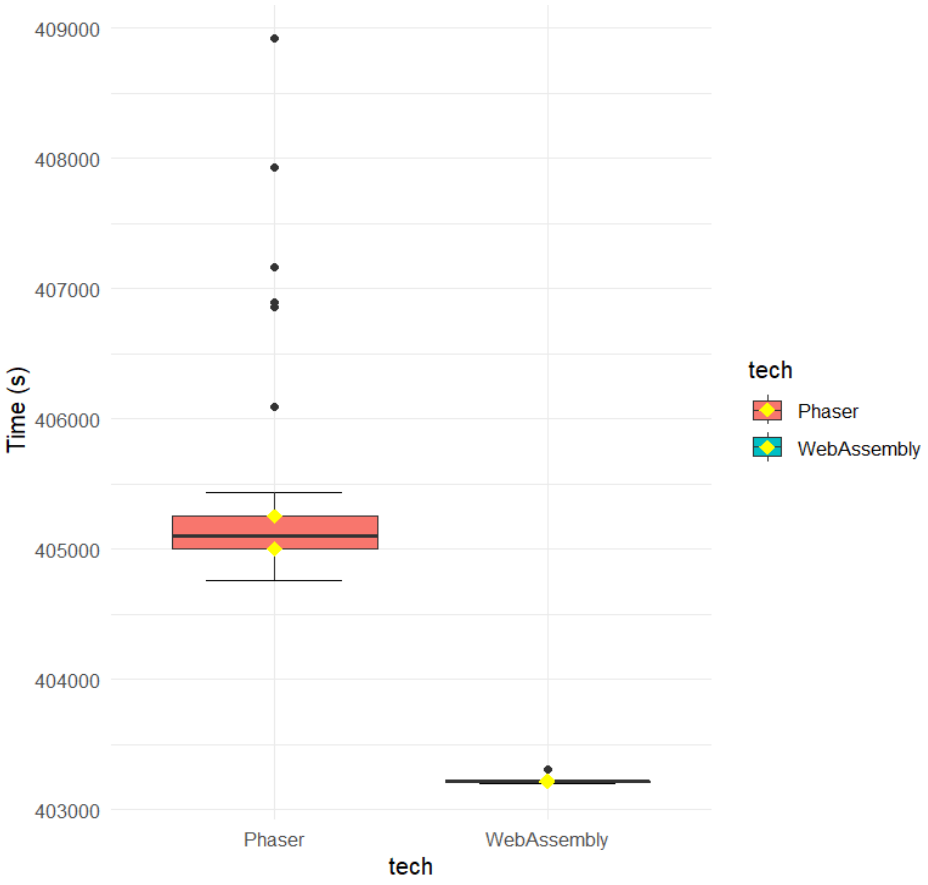

Figure 3. Boxplot of execution time in milliseconds for 110x110 dimension

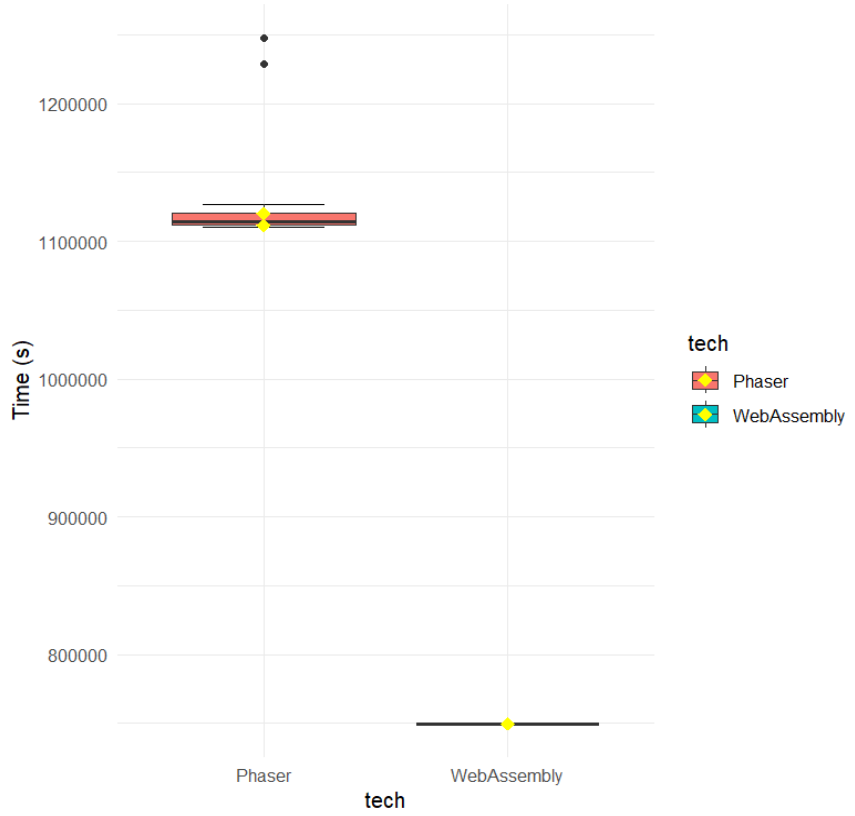

Figure 4. Boxplot of execution time in milliseconds for 150x150 dimensions

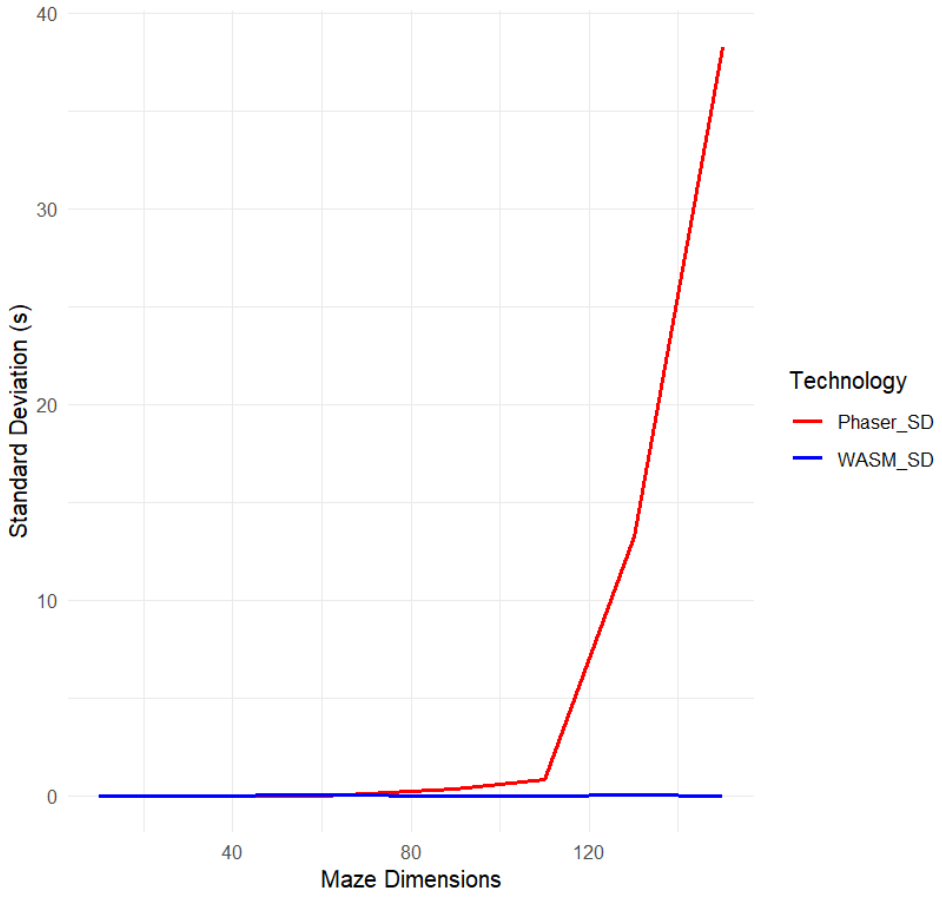

Figure 5. Comparison of standard deviation in performance times between Phaser and WebAssembly across maze dimensions

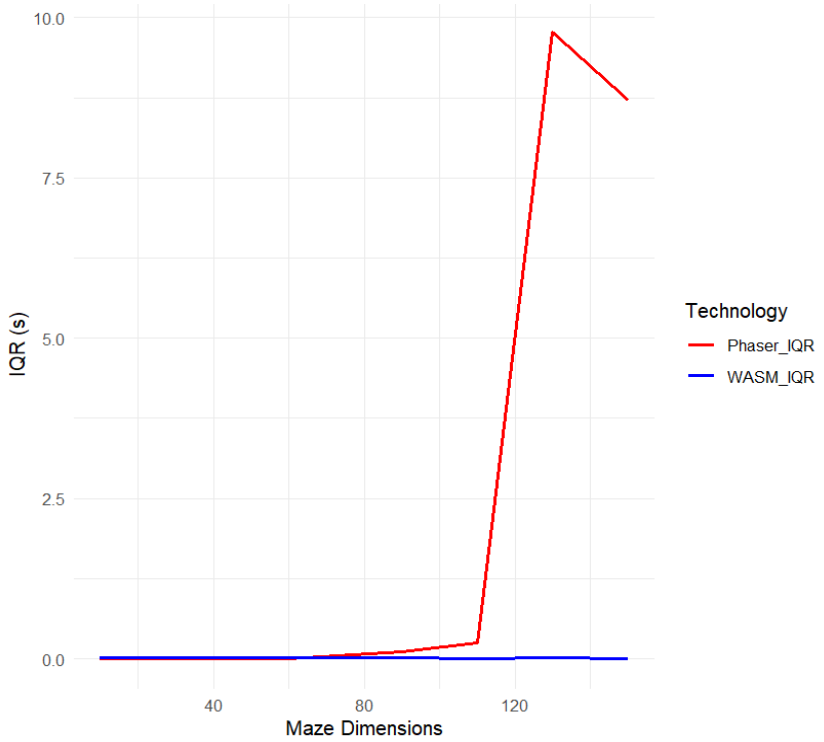

Figure 6. Comparison of interquartile range (IQR) in performance times between Phaser and WebAssembly across maze dimensions

Discussion

To determine whether a parametric or non-parametric test should be used to assess whether the difference in average execution time between Phaser and WebAssembly is statistically significant, Shapiro-Wilks tests were conducted on the data for each maze dimension. All dimensions for both technologies failed the normality test (p-values <0.05, as shown in Table 3, indicating that the execution time data does not follow a normal distribution. As a result, the non-parametric Mann-Whitney-Wilcoxon test was chosen over the parametric t-test to evaluate statistical significance.

Table 3. Comparison of average time in milliseconds to complete maze generation for different maze dimensions between WebAssembly and Phaser

Dimension	p-value	Significance	Faster
10x10	< 2,2e-16	Significant	Phaser
30x30	< 2,2e-16	Significant	Phaser
60x60	< 2,2e-16	Significant	Phaser
90x90	< 2,2e-16	Significant	WebAssembly
110x110	< 2,2e-16	Significant	WebAssembly
130x130	5,181e-08	Significant	WebAssembly
150x150	4,695e-08	Significant	WebAssembly

All evaluated dimensions demonstrate significant differences between the two subsets, with very low p-values (< 0.001) providing strong evidence against the null hypothesis that the location shift is equal to zero, indicating that there is no significant difference in time performance between the two technologies. Regarding the number of test runs performed (as listed in Table 1), the time required for maze generation increases dramatically with maze dimensions. Due to time constraints, it was not feasible to run 100 tests for each dimension. Consequently, 50 test runs were performed for 110x110 maze, while 20 test runs were conducted for 130x130 and 150x150 mazes.

The p-values for 130x130 and 150x150 dimensions (p = 5,181e-08 and p = 4,695e08, respectively), though still very small, are larger than those for other dimensions, indicating a less pronounced difference in performance times between Phaser and WebAssembly in these cases. One possible explanation is the smaller number of test runs for these higher dimensions (20 runs, compared to 50 or 100 for others), which reduces the power of the

statistical tests, making them less sensitive to detecting differences. Another factor could be the wider spread in data distribution at higher dimensions. Since the Mann-Whitney test compares ranks rather than actual values, this increased variability may cause overlapping ranks between Phaser and WebAssembly. Although the mean values show the greatest differences between the two technologies at these dimensions, the test may detect overlapping distributions, resulting in a larger p-value.

Based on the analysis of the results, we can conclude that there is a statistically significant difference in execution times across all dimensions, with WebAssembly generally performing faster than Phaser across higher dimensions. The primary reason for WebAssembly's superior performance at higher dimensions appears to be the growth curve of average execution times. WebAssembly shows a more linear increase, whereas Phaser's performance time escalates more rapidly, particularly at larger maze sizes (Figure 1). Given this trend, it could be expected that the gap between Phaser and WebAssembly will continue to widen in favour of WebAssembly as dimensions increase.

In terms of performance variability, while Phaser is consistent with smaller mazes, its performance becomes increasingly variable for larger maze dimensions, as indicated by the greater spread and outliers in the boxplots from dimension 60x60 onwards. The strong positive skew in Phaser's execution times for higher dimensions suggests that a small number of outliers with longer execution times pulls the mean upwards. This indicates that Phaser occasionally takes significantly longer to perform in certain cases, contributing to the higher average. As maze complexity grows, Phaser may experience more frequent performance bottlenecks compared to WebAssembly. In contrast, WebAssembly's lower skew and more stable performance indicate that it is more predictable and less variable across test runs.

One limitation of the testing process was the reduced number of test runs for the 110x110, 130x130 and 150x150 dimensions, which was necessary due to time constraints. Another potential limitation are the possible differences in the implementations of the algorithms, as Phaser and WebAssembly use different programming languages, which may require a slightly different coding approaches, even though the underlying logic remains the same. Additionally, a potential constraint for WebAssembly is the use of a JavaScript function to reload timers for measuring execution time. However, any slowdown resulting from this appears to be negligible compared to measuring the time directly in C++ code.

The performance differences in large maze dimensions may also be attributed to how memory is managed in WebAssembly compared to JavaScript (Phaser). WebAssembly uses a linear memory model similar to lower-level languages, where memory is allocated in contiguous blocks, enabling faster memory access. In contrast, JavaScript relies on automatic garbage collection, which simplifies development but can lead to unpredictable performance drops during long-running tasks as indicated in Haas et al. (2017). As maze sizes increase, the added complexity may strain Phaser's memory management, resulting in slowdowns and greater variability in execution times for larger dimensions.

As a result, depending on the application's complexity and performance requirements, WebAssembly may be the preferred option for generating more complex structures, particularly when execution time is a critical factor. For simpler use cases, however, WebAssembly may not provide a significant speed advantage, making Phaser a more optimal choice due to its simplicity and lack of need for prior compilation.

Conclusion

In this paper, we conducted a comparison of procedural maze generation using WebAssembly and Phaser. The results demonstrate a statistically significant difference in execution times across various maze dimensions, with very low p-values providing strong evidence against the null hypothesis. While both technologies showed notable performance variations, Phaser outperformed WebAssembly up to dimension 60x60. On the other hand, WebAssembly outperformed Phaser from dimension 90x90 onwards, especially at larger maze dimensions. This trend can be attributed to WebAssembly's more linear growth in execution times, in contrast to the steeper increase observed in Phaser. Moreover, Phaser's performance became increasingly variable as maze complexity grew, indicating a greater likelihood of performance bottlenecks. Although limitations, such as a reduced number of test runs for larger dimensions and potential differences in algorithm implementations, may have influenced the results, the findings underscore the advantages of WebAssembly for generating complex structures, while Phaser might be preferable for simpler use cases.

Further research could explore the underlying causes of the observed performance differences, such as optimisation techniques or algorithmic complexity in Phaser versus WebAssembly. Additionally, performance comparisons across different browsers or analyses of memory complexity could provide deeper insights.

Recommendations

This paper is relevant for researchers, developers, and practitioners involved in the optimization of web technologies, game development, and procedural generation. It will be of interest to those exploring performance trade-offs between WebAssembly and JavaScript frameworks like Phaser, particularly in scenarios involving the generation of complex structures such as mazes. Additionally, the paper is suitable for those investigating performance optimization, as well as those interested in understanding the impact of different technologies on execution time and scalability in web-based applications. Developers working on applications requiring efficient real-time performance, especially those using WebAssembly or Phaser, will find the findings useful for selecting the most appropriate technology based on their specific use case and system requirements.

Scientific Ethics Declaration

* The authors declare that the scientific ethical and legal responsibility of this article published in EPSTEM Journal belongs to the authors.

Conflict of Interest

* The authors declare that they have no conflicts of interest

Funding

* This research received no specific grant from any funding agency in the public, commercial, or not-for-profit sectors.

Acknowledgements or Notes

* This article was presented as an oral presentation at the International Conference on Basic Sciences, Engineering and Technology (www.icbaset.net) held in Trabzon/Türkiye on May 01-04, 2025.

References

Battagline, R. (2019). *Hands-on game development with WebAssembly: Learn WebAssembly C++ programming by building a retro space game*. Packt Publishing Ltd.

Cagiltay, N. E. (2007). Teaching software engineering by means of computer-game development: Challenges and opportunities. *British Journal of Educational Technology, 38*(3), 405–415.

Faas, T. (2017). *An introduction to HTML5 game development with Phaser.js*. AK Peters/CRC Press.

Haas, A., Rossberg, A., Schuff, D. L., Titzer, B. L., Holman, M., Gohman, D., Wagner, L., Zakai, A., & Bastien, J. (2017). Bringing the web up to speed with WebAssembly. *Proceedings of the 38th ACM SIGPLAN Conference on Programming Language Design and Implementation* (pp. 185–200).

Herrera, D., Chen, H., Lavoie, E., & Hendren, L. (2018, March 14). *WebAssembly and JavaScript challenge: Numerical program performance using modern browser technologies and devices*. McGill University, Montreal: QC, Technical Report SABLE-TR-2018-2. Retrieved from http://www.sable.mcgill.ca/publications/techreports/2018-2/techrep.pdf

Macedo, J. D., Abreu, R., Pereira, R., & Saraiva, J. (2022). WebAssembly versus JavaScript: Energy and runtime performance. *Proceedings of the 2022 International Conference on ICT for Sustainability (ICT4S 2022)* (pp. 24–34).

Midžić, N. (2024). *Using C++ programming language in web application development.* (Bachelor thesis, Faculty of Organization and Informatics at University of Zagreb).

Mustonen, M. (2023). *Web based game engine design.* (Master thesis, School of Engineering Science, Information Technology at Lappeenranta–Lahti University of Technology).

Pavkov, S., Franković, I., & Hoić Božić, N. (2017). Comparison of game engines for serious games. *2017 40th International Convention on Information and Communication Technology, Electronics and Microelectronics (MIPRO)* (pp. 728–733). IEEE.

Reiser, M., & Bläser, L. (2017). Accelerate JavaScript applications by cross-compiling to WebAssembly. *Proceedings of the 9th ACM SIGPLAN International Workshop on Virtual Machines and Intermediate Languages* (pp. 10–17).

Wilson, K. N., Ghansah, B., Ananga, P., Oppong, S. O., Essibu, W. K., & Essibu, E. K. (2024). Exploring the efficacy of computer games as a pedagogical tool for teaching and learning programming: A systematic review. *Education and Information Technologies, 30*(4),4157-4184.

Wu, B., & Wang, A. I. (2012). A guideline for game development-based learning: A literature review. *International Journal of Computer Games Technology, 2012*(1), 103710.

Ylenius, S. (2020). *Mitigating JavaScript's overhead with WebAssembly*. (Master's thesis, Faculty of Information Technology and Communication Sciences at Tampere University).

Author(s) Information

Noa Midzic
University of Zagreb, Faculty of Organization and Informatics, Pavlinska 2, 42000 Varaždin, Croatia

Matija Novak
University of Zagreb, Faculty of Organization and Informatics, Pavlinska 2, 42000 Varaždin, Croatia
Contact e-mail: *matija.novak@foi.unizg.hr*

To cite this article

Midzic, N., & Novak, M. (2025). Performance comparison of WebAssembly and Phaser in procedural maze generation. *The Eurasia Proceedings of Science, Technology, Engineering and Mathematics (EPSTEM), 34*, 172-181.

The Eurasia Proceedings of Science, Technology, Engineering & Mathematics (EPSTEM)
ISSN: 2602-3199

The Eurasia Proceedings of Science, Technology, Engineering and Mathematics (EPSTEM), 2025

Volume 34, Pages 182-194

ICBASET 2025: International Conference on Basic Sciences, Engineering and Technology

Longitudinal Fracture of Inhomogeneous Viscoelastic Beams Subjected to Combined Time-Dependent Loading: A Parametric Study

Victor Rizov
University of Architecture, Civil Engineering and Geodesy

Abstract: A parametric study of longitudinal fracture in continuously inhomogeneous viscoelastic beam structures subjected to combined time-dependent loadings is described in this paper. The beams are under angle of twist and vertical displacement which change continuously with time. Beams with different cross-sections (T-shape, I-shape, trapezium, and rightangled triangle) are considered in order to assess the influence of the beam cross-section on the longitudinal fracture. The viscoelastic behaviour under bending and torsion is treated by using time-dependent modulus of elasticity and shear modulus, respectively. A viscoelastic mechanical model with two springs and a dashpot under time-dependent strains is used in order to derive the time-dependent moduli. These moduli are applied when obtaining solution of the strain energy release rate. The compliances of the beam configuration under time-dependent angle of twist and vertical displacement are analyzed in order to derive the strain energy release rate for verification. The parametric study is carried-out by using the solution of the strain energy release rate.

Keywords: Cross-section shape, Continuously inhomogeneous beam, Longitudinal fracture, Viscoelastic behavior

Introduction

Structural materials whose properties vary continuously in the solid are known in the engineering community as continuously inhomogeneous materials. Their material properties represent continuous mathematical functions of one or more coordinates. A typical example of modern continuously inhomogeneous material with numerous applications in various areas of engineering is the functionally graded material (Gandra et al., 2011; Gururaja-Udupa et al., 2014; Nagaral et al., 2019). The attractiveness of functionally graded materials is due mainly to the fact that continuous distribution of their properties in the structural component can be formed during manufacturing with aim to improve the structural component performance under given loading combinations and external influences (Gasik, 2010; Radhika et al., 2020). An essential disadvantage of functionally graded materials is that they are prone to longitudinal fracture. The reason for this is that the functionally graded materials can be built up layer by layer (Dowling, 2007; Mahamood & Akinlabi, 2017; Rizov, 2018, 2019) which favours appearance of longitudinal cracks between layers. Certainly, these cracks have negative effect on the structural integrity. The longitudinal cracks reduce the stiffness and the load-carrying ability of the structure and may cause catastrophic collapse.

Although the application of fracture mechanics in continuously inhomogeneous structural components is relatively well established, there are some topics which have not been studied enough. In particular, such subject as the time-dependent longitudinal fracture of inhomogeneous viscoelastic beams under loading combinations which include torsion in not clarified from both theoretical and applied point of view and needs more attention. This is especially true for beam structures with cross-sections other than rectangular although such beam cross-sections have numerous applications in practice.

Our goal is to carry-out a detailed parametric study of the longitudinal fracture in a viscoealstic continuously inhomogeneous beam structure subjected to a combined time-dependent loading. In this way, we aim to clarify the influence of various factors including the beam cross-section on the longitudinal fracture. A time-dependent solution of the strain energy release rate (SERR) is derived. The solution is applied in the parametric study. In order to verify the solution, the SERR is found also by using the time-dependent compliances of the beam. Four beam configurations with T-shaped, I-shaped, trapezoidal and triangular cross-sections are considered in the parametric study of the SERR. Besides, the influence of the parameters of the combined loading on the SERR is also examined.

Analysis

Consider the beam structure depicted in Figure 1. The length and thickness of the beam are l and h, respectively. There is a longitudinal crack of length, a, in the beam as depicted in Figure1.

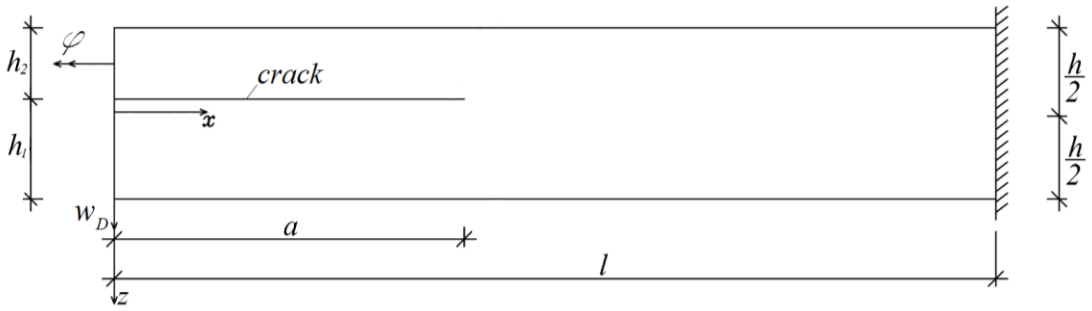

Figure 1. Geometry of a beam structure

The lower and the upper crack arm have thicknesses, h_1 and h_2, respectively.

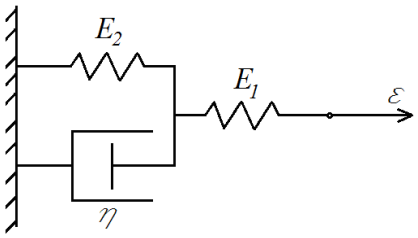

Figure 2. Viscoelastic model

The upper crack arm end is loaded in torsion so as the angle of twist, φ, changes with time, t, as given below, i.e.

$$\varphi = \beta t^2, \tag{1}$$

where β is a parameter. The lower crack arm end is loaded by in bending by a vertical force so as the variation of the vertical displacement, w_D, is described as

$$w_D = \delta t^2. \tag{2}$$

Here, δ is a parameter.

The beam has viscoelastic behaviour that is described by the viscoelastic model depicted in Figure 2. The model has two springs and a dashpot. The moduli of elasticity of the two springs are E_1 and E_2. The coefficient of viscosity of the dashpot is η. The model is under strain, ε. The variation of ε with time is expressed as

$$\varepsilon = \theta t^2, \tag{3}$$

where θ is a parameter. The equilibrium of the viscoelastic model yields the following differential equation:

$$\dot{\varepsilon}_2 + \psi_1 \varepsilon_2 = \psi_2 t^2, \tag{4}$$

where ε_2 is the strain in the spring with modulus of elasticity, E_2. The quantities, ψ_1 and ψ_2, are written as

$$\psi_1 = \frac{E_1 + E_2}{\eta}, \tag{5}$$

$$\psi_2 = \frac{E_1 \theta}{\eta}. \tag{6}$$

The equation (4) is inhomogeneous. Its solution is found as

$$\varepsilon_2 = C_1 e^{-\psi_1 t} + \varepsilon_{2n}. \tag{7}$$

The particular solution, ε_{2n}, is written in the form

$$\varepsilon_{2n} = \psi_3 t^2 + \psi_4 t + \psi_5. \tag{8}$$

After substituting of (8) in (4), one obtains

$$\psi_3 = \frac{\psi_2}{\psi_1}, \tag{9}$$

$$\psi_4 = -2\frac{\psi_2}{\psi_1^2}, \tag{10}$$

$$\psi_5 = -2\frac{\psi_2}{\psi_1^3}. \tag{11}$$

The initial condition is written as

$$\varepsilon_2(0) = 0. \tag{12}$$

Thus, the final form of (7) is obtained as

$$\varepsilon_2 = \psi_5\left(1 - e^{-\psi_1 t}\right) + \psi_3 t^2 + \psi_4 t. \tag{13}$$

The stress, σ, is found as

$$\sigma = E_1(\varepsilon - \varepsilon_2). \tag{14}$$

The time-dependent modulus of elasticity, E_*, of the viscoelastic model is defined as

$$E_*(t) = \frac{\sigma}{\varepsilon}. \tag{15}$$

By substituting of (3), (5), (6), (9), (10), (11), (13) and (14) in (15), one derives

$$E_*(t)=\frac{E_1\left[t-\frac{2\zeta}{\psi_1^3}\left(1-e^{-\psi_1 t}\right)-\frac{\zeta t^2}{\psi_1}-2\frac{\zeta t}{\psi_1^2}\right]}{t^2}, \tag{16}$$

where

$$\zeta=\frac{E_1}{\eta}. \tag{17}$$

The viscoelastic behaviour of the beam under torsion is treated also by using the model in Figure 2. Thus, formula (16) is applied to determine the time-dependent shear modulus, G_*, under torsion. For this purpose, E_1, E_2 and η are replaced with G_1, G_2 and η_τ, respectively. Here, G_1 and G_2 are the shear moduli of the two springs, η_τ is the coefficient of viscosity. The beam in Figure 1 exhibits smooth material inhomogeneity in longitudinal direction. The distributions of material properties along the beam length are written as

$$E_1=E_{1L}e^{\mu_1\frac{x}{l}}, \tag{18}$$

$$E_2=E_{2L}e^{\mu_2\frac{x}{l}}, \tag{19}$$

$$\eta=\eta_L e^{\mu_3\frac{x}{l}}, \tag{20}$$

$$G_1=G_{1L}e^{\mu_4\frac{x}{l}}, \tag{21}$$

$$G_2=G_{2L}e^{\mu_5\frac{x}{l}}, \tag{22}$$

$$\eta_\tau=\eta_{\tau L}e^{\mu_6\frac{x}{l}}, \tag{23}$$

where

$$0\le x\le l \tag{24}$$

In formulae (18) – (24), E_{1L}, E_{2L}, η_L, G_{1L}, G_{2L} and $\eta_{\tau L}$ are the values of E_1, E_2, η, G_1, G_2 and η_τ at $x=0$ (the axis, x, is shown in Fig. 1), μ_i are parameters (here, $i=1,2,...,6$).

The torsion moment, T, at the upper crack arm end is found in the following way. First, the angle of twist is expressed by using the integrals of Maxwell-Mohr. The result is

$$\varphi=\int_0^a\frac{T_1}{S_1}dx+\int_a^l\frac{T_2}{S_2}dx, \tag{25}$$

where S_1 and S_2 are the stiffness in torsion of the upper crack arm and the un-cracked beam portion (S_1 and S_2 depend on the beam cross-section shape), T_1 and T_2 are the torsion moments. Figure 1 indicates that

$$T_1 = T\,, \tag{26}$$

$$T_2 = T\,. \tag{27}$$

By using of (25), (26) and (27), one obtains

$$T = \frac{\varphi}{\varsigma_1 + \varsigma_2}\,, \tag{28}$$

where

$$\varsigma_1 = \int_0^a \frac{1}{S_1}\,dx\,, \tag{29}$$

$$\varsigma_1 = \int_a^l \frac{1}{S_2}\,dx\,. \tag{30}$$

S_1 and S_2 are functions of x since the beam is continuously inhomogeneous in longitudinal direction (S_1 and S_2 depend on the G_* where G_* is function of x). The integrals (29) and (30) are solved by the MatLab. The vertical force, F, at the lower crack arm end is derived in a similar manner. The vertical displacement is written as

$$w_D = \int_0^a \frac{Fx^2}{E_* I_1}\,dx + \int_a^l \frac{Fx^2}{E_* I_2}\,dx\,, \tag{31}$$

where I_1 and I_2 are the moments of inertia of the cross-sections of the lower crack arm and the un-cracked beam portion (I_1 and I_2 are determined depending on the shape of the cross-section). From (31), one derives

$$F = \frac{w_D}{\vartheta_1 + \vartheta_2}\,, \tag{32}$$

where

$$\vartheta_1 = \int_0^a \frac{x^2}{E_* I_1}\,dx\,, \tag{33}$$

$$\vartheta_2 = \int_a^l \frac{x^2}{E_* I_2}\,dx\,. \tag{34}$$

The MatLab is used to solve the integrals (33) and (34).

The SERR, G, is obtained as

$$G = \frac{dU}{bda}, \tag{35}$$

where U is the strain energy, b is the beam width at height, h_1, above the beam lower surface (b depends on the beam cross-section shape).

The strain energy is found as

$$U = U_1 + U_2 + U_3 + U_4, \tag{36}$$

where U_1 and U_2 are the strain energies in the upper crack arm and the un-cracked beam portion due to torsion, U_3 and U_4 are the strain energies in the lower crack arm and the un-cracked beam portion due to bending.

The strain energy, U_1, is written as

$$U_1 = \int_0^a \frac{T^2}{2S_1} dx \ . \tag{37}$$

U_2 is derived as

$$U_2 = \int_a^l \frac{T^2}{2S_2} dx \ . \tag{38}$$

The strain energies, U_3 and U_4, are determined as

$$U_3 = \int_0^a \frac{F^2 x^2}{2E_* I_1} dx \ , \tag{39}$$

$$U_4 = \int_a^l \frac{F^2 x^2}{2E_* I_2} dx \ . \tag{40}$$

By combining of (35) – (40), one obtains

$$G = \frac{1}{b}\left(\frac{T^2}{2S_1} + \frac{F^2 a^2}{2E_* I_1} - \frac{T^2}{2S_2} - \frac{F^2 a^2}{2E_* I_2} \right). \tag{41}$$

The material properties involved in S_1, S_2 and E_* are determined at $x = a$. The SERR is calculated by (41) for different beam cross-sections. The time-dependent beam compliances are analyzed to derive an alternative solution of the SERR for verification of (41). The beam compliances under torsion and bending, C_T and S_F, are determined as

$$C_T = \frac{\varphi}{T}, \tag{42}$$

$$C_F = \frac{w_D}{F}. \tag{43}$$

The SERR, G_T and G_F, due to torsion and bending are found as

$$G_T = \frac{T^2}{2b}\frac{dC_T}{da}, \tag{44}$$

$$G_F = \frac{F^2}{2b}\frac{dC_F}{da}. \tag{45}$$

Finally, the SERR is obtained as

$$G = G_T + G_F. \tag{46}$$

The results derived by using (46) for different beam cross-sections match these found by (41) which verifies the SERR solution.

Results of Parametric Study

The results are obtained by using four different cross-sections of the beam in Figure 1.

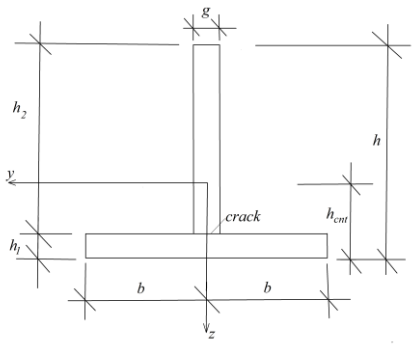

Figure 3. T-shaped cross-section

First, the SERR is determined for the beam whose cross-section has a T-shape. The geometry of this cross-section is depicted in Figure 3. The longitudinal crack is situated in the plane of contact of the flange and the web. The thicknesses of the flange and the web are h_1 and h_2, respectively. The width of the flange is $2b$. The upper crack arm has width, g, and thickness, h_2. The stiffness in torsion of the upper crack arm and the un-cracked beam portion which is involved in the SERR solution is calculated by applying the formula presented in Chobanian (1997). The moments of inertia of the lower crack arm and the un-cracked beam portion are found by using methods of strength of materials (Obodovski & Hanin, 1981).

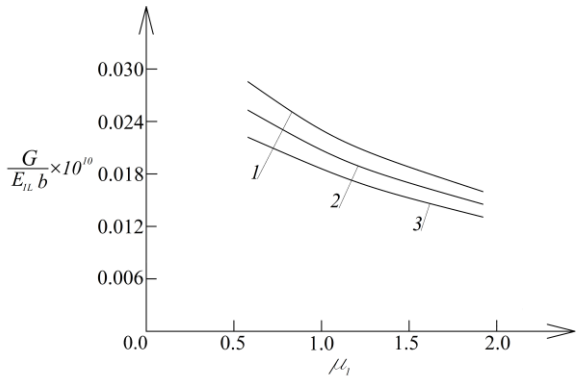

Figure 4. The SERR versus μ_1 for T-shaped cross-section

A parametric study of the SERR is carried-out. The main aim of the parametric study is to assess the influence of the cross-section geometry on the SERR. The effects of the material inhomogeneity and the loading conditions are also evaluated. It is assumed that $b = 0.015$ m, $h = 0.035$ m, $l = 0.700$ m, $\beta = 0.003 \times 10^{-8}$ rad/s^2 and $\delta = 0.004 \times 10^{-7}$ m/s^2.

The variation of the SERR with increasing of parameter, μ_1, at $h_1 / b = 0.02$ (curve 1), $h_1 / b = 0.04$ (curve 2) and $h_1 / b = 0.08$ (curve 3) is depicted in Figure 4. One can observe that the SERR reduces when μ_1 and h_1 / b increase (Figure 4). One can examine the effect of the parameter, β, on the SERR at $g / b = 0.03$ (curve 1), $g / b = 0.06$ (curve 2) and $g / b = 0.09$ (curve 3) in Figure 5. The curves in Figure 5 indicate that when β increases, the SERR increases too. However, increase of g / b ratio causes reduction of the SERR (Figure 5).

Next cross-section is I (Figure 6). The width and thickness of the lower flange are $2b$ and h_1, respectively. The dimensions of the upper flange are the same (Figure 6). The width of the web is g. The longitudinal crack is situated in the plane of contact of the lower flange and the web. The stiffness in torsion and the moments of inertia are determined by applying the formulae presented in (Chobanian, 1997).

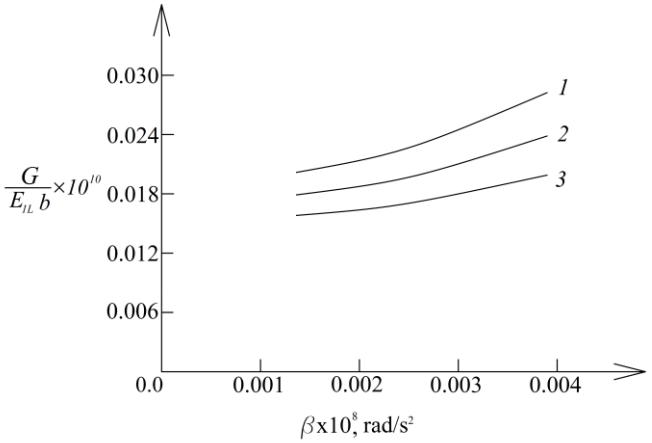

Figure 5. The SERR versus β for T-shaped cross-section

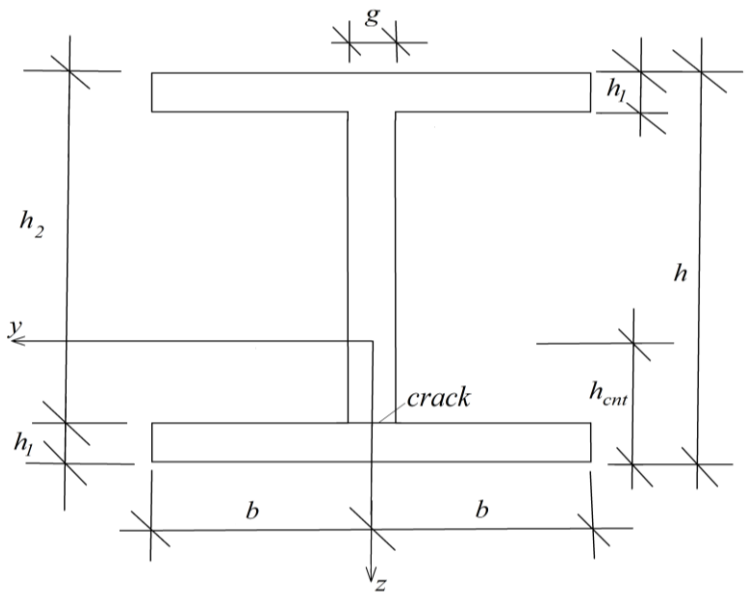

Figure 6. I-shaped cross-section

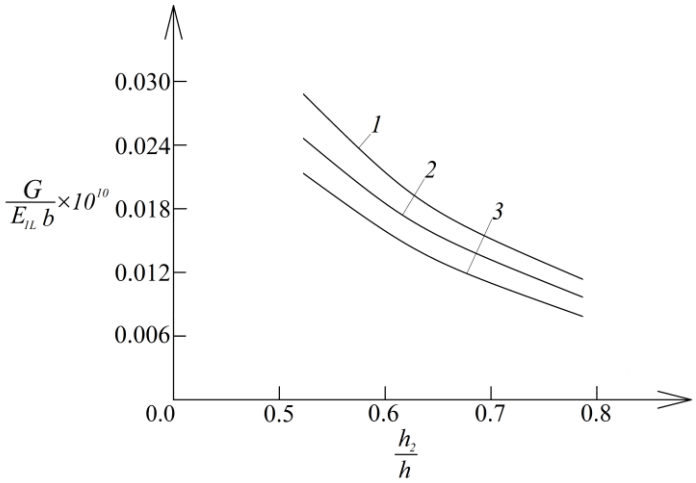

Figure 7. The SERR versus h_2 / h for I-shaped cross-section

The influence of h_2 / h on the SERR at $g / h = 0.004$ (curve 1), $g / h = 0.008$ (curve 2) and $g / h = 0.012$ (curve 3) is illustrated in Figure 7. The inspection of Figure 7 indicates that the SERR reduces when h_2 / h and g / h ratios increase.

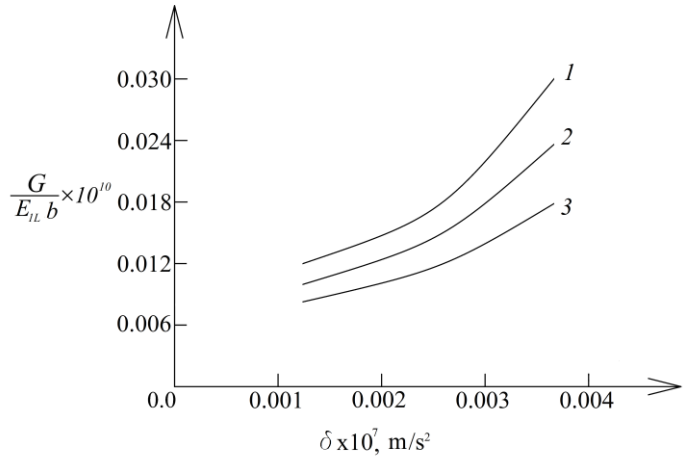

Figure 8. The SERR versus δ for I-shaped cross-section

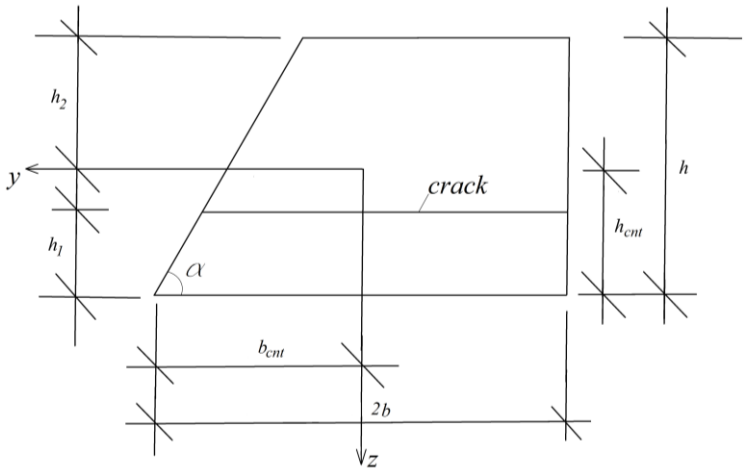

Figure 9. Trapezoidal cross-section

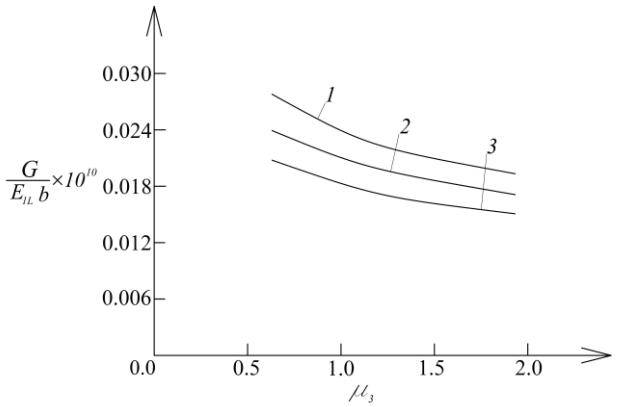

Figure 10. The SERR versus μ_3 for trapezoidal cross-section

The SERR is presented as a function of parameter, δ, at $\mu_2 = 0.5$ (curve 1), $\mu_2 = 1.0$ (curve 2) and $\mu_2 = 2.0$ (curve 3) in Figure 8. The SERR increases quickly with increase of δ (Figure 8). The increase of μ_2 induces reduction of the SERR (Figure 8).

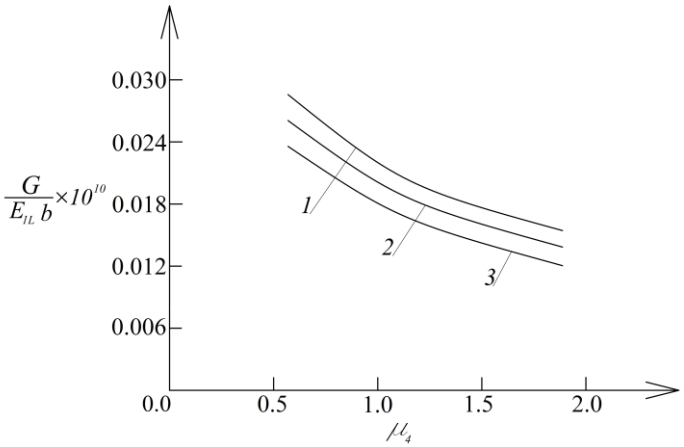

Figure 11. The SERR versus μ_4 for trapezoidal cross-section

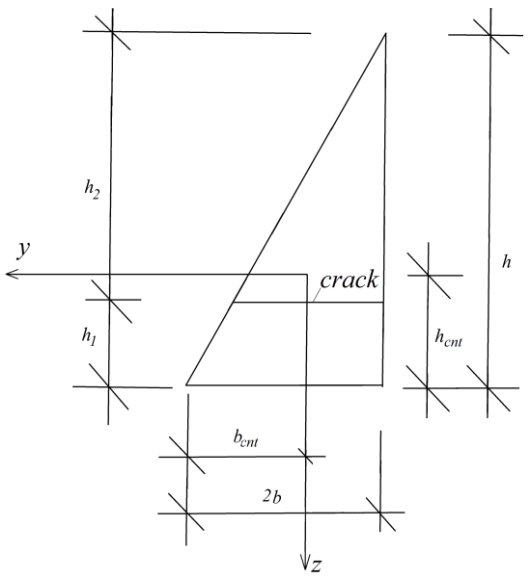

Figure 12. Cross-section in the shape of rightangled triangle

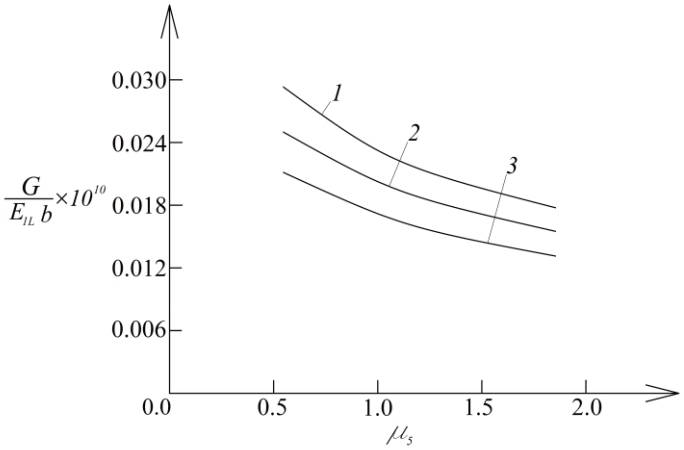

Figure 13. The SERR versus μ_5 for rightangled triangle

The SERR is analyzed assuming that the beam has trapezoidal cross-section. The geometry of this cross-section is shown in Figure 9. The lower base and thickness of the cross-section are denoted by $2b$ and h, respectively. The formulae in Chobanian (1997) are used to determine the stiffness in torsion and the moments of inertia which are needed to calculate the SERR.

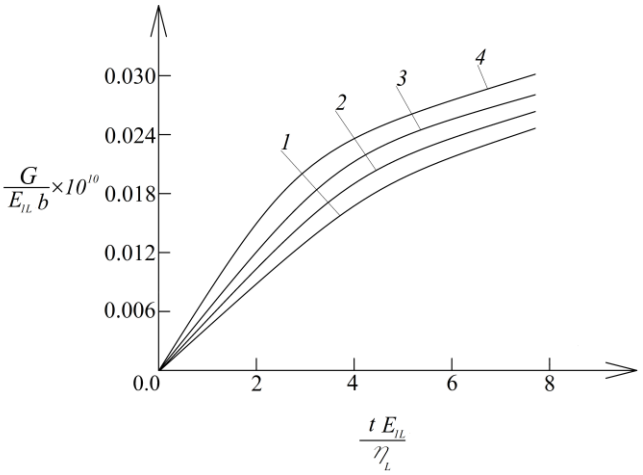

Figure 14. The SERR versus time

The effect of the parameter, μ_3, on the SERR at $h/2b=1.3$ (curve 1), $h/2b=1.6$ (curve 2) and $h/2b=1.9$ (curve 3) is presented in Figure 10. The curves in Figure 10 indicate that the SERR reduces when μ_3 and $h/2b$ ratio increase. One can examine the influence of μ_4 on the SERR at $\alpha=45^\circ$ (curve 1), $\alpha=60^\circ$ (curve 2) and $\alpha=75^\circ$ (curve 3) in Figure 11 (the angle, α, is depicted in Figure 9). Increase of α and μ_4 causes reduction of the SERR (Figure 9).

Finally, the SERR is investigated assuming that the cross-section is a rightangled triangle (Figure 12). The base and thickness of this cross-section are denoted by $2b$ and h, respectively (Figure 12). The stiffness in torsion and the moments of inertia are taken from (Chobanian, 1997).

The SERR is presented as a function of μ_5 in Figure 13 at $\mu_6=0.5$ (curve 1), $\mu_6=1.0$ (curve 2) and $\mu_6=2.0$ (curve 3). The curves show that the strain energy release rate reduces when μ_5 and μ_6 increase (Figure 13).

The SERR is presented in Figure 14 as function of time for I-shaped cross-section (curve 1), T-shaped cross-section (curve 2), trapezoidal cross-section (curve 3) and triangular cross-section (curve 4). The SERR in Figure 14 is found for the case when the four beam cross-sections have the same area. The lowest SERR is obtained for I-shaped cross-section.

Conclusion

Parametric study of longitudinal fracture in a viscoelastic continuously inhomogeneous beam configuration subjected to a combined time-dependent loading is carried-out. The loading represents a combination of angle of twist and vertical displacement which vary smoothly with time. Solution of the SERR is found. The beam compliances are analyzed to verify the SERR. The study reveals that the SERR reduces with increasing of parameters, μ_i, where $i = 1, 2, ..., 6$. The increase of h_1 / b, g / b, h_2 / h, g / h and $h / 2b$ ratios and angle, α, also causes reduction of the SERR. These findings are linked with beam stiffness increase. Concerning the influence of parameters, β and δ, the study indicates that the SERR increases when β and δ increase. The influence of the shape of the beam cross-section on the SERR is examined closely. Four cross-sections (T-shaped, I-shaped, trapezium and rightangled triangle) are considered. It is found that the SERR is minimal for I-shaped cross-section. Since this finding is obtained assuming that the four cross-sections have the same area, it can be concluded that the I-shaped cross-section is optimal for improving the longitudinal fracture behaviour of viscoelastic inhomogeneous beams subjected to combined time-dependent loadings.

Recommendations

The analysis presented in this paper can be sophisticated by applying non-linear viscoelastic models of the beams. In this way, the effect of the cross-section shape on the longitudinal fracture behavior of non-linear viscoelastic inhomogeneous beams can be examined.

Scientific Ethics Declaration

* The author declares that the scientific ethical and legal responsibility of this article published in EPSTEM Journal belongs to the author.

Conflict of Interest

* The author declares that he has no conflicts of interest.

Acknowledgements or Notes

* This article was presented as an oral presentation at the International Conference on Basic Sciences, Engineering and Technology (www.icbaset.net) held in Trabzon/Türkiye on May 01-04, 2025.

References

Dowling, N. (2007). *Mechanical behavior of materials*. Pearson.

Chobanian, K.S. (1997). *Stresses in combined elastic solids*. Science.

Gandra, J., Miranda, R., Vilaca, P., Velhinho, A., & Teixeira, J.P. (2011). Functionally graded materials produced by friction stir processing. *Journal of Materials Processing Technology, 211,* 1659-1668.

Gasik, M.M. (2010). Functionally graded materials: Bulk processing techniques, *International Journal of Materials and Product Technology, 39,* 20-29.

Gururaja Udupa, Shrikantha Rao, S., & Rao Gangadharan, K. (2014). Functionally graded composite materials: An overview. *Procedia Materals Science, 5,* 1291-1299.

Mahamood, R. C., & Akinlabi, E. T. (2017). *Functionally graded materials*. Springer.

Nagaral, M., Nayak, P. H., Srinivas, H. K., & Auradi V. (2019). Characterization and tensile fractography of nano zro2 reinforced copper-zinc alloy composites. *Frattura ed Integrità Strutturale, 13,* 370-376.

Obodovski, B. A., & Hanin, S. E. (1981). *Strength of materials*. Vishta shkola.

Radhika, N., Sasikumar, J., Sylesh, J. L., & Kishore, R. (2020). Dry reciprocating wear and frictional behaviour of B4C reinforced functionally graded and homogenous aluminium matrix composites. *Journal of Materials Research and Technology*, *9,* 1578-1592.

Rizov, V. I. (2018). Non-linear delamination in two-dimensional functionally graded multilayered beam. *International Journal of Structural Integrity, 9,* 646-663.

Rizov, V.I. (2019). Influence of material inhomogeneity and non-linear mechanical behaviour of the material on delamination in multilayered beams. *Frattura ed Integrità Strutturale, 47,* 468-481.

Author Information

Victor Rizov
Department of Technical Mechanics
University of Architecture, Civil Engineering and Geodesy
1 Chr. Smirnensky blvd.
1046 – Sofia
Bulgaria
Contact e-mail: *v_rizov_fhe@uacg.bg*

To cite this article:

Rizov, V. (2025). Longitudinal fracture of inhomogeneous viscoelastic beams subjected to combined time-dependent loading: A parametric study. *The Eurasia Proceedings of Science, Technology, Engineering and Mathematics (EPSTEM), 34,* 182-194.

The Eurasia Proceedings of Science, Technology, Engineering & Mathematics (EPSTEM)
ISSN: 2602-3199

The Eurasia Proceedings of Science, Technology, Engineering and Mathematics (EPSTEM), 2025

Volume 34, Pages 195-201

ICBASET 2025: International Conference on Basic Sciences, Engineering and Technology

WCAG Success Criteria to Support Accessibility of Elderly Users in Bi-lingual Websites

Baha Khasawneh
Princess Sumaya University for Technology

Abstract: The Internet has provided significant opportunities for the inclusion of older adults through their use of websites specializing in medical information, news, and government services. Even though most websites are monolingual, mainly in English, many websites are bilingual or use multilingual content. To make websites senior-friendly and more accessible, it's important to study the impact of localization on the usability of bilingual websites for older adults. To overcome potential digital accessibility or lingual confusion, web pages must be designed to be natively accessible. The website URL and standardizing icons, error messages, warnings, and form filling are very important to web accessibility. A study was conducted to determine accessibility for older users on bilingual websites. Based on the Analysis of the responses, the study established the need for new accessibility success criteria to overcome some language-related challenges using bilingual websites. The study proposes six accessibility criteria supplementary to the WCAG guidelines, with rationale and intent for each recommended criterion.

Keywords: Web accessibility, WCAG, Accessibility, Bilingual websites

Introduction

For the last decade, the world has faced two important challenges, mainly the advancement in ICT-based technologies and the demographic shift in population aging. According to United Nations estimates (Carrillo, 2021; UN, 2020), the world's aging population will increase from 12% to 22% by the year 2050, mainly in developing countries, with women accounting for the largest proportion by 2050. We are witnessing great advancements, mainly the development of information and communication technology and the spread of web applications on various devices, including fixed and portable computers, smartphones, tablets, and wearable devices. WEB accessibility for people with disabilities and the elderly is gaining significant attention to keep pace with these rapid advancements. This is because technology provides easier options for accessing government services and getting much-needed information (Juristic & Bogataj, 2024). This fact is very significant for the elderly and people with disabilities since technology helps to improve their skills to live more easily while maintaining their independence and dignity and enables them to communicate socially and obtain information and services within a digital environment, also improving digital inclusion for all.

Many countries, international institutions, designers, and developers have adopted different web accessibility standards to make new technologies and applications more accessible and easier to use for all web users, mainly people with disabilities and the elderly (Chen &Yang, 2015). The World Wide Web Consortium and the Standards Organization have developed accessibility standards and guidelines for the web and all digital communication, as well as principles and standards for developers and designers alike. Many standards for digital accessibility are officially recognized in many countries, but they are all largely derived from or built on the WCAG Guidelines. Although these principles were developed for people with different functional disabilities, they help web users facilitate access and accessibility in general, including older persons (W3C, 2008).

While most web pages are designed in one language, mainly English (Ding et al., 2023), non-English websites or multilingual or bilingual websites are on the rise due to the proliferation of web technology globally (Miraz et al., 2013). Many of these websites use scripts written from right to left and numbers or symbols from left to right, like Arabic, Hebrew, and Urdu (Goldenberg & Tractinsky, 2021). The accessibility of such bilingual web pages represents a challenge for people with disability and generally for older users (Sayago & Blat, 2009). Mostly in switching from one direction to another, and in the use of English abbreviations and technical terms. Moreover, when localization issues are ignored or overlooked (Ishida, 2010).

In this paper, we will examine web accessibility guidelines in bilingual web pages as they relate to older people and how it developed across different versions. We will also propose a set of new guidelines to address the difficulties of older adults. These criteria were based on the findings of our study. Adopting these new criteria would make bilingual websites more accessible for older persons, by overcoming the challenges when using two different languages, mainly Arabic and English. The rest of the paper is organized as follows: in Section 2 we present the web accessibility guidelines structure and criteria with detailed accessibility needs and challenges for the elderly. In Section 3, we review related literature. Section 4 describes our survey and findings. In section 5 we propose a set of accessibility criteria for bilingual websites for old users, and Section 6 includes final remarks and future work.

WEB Accessibility Guidelines Overview

WCAG 1.0 is part of the Web Accessibility Initiative (WAI) by the World Wide Web Consortium (W3C). These guideline recommendations were introduced in 1999 to promote accessibility among web developers, not only to persons with hearing disability, blindness, or cognitive and learning disabilities but to all users (W3C, 1999). The standard is organized to include a guideline title, rationale, and the group of users who benefit from it. In addition, a checkpoint definition (for developers) with three priorities (Must, Should, May) and 3 conformance levels (A, AA, AAA). The set of recommendations includes 14 guidelines with 65 techniques, 16 of which are priority 1, 30 of priority 2, and 19 of priority 3. It also includes how to implement each checkpoint, with detailed examples of using HTML, CSS, SMIL, and MathML (W3C, 1999).

The next major guideline, WCAG 2.0, was introduced in 2008 and revised in 2018 (W3C, 2018) with a significant shift in its structure. It divides the guidelines into four main principles, Perceivable, Operable, Understandable, and Robust (POUR), while keeping the three levels of conformance. Table 1 details the hierarchy of these guidelines.

Table 1. WCAG 2.0 guidelines hierarchy

Principle	Guidelines	Success criteria	Level A	Level AA	Level AAA
Perceivable	4	22	9	5	8
Operable	4	20	9	3	8
Understandable	3	16	5	5	7
Robust	1	2	2	0	0

WCAG 2.1, published in 2018 introduced 17 newer success criteria to improve compliance with WCAG 2.0 and to provide room for future improvements (W3C, 2024). Both WCAG 2.0 and WCAG 2.1 guidelines had no criteria just for older people in particular but highlighted the criteria that meet the needs of older people's web accessibility, which overlaps with users with disabilities (W3C, 2018). In their literature review (Henry & Arch, 2018), WAI highlighted 20 success criteria with full explanation and techniques for how to apply them for old users.

The newer WCAG 2.2 guidelines extended the work of WCAG 2.1 with the addition of 8 new criteria to support accessibility for older users. However, the issue of multilingual or bilingual in particular received little attention in all the guidelines, nonetheless, it included a few techniques for using HTML language attribute or setting a default language for a page or a PDF document (W3C, 2024).

Elderly Accessibility Needs and Challenges

The use of the Internet by older adults is as important as any other age group for what it can offer for their mental or physical health, and social interaction (Ding et al., 2023; Yang et al., 2022; Rasi-Heikkinen & Doh,

2023). Their digital inclusion is also deemed important in developed countries, while in the rest of the world, the issue of older adults' inclusion is greatly influenced by Internet availability, digital skills, and accessibility issues (Helsper, 2021).

The Web accessibility initiative (WAI, https://www.w3.org/WAI/) aims at making the Internet available for all web users mainly people with functional disabilities, has identified 6 functional disabilities affecting accessibility such as vision disability, hearing disability, physical impairment, and cognitive and learning disabilities. While older adults may share similar disabilities, the cause of these impairments is due mainly to aging. Table 2 below lists 4 age-related impairments and 4 age-related challenges that influence accessibility for older users. The recent standard.

Table 2. Old adults' impairments and challenges

İmpairment	Effects
Declining vision	Reduction in color contrast and sensitivity, and focus
Declining physical capability	Reduced motor control
Declining hearing	Difficulty hearing
Declining mental abilities	Decline in short-term memory, lower mental concentration, and being easily distracted
Geographical challenge	Low connection speed
Technological challenge	Use of old technology
Skills Challenge	New to the web
Skills challenge	Infrequent user

*Source w3c

Czaja et al. (2019) argue that older users are slower in learning new techniques if multiple tasks are required at the same time. These abilities tend to decline with age, and it is essential to take that into account when designing web pages, and even more for multilingual or bilingual pages (Ding et al., 2023). Numerous studies focused on the older person's accessibility of health-related sites or common services web pages (Fernandes et al., 2023; Acosta et al., 2020), but few researched the adequacy and accessibility of multi-lingual or bi-lingual pages (Vázquez & Bolfing, 2013; Ishida, 2010). For this reason, and to promote better and less confusing interaction, we propose several accessibility criteria as an addition to the WCAG standards to facilitate the use of bi-lingual web pages for older people.

Related Work

Web accessibility for older people has been extensively studied and researched while focusing on common disabilities shared amongst people with disabilities and older people (Sayago & Blat, 2009; Affonso et al., 2010). With many studies that suggested making websites more accessible and friendly to use, the National Institute on Aging (https://www.nia.nih.gov/), enforced a policy to make websites more elderly-friendly that is based on WCAG standards. These include designing readable text, information presentation, and audiovisual content.

Website accessibility evaluation also received more attention across many disciplines such as education, healthcare, and government services, covering all disabilities and elderly needs (ltinier et al., 2022; Bhagat & Joshi, 2019; Vigo & Conway, 2013). Acosta et al. (2020) identified the challenges and suggested improvements in health services website Accessibility by integrating intelligent human systems. Orbán-Mihálykó and Sik-Lany (2019), evaluated the accessibility of European health-related websites in 48 EU countries and found that the percentage of elderly does not affect the software testing results in any of the respective countries. Fernandes et al. (2023) and Mason et al. (2021) and Alajarmeh (2021) evaluated the web accessibility of international and popular health websites, in which they identified different inaccessibility challenges and suggested recommendations and evaluation tools for all challenged groups, including the elderly.

Since the start of the WAI-AGE initiative (WAI, (https://www.w3.org/WAI/WAI-AGE/), Abou-Zahra et. al. (2008), highlighted the need to consider the accessibility of aging web users as important as it is for people with disabilities. Their recommendations are for developers, researchers, and users to review and develop better accessibility practices that are based on the real needs of the aging Web users. The study highlighted the five main objectives of the initiative to overcome the digital divide for those with age-related needs. These objectives have influenced research directions for the next two decades. The set of objectives focused on developing

guidelines to include older people and to create a continuing exchange of ideas between all accessibility stakeholders, mainly developers.

Many studies since, focused on the different needs, challenges, and problems facing elderly web users Junqueira, (2023), Ran et al. (2024), Martin-Hammond et al. (2021) and Sayago and Blat, (2009). For example, Lara et al., (2010) proposed a set of 30 success criteria based on the four accessibility principles that address older users' accessibility WCAG2.0 standard. None of these success criteria focus on multilingual or bilingual websites. However, Vázquez and Bolfing (2013), observed common gaps in multilingual websites by not following a standardized pattern in lingual and culture-related settings. The study also emphasized the need for localization rather than only the translation of terms and abbreviations. Other studies addressed multilingual website usability (Miraz et al., 2013), bilingual user interface challenges (Goldenberg & Tractinsky, 2021), and localization (Guptaet al., 2012).

Survey and Key Findings

To identify specific accessibility issues for older users in bilingual websites (Arabic and English), we conducted a survey, analyzed our findings, and reported the main outcomes of the survey. The questions focused on six important accessibility issues. The first is on the suitability of the website URL, and the second is related to pop-up windows. The next two issues investigate the use of localized Icons, measurement units, abbreviations, and symbols. The last two topics address filling forms and error messages, and alerts. The main contribution is to derive appropriate accessibility guidelines that could be amended to the current WCAG standards, based on needs as they relate to elderly users of bilingual webpages.

The survey was distributed to 50 old web users aged 60+, 35 attempted the survey questions, and only 30 responses were used. All persons surveyed describe themselves as frequent web users who are fluent in Arabic but English illiterate. We suggested a few bilingual websites in the areas of news, healthcare, and telecommunication, in addition to their regularly visited websites.

Almost all surveyed (90%) believe that if the URL were in Arabic, and not in English, abbreviated letters, the site would be easier to remember and track, particularly when accessing other pages on the same site. On the question of pop-up windows, all respondents feel confused and annoyed when pop-ups appear. Pop-ups are confusing, particularly if accompanied by English audio, and do not offer the option of closing the window. Many think either an error has occurred or they did something wrong, and often react by closing the main page rather than the pop-up window. On the questions of localized icons, units, abbreviations, and symbols, 90% of respondents are not familiar with localized icons, and 70% do not prefer abbreviations and measurement units even in their native language. For example, the lack of standardized Icons requires knowing the different Icons on different sites, and many times leads to confusion and mistakes.

Filling forms presents a challenge for 90% of respondents, mainly when some information is required in the second language, such as medical information like medicine names and laboratory information, or when filling forms for travel. The confusion comes from having to fill in forms in bi-directional text and the need to change keyboard settings to do so.

Proposed New Success Criteria

In this section, we propose a set of new success criteria that could be integrated into the latest WCAG 2.2 guidelines to ensure better accessibility for older people in bilingual web pages. The proposed success criteria are derived from the survey and are designed to align with the four WCAG principles of Perceivable, Operable, Understandable, and Robust. Each criterion will have a suggested level, description, rationale, and to whom it is intended.

• *Success Criteria* (Level AAA): The URL of the main page and all pages in the preferred language.
Rationale: The main web page and all other pages must have the URL in the preferred language with no abbreviations to prevent confusion and distraction.
Intent: Reading disabilities and language literacy.

• *Success Criteria* (Level A): No pop-up windows
Rationale: Pop-up windows tend to distract old users and give the impression of wrong action.

Intent: For old people who are technically challenged.

• *Success Criteria* (Level AA): All units and abbreviations are localized
Rationale: Old users find it hard to convert between metric and non-metric systems like temperature, weigh units, and measurements.
Intent: For old people who are technically challenged.

• *Success Criteria* (Level AA): Form filling forms accept only the language of the page
Rationale: Old users might get confused if two languages are required to fill a form more apparent in languages with right-to-left text directions.
Intent: For old people with impaired vision or with learning disabilities.

• *Success Criteria* (level AA): Errors and alerts in the language of the page
Rationale: This makes it easier to recognize what went wrong to prevent confusion and to be able to correct.
Intent: Suitable for all users.

Conclusion

Web accessibility is of great importance not only for people with disabilities but also for the elderly. As the world is increasingly digital, more aging users rely on services and information provided by different electronic means and applications. While WCAG guidelines are designed to overcome accessibility barriers, new guidelines are still needed due to technological advancements and to accommodate ever-changing needs. In this study, we proposed to help aging users who are English illiterate overcome accessibility barriers that arise when using bilingual websites. The proposed success criteria could be extended to popular Apps and digital platforms. Our future work will focus on using AI tools to dynamically make website content more accessible based on users' age and their knowledge of technology.

Scientific Ethics Declaration

* The authors declare that the scientific ethical and legal responsibility of this article published in EPSTEM Journal belongs to the authors.

Conflict of Interest

* The authors declare that they have no conflicts of interest

Funding

* This research received no specific grant from any funding agency in the public, commercial, or not-for-profit sectors.

Acknowledgements or Notes

* This article was presented as an oral presentation at the International Conference on Basic Sciences, Engineering and Technology (www.icbaset.net) held in Trabzon/Türkiye on May 01-04, 2025.

References

Abou-Zahra, S., Brewer, J., & Arch, A. (2008). Towards bridging the accessibility needs of people with disabilities and the ageing community. *International Cross-Disciplinary Conference on Web Accessibility*, 83–86.

Acosta-Vargas, P., Hidalgo, P., Acosta-Vargas, G., Gonzalez, M., Guaña-Moya, J., & Salvador-Acosta, B. (2020). Challenges and improvements in website accessibility for health services. *International Conference on Intelligent Human Systems Integration* (pp. 875–881). Springer.

Affonso de Lara, S. M., Watanabe, W. M., dos Santos, E. P. B., & Fortes, R. P. M. (2010). Improving WCAG for elderly web accessibility. *Proceedings of the 28th ACM International Conference on Design of Communication - SIGDOC,* 175-182.

Alajarmeh, N. (2021). Evaluating the accessibility of public health websites: An exploratory cross-country study. *Universal Access in the Information Society*, *21*(3), 771-789.

Bhagat, S., & Joshi, P. (2019). Evaluation of accessibility and accessibility audit methods for e-governance portals. *Proceedings of the 12th International Conference on Theory and Practice of Electronic Governance*, 220-226.

Carrillo, A. M. (2021) *Ageing in a digital world – from vulnerable to valuable*. ITU Publication Report. Retrieved from https://www.itu.int/dms_pub/itu.pdf

Czaja, S.J., Boot, W.R., Charness, N., & Rogers, W.A. (2019). *Designing for older adults: Principles and creative human factors approaches* (3rd ed.). CRC Press.

Eberhard, D., Simons, G., & Fennig, C. (2020). Ethnologue: Languages of the world, *Abgerufen am*, *4*, 30.

Fernandes, K., Paramananthan, S., Cockburn, L., & Nganji, J. (2023). Readily available but how accessible? An analysis of the web accessibility of healthcare-related resources. *Journal of Accessibility and Design for All*, *13*(2), 188–215.

Goldenberg, Y., & Tractinsky, N. (2021). Towards the right direction in bidirectional user interfaces. *Proceedings of the 2021 CHI Conference on Human Factors in Computing Systems*, 1-13.

Gupta, N., Fischer, A. R., & Frewer, L. J. (2012). Socio-psychological determinants of public acceptance of technologies: A review. *Public Understanding of Science, 21*(7), 782–795.

Helsper, Ellen (2021) *The digital disconnect*. SAGE Publications.

Henry, S. L., & Arch, A. (2018, February 22). Overview of "web accessibility for older users: a literature review. Retrieved from https://www.w3.org

Ishida, R. (2010). The multilingual web: Where are we?. Retrieved from http://www.multilingualweb.eu

Junqueira, L.D., Freire, A.P., GrUtzmann, A., & Zitkus, E. (2023). Challenges and barriers faced by older adults to access legislative e-participation platforms in Brazil. *The Electronic Journal of Information Systems in Developing Countries*, 89.

Jurišić, I., & Bogataj, D. (2024). Enhancing Digital Government Engagement among Older Adults: Literature Review and Research Agenda. *IFAC-PapersOnLine*, *58*(3), 256-261.

ltinier, A., Oncins, E., Sauberer, G., & Mehigan, T. (2022). Demystifying digital accessibility and fostering inclusive mindsets. compliance with the European Standard for digital accessibility EN 301 549. *European Conference on Software Process Improvement (EuroSPI),* 595-609.

Martin-Hammond, A., Patil, U., & Tandukar, B. (2021). A case for making web accessibility guidelines accessible: Older adult content creators and web accessibility planning. *Proceedings of the 23rd International ACM SIGACCESS Conference on Computers and Accessibility,* 1-6.

Mason, A. M., Compton, J., & Bhati, S. (2021). Disabilities and the digital divide: Assessing web accessibility, readability, and mobility of popular health websites. *Journal of Health Communication*, *26*(10), 667–674.

Miraz, M. H., Ali, M., & Excell, P. (2013). Multilingual website usability analysis based on an international user survey. *Proceedings of the Fifth International Conference on Internet Technologies and Applications*, 236-244.

Ran, D., Fu, Y., He, Y., Chen, T., Tang, X., & Xie, T. (2024). Path toward elderly friendly mobile apps. *Computer*, *57*(6), 29–39.

Rasi-Heikkinen, P., & Doh, M. (2023). Older adults and digital inclusion. *Educational Gerontology*, *49*(5), 345–347.

Sayago, S., & Blat, J. (2009). About the relevance of accessibility barriers in the everyday interactions of older people with the web. *International Cross-Disciplinary Conference on Web Accessibility* (W4A), 104 – 113.

Sik-Lanyi, C., & Orbán-Mihálykó, É. (2019). Accessibility testing of European health-related websites. *Arabian Journal for Science and Engineering*, *44*(11), 9171–9190.

United Nations Department of Economic and Social Affairs, Population Division. (2020). *World population ageing 2020 highlights: Living arrangements of older persons*. Retrieved from https://digitallibrary.un.org/record/3898412/files/undesa_pd2020_world_population_ageing_highlights.pdf

Vázquez, S. R., & Bolfing, A. (2013). Multilingual website assessment for accessibility: a survey on current practices. *Proceedings of the 15th International ACM SIGACCESS Conference on Computers and Accessibility* (ASSETS '13), *59*, 1–2.

Vigo, M., Brown, J., & Conway, V. (2013). Benchmarking web accessibility evaluation tools: measuring the harm of sole reliance on automated tests. *Proceedings of the 10th International Cross-Disciplinary Conference on Web Accessibility*, 1–10.

W3C .(2008). The world wide web consortium. Retrieved from https://www.w3.org/

W3C. (1999, May 5). Web content accessibility guidelines 1.0. Retrieved from https://www.w3.org/TR/WCAG10/

W3C. (2018, January 1). *Developing websites for older people: How web content accessibility guidelines (WCAG) 2.0 applies.* Retrieved from https://www.w3.org/WAI/older-users/developing/

W3C. (2024, December 12). *Web content accessibility guidelines (WCAG) 2.2*. Retrieved from https://www.w3.org/TR/WCAG22/

Yang, Y. T., & Chen, B. (2015). Web accessibility for older adults: A comparative analysis of disability laws. *The Gerontologist, 55*(5), 854–864.

Yang, Y., Zeng, D., & Yang, F. (2022). Internet use and subjective well-being of the Elderly: An analysis of the mediating effect based on social capital. *International Journal of Environmental Research and Public Health*, *19*(19), 12087.

Author Information

Baha Khasawneh
Princess Sumaya University for Technology
Amman, Jordan
Contact e-mail: *baha@psut.edu.jo*

To cite this article:

Khasawneh, B. (2025). WCAG success criteria to support accessibility of elderly users in bi-lingual websites. *The Eurasia Proceedings of Science, Technology, Engineering and Mathematics (EPSTEM), 34,* 195-201.

The Eurasia Proceedings of Science, Technology, Engineering & Mathematics (EPSTEM)
ISSN: 2602-3199

The Eurasia Proceedings of Science, Technology, Engineering and Mathematics (EPSTEM), 2025

Volume 34, Pages 202-208

ICBASET 2025: International Conference on Basic Sciences, Engineering and Technology

Study of Secondary Metabolites of Georgian Grape Wine Processing Waste Using UPLC-PDA-MS Methods and Prospects for Using Products Obtained from It

Maia Vanidze
Batumi Shota Rustaveli State University

Khatuna Diasamidze
Batumi Shota Rustaveli State University

Indira Japaridze
Batumi Shota Rustaveli State University

Ruslan Davitadze
Batumi Shota Rustaveli State University

Aleko Kalandia
Batumi Shota Rustaveli State University

Abstract

There is increasing interest in harnessing natural biologically active compounds for preventive and therapeutic purposes. However, the byproducts of wine production from endemic Georgian grape varieties have not been extensively studied using modern analytical methods and are typically left unutilized.This study aimed to analyze the chemical composition of grape wine production residues from cultivated grape varieties in Western Georgia and to evaluate their potential applications. An optimized processing technology was established for grape wine production residues, enabling the extraction of cold-pressed buckwheat oil (rich in unsaturated fatty acids) and hydrophilic preparations enriched with proanthocyanidins, catechins, and phenolic acids. The extraction process utilized green technologies, including high-pressure and ultrasonic-assisted extraction with a water-alcohol solvent system. The obtained extracts were concentrated under vacuum and subsequently freeze-dried to preserve biologically active compounds.This study provides valuable insights into the sustainable utilization of grape processing residues, demonstrating their potential for the production of functional food ingredients and bioactive preparations.

Keywords: Grape processing waste, UPLC-PDA-MS, Green extraction, Antioxidant activity, Anthocyanins.

Introduction

Georgia is home to more than 500 indigenous grape varieties, each displaying distinct morphological traits and unique chemical profiles. This diversity extends not only to the grape berries themselves but also to by-products such as grape skins and seeds, which constitute approximately 25–30% of winemaking waste. The chemical composition of these by-products is influenced by a range of factors, including grape variety, viticultural practices, soil type, climatic conditions, and processing technologies (Vanidze et al., 2020).

In Georgian winemaking, two primary fermentation methods are employed: the European method and the traditional Kakhetian method. The European approach involves fermenting only the grape juice, with solid residues such as skins and seeds removed early in the process. As a result, the chemical composition of the removed materials remains largely unchanged by fermentation. In contrast, the Kakhetian method involves the fermentation of the juice along with skins, seeds, and stems (pomace), leading to extended contact between the solid residues and the fermenting must (Kharadze et al., 2020).

In this latter method, several fermentation-dependent factors—such as initial sugar concentration, alcohol content, and fermentation duration—can significantly alter the chemical profile of the grape skins and seeds. This prolonged exposure to alcohol and enzymatic activity often enhances the extraction and transformation of phenolic compounds, especially in red grape varieties, where the skins are rich in anthocyanins and other bioactive constituents.

Notably, anthocyanins are predominantly located in the grape skin and contribute to the coloration and antioxidant properties of red wines. These compounds are more prevalent in unfermented or minimally processed grape skins. Therefore, understanding the interplay between grape variety, processing method, and chemical composition of winemaking by-products is critical for optimizing their valorization in food, cosmetic, and pharmaceutical applications.

Grape seeds are distinguished by their high content of biologically active compounds. (Kadri, S.et al.,2019), Interest in such studies is very high (Morazzoni et al.,2021), studies focus on obtaining biologically active compounds through the so-called "green extraction" (Beilankouhiet al.,2024), biologically active compounds have been discovered (Montero et.al. 2013; Dabetic et al., 2022; Beilankouhi et al., 2024). Grape seeds also contain lipids (Pérez-Navarro et al., 2019), unfortunately, the chemical composition of the seeds of Georgian grape varieties and their potential uses have been poorly studied.

Plant Material and Sample Preparation

The object of the research was the seeds and skins of grapes (“Ockhanuri saphere”) grown in western Georgia (42.1874° N, 42.9357° E), which underwent various degrees of extraction.

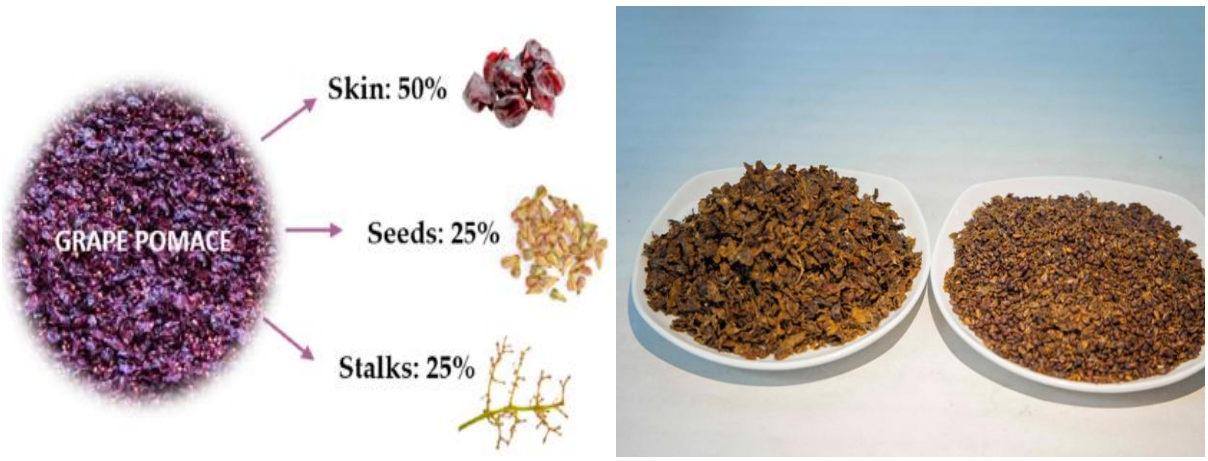

Extraction Methods

Ultrasonic Extraction (USE)

Ultrasonic extraction leverages the dual impact of mechanical vibration and acoustic cavitation generated by ultrasonic waves to enhance the mass transfer during the extraction process. The mechanical aspect involves the transmission of ultrasonic energy through the solvent, which promotes particle agitation, enhancing solvent diffusion and penetration into plant matrices. Cavitation—the formation and implosion of microbubbles—produces localized high temperatures and pressure differentials that rupture cell walls, thereby liberating bioactive constituents into the solvent medium. This approach significantly boosts extraction efficiency and rate while preserving thermally sensitive compounds (Surmanidze et al., 2024).

Pressurized Hot Water Extraction (PHWE)

PHWE operates by employing water under high temperature and pressure to remain in a liquid state above its standard boiling point, thus modifying its solvent characteristics. In this state, water's polarity decreases, enabling it to extract a broader spectrum of compounds, from polar to moderately nonpolar. The technique is considered sustainable due to its minimal environmental impact and effective energy use. Precise temperature regulation is crucial, as excessive heat (above 160 °C) may lead to degradation of heat-sensitive antioxidants. Enhancements in selectivity and yield can be achieved through the inclusion of natural deep eutectic solvents (NADES) or by coupling the process with pulsed electric field (PEF) treatments.

Anthocyanin Analysis

The characterization of anthocyanin compounds was carried out using ultra-performance liquid chromatography coupled with photodiode array and mass spectrometry detection (UPLC-PDA-MS). Separation was performed on a BEN C18 column under positive electrospray ionization (ESI+) conditions. The mobile phase consisted of 2% formic acid (Solvent A) and methanol (Solvent B), applied in a gradient elution mode. Chromatographic parameters included a constant flow rate of 0.3 mL/min and a column temperature set at 30 °C. The mass spectrometer scanned ions in the m/z range of 100–1200 Da, with a probe temperature of 500 °C, a spray voltage of 0.8 kV, and a capillary voltage of 1.5 kV. This analytical setup enabled accurate detection of cyanogenic anthocyanins, compounds with established anticancer potential (Abashidze et al.,2024).

Identification of Non-Anthocyanin Phenolic Compounds

To analyze non-anthocyanin phenolics, ultra-high-performance liquid chromatography (UHPLC) paired with a photodiode array and mass spectrometric detector (PDA-MS) was used. The separation process employed a BEH C18 column (1.7 µm) with a binary solvent gradient: 0.2% formic acid in water (A) and acetonitrile (B), at a consistent flow of 0.3 mL/min and a column temperature of 30 °C. The MS operated in negative ionization mode, with parameters set to enhance sensitivity and resolution (e.g., 500 °C probe temperature, 0.8 kV spray voltage). Data were acquired across a mass range of m/z 100–1200 and matched with standard compounds and the METLIN database. All samples and eluents were filtered through 0.45 µm membranes before injection (Sarker et al., 2013).

Determination of Antioxidant Activity

The antioxidant properties of extracts were evaluated using the DPPH radical scavenging assay. In this assay, a 1 mL sample of the extract was combined with 3 mL of DPPH solution and incubated in the dark for 15 minutes to allow the reaction. The absorbance was then measured at 517 nm using a UV-Vis spectrophotometer. Antioxidant effectiveness was expressed as the IC_{50} value, representing the concentration necessary to neutralize 50% of DPPH radicals, calculated from absorbance differences and sample mass (Abashidze et al., 2024).

Table.1 Influence of extraction methods on the content of phenolic compounds

Sample name (dray)	Total phenol mg/g	Phenol carbonic acids mg/g	Flavonoids, mg/ml	Catechins mg/ml	Proanthocyanins mg/ml
Grape "Ockhanuri saphere" seeds - SWE	68,694	8,5490	48,599	13,613	24,033
Grape "Ockhanuri saphere" seeds - US	74,902	8,7329	54,699	16,039	30,477
Grape "Ockhanuri saphere" - maceration	61,429	7,8685	42,344	12,228	24,051
Grape "Ockhanuri saphere" skine - SWE	59,704	6,8134	49,523	11,855	13,274
Grape "Ockhanuri saphere" skine - US	62,885	6,8670	53,998	13,125	14,781
Grape "Ockhanuri saphere" skine - maceration	47,725	6,5610	38,423	10,618	11,708

The pods taken for the study were prepared in advance. They were divided into pods and skins. The samples were extracted by maceration (classical method), Ultrasonic Extraction (USE) and Pressurized Hot Water Extraction (PHWE). Pod extraction by the US method gives the best results (68.7 mg/g), respectively, such an extract contains more phenolic acids (8.7 mg/g), flavonoids (54.7 mg/g), catechins (16.0 mg/g) and proanthocyanidins (30.5 mg/g). The results are relatively lower under PHWE conditions (total phenols 68.7 mg/g), respectively, other compounds are relatively less. Maceration achieves the worst results (61.4 mg/g). (Table 1)

Similar results are obtained in grape skin extraction. The best results are obtained here by the US method (62.9 mg/g), respectively phenolic acids (6.9 mg/g), flavonoids (49.5 mg/g), catechins (13.1 mg/g) and proanthocyanidins (14.8 mg/g). Relatively lower results are obtained under PHWE conditions (total phenols 59.7 mg/g), respectively other compounds are relatively less. The worst result is achieved by maceration (47.7 mg/g). The content of anthocyanins is not observed in the seed extracts. The extracts are distinguished by high antioxidant activity. This indicator is proportional to the content of phenolic compounds, the higher their content, the less sample is required 50% inhibition of 0.1 mM DPPH (0.414 mg).

Table 2. Effect of extraction methods on anthocyanin content and antioxidant activity

Sample name (dray)	**Total anthocyanins mg/g**	**Monomeric anthocyanins mg/g**	AA, mg Sample **50%** inhibition of 0.1 mM DPPH	**1/ AA,** mg Sample **50%** inhibition of 0.1 mM DPPH
Grape “Ockhanuri saphere” seeds - SWE	-	-	0,720	1,389
Grape “Ockhanuri saphere” seeds - US	-	-	0,414	2,415
Grape “Ockhanuri saphere” seeds - maceration	-	-	0,783	1,277
Grape “Ockhanuri saphere” skine - SWE	1,480	1,079	0,361	2,771
Grape “Ockhanuri saphere” skine - US	2,467	2,127	0,240	4,170
Grape “Ockhanuri saphere” skine - maceration	1,764	1,511	0,419	2,387

US extracted grape skins have a high content of anthocyanins (2.5 mg/g), therefore it is distinguished by a higher antioxidant activity (0.24 mg Sample 50% inhibition of 0.1 mM DPPH) than other extracts (0.36 mg SWE and 0.42 mg-maceration) (Table 2.).

The dominant anthocyanin was identified in the composition of the seeds ESI [M+H] - m/z 493.04 is recorded on the chromatogram with a retention time of 5.437 min, with absorption maxima at 282.7 nm and 518.4 nm. The obtained results, as well as the METLIN (https://metlin.scripps.edu) mass database of compounds, were compared with the standard compound malvidin-3-O-glucoside (C17H13O7).

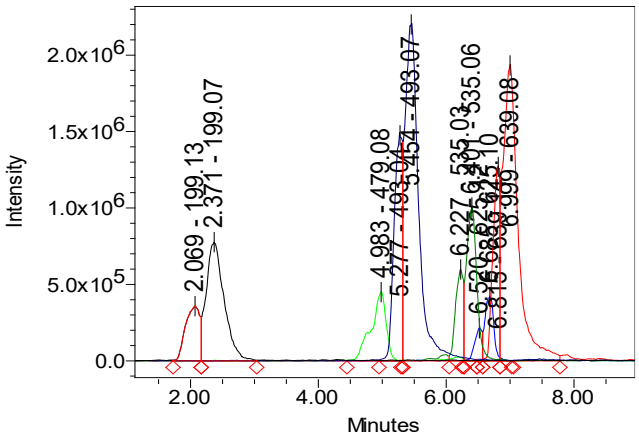

Figure 1. ESI [M+H] –anthocyanidins chromatograms of grape seeds

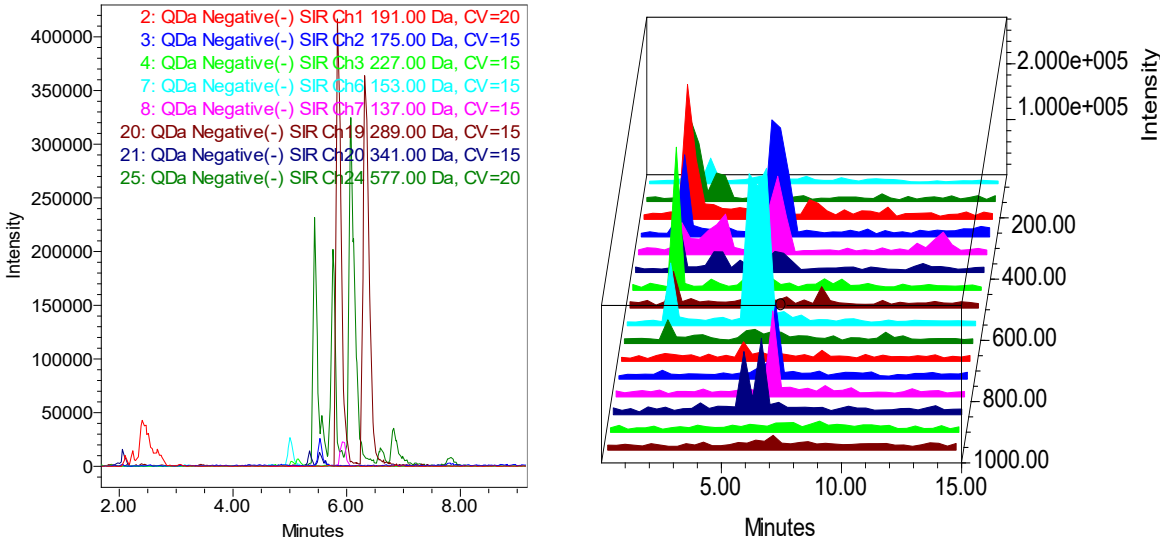

Figure 2. ESI [M-H] – chromatograms of grape seeds

ESI [M-H] - m/z 288.87 and 288.91 are recorded on the chromatogram with retention times of 6.748 min and 7.379 min, with an absorption maximum at 281.7 nm. By comparing the obtained results, as well as according to the mass database of compounds (https://metlin.scripps.edu), these compounds correspond to catechin, (MF C15H14O6, MW: 290.27g/mol Catechin (2R,3S)-2-(3,4-dihydroxyphenyl)-3,4-dihydro-2H-chromene-3,5,7-triol) and epicatechin MF C15H14O6, MW: 290.27g/mol epi-Catechin (2R,3R)-2-(3,4-dihydroxyphenyl)- 3,4-dihydro-2H-chromene-3,5,7-triol). (Figure 3)

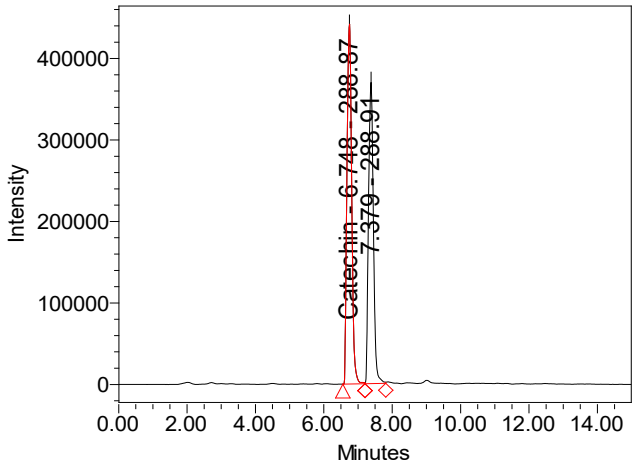

Figure 3. ESI [M-H] – 289 chromatograms of grape seeds

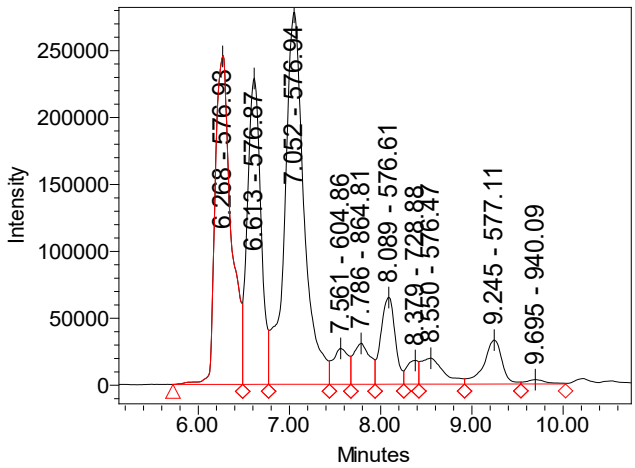

Figure 4. ESI [M-H] – 577 chromatograms of grape seeds

ESI [M-H] - m/z 576.93 is recorded on the chromatogram with a retention time of 6.268 min, with an absorption maximum at 278 nm. By comparing the obtained results, as well as according to the mass database of compounds (https://metlin.scripps.edu), procyanidin B1, (Procyanidin B1) MF: C30H26O12 MW: 578.5 g/mol, IUPAC Name: (2R,3S)- 2-(3,4-dihydroxyphenyl)-8-[(2R,3R,4R)-2-(3,4-dihydroxyphenyl)-3,5,7-trihydroxy-3,4-dihydro2H-chromen-4-yl]-3,4-dihydro-2H-chromene-3,5,7-triol, and ESI [M-H] - m/z 576.87 is recorded on the chromatogram with a retention time of 6.613 min, with an absorption maximum at 278 nm. According to the results obtained, as well as the mass database of compounds (https://metlin.scripps.edu), procyanidin B2 is (Procyanidin B1) MF: C30H26O12 MW: 578.5g/mol, IUPAC Name: (2R,3S)- 2-(3,4-dihydroxyphenyl)-8-[(2R,3R,4R)-2-(3,4-dihydroxyphenyl)-3,5,7-trihydroxy-3,4-dihydro2H-chromen-4-yl]-3,4-dihydro-2H-chromene-3,5,7-triol. (Fig. 4.)

Conclusion

Catechin, epicatechin, procyanidin B1 and procyanidin B2 were identified in the composition of the seeds of the grape variety "Otskhanuri Sapere", which is widespread in Western Georgia, and the dominant anthocyanidin in the composition of the skin is malvidin-3-O-glucoside. Ultrasonic Extraction is used for the extraction of biologically active compounds from seeds and skin.

Recommendations

The grape variety "Otskhanuri Sapere" is a good raw material for the production of preparations rich in biologically active catechins and procyanidins, and in the case of the skin, it is additionally possible to obtain a natural red dye. Biologically active compounds are obtained using Ultrasonic Extraction "green technology".

Scientific Ethics Declaration

* The authors declare that the scientific ethical and legal responsibility of this article published in EPSTEM Journal belongs to the authors.

Conflict of Interest

* No conflict of interests is declared.

Funding

* This work was done with grant financing. Development of innovative technologies for the valorization of plant raw materials and processing waste to reduce the negative impact on the environment using the principles of a circular economy GRANT_NUMBER: FR-22-4236 LEPL Shota Rustaveli National Science Foundation (Tbilisi, GE)

Acknowledgements or Notes

* This article was presented as a poster presentation at the International Conference on Basic Sciences, Engineering and Technology (www.icbaset.net) held in Trabzon/Türkiye on May 01-04, 2025.

References

Abashidze, N., Djafaridze, I., Vanidze, M., Khakhutaishvili, M., Kharadze, M., Kartsivadze, I., Davitadze, R., & Kalandia, A. (2024). Physicochemical characterization and antioxidant activity of Jara honey produced in Western Georgia. *Applied Sciences, 14*(16), 6874.

Beilankouhi, S., Pourfarzad, A., Ghanbarzadeh, B., Rasouli, M., & Hamishekar, H. (2024). Identification of polyphenol composition in grape (*Vitis vinifera* cv. Bidaneh Sefid) stem using green extraction methods and LC–MS/MS analysis. *Food Science & Nutrition, 12*(9), 6789–6798.

Dabetic, N., Todorovic, V., Malenovic, A., Sobajic, S., & Markovic, B. (2022). Optimization of extraction and HPLC–MS/MS profiling of phenolic compounds from red grape seed extracts using conventional and deep eutectic solvents. *Antioxidants, 11*(8), 1595.

Kadri, S., El Ayed, M., Cosette, P., Jouenne, T., Elkhaoui, S., Zekri, S., Limam, F., Aouani, E., & Mokni, M. (2019). Neuroprotective effect of grape seed extract on brain ischemia: A proteomic approach. *Metabolic Brain Disease, 34*(3), 889–907.

Kharadze, M., Djaparidze, I., Shalashvili, A., Vanidze, M., & Kalandia, A. (2018). Phenolic compounds and antioxidant properties of some white varieties of grape wines spread in Western Georgia. *Bulletin of the Georgian National Academy of Sciences, 12*(3), 16.

Montero, L., Herrero, M., Prodanov, M., Ibáñez, E., & Cifuentes, A. (2013). Characterization of grape seed procyanidins by comprehensive two-dimensional hydrophilic interaction × reversed phase liquid chromatography coupled to diode array detection and tandem mass spectrometry. *Analytical and Bioanalytical Chemistry, 405*(13), 4627–4638.

Morazzoni, P., Vanzani, P., Santinello, S., Gucciardi, A., Zennaro, L., Miotto, G., & Ursini, F. (2021). Grape seeds proanthocyanidins: Advanced technological preparation and analytical characterization. *Antioxidants, 10*(3), 418.

Pérez-Navarro, J., Da Ros, A., Masuero, D., Izquierdo-Cañas, P. M., Hermosín-Gutiérrez, I., Gómez-Alonso, S., Mattivi, F., & Vrhovsek, U. (2019). LC-MS/MS analysis of free fatty acid composition and other lipids in skins and seeds of *Vitis vinifera* grape cultivars. *Food Research International, 125*, 108556.

Surmanidze, N., Vanidze, M., Djafaridze, I., Davitadze, R., Qarcivadze, I., Khakhutaishvili, M., & Kalandia, A. (2024). Optimization of the method of ultrasonic extraction of lycopene with a green extract from the fruit of *Elaeagnus umbellata*, common in Western Georgia. *Food Science & Nutrition*, *12*(5), 3593-3601.

Vanidze, M., Kharadze, M., Djafaridze, I., & Kalandia, A. (2020). Characterization of phenolic acids in several autochthonic wines. *Bulletin of the Georgian National Academy of Sciences, 14*(4), 82-88.

Author(s) Information

Maia Vanidze
Batumi Shota Rustaveli State University, Batumi. Ninoshvili av. 35, Georgia
Contact e-mail: *maia.vanidze@bsu.edu.ge*

Khatuna Diasamidze
Batumi Shota Rustaveli State University, Batumi. Ninoshvili av. 35, Georgia

Indira Japaridze
Batumi Shota Rustaveli State University, Batumi. Ninoshvili av. 35, Georgia

Ruslan Davitadze
Batumi Shota Rustaveli State University, Batumi. Ninoshvili av. 35, Georgia

Aleko Kalandia
Batumi Shota Rustaveli State University, Batumi. Ninoshvili av. 35, Georgia

To cite this article:

Vanidze, M., Diasamidze, K., Japaridze, I., Davitadze, R., & Kalandia, A. (2025). Study of secondary metabolites of Georgian grape wine processing waste using UPLC-PDA-MS methods and prospects for using products obtained from it. *The Eurasia Proceedings of Science, Technology, Engineering and Mathematics (EPSTEM), 34,* 202-208.

The Eurasia Proceedings of Science, Technology, Engineering & Mathematics (EPSTEM)
ISSN: 2602-3199

The Eurasia Proceedings of Science, Technology, Engineering and Mathematics (EPSTEM), 2025

Volume 34, Pages 209-214

ICBASET 2025: International Conference on Basic Sciences, Engineering and Technology

Effect of Pasture-Based Feeding Systems on Milk Production and Composition of Dairy Goats in Different Mountainous Areas

Azeddine Mouhous
Mouloud Mammeri University of Tizi-Ouzou

Nassima Zirmi-Zembri
Mouloud Mammeri University of Tizi-Ouzou

Zahia Dorbane
Mouloud Mammeri University of Tizi-Ouzou

Si Ammar Kadi
Mouloud Mammeri University of Tizi-Ouzou

Ali Bouzourene
Mouloud Mammeri University of Tizi-Ouzou

Rabia Cherfouh
Mouloud Mammeri University of Tizi-Ouzou

Idir Moualek
Mouloud Mammeri University of Tizi-Ouzou

Hocine Guermah
Mohammed Boudiaf University of M'sila

Farid Djellal
Ferhat Abbas University of Setif, Algeria

Dyhia Saidj
SAAD Dahleb University

Abstract: The aim of this study is to assess the effect of pasture-based feeding systems on milk production of goats raised in different mountainous regions of Kabylia (Algeria), with a view to geographically labelling the cheeses produced in each region. A one-year survey was performed on about fifty goat farms in four Kabylian mountainous regions (Tigzirt, Yakourene, Boghni and Ouacifs). The results shows that farmers are raise in general 30 goats' heads per farmer. The average grazing times are 3.30, 8, 7 and 5 hours, respectively for winter, spring, summer and autumn. A high significant difference is reported in winter ($P < 0.0001$) where farmers in the Boghni region spend the most time on pasture (on average 4.3 hours), and a relative difference in autumn ($P=0.052$). The average milk production is 2 litres/goat/day. There is no significant difference in milk production between the herds ($P=0.155$) in the four regions. On the other hand, the analysis of pasture vegetation shows a significant difference for all four regions ($P<0.0001$). On average, results of the milk physico-chemical composition were similar to those expected: 4.05±0.57 for fat, 2.88±0.18 for protein, 17.29±0.37 for titratable acidity expressed in Dornic Degree, 7.92±0.42 for total dry extract, -0.506±0.029 for freezing point and 4.20±5.07 for wetting. For the four regions and for all parameters, only the fat parameter

shows a significant difference (p = 0.009). Also, the comparison between the two regions Ouacifs and Tigzirt shows a non-significant difference for the same parameter (P = 0.291). In conclusion, analysis of farming systems and milk do not show a great difference between the regions studied. Other studies, such as bacteriological and other tests, should be carried out to investigate these differences.

Keywords: Goat, Breeding systems, Pasture vegetation, Milk quality

Introduction

Goat farming plays a crucial socio-economic role in mountainous regions, where production systems are often traditional and extensive, heavily relying on freely available pastoral resources. Pasture-based feeding systems are commonly practiced in these areas due to their low cost and their contribution to the valorization of local forage resources (Morand-Fehr et al., 2007). According to Alary et al. (2011), goat farming serves as a means to achieve food security for populations in extreme environments such as mountainous areas.

In mountainous areas, the predominant system is the extensive system, which relies on pasture-based feeding and the use of local breed animals (Mouhous et al., 2013). These systems are strongly influenced by seasonal variations and the specific agro-ecological conditions of each zone (Chebli et al., 2020). Several studies have demonstrated that feeding practices play a decisive role in the nutritional quality of milk, particularly by altering the fatty acid profile and the concentration of essential micronutrients (Chilliard et al., 2013).

According to Morand-Fehr et al. (2004), the use of pastoral forage resources, which are climate-dependent, has a significant impact on goat milk productivity and its composition. However, the quality and availability of pastures vary according to seasons and edapho-climatic conditions, directly influencing milk production and its composition in terms of fat, proteins, and minerals (López et al., 2019). Furthermore, variations in the agro-ecological conditions of mountainous areas (considering parameters such as altitude, climate, and vegetation) can lead to differences in the quality and quantity of milk produced (Boyazoglu et al., 2005; Mellado et al., 2020). In this context, our study aims to analyze the impact of pastoral feeding systems on the productivity and quality of goat milk in mountainous areas of Kabylia. To this end, this study focused on the physico-chemical composition of goat milk samples collected from four mountainous regions.

Method

The Study Area

Our choice of survey location focused on the Tizi-Ouzou province, a mountainous region located in the center of the Algerian coastline. Its physical environment is composed of several distinct geographical features, including the central massif, the Draa-El-Mizan depression, coastal plains and valleys, the central massif, and the Djurdjura mountain range. More than 52% of the study area is characterized by significant slopes (DPAT, 2012). Dense forested areas span the entire region, providing high-quality pastures for goat farming. The surveys concerned only extensive dairy goat farms in mountain areas. The farms surveyed were those that used pasture all year round. The number of farms monitored during a year is 50 dairy goat farms. İthey are spread over four regions with different bioclimatic stages. These four regions are Ouacif, Boghni, Tigzirt and Yakourene. Milk samples were taken on a regular basis, once a week for each farm. The number of milk samples for each farm was three (3). Sometimes more, as samples with a high percentage of added water are eliminated.

Analysis Methods

To analyze the milk samples, we used a device called the "Lactoscan." For the physico-chemical analyses, the various parameters measured included: fat content, density, lactose, proteins, dry extract, freezing point, water addition, temperature, and mineral salts. The results are expressed as percentages.

Statistical Analyses

The results were subjected to descriptive statistical analyses, including mean, standard deviation, and percentage. Additionally, an analysis of variance (ANOVA) using Levene's test and the Kruskal-Wallis test was applied to assess the correlations between the different studied variables. The statistical analysis was performed using XLSTAT software, version 2019.

Results and Discussion

Functioning of Goat Farms

Table 1 shows that the number of goats is higher because they represent the productive portion of the herd. In contrast, the number of kids is low. One or two are raised for the replacement of breeding males, while the rest are destined for sale or self-consumption. The number of young females (chevrettes) represents an average proportion of the herd. They are used to replace culled females.

Table 1. Distribution of goat herd numbers

Herd numbers/regions	Goats	Bucks	Young goats	Young females goats
Ouacifs	42	9	42	15
Boghni	267	16	60	46
Tigzirt	162	27	154	103
Yakourene	74	21	35	30

Dry cleaning is a method found among all the surveyed farmers. Approximately 40% of farmers in Ouacif and Boghni use this method. However, this rate drops to 8% and 15% in the regions of Tigzirt and Yakourene, respectively (Figure 1). The most commonly used method combines dry cleaning with the use of water. This method is employed by 77% of farmers in Yakourene and 63% of those in Ouacif. In Boghni and Tigzirt, the rates are 35% and 33%, respectively. The exclusive use of water as a cleaning method represents low percentages, with 33% of farmers in Tigzirt, 26% in Boghni, and only 8% in Yakourene. Finally, the use of pressurized water is observed only among 25% of farmers in Tigzirt. In these farms, the semi-intensive system is prevalent.

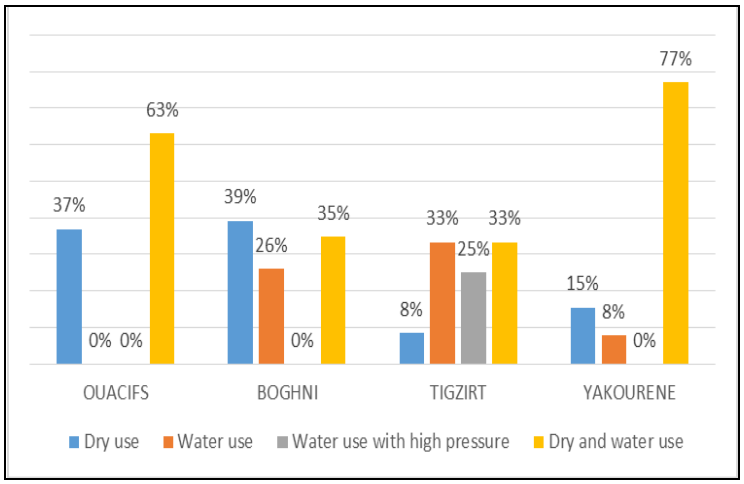

Figure 1. Cleaning methods

Furthermore, Table 2 highlights some characteristics inherent to the surveyed farms. The number of goats shows a significant difference between regions ($p = 0.009$). The Tigzirt region, with an average of 39 goats per herd, is known for its abundance of forest pastures. Additionally, the semi-intensive system is dominant in this area. For milk production, there is no significant difference between regions. On average, milk production does not exceed 2.12 liters/goat/day. In the regions of Ouacif and Tigzirt, the average milk production exceeds 2 liters/goat/day. Our results align with those of Mellado et al. (2020), who reported similar milk production levels (1.5 to 2.5 liters/goat/day) in goats raised under extensive systems in arid environments. Grazing is an important practice in goat farming. It is noted that during winter and spring, the duration of grazing does not show a significant difference across the four regions. Moreover, García-Rodríguez et al. (2022) emphasized that winter and spring grazing play a crucial role in maintaining goat productivity due to the increased availability of high-quality forage.

Table 2. Characteristics of dairy goat farms.

	Ouacıfs	Boghnı	Tıgzırt	Yakourene	*K*	P-Value
Herd size (goats)	14±2,905	33,42±27,317	39,50±23,296	32,10±8,799	11,662	**0,009**
Milk production (liters/goat/day)	2,40±0,774	1,85±0,864	2,30±0,537	1,95±0,368	5,861	0,119
Grazing duration (hours/day) – Winter	2,7±0,674	4,42±2,101	3,10±0,994	3,30±0,948	5,774	0,123
Grazing duration (hours/day) – Spring	8,10±1,286	8,78±1,121	7,60±1,577	7,90±0,875	5,004	0,172
Grazing duration (hours/day) – Summer	8,10±1,286	8,14±1,875	4±1,247	6±0,816	26,769	**< 0,0001**
Grazing duration (hours/day) – Autumn	5,10±0,994	6,92±1,899	2,50±1,080	4,60±0,966	27,642	**< 0,0001**

In winter, the time spent grazing does not exceed 4 hours per day. However, in spring, the animals are often outdoors grazing, spending an average of 8 hours per day. Significant differences in grazing duration are observed only in summer and autumn ($P < 0.0001$). In summer, farmers in Ouacif and Boghni spend an average of 8 hours/day grazing, while those in Tigzirt and Yakourene, which are forested areas, spend 4 and 6 hours/day, respectively. In autumn, the regions of Ouacif and Boghni again show longer grazing durations (5 and 6.9 hours/day). Benyoucef et al. (2018) highlighted the importance of forest pastures in supporting larger goat herds.

Quality of Goat Milk in Different Regions

Table 3 presents the physico-chemical results of goat milk from the four study regions. The values obtained for the analyzed milk samples are consistent with those reported by Noutfia et al. (2011). For fat content, the overall average across all regions is 4.05 ± 0.57%. However, a significant difference is observed between regions ($P = 0.009$). The regions of Yakourene and Boghni recorded the highest fat levels, while Tigzirt and Ouacif did not reach 4%.

Our results align with those of Mellado et al. (2020), who reported similar values (3.5% to 4.5%). The type of feed provided influences milk composition. For instance, energy-rich diets do not promote the production of acetyl compounds, which contributes to a reduction in milk fat content (Morel et al., 2006). Lipids are the most important milk components in terms of cost, nutrition, and the physical and sensory characteristics they impart to dairy products (Park et al., 2007). For titratable acidity in Dornic degrees (°D), the overall average recorded is 17.29 ± 0.37 °D, with no significant difference between regions. Our results fall within the range reported by the FAO (2010), which is 15–17 °D. Chebli et al. (2020) reported titratable acidity values between 16.5 °D and 18.0 °D in extensive systems. The protein content in our farms averages 2.88 ± 0.28%, with no significant difference between the four regions. This protein level is lower than that reported by Benyoub (2015), which is 4.3%. The average lactose content in the milk from the four regions is 4.36 ± 0.25%, with a slight but significant difference between regions. Our results align with those of Morand-Fehr et al. (2004), who indicated that the lactose content of goat milk typically ranges between 4.0% and 4.8%.

Table 3. Physico-chemical parameters of goat milk

	Ouacıfs	Boghnı	Tıgzırt	Yakourene	Overall average	*F*	P-Value
Fat %	3.63±0.217	4.56±0.572	3.81±0.480	4.00±0.405	405±0.57	4.451	0.00863
Titrabl Acidity (°D)	17.26±0.210	17.38±0.430	17.51±0.419	17±1.154	17.29±0.37	2.008	0.128
Lactose (%)	4.56±0.190	4.31±0.324	4.29±0.269	4.32±0.079	4.36±0.25	2.489	0.0741
Protein (%)	2.99±0.103	2.87±0.194	2.85±0.176	2.80±0.202	2.88±0.28	0.61	0.612
Dry extract (%)	8.18±0.270	7.83±0.539	7.77±0.456	7.93±0.217	7.92±0.82	2.295	0.0923
Ash Content (%)	0.661±0.0463	0.646±0.0450	0.643±0.0393	0.648±0.0283	0.64±0.03	0.732	0.538
Wetting Index (%)	1.31±1.734	4.66±6.087	6.78±5.854	3.85±3.905	4.20±5.07	2.435	0.0787
Freezing Point (°C)	-0.52±0.019	-0.50±0.034	-0.49±0.036	-0.500±0.0168	-0.50±0.02	1.919	0.1418

A slight but significant difference is observed in the dry extract (P = 0.09) and the wetting index (P = 0.07). The averages for these parameters are 7.92 ± 0.82% and 4.20 ± 5.07%, respectively. For the dry extract, the region of Ouacif shows the highest value at 8.18%. Our results align with those of Silanikove et al. (2010), who indicated that the dry extract of goat milk typically ranges between 7.5% and 8.5%. For the wetting index, the region of Tigzirt records the highest value (6.78%), while Ouacif shows the lowest value (1.31%). The ash content in the milk does not show a significant difference between regions, with an average of 0.64 ± 0.03%. The analyzed samples indicate no significant difference in the freezing point between regions, with an overall average of -0.50 ± 0.02 °C. García-Rodríguez et al. (2022) reported similar results, ranging between -0.50 °C and -0.55 °C.

Conclusion

The extensive system is the most commonly practiced in the study area. Significant differences are observed in the number of goats per region, with areas that have forested massifs recording the largest herds. Additionally, differences are noted in grazing duration during summer and autumn. The productivity of goats in terms of milk remains low, averaging 2.12 liters/goat/day. For cleaning, dry and water-based methods are the most prevalent across the four regions.The results of the physico-chemical analyses revealed a highly significant difference in fat content among the four regions. This suggests the potential to produce distinct, region-specific labeled cheeses. Slight but significant differences were recorded in certain parameters, such as lactose, dry extract, and wetting index. Overall, the results showed nuanced differences between the milk from the four regions.

Recommendations

To better understand the differences between regions, it is recommended to conduct more in-depth studies, such as analyses of farming systems, focusing on feeding practices and the examination of consumed plants. Additional analyses, such as bacteriological studies, are also recommended.

Scientific Ethics Declaration

* The authors declare that the scientific ethical and legal responsibility of this article published in EPSTEM Journal belongs to the authors.

Conflict of Interest

* The authors declare that they have no conflicts of interest

Acknowledgements or Notes

* This article was presented as an oral presentation at the International Conference on Basic Sciences, Engineering and Technology (www.icbaset.net) held in Trabzon/Türkiye on May 01-04, 2025.

References

Alary, V., Duteurtre G., & Faye B. (2011). Élevages et sociétés : les rôles multiples de l'élevage dans les pays tropicaux. *INRA Productions Animales, 24* (1), 145-156

Benyoucef, M. T., Boukhelkhal, A., & Yakhlef, H. (2018). Role of forest rangelands in sustaining goat farming systems in mountainous areas of northern Algeria. *Small Ruminant Research, 160*, 1-8.

Boyazoglu, J., Hatziminaoglou, I., & Morand-Fehr, P. (2005). The role of the goat in society : Past, present and perspectives for the future. *Small Ruminant Research, 60*(1-2), 13-23.

García-Rodríguez, J., López-Díaz, A., & González, M. (2022). Impact of seasonal grazing on dairy goat productivity in Mediterranean mountain systems. *Journal of Animal Science, 100*(3), 1-10.

Chebli, Y., El Otmani, S., Hornick, J. L., Keli, A., & Cabaraux, J. F. (2020). Effects of feeding management and climate on milk production and composition in dairy goats in northern Morocco. *Journal of Animal Physiology and Animal Nutrition, 104*(1), 1-10.

Chilliard, Y., Glasser, F., Ferlay, A., Bernard, L., Rouel, J., & Doreau, M. (2013). Diet, rumen biohydrogenation and nutritional quality of cow and goat milk fat. *European Journal of Lipid Science and Technology*, *115*(7), 706-717.

DPAT. (2012). Directorate of Planning and Territorial Development. *Statistical Data. Wilaya of Tizi-Ouzou.*

López, A., Vasconi, M., Barone, G., & Moretti, V. M. (2019). Chemical and nutritional quality of commercial goat milk. *Journal of Dairy Science*, *102*(12), 10705-10715.

Mellado, M., Valdez, R., Lara, L. M., & García, J. E. (2020). Factors affecting the reproductive performance of goats under extensive conditions in a hot-arid environment. *Small Ruminant Research, 183*, 106034.

Morand-Fehr, P., Boutonnet, J. P., Devendra, C., Dubeuf, J. P., Haenlein, G. F. W., Holst, P., ... & Capote, J. (2004). Strategy for goat farming in the 21st century. *Small Ruminant Research, 51*(2), 175-183.

Morand-Fehr, P., Fedele, V., Decandia, M., & Le Frileux, Y. (2007). Influence of farming and feeding systems on composition and quality of goat and sheep milk. *Small Ruminant Research*, *68*(1-2), 20-34.

Morel, L., Wyss, U., & Collomb, M. (2006). Influence de la composition botanique de l'herbe ou du foin sur la composition chimique du lait. *Revue Suisse Agriulture,38* (1), 9 -15.

Mouhous, A., Bouraine. N., & Bouaraba, F. (2013). L'élevage caprin dans la zone montagneuse. Cas de la région de Tizi Ouzou (Algérie). (Doctoral dissertation). Retrieved from www.journees3r.fr/spip.php?article3712

Noutfia, Y., Ibnelbachir, M., & Zantar, S. (2011). Apercu sur le secteur de fabrication de fromage e chèvre dans la région d'Ouarzazate. In *Options Méditerranéennes n°100, economic, social and environnemental sustainability in sheep and goat production systes.* CIHEAM.Retrieved from http://www.ciheam.org/

Park, W.Y., Juarez, M., Ramos, M., & Haenlein, G.F.W. (2007). Physicochemical characteristics of goat and sheep milk. *Small Ruminant Research. 68*, 88 113.

Silanikove, N., Leitner, G., Merin, U., & Prosser, C. G. (2010). Recent advances in exploiting goat's milk: Quality, safety and production aspects. *Small Ruminant Research, 89*(2-3), 110-124.

Author(s) Information

Azeddine Mouhous
Department of Agronomic Sciences, Faculty of Biological Sciences and Agronomic Sciences, Mouloud Mammeri University of Tizi-Ouzou, Algeria
Contact e-mail: *mouhousazeddine@yahoo.fr*

Zahia Dorbane
Department of Agronomic Sciences, Faculty of Biological Sciences and Agronomic Sciences, Mouloud Mammeri University of Tizi-Ouzou, Algeria

Ali Bouzourene
Department of Agronomic Sciences, Faculty of Biological Sciences and Agronomic Sciences, Mouloud Mammeri University of Tizi-Ouzou, Algeria

Idir Moualek
Department of Biological Sciences, Faculty of Biological Sciences and Agronomic Sciences, Mouloud Mammeri University of Tizi-Ouzou, Algeria

Farid Djellal
Faculty of Agronomic Sciences, Ferhat Abbas University of Setif, Algeria

Nacima Zirmi-Zembri
Department of Agronomic Sciences, Faculty of Biological Sciences and Agronomic Sciences, Mouloud Mammeri University of Tizi-Ouzou, Algeria

Si Ammar Kadi
Department of Agronomic Sciences, Faculty of Biological Sciences and Agronomic Sciences, Mouloud Mammeri University of Tizi-Ouzou, Algeria

Rabia Cherfouh
Department of Agronomic Sciences, Faculty of Biological Sciences and Agronomic Sciences, Mouloud Mammeri University of Tizi-Ouzou, Algeria

Hocine Guermah
Faculty of Agronomic Sciences, Mohammed Boudiaf University of M'sila, Algeria

Dyhia Saidj
Veterinary Sciences Institute, SAAD Dahleb University, Blida1, Algeria

To cite this article:

Mouhous, A., Zirmi-Zembri, N., Dorbane, Z., Kadi, S.A., Bouzourene, A., Cherfouh, R., Moualek, I., Guermah, H., Djellal, F., & Saidj, D. (2025). Effect of pasture-based feeding systems on milk production and composition of dairy goats in different mountainous areas. *The Eurasia Proceedings of Science, Technology, Engineering and Mathematics (EPSTEM), 34,* 209-214.

The Eurasia Proceedings of Science, Technology, Engineering & Mathematics (EPSTEM)
ISSN: 2602-3199

The Eurasia Proceedings of Science, Technology, Engineering and Mathematics (EPSTEM), 2025

Volume 34, Pages 215-220

ICBASET 2025: International Conference on Basic Sciences, Engineering and Technology

Identification of Possibilities of Controlling Plastic Processing Processes in Conditions of Complex Loading

Valery Chigirinsky
Rudny Industrial University

Abdrakhman Naizabekov
Rudny Industrial University

Sergey Melentyev
Rudny Industrial University

Irina Volokitina
Karaganda Industrial University

Evgeniy Panin
Karaganda Industrial University

Abstract: The combination of different loads in the process of plastic deformation makes it possible to find sufficiently effective technological modes of deformation associated with the control of plastic shaping of the deformable metal. These approaches are manifested in the fact that it is possible to reduce the force load on the deformation site, or the implementation of processing in which it is possible to improve the quality of finished products, mill productivity. Therefore, the task of finding process parameters that allow you to control and influence the deformation center during rolling in a special way becomes urgent. The analysis of scientific and technical literature shows that such parameters can be impacts that, according to deformation and force loading, should not be comparable with the main load, due to which the process of plastic deformation is realized. In this case, the factor of unevenness of plastic deformation can be controlling if its loading on the deformation site is less than the main one. This work, carried out within the framework of grant № AP23488953, funded by the Science Committee of the Ministry of Science and Higher Education of the Republic of Kazakhstan, presents experimental studies of the effect of asymmetric unevenness of plastic processing along the width of the deformation zone during rolling on the conditions of rectilinear movement of the strip in the deformation zone and the force characteristics of ensuring this movement. Experimental data show that the force effect on the deformation site from the unevenness of compression is significantly less than the main load, which gives reason to consider this type of loading as controlling. The imposition of unevenness of plastic deformation on the plastic treatment zone causes the appearance of additional regulatory stresses, which significantly affect the stress state of the deformation site as a whole.

Keywords: Plastic deformation, Rolling, Deformation zone, Unevenness of deformation, Complex loading

Introduction

The combination of different loads in the plastic deformation makes it possible to find sufficiently effective processing modes related to the control of plastic shaping. These approaches are manifested in the fact that it is possible to reduce the force load on the deformation zone, or to implement processing modes while improving the

quality of the finished product and mill productivity. In this regard, it becomes important to find the process parameters that allow to control and influence the deformation zone in a special way.

The combination of different pressure treatment operations in the deformation zone is presented as primary and auxiliary or additional. The difference lies in the power load. If the combined effects of metal pressure treatment are characterized by different force parameters, then, accordingly, these effects are characterized by different effects on the plastic shaping process itself. In this case, the effects with lower force parameters on the deformation zone and the factors that can implement such effects are of the greatest interest. Based on experimental data, it was shown that the factors that can affect the deformation zone with lower force parameters can include the factor of uneven plastic deformation (Chigirinsky & Volokitina, 2024).

Let's consider the features of uneven plastic shaping from the point of view of the controlling factor. Different compression by volume of the deformable workpiece forms the geometry of the finished product, and accordingly causes uneven deformation. At the same time, this leads not only to a change in the stress state, but also to a change in the flow pattern of the metal in different directions. Figure 1a shows a "template" of a cross-section of a complex roll with "witnesses" after compression in the rough passage. It can be seen that local plastic deformations, unrelated to the extraction capabilities of rough gauges, significantly change the flow of metal in the transverse direction (Chigirinsky et al., 2014).

The metal moves from areas of greater compression to areas with less compression. This is clearly visible in Figure 1b, where the circles show the centers of the "witnesses" before and after rolling. The graph of the compression distribution over the strip width, which is also shown in Figure 1b, characterizes the deformation in this case as extremely uneven.

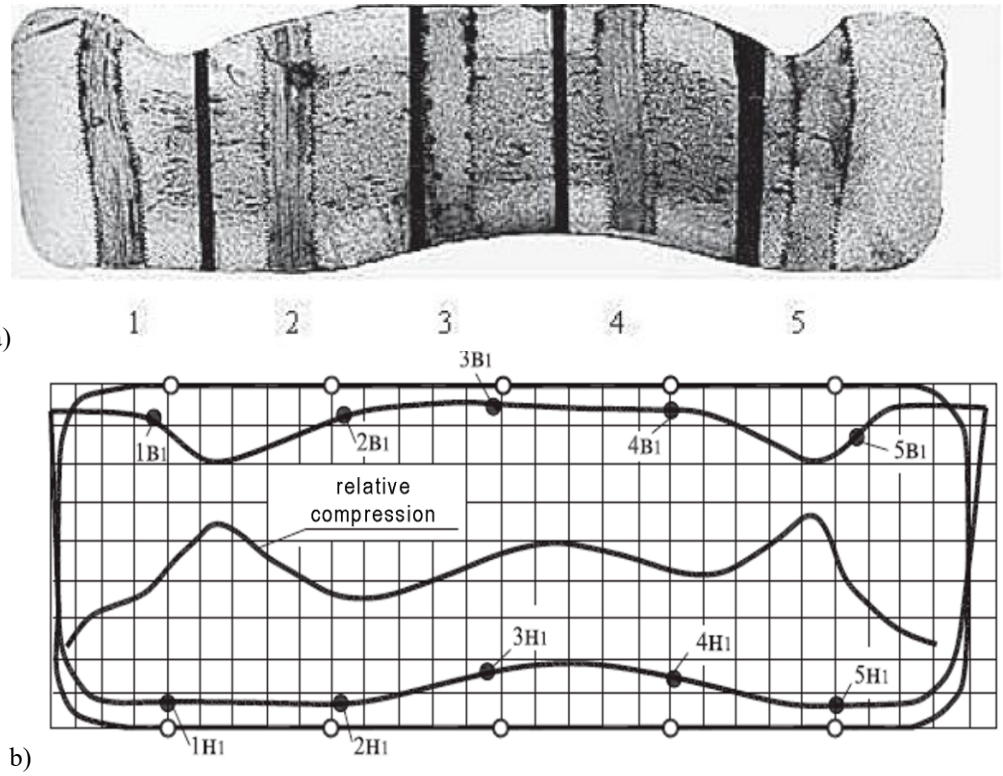

Figure 1. Location of the "witnesses" (a) and diagram of the transverse displacement with a graph of the compression distribution across the strip width (b)

The movements of the "witness" centers show the flows of the plastic flow of the medium in the transverse direction. Local (additional) deformations associated with uneven compression are those controlling influences that, based on the drawing capacity of the caliber, form plastic metal flows.

As a result of the interaction of the elements, there is a forceful external support and tension in individual zones of the strip, as an additional external effect on the deformation zone, similar to external forces in the intercellular gap of a continuous mill. As a result, contact stresses in the deformation zone change, which is widely used in

regulating the rolling process of continuous mills (Chekmarev et al., 1967). The above example indicates the regulating effect of external forces on the deformation zone, which is also indicated in case of uneven deformation.

Such deformation modes are typical for rolling profiles of complex asymmetrical shape. Their peculiarity is that the rolled strip is prone to sickling in the horizontal plane at the entrance and exit from the deformation zone. In this case, it becomes experimentally possible to establish a correspondence between uneven deformation and an external additional effect on the compression zone.

Method

As noted above, an assessment of the additional impact on the deformation zone is necessary in order to verify how effective and efficient this loading is for regulating the stress-strain state of the plastic medium. Therefore, a physical experiment was conducted to evaluate the additional effect on the deformation site under difficult loading conditions. The experiment was carried out at the DUO-150 rolling mill, with different ratios B_1/B_0 and H_1/H_0, which ranged from B_1/B_0 from 0.50 to 0.93 and H_1/H_0 from 0.65 to 0.91, respectively, were rolled on this mill (Fig. 2). The parameters H_1/H_0 and B_1/B_0 characterize to a certain extent the unevenness of plastic deformation along the width of the profile. The H_1/H_0 ratio quantifies the interaction between two adjacent elements. The ratio B_1/B_0 is the weight of each element in case of uneven deformation.

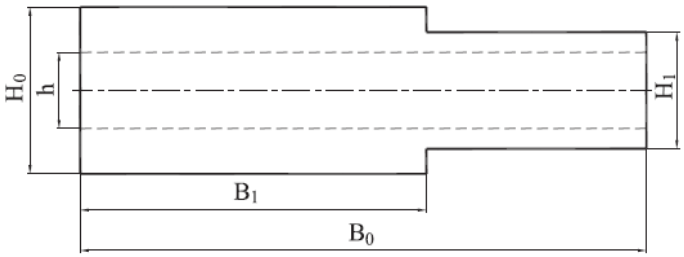

Figure 2. Asymmetrical step sample

During the experiment, the pressure of the strip on the side roll rulers of a special design was measured. Some of the experimental data on measuring the pressure of the strip on the side rulers are shown in Table 1. To assess the effect of the impact, it must be compared with the main one, which implements plastic deformation. The torques from the side lines, as external additional ones, and the torques of plastic bending, as the main load, were compared:

$$M_{pl} = \beta \cdot \sigma_y \cdot W_{pl}, \quad (1)$$

where β - characterization of the stress state at a point; σ_y - yield stress; W_{pl} - torque of plastic resistance.

Table 1. Experimental values of forces and torques from the side rulers

№	B_1/B_0	H_1/H_0	Values of force, N		Values of torque, N·m		Force ratio P_{ent}/P_{ex}	Torque ratio M_{ent}/M_{ex}
			Entrance	Exit	Entrance	Exit		
1	0,93	0,73	932	376	75,6	54,1	2,5	1,4
2	0,77	0,76	1340	550	110,7	79,2	2,5	1,4
3	0,62	0,72	1952	780	162,0	112,3	2,5	1,4
4	0,52	0,77	1783	770	153,0	111,0	2,3	1,4
1	0,93	0,82	480	212	40,5	30,5	2,3	1,3
2	0,78	0,83	888	380	75,8	54,7	2,3	1,4
3	0,63	0,79	1325	580	115,5	83,5	2,3	1,4
4	0,52	0,82	1250	559	109,0	80,6	2,2	1,5
1	0,92	0,76	772	319	62,4	46,5	2,4	1,4
2	0,77	0,75	1225	478	100,2	69,0	2,6	1,5
3	0,62	0,75	1805	786	151,2	113,2	2,3	1,3
4	0,52	0,74	1860	838	157,5	120,9	2,2	1,3

The data in Table 1 show that the torques of forces from the rulers uniquely respond to changes in the unevenness of deformation. The parameters B_1/B_0 and H_1/H_0 are able to assess the process of unevenness to a certain extent

when the number of elements is minimal. But they do not give a complete picture of the asymmetry of loading for profiles of complex construction, when their number is more than two and with other qualitative indicators. Fragments of such indicators can be static torques of a given section, as well as factors that take into account the longitudinal interaction in the deformation zone $\ln\mu_{av}/\mu_i$. Therefore, in our opinion, for a more complete characterization of uneven deformation, it is necessary to use the dimensionless parameters from the side of the entrance and exit of the metal from the deformation zone:
- entrance:

$$\delta_{ent} = \frac{\sum 2\frac{a_i}{1+a_i}\cdot \ln\frac{\mu_{av}}{\mu_i} F_{0i} y_{0i}}{W_{pl.ent}}, \tag{2}$$

- exit:

$$\delta_{ex} = \frac{\sum 2\frac{a_i}{1+a_i}\cdot \ln\frac{\mu_{av}}{\mu_i} F_{1i} y_{1i}}{W_{pl.ex}}, \tag{3}$$

where W_{pl} - torque of plastic resistance at the entrance and exit from the deformation zone; μ_{av} - average stretching in the compression zone; μ_i - private stretching.

In addition to the dimensionless indicators (2) and (3), it is advisable to use a dimensionless indicator for torques from the rulers M_{exp}/M_{pl}. For this purpose, the torques of plastic bending for the sections used in the experiment were calculated within the limits: at the entrance: 152.0-234.2 N·m, at the exit: 97.9-197.5 N·m.

Results and Discussion

Comparing the plastic torques with the data given in Table 1, it can be seen that they are higher than the values obtained experimentally. The use of relative data for torques and parameters δ makes it possible to eliminate the influence of yield strength and absolute band sizes when constructing a mathematical model under conditions of asymmetric impact. Also, when comparing the results of the measurement and calculation of the torques, it can be seen that the additional impact, through uneven deformation, is less than the main load, and the ratio of torques M_{exp}/M_{pl} is less than one and ranges from 0.2 to 0.8. Analysis of the data obtained shows that the torques of forces from the lateral rulers in relation to the torques of plastic bending in this range plastic interaction is always less than one. This is evidence that the additional load from the rulers on the deformation zone is less than the main one, which determines the plastic deformation process. Based on the processing of experimental data, some of which were given in Table 1, the dependence of the ratio of loading torques on a dimensionless indicator characterizing the unevenness of deformations was constructed (Fig. 3).

a)

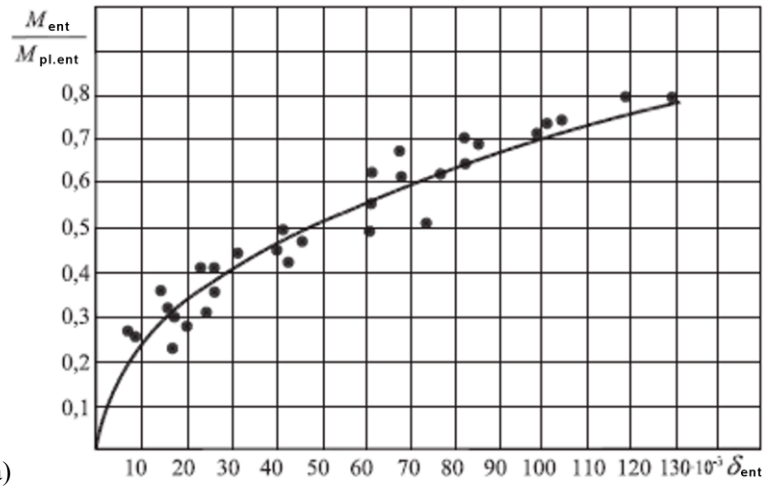

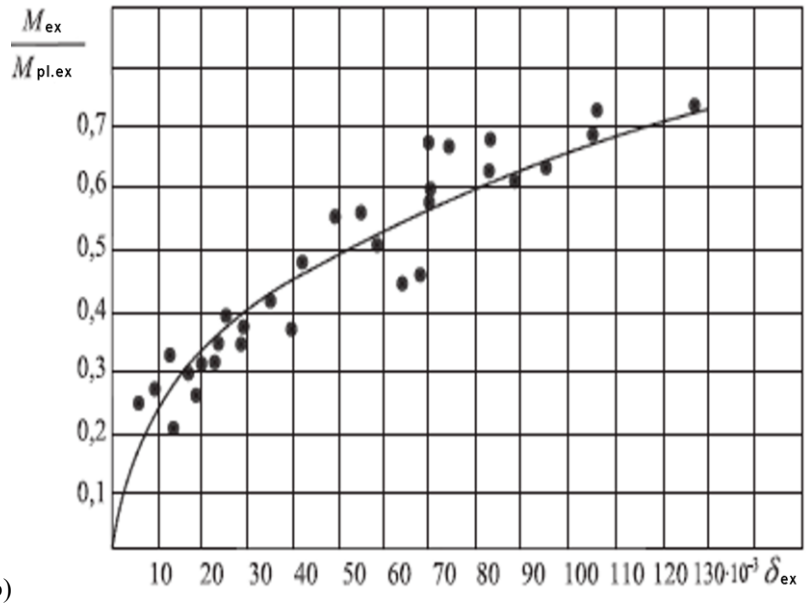

b)

Figure 3. Dependences of the ratios of the M_{exp}/M_{pl} torques at the entrance (a) and at the exit (b) from the deformation zone on the δ parameters

Mathematical processing of experimental results using the least squares method for a power function allowed to obtain expressions of the form:

- entrance:

$$M_{ent} = 1.938 \cdot M_{pl.ent} \cdot \left[\frac{\sum 2 \frac{a_i}{1+a_i} \cdot \ln \frac{\mu_{av}}{\mu_i} F_{0i} y_{0i}}{W_{pl.ent}} \right]^{0.443}, \quad (4)$$

- exit:

$$M_{ex} = 1.827 \cdot M_{pl.ex} \cdot \left[\frac{\sum 2 \frac{a_i}{1+a_i} \cdot \ln \frac{\mu_{av}}{\mu_i} F_{1i} y_{1i}}{W_{pl.ex}} \right]^{0.485}. \quad (5)$$

The closeness of the relationships between the studied parameters for the input and output, respectively, is 0.946 and 0.937. Expressions (4) and (5) make it possible to calculate the torque values for asymmetric rolling of different profiles of any size and with any number of elements. Attention should be paid to the difference in the values of the main and additional loads, which can be explained by different physical processes occurring during plastic deformation. During plastic bending, the stresses of the latter reach maximum values equal to the yield strength, which characterizes the main load. When rolling with uneven compression, longitudinal interaction forces appear in the deformation zone, determined by additional stresses. The magnitude of the additional stresses, as can be seen from the studies carried out, is less than the yield strength. It is characterized not by plastic loading, but by different extracts in the deformation zone, obeying the laws of mathematical models (4) and (5).

Conclusion

This experiment has shown that an external additional effect on the deformation zone meets the basic requirements for additional control effects - these are different force characteristics of additional and main loading (Figure 3, expressions 4 and 5). The ratio of the external moment to the plastic moment over the entire range of change is less than one, and it can be regulated by the parameter δ and everything that determines it. It follows that additional stresses may be the regulating factor that changes the stress state of the deformation zone.

Scientific Ethics Declaration

* The authors declare that the scientific ethical and legal responsibility of this article published in EPSTEM Journal belongs to the authors.

Conflict of Interest

* The authors declare that they have no conflicts of interest

Funding

* This work was funded by the Science Committee of the Ministry of Science and Higher Education of the Republic of Kazakhstan. (Grant № AP23488953).

Acknowledgements or Notes

* This article was presented as a poster presentation at the International Conference on Basic Sciences, Engineering and Technology (www.icbaset.net) held in Trabzon/Türkiye on May 01-04, 2025.

References

Chekmarev, A. P., Grechko, V. P., Getmanets, V. V., & Khovrin, B. V. (1967). *Rolling on small-grade mills*. Moscow: Metallurgiya.

Chigirinsky, V. V., Krisanov, Y. S., Kachan, A. Ya., & Slepynin, A. G. (2014). *Production of thin–walled rolled products for special purposes*. Zaporizhia: Accent IT - VALPIS.

Chigirinsky, V., & Volokitina, I. (2024). Additional effect on the deformation zone during plastic metal flow. *Engineering Solid Mechanics, 12*, 113-126.

Author(s) Information

Valery Chigirinsky
Rudny Industrial University
38, 50 let Oktyabrya str., Rudny, Kazakhstan
Contact e-mail: *chigirinvv18@gmail.com*

Abdrakhman Naizabekov
Rudny Industrial University
38, 50 let Oktyabrya str., Rudny, Kazakhstan

Sergey Melentyev
Rudny Industrial University
38, 50 let Oktyabrya str., Rudny, Kazakhstan

Irina Volokitina
Karaganda Industrial University
30, Republic av., Temirtau, Kazakhstan

Evgeniy Panin
Karaganda Industrial University
30, Republic av., Temirtau, Kazakhstan

To cite this article:

Chigirinsky, V., Naizabekov, A., Melentyev, S., Volokitina, I., & Panin, E. (2025). Identification of possibilities of controlling plastic processing processes in conditions of complex loading. *The Eurasia Proceedings of Science, Technology, Engineering and Mathematics (EPSTEM), 34,* 215-220.

The Eurasia Proceedings of Science, Technology, Engineering & Mathematics (EPSTEM)
ISSN: 2602-3199

The Eurasia Proceedings of Science, Technology, Engineering and Mathematics (EPSTEM), 2025

Volume 34, Pages 221-233

ICBASET 2025: International Conference on Basic Sciences, Engineering and Technology

Designing Intelligent Models with ARIMAANN for Visionary Forecasts

Morena Breshanaj
University of Vlora

Areti Stringa
University of Tirana

Abstract: It is essential to choose the right model that can explain the growth of tourism in Albania and, therefore, to make the right decisions and direct the flow of tourists. This research aims to compare and apply three forecasting models: ARIMA, Artificial Neural Networks (ANN), and the hibrid ARIMAANN model to forecast the number of international tourists in Albania. The outcomes indicate that the interaction between the two approaches, ARIMAANN, is the first model to explain 96% of the data variation and provides the minimum mean absolute percentage error (MAPE) of 21.6%. In order to enhance the model's precision, the refined model, ARIMAANN 21-24, was suggested, which excluded the pre-pandemic and pandemic periods. This adjustment resulted in significant enhancements where the accuracy was 0.99, and MAPE was 7.09 %, making it the most accurate forecast. The proposed model shows that tourism will keep increasing in the next five years. The most tourists are expected in August 2029, with 2.9 million international tourists. This research provides a predictive tool for policymakers, tourism operators, and government agencies to capitalize on the benefits of hybrid modelling to enhance sustainable tourism's strategic development and management. All data and analyses were processed in RStudio with the latest advancements in time series modelling.

Keywords: Tourism demand forecasting, ARIMA, ANN, ARIMAANN

Introduction

Tourism is one of the strongest sectors of the economy of almost any country. The number of international visitors has increased dramatically, from 25.2 million in 1950 to 439 million in 1990, to 1.4 billion in 2019 and 1.4 billion in 2024. (UN Tourism World Tourism Barometer | Global Tourism Statistics, 2025) As per the Global Economic Impact & Trends, tourism is one of the critical components of 10.4% of the global GDP and 10.6% of total employment. (WTTC: World Travel & Tourism Council). In the last World Tourism Report by the United Nations World Tourism Organisation, the number of international arrivals was 1.4 billion in 2024, a 99% recovery from 2019 and 11% growth from 2023 or 140 million more international tourists. (UN Tourism World Tourism Barometer:Global Tourism Statistics, 2025)

The Secretary General of the United Nations, Zurab Pololikashvili, noted, "In 2024, international tourism has rebounded fully from the pandemic, and in many countries, the number of arrivals and, particularly, revenue is even higher than in 2019. The growth is expected to maintain its direction through 2025, with high demand as a major force for socio-economic impact for mature and emerging markets. This is evidence of our role as a sector in the globalization of the sector and making the sector more sustainable in terms of people and the planet. This is why it is our responsibility as a sector to build on this and ensure that people and the planet are at the centre of development in tourism." (UN Tourism | Bringing the world closer). In 2024, Europe was the largest region in the world, with 747 million international arrivals, 1% more than before the pandemic and 5% more than in 2023. Europe's sub-regions have seen a rise in arrivals compared to the pre-pandemic figures, except Central and Eastern Europe.

As one of the European countries with the highest rate of growth in the tourism industry, Albania has also experienced an increase in the number of tourist visits and 11,700,340 million non-resident visitors in 2024, which is 45% more than in 2019. However, these figures need to be supported by sound models to ensure the sustainable management of the flows and the formulation of policies. This research proposes a combined model to predict the number of tourists visiting Albania. This study has applied an enhanced version of the hybrid model, ARIMAANN 21-24, to enhance the model's accuracy and exclude the impact of the COVID-19 pandemic. This approach has also helped attain a better fit for the recent trends in tourism and has lower forecast errors than the previous models. The improved model has provided more accurate forecasts for the next five years that correctly capture the tourism trends in Albania. The purpose of this research is to provide empirical evidence that can be used by the tourism industry, government agencies and investors to shape policy and decision-making towards the sustainable management and development of tourism in Albania and thus contribute to the national economy and defend the natural and cultural heritage of the area. Lastly, the implications of this study for tourism management and economic development are discussed, and the possible application of the model developed in this study to policy making and resource allocation are discussed. Hence, the accurate prediction of the trends in tourism is crucial because the stakeholders can prepare and manage their resources to address the challenges, develop the right marketing strategies, and establish policies that can help the growth of sustainable tourism in the region. The research carried out in this paper provides important findings that can be used to help Albania properly utilize its tourism resources, pursue good economic development and conservation, and ensure the sustainability of the population. The number of non-resident visitors to Albania for 2016-2024 is presented in the table below.

Table 1. Number of non-resident tourists in Albania for the period 2016-2024

	2016	**2017**	**2018**	**2019**	**2020**	**2021**	**2022**	**2023**	**2024**
January	173534	172757	232338	209520	249461	185392	194237	377211	489599
February	169556	185721	190531	201597	228941	158173	200997	309325	480539
March	218858	243462	254020	283910	95321	170279	275976	384028	564975
April	285902	359452	351610	410060	12188	241015	402051	614256	794129
May	358484	360082	394869	401531	16389	328742	604430	705079	973688
June	394361	437820	496137	630334	179594	604381	876056	1007033	1244967
July	864718	864023	1028182	1176810	387716	1158962	1403333	1770724	1818378
August	1124615	1142198	1449952	1556826	575559	1537191	1710041	2022754	2167665
September	406582	459168	664184	591414	377033	494332	761544	1104190	1146090
October	302834	379327	337603	387152	206439	298712	365237	696825	761636
November	210377	256216	246678	268176	148362	244061	358350	547221	604332
December	225690	257474	280699	288708	180815	267409	391565	616994	654342

We have presented a visual representation of these values in the interactive graph https://rpubs.com/Breshanaj/1265708, which shows the increasing trend and seasonality of the data. The graphs were built in the R programming language with the help of the " *plotly* " package.

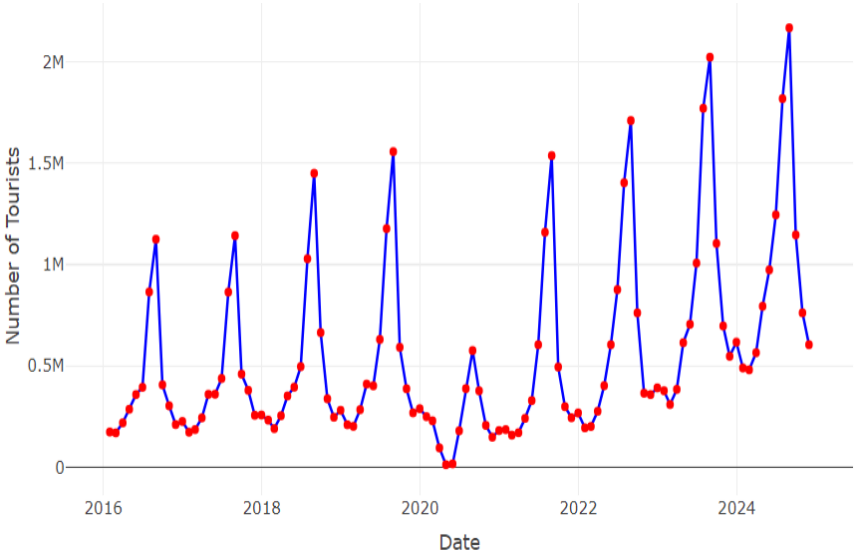

Figure 1. Number of non-resident tourists in Albania (2016-2024)

The interactive graph shows that the period with the least historical data is April 2020, which had 12,188 tourists. This is a sharp decrease from an increasing trend due to the global restrictions due to the COVID-19 pandemic. The highest monthly figure in these data is the 2,167,665 tourists recorded in August 2024. Because of the rapid growth in the number of tourists and the effects of seasonal variations, this study aims to analyze and predict future trends in tourism in Albania using advanced time series modelling techniques.

The second section outlines the methods applied in this study, and the third section gives some examples of applying the methods under study in different real-life situations. The fourth section explains how the ARIMA, ANN, and combined ARIMAANN models can forecast and model the number of non-resident tourists in Albania. The fifth section discusses the significant implications of the study, and the last section compares the findings of this study with other similar studies and presents the major conclusions.

Method

The approach used for this research in modelling and forecasting international tourist arrivals is based on a series of procedures to ensure that the modelling is done as effectively as possible. Figure 2 shows the strategy of the methodological approach, which describes the main phases from data preparation to model fitting and forecasting. All steps are implemented systematically to gain knowledge and improve the accuracy of the forecast.

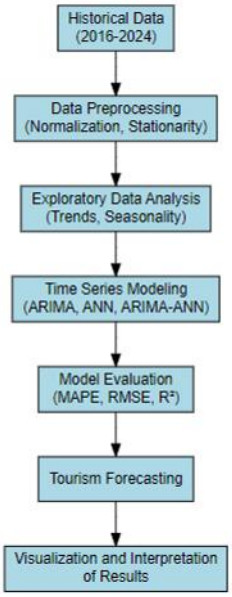

Figure 2. Structure of the methodology

This study's research design consists of formulating and comparing three statistical models for forecasting international tourist arrivals in Albania: ARIMA, ANN, and their combination ARIMAANN. The data set for this study includes monthly data from 2016-2024, which was collected from the Institute of Statistics of Albania (INSTAT) and divided into two sets: the training set, which is 80%, and the testing set, which is 20%.

The ARIMA(1,1,2)(0,1,2) [12] model is used to identify and model linear trends in time series data. In contrast, the ANN model uses a neural network with five inputs, two hidden layers, and one product to model nonlinear trends. The combined ARIMAANN method integrates the best features of both models to enhance the accuracy of the forecasts. This paper evaluates the models discussed based on accuracy metrics such as RMSE, MAE, MAPE and the R^2 coefficient of fit.

- Root Mean Squared$RMSE = \sqrt{\frac{1}{n}\sum_{t=1}^{n}(y_t - \hat{y}_t)^2}$
- Mean Absolute Error$MAE = \frac{1}{n}\sum_{t=1}^{n}|y_t - \hat{y}_t|$

- Mean Absolute Percentage Error$MAPE = \frac{1}{n}\sum_{i=1}^{n}\left|\frac{y_t-\widehat{y_t}}{y_t}\right| x100$

- R-squared$R^2 = 1 - \frac{\sum_{t=1}^{n}(y_t-\widehat{y_t})^2}{\sum_{t=1}^{n}(y_t-\bar{y})^2}$

On this note, the hybrid ARIMAANN21-24 method is the best as it is 96% fit to historical data and is more accurate in forecasting arrivals in the next five years. The modelling and analysis were done in RStudio, which provided a better visualization of the tourism dynamics and a reasonable basis for strategic planning in the Albanian tourism industry.

Literature Review

The ARIMAANN method combines the ARIMA (AutoRegressive Integrated Moving Average) model and ANN, an Artificial Neural Network. ARIMA models the linear components of a time series, while ANN models the nonlinear structure that ARIMA cannot capture. This method is adapted to increase the model's accuracy, especially for models with complex characteristics.

In 2003, Guangping Zhang, in his study "Time Series Forecasting Using a Hybrid ARIMA and Neural Network Model," introduced this combination. In this study, a hybrid methodology was introduced that combines both ARIMA and ANN models to take advantage of the unique power of ARIMA and ANN models in linear and nonlinear modelling (Mentes. & Yetkin, 2020). Experimental results with real data sets show that the combined model can effectively improve the forecast accuracy achieved by each of the models used separately (Zhang, 2003).

While Zhang (2003) first introduced the ARIMA-ANN model, subsequent studies such as those of Atesongun and Gulsen (2024) and Rahayu et al. (2023) etc. have shown significant improvements in this method in different time models. Adil Atesongun and Mehmet Gulsen studied a particular and interesting application of the ARIMAANN method in their article "A Hybrid Forecasting Structure Based on Arima and Artificial Neural Network Models" they have described in detail the functioning of the hybrid ARIMAANN method. They have applied this method to several issues, such as Turkish wheat yield, which was, in fact, the primary motivation for their article: sunspot observations, Canadian lynx counts, airline passenger data, and hourly electricity rates. They used the accuracy metrics MAD, MSE and MAPE to compare the hybrid model. These metrics have also been used in studies with other methods but with the same data, where the hybrid ARIMA-ANN method has resulted in the most successful. According to the metrics calculated in their study, the performance of the hybrid model is much higher than that of independent ARIMA or ANN. (Atesongun & Gulsen, 2024). These results indicate that the ARIMAANN model can provide higher accuracy for complex and variable data and may be suitable for forecasting tourism demand.

Rahayu et al. (2023) have presented in their study " Hybrid ARIMA-ANN Model for Solving Nonlinearity In Time Series Data" the ARIMA, ANN and hybrid ARIMA-ANN methods for estimating and forecasting the price of "shallots". They used daily data for the price of shallots for October 1, 2022 - September 30, 2023, which they divided into 90% training data and 10% testing data. From the metrics found, it was found that the hybrid ARIMA-ANN method is more accurate, with RMSE 2601 and MAPE 15.71%, respectively than the ARIMA model, which has RMSE 2888 and MAPE 17.51%. (Rahayu et al., 2023)

The research " Pemodelan ARIMAANN pada harga saham bank Mandiri" by authors Fadhillah et al. (2024) stock price data using the hybrid ARIMAANN method. This study used 493 daily data from January 2021 to December 2022. The authors built the ARIMA (0,1,1) model and the ANN model with four neurons in the hidden layer. The training and testing MAPE values for ARIMA-ANN resulted in 1.32% and 5.49%, values less than 10%, indicating that the ARIMA-ANN method is considered very good (Fadhillah et al., 2024).

The study "Application of Hybrid ARIMA and Artificial Neural Network Modeling for Electromagnetic Propagation: An Alternative to the Least Squares Method and ITU Recommendation P.1546-5 for Amazon Urbanized Cities" by Fraiha - Lopes et al. (2020) presents an empirical hybrid model integrating moving average (ARIMA) and artificial neural network (ANN), designed to estimate the propagation of electromagnetic waves in densely forested urban areas. The signal power intensity data was obtained through measurement campaigns in the Metropolitan Area of Belem (MAB) in the Brazilian Amazon (Fraiha- Lopes et al., 2020).

Authors Naheeda Perveen, Khadija Tariq and Hafiz Shabir Ahmad combined the ARIMA model and artificial neural network by adopting an equal-weight approach and a profit-weighted approach to capture the exchange rate's linear and nonlinear components. They developed a hybrid technique using the ARIMA-ANN model in their paper " Comparative Studies of Hybrid ARIMA and Artificial Neural Network (ANN) Techniques for Predicting Exchange Rate in Pakistan". The effectiveness of the models was analyzed for foreign exchange rate, imports and exports data and concluded that the hybrid techniques gave the best forecasting results (Perveen, et al., 2024).

A similar study to ours is the article “Hybrid Model of Seasonal ARIMA-ANN to Forecast Tourist Arrivals through Minangkabau International Airport”, which uses the hybrid ARIMAANN method to model and predict number of tourists arriving at Minangkabau International Airport, Indonesia. First, they use a SARIMA (1, 0, 1) (1, 1, 0) 12 model to model the linear and seasonal components of the data. Then, an Artificial Neural Network (ANN) with a 2–2–2–1 architecture is applied to the SARIMA residuals to address the nonlinear patterns. The results show that the combination of SARIMA and ANN significantly improves the accuracy of the predictions, with a MAPE of 17.0963%, lower than that of SARIMA (17.1770%).

In the article "Tourism Demand Modelling and Forecasting: A Review of Literature" by Abdou et al. (2021), the authors conduct an in-depth review of different methods for forecasting tourism demand, analyzing 145 studies conducted from 1979 to 2020. They categorize the main methods into three groups: econometric models, time series models and artificial intelligence (AI) models. The study's findings show that while traditional methods such as ARIMA and econometric models help capture trends and seasonality, they cannot model the nonlinear complexity of tourism demand. On the other hand, artificial intelligence models, such as artificial neural networks (ANN) and Support Vector Machines (SVM), have great potential to improve forecast accuracy but can be more challenging to interpret. The authors emphasize that combining traditional methods with artificial intelligence through hybrid models such as ARIMAANN brings more accurate and reliable results in tourism demand forecasting. This review is important for our study, as it highlights the need for advanced approaches in tourism demand modelling, justifying the choice of the ARIMAANN model for forecasting the number of tourists in Albania.

The ARIMANN method has been widely applied in various real-life fields such as finance, energy and demand forecasting, tourism, etc. The choice of the ARIMAANN model in this study is applied after the performance of the ARIMA and ANN methods, which resulted in a need for improvement. To our knowledge, this method has no application in modelling and forecasting tourist flows in Albania. This lack of literature creates a space for exploring and evaluating the performance of this method in a new context. The results of this study will contribute to the scientific literature and will provide a valid model for the analysis of tourist flow forecasting in the country.

All these studies, which have been applied or not in the field of tourism, show the effectiveness of the ARIMAANN model in modelling complex data and seasonality, a characteristic that is essential for the analysis of tourist flows. Considering the results of the above works, our study aims to apply and evaluate this method in a field that has not yet been applied: tourism forecasting in Albania. This will help policymakers, tourism businesses, and government institutions improve the design of strategies for managing tourist flows and promoting Albanian tourism.

Modelling the Number of İnternational Tourists in Albania

Understanding and correctly predicting the number of international tourists visiting Albania is vital for effective planning, resource allocation, and policy-making in the tourism industry. As there are significant seasonal variations and more visitors today than before, it is imperative to use the right model that can capture both short-term fluctuations as well as long-term trends. Different forecasting methods can analyze historical data, each with advantages and disadvantages. This section examines the application of three techniques, ARIMA, ANN, and a combined ARIMAANN model, to explain the trends and forecast international tourist arrivals in Albania.

AutoRegressive Integrated Moving Average

ARIMA (AutoRegressive Integrated Moving Average) is one of the oldest methods of modelling and forecasting time series. However, at the same time, it is one of the best and has proved effective in many recent studies. It functions by using historical values (AutoRegresive), smoothing the series to make it stationary

(Integrated) and studying the errors or residuals using the moving average method (Moving Average). We used the "auto.arima" function in Rstudio to fit the ARIMA model to our data on international tourists' arrival in Albania. According to this procedure, ARIMA(1,1,2)(0,1,2)[12] was chosen as the best-fit model. The point forecasts and corresponding confidence intervals of the model selected by auto.arima are illustrated in the following figure.

```
Coefficients:
          ar1      ma1      ma2     sma1    sma2
      0.6531  -0.5172  -0.3340  -0.8235  0.1917
s.e.  0.1485   0.1663   0.1077   0.1175  0.1172

sigma^2 = 1.33e+10:  log likelihood = -1231.18
AIC=2474.37   AICc=2475.33   BIC=2489.63
```

Figure 3. ARIMA(1,1,2)(0,1,2)[12]

The parameters (1, 1, 2) are for the non-seasonal component and the parameters (0,1,2)[12] for the seasonal component.

- p = 1 indicates a first-order autoregressive (AR) component, which means that a linear combination of the previous value gives the current value. The value of this parameter tells us that our modelling will have the form $y_t = 0.6531\ y_{t-1} + \varepsilon_t$, y_t is the current value of the series at time t, $y_{t-1}$is the previous value and $\varepsilon_t$is the error at the time t(the difference between the predicted value and the actual value).
- d = 1 indicates that The differentiation process is used once to make the time series stationary. In the case of our series of the number of incoming tourists, the number of tourists increases every year, showing a clear upward trend. After the first differentiation, the limits of this series are transformed into differences between consecutive months, turning the series into a stationary series. The formula after this step will be $y_t - y_{t-1} = 0.6531(\ y_{t-1} - y_{t-2}) + \ \varepsilon_t$.
- q = 2 shows that The model uses error terms from the last two months in the moving average. Which will help correct the forecasts for the current month. The model is also restated as:

$$y_t - y_{t-1} = 0.6531(\ y_{t-1} - y_{t-2}) - 0.5172\ \varepsilon_{t-1} - 0.334\ \varepsilon_{t-2} + \ \varepsilon_t$$
$$y_t = 1.6531\ y_{t-1} - 0.6531\ y_{t-2} - 0.5172\ \varepsilon_{t-1} - 0.334\ \varepsilon_{t-2} + \ \varepsilon_t$$

- P = 0, the absence of a seasonal autoregressive component means that this model does not use past seasonal values to generate forecasts.
- D = 1, A seasonal difference is made to station the series as a seasonally unadjusted series. This is achieved by making the differences between each month and the previous year's respective month.
- Q = 2 shows that the model includes the impact of two preceding seasonal value $y_t$errors. In our case, since the series has a frequency of 12, the error of periods $t - 12$will be included in the modelling$t - 24$.
- [12] shows that our data are monthly, meaning the seasonality has a periodicity of 12.

The modelling expresses the combination of the above seasonal and non-seasonal components

$$y_t - 0.6531\ y_{t-1} - y_{t-1} + 0.6531 y_{t-2} - y_{t-12} + 0.6531\ y_{t-13} + y_{t-13} - 0.6531\ y_{t-14}$$
$$= \varepsilon_t - 0.5172\ \varepsilon_{t-1} - 0.334\ \varepsilon_{t-2} - 0.8235\ \varepsilon_{t-12} + 0.1917\ \varepsilon_{t-24}$$

Let us evaluate the statistical indicators for this method to understand how effective and accurate this model is.
Table 2. Statistical metrics of ARIMA model accuracy

Table 2. Statistical metrics of ARIMA model accuracy

Model	**RMSE**	**MAE**	**MAPE**	R^2
ARIMA (1,1,2)(0,1,2)[12]	105171.1	67609.17	31.57071	0.9463824

According to the calculations of the above statistical coefficients, we can accept that this is a good model for modelling and forecasting the number of tourists in Albania since the MAE and RMSE are about 12% and 19% of the average value of historical data, values that categorize the implemented model as a good model. The value of the coefficient of determination $R^2 = 0.95$ shows that the model performs very well, representing about 95% of the data and leaving only 5% of the variation unexplained, but MAPE= 31.57071 is a value that

leaves room for improvement. The modelling results and the forecast for the next 5 years according to the ARIMA method are graphically presented in Figure 4. (https://rpubs.com/Breshanaj/1268987)

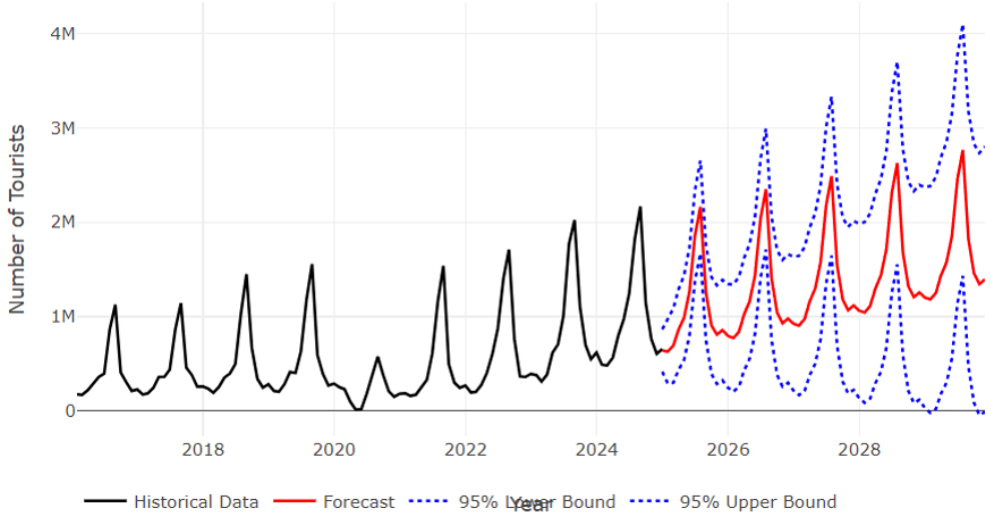

Figure 4. Forecasting tourist flow with the ARIMA method

Graphically, the optimistic forecast for the next five years is evident. According to the ARIMA (1,1,2)(0,1,2) model[12], the upward trend and seasonality of the monthly data on the number of non-resident tourists in Albania are expected to continue. The highest value, predicted according to this model, is expected to be recorded in August 2029 with a figure of about 2.8 million visitors. ARIMA works well in studying linear models but cannot study and process nonlinear data. We use the ANN method to fill this gap, which has shown efficiency in modelling nonlinear or complex data.

Artificial Neural Networks

The Artificial Neural Network (ANN) method is a powerful and advanced artificial intelligence and machine learning technique. It is based on imitating the structure and function of the human brain to analyze and process information (Breshanaj & Bakaj, 2024). An artificial neural network (ANN) is a computer simulation of the human brain in its most basic form (Fang et al., 2022). A normal brain can adapt to different environments and learn new things. The brain can evaluate partial, ambiguous, and ambiguous information and generate its own conclusions (Bharath et al., 2016).

Tourism time series usually have nonlinear data content and strong seasonality, which are handled quite well by artificial neural networks (ANN). We use the "neuralnet " package in Rstudio to model our historical data on the number of non-resident tourists in Albania. The Artificial Neural Network model has three layers: input, hidden, and output. The input layer in this study uses five input values: the number of tourists in the previous month, the number of tourists in the past 2, 3 and 6 months, and the corresponding value from a year ago to understand historical trends and seasonality.

In the architecture of this model, we have built two hidden layers with 12 and 6 neurons, respectively. The first layer, with 12 neurons, receives information from the input layer, processes it by analyzing the relationships between the data, trends, and seasonality and, based on this information, creates the model. The sigmoid ("logistic") function is used in this layer to help model nonlinear data. With six neurons, the second layer processes the model obtained from the first hidden layer, making it more sophisticated and sending the information to the output layer. The interaction of both layers helps in improving the accuracy of the predictions. The output layer contains only one neuron, which forecasts the number of tourists for the next month. The function in this layer is linear, allowing the ANN to produce continuous values. In the figure below, the corresponding architecture of the ANN model is built.

After processing, modelling and forecasting data for international tourism in Albania with the ANN method in Rstudio, it turns out that the model has been adapted to 89% of the variance of historical data ($R^2 = 0.89$) and can deviate on average 22.7% from absolute values (MAPE=22.7).

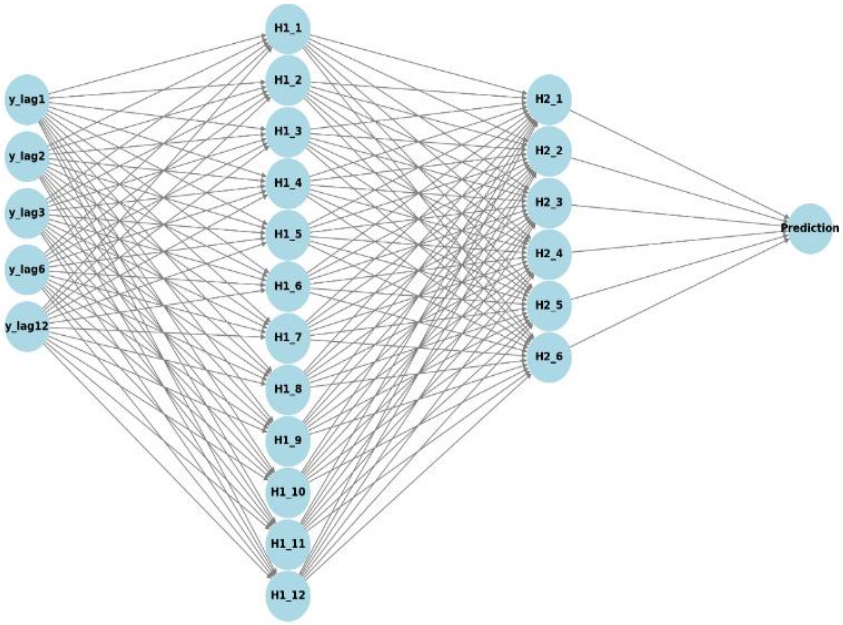

Figure 5. Architecture of the artificial network for tourism forecasting

Table 3. Statistical metrics of ANN model accuracy

Model	**RMSE**	**MAE**	**MAPE**	R^2
ANN	234026.4	187720.7	23.1	0.889

The ANN results show an $R^2 = 0.89$ and a MAPE = 23.1%, indicating that the model is effective in enhancing the forecast accuracy compared to ARIMA. The main advantage of ANN is that it is pretty flexible in capturing complex relationships and anomalies in the data, which helps forecast sudden changes in tourism. However, the model has a higher RMSE and MAE than ARIMA, which means there might be overfitting or lack of interpretability. The tables show that ARIMA has a higher accuracy in terms of RMSE and MAE, which indicates that its models are more robust to historical data. On the other hand, ANN has a lower MAPE, which indicates an enhancement in the capacity to model nonlinear variations in the data.In conclusion, there is no perfect method on its own. ARIMA is good at analyzing linear and seasonal data, while ANN is good at nonlinear patterns and anomalies. This has resulted in applying a hybrid ARIMAANN model that combines the best features of both models to develop a single model that can provide a better and more holistic forecast of tourism in Albania.

ARIMAANN

Complex real-world problems, in which nonlinearity is often present, can be successfully modelled using this technique (Perveen et al., 2024). It is universally stated that no single method is sufficient for problem-solving in every possible situation (Perveen et al., 2024). This has led researchers to combine different methods to achieve the best results for modelling or forecasting time series in various real-life problems. One of the most potent combinations has resulted in the ARIMAANN method, which manages data by dividing tasks between the traditional ARIMA and ANN artificial intelligence methods. The ARIMA model includes the linear trends and seasons in the time series data, and it works by identifying and extracting the regular patterns that can be expected to occur in the data set. The ANN model is designed to work with the nonlinear components of the time series, given its capability to learn and generalize from the data where the ARIMA model may be lacking. This way, the model can enhance the forecast precision to avoid the consequences of using a single method. This way, the data is first employed to build the ARIMA model to learn the linear structure of the data. Then, the residuals (the errors from the ARIMA model) are further analyzed using ANN to learn the nonlinear relationships in the data.

We have applied the hybrid ARIMAANN method to model and forecast the number of tourists in Albania. We have used the "ARIMAANN" package in Rstudio to model and forecast our monthly data. The accuracy metrics for this model show us that the model fits 96% of the data and can deviate on average 21.6% from the actual values (MAPE=21.6).

Table 4. Statistical metrics of the accuracy of the ARIMAANN model

Model	RMSE	MAE	MAPE	R^2
ARIMAANN	93012.66	64528.77	21.6	0.96

According to the ARIMA-ANN hybrid model, which was applied for modelling and forecasting the tourists in Albania, the result fit the historical data (R^2 = 0.96). Although the model is quite precise, the mean absolute error estimate (MAPE = 21.6%) suggests that other factors can significantly affect the variations in the number of tourists. Nevertheless, this model can be considered a potentially effective method of tourist flow analysis and forecasting in the Albanian context and can be helpful for decision-makers in the tourism industry. To enhance the precision of the forecasts, it is possible to try other combinations of methods or to use other factors that may impact tourist movement. In the graph below (https://rpubs.com/Breshanaj/1268516), built with "plotly" in R, we have reflected the monthly values of tourist arrivals in Albania and the forecast for the next five years.

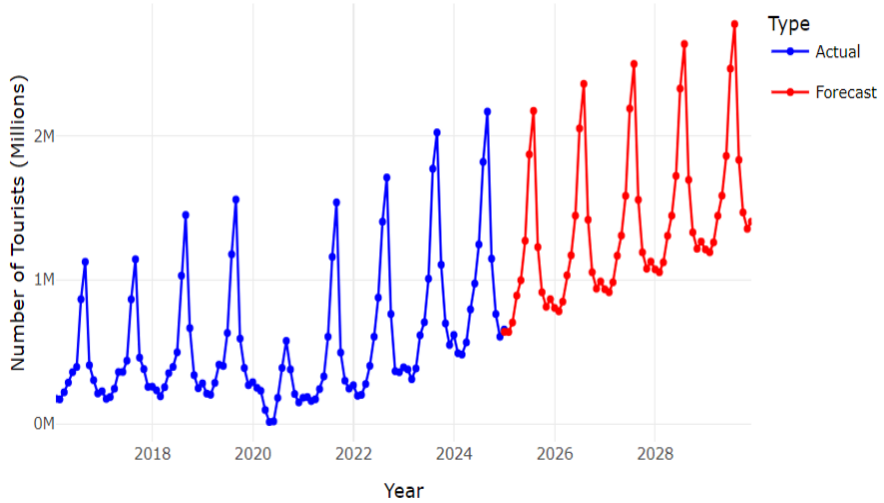

Figure 6. Forecasting tourist flow with the hybrid ARIMAANN method

The forecast graph shows a clear upward trend for the coming years, reflecting a continued expansion of the tourism sector in Albania. According to the ARIMAANN hybrid model, the projections show that the number of international arrivals will continue to increase, reaching a predicted peak of 2,775,862 tourists in August 2025. This result suggests a stabilization of tourism growth after the pandemic and a strong seasonal trend, with the summer months continuing to be the periods with the highest intensity of visitors. The modelling in this paper can aid in resolving decisions by all concerned in managing tourism demand and ensuring the highest quality of tourism.

ARIMAANN for the Period 2021-2029

To avoid the impact of the COVID-19 pandemic period (Sá et al., 2023), we applied the ARIMAANN model to the monthly data of non-resident tourist arrivals in Albania for 2021-2029. As shown in Table 5, this significantly improved model, referred to as ARIMAANN 21-24, showed a significant improvement in all performance metrics compared to the previous models. Statistical evaluations show an RMSE of 48761.5, an MAE of 39700.84, a MAPE reduced to 7.09%, and an R^2 of 0.99, suggesting an almost perfect fit to historical data and a reliable forecast for tourism for the coming years.

Table 5. Statistical metrics of the accuracy of the ARIMAANN model

Model	RMSE	MAE	MAPE	R^2
ARIMAANN 21-24	48761.5	39700.84	7.09	0.99

The graph below shows the trend in the number of intern.ational tourists in Albania for the next five years. The forecasts confirm a progressive increase in tourism, with the highest points during the summer season, where the maximum number of visitors is expected to reach approximately 2.9 million in August 2029. https://rpubs.com/Breshanaj/1269266

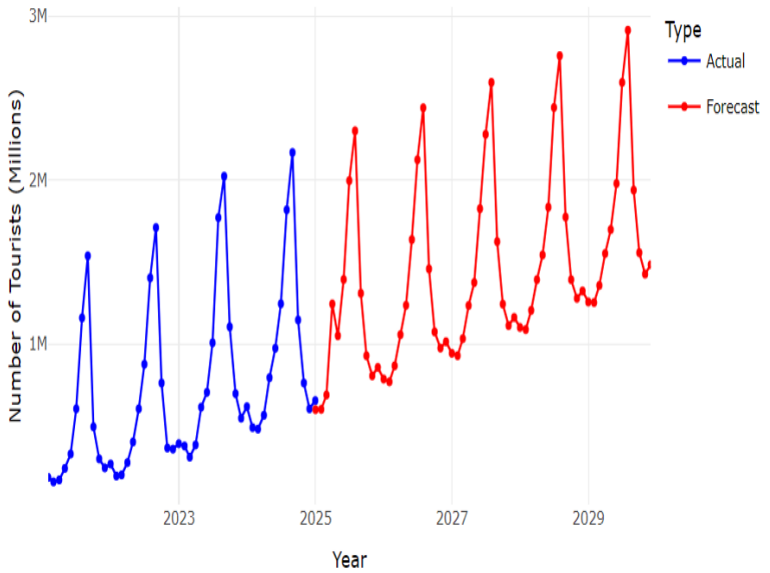

Figure 7. Hybrid ARIMAANN forecasting 2021-2029

These findings highlight the importance of hybrid models, where combining traditional methods with advanced artificial intelligence methods helps in strategic planning and careful management, becoming the foundation for sustainable growth in the tourism sector.

Results and Discussion

The results of this study clearly show that the models used to forecast the number of international tourists in Albania have significant differences in accuracy and appropriateness with historical data. To compare the ARIMA, ANN and ARIMAANN models, we use statistical indicators such as Root Mean Squared Error (RMSE), Mean Absolute Error (MAE), Mean Absolute Percentage Error (MAPE) (Narváez-Villa et al., 2021) and the coefficient of fit (R^2). The accuracymeasurement results are presented in the table below.

Table 6. Performance of ARIMA, ANN, and ARIMANN models

Model	RMSE	MAE	MAPE	R^2
ARIMA	105171.1	67609.17	31.57071	0.946
ANN	234026.4	187720.7	23.1	0.889
ARIMAANN	93012.66	64528.77	21.6	0.96
ARIMAANN 21-24	**48761.5**	**39700.84**	**7.09**	**0.99**

The combined ARIMAANN model, which integrates the two approaches, was the most accurate and best fitting of the three models, with the highest value $R^2$of 0.96 and fewer errors than the other models. This result shows that the combination of ARIMA, which models the linear and seasonal components of the data, and the nonlinear trends of ANN creates a better and more complete model for forecasting tourist flows.

The five-year future forecasts are optimistic and can be seen in all models applied in this study: ARIMA, ANN and ARIMAANN. Based on these models, it is predicted that the highest number of international tourists is expected during the summer months, and the peak is expected to be in August 2029, when the tourist could reach 2.8-2.9 million visitors. This result also supports the existence of a strong seasonality, where the summer months are peak seasons in terms of tourist arrivals while the winter months are low seasons. These findings are significant for policymakers, tourism managers, and government agencies as they can be used to effectively manage tourism dynamics concerning resource allocation and infrastructure development. The model suggested in this paper can also be employed to design marketing strategies and enhance the capacity of the tourism sector to address growing demands, thereby contributing to the sustainable development of the tourism sector in Albania.

Based on the study's findings, the hybrid ARIMAANN approach is a more complex and appropriate model for forecasting tourism demand than the application of individual models. While the ARIMAANN model has

demonstrated a significant improvement compared to the individual ARIMA and ANN models, a more advanced approach, referred to as ARIMAANN 21-24, has shown even more accurate results by eliminating the effects of the COVID-19 pandemic. Compared to the previous version of the ARIMAANN model, the RMSE value has been reduced from 93012.66 to 48761.5; the MAPE has undergone an improvement from 21.6% to 7.09%, a value that categorizes the model as very good. This shows that the new model fits better with recent historical data, providing a more accurate and reliable forecast for tourist flows in Albania. Furthermore, the R^2number has increased from 0.96 to 0.99, suggesting an almost perfect fit for the model with the data used for training. These findings are important to policymakers, tourism managers, and government agencies because they can assist in effectively managing tourism dynamics regarding resource allocation and infrastructure development. The model suggested in this paper can also be employed to design marketing strategies and enhance the capacity of the tourism sector to address growing demands, thereby contributing to the sustainable development of the tourism sector in Albania.

From the study's findings, the hybrid ARIMAANN21-24 approach is a more sophisticated and suitable model for forecasting tourism demand than individual models. The combination of classical approaches and artificial intelligence has led to a significant improvement in the accuracy of forecasts and a better fit to historical data, providing more accurate and reliable results.

Conclusion

Tourism is a rapidly growing industry in most countries (Saba et al., 2022) and requires more accurate modelling and forecasting of tourist arrival data for many purposeful decisions. (Tanzila Saba, Mirza Naveed Shahzad, Sonia Iqbal, Amjad Rehman, Ibrahim Abunadi, 2022) The results of our study clearly show that the hybrid ARIMAANN model has provided the best performance compared to the individual ARIMA and ANN models, confirming the conclusions of previous studies that support the power of combining traditional statistical methods with artificial intelligence.

In line with the studies of Zhang (2003), Atesongun and Gulsen (2024) and Rahayu et al. (2023), this study demonstrates that the hybrid approach provides a significant improvement in forecast accuracy, especially for time series with nonlinear trends and pronounced seasonality, as in the case of Albanian tourism. Also, the results of our study converge to the same conclusion as the findings of Musonera et al. (2021), highlighting the need for advanced models that combine statistical analysis and artificial intelligence algorithms to increase the reliability of forecasts.

In addition to the higher accuracy of the ARIMAANN21-24 model, this study has shown that the trend of increasing international tourist arrivals in Albania will continue in the coming years, with a peak predicted during the summer months. In line with existing studies on hybrid models, this study shows that the selection of the training period significantly impacts the accuracy of the forecasts. Through ARIMAANN 21-24, it is demonstrated that by eliminating the effects of exceptional periods such as the COVID-19 pandemic, a significant reduction in forecast errors and an increase in the fit to recent tourism data in Albania can be achieved. This model's improvement of MAPE and RMSE reinforces the importance of using the most appropriate training periods and hybrid methods to optimize future forecasts in the tourism sector. These results have important implications for strategic tourism management, helping policymakers and tourism operators to improve resource allocation and infrastructure development more efficiently. Although the hybrid model has provided promising results, it cannot capture all the factors that affect tourism, such as sudden political, economic, or climatic changes.

This study leaves room for further studies, where the integration of external influencing factors in the field of tourism or the application of other hybrid methods, such as SARIMA + LSTM**,** ARIMA + XGBoost, or Wavelet Transform + ARIMA + ANN, etc., could further improve the forecast of tourist flows in Albania. These results can be generalized to predict tourist arrivals in any country or region with a complicated data model.

Recommendations

The results of this study highlight the efficiency of hybrid models, especially ARIMAANN 21-24, for enhancing the accuracy of tourism demand forecasting. Policymakers, tourism operators, and government agencies should include such models in their decision-making process for better resource management, infrastructure, and marketing strategies. The interaction between academic institutions, government, and tourism

organizations is vital in encouraging innovation and ensuring that the forecasting models are relevant to the practice. Future work should also incorporate other external factors like political risk, climate change and economic factors to enhance the precision of the forecasts. Also, applying advanced hybrid models such as SARIMA + LSTM, ARIMA + XGBoost, or Wavelet Transform + ARIMA + ANN can produce even better results. The forecasts obtained from the models should be used as a basis for the formulation of sustainable tourism policies that can support the economic development of the country while at the same time protecting the environment and improving the quality of services offered to tourists. These suggestions are meant to assist in the growth of a strong and strategic tourism sector in Albania.

Scientific Ethics Declaration

* The authors declare that the scientific, ethical, and legal responsibility of this article published in EPSTEM journal belongs to the authors.

Conflict of Interest

* The authors declare that they have no conflicts of interest.

Funding

* We thank the "Ismail Qemali" University of Vlora for supporting this work. A special recognition also goes to the Faculty of Technical and Natural Sciences, which provides an inspiring academic environment and encourages the development of scientific research.

Acknowledgements or Notes

* This article was presented as a poster presentation at the International Conference on Basic Sciences, Engineering and Technology (www.icbaset.net) held in Trabzon/Türkiye on May 01-04, 2025.

References

Abdou, M., Musabanganji, E., & Musahara, H. (2021). Tourism demand modelling and forecasting: A review literature. *African Journal of Hospitality, Tourism and Leisure*, *10*(4), 1370-1393.

Atesongun, A., & Gulsen, M. (2024). A hybrid forecasting structure based on arima and artificial neural network models. *Applied Sciences, 14*(1671), 1-10.

Breshanaj M., & Bakaj, A. (2024). Application of ANN in the tourism industry in Albania. *The Albanian Journal of Economy and Business*, 85-102.

Fadhillah, R., Kusnandar, D., & Huda, N. M. (2024). Pemodelan Arima-ann pada harga saham bank mandiri. *Bimaster: Buletin Ilmiah Matematika, Statistika dan Terapannya*, *13*(1), 117-126.

Fang, H., Tu, Y., Wang, H., He, S., Liu, F., Ding, Z., & Cheng, S. S. (2022). Fuzzy-based adaptive optimization of unknown discrete-time nonlinear Markov jump systems with off-policy reinforcement learning. *IEEE Transactions on Fuzzy Systems*, *30*(12), 5276-5290.

Fraiha- Lopes, R. L., Fraiha, S. G., Gomes, H. S., Lima, V. D., & Cavalcante, G. P. (2020). Application of hybrid ARIMA and artificial neural network modelling for electromagnetic propagation: An alternative to the least squares method and ITU recommendation p. 1546-5 for Amazon urbanized cities. *International Journal of Antennas and Propagation*, *2020*(1), 8494185.

Kukreja, H., Bharath N., Siddesh C., & Kuldeep, S. (2016). An introduction to artificial neural network. *International Journal of Advance Research and Innovative Ideas in Education, 1*(5), 27-30.

Mentes, A. & Yetkin, M. (2020). An application of soft computing techniques to predict dynamic behaviour of mooring systems. *Brodogradnja: An International Journal of Naval Architecture and Ocean Engineering for Research and Development*, *73*(2), 121-137.

Narváez-Villa, P., Arenas-Ramírez, B., Mira, J., & Aparicio-Izquierdo, F. (2021). Analysis and prediction of vehicle kilometers traveled: A case study in Spain. *International Journal of Environmental Research and Public Health*, *18*(16), 8327.

Perveen, N., Tariq, K., & Ahmad, H. S. (2024). Comparative studies of hybrid ARIMA and artificial neural network (ANN) techniques for predicting exchange rate in Pakistan. *Bulletin of Business and Economics (BBE)*, *13*(2), 630-636.

Sá, J., & Luís, A. L. (2023). Industrialization is not the solution for creating wealth. *The Journal of Social, Political, and Economic Studies*, *47*(3/4), 324-332.

Saba, T., Shahzad, M. N., Iqbal, S., Rehman, A., & Abunadi, I. (2022). A new hybrid SARFIMA-ANN model for tourism forecasting. *Cmc-Computer Materials and Continua*, *71*, 4785-4801.

Zhang, G. P. (2003). Time series forecasting using a hybrid ARIMA and neural network model. *Neurocomputing*, *50*, 159-175.

Author(s) Information

Morena Breshanaj
University "Ismail Qemali"
Vlore, Albania
Contact e-mail: *morena.breshanaj@univlora.edu.al*

Areti Stringa
University of Tirana
Tirana, Albania

To cite this article:

Breshanaj, M., & Stringa, A. (2025). Designing intelligent models with ARIMAANN for visionary forecasts. *The Eurasia Proceedings of Science, Technology, Engineering and Mathematics (EPSTEM), 34,* 221-233.

The Eurasia Proceedings of Science, Technology, Engineering & Mathematics (EPSTEM)
ISSN: 2602-3199

The Eurasia Proceedings of Science, Technology, Engineering and Mathematics (EPSTEM), 2025

Volume 34, Pages 234-243

ICBASET 2025: International Conference on Basic Sciences, Engineering and Technology

Energy Saving Measures in Enterprise from Canning Industry

Slav Valchev
University of Food Technology

Stanislava Tasheva
University of Food Technology

Ana Semerdzhieva
University of Food Technology

Abstract: An energy survey of an enterprise from the canning industry was carried out. This survey includes: collection of primary information on the energy costs of the enterprise for a period of three consecutive years and analysis in order to determine the potential for energy savings, determination of a reference year, on the basis of which the baseline of energy consumption of the enterprise is determined, determination of specific energy consumption depending on the production in the enterprise, determining the amount of energy savings as saved energy and as separated carbon emissions to the environment. The baseline for energy consumption is determined, depending on the energy consumption in the enterprise for the considered period of the survey. The specific costs for energy carriers in the enterprise were calculated, and on this basis an economic and ecological assessment of the proposed energy-saving measures was carried out. A regression equation was derived to determine the energy consumption depending on the processed output of an industrial system.

Keywords: Energy audit, Energy survey, Saved carbon emissions

Introduction

Energy in industry plays an important role in determining the price of manufactured products. In addition, energy consumption largely determines its quality. Subject to mandatory energy efficiency audit in accordance with regulation act in Bulgaria are large enterprises for the production of goods, large service providers, industrial systems whose annual energy consumption is over 3000 MWh (Ordinance №E-RD-04-3, 2016; Ordinance №E-RD-04-05, 2016). Improving energy efficiency of enterprise has one of the following two objectives:

- while preserving the production result, to ensure lower costs of energy resources for enterprise or
- while maintaining the costs of energy resources for the enterprise to increase its production result.

In both cases, as a result of introduced energy-saving measures in enterprise, we ensure reduction of specific energy consumption per unit of manufactured product (Baev et al.,2015; Kaloyanov et al, 2020). Industrial systems are also subject to an energy audit one year after major changes have been made to technological equipment and/or production systems, changing the fuel base and the way energy is converted (Ivanov et al., 2021; Kamburova et al., 2017; Iliev et al., 2013; Berk, 2009; Fellows, 2000; Balentas et al., 1997; Brennan, 2006).

Method

- Selection and peer-review under responsibility of the Organizing Committee of the Conference

The object of the present survey for energy efficiency of an industrial system is a canning enterprise in Bulgaria. The enterprise specializes in processing seasonal fruits and vegetables, mainly for export to European countries. It processes about 2,000 tons of different fruits and vegetables per season. The product range also includes a variety of canned products from fruits, vegetables, ready meals, sauces and jams. In enterprise for canning industry the following technological processes are carried out:

- Technological lines for processing peaches;
- Filling and closing section;
- Equipment for pasteurization and sterilization;
- Equipment for the production of compote from cherries, sour cherries, prunes and apricots;
- Equipment for the production of roasted pepper;
- Equipment for the production of tomatoes with salty-sour topping or tomato juice topping;
- Preparation of tomato juice for topping;

The choice of energy-saving measures, guaranteeing highest value energy savings in form of energy and carbon emissions released into the environment, requires a detailed energy analysis of enterprise's energy costs This analysis includes:

- collection of primary information on the energy costs of the enterprise for a period of 3 consecutive years and analysis in order to determine potential for energy savings;
- determination of a reference year, on the basis of which baseline of energy consumption of enterprise is determined;
- determination of specific energy consumption depending on production in enterprise;
- determining amount of energy savings as saved energy and as saved carbon emissions to the environment.

The introduction of energy-saving measures in enterprise, such as supply of new energy-efficient equipment, should not conflict with the requirements for:

- reducing amount of waste from enterprise (includes management of production storage processes, monitoring expiration dates of food products, use of artificial intelligence to predict future consumption of food products) ;
- recycling materials used in production process (using food waste to obtain innovative food products and bio fuels for needs of enterprise);
- using innovative biodegradable materials for product packaging (switching to biodegradable or recycled packaging in order to reduce plastic waste from enterprise);
- circular agriculture (integrating livestock and crop production can also create a balanced ecosystem, reducing need for chemical fertilizers and pesticides used in growing vegetables).

The energy survey used data provided by the owner of the enterprise and the engineering team that developed the technological project for reconstruction, as well as technical catalogs for technological equipment.

Results and Discussion

The energy carriers used for enterprise needs are natural gas and electricity. The factory is fully gasified. Natural gas is used to obtain process steam. Steam is used for pasteurization and sterilization of finished products. Electricity is used to power the production machines and equipment, as well as for lighting. The available electrical power of the company is 250 kW. A 200 kVA diesel generator is used for emergencies. In Table 1 are shown data on installed electrical power of the facilities in the enterprise. The annual consumption of electricity for needs of the technological process and produced output before energy savings measures are presented in Table 2. Process steam is used for needs of the pasteurization tunnels and autoclaves. It is obtained from a steam boiler with a productivity of 4000 kg steam/hour. The burner of steam boiler use natural gas. Annual consumption of electrical energy of enterprise for 2017, 2018 and 2019 year are presented in Table 2. In Table 3 are shown data for annual consumption of natural gas in enterprise for 2017, 2018 and 2019 year.

Used energy (electrical and natural gas) is reported for production period of three years 2017, 2018 and 2019. Data in table show that the total energy consumption are the highest for 2019 year. This is why this year was chosen as a reference year for energy audit. Using this data the baseline for energy consumption of the enterprise is determined. On Figure 1 is shown percentage distribution of energy consumed in enterprise for 2019 year.

Table 1. Installed electrical power of the facilities in the enterprise

Name	Value	Power, kW	Total power, kW
Pallet turning machine	1	2.0	2.0
Fan washing machine	1	3.7	3.7
Inspection line	1	1.1	1.1
Calibrator for whole peaches	1	1.5	1.5
Conveying belt	1	0.6	0.6
Elevator	1	2.0	2.0
Bone grafting machine	10	0.56	5.6
Inspection line	1	0.8	0.8
Conveying belt	1	0.6	0.6
Inspection line	1	0.8	0.8
Elevator	1	3.0	3.0
Reception tub with pressure pump	2	4.0	8.0
Buffer tank	1	4.0	4.0
El. motor	1	2.2	2.2
El. motor	1	2.2	2.2
Conveyor belts	5	0.56	2.8
Rotating tables	6	0.55	3.3
Filling tables	3	4.5	13.5
Conveyor belt (full jars)	2	0.75	1.5
Distribution belt	3	0.57	1.7
Metal box stopper	1	7.5	7.5
Tunnel - pasteurizing	1	18.0	18.0
Compressor	1	15.0	15.0
Boiler pump	1	5.5	5.5
Burner	1	9.7	9.7
Lighting	150	2x0.058	17.4
Total usable power			133.7

Table 2. Annual consumption of electrical energy of enterprise for 2017, 2018 and 2019 year

Year	2017	2018	2019
Month	kWh	kWh	kWh
January	7746	3878	5228
February	7214	6454	3791
March	8041	7449	3550
April	5922	6668	3518
May	6801	7868	2815
June	13580	5459	8311
July	24450	16210	24710
August	39065	28004	37215
September	1235	1146	17142
October	1461	2210	13683
November	2551	2884	9653
December	3064	3470	9079
Total	121130	91700	138695

Table 3. Annual consumption of natural gas for enterprise for 2017, 2018 and 2019 year

Year	2017	2018	2019
Month	kWh	kWh	kWh
January	0	0	0
February	0	0	0
March	0	0	0
April	0	0	0
May	9207	7306	0
June	140567	135761	137350
July	266536	270628	298292
August	519158	540031	600975
September	0	200147	220713
October	0	88225	101961

November	0	0	0
December	0	0	0
Total	935468	1242098	1359291

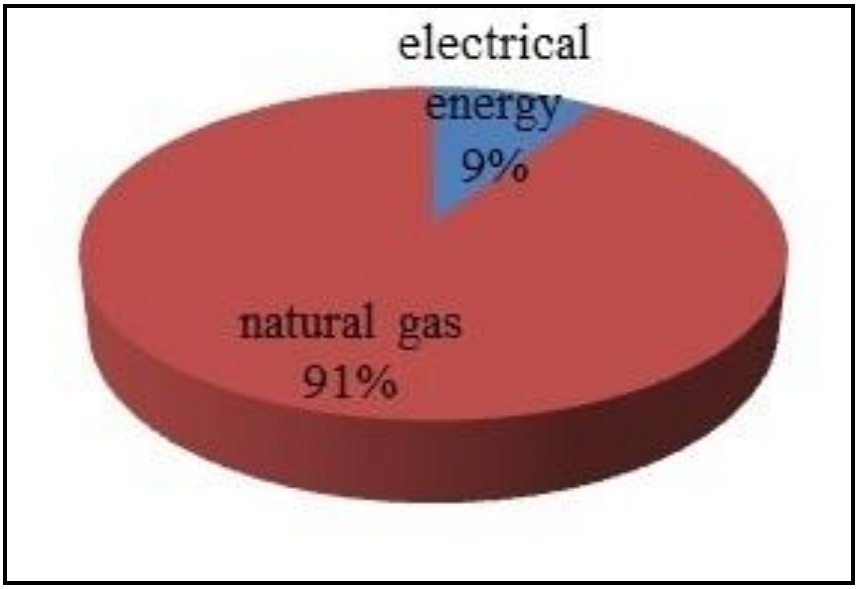

Figure 1. Percentage distribution of energy consumed by enterprise 2019 year

The graph shows that there is great potential for saving energy in enterprise in optimization and replacement of facilities consuming fuel - natural gas. Annual consumption of electricity for needs of the technological process and produced output before energy saving measures are presented in Table 4. Annual energy cost for autoclaves, steam pasteurizing tunnel and roasting peppers before energy saving measures are presented in Table 5.

Table 4. Annual consumption of electricity for needs of the technological process and produced output before energy saving measures

Name	Value	Unit of measure
Total usable power	133.7	kW
Consumed electrical energy	138695	kWh/year
Hours of equipment operation	1037.36	hours/year
Produced output	3629182	units/year
Production capacity of technological line	3498	units/hour
Specific energy consumption	0.038	kWh/unit

Table 5. Annual energy cost for autoclaves, steam pasteurizing tunnel and roasting peppers before energy saving measures

Name	Value	Unit of measure
Autoclaves		
Steam consumption	220	kg/ hour
Autoclave	7	cycle/day
Total autoclaves (10 pcs.)	2200	kg/ hour
Total autoclaves (10 pcs.)	70	cycle/day
Packs per cycle	500	units
Total autoclaves (10 pcs.)	35000	units/day
Total autoclaves (10 pcs.)	17600	kg/ day
Number of packages processed	1957188	unit/year
Operation of autoclaves	55.9	days
Used steam autoclaves	983.8	t/year
Used heat energy autoclaves	619819	kWh/year
Specific energy consumption	0.317	kWh/unit
Pasteurization tunnel		
Steam consumption	1600	kg/ hour
Pasteurization tunnel capacity	3000	units/hour
Number of packages - boxes	1671994	units

Operation of pasteurizing tunnel	557.3	hours
Used steam pasteurizing tunnel	851.7	t/year
Used heat energy pasteurizing tunnel	536558	kWh/year
Specific energy consumption	0.321	kWh/unit
Roasting peppers		
Energy for roasting peppers	79303	kWh/year
Annual cost		
Total steam consumption	1835.5	t/year
Natural gas energy consumption	1359291	kWh/year
Specific energy consumption natural gas	741	kWh/t steam

In Table 6 data are shown for specific energy consumption of final product for 2017, 2018 and 2019 year.

Table 6. Specific energy consumption for final product 2017, 2018 and 2019 year

Year		2017	2018	2019
Manufactured product	Unit/ year	2554401	3299545	3629182
Consumed electrical energy	kWh/ year	121130	91700	138695
Specific electricity consumption	kWh/ unit	0.047	0.028	0.038
Consumed natural gas	kWh/ year	935468	1242098	1359291
Specific natural gas consumption	kWh/ unit	0.366	0.376	0.385
Consumed electrical + natural gas energy	kWh/ year	1056598	1333798	1497986
Specific energy consumption for final product	kWh/ unit	0.414	0.404	0.424

The enterprise intends to make the following investments:

- Peach pitting machines – 3 pieces;
- Bottling machine by level - 3 pieces;
- Monobloc – 1 piece;
- Automatic machine for closing and orienting caps - 1 piece;
- Linear rinser - 1 piece;
- Automatic flotation machine - 1 piece;
- Sealing machine for metal cylindrical boxes - 3 pieces;
- Compressor installation - 1 piece;
- Gas forklift - 1 piece;
- Electric car – 3 pieces;
- Automatic titrator - 1 piece;
- System for weight control of products in rigid packaging – 4 pieces;
- Peach elevator tub - 3 pieces;
- Inspection tape, roll - 1 piece;
- Transport road feeding pasteurization tunnel - 1 piece;
- Pasteurization tunnel-cooler for cans 1 kg -1 piece;
- Buffer table - 1 piece;
- Aerial transport line for empty metal cans (1kg) - 1 piece;
- Reconstruction of a boiler plant installation of a second boiler 2.5 t/h - 1 piece;

The delivery of the new equipment will lead to an increase in production at the enterprise. This necessitates the determination of adjusted baseline energy consumption for new higher amount of output produced. The data are shown in Table 7.

Table 7. Baseline of enterprise according to new produced output

Name	Value	Unit of measure
Produced output according to the plan of enterprise	5740000	Unit/ year
Specific electricity consumption 2019	0.038	kWh/ unit
Specific natural gas consumption 2019	0.385	kWh/ unit
Baseline electrical energy consumption	218120	kWh/year
Baseline natural gas energy consumption	2209900	kWh/year
Total energy consumption by baseline	2428020	kWh/year

In Table 8 data are shown on installed electrical power of facilities in enterprise after energy saving measures.

Table 8. Installed electrical power of facilities in enterprise after energy saving measures

Name	Value	Power, kW	Total power, kW
Pallet turning machine	1	2.0	2.0
Fan washing machine	1	1.1	1.1
Inspection tape - roll type	1	1.1	1.1
Calibrator for whole peaches - 3+2 classes	1	1.0	1.0
Conveyor belt - distributed	1	0.55	0.55
Elevator with water bath	3	0.8	2.4
Peach pitting machine	3	8.0	24.0
Inspection tape - collection	1	0.55	0.55
Conveyor belt - feeding	1	0.55	0.55
Elevator - feeder	1	1.1	1.1
Elevator - feeder	1	1.1	1.1
Conveyor belt - distributed	1	0.55	0.55
"cup up" pitting machine	2	1.5	3.0
Inspection tape	1	0.55	0.55
Inspection tape	1	0.55	0.55
Inspection tape - collection	1	0.55	0.55
Elevator - feeder	1	0.75	0.75
Conveying belt	1	0.55	0.55
"cup down" peach orienteering track	1	1.5	1.5
Installation for thermochemical peeling	1	5.0	5.0
Reception tub with pressure pump	1	3.0	3.0
Water transport road - circulation	1	22.0	22.0
Calibrator for peach halves - 3+2 classes	1	2.2	2.2
Conveyor belt - distributed	1	0.55	0.55
Elevator	3	1.1	3.3
Trasina "cup up" - 3 pcs. Trasina "cup down" - 3 pcs.	6	1.5	9.0
Inspection tape	6	0.55	3.3
Jar feeding station	1	2.0	2.0
Transport route for empty jars	1	1.5	1.5
Linear rinser	1	11.5	11.5
Filling table for products in metal boxes - paired	1	2.2	2.2
Filling table for products in metal boxes	1	1.5	1.5
Filling table for products in glass jars	1	2.2	2.2
Transport road - single	3	0.75	2.25
Conveyor track for boxes	1	0.75	0.75
Transport route for jars	1	0.75	0.75
Transport route for jars	1	0.75	0.75
Weight control system	4	0.25	1.0
Vacuum filling machine	3	0.75	2.25
Bruiser type filling machine	1	0.75	0.75
Transport road	3	0.75	2.25
Sealing machine for metal cans	3	3.0	9.0
Feed elevator for caps	2	0.75	1.5
Sealing machine for jars	1	0.75	0.75
Filling and closing monobloc for glass jars	1	1.5	1.5
Transport route for jars	1	0.75	0.75
Packaging printer	4	0.75	3.0
Transport road	1	0.75	0.75
Set with printer	1	0.35	0.35
Stacking machine. The machine automatically packs ready cans in shrink wrap.	1	26.0	26.0
Tunnel pasteurizer	1	18.0	18.0
Accepted transport route	1	0.75	0.75
Labeling machine	1	2.2	2.2
Transport road feeding pasteurization tunnel.	1		
Pasteurization tunnel-cooler for cans. Set with outgoing transport path.		33.0	33.0

Water cooling tower and buffer table. Overhead conveyor line for metal boxes			
Transport road	1	0.75	0.75
Set with printer	1	0.35	0.35
Stacking machine. The machine automatically packs ready cans in shrink wrap.	1	26.0	26.0
Compressor equipment. Compressed air compressor. Complete with a microfilter.	1	9.0	9.0
Compressor	1	15.0	15.0
Forklift. Engine fuel type - gas. Load capacity-3 t.	1	0.0	0.0
Electric car. Load capacity - 1.5 t.	3	0.0	0.0
Automatic titrator. Intended for use in the food industry.	1	0.5	0.5
Lighting	150	2x0.058	17.4
Lighting new warehouses	58	2x0.054	6.26
Total usable power			152.0

In Table 9 data are shown on consumed electrical energy in enterprise after energy saving measures. Consumption of natural gas for the needs of pasteurization tunnels is presented in Table 10. Consumption of natural gas for the needs of autoclaves after energy saving measures is presented in Table 11.

Table 9. Consumed electrical energy after energy-saving measures

Name	Value	Unit of measure
Total usable power	kW	152.0
Production capacity of the new line	Unit/hour	5000
Production plan of the enterprise after energy-saving measures	Unit/year	5740000
Hours of operation on new equipment	Hour/year	1148
Consumed electrical energy after energy-saving measures	kWh/year	174496

Table 10. Consumption of natural gas pasteurization tunnels

Name	Value	Unit of measure
Pasteurization tunnel – new line		
Steam consumption	2200	Kg/ hour
Pasteurization tunnel capacity	5000	Unit/ hour
Number of packages	3650000	Unit/ year
Operation of the pasteurizing tunnel - new	730	Hour/ year
Used steam pasteurizing tunnel	1606	t/ year
Used thermal energy pasteurizing tunnel	1011780	kWh/year
Specific energy consumption	0.277	kWh/unit
Pasteurization tunnel – existing		
Steam consumption	1600	Kg / hour
Pasteurization tunnel capacity	3000	Unit/ hour
Number of packages	1120000	Unit/ year
Operation of the pasteurizing tunnel - existing	373.33	Hour/ year
Used steam pasteurizing tunnel	597.33	t/ year
Used thermal energy pasteurizing tunnel	376320	kWh/year
Specific energy consumption	0.336	kWh/unit
Annual cost		
Number of packages	4770000	Unit/ year
Used steam pasteurizing tunnels	1327.33	t/ year
Used thermal energy pasteurizing tunnels	1388100	kWh/year
Specific energy consumption	0.291	kWh/unit

The distribution of natural gas energy after energy saving measures is shown in Table 12. The summary analysis energy costs of enterprise after the introduction of the energy saving measure is shown in Table 13.

Table 11. Consumption of natural gas for the needs of autoclaves after energy saving measures

Name	Value	Unit of measure
Autoclave	220	Kg steam/ hour
Autoclave	7	Cycles/day
Total autoclaves (10 pcs.)	2200	Kg steam/ hour
Total autoclaves (10 pcs.)	70	Cycles/day
Packs per cycle	500	units
Total autoclaves (10 pcs.)	35000	units/day
Total autoclaves (10 pcs.)	17600	Kg steam/ hour
Number of packages processed	970000	Units/ year
Operation of the autoclaves	27.7	days
Used steam autoclaves	487.8	t steam/ year
Used heat energy autoclaves	307296	kWh/year

Table 12. Distribution of natural gas after energy saving measures

Name	Value	Unit of measure
Production plan of the enterprise after energy-saving measures	Unit/year	5740000
Used steam pasteurizing tunnel – new line	1606	t/ year
Used thermal energy pasteurizing tunnel – new line	1011780	kWh/year
Used steam tunnel pasteurizer - existing	597.33	t/ year
Used thermal energy pasteurizing tunnel - existing	376320	kWh/year
Used steam autoclaves	487.8	t/ year
Used heat energy autoclaves	307296	kWh/year
Total steam	2691.13	t/ year
Total steam energy	1695396	kWh/year
Energy /natural gas/ for roasting peppers	79303	kWh/year
Disposal in an integrated economizer	50862	kWh/year
Thermal efficiency of a boiler	95	%
Heat losses in a boiler	84770	kWh/year
Necessary amount of natural gas	1808607	kWh/year
Specific energy consumption (natural gas)	672	kWh/t steam
Specific energy consumption (natural gas)	0.315	kWh/unit

Table 13. Analysis energy costs of enterprise after energy saving measures

Name	Value	Unit of measure
Quantity produced after energy saving measures	5740000	Units/ year
Baseline electrical energy consumption	218120	kWh/year
Baseline natural gas energy consumption	2209900	kWh/year
Total energy consumption by baseline	2428020	kWh/year
Consumed electrical energy after energy saving measures	174496	kWh/year
Energy consumed from natural gas after energy saving measures	1808607	kWh/year
Total required energy after energy saving measures	1983103	kWh/year
Electical energy savings	43624	kWh/year
Natural gas energy savings	401293	kWh/year
Overall energy savings	452020	kWh/year
Specific energy saving /electical energy/	0.008	kWh/unit
Specific energy savings /natural gas/	0.070	kWh/unit
Total specific energy savings	0.078	kWh/unit
Specific electrical energy consumption after energy saving measures	0.030	kWh/unit
Specific consumption of energy from natural gas after energy saving measures	0.315	kWh/unit
Total specific energy expenditure after energy saving measures	0.345	kWh/unit

Table 14. Energy savings

Energy saving measures	Energy carrier	Energy savings		Ecological equivalent
		kWh	%	t CO_2/ year
Modernization of a canning enterprise	electricity	43624	19.83	35.4
	natural gas	401293	18.16	81.1
Total:		444557	18.31	116.5

The share of the enterprise's energy savings compared to the reference year 2019 has been determined in energy value (in kWh) and ecological equivalent (t CO_2/ year). The results are shown in Table 14.

Conclusion

Upon implementation of energy saving measures, the enterprise will realize an energy saving of 18.31% compared to the baseline of energy consumption, which is equal to an energy saving of 444557 kWh/ year with an ecological equivalent of 116.5 tons of CO_2 emissions saved.

Scientific Ethics Declaration

* The authors declare that the scientific ethical and legal responsibility of this article published in EPSTEM. Journal belongs to the authors.

Conflict of Interest

* The authors declare that they have no conflicts of interest

Funding

* This research received no specific grant from any funding agency in the public, commercial, or not-for-profit sectors.

Acknowledgements or Notes

* This article was presented as an oral presentation at the International Conference on Basic Sciences, Engineering and Technology (www.icbaset.net) held in Trabzon/Türkiye on May 01-04, 2025.

References

Baev, D., Georgiev, Z., Manchev, P., Simeonov, K., Ivanova, D., Hristov, H., Canev, D., Haladzhova, R., & Stankov, A. (2024, October 16). *Manual on energy efficiency management in.* Retrieved from https://seea.government.bg/documents/narachnik.pdf

Berk, Z. (2009). *Food process engineering and technology*. Academic Press.

Brennan, J. (2006). *Food processing handbook*. Wiley-VCH Publishing

Fellows, P. (2000). *Food processing technology* (2nd ed.). CRC Press.

Iliev, I., Kaloyanov, N., Gramatikov, P. Terziev, A., Pavlov, I., Stefanov, S., Sirakov, K., & Kamburova, V. (2024, 16 October). *Energy efficiency and energy management handbook*. Retrieved from https://www.exergia-max.com/sites/default/files/documents/EEEM_Handbook_ENG.pdf

Ivanov, K., Georgieva, N., Tasheva, S., & Gandova, V. (2021). Analysis of energy efficiency of an industrial system. *IOP Conference Series: Materials Science and Engineering, 1031*(1), 012080.

Kaloyanov, N., Kasabov, I., Bojkov, C., Matanov, N., Penkova, N., Vasilev, M., Cekov, R., Tomova, M., Djabarska, S., Markova, S., & Todorov, C. (2024, October 16). *Methodological instructions for do a survey for energy efficiency and evaluation of industrial energy savings systems and enterprises* Retrieved from https://seea.government.bg/documents/metodicheski_ukazania.pdf

Kamburova, V., Iliev, I., Velikanov, M., Terziev, A., Ahmedov, A., & Iliev, K. (2017). Energy efficiency of large industrial enterprises. *Journal Energetika, 3,* 40-50.

Ordinance № E-RD-04-05. (2016, September 8). *On determining energy consumption indicators, energy performance of enterprises, industrial systems and outdoor artificial lighting systems, as well as on determining conditions and procedure for conducting inspections for energy efficiency and preparation of energy savings assessment.* Retrieved from https://seea.pdf

Ordinance № E-RD-04-3. (2016, May 4). *On admissible measures for implementation of energy savings in final consumption, ways of proving the achieved energy savings, requirements to methodologies for their evaluation and ways for their confirmatio.* Retrieved from https://seea.government.bg/documents.pdf

Valentas, K., Rotstein, E., & Singh. R. (1997). *Food engineering practice*. CRC Press.

Author(s) Information

Slav Valchev
University of Food Technology
Plovdiv, 26 Maritza Boulevard, Bulgaria
Contact e-mail: *slavvalchev@uft-plovdiv.bg*

Stanislava Tasheva
University of Food Technology
Plovdiv, 26 Maritza Boulevard, Bulgaria

Ana Semerdzhieva
University of Food Technology
Plovdiv, 26 Maritza Boulevard, Bulgaria

To cite this article:

Valchev, S., Tasheva, S., & Semerdzhieva, A. (2025). Energy saving measures in enterprise from canning industry. *The Eurasia Proceedings of Science, Technology, Engineering and Mathematics (EPSTEM), 34,* 234-243.

The Eurasia Proceedings of Science, Technology, Engineering & Mathematics (EPSTEM)
ISSN: 2602-3199

The Eurasia Proceedings of Science, Technology, Engineering and Mathematics (EPSTEM), 2025

Volume 34, Pages 244-252

ICBASET 2025: International Conference on Basic Sciences, Engineering and Technology

The Influence of Soil Flexibility on Structural Seismic Behavior

Sonia Outayeb
Mouloud Mammeri University of Tizi Ouzou

Samia Louadj
Mouloud Mammeri University of Tizi Ouzou

Amar Louzai
Mouloud Mammeri University of Tizi Ouzou

Abstract: The dynamic behavior of buildings during earthquakes is deeply influenced by the interaction between the structure and the supporting soil. This work investigates the influence of soil-structure interaction (SSI) on the seismic behavior of 3-, 6-, and 9-story reinforced concrete moment-resisting frames designed in accordance with the Algerian seismic code RPA99 (Version 2003). The numerical analyses are carried out using the FLAC2D software, where the soil is modeled as a homogeneous profile with elastic perfectly plastic behavior, and the structural components remain within the linear elastic domain. Two scenarios are compared: a fixed-base model and a flexible-base model that accounts for SSI effects. The frames are subjected to three recorded ground motions. The comparison is made in terms of spectral acceleration, top lateral displacements, and base shear. The results indicate that SSI modifies the dynamic response of structures and can induce resonance effects that amplify structural response, highlighting the necessity of considering these phenomena in seismic design.

Keywords: Soil-structure interaction, Numerical analysis, Reinforced concrete frames, Resonance effects.

Introduction

Soil-structure interaction (SSI) plays a crucial role in seismic analysis, as the flexibility of supporting soil significantly influences the way dynamic forces are transmitted and dissipated. Unlike a rigid base, which imposes uniform motion on the structure without deformation, a flexible soil absorbs part of the seismic energy and alters the structural response. This interaction leads to modifications in natural frequencies, damping, and internal force distribution, thereby affecting the overall seismic behavior of buildings. One of the most notable effects of SSI is the elongation of the fundamental period due to the overall softening induced by soil deformability (Ramadan et al., 2012; Scarfone et al., 2020). This elongation directly impacts seismic response by altering the internal force distribution and increasing lateral displacements. In fact, lateral displacements in structures with SSI tend to be larger than those in fixed-base structures, as they result from the combined effects of soil deformations and structural oscillations (Tabatabaiefar & Fatahi, 2014; Outayeb et al., 2023). This increase can have adverse consequences, particularly in terms of occupant comfort and additional stresses on non-structural elements. Furthermore, SSI affects base shear forces, as soil flexibility modifies the way seismic energy is absorbed and redistributed. In some cases, this results in a reduction of base shear compared to fixed-base conditions, but the extent of this variation depends on multiple factors (Hokmabadi et al., 2014; Yeganeh et al., 2015).

Beyond these effects, a particularly critical aspect of SSI is the potential resonance between the structure and the supporting soil. This phenomenon occurs when the modified fundamental period of the structure aligns with a

frequency range of the seismic motion, leading to excessive amplification on internal forces (Scholl, 1989; Mylonakis & Gazetas, 2000; Torabi & Rayhani, 2014). The severity of resonance depends on soil stiffness, structural height, and seismic input characteristics, potentially increasing the vulnerability of the building.

Given these considerations, incorporating SSI into seismic analysis is essential for refining numerical models and improving the accuracy of structural response assessments under earthquake loading. In this context, this present study investigates SSI effects on reinforced concrete moment-resisting frames, considering 3-, 6-, and 9-story structures designed according to the Algerian seismic code RPA99/Version 2003. The frames are supported by a homogeneous soil modeled with an elastic perfectly plastic behavior, while the structural elements are assumed to remain within the linear elastic range. Numerical simulations are conducted using FLAC2D, employing the global method to compare fixed-base and flexible-base conditions. The models are subjected to three recorded seismic events, and the effects of SSI are evaluated in terms of spectral acceleration, top lateral displacements, and base shear.

Development of a 2D Numerical Model

For comparative investigation of fixed and flexible base support conditions of the structures, a set of three structural models, consisting of 3, 6, and 9-story RC building frames, is adopted herein, representing conventional types of low and mid-rise moment-resisting building frames. The building site was assumed to have a 30-meter-thick deposit of very flexible homogeneous soil with a shear wave velocity V_s constant with depth and less than 200 m/s, underlain by the bedrock.

RC Frame Structures

The model buildings considered are located in the Algiers area and have a plan that represents an ordinary architectural plan. Figure 1 shows the plan view of the repetitive story of the three buildings.

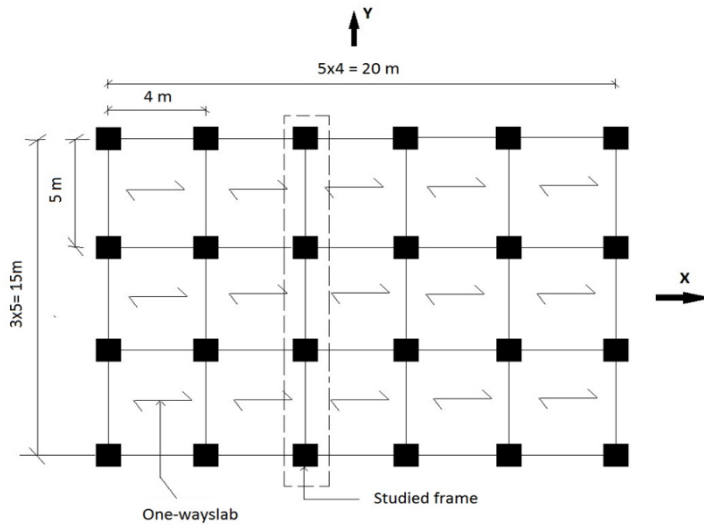

Figure 1. Typical floor plan for model buildings of 3-, 6-, and 9- story

Structural components and dimensions of the studied frames are presented in Table 1. All structures are regular in elevation and in plan to remove secondary effects due to irregularity when analyzing the dynamic behavior of building frames with the effect of soil-structure interaction. Columns and beams of frames are considered to be made of reinforced concrete with the same material properties. The structural design was performed in accordance with the criteria specified by the Reinforced Concrete Code BAEL 91 and Algerian Seismic Design Code Provisions RPA 99/version 2003 under the design seismic action of PGA = 0.25 g, which corresponds to a high seismicity zone (Zone III), soil type S3 (soft soil), a quality factor of 1, and a viscous damping ratio of 5%.

A seismic behavior factor of 5 was adopted for frames without masonry infill. The gravity loads assigned to the buildings were the own weight of structural components, including the reinforced concrete beams, columns, and slabs, and the live loads they support. Therefore, the imposed load in weight calculation is a uniform story live load of LL = 2.5 kN/m^2 and a roof live load of LL = 1.0 kN/m^2. Also, a story dead load of LD = 5.1 kN/m^2 and a

roof dead load of LD = 5.8 kN/m^2 are adopted. A characteristic cylinder strength of 25 MPa for concrete and a yield strength of 500 MPa for steel are utilized. Structures are assumed to be built over shallow foundations that are 0.5 m thick and 15 m length and assumed to be located close to the ground; the effect of the embedment depth of the foundation has been ignored in soil-structure interaction.

Table 1. Structural components and dimensions of the studied frames.

Number of Stories	Total Height (m)	Bay Spacing (m)	Beam Cross-Section (cm × cm)	Column Cross-Section (cm × cm) per Story
3 stories	9	5	30 × 40	40 × 40 (all stories) 50 × 50 (1st–2nd stories)
6 stories	18	5	30 × 40	45 × 45 (3rd–4th stories) 45 × 45 (5th–6th stories) 60 × 60 (1st–2nd stories)
			30 × 45 (1st–4th stories)	55 × 55 (3rd–4th stories)
9 stories	27	5	30 × 40 (5th–9th stories)	50 × 50 (5th–6th stories) 45 × 45 (7th–8th stories) 40 × 40 (9th stories)

The structural frame was modeled using standard 1D beam elements, with soil-structure interaction (SSI) incorporated in FLAC2D by connecting beam elements to the soil grid points via the GRID keyword. The superstructure, supported by an elastic concrete foundation, was installed after achieving equilibrium. As reported by Rayhani and Naggar (2006) and Yue and Wang (2012), both the frame and foundation remained elastic under static and dynamic conditions. While slabs were not explicitly modeled, their weight and live load were accounted for by distributing their reactions onto the supporting girders. To reflect these loads in both static and dynamic analyses, the mass density of beams was adjusted accordingly.

To ensure a realistic representation of energy dissipation, Rayleigh damping was introduced in the numerical model. The α and β coefficients determined based on the dominant modal frequencies extracted from a modal analysis in SAP2000. The fundamental and secondary periods of the 3-, 6-, and 9-story frames were identified respectively as 0.42 s and 0.12 s for the 3-story frame, 0.77 s and 0.25 s for the 6-story frame, and 1.00s and 0.35 s for the 9-story frame. Using these values, the minimum critical damping ratio (ξ_{min}) and the minimum center frequency (f_{min}) were computed for each structural frame according to the following equations:

$$\xi_{min} = \left(\alpha\beta^{1/2}\right) \tag{1}$$

$$f_{min} = \frac{1}{2\pi}\left(\frac{\alpha}{\beta}\right)^{1/2} \tag{2}$$

The results yielded $\xi_{min} = 4.1\%$ and $f_{min} = 4.4\,Hz$ for the 3-story frame, $\xi_{min} = 4.4\%$ and $f_{min} = 2.15\,Hz$ for the 6-story frame, and $\xi_{min} = 4.4\%$ and $f_{min} = 1.6\,Hz$ for the 9-story frame. These parameters were implemented in FLAC2D to accurately capture damping effects in the numerical simulations.

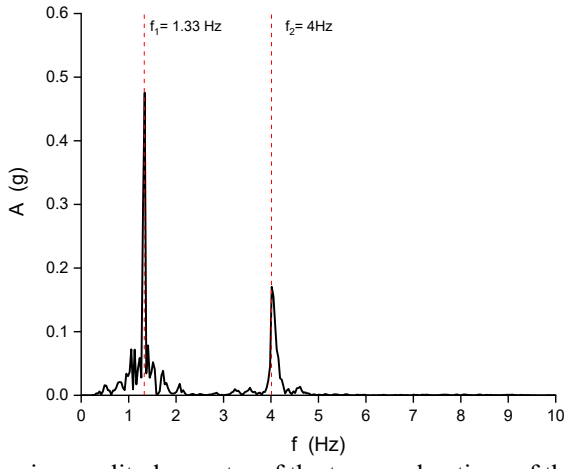

Figure 2. Fourier amplitude spectra of the top accelerations of the 6-story frame

The effectiveness of this approach is confirmed by the Fourier amplitude spectra presented in Figure 2, where the first two natural frequencies of the fixed-base 6-story frame ($f_1 = 1.30\ Hz$ and $f_2 = 4\ Hz$) are clearly identified. Furthermore, the computed natural frequencies exhibit excellent agreement with those obtained from a numerical analysis performed in SAP2000 on an identical 2D model of the fixed-base structure.

Soil Profile

The soil we are concerned with is basically a very simple one. A horizontal soil layer, bounded by the free surface and below by a semi-infinite elastic medium representing the bedrock, is postulated. The soil deposit is located at El Biar, in Algeria with the geotechnical characteristics based on the available in-situ tests and illustrated in Table 2 (Saci 2011). With a constant shear velocity V_s of 180 m/s, this soil is classified as a very flexible soil according to the Algerian seismic code RPA2003.

Table 2**.** Details of soil parameters

Mass density (kg/m^3)	Shear velocity (m/s)	Shear modulus (MPa)	Bulk modulus (MPa)	Friction angle	Cohesion (KPa)
1520	180	49.2	90.1	10°	60

To properly account for wave propagation effects in soil-structure interaction (SSI) modeling, the soil domain was set to five times the structure's width, minimizing boundary effects as recommended by Rayhani and Naggar (2009). The soil deposit, discretized into 2250 quadrilateral elements (75 m × 30 m), was meshed following Kuhlemeyer and Lysmer's (1969) criterion to ensure accurate wave transmission. A rigid bedrock boundary was assumed for the underlying layer, as suggested by Kocak and Mengi (2000), ensuring realistic seismic wave reflections.

To characterize the mechanical response of the soil under seismic loading, an elastic-perfectly plastic model with a Mohr-Coulomb failure criterion and a non-associated flow rule ($\psi = 0$) was adopted. Given the limited availability of site-specific soil data, this approach was chosen for its balance between simplicity and effectiveness in SSI studies. To account for nonlinear soil behavior, a hysteretic damping model based on Masing rules (1926) was implemented. This model was calibrated using the backbone curves proposed by Sun et al. (1988) for clayey soils, with the fitting parameters $a = 1.017, b = -0.479$, and $x_0 = -1.249$, defining the relationship between shear modulus reduction (G/G_0) and cyclic shear strain. These relationships, along with the variation of the material damping ratio as a function of cyclic shear strain, are illustrated in Figure 3, where Figure 3a depicts the evolution of G/G_max, while Figure 3b presents the corresponding damping ratio curves.

Beyond hysteretic damping, Rayleigh damping was applied to mitigate high-frequency numerical noise and capture small-strain frequency-dependent behavior. A viscous damping ratio of 0.2% was assigned at $f = 1.5\ Hz$, ensuring a realistic dynamic response of the soil model.

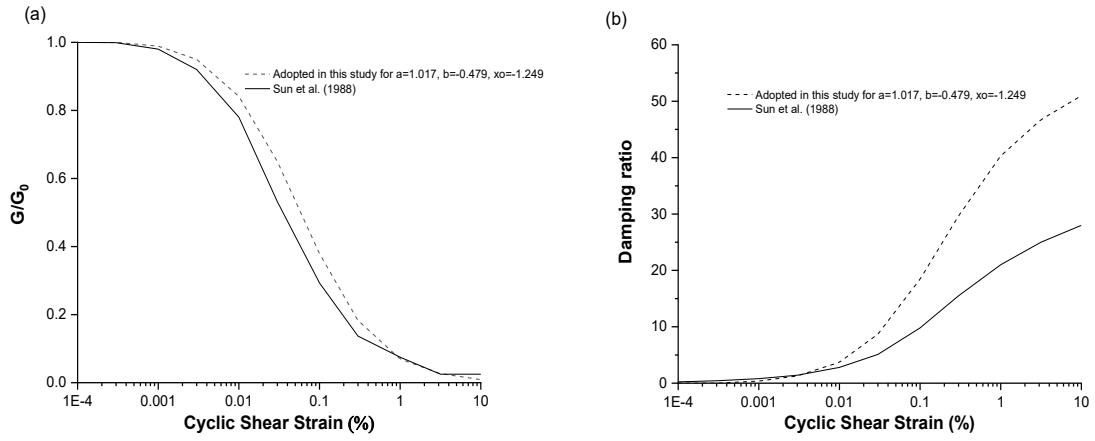

Figure 3. (a) Relationships between G/G_{max} and the cyclic shear strain and (b) Relationships between the material damping ratio and the cyclic shear strain

Ground Motion Excitations

The ground motion time histories adopted in this study are representative of the maximum probable earthquakes expected to occur at the site of interest during the lifetimes of the systems considered. Three well-known earthquakes are taken from the Canadian Association for Earthquake Engineering (CAEE) (Naumoski, 1988) as real-world input data. The names and seismic parameters of the earthquakes are presented in Table 3, and the corresponding elastic acceleration response spectra are shown in Figure 5. Once the selected ground input motions are scaled to a peak ground acceleration of the design spectrum of the Algerian seismic code (RPA 2003) as a PGA=0.25g according to the PGA scaling method (Choopool & Boonyapinyo 2011), they are low-pass filtered to remove frequencies higher than 15 Hz, aiming at limiting the element dimension adopted in the mesh, and baseline corrected using a standard polynomial detrending algorithm.

Table 3. Ground motions used in time-history analysis

Earthquake	Date	Site	Comp	Mag.(Ms)	Max. Acc. A (g)	Max. Vel. V (m/s)	A/V ratio*
San Fernando-1 California	09/02/1971	Lake Hughes 4 S21W	Station	6.4	0.146	0.085	1.72
Imperial Valley California	18/05/1940	El Centro	S00E	6.6	0.348	0.334	1.04
San Fernando-2 California	09/02/1971	3470 Wilshire Blvd L A	S90W	6.4	0.114	0.186	0.61

*A/V>1.2: high frequency content; 0.8<A/V<1.2: intermediate frequency content; A/V<0.8: low frequency content (Naumoski, 1988).

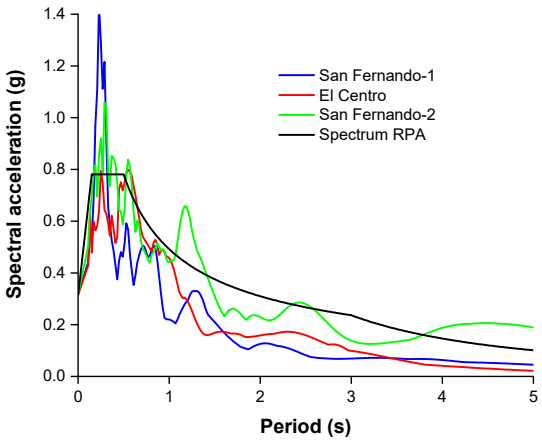

Figure 4. Acceleration response spectrum for the selected earthquakes and the RPA99/Version 2003 elastic design spectrum

Dynamic Analysis and Boundary Conditions

To carry out all the analyses, an initial static stage is performed, during which the construction of the structure is simulated and the system is brought to an initial equilibrium state under only gravity loads. During the static stages, the boundary conditions are the usual ones, i.e., nodes on the lateral sides are permitted to move only along the vertical direction, whereas entire fixities are imposed on the nodes at the base of the model.

The static stage is followed by the dynamic stage, which is achieved when the seismic input is applied to the base of the model at the level of the bedrock. As stated by Wegner and Zhang (2005), the generally considered seismic wave model is that of volume waves propagating vertically from assumed rigid horizontal bedrock. Subsequently, dynamic loading is applied at the base of the model as an acceleration excitation, assuming horizontally polarized shear waves propagating vertically. For lateral boundaries of the soil medium, the procedure of quiet (viscous) boundaries developed by Lysmer and Kuhlemeyer (1969) and available in the FLAC2D library is activated in order to represent the effect of the truncated soil by using viscous spring dashpot

dampers at the boundaries, which can fully absorb waves and prevent outward propagating waves from returning into the boundary of the model. The independent dashpots in the normal and shear directions are coupled to the free-field columns at the sides of the model to reproduce the free-field motion that would exist in the absence of the structure.

Results and Discussions

The acceleration response spectra shown in Figure 5 illustrate the effects of soil-structure interaction (SSI) on the amplification of accelerations at the top of the 3-, 6-, and 9-story reinforced concrete frames. For each structure, the comparison between the fixed-base models and those incorporating soil flexibility highlights an overall reduction in peak accelerations when SSI is considered. This attenuation is primarily due to the soil's hysteretic behavior and energy dissipation in a plastic soil medium. The reduction is more pronounced for low-rise structures, particularly the 3-story frame, where the interaction with the soil induces significant energy dissipation. However, spectral ordinates are higher for the 6-story structure, particularly at the second natural period $T_2 = 0.25\ s$. This period is close to the second natural period of the soil, calculated as follows:

$$f_n = (2n - 1)\ \frac{V_S}{4H}$$

where Vs is the shear wave velocity, H is the height of the soil deposit, and n represents the corresponding mode number. This proximity between structural and soil natural frequencies may lead to a resonance phenomenon. Furthermore, the spectral curves exhibit a shift of peak values towards longer periods in the presence of SSI, indicating an increase in the fundamental period of the structure due to soil flexibility. This effect is more pronounced for taller buildings, as they are more sensitive to softening effects induced by soil deformability. In contrast, the fixed-base models display higher spectral peaks concentrated over shorter periods, reflecting a globally stiffer behavior. The impact of SSI is therefore twofold: on the one hand, it reduces peak accelerations, which can be beneficial for the protection of internal equipment; on the other hand, it alters the dynamic response of the structure, making it more flexible, which can influence seismic design considerations.

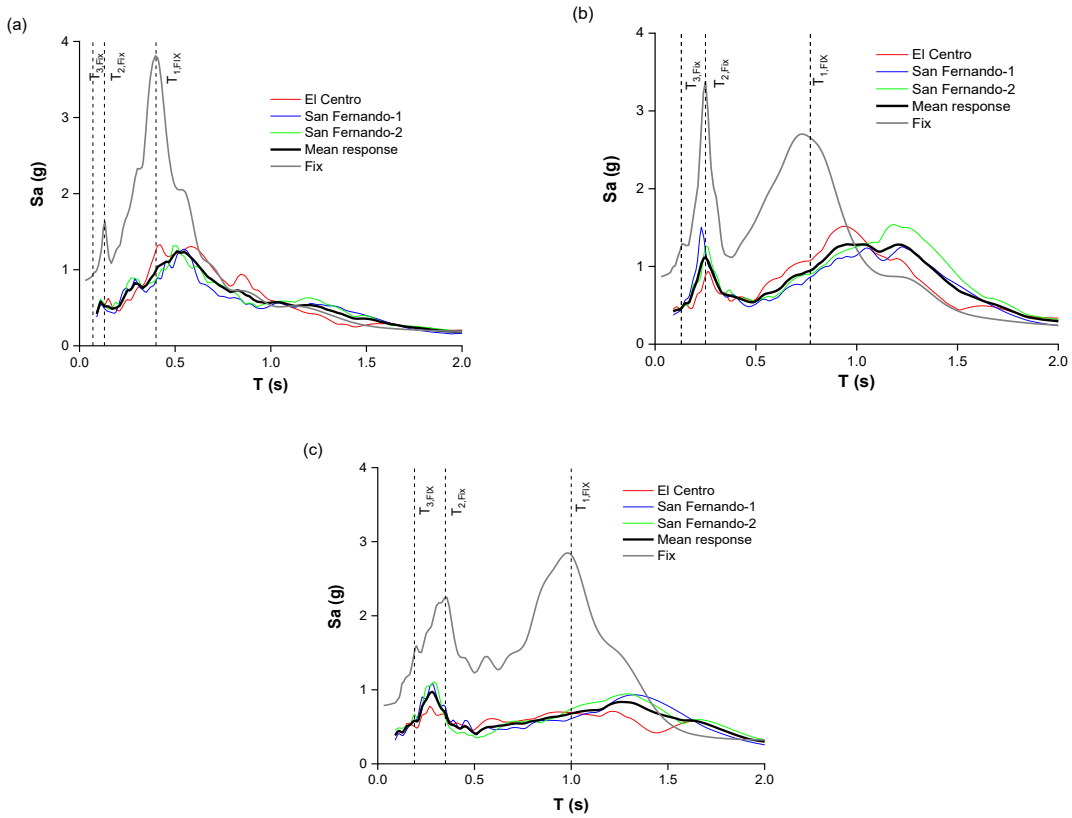

Figure 5. Acceleration response spectra at the roof of the frames: (a) 3-story frame, (b) 6-story frame, and (c) 9-story frame for fixed and flexible base models

The results in Figure 6 highlight the influence of soil-structure interaction (SSI) on the dynamic behavior of reinforced concrete frames with 3, 6, and 9 stories. The pie chart shows that the ratio of top lateral displacements between the SSI and fixed-base configurations is highest for the 3-story frame (45.34 %), followed by the 6-story frame (32.89 %) and the 9-story frame (21.97 %). This indicates that SSI amplifies displacements more significantly in low-rise structures, where soil flexibility plays a dominant role.

In parallel, the bar chart reveals that the maximum base shear force is consistently lower in the SSI case compared to the fixed-base case. This reduction is attributed to energy dissipation induced by soil deformability, which acts as a natural damper, as well as the hysteretic behavior of the soil, which contributes to additional energy dissipation through loading-unloading cycles. However, for the 6-story frame, the base shear force remains relatively higher than for the 3- and 9-story structures in the SSI case. This phenomenon can be attributed to resonance effects, resulting from the proximity between the fundamental period of the structure and that of the soil, thereby amplifying the dynamic response. These findings emphasize the importance of incorporating soil flexibility in seismic assessments to better capture dynamic effects and adapt seismic design accordingly.

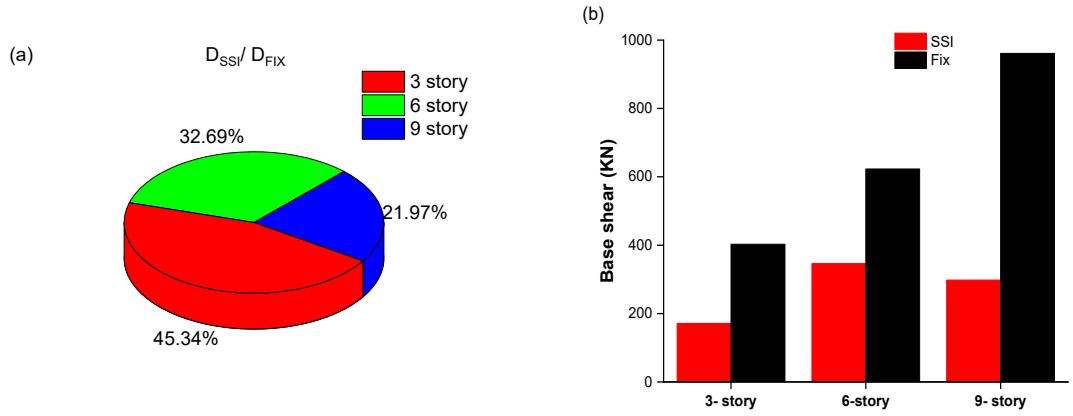

Figure 6. (a) Ratio of top lateral displacement between soil-structure interaction and fixed-base configurations, and (b) maximum base shear for 3-, 6-, and 9-story frames

Conclusion

This study examines the effects of soil-structure interaction (SSI) on the dynamic response of reinforced concrete moment-resisting frames of 3, 6, and 9 stories, designed according to the Algerian seismic code RPA99/Version 2003. The numerical analyses, conducted using FLAC2D, compare fixed-base and flexible-base conditions under three recorded seismic events, with SSI effects evaluated in terms of spectral acceleration, top lateral displacements, and base shear. The results indicate that:

- Peak spectral accelerations are reduced, with a more significant effect observed in low-rise structures. However, resonance effects in the 6-story frame, influenced by soil-structure interaction (SSI), lead to higher spectral ordinates at certain periods.
- Soil-structure interaction results in an elongation of the fundamental period, particularly for taller buildings, emphasizing the need to incorporate soil flexibility into seismic design for more accurate dynamic predictions.
- Lateral displacements are amplified due to SSI, with the 3-story frame experiencing the most pronounced increase, underlining the effect of soil deformability on structural deformations.
- SSI leads to a systematic reduction in base shear through energy dissipation from soil deformability and hysteretic effects. However, for the 6-story frame, resonance effects mitigate the reduction, amplifying the overall structural response.

SSI alters the dynamic response by increasing structural flexibility and modifying frequency content. The combined effects of soil deformability and energy dissipation mechanisms must be considered in seismic design to accurately assess structural performance.

Scientific Ethics Declaration

* The authors declare that the scientific ethical and legal responsibility of this article published in EPSTEM Journal belongs to the authors.

Conflict of Interest

* The authors declare that they have no conflicts of interest

Funding

* This research received no specific grant from any funding agency in the public, commercial, or not-for-profit sectors.

Acknowledgements or Notes

* This article was presented as a poster presentation at the International Conference on Basic Sciences, Engineering and Technology (www.icbaset.net) held in Trabzon/Türkiye on May 01-04, 2025.

References

BAEL 91. (1992). *Règles techniques de conception et de calcul des ouvrages et constructions en béton armé suivant la méthode des états limites*. Paris: France

Choopool, N., & Boonyapinyo, V. (2011). Seismic performance evaluation of reinforced concrete moment resisting frames with various ductility in low seismic zone. *American Journal of Engineering and Applied Sciences, 4*(1), 17-36.

Hokmabadi, A. S., Fatahi, B., & Samali, B. (2014). Assessment of soil–pile–structure interaction influencing seismic response of mid-rise buildings sitting on floating pile foundations. *Computers and Geotechnics, 55*, 172-186.

Itasca User's Manual FLAC2D. (2011). *Fast lagrangian analysis of continua version 7.0.* Minneapolis: Itasca Consulting group.

Kocak, S., & Mengi, Y. (2000). A simple soil–structure interaction model. *Applied Mathematical Modelling, 24*(8–9), 607–635.

Lysmer, J., & Kuhlemeyer, R. L. (1969). Finite dynamic model for infinite media. *Journal of the Engineering Mechanics Division, 95*(4), 859–877.

Masing, G. (1926). Eigenspannungen und verfestigung beim messing. *Second International Congress of Applied Mechanics* (pp. 332-335).

Mylonakis, G., & Gazetas, G. (2000). Seismic soil-structure interaction: beneficial or detrimental*?*. *Journal of Earthquake Engineering, 4*(3), 277-301.

Naumoski, N. (1988). Representative ensembles of strong earthquake records. *CAEE—The Canadian Association for Earthquake Engineering.*

Outayeb, S., Louadj, S., & Louzai, A. (2023). Soil-class effects on the seismic response of RC moment-resisting frames considering soil-structure interaction. *Asian Journal of Civil Engineering, 24*(8), 2739-2754.

Ramadan, O. M. O., Al-Anany, Y. M. M., & Sanad, A. M. (2012). Effects of soil-structure interaction on nonlinear seismic response of buildings. *15th World Conference on Earthquake Engineering*.

Rayhani, M. H., & El Naggar, M. H. (2008). Numerical modelling of seismic response of rigid foundation on soft soil. *International Journal of Geomechanics, 8*(6), 336–346.

Saci, L. (2011). *Etude de l'évolution des paramètres dynamiques des sols à partir d'essais geophysiques*. (Doctoral dissertation, Université Mouloud Mammeri).

Scarfone, R., Morigi, M., & Conti, R. (2020). Assessment of dynamic soil-structure interaction effects for tall buildings: A 3D numerical approach. *Soil Dynamics and Earthquake Engineering, 128*, 105864.

Scholl, R. E. (1989). Observations of the performance of buildings during the 1985 Mexico earthquake, and structural design implications. *International Journal of Mining and Geological Engineering, 7(*1), 69-99.

Sun, J. I., Golesorkhi, R., & Seed, H. B. (1988). *Dynamic moduli and damping ratios for cohesive soils* (Vol. 88). Berkeley: Earthquake Engineering Research Center, University of California.

Tabatabaiefar, H. R., & Fatahi, B. (2014). Idealisation of soil–structure system to determine inelastic seismic response of mid-rise building frames. *Soil Dynamics and Earthquake Engineering, 66*, 339-351.

Torabi, H., & Rayhani, M. T. (2014). Three-dimensional finite element modeling of seismic soil–structure interaction in soft soil. *Computers and Geotechnics, 60,* 9-19.

Wegner, J. L., & Zhang, X. (2005). Dynamic wave soil structure interaction analysis in the time domain. *Computers & Structures, 83*(27), 2206–2214.

Yeganeh, N., Bazaz, J. B., & Akhtarpour, A. (2015). Seismic analysis of the soil–structure interaction for a high rise building adjacent to deep excavation. *Soil Dynamics and Earthquake Engineering, 79,* 149-170.

Yue, M. G., & Wang, Y. Y. (2009). Soil-structure interaction of high-rise building resting on soft soil. *The Electronic Journal of Geotechnical Engineering, 13*, 1–8.

Author(s) Information

Sonia Outayeb
Civil engineering department, Mouloud Mammeri University of Tizi Ouzou, 15000, Algeria.
Contact e-mail : *sonia.outayeb@ummto.dz*

Samia Louadj
Civil engineering department, Mouloud Mammeri University of Tizi Ouzou, 15000, Algeria.

Amar Louzai
Civil engineering department, Mouloud Mammeri University of Tizi Ouzou, 15000, Algeria.

To cite this article:

Outayeb, S., Louadj, S., & Louzai, A. (2025). The influence of soil flexibility on structural seismic behavior. *The Eurasia Proceedings of Science, Technology, Engineering and Mathematics (EPSTEM), 34,* 244-252.

The Eurasia Proceedings of Science, Technology, Engineering & Mathematics (EPSTEM)
ISSN: 2602-3199

The Eurasia Proceedings of Science, Technology, Engineering and Mathematics (EPSTEM), 2025

Volume 34, Pages 253-260

ICBASET 2025: International Conference on Basic Sciences, Engineering and Technology

Influence of Perpendicular Magnetic Field Strength on Corrosion Resistance of 316 Stainless Steel in Nitric Acid

Djedjiga Ben-Abdesselam
Mouloud Mammeri University of Tizi-Ouzou

Nacer Zazi
Mouloud Mammeri University of Tizi-Ouzou

Youcef Hadj-Ali
Mouloud Mammeri University of Tizi-Ouzou

Belkacem Korichi
Mouloud Mammeri University of Tizi-Ouzou

Fatah Hellal
Ecole Nationale Polytechnique

Jean Paul Chopart
University of Reims Champagne-Ardenne

Abstract: Austenitic stainless steels find extensive applications across various industries. The versatility of these steels stems from their impressive combination of properties, such as high resistance to general corrosion, exceptional mechanical characteristics, and cost-effectiveness. This study aims to analyze the impact of perpendicular magnetic field strength in an aerated solution of 68% weight nitric acid on the corrosion kinetics of AISI 316 austenitic stainless steel after one hour of immersion. Studies were conducted on open circuit potential (OCP), polarization and electrochemical impedance spectroscopy (EIS) tests. All tests were performed at a temperature of 22 °C. The results show that increased magnetic field strength decreases open circuit potential (OCP) and transfer resistance (Rt), and increases double layer capacity (Cd), polarization resistance (Rp), and corrosion potential (Ecorr) of AISI 316 stainless steel in a nitric acid solution. The magnetic field intensity influences the parameters of corrosion kinetics of 316 stainless steel in an aerated solution of 68 % weight nitric acid.

Keywords: Corrosion kinetics, Corrosion resistance, Magnetic field, Nitric acid, Double layer capacity (Cd)

Introduction

Industries, including the food, medical and construction sectors, use austenitic stainless steels extensively (González et al., 2021; Hilbert et al., 2003; Rokicki et al., 2008; Lorsbach & Schmitz, 2018; Manivasagam et al., 2010; Sumita et al., 2004; Varmaziar et al., 2022). The versatility of these steels stems from their impressive combination of properties, such as high resistance to general corrosion, exceptional mechanical characteristics, and low cost. However, despite their wide-ranging utility, austenitic steels have a low resistance to localized corrosion, particularly in highly aggressive environments (Lorsbach & Schmitz, 2018; Steinemann, 1968; Varmaziar et al., 2022). While these metals inherently possess the ability of passivation upon exposure to air and humid conditions, resulting in the formation of a protective oxide layer known as the "passive layer,"

- Selection and peer-review under responsibility of the Organizing Committee of the Conference

typically a few nanometers thick, this self-protective mechanism is challenged when these materials come into direct contact with aggressive environments (Hryniewicz, et al., 2008; Jokar et al., 2016; Lorsbach & Schmitz, 2018; Steinemann, 1968).

Numerous researchers have dedicated significant attention to enhancing the corrosion resistance of stainless steels, aiming to prolong their service life (Bond et al., 1973; Colombié et al., 1973; Condylis et al., 1970; Gwinner et al., 2010; Lorsbach & Schmitz, 2018; Noh et al., 2000; Ručinskien et al., 2002; Salvago & Fumagalli, 1994; Shalash & Nasher, 2010; Steinemann, 1968). Numerous studies have explored the influence of magnetic fields on the corrosion resistance of metals in various corrosive environments (Bech-Nielsen & Jaskuła, 2008; Costa et al., 2004; Fahidy, 2002; Rokicki, et al., 2008; Hryniewicz et al., 2008; Ručinskien et al., 2002; Shalash & Nasher, 2010; Slimani et al., 2016; Taleb et al., 2019; Zazi et al., 2018). Some investigations suggest that magnetic fields contribute to a reduction in the corrosion rates of metals (Chiba et al., 1994; Hryniewiczet al., 2008; Ručinskien et al., 2002; Sagawa, 1982). Several studies have noted the effect of the magnetic field on polarization resistance and the corrosion potential and passivation. For instance, a recent study demonstrated that applying a magnetic field during electrochemical testing significantly enhanced the polarization resistance of stainless steel, indicating improved corrosion resistance. This finding suggests that the manipulation of magnetic fields could be a viable strategy for protecting metals in environments prone to corrosion. Hryniewicz et al. demonstrated that the concurrent application of a magnetic field during surface treatment enhances the corrosion resistance of austenitic 316L stainless steels, resulting in a decreased presence of corrosive products in Ringer body fluid (Rokicki, et al., 2008; Hryniewicz et al., 2008). The magnetic field shifts the corrosion potential to higher values and increases the anodic polarization resistance of aluminum. Weight loss decreased from 5% to 38% in the presence of a magnetic field (Chiba et al., 1994). The magnetic field increases passivation potential and reduces pitting and weight loss of stainless steels (Ručinskien et al., 2002). A low magnetic field modifies the polarization curve in the anodic region of ZnO deposits and modifies corrosion potential and polarization resistance (Tacken & Janssen, 1995; Taleb et al., 2019).

The maximum benefit of HNO3 treatment was associated with obtaining optimal corrosion potential by pretreatment (Kannan et al., 2005; Noh et al., 2000; Shoji & Shibata, 1997). Kannan et al. (Kannan et al., 2005) found that all treated 316 SSL samples show an increased burst potential value compared to untreated 316 SSL, and they also found that 50% acid treatment indicated a reduction in the Ecorr value as well as the degradation potential. The impedance results showed that total impedance |Z| and polarization resistance (Rp) increased for treatments in nitric acid HNO_3. The increase in nitric acid concentration during processing increases corrosion potential (Shoji & Shibata, 1997). Noh et al. (2000) showed that the effectiveness of the passivation treatment depends on the concentration of nitric acid pretreatment and that the puncture potential of 316 SS steel varies according to the concentration of nitric acid. The pitting potential increases by up to 25% by weight of nitric acid and then decreases by increasing the concentration of nitric acid. Ben Abdesselam et al. (2024) studied the effect of preliminary nitric chemical treatment on the corrosion resistance of 316 stainless steel in 0.9% NaCl-containing glucose solution; they noticed that the chemical treatment with nitric acid changed the open circuit potential of AISI 316 SS in the chlorinated solution, and the corrosion potential increased, while the polarization resistance decreased for the treated samples.

The determination of corrosion resistance in a given solution for stainless steel can be carried out through electrochemical techniques. However, it is crucial to acknowledge that test conditions can influence the results. This study specifically aims to investigate the corrosion behavior of an austenitic 316 stainless steel, containing 2.19 % molybdenum, in a solution of 68 wt. % of nitric acid. The evaluations are conducted at a temperature of 22°C under natural aeration. The study further explores the impact of the intensity of the perpendicular magnetic field on the corrosion resistance of 316 SS steel.

Experimental Methods

Materials and Procedures

The factory-annealed AISI 316 SS alloy sheet was cut into 10 mm x 10 mm x 2 mm pieces. The detailed chemical composition of this alloy is presented in (Table 1) Prior to the commencement of the study, the samples underwent preparation following the standard metallographic procedure. A designated 1 cm^2 area of each sample remained active, while the remaining portion was isolated with resin. Since the electrical contact is ensured by a copper wire.

Table 1. AISI 316 SS chemical composition.

Elements (wt. %)	AISI 316	Elements (wt. %)	AISI 316	Elements (wt. %)	AISI 316
C	0.049	Cu	0.12	Bi	0.009
Si	0.63	Nb	0.016	Ca	0.0006
Mn	0.95	Ti	0.006	Ce	0.012
P	0.007	V	0.066	Sb	<0.002
S	0.004	W	<0.007	Se	<0.001
Cr	16.65	Pb	<0.002	Te	0.005
Mo	2.19	Sn	0.017	Ta	0.057
Ni	10.43	Mg	0.012	B	0.0004
Al	0.003	As	0.013	Zn	0.002
Co	0.31	Zr	0.004	La	0.001
				Fe	68.4

To induce a magnetic field, the electrochemical cell was placed within an electromagnet of the Bouhnik 13181B type, ensuring that the magnetic field was perpendicular to the surface of the samples. The applied magnetic field strengths were B=0.05T, B=0.1T and B=1T. Electrochemical studies in solutions of 68 wt. % of nitric acid. Detailed characteristics of these samples are presented in (Table 2).

Table 2. Sample types used for different electrochemical tests.

Samples	Conditions
1	Immersed in the presence of a perpendicular magnetic field with an intensity of 0.05T
2	Immersed in the presence of a perpendicular magnetic field with an intensity of 0.1T
3	Immersed in the presence of a perpendicular magnetic field with an intensity of 1T

Corrosion Behavior

Corrosion measurements were conducted using a three-electrode cell at 22°C in solutions of 68 wt. % of nitric acid aerated medium, in the presence of a perpendicular magnetic field. The test environment remained undisturbed during these assessments. This medium was chosen for its suitability in studying corrosion. The working electrode was the AISI 316 (WE) stainless steel substrate, with an Ag/AgCl (RE) reference electrode and a thick platinum wire serving as the counter electrode (CE). Open circuit potential measurements (EOCP) utilized an Ag/AgCl reference electrode. Potentiodynamic bias test measurements covered a range from -1000 mV to 1000 mV, with an acquisition rate of 1 mV/s, and current-potential curves were obtained after 1 hour of immersion. Electrochemical impedance spectroscopy (EIS) spectra were recorded after 1 hour of immersion in the corrosive medium, spanning a frequency range from 60 kHz to 10 mHz with 10 frequency points per decade and a magnitude of the potential disturbance set at 20 mV. Open-circuit potential, current-potential curves, and electrochemical impedance spectroscopy (EIS) spectra were obtained using PGZ100 VoltaLab.

Results and Discussion

Figure 1 shows the variation of open circuit potential (OCP) over immersion time for AISI 316 SS, immersed in a 68 % by weight aerated solution of nitric acid in the presence of different perpendicular magnetic field intensities. The potential of sample 1 immersed in nitric acid with 0.05T magnetic field intensity is more noble than that of samples 2 and 3 immersed in nitric acid with 0.1T and 1T magnetic field intensity respectively. The potential of 316 stainless steel is found to increase with the decrease in magnetic field intensity. The intensity of the magnetic field has a considerable influence on the potential (Chiba et al., 1994; Ručinskien≐ et al., 2002; Taleb et al., 2019). Over time, the potential increases steadily (sample1 E= 0.915 V to E= 0.967 V, sample2 E= 0.791 V to E= 0.884 V and sample 3 E= 0.758 V to E= 0.876 V), which means a passivation of stainless steel in nitric acid. These results confirm that nitric acid improves the passivation of stainless steels (Ahmadian et al., 2014; Noh et al., 2000).

The Nyquist impedance plots for samples 1, 2, and 3, after one hour of immersion in a 68 % by weight aerated solution of nitric acid in the presence of different perpendicular magnetic field intensities, are represented in (Figures 2). The solution resistance (Rs), transfer resistance (Rt), and double layer capacity (Cd) of AISI 316 SS are shown in Table 3. The transfer resistance (Rt) is 25324 Ω/cm2 for sample 1 (B = 0.05T), the transfer resistance (Rt) for sample 2 (B =0.1T) is 24213.1 Ω/cm2, and for sample 3 the transfer resistance (Rt) is about 6862.7 Ω/cm2, we found that the transfer resistance decreases with the increase of the magnetic field intensity.

The capacity of the double layer (Cd) is about 62.84 µF/cm2 for sample 1, about 65.76 µF/cm2 for sample 2 and 73.59 µF/cm2 for sample 3, we found that the double layer capacity increases with the increase of the magnetic field intensity the (Rt and Cd) are influenced by the magnetic field intensity. It is evident that the corrosion behavior of 316 stainless steel is significantly affected by the magnetic field intensity.

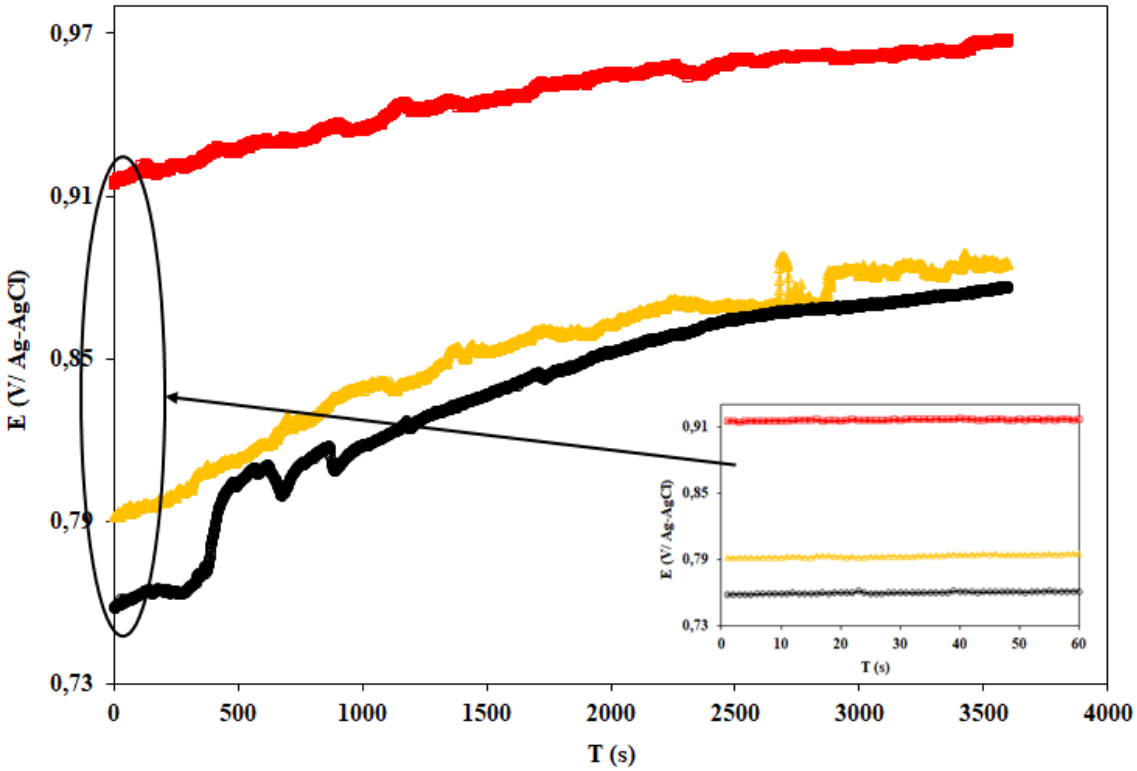

Figure 1. Variation of the open circuit potential (OCP) over the immersion time for samples 1, 2 and 3 in 68 wt.% nitric acid aerated solutions, during one hour, immersed in the presence of perpendicular magnetic field, □ B=0.05 T, △ B=0.1 T and ○ B=1 T.

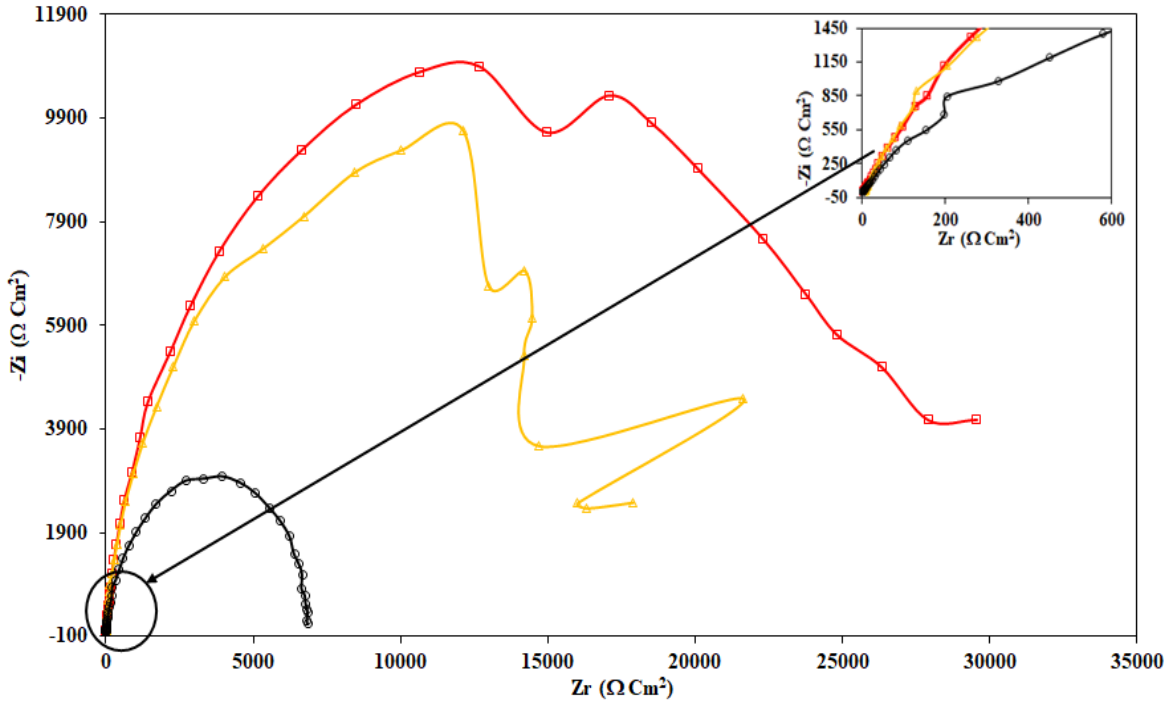

Figure 2. Nyquist plots for 316 stainless steel over the immersion time in 68 wt.% nitric acid aerated solutions, in the presence of perpendicular magnetic field, during one hour, □ B =0.05 T, △ B =0.1 T and ○ B =1 T.

Table 3. Solution resistance, transfer resistance and double layer capacity of the samples 1, 2 and 3.

Samples	Rs (Ω)	Rt (Ω/cm^2)	Cd (µF/cm^2)
1	2	25324	62.84
2	5.5	24213.1	65.76
3	1.30	6862.7	73.59

Based on the current-voltage curves (i(E)), we calculated the polarization resistance (Rp) and corrosion potential (Ecorr). These values are precisely listed in table 4. From the curves i(E) and log i(E) and table 4, we found that sample 3 in immersion in the presence of the magnetic field with a higher intensity presents a more noble corrosion potential (Ecorr = 0.701 V) and a greater polarization resistance (Rp = 234 Ω/cm2) compared to the other two samples 1 and 2. The magnetic field intensity influences the polarization resistance and corrosion potential of 316 SS (Chiba et al., 1994; Ručinskien≐ et al., 2002; Taleb et al., 2019). Figure 3 a and b) shows the results of the polarization tests performed on samples 1, 2 and 3, a) representing curve i(E) and a$_1$) magnifying effect, and b) showing log curve i(E).

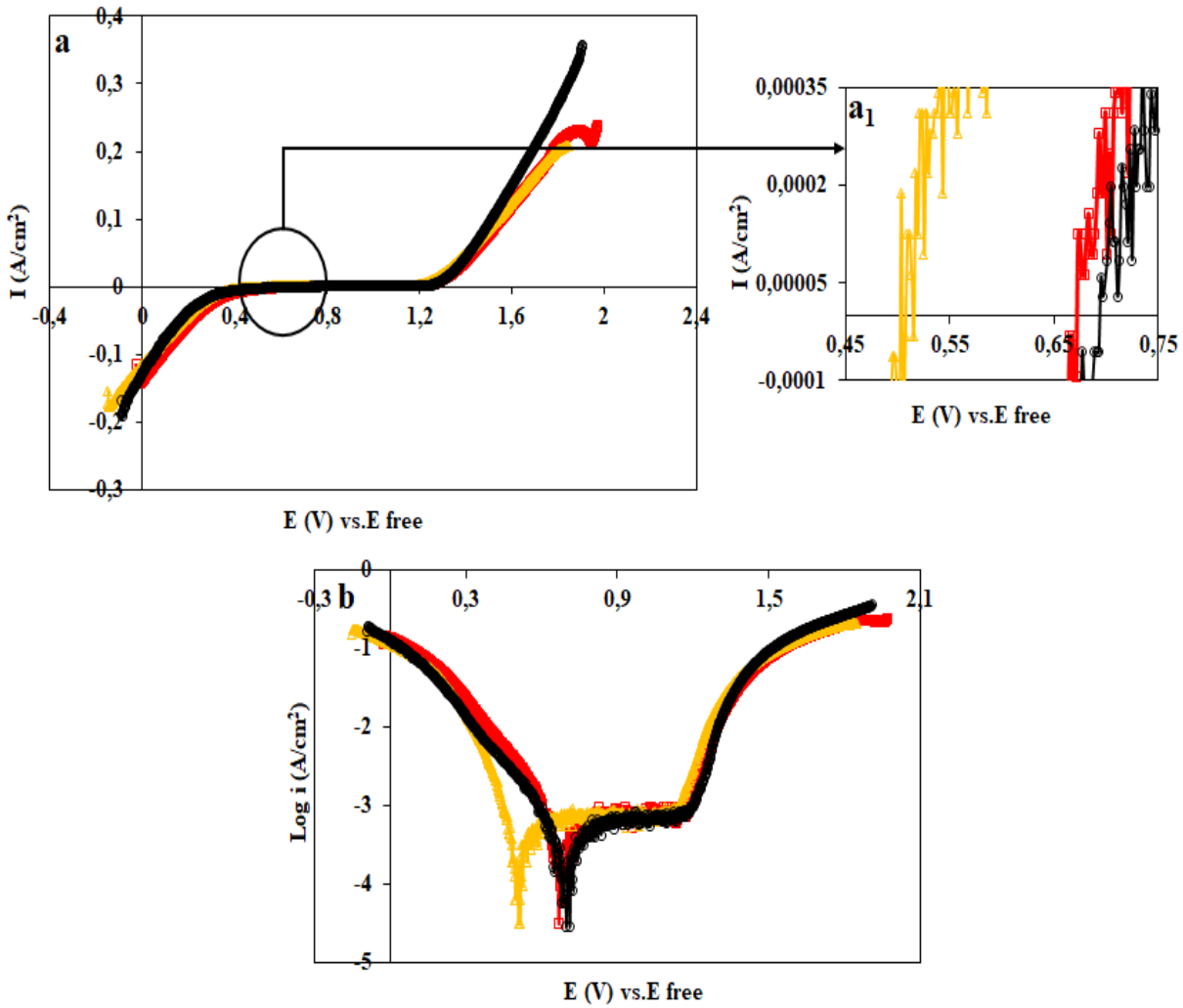

Figure 3. Illustrates the polarization curves of samples 1, 2, and 3 in a 68 wt. % nitric acid solution one hour after immersion. a) presents the i(E) curve and a1) the magnification effect, while b) showcases the log i(E) curve.

Table 4. Polarization resistance and corrosion potential of the sample 1, 2 and 3.

Samples	**E_{corr} (v)**	**R_p (Ω/cm^2)**
1	0,673	127
2	0,511	179
3	0,701	234

Conclusion

The study examines the impact of perpendicular magnetic field strength in an aerated solution of 68% weights nitric acid on the corrosion of AISI 316 SS. The analyses were carried out on open circuit potential (OCP), as well as on polarization and impedance tests. The main conclusions are as follows:

- The potential of 316 stainless steel is increase with the decrease in the magnetic field intensity;
- Stainless steel 316 is passivated in nitric acid;
- The transfer resistance (Rt) decreases with the increase of the magnetic field intensity;
- The double layer capacity increases with the increase of the magnetic field intensity;
- The (Rt and Cd) are influenced by the magnetic field intensity;
- The magnetic field intensity influences the polarization resistance and corrosion potential of 316 SS;
- the corrosion potential of 316 SS is more noble in the presence of the magnetic field with a high intensity;
- AISI 316 SS presents a better polarization resistance in the presence of magnetic field with greater intensity.

Scientific Ethics Declaration

* The authors declare that the scientific ethical and legal responsibility of this article published in EPSTEM Journal belongs to the authors.

Conflict of Interest

* The authors declare that they have no conflicts of interest

Funding

* This research received no specific grant from any funding agency in the public, commercial, or not-for-profit sectors.

Acknowledgements or Notes

* This article was presented as a poster presentation at the International Conference on Basic Sciences, Engineering and Technology (www.icbaset.net) held in Trabzon/Türkiye on May 01-04, 2025.

References

Ahmadian, Z., Danaee, I., & Golozar, M. A. (2014). Effect of surface treatment on corrosion resistance of 304 stainless steel implants in tyrode solution. *Archives of Metallurgy and Materials, 59*(1), 25-30.

Bech-Nielsen, G., & Jaskuła, M. (2008). The influence of a magnetic field on the non-electrochemical dissolution of iron. *Journal of Electroanalytical Chemistry, 624*(1-2), 327-328.

Ben - Abdesselam, D., Zazi, N., Hadj - Ali, Y., Hellal, F., Chopart, J. P., Abrudeanu, M., & Negrea, D. (2024). Effect of preliminary nitric chemical treatment on corrosion behavior of 316 stainless steel in chloride solution contain glucose. *The Eurasia Proceedings of Science Technology Engineering and Mathematics, 32,* 66-79.

Bond, A. P., Dundas, H. J., Schmidt, W., & Wol, M. (1973). Etude de la résistance à la corrosion d'aciersinoxydables en vue de leur utilisationen distribution d'eau chaude. *Revue de Métallurgie, 70*(1), 33-42.

Chiba, A., Kawazu, K., Nakano, O., Tamura, T., Yoshihara, S., & Sato, E. (1994). The effects of magnetic fields on the corrosion of aluminum foil in sodium chloride solutions. *Corrosion Science, 36*(3), 539-543.

Colombié, M., Condylis, A., Desestret, A., Grand, R., & Mayoud, R. (1973). Les aciers ferritiques inoxydables ductiles à haute teneur en chrome. Nouveaux matériaux résistant à la corrosion par piqûre, par crevasse et à la corrosion sous tension. *Revue de Métallurgie, 70*(12), 949-962.

Condylis, A., Bayon, F., & Desestret, A. (1970). Aciers inoxydables austénitiques au chrome-nickel-manganèse-azote. *Revue de Métallurgie, 67*(5), 427-442.

Costa, I., Oliveira, M. C. L., de Melo, H. G., & Faria, R. N. (2004). The effect of the magnetic field on the corrosion behavior of Nd–Fe–B permanent magnets. *Journal of Magnetism and Magnetic Materials, 278*(3), 348-358.

Fahidy, T. Z. (2002). The effect of magnetic fields on electrochemical processes. In B. E. Conway, J. O. Bockris, & R. E. White (Eds.), *Modern aspects of electrochemistry* (Vol. 32, p. 333-354). Kluwer Academic Publishers.

González, A. S., Riego, A., Vega, V., García, J., Galié, S., Gutiérrez del Río, I., Martínez de Yuso, M. del V., Villar, C. J., Lombó, F., & De la Prida, V. M. (2021). Functional antimicrobial surface coatings deposited onto nanostructured 316L food-grade stainless steel. *Nanomaterials, 11*(4), 4.

Gwinner, B., Auroy, M., Bague, V., Chaachoua, S., Fieulaine, B., Tran, Q. T., & Tricoit, S. (2010). Corrosion intergranulaire dans l'acide nitrique des aciers inoxydables austénitiques non sensibilisés. *Revue de Métallurgie, 107*(10-11), 441-443.

Hilbert, L. R., Bagge-Ravn, D., Kold, J., & Gram, L. (2003). Influence of surface roughness of stainless steel on microbial adhesion and corrosion resistance. *International Biodeterioration & Biodegradation, 52*(3), 175-185.

Hryniewicz, T., Rokicki, R., & Rokosz, K. (2008). Corrosion Characteristics of Medical-Grade AISI Type 316L Stainless Steel Surface After Electropolishing in a Magnetic Field. *Corrosion, 64*(8), 660-665.

Hryniewicz, T., Rokosz, K., & Rokicki, R. (2008). Electrochemical and XPS studies of AISI 316L stainless steel after electropolishing in a magnetic field. *Corrosion Science, 50*(9), 2676-2681.

Jokar, M., Darvishi, S., Torkaman, R., Kharaziha, M., & Karbasi, M. (2016). Corrosion and bioactivity evaluation of nanocomposite PCL-forsterite coating applied on 316L stainless steel. *Surface and Coatings Technology, 307*, 324-331.

Kannan, S., Balamurugan, A., & Rajeswari, S. (2005). Electrochemical characterization of hydroxyapatite coatings on HNO3 passivated 316L SS for implant applications. *Electrochimica Acta, 50*(10), 2065-2072.

Lorsbach, B., & Schmitz, E. (2018). Influence of test parameters of potentiodynamic current density measurements on the determination of the pitting corrosion resistance of austenitic stainless steels. *Materials and Corrosion, 69*(1), 37-43.

Manivasagam, G., Dhinasekaran, D., & Rajamanickam, A. (2010). Biomedical implants: Corrosion and its prevention - a review. *Recent Patents on Corrosion Science, 2*(1), 40-54.

Noh, J. S., Laycock, N. J., Gao, W., & Wells, D. B. (2000). Effects of nitric acid passivation on the pitting resistance of 316 stainless steel. *Corrosion Science, 42*(12), 2069-2084.

Ručinskien≒, A., Bikulčius, G., Gudavičiūt, L., & Juzeliūnas, E. (2002). Magnetic field effect on stainless steel corrosion in FeCl3 solution. *Electrochemistry Communications, 4*(1), 86-91.

Sagawa, M. (1982). Effect of a local magnetic field on the dissolution of copper and iron in nitric acid solution. *Transactions of the Japan Institute of Metals, 23*(1), 38-40.

Salvago, G., & Fumagalli, G. (1994). The distribution of stainless-steel breakdown potentials: The effect of surface finishing degree and HNO3 treatment. *Corrosion Science, 36*(4), 733-742.

Shalash, L. B. T., & Nasher, L. S. H. (2010). Study the effect of magnetic field on the corrosion of steel in sodium chloride solution (NaCl). *Misan Journal of Academic Studies, 9,* 30-38.

Shoji, T., & Shibata, T. (1997). *Proceedings of the International Symposium on Plant Aging and Life Prediction of Corrodible Structures* : May 15-18, 1995, Sapporo, Japan. NACE.

Slimani, R., Zazi, N., & Chopart, J.-P. (2016). Investigation of nickel deposition onto section and central longitudinal surfaces of AA1370 aluminum electrical wire with and without a weak permanent magnetic field. *Protection of Metals and Physical Chemistry of Surfaces, 52*(1), 111-118.

Steinemann, S. (1968). Résistance à la corrosion par piqûres de l'acier inoxydable au chrome-nickel-molybdène élaboré normalement à haute fréquence et refondu sous laitier électroconducteur (ESR). *Revue de Métallurgie, 65*(10), 651-658.

Sumita, M., Hanawa, T., & Teoh, S. H. (2004). Development of nitrogen-containing nickel-free austenitic stainless steels for metallic biomaterials—review. *Materials Science and Engineering: C, 24*(6-8), 753-760.

Tacken, R. A., & Janssen, L. J. J. (1995). Applications of magnetoelectrolysis. *Journal of Applied Electrochemistry, 25*(1).

Taleb, S., Dokhan, N., Zazi, N., & Chopart, J.-P. (2019). Perpendicular weak permanent magnetic field effect on the electrodeposited nanostructured ZnO film and its kinetic corrosion behavior. *Protection of Metals and Physical Chemistry of Surfaces, 55*(4), 781-788.

Varmaziar, S., Atapour, M., & Hedberg, Y. S. (2022). Corrosion and metal release characterization of stainless steel 316L weld zones in whey protein solution. *Npj Materials Degradation, 6*(1), 1.

Zazi, N., Aouchiche, H., Benbaha, C., & Chopart, J. P. (2018). Sulfuric containing sugar bath and permanent weak magnetic field effect during anodizing AlCu6Si alloy sheet surfaces. *Russian Journal of Non-Ferrous Metals, 59*(2), 123-134.

Author(s) Information

Djedjiga Ben-Abdesselam
Mouloud Mammeri University of Tizi-Ouzou Faculty of Construction Engineering Department of Mechanical Engineering Laboratory of Structural Mechanics and Energy (LMSE) B.P.17 RP Tizi-Ouzou, Algeria.
Contact e-mail: *djedjiga.benabdesselam@ummto.dz*

Nacer Zazi
Mouloud Mammeri University of Tizi-Ouzou Faculty of Construction Engineering Department of Mechanical Engineering Laboratory of Structural Mechanics and Energy (LMSE) B.P.17 RP Tizi-Ouzou, Algeria.

Fatah Hellal
Ecole Nationale Polytechnique, Department of Metallurgy, LSGM, BP 182, 16051, El Harrach, Algiers, Alegria.

Youcef Hadj-Ali
Mouloud Mammeri University of Tizi-Ouzou Faculty of Construction Engineering Department of Mechanical Engineering Laboratory of Structural Mechanics and Energy (LMSE) B.P.17 RP Tizi-Ouzou, Algeria.

Jean Paul Chopart
MATIM Laboratory, University of Reims Champagne-Ardenne, 51687 Reims, France.

Belkacem Korichi
Mouloud Mammeri University of Tizi-Ouzou Faculty of Construction Engineering Department of Mechanical Engineering Laboratory of Structural Mechanics and Energy (LMSE) B.P.17 RP Tizi-Ouzou, Algeria.

To cite this article:

Ben-Abdesselam, D., Zazi, N., Hadj-Ali, Y., Korichi, B., Hellal, F., & Chopart, J. P. (2025). Influence of perpendicular magnetic field strength on corrosion resistance of 316 stainless steel in nitric asid. *The Eurasia Proceedings of Science, Technology, Engineering and Mathematics (EPSTEM), 34,* 253-260.

The Eurasia Proceedings of Science, Technology, Engineering & Mathematics (EPSTEM)
ISSN: 2602-3199

The Eurasia Proceedings of Science, Technology, Engineering and Mathematics (EPSTEM), 2025

Volume 34, Pages 261-267

ICBASET 2025: International Conference on Basic Sciences, Engineering and Technology

Modeling the Mechanical Behavior of a Cement Mortar Based on Plant Fibers

Toufik Djadoun
University Mouloud Mammeri of Tizi Ouzou

Fatma Taouche-Kheloui
University Mouloud Mammeri of Tizi Ouzou

Ourdia Fedaoui-Akmoussi
University Mouloud Mammeri of Tizi Ouzou

Abdelmadjid Si-Salem
University Mouloud Mammeri of Tizi Ouzou

Souad Ait-Taleb
University Mouloud Mammeri of Tizi Ouzou

Fatma Bouzeboudja
University Mouloud Mammeri of Tizi Ouzou

Abstract: Today, technological progress demands the use of innovative materials that offer superior thermal and acoustic properties alongside high mechanical performance, all while maintaining economic competitiveness. This need has driven researchers to create a new generation of advanced materials. In Algeria, building facades are primarily made of bricks, which add to the structural weight, prolongs construction time, and offers insufficient thermal and acoustic insulation. The objective of this experimental modeling is to design a new material incorporating plant fibers. This experimental study aims to examine the effect of sisal fiber slenderness by using two different fiber lengths (7cm and 3cm). Various fiber percentages were tested: 0%, 0.25%, 0.5%, 0.75%, 1%, 1.25%, and 1.5%. After 28 days of curing, mechanical performance was evaluated through compression tests on 4×4×4 cm³ specimens and three-point bending tests on 4×4×16 cm³ specimens. The best variant will be used for manufacturing multi-layer panels. The results showed that fiber-reinforced mortars exhibited higher strength compared to the control mortar.

Keywords: Sisal fiber, Mortar, Valorization, Mechanical tests

Introduction

For centuries, humans have sought to improve the strength of fragile construction materials by incorporating various types of fibers. Well-known historical examples include clay bricks reinforced with straw (Achour, 2017), lime mortars mixed with animal hair, and plasters combined with tow (flax fibers). Over time, a wide range of fibers has been experimented with, including glass, steel, plastic, and carbon fibers, as well as plant-based fibers (Ponce-Antón et al., 2024; Ascione et al., 2024)

Nowadays, research has shifted toward more environmentally friendly solutions in response to current sustainable development challenges (Duffy, 2009). As a result, plant-based fibers, mainly derived from agricultural and forestry sectors, have emerged as a potential alternative to conventional fibers such as glass and

carbon. Lightweight, renewable, low-cost, and offering acceptable mechanical strength, these fibers present numerous advantages. Due to the low fiber consumption in many developing countries, it is possible to achieve reduced energy and technological impact (Dufresne, 2003; Elfaleh et al., 2023; Dallel, 2012).

From a technical perspective, plant-based fibers possess a porous structure that grants them excellent thermal and acoustic insulation properties (Dallel, 2013; Shinoj et al., 2010). Their flexibility also facilitates implementation, particularly when the incorporation rate within the matrix is high. In contrast to metallic fibers, such as steel, they are easier to handle and integrate into materials. These characteristics make natural fibers key components in a new generation of sustainable, lightweight, and cost-effective materials (Yousif & Shallwan, 2013; Habibi et al., 2020). Sisal fiber, extracted from the leaves of *Agave sisalana*, is one of the most widely used natural fibers in the world (Bessell, 1982). It originates from the tropical and subtropical regions of North and South America (Ramamoorthy et al., 2015). Each sisal plant has approximately 200 to 250 leaves, each containing 1,000 to 1,200 bundles, with an average length of 3 mm per elementary fiber (Sanjay et al., 2016; Ramesh et al.,2017). Easy to cultivate, it is produced on a large scale, and its use continues to grow due to its versatility. Rich in cellulose, it exhibits good mechanical strength, particularly in tension (Baley et al., 2005; Bongarde et al., 2014), while having a low moisture absorption capacity, which makes it especially suitable for construction materials (Savastano Jr et al., 2000; Dufresne et al., 2003).

The study presented is part of an ecological approach. Its objective is to develop a construction material that combines lightness with sufficient mechanical strength, primarily for wall insulation applications. The aim is twofold: to improve the thermal and acoustic performance of structures while maintaining acceptable structural integrity. To this end, the influence of sisal fiber fineness was examined by testing two lengths: 3 cm and 7 cm. Several incorporation rates were evaluated: 0%, 0.25%, 0.5%, 0.75%, 1%, 1.25%, and 1.5%. After a 28-day curing period, the mechanical strength of the samples was assessed through three-point bending tests on specimens measuring 4×4×16 cm^3. The results showed a significant improvement in the mechanical performance of fiber-reinforced mortars compared to the reference mortar. Among the various configurations tested, the mortar containing 1% sisal fibers exhibited the best results, demonstrating the effectiveness of this natural reinforcement in optimizing construction materials

Experimental Analysis

Materials Used

Only one variety of cement mortar was utilized in producing the various specimens.

Cement

The cement used is a Portland cement of class CEM I 42.5R. Its chemical composition and physical properties are presented in Tables 1 and 2.

Table 1. Chemical composition of cement

SiO2	22
Al2 O3	5.5
Fe2O3	3
CaO	64.5
MgO	1.7
SO3	1.9
Na2O et K2O	0.2-1.3
Cl-	0.02
PAF	< 1.5

Table 2. Physical properties of cement

Physical characteristic	Value
Apparent density (kg/m^3)	1130
Absolute density (kg/m^3)	3100
Specific surface (cm^2/g)	3917
Normal consistency(%)	27.48

The Sand

Granular class 0/3 sand sourced from a sand pit in the Tizi-Ouzou region was used, and tap water was employed as the mixing water. To identify the sand, characterization tests were conducted, with all results presented in Table 3.

Table 3. Characteristics of sand

Gravel	Apparent density(g/cm^3) NF P 18-554	Absolute density (g/cm^3) NF P 18-555	Fineness module MF NF P 18-101	Sand equivalent (%) NFP18-598
Sand 0/3	1,485	2,63	2,87	79.25

Sisal Fiber

Natural sisal fibers were used to reinforce the mortar matrix, with their characteristics and the amounts incorporated presented in Tables 4 and 5.

Table 4. Property of sisal fiber

Width or diameter	50-300
Density (kgm^{-3})	1450
Cellulose / lignin content (%)	67/12
Module E (GNm^{-2})	9.4-22
Tensile strength (MNm^{-2})	530-640
Élongation (%)	3-7

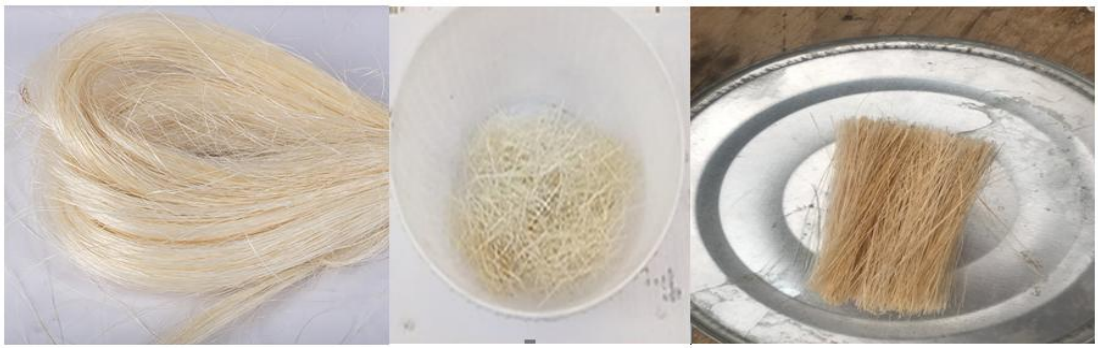

Figure 1. a) Sisal fiber, b) length sisal fiber 3cm, c) length sisal fiber 7cm.

Mix Proportions

Our specimens were prepared using a single composition. After 24 hours, the samples were removed from the molds and kept submerged in a water basin. The proportions of the various constituents are shown in Table 5 and the table.

Table 5. Mortar composition ($1m^3$).

Components	Quantities (Kg)
Cement	450
Sand	1350
Water (L)	225
W/C	0.5

Table 6. Sisal fiber quantities (length 3 and 7cm)

Percentage (%)	0.25	0.5	0.75	1	1.25	1.5
Sisal fibers (g)	0.96	1.92	2.88	3.84	4.8	5.76

Figure 2. Experimental procedure.

Behavior in Three-Point Bending

Bending tests are carried out on specimens of dimensions (4×4×16) cm^3 according to standard NF T 54-606.

Figure 3. Bending test

This table provides the mechanical flexural strength results of the fiber-reinforced mortars and the control mortar, assessed under two different fiber size configurations.

Table 7. Flexural strength of the mortars studied

	Flexural strength (MPa)						
% / Mortar	MT	0.25	0.5	0.75	1	1.25	1.5
MFS3	7.2	7.26	7.05	7.30	7.25	6.95	7.45
MFS7	7.2	7.53	7.37	7.34	8.11	7.99	7.92

MFS3: Sisal fiber mortar with a fiber length of 3 cm.
MFS7: Sisal fiber mortar with a fiber length of 7 cm.

Figure 4 shows the evolution of the flexural strengths of unreinforced and sisal fiber reinforced mortars using two fiber lengths (MFS3) and (MFS7).

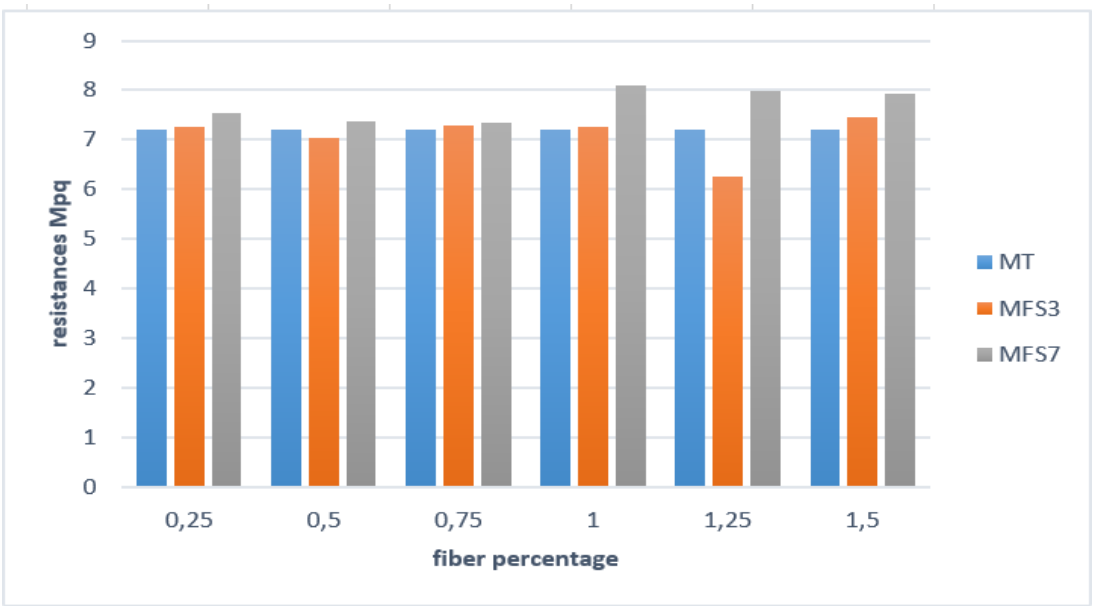

Figure 4. Three-point bending strength of the mortars studied.

According to the figure above, the incorporation of 7 cm sisal fibers significantly enhances the flexural strength of the mortar compared to the control. The optimal performance is observed at a 1% fiber dosage. A moderate increase in strength is also noted for mortars reinforced with 3 cm fibers.

Influence of Fiber Length

In this section, the influence of the length of Sisal fibers in the different mortars is presented and analyzed in Figure 5.

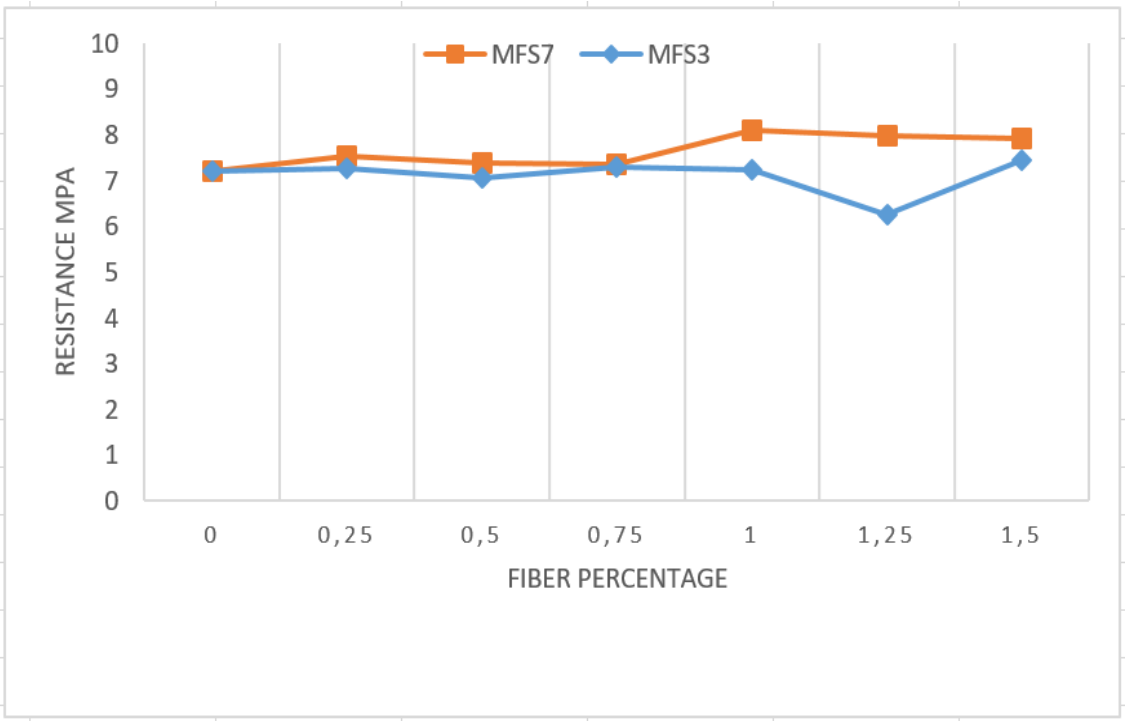

Figure 5. Influence of fiber length

The MFS7 mortar exhibited superior post-peak behavior compared to other formulations, particularly MFS3, highlighting the significant influence of fiber length on flexural strength. Indeed, MFS7 achieved a maximum strength of 8.11 MPa, compared to 7.25 MPa for MFS3, representing an 11% increase. For comparison, the

control mortar recorded a strength of 7.2 MPa. The incorporation of 7 cm fibers enhances the cohesion of the mortar by limiting the initiation, propagation, and widening of cracks through a bridging effect, thereby optimizing its strength and durability.

Conclusion

Based on the results obtained in this experimental investigation, we were able to draw the following conclusions:

- The length parameter of the Sisal fibers influences the resistance of these mortars.
- The maximum tensile strength by bending is higher for mortars with 7 cm long fibers than for the reference mortar (without fibers).
- The mortars with fibers 7 cm in length presented better performances, in tractions by bending, compared to the mortar of fibers of 3 cm. There is a difference of 11%.
- The best resistances for the 7 cm fiber are recorded for a dosage of 1%, on the other hand for the 3 cm fiber the best performance is recorded for a dosage of 1.5%.

Scientific Ethics Declaration

* The authors declare that the scientific ethical and legal responsibility of this article published in EPSTEM Journal belongs to the authors.

Conflict of Interest

* The authors declare that they have no conflicts of interest

Funding

* This research received no specific grant from any funding agency in the public, commercial, or not-for-profit sectors.

Acknowledgements or Notes

* This article was presented as a poster presentation at the International Conference on Basic Sciences, Engineering and Technology (www.icbaset.net) held in Trabzon/Türkiye on May 01-04, 2025.

References

Achour, A. (2017). *Étude des performances des mortiers renforcés de fibres naturelles: valorisation des plantes locales*. (Doctoral dissertation, Université Aboubakr Belkaïd– Tlemcen).

Ascione, F., Maselli, G., & Nesticò, A. (2024). Sustainable materials selection in industrial construction: A life-cycle based approach to compare the economic and structural performances of glass fibre reinforced polymer (GFRP) and steel. *Journal of Cleaner Production*, *475*, 143641.

Baley, C. (2005). Fibres naturelles de renfort pour matériaux composites. *Techniques de l'Ingénieur, 5*(130), 1-12.

Bessell, T. J., & Mutuli, S. M. (1982). The interfacial bond strength of sisal—cement composites using a tensile test. *Journal of Materials Science Letters*, *1*(6), 244-246.

Bongarde, U. S., & Shinde, V. D. (2014). Review on natural fiber reinforcement polymer composites. *International Journal of Engineering Science and Innovative Technology*, *3*(2), 431-436.

Dallel, M. (2012). *Evaluation du potentiel textile des fibres d'Alfa (Stipa Tenacissima L.): Caractérisation physico-chimique de la fibre au fil.* (Doctoral dissertation, Université de Haute Alsace).

Duffy, S., & Verges, M. (2009). It matters a hole lot: Perceptual affordances of waste containers influence recycling compliance. *Environment and Behavior*, *41*(5), 741-749.

Elfaleh, I., Abbassi, F., Habibi, M., Ahmad, F., Guedri, M., Nasri, M., & Garnier, C. (2023). A comprehensive review of natural fibers and their composites : An eco-friendly alternative to conventional materials. *Results in Engineering*, *19*, 101271.

Faruk, O., Bledzki, A. K., Fink, H. P., & Sain, M. (2012). Biocomposites reinforced with natural fibers: 2000–2010. *Progress in Polymer Science*, *37*(11), 1552-1596.

Habibi, M., Selmi, S., Laperrière, L., Mahi, H., & Kelouwani, S. (2020). Post-impact compression behavior of natural flax fiber composites. *Journal of Natural Fibers*, *17* (11), 1683-1691.

Ponce-Antón, G., Cultrone, G., Zuluaga, M. C., Ortega, L. Á., & Gómez-Val, R. (2024). Investigation on 19th century fired bricks and lime plaster for the conservation of historical building materials: A case study of the Church of Sant Rafael (Barcelona, Spain). *Case Studies in Construction Materials*, *21*, e03870.

Ramamoorthy, S. K., Skrifvars, M., & Persson, A. (2015). A review of natural fibers used in biocomposites: Plant, animal and regenerated cellulose fibers. *Polymer Reviews*, *55*(1), 107-162.

Ramesh, M., Palanikumar, K., & Reddy, K. H. (2017). Plant fibre based bio-composites : Sustainable and renewable green materials. *Renewable and Sustainable Energy Reviews*, *79*, 558-584.

Sanjay, M. R., Arpitha, G. R., Naik, L. L., Gopalakrishna, K., & Yogesha, B. J. N. R. (2016). Applications of natural fibers and its composites : An overview. *Natural Resources*, *7*(3), 108-114.

Savastano Jr, H., Warden, P. G., & Coutts, R. S. P. (2000). Brazilian waste fibres as reinforcement for cement-based composites. *Cement and Concrete Composites*, *22*(5), 379-384.

Shalwan, A., & Yousif, B. F. (2013). In state of art : Mechanical and tribological behaviour of polymeric composites based on natural fibres. *Materials & Design*, *48*, 14-24.

Shinoj, S., Visvanathan, R., & Panigrahi, S. (2010). Towards industrial utilization of oil palm fibre: Physical and dielectric characterization of linear low density polyethylene composites and comparison with other fibre sources. *Biosystems Engineering*, *106*(4), 378-388.

Author(s) Information

Toufik Djadoun
University Mouloud Mammeri of Tizi Ouzou
Route de Hasnaoua BP 47, Algeria
Contact e-mail : *toufik.djadoun@ummto.dz*

Fatma Taouche-Kheloui
University Mouloud Mammeri of Tizi Ouzou
Route de Hasnaoua BP 47, Algeria

Ourdia Fedaoui-Akmoussi
University Mouloud Mammeri of Tizi Ouzou
Route de Hasnaoua BP 47, Algeria

Abdelmadjid Si-Salem
University Mouloud Mammeri of Tizi Ouzou
Route de Hasnaoua BP 47, Algeria

Souad Ait-Tayeb
University Mouloud Mammeri of Tizi Ouzou
Route de Hasnaoua BP 47, Algeria

Fatma Bouzeboudja
University Mouloud Mammeri of Tizi Ouzou
Route de Hasnaoua BP 47, Algeria

To cite this article:

Djadoun, T., Taouche-Kheloui, F., Fedaoui-Akmoussi, O., Si-Salem, A., Ait Taleb, S., & Bouzeboudja, F. (2025). Modeling the mechanical behavior of a cement mortar based on plant fibers. *The Eurasia Proceedings of Science, Technology, Engineering and Mathematics (EPSTEM),34,* 261-267.

The Eurasia Proceedings of Science, Technology, Engineering & Mathematics (EPSTEM)
ISSN: 2602-3199

The Eurasia Proceedings of Science, Technology, Engineering and Mathematics (EPSTEM), 2025

Volume 34, Pages 268-277

ICBASET 2025: International Conference on Basic Sciences, Engineering and Technology

A GIS and Drone-Based Risk Assessment Framework for Hydroelectric and Solar Energy Infrastructure in Disaster-Prone Areas with High Forestry and Agricultural Activity

Oyku Alkan
Alkan Harita Co.

M.Nurullah Alkan
Hitit University

Abstract: The increasing global demand for renewable energy has accelerated the expansion of hydroelectric (HEPPs) and solar power plants (SEPs), frequently located in ecologically fragile and geologically hazardous areas. This study proposes an integrated geospatial risk assessment framework combining Geographic Information Systems (GIS) and Unmanned Aerial Vehicles (UAVs) to evaluate and mitigate multi-hazard risks affecting renewable energy infrastructure. Focusing on Turkey's North-Middle Black Sea Region intersected by the seismically active North Anatolian Fault (NAF) and encompassing the geologically complex Obruk Dam basin this research addresses an area with dense renewable energy installations and high susceptibility to tectonic and climate-induced hazards. High-resolution UAV imagery, coupled with 3D terrain modeling, was utilized to assess infrastructure vulnerabilities. GIS-based spatial overlay techniques integrated multiple data layers, including active fault lines, slope instability, flood-prone zones, and land use classifications. Time-series change detection analyses were conducted to monitor landscape dynamics related to erosion, vegetation loss, and anthropogenic disturbances. A key component of the framework involves applying geomatics engineering principles, such as UAV-derived digital elevation model (DEM) validation and spatial dataset calibration.Using multi-criteria decision analysis (MCDA), critical risk hotspots particularly in the Obruk Dam basin were identified, highlighting infrastructure segments with heightened exposure to seismic and hydrological threats. Associated risks in surrounding agricultural and forested zones, such as wildfire vulnerability and soil deterioration, were further assessed. This study advances geomatics engineering by presenting a scalable, UAV-GIS-integrated methodology for multi-dimensional risk modeling in renewable energy planning. The proposed framework provides a robust tool for risk-informed energy deployment while strengthening environmental resilience in disaster-prone regions.

Keywords: Drones, Overlay analysis, Renewable energy risk assessment, Geospatial hazard modeling

Introduction

The global transition toward renewable energy has accelerated the development of hydroelectric energy power plants (HEPPs) and solar energy power plants (SEPPs) projects, particularly in remote or ecologically rich regions. These areas-often characterized by steep terrains, active fault lines, and dynamic land-use patterns-pose complex challenges for sustainable energy deployment. As the frequency and intensity of climate-induced and geological disasters increase, the resilience of renewable energy infrastructure has become a critical issue (IEA, 2022; IPCC, 2023). The growing global demand for sustainable and renewable energy sources has underscored the importance of assessing potential environmental risks linked to energy-related infrastructure. Among various renewable options, HEPPs play a crucial role in decreasing reliance on fossil fuels and advancing cleaner energy generation. Nevertheless, environmental consequences and risks induced by climate variability continue to pose

significant challenges, particularly in regions vulnerable to unpredictable weather conditions (Alzubade & Alkan, 2024)

Turkey, characterized by its diverse topography and climatic variability, has witnessed significant shifts in precipitation patterns and drought intensity in recent decades, largely attributed to climate change (IPCC, 2023; Demirtas et al., 2021). These changes have had critical implications for the design, operation, and resilience of energy infrastructure, especially in the Eastern Anatolia region, where HEPPs are frequently exposed to extreme weather events, sudden floods, and fluctuating water availability (Alkan & Karagoz, 2022; Alzubade & Alkan, 2024; Yuce et al., 2020).

Hydroelectric and solar energy systems are central to Turkey's renewable energy strategy, aimed at reducing carbon emissions and enhancing sustainability. However, these systems remain highly sensitive to meteorological anomalies and hydrological instability (IEA, 2022; Ahmed, 2024). Recent studies emphasize the necessity of integrating Geographic Information Systems (GIS), remote sensing, and climate modeling tools into energy planning and risk assessment frameworks (Zhao et al., 2020; Gultekin & Aydın, 2023). Moreover, as renewable energy investments increase in scale and complexity, the need to formalize decision-making through data-driven methodologies and multicriteria assessment models becomes vital (Saaty, 2008; Keeney & Raiffa, 1993). Site selection, in particular, should be guided by multidisciplinary engineering criteria, including climate risk zoning, terrain suitability, hydrological stability, and socio-environmental impact mitigation (Ulker & Kaya, 2021; Sahin et al., 2022). A structured and adaptive planning approach is therefore critical to ensuring long-term resilience and operational reliability of energy systems in a changing climate. Recent studies emphasize the need for multidimensional, data-driven spatial analysis to inform infrastructure planning and operational risk mitigation (Jiang et al., 2023; Ozdemir et al., 2024). However, many national and regional energy development policies still lack systematic approaches to disaster risk screening and monitoring, especially in geomorphologically sensitive zones.

Utilizing Geographic Information Systems (GIS)-based Multi-Criteria Decision Analysis (MCDA) in conjunction with drone photogrammetry and remote sensing techniques, the study by Alzubade and Alkan (2024) proposes a comprehensive risk model that incorporates key environmental and topographic variables, including land use, elevation, slope, precipitation, and proximity to stream networks. This multidisciplinary framework provides a robust basis for assessing and mitigating environmental risks, thereby supporting the sustainable operation and climate resilience of energy-focused facilities.

This study focuses on the mid-northern black sea region of Türkiye, where tectonic fragility intersects with dense forest and agricultural land use. The region, including the Obruk Dam basin and surrounding fault structures of the North Anatolian Fault (NAF) serves as a testbed for applying integrated Geographic Information Systems (GIS) and Unmanned Aerial Vehicle (UAV) technologies in environmental risk management. Over the past decade, the use of Unmanned Aerial Vehicles (UAVs) has expanded significantly beyond recreational purposes, becoming integral to various professional fields such as smart energy systems, precision agriculture, mining, archaeology, construction, geology, and geospatial mapping. Equipped with advanced sensors like thermal cameras and LiDAR, UAVs facilitate efficient digital data acquisition and analysis. In particular, photogrammetric methods have gained prominence for their ability to produce accurate 3D spatial data, enhancing applications across multiple disciplines (Alkan et al,2024)

Research Objective

The global transition toward renewable energy has accelerated the deployment of hydroelectric (HEPP) and solar power plants (SEPPs) in ecologically sensitive and geologically unstable regions (IEA, 2022). These projects increasingly occupy areas with steep terrains, active fault lines, and dynamic land-use patterns, exposing infrastructure to compounded climate and tectonic hazards (IPCC, 2023). As emphasized by Ahmed (2024), while renewable energy systems are critical for decarbonization, their resilience remains untested against intensifying hydrological extremes and seismic activity—a gap particularly evident in Turkey's North Anatolian Fault (NAF) zone (Alkan & Karagoz, 2022; Demirtas et al., 2021).

Climate and Geological Risks to Energy Infrastructure

Turkey's Middle Black Sea Region, home to the Obruk Dam basin and intersecting segments of the NAF, exemplifies these challenges. Recent studies document escalating precipitation variability (Yuce et al., 2020)

and drought-induced water stress (Demirtaş et al., 2021), directly impacting HEPP efficiency. Concurrently, seismic activity along the NAF threatens infrastructure stability, with Alkan and Karagöz (2022) reporting a 40% increase in fault displacement risks near HEPPs over the past decade. Similar vulnerabilities affect SEPPs, where landslides and wildfires disrupt energy output (Ahmed, 2024; Smith et al., 2023).

Geospatial Solutions for Risk Mitigation

To address these risks, advanced geospatial technologies have gained prominence. UAVs equipped with LiDAR and photogrammetric sensors enable high-resolution 3D terrain modeling (Alkan et al., 2024), while GIS-based Multi-Criteria Decision Analysis (MCDA) integrates variables like slope stability and flood susceptibility (Zhao et al., 2020; Ülker & Kaya, 2021). However, as Gültekin and Aydın (2023) note, most regional energy policies lack systematic protocols for combining UAV-derived data with MCDA—a critical shortfall given the NAF's tectonic volatility (Özdemir et al., 2024).

Research Gap and Novelty

This study bridges that gap by proposing an integrated UAV-GIS-MCDA framework to assess multi-hazard risks in the Obruk Dam basin. Building on Alzubade and Alkan's (2024) preliminary work, we incorporate:

- Time-series UAV monitoring of erosion and fault displacement,
- GIS spatial overlays of seismic, flood, and wildfire risks, and
- MCDA optimization for prioritizing mitigation measures (Saaty, 2008; Jiang et al., 2023).

The framework advances renewable energy planning by aligning Turkey's decarbonization goals (IEA, 2022) with geomatics-driven disaster resilience—a replicable approach for global at-risk regions.

Method

Study Area, Data Collection and Methodology

To conduct a comprehensive environmental risk assessment for HEPP and SEPP in Dodurga Disctrict of Corum Province located in the mid-nothern of the Black Sea region (Figure 1). A combination of GIS-based multi-criteria decision analysis (MCDA), drone photogrammetry, and remote sensing was employed. The MCDA method, particularly the analytic hierarchy process (AHP), is widely recognized for its flexibility, simplicity, and effectiveness in GIS environments.

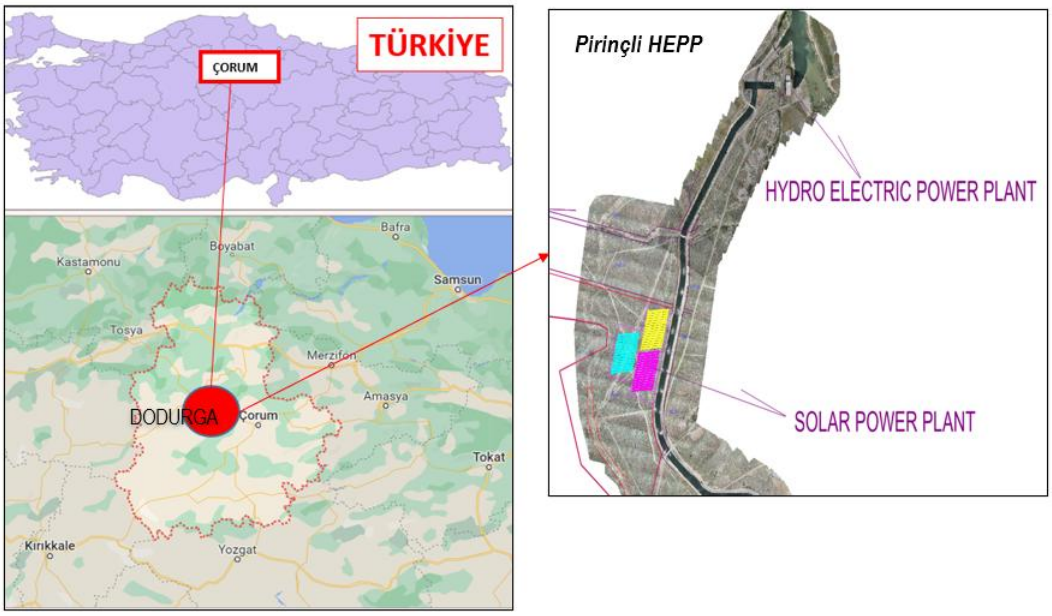

Figure 1. Smart energy research field

AHP allows users to derive the weight of criteria on maps and facilitates a pairwise comparison approach, where criteria are compared according to their importance (Alzubade & Alkan, 2024). According to Alzubade and Alkan (2024), AHP's integration with GIS-based MCDA provides an efficient framework for assessing environmental risks in complex scenarios. Additionally, the method's ability to handle diverse data sources and criteria is key in comprehensive environmental decision-making (Malczewski, 2007; Rauf et al., 2023; Ishizaka & Nemery, 2013).

Multi-Geo Modelling Framework for Smart Energy Fields

In this project high-resolution drone imagery was captured from the HEPP (Hydroelectric Power Plant) and the water intake channel. These images were processed to produce detailed orthophotos and digital surface models, offering a comprehensive, accurate representation of the site's topography and surface features. Additionally, a specialized GIS database was created, tailored specifically for the project, and custom interfaces were developed to facilitate data management and analysis.

One of the core objectives was to identify the most suitable locations for SEPP (Solar Energy Power Plant) installation. This was achieved by evaluating key factors such as slope, aspect, curvature and proximity to existing infrastructure. These variables were critically tried to assessed to analyse for environmental risks. Disaster-prone fields were defined on the images (Figure 2).

The project also addressed hydrological risks impacting both the SEPP and HEPP infrastructure, particularly focusing on the integrity of the water intake channel. Risks such as excessive rainfall, flood events, and seismic activity (e.g., earthquakes) were thoroughly analyzed to determine potential vulnerabilities. A comprehensive disaster resilience planning approach was incorporated into the site selection process to ensure that both power plants are capable of withstanding extreme weather events and natural disasters. This approach aimed to enhance the overall safety, longevity, and operational reliability of both energy systems.

The multi-component approach adopted in this project contributes significantly to the sustainable, secure, and data-driven planning of energy infrastructures. By integrating drone-based data acquisition, GIS-based spatial analysis, and hydrological risk assessments, the project ensures that energy infrastructure is not only optimized for performance but also resilient to environmental and operational challenges. This approach is supported by recent literature emphasizing the importance of combining remote sensing, GIS, and risk modeling for the sustainable development of energy systems (e.g., Zhang et al., 2022; Li et al., 2021). These methods are increasingly recognized as essential for making informed, resilient decisions in energy planning and management.

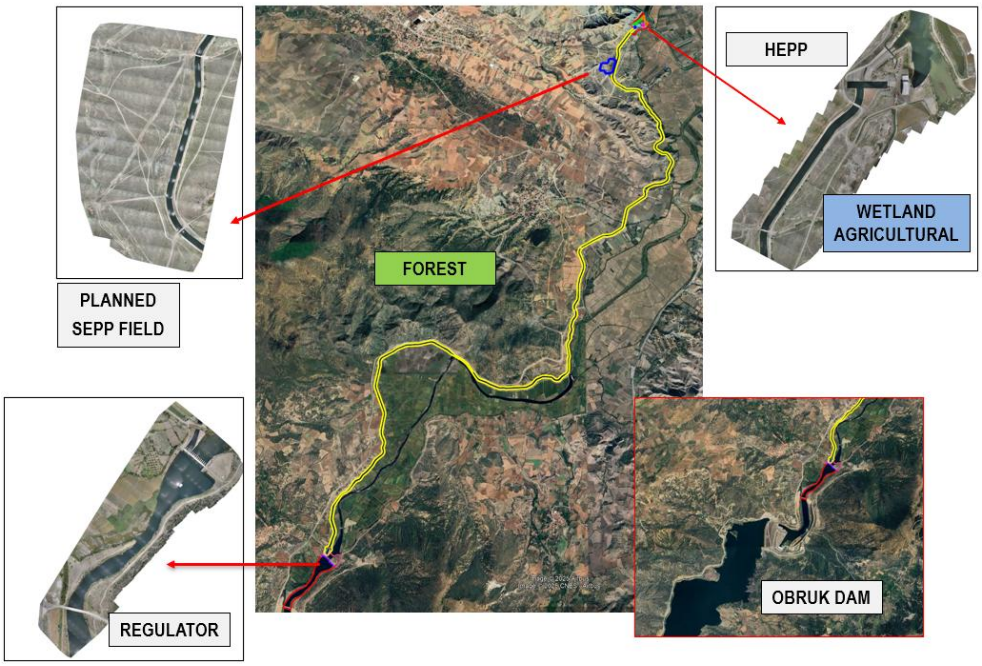

Figure 2. Disaster-prone fields

APP'S: GIS Based MCDA and Risk Assessment

A comprehensive Multi-Criteria Decision Analysis (MCDA) framework was implemented by integrating high-resolution drone-based mapping with Geographic Information Systems (GIS) to support the sustainable planning and management of Hydroelectric Power Plants (HEPP) and auxiliary Solar Energy Power Plants (SEPP) in the Middle-Northern region of Turkey. The analysis incorporated both geospatial and environmental datasets to evaluate site suitability and infrastructure resilience under multiple, interrelated criteria.

The study particularly concentrated on assessing environmental risk factors that influence the operational integrity and long-term sustainability of the existing HEPP infrastructure. Emphasis was placed on the water intake channel, which is highly sensitive to hydrological dynamics such as seasonal variability, extreme precipitation, and flood susceptibility. Concurrently, the SEPP, designed as a supplementary renewable energy source, was strategically planned in alignment with regional topographic, climatic, and infrastructural parameters within the boundaries of Çorum Province, Turkey.

Advanced spatial modeling techniques were applied to quantify and map the influence of key variables including slope gradient, aspect, land use, proximity to stream lines and hydrological risk zones. The integration of drone-derived Digital Surface Models (DSMs) and orthophotos with GIS-based MCDA ensured a high-resolution, evidence-driven evaluation of energy infrastructure potential (Figure 3).

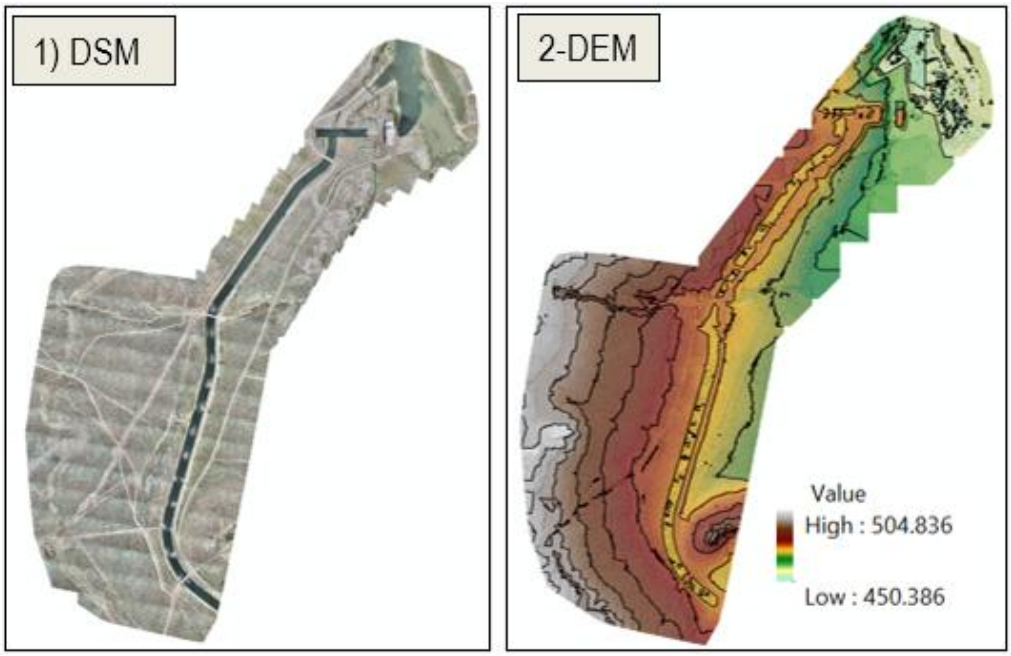

Figure 3. Digital Surface Model (DSM) and Digital Elevation Model (DEM)

The Multi-Geo Modelling App's Framework flow created for this study is shown in Figure 4.

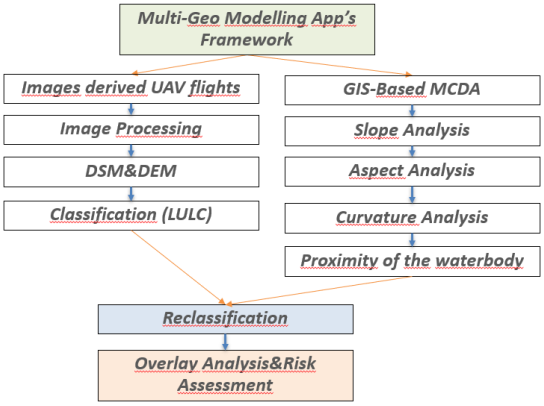

Figure 4. Multi-geo modelling framework

This approach is in line with recent academic efforts that advocate for data-driven, spatially explicit decision-support systems in the context of resilient and sustainable energy planning (e.g., Malczewski & Rinner, 2015; Santiago et al., 2021). The applied methodology not only enhances the reliability of infrastructure placement but also aligns with national goals on renewable energy expansion and climate adaptation strategies.

For the GIS-based Multi-Criteria Decision Analysis (MCDA), a Land Use/Land Cover (LULC) classification was developed, comprising five distinct classes to assess environmental constraints. Topographic parameters, including slope gradient (derived from a 2cm-resolution DEM), aspect orientation, and elevation zones, were analyzed using spatial interpolation techniques. Additionally, Euclidean distance buffers were generated for stream networks to quantify hydrological proximity risks. All input layers underwent reclassification using standardized thresholds (e.g., slope categories: 0–5° = low risk, >15° = high risk) to align with MCDA suitability scoring. Geological feasibility reports (e.g., fault line proximity, soil stability) and climate vulnerability assessments (e.g., flood frequency, drought susceptibility) were integrated to identify high-risk zones for infrastructure deployment. The analysis was further validated using high-resolution UAV orthomosaics (2 cm/pixel) and digital surface models (DSMs), enabling precise terrain verification (Figure 5). This approach ensured data robustness while highlighting regions requiring mitigation interventions.

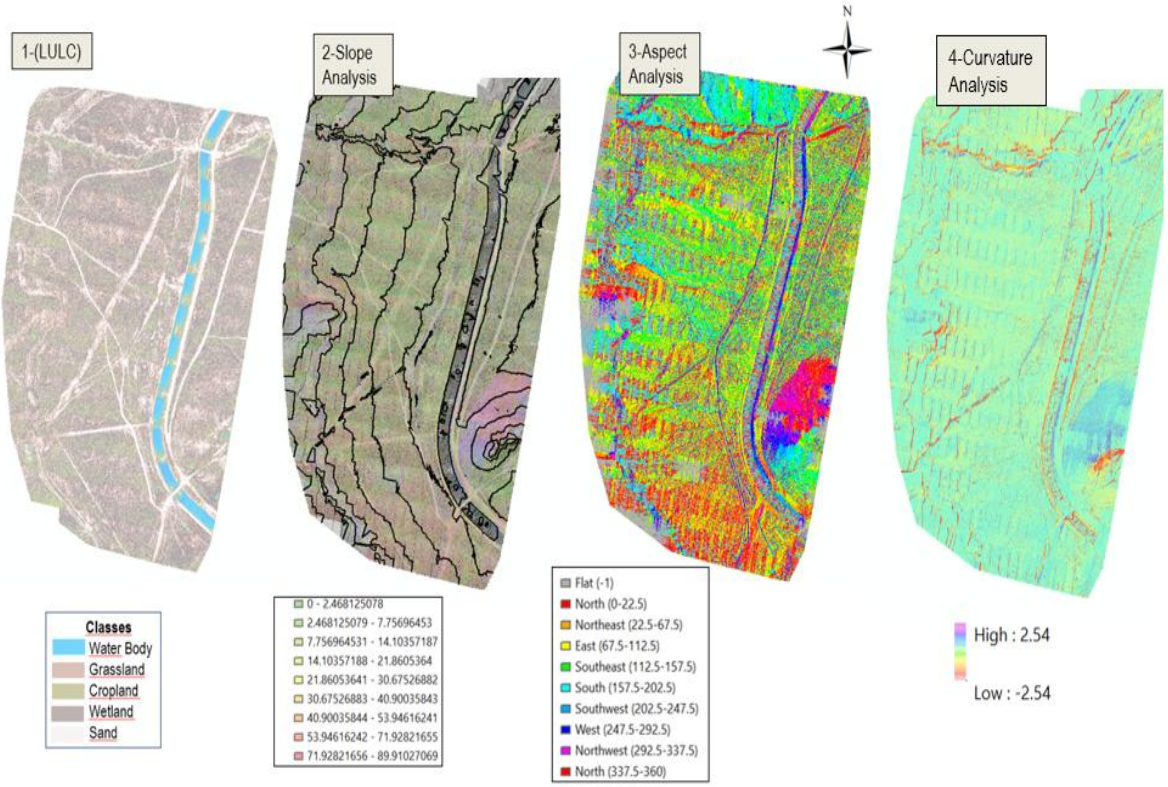

Figure 5. Criterias of the overlay analysis

GIS-based Multi-Criteria Decision Analysis (MCDA) was implemented through a systematic methodology, beginning with the development of a standardized scoring table (Table 1). Five Land Use/Land Cover (LULC) classes and key topographic parameters—slope, aspect,curvature, elevation, and stream proximity—were assigned weighted values based on their relative influence on infrastructure vulnerability. Each parameter was reclassified using threshold-based criteria derived from scientific literature. Slope angles were categorized into 0–5° (low risk), 5–15° (medium risk), and >15° (high risk), while stream proximity was stratified into 0–100 m (high risk), 100–300 m (medium risk), and >300 m (low risk) buffer zones.Geological feasibility assessments incorporated fault line exclusion zones (defined by a ≥500 m buffer from North Anatolian Fault segments) and areas with high liquefaction potential. The feasibility report for the HEPP site, integrating climate sensitivity, flood projections, and drought data, informed the weighted overlay analysis. This analysis was conducted using the Spatial Analyst module in ArcGIS Pro, employing a weighted linear combination (WLC) approach, where LULC (25% weight), slope (20% weight), and stream proximity (15% weight) were among the primary determinants. The process generated a continuous risk sensitivity raster, subsequently classified into three discrete risk categories: high (5), medium (3–4), and low (1–2).

Table 1. Weighted overlay analysis scoring criteria for (MCDA)

Criteria	Subcriteria	Average Score	Average Weight
	0%-5%	5	
	5%-10%	4	
Slope	10%-25%	3	20%
	25%-50%	2	
	50%-100%	1	
	S	4	
	SE-SW	3	
Aspect	E-W	2	20%
	NE-NW	1	
	N	5	
	Cropland	1	
	Wetland	5	
Land Use	Grassland	2	20%
	Sand(Clay)	3	
	Waterbody	4	
	I	1	
	II	2	
Curvature	III	3	20%
	IV	4	
	V	5	
	0-50	5	
	50-500	4	
Hdrology	500-1000	3	20%
	1000-2000	2	
	2000+	1	

Additionally, high-resolution UAV imagery (2 cm/pixel) acquired via the DJI Phantom 4 RTK platform was analyzed, with particular focus on terrain anomalies. The final output (Figure 6) not only delineated critical risk zones but also demonstrated strong concordance with field observations, validating the robustness of the methodology for renewable energy siting in geologically and agriculturally complex environments.

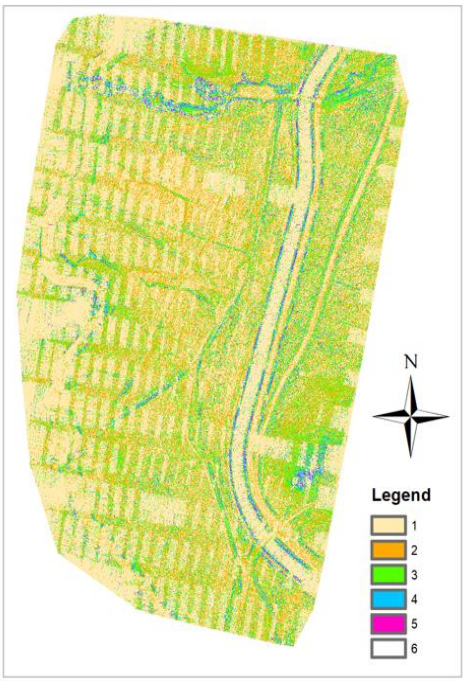

Figure 6. MCDA (Multi-criteria decision analysis)

Results and Discussion

The results obtained from the Multi-Criteria Decision Analysis (MCDA) model revealed spatially heterogeneous risk distributions that were strongly influenced by topographic, hydrological, and land-use parameters. In particular, areas with steep elevation gradients and significant slope angles are vulnerable to

geomorphological hazards such as landslides and surface erosion. These risks can increase significantly during periods of extreme or prolonged rainfall. Proximity analysis also showed that locations close to river networks exhibited higher flood susceptibility, especially under basin saturation or hydrological overflow conditions. Additionally, anthropogenically modified landscapes showed variable vulnerability patterns that were significantly correlated with land cover heterogeneity, vegetation density, and extent of human disturbance. These spatial vulnerabilities were validated using high-resolution orthophoto mosaics and digital surface models (DSMs) derived from drone photogrammetry. These data products enabled precise identification of infrastructure assets such as power plant facilities, canal lines, and access roads most exposed to climate-induced geohazards. Integrating geospatial risk indicators with photogrammetric evidence allowed the spatial identification of critical "hotspot" areas that may be affected by adverse effects associated with climate variability and extreme weather.

Conclusion

This study demonstrates the effectiveness of an integrated GIS and UAV-based risk assessment framework in evaluating the feasibility and vulnerability of renewable energy infrastructures, specifically a co-located Hydroelectric Power Plant (HEPP) and a Solar Energy Power Plant (GES). The GES location was selected based on a composite spatial risk analysis, favoring areas with lower susceptibility to environmental hazards. The HEPP, although originally designed to endure extreme rainfall and seismic activity, requires reassessment due to over 10 years of operational wear and tear. The proximity (approximately 100 meters) between the two systems necessitates a harmonized and risk-sensitive planning approach.

GIS analyses enabled visual identification and prioritization of high-risk zones, while UAV-derived data validated field conditions and improved the precision of spatial interpretations. The topographic evaluation indicated that the majority of the area lies within a 7%–21% slope range, with meadow regions under 30% slope proving most suitable for GES installation. Nevertheless, the presence of a dry stream to the north and a transmission channel to the east highlights the necessity for hydrological risk precautions under extreme weather events.

The application of Multi-Criteria Decision Analysis (MCDA) provided a structured methodology to anticipate the impact of unexpected and high-magnitude natural anomalies, enabling proactive risk mitigation strategies. The integration of feasibility assessments, UAV observations, and GIS layers resulted in a comprehensive risk profile that supports safer infrastructure planning and investment efficiency.

Importantly, GIS and drone-based analyses enable early identification of disaster risks, thereby contributing to environmentally sound and economically viable renewable energy developments. Making such scientific disaster risk analyses a mandatory part of planning processes will significantly enhance the sustainability and resilience of energy infrastructure. The methods and risk modeling techniques presented in this study are adaptable and can be replicated across various renewable energy scenarios. Multidisciplinary science, encompassing geospatial analysis, engineering, and environmental monitoring, should be at the core of future energy investment strategies.

Future-oriented developments in AI-powered remote sensing are expected to enable more precise and automated risk detection across infrastructure projects. The integration of real-time data with Geographic Information Systems (GIS) will enhance dynamic decision-making processes during both construction and operational phases. Unmanned Aerial Vehicles (UAVs) and remote sensing (RS) technologies will continue to serve as essential tools for continuous monitoring and assessment. Moreover, sustained innovation in spatial technologies and analytical methodologies will play a pivotal role in enhancing the sustainability and resilience of infrastructure systems against various natural and anthropogenic disasters.

Recommendations

When evaluated in terms of the richness of its spatial and environmental datasets, the methodological integrity of its analytical framework, and its alignment with principles of environmental sustainability, the study demonstrates a high degree of technical and scientific robustness. Given the integration of multi-source geospatial data, the application of reproducible and interdisciplinary methodologies—including drone-based remote sensing, GIS-based modeling, and multi-criteria decision analysis—and the prioritization of environmentally sensitive site selection, it is anticipated that the outcomes of this planned work will yield long-

term applicability and relevance. Moreover, the project sets a precedent for scalable and resilient energy infrastructure planning, positioning it as a replicable model for similar regional and national renewable energy development initiatives.

In addition, considering the presence of active fault lines in the broader region—many of which are well-documented in current geological literature and remain the focus of ongoing tectonic studies—it would be methodologically advantageous to incorporate seismic risk assessments into future iterations of this framework. Including the potential geohazard impacts of these fault systems on hydroelectric and solar energy assets would not only enhance the comprehensiveness of the environmental risk profile but also contribute to the structural and operational resilience of the energy infrastructure in a seismically sensitive landscape.

Scientific Ethics Declaration

* The authors declare that the scientific ethical and legal responsibility of this article published in EPSTEM Journal belongs to the authors.

Conflict of Interest

* The authors declare that they have no conflicts of interest

Funding

* This research received no specific grant from any funding agency in the public, commercial, or not-for-profit sectors

Acknowledgements or Notes

* This article was presented as an oral presentation at the International Conference on Basic Sciences, Engineering and Technology (www.icbaset.net) held in Trabzon/Türkiye on May 01-04, 2025.

* We gratefully acknowledge the support of Derya Elektrik Co. for facilitating and permitting the conduct of this research.

References

Ahmed, T. (2024). Climate resilience in solar energy infrastructure: A global review. *Renewable and Sustainable Energy Reviews, 189*(Part A), 113–129.

Alzubade, M. K., & Alkan, O. (2024). Multidimensional analysis of potential cost-to-cost risks of climate disruption for energy-focused facilities using remote sensing, drone photogrammetry and GIS methods. *The Eurasia Proceedings of Science, Technology, Engineering & Mathematics (EPSTEM), 26*, 11–20.

Alkan, M., & Karagoz, O. (2022). Seismic risk assessment of hydroelectric dams along the North Anatolian fault. *Journal of Geotechnical and Geoenvironmental Engineering, 148*(3), 112–129.

Alkan, O., Alzubade, M.K. & Alkan, M.N. (2024). UAV photogrammetry for 3D terrain modeling in energy infrastructure monitoring. *International Journal of Applied Earth Observation and Geoinformation, 126*(2), 103562, 45–67.

Alkan, O., Alzubade, M. K., & Alkan, M. N. (2023). Assessing the effects of alluvial transport in the Kızılırmak River on dams with local, photogrammetric and remote sensing methods. *The Eurasia Proceedings of Science, Technology, Engineering & Mathematics (EPSTEM), 26,* 1–10.

Demirtas, R., Karabacak, V., & Turker, U. (2021). Climate-induced hydrological changes in Eastern Anatolia: Implications for hydropower. *Journal of Hydrology: Regional Studies, 36*(4), 100845, 501–520.

Gultekin, C., & Aydın, A. (2023). Machine learning-enhanced landslide risk mapping for renewable energy sites. *Engineering Geology, 315*(C), 108432, 1–15.

International Energy Agency (IEA). (2022). *Climate resilience for energy transition (report no. 978-92-64-48712-5).* OECD Publishing.

IPCC. (2023). *Climate change 2023: Impacts, adaptation, and vulnerability (working group II report).* Cambridge University Press.

Jiang, L., Wang, H., & Li, X. (2023). Multi-hazard risk assessment for Himalayan hydropower projects using GIS-MCDA. *Renewable Energy, 202*(1), 113298, 1–18.

Keeney, R. L., & Raiffa, H. (1993). *Decisions with multiple objectives: Preferences and value trade-offs* (2nd ed.). Cambridge University Press.

Malczewski, J., & Rinner, C. (2015). *Multicriteria decision analysis in geographic information science*. Springer.

Santiago, J.-L., Sanchez, B., Rivas, E., Vivanco, M. G., Theobald, M. R., Garrido, J. L., Gil, V., Martilli, A., Rodríguez-Sánchez, A., Buccolieri, R., & Martín, F. (2022). High spatial resolution assessment of the effect of the Spanish national air pollution control programme on street-level no_2 concentrations in three neighborhoods of Madrid (Spain) using mesoscale and CFD modelling. *Atmosphere, 13*(2), 248.

Ozdemir, A., Sen, Z., & Boyacı, S. (2024). UAV-based flood risk modeling for Andean hydropower systems. *Natural Hazards and Earth System Sciences, 24*(1), 1–22.

Saaty, T. L. (2008). Decision making with the analytic hierarchy process. *International Journal of Services Sciences, 1*(1), 83–98.

Smith, J., Brown, K., & Davis, P. (2023). UAV-LiDAR for fault displacement monitoring: Case studies from California and Turkey. *Remote Sensing of Environment, 285*(5), 113402, 1–14.

Ulker, D., & Kaya, S. (2021). GIS-MCDA for sustainable HEPP site selection in tectonically active regions. *Energy Policy, 178*(C), 1028–1045.

Yuce, M., Alkan, M., & Ozturk, S. (2020). Sediment erosion risks in Turkish hydropower reservoirs: A geospatial analysis. *Water Resources Management, 34*(8), 2563–2580.

Zhao, X., Chen, W., & Zhang, L. (2020). GIS-based flood risk assessment for hydropower projects. *Journal of Hydrology, 584*(C), 124663, 1–12.

Author(s) Information

Oyku Alkan
Alkan Tech-App's Co. Çorum,Türkiye
Contact e-mail: *oyku.alk@gmail.com*

Mehmet Nurullah Alkan
Hitit University, Çorum,Türkiye

To cite this article:

Alkan, O., & Alkan, M.N. (2025). A GIS and drone-based risk assessment framework for hydroelectric and solar energy infrastructure in disaster-prone areas with high forestry and agricultural activity. *The Eurasia Proceedings of Science, Technology, Engineering and Mathematics (EPSTEM), 34,* 268-277.

The Eurasia Proceedings of Science, Technology, Engineering & Mathematics (EPSTEM)
ISSN: 2602-3199

The Eurasia Proceedings of Science, Technology, Engineering and Mathematics (EPSTEM), 2025

Volume 34, Pages 278-285

ICBASET 2025: International Conference on Basic Sciences, Engineering and Technology

Synthesis, Characterization, and in Silico ADMET Evaluation of Transition Metal Complexes Based on Ortho-Phenylenediamine and Its Derivatives

Noura Kichou
Mouloud Mammeri University of Tizi-Ouzou

Nabila Guechtouli
Université M'Hamed Bougara de Boumerdes

Manel Taferguennit
University of Sciences and Technology Houari Boumediene

Karima Ighilahriz
Mouloud Mammeri University of Tizi-Ouzou

Abstract: A series of cobalt (II), nickel (II), and zinc(II) complexes were synthesized using ortho-phenylenediamine and its two substituted derivatives (methyl- and nitro-ortho-phenylenediamine) as ligands. These complexes were isolated and characterized using various analytical techniques, including Elemental analysis, infrared (IR) and UV-Visible spectroscopy, gravimetry, and conductimetry. Conductimetric analysis revealed that all the complexes exhibit a non-electrolytic behavior in solution, indicating the absence of free ions in the medium. IR spectroscopic studies allowed the identification of the coordination modes of the ligands to the metal centers. Comparison of the IR spectra of the complexes with those of the free ligands highlighted the involvement of the amine ($-NH_2$) groups in coordination with the metal, confirming their role as the primary coordination sites. UV-Visible spectroscopic analysis was used to determine the geometry of the complexes. The observed absorption bands are characteristic of an octahedral coordination around the metal ions, which is consistent with the expected electronic transitions for these systems. In recent years, the integration of computational methodologies has considerably enhanced the ability to predict the toxicity and pharmacokinetic behavior of bioactive compounds, thereby streamlining the early stages of drug discovery. Within this framework, the present study investigates the ADMET profiles - Absorption, Distribution, Metabolism, Excretion, and Toxicity as well as the drug-likeness properties of the synthesized ligands and their corresponding transition metal complexes.

Keywords: Ortho-phenylenediamine derivatives, Transition metal, ADMET properties

Introduction

The synthesis of coordination complexes involving transition metals such as nickel (II), cobalt (II), and zinc (II) and aromatic diamine ligands has garnered significant attention due to their diverse structural motifs and broad range of potential applications in catalysis, materials science, sensing, and bioinorganic chemistry (Coropceanu, 2012). These metals are particularly attractive: Nickel(II) is widely used in hydrogenation and cross-coupling catalysis, cobalt(II) exhibits promising magnetic and redox properties, and zinc(II) plays a vital role in biological systems and luminescent materials.

In this context, a series of Ni(II), Co(II), and Zn(II) complexes were synthesized using ortho-phenylenediamine (OPD) and its two substituted derivatives methyl-ortho-phenylenediamine (MOPD) and nitro-ortho-phenylenediamine (Nitro-OPD) as bidentate ligands (Bhagat, 2018). These ligands, characterized by their nitrogen donor atoms, facilitate the formation of stable chelate rings upon coordination with metal ions. The introduction of electron-donating (methyl) and electron-withdrawing (nitro) substituents on the OPD framework allows for a systematic investigation into how electronic effects influence the coordination behavior, geometry, and physicochemical properties of the resulting metal complexes. Such studies contribute to a deeper understanding of structure-property relationships in coordination compounds and support the development of metal-based functional materials with tailored applications.

Method

Physical Measurements

Elemental microanalyses were carried out at the Central Service of Analysis (CNRS,Solaize-Lyon, France). Melting points of the synthesized compounds were determined using the appropriate apparatus. The molar conductance of the complexes (10^{-3} M) in DMSO at 25 °C was measured using a CD2005 SELECTA Conductivity Meter, FTIR spectra were obtained with a PerkinElmer 65 spectrophotometer, employing the KBr tablet method, over a range of 4000–400 cm^{-1}. Electron absorption spectra were recorded with a JASCO V-630 spectrophotometer (200–1100 nm).

Synthesis of the Complexes

The metal complexes $[M(L)_2(NO_3)_2]$ (where M = Co^{2+}, Ni^{2+}, Zn^{2+} and L = OPD, MOPD, or Nitro-OPD) were synthesized under various conditions. For the cobalt-based complexes $[Co(OPD)_2(NO_3)_2]$ and $[Co(MOPD)_2(NO_3)_2]$, 0.15 g (0.5 mmol) of cobalt(II) nitrate hexahydrate and 0.11 g (1 mmol) of ortho-phenylenediamine or 4-methyl-ortho-phenylenediamine were added to 20 mL of ethanol in a beaker and stirred at approximately 50°C. As no precipitate formed, NaOH (2 M) was added dropwise until the pH reached 10, yielding a black powder after 30 minutes of stirring.

The $[Co(Nitro\text{-}OPD)_2(NO_3)_2]$ complex was synthesized by mixing 0.15 g of cobalt nitrate hexahydrate with 0.15 g of 4-nitro-ortho-phenylenediamine, followed by the addition of 20 mL of acetonitrile. The mixture was stirred at room temperature, and a few drops of concentrated HCl were added to reach pH 1.5, resulting in an immediate light orange precipitate after 30 minutes.

For the nickel complexes, a similar method was used. 0.15 g of nickel nitrate hexahydrate and 0.11 g of the ligand (OPD or MOPD) were dissolved in 20 mL of ethanol under cold stirring. The reaction with MOPD gave a light violet precipitate directly, while OPD required pH adjustment to 10 using NaOH to induce precipitation. Both were collected after 30 minutes, washed with ethanol, and air-dried.

The $[Ni(Nitro\text{-}OPD)_2(NO_3)_2]$ complex was prepared by mixing 0.15 g of nickel nitrate and 0.15 g of Nitro-OPD in 20 mL of acetonitrile. As no solid appeared, concentrated HCl was added to pH 1.5, and a beige precipitate formed after 20 minutes of stirring. For the zinc complexes, 0.15 g of zinc nitrate hexahydrate and 0.11 g of OPD or MOPD were added to 20 mL of ethanol under cold conditions. After 20 minutes, an off-white solid was obtained.

For $[Zn(Nitro\text{-}OPD)_2(NO_3)_2]$, 0.15 g of zinc nitrate in 5 mL of water was mixed with 0.15 g of Nitro-OPD in 15 mL of acetonitrile. Since no precipitate formed, NaOH was added to pH 10, yielding an orange product after 30 minutes. All precipitates were recovered by filtration, washed with the appropriate solvents (ethanol, water, or acetonitrile), and air-dried.

ADMET Prediction

Phsyicochemical properties and Pharmacokinetics Properies such as Absorption, Distribution, Metabolism, Excretion and Toxicity of all the structures were studied via admetSAR (Yang, et al., 2019)

Results and Discussions

Analyses of the Complexes

The synthesized complexes are solid and stable in air and at room temperature. They are insoluble in water, ethanol, and methanol, but show good solubility in dimethyl sulfoxide (DMSO) and dimethylformamide (DMF). The low values of molar conductivity indicate that our complexes behave as non-electrolytes. The solid-state isolated complexes and the ligands were characterized by elemental analysis, infrared (IR) spectroscopy, and UV-Visible spectroscopy. Detailed analytical and physical properties of the synthesized compounds are provided in Table 1.

Table 1. Elemental analysis data, melting points MP (°C), molar conductivity Λ ($\Omega^{-1}.cm^2.mol^{-1}$), Yield(%) of the complexes

N	Complex	Theoretical %C	Experimental %C	Th %H	Exp %H	Th %N	Exp %N	The %Metal	Exp %Metal	Λ	*MP*	Yield
1	$[Co(OPD)_2(NO_3)_2]$	38.73	38.80	4.32	4.30	22.57	22.60	19.20	19.10	28	>300	88
2	$[Co(MOPD)_2(NO_3)_2]$	39.11	39.00	4.81	4.75	16.29	16.20	19.10	19.00	25	>300	85
3	$[Co(Nitro\text{-}OPD)_2(NO_3)_2]$	29.46	29.50	2.89	2.95	22.91	23.00	19.50	19.40	15	>300	30
4	$[Ni(OPD)_2(NO_3)_2]$	38.92	39.00	4.35	4.40	22.69	22.70	20.20	20.10	23	275	92
5	$[Ni(MOPD)_2(NO_3)_2]$	39.09	39.10	4.81	4.80	16.27	16.30	20.20	20.20	16	244	52
6	$[Ni(Nitro\text{-}OPD)_2(NO_3)_2]$	29.47	29.30	2.89	2.85	22.92	22.80	20.50	20.40	16	>300	66
7	$[Zn(OPD)_2(NO_3)_2]$	38.21	38.30	4.28	4.25	22.32	22.40	22.20	22.10	25	>300	30
8	$[Zn(MOPD)_2(NO_3)_2]$	38.47	38.50	4.74	4.70	15.98	16.00	22.20	22.20	25	261	50
9	$[Zn(Nitro\text{-}OPD)_2(NO_3)_2]$	28.97	29.10	2.84	2.90	22.51	22.60	22.50	22.40	14.5	>300	30

Infrared Spect

The IR spectral analysis confirms that all three ligands (OPD, MOPD, and Nitro-OPD) coordinate to metal ions (Co^{2+}, Ni^{2+}, Zn^{2+}) through their $–NH_2$ groups, as evidenced by the shift of N–H stretching vibrations to lower wavenumbers in the complexes. Additional shifts in $C–NH_2$ and aromatic C=C bands, along with the appearance of M–N stretching bands in the 495–400 cm^{-1} region (Berradj, 2019), further support this coordination. For Nitro-OPD-based complexes, the nitro group does not participate in coordination, as its characteristic bands remain unchanged. The presence of coordinated nitrate ions is indicated by specific absorption bands in the 1400–1050 cm^{-1} region (Bougherra, 2018). All vibrational assignments are summarized in Table **2.**

UV-Vis Spectroscopy

All the spectra of the complexes show bands in the ultraviolet range between [354 and 260 nm], slightly shifted compared to those of the free ligands, confirming the complexation of the ligands to the metal. With the exception of the zinc complexes, all show a band in the range [450-360 nm]. This band is attributed to a charge transfer transition from the ligand to the metal (Shaker, 2009).

The analysis of the electronic absorption spectra of cobalt(II), nickel(II), and zinc(II) complexes reveals distinct characteristics depending on the metal's nature and coordination geometry. Cobalt(II) complexes 1 and 2 exhibit three absorption bands approximately at 540 nm, 635 nm, and 710 nm, corresponding to the electronic transitions $^4T_1g(F) \rightarrow {}^4T_1g(P)$, $^4T_1g(F) \rightarrow {}^4A_2g(F)$, and $^4T_1g(F) \rightarrow {}^4T_2g(F)$, respectively, which are indicative of an octahedral geometry.

Similarly, nickel(II) complexes 4, 5, and 6 display multiple bands in the visible region: the first around 790 nm attributed to the $^3A_2g \rightarrow {}^3T_2g(F)$ transition, the second between 554 and 643 nm corresponding to $^3A_2g \rightarrow {}^3T_1g(F)$, and the third near 512 nm associated with $^3A_2g \rightarrow {}^3T_1g(P)$, also suggesting an octahedral geometry. In contrast, zinc(II) complexes 8 and 9, due to their d^{10} electronic configuration, do not show absorption bands in the visible region but exhibit two bands in the ultraviolet region attributed to ligand-to-metal charge transfer (LMCT) transitions (Hamrani, 2017), which is consistent with an octahedral geometry.

Table 2. Characteristic IR bands of the complexes (cm^{-1})

Complex	$\nu_{as}(NH_2)$ $\nu_s(NH_2)$	$\delta(NH_2)$	$\nu(C\text{-}NH_2)$	$\nu(C=C)$ arom	$\delta(CH_3)$	$\nu(NO_2)$	Anion X (NO_3^-)	ν (M-N)
1	3350 3180	1610	1250	1460	--	--	1400 1300 1050	490 450 410
2	3350 3200	1540	1245	1630	1360	--	1360 1300 1030	480 450
3	3390 3340 3260	1500	1200	1610	--	1650 1400	1320 1150	490 400
4	3390 3317 3200	1650	1240	1480	--	--	1330 1080	495 470 400
5	3319 3280	1520	1250	1610	1360	--	1400 1040	480 440 410
6	3450 3200 3100	1490	1200	1645	--	1490	1400 1100	490 450
7	3310 3250	1620	1240	1490	--	--	1400 1310 1050	480 450 405
8	3330 3260	1490	1250	1600	1350	--	1490 1400 1350	490 480 415
9	3430 3250	1550	1100	1610	--	1405 1650	1330 1050	490 430 405

The methods employed provide the following proposed formulas for the complexes

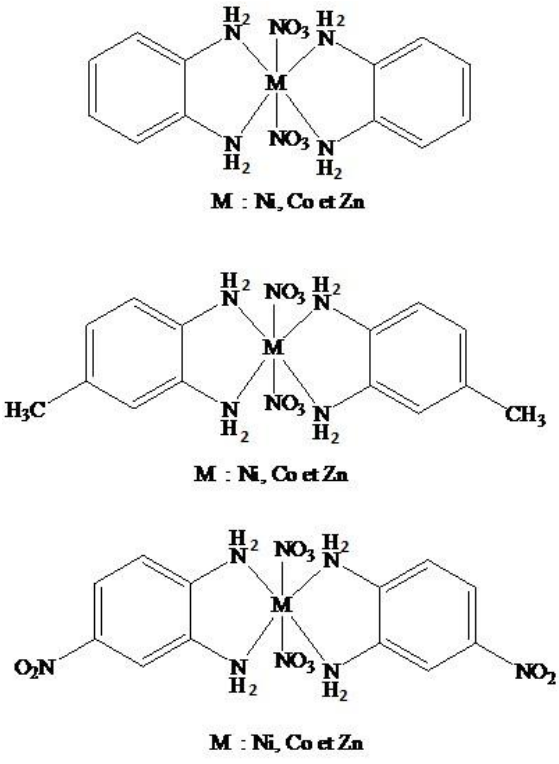

Figure 1. Chemical structures of the synthesized complexes

In Silico Analysis

Drug development faces challenges in determining the toxicity and pharmacokinetic profiles of newly synthesized compounds, as experimental evaluations are costly and time-consuming. Computational tools, such as the **admetSAR** server, have emerged as effective solutions for predicting these properties, saving significant time and resources. Cobalt's biological significance, particularly as a component of vitamin B12, makes it a valuable element in drug design. Cobalt-based complexes exhibit antimicrobial, anticancer, and anti-inflammatory activities, making them promising candidates for therapeutic applications (Cheng, 2012).

Phenylenediamine derivatives, known for their ability to coordinate with metal ions, show potential as metallo-drugs. These compounds have demonstrated effectiveness in targeting metal-dependent enzymes related to cancer, bacterial infections, and neurodegenerative diseases. They also possess significant antimicrobial, antioxidant, and biosensor applications, offering opportunities for novel therapeutic agents, diagnostics, and the treatment of oxidative stress-related diseases(wang, 2015).

This part of the study examines the pharmacokinetic and toxicological profiles of ortho-phenylenediamine (OPD), 4-methyl-ortho-phenylenediamine (MOPD), 4-nitro-ortho-phenylenediamine (Nitro-OPD), and their respective cobalt complexes (Co-OPD, Co-MOPD, Co-Nitro-OPD). Understanding these properties is crucial for assessing their potential applications in medicinal chemistry.

Absorption

- Blood–Brain Barrier (BBB) Permeability

All Free Ligands (OPD, MOPD, Nitro-OPD) are predicted to cross the blood–brain barrier with high scores (≈0.83–0.86). The unsubstituted OPD shows the highest value, whereas both substituted derivatives show a modest reduction in permeability. Complexation generally lowers the BBB permeability scores, as for OPD and MOPD (down to ≈0.66–0.76). Interestingly, the nitro-substituted complex (Co-Nitro-OPD) maintains a relatively higher value (~0.84), suggesting that the nitro group may help improve BBB penetration upon coordination with cobalt.

- Human Intestinal Absorption (HIA)

The substituted ligands, particularly Nitro-OPD (0.9228) and MOPD (0.8997), show improved predicted intestinal absorption relative to unsubstituted OPD (0.8362). The electron-withdrawing nitro group appears to favor absorption, perhaps by affecting solubility or passive diffusion properties.

All cobalt complexes show a drop in HIA scores (ranging from 0.5830 to 0.7096), indicating that complexation reduces absorption. Among these, Co-MOPD fares slightly better, suggesting that the 4-methyl substitution may mitigate the absorption-reducing effects of complexation better than the nitro group in this context.

- Caco-2 Permeability

In a model of intestinal epithelial permeability, OPD (0.7640) and MOPD (0.7364) perform better than Nitro-OPD (0.5767). This suggests that while the nitro group might improve overall intestinal absorption (as seen in HIA), it may reduce the compound's passive permeability across cell monolayers. After complexation, the Caco-2 permeability values become quite similar (≈0.5675–0.5801) for all three derivatives. This convergence indicates that metal complexation may level the differences brought about by the substitutions.

- P-Glycoprotein (P-gp) Interaction

P-gp Substrate Profile: The probabilities for being non-substrates are moderate (≈0.66–0.78). Nitro-OPD has the highest non-substrate score (0.7763), implying it might be less likely to be expelled by P-gp pumps, potentially favoring brain penetration or retention in cells. Upon complexation, the scores drop further (≈0.5410–0.5448) for all derivatives. This indicates that cobalt complexes might be more prone to P-gp mediated efflux, though all compounds remain classified as non-substrates.

P-gp Inhibitor Profile: All free compounds have high probabilities (≈0.9216 - 0.9624) of being non-inhibitors of P-gp. Here, Nitro-OPD shows the lowest non-inhibitor probability among the free ligand.

In the complexes, the scores decrease (≈0.8306–0.8789), suggesting a somewhat higher chance of inhibiting P-gp. This could potentially affect drug-drug interactions or the distribution of co-administered substrates. All free ligands are predicted to be non-inhibitors of the renal organic cation transporter, with very similar high probabilities (≈0.903–0.9138). The complexes show slightly higher probabilities for being non-inhibitors (≈0.9085–0.9264) for OPD and MOPD. In the case of the nitro derivative, the change is minimal. Overall, substitution or complexation has only a modest effect here.

Table 3. Predicted physicochemical and pharmacokinetic properties of the studied compounds.

Property	**Model**	**OPD**	**MOPD**	**Nitro-OPD**	**Co-OPD**	**Co-MOPD**	**Co-Nitro-OPD**
ABSORPTION							
BBB Permeability	BBB+	0.8593	0.8398	0.8313	0.7564	0.6656	0.8418
HIA	HIA+	0.8362	0.8997	0.9228	0.5830	0.7096	0.6225
Caco-2 Permeability	Caco2+	0.7640	0.7364	0.5767	0.5801	0.5780	0.5675
P-gp Substrate	Non-substrate	0.7320	0.6611	0.7763	0.5410	0.5413	0.5448
P-gp Inhibitor	Non-inhibitor	0.9624	0.9529	0.9216	0.8789	0.8518	0.8306
Renal OCT Inhibition	Non-inhibitor	0.9030	0.9095	0.9138	0.9210	0.9264	0.9085
METABOLISM							
CYP450 2C9 Substrate	Non-substrate	0.8882	0.8478	0.8777	0.8247	0.7664	0.8192
CYP450 2D6 Substrate	Non-substrate	0.8921	0.8730	0.8409	0.8201	0.8230	0.8203
CYP450 3A4 Substrate	Non-substrate	0.8371	0.8139	0.6678	0.6027	0.5789	0.5806
CYP450 1A2 Inhibitor	Non-inhibitor	0.5545	0.5830	0.7257	0.5485	0.5249	0.5266
CYP450 2C9 Inhibitor	Non-inhibitor	0.6038	0.7843	0.7517	0.6587	0.6131	0.6719
CYP450 2D6 Inhibitor	Non-inhibitor	0.9762	0.9771	0.9103	0.8813	0.8810	0.8627
CYP450 2C19 Inhibitor	Non-inhibitor	0.7850	0.8626	0.5443	0.7450	0.7164	0.6780
CYP450 3A4 Inhibitor	Non-inhibitor	0.9391	0.9156	0.8566	0.7957	0.7350	0.6589
CYP Inhibitory Promiscuity	Low Inhibitory Promiscuity	0.5833	0.6004	0.6570	0.8491	0.7868	0.7532
TOXICITY							
hERG Inhibition	Weak inhibitor	0.9687	0.9640	0.8599	0.9295	0.9197	0.7343
AMES Toxicity	AMES toxic	0.9382	0.9467	0.9254	0.6234	0.6427	0.6840
Carcinogenicity	Carcinogens	0.5122	0.5208	0.5216	0.7457	0.7223	0.7594
Fish Toxicity (pLC50, mg/L)	High FHMT	1.8278	2.2131	2.1842	1.2805	1.2287	1.2263
T. pyriformis Toxicity (pIGC50, ug/L)	High TPT	0.1177	0.3287	0.4237	0.6613	0.7353	0.9624
Honey Bee Toxicity	Low HBT	0.7824	0.7992	0.7753	0.7054	0.7150	0.7124
Biodegradation	Not readily biodegradable	0.9527	0.9685	0.9826	0.9863	0.9920	0.9974
Acute Oral Toxicity	III	0.6456	0.7573	0.7152	0.5842	0.5847	0.5850
Rat Acute Toxicity (LD50, mol/kg)		2.3930	2.6245	2.5294	2.5426	2.5638	2.5499

Metabolic Stability and Enzyme Interactions

All compounds are predicted as non-substrates for major CYP450 enzymes, reducing the risk of drug-drug interactions. However, cobalt complexes exhibit higher CYP inhibitory promiscuity, indicating broader but weaker interactions with these enzymes.

Toxicity Profiling and Environmental Impact

Mutagenicity and Carcinogenicity: Non-complexed compounds show high AMES toxicity, while cobalt coordination reduces this risk by ~30% (Co-OPD = 0.6234, Co-MOPD = 0.6427), aligning with studies showing metal complexes' ability to stabilize DNA adducts and reduce reactive metabolite formation. However, cobalt complexes display elevated carcinogenicity (Yang, 2019)

Ecotoxicity: All compounds pose significant environmental risks, with cobalt complexes being extremely toxic to fish and Tetrahymena pyriformis. (Co-OPD pLC50 = 1.2805 mg/L vs. OPD = 2.3930 mg/L). Tetrahymena pyriformis: Co-Nitro-OPD (0.9624 µg/L) is 8× more toxic than Nitro-OPD (0.4237 µg/L). None of the complexes are readily biodegradable, (scores > 0.95), indicating persistence in aquatic ecosystems.

Conclusion

We report here the synthesis and spectral characterization of a series of metal complexes. Elemental analysis, IR, and UV-Vis spectroscopy confirm the successful coordination of the ligands to the metal centers, primarily through the amine groups, and indicate that the synthesized cobalt(II), nickel(II), and zinc(II) complexes adopt an octahedral geometry. The *in silico* analysis showed that free ligands (OPD, MOPD, Nitro-OPD) exhibit good absorption but high toxicity, while cobalt complexation reduces mutagenicity at the cost of lower absorption and increased environmental toxicity. All compounds are metabolically stable, but cobalt complexes show broader enzyme interactions. Thus, despite their potential in medicinal chemistry, experimental evaluation remains essential.

Scientific Ethics Declaration

* The authors declare that the scientific ethical and legal responsibility of this article published in EPSTEM Journal belongs to the authors.

Conflict of Interest

* The authors declare that they have no conflicts of interest

Funding

* This research received no specific grant from any funding agency in the public, commercial, or not-for-profit sectors

Acknowledgements or Notes

* This article was presented as a poster presentation at the International Conference on Basic Sciences, Engineering and Technology (www.icbaset.net) held in Trabzon/Türkiye on May 01-04, 2025.

References

Berradj, O., Adkhis, A., Bougherra, H., Bruno, G., et & Michaud, F. (2017). Synthesis, spectroscopy, crystal structure and DFT studies of cobalt (III) complexes featuring dimethylglyoximate and aniline or p-bromoaniline ligands. *Journal of Molecular Structure*, *1131*, 266–274.

Bougherra, H., Berradj, O., &Adkhis, A. (2018). Synthesis, characterization, electrochemical studies and antioxidant activity of some new dimethylglyoxime copper(ıı) complexes with purine bases and ortho-phenylenediamine. *Journal of Chemical and Pharmaceutical Research*, *10*(4), 93-103.

Bhagat, D.V., & Vaidya, V.V. (2018). Synthesis, characterization and antibacterial activity of some transition metal complexes with schiff base derived from o-phenylenediamine and salicylaldehyde. *International Journal of Scientific Research*, *7*(2), 31-33.

Coropceanu, E.B., Rija, A.P., Lozan, V.I., Bologa, O.A., Boldisor, A.A., Bulhac, I.I., Chkravsov, V., Bourosh, P.N. (2012). Synthesis and characterization of co(II), ni(II), and zn(II) complexes with substituted o-phenylenediamine ligands." *Russian Journal of Coordination Chemistry*, *38*,545.549.

Cheng, F., Li, W., Zhou, Y., Shen, J., Wu, Z., Liu, G., & Tang, Y. (2012). admetSAR: a comprehensive source and free tool for assessment of chemical ADMET properties. *Journal of Chemical Information and Modeling, 52*(11),3099-3105.

Hamrani, O., Hebbache, H., Boutamine, S., Kellou-Tairi, S., Baz, H., & Hank, Z. (2017). Reaction of thiosemicarbazide with some divalent ions: Synthesis, characterization, molecular modeling, and evaluation of the catalytic and biological activity of the complexes. *Inorganic and Nano-Metal Chemistry*, *47*(7), 1070–1079.

Shaker, S. A., Farina, Y., & Al-Hamdani, A. A. S. (2009). Synthesis and characterization of mixed ligand complexes of 8-hydroxyquinoline and hydroxylbenzylidene-1-phenyl-2,3-dimethyl-4-amino-3-pyrazolin-5-one with Fe(II), Co(II), Ni(II), and Cu(II) ions. *European Journal of Scientific Research, 33*(4), 702–709.

Wang, Y., Xing, J.,…& Xu, Y. (2015). In silico ADME/T modelling for rational drug design. *Quarterly Reviews of Biophysics*, *48*, 488-515.

Yang, H., Lou, C., Sun, L., Li, J., Cai, Y., Wang, Z., Li, W., Liu, G., & Tang, Y. (2019). admetSAR 2.0 : Web-service for prediction and optimization of chemical ADMET properties. *Bioinformatics*, *35*(6), 1067-1069.

Zhang, P., Peng, J., Xiantion, A., Jing-Quan, S., Hai-Jun, P., Zhu, M., & Wong, Y. (2009). Synthesis and structural characterization of transition metal complexes with Schiff base ligands derived from 2-hydroxy-1-naphthaldehyde and 3-amino-2-methylquinazoline. *Journal of Molecular Structure*, *931,* 50–54.

Author(s) Information

Noura Kichou
Department of Chemistry, Faculty of Sciences, University Mouloud Mammeri of Tizi-Ouzou, Tizi-Ouzou, Algeria
Laboratory of Electrochemistry-Corrosion, Metallurgy and Mineral Chemistry, Faculty of Chemistry, USTHB, BP 32 El Alia, Algiers, Algeria.
Contact e-mail: *noura.kichou@ummto.dz*

Nabila Guechtouli
Université M'Hamed Bougara de Boumerdès, 35000 Algeria

Manel Taferguennit
Laboratory of Electrochemistry-Corrosion, Metallurgy and Mineral Chemistry, Faculty of Chemistry, USTHB, BP 32 El Alia, Algiers, Algeria

Karima Ighilahriz
Laboratory de Physic and Chemistry of Materials LPCM, Departement of Chemistry, Faculty of Sciences, University Mouloud Mammeri, 15000, TiziOuzou, Algeria

To cite this article:

Kichou, N., Guechtouli, N., Taferghennit, M., & Ighilahriz, K. (2025). Synthesis, characterization, and in silico ADMET evaluation of transition metal complexes based on ortho-phenylenediamine and its derivatives. *The Eurasia Proceedings of Science, Technology, Engineering and Mathematics (EPSTEM), 34,* 278-285.

The Eurasia Proceedings of Science, Technology, Engineering & Mathematics (EPSTEM)
ISSN: 2602-3199

The Eurasia Proceedings of Science, Technology, Engineering and Mathematics (EPSTEM), 2025

Volume 34, Pages 286-295

ICBASET 2025: International Conference on Basic Sciences, Engineering and Technology

Enhancing Highway Safety through Intelligent Transportation System

Hillary Makonise
Near East University

Mustafa Alas
Near East University

Abstract: The transportation industry has to deal with two major, ongoing problems: congestion and accidents. These issues pose a serious risk to public safety and could cause fatalities or serious injuries. The transportation industry is predicted to undergo a revolutionary shift with the introduction of Intelligent Transportation Systems (ITS). This research uses a qualitative design to provide a thorough understanding of the factors impacting highway safety and the effectiveness of Intelligent Transportation Systems (ITS). Semi-structured interviews and focus groups with key stakeholders, including tech developers, user groups, and transportation authorities, were conducted during the research. Thematic analysis of the responses was performed using NVivo Software. Key findings show that ITS shows promise in improving traffic flow, raising driver awareness and enabling effective emergency response. Nonetheless, key barriers still exist like data security and infrastructure updates. In line with suggestions from earlier research, the study emphasizes the significance of stakeholder collaboration, public-private partnerships, and capacity building to optimize the potential of ITS.

Keywords: Intelligent transportation system, Highway safety, Traffic

Introduction

The transportation industry has to deal with two major, ongoing problems: congestion and accidents. In addition to being very expensive, these issues pose a serious risk to public safety and could cause fatalities or serious injuries. The transportation industry is predicted to undergo a revolutionary shift with the introduction of Intelligent Transportation Systems (ITS), even if existing solutions have not been able to fully address these problems (Alam et al., 2016). Intelligent transportation systems (ITS) are revolutionizing the field of transportation management by establishing a dynamic, interconnected ecosystem based on data analytics, sensor networks, and cutting-edge communication technologies. The interconnection of this network allows people, vehicles, and infrastructure to share information in real time, increasing the intelligence and responsiveness of the transportation system (Lin et al., 2017).

Traffic congestion and accidents in North Cyprus continue to plague highways, posing a significant threat to public safety and causing economic burdens. Traditional transportation systems have limitations in comprehensively addressing these issues. While the emergence of Intelligent Transportation Systems (ITS) offers a promising solution, several key challenges hinder its widespread adoption and full effectiveness. These challenges include ensuring data security and privacy. The integration of ITS with connected vehicles and the Internet of Things (IoT) necessitates robust cybersecurity measures to protect sensitive data collected from users and the environment (Ibáñez et al., 2015). As ITS integrates connected vehicles and the Internet of Things (IoT) into a vast network, the risk of data breaches and privacy violations rises (Hammi et al., 2018; Ibáñez et al., 2015). To lessen these risks, several tactics are needed. (Hahn et al., 2021) states that encryption is necessary to safeguard data flow between central servers, roadside infrastructure, and automobiles.

Interoperability is necessary for accurate data interchange and communication between different ITS systems in order to effectively exploit this technology. Since ITS components operate separately, creating a connected and responsive transportation ecosystem is more challenging in the absence of a standard language (Lin et al., 2017). Interoperability allows for a broader view of the condition of the roads, which improves the ability of emergency response teams to handle collisions and other crises i.e., prioritizing safety (Alanazi & Alenezi, 2024).

The study will examine specific enhancing highway safety methods by which ITS might improve road safety in North Cyprus. By using qualitative methods, the research will utilize a combination of data collection methods, potentially including semi-structured interviews with key stakeholders like transportation officials, IT specialists, and ITS developers. This study will contribute to the development of a safer and more effective transportation system in the future, by examining the most recent technological developments, pinpointing best practices, and addressing urgent problems.

Method

The research used a qualitative design to provide a thorough understanding of the factors impacting highway safety and the effectiveness of Intelligent Transportation Systems (ITS). Semi-structured interviews and focus groups with key stakeholders, including tech developers, user groups, and transportation authorities, were conducted. Semi-structured interviews were conducted with stakeholders of the North Cyprus government. Qualitative information was gathered from semi-structured interviews with 30 important North Cyprus stakeholders. Among these stakeholders were representatives from the appropriate transportation departments as well as government authorities.

Thematic analysis was used to examine the information acquired in order to investigate how Intelligent Transportation Systems (ITS) might improve road safety. NVivo Software (V14) was used for the thematic analysis, it entails a thorough coding process of interview transcripts in order to find reoccurring themes, patterns, and insightful observations. The initial coding stage of the analysis involved classifying the data segments according to their content. The substance of the participants' experiences and viewpoints on the implementation of ITS and its effect on highway safety will then be captured by further refining these initial codes and organizing them into more comprehensive thematic categories. Participant quotes were then thoughtfully incorporated into the analysis to highlight these major themes and improve the depth and veracity of the conclusions.

Results and Discussion

Government Departmental Representation

Three different sectors of the North Cyprus government departments were for data collection in this study as shown below in Table 1. This allowed for a full understanding of the government's position and opinions regarding the deployment of ITS in North Cyprus.

Table 1. The variety of government agencies that are directly involved in transportation safety and make up the participant pool.

N. Cyprus Govt Departments	Number of Participants
Ministry of transport	13
Department of motor vehicles	8
Other transport stakeholders	9
Total	30

As seen in Table 1 and Figure 1, The Ministry of Transport had the highest representation, with 13 participants 43.33%, followed by the Department of Motor Vehicles with 8 participants 26.66%. Stakeholder organizations and other pertinent transportation departments provided nine participants 30.01%. The diverse departmental participation made it easier to conduct a thorough analysis of the existing transportation environment and potential opportunities for ITS integration across many government departments.

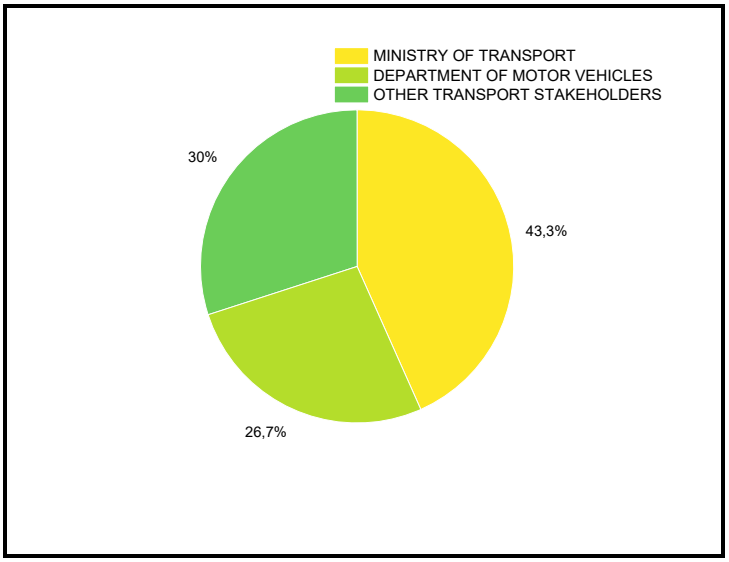

Figure 1.Frequency distribution of the government department representation.

Participant Experience Levels

The participants' varying levels of industrial experience in the transportation sector are shown in Table 2. This range contained enlightening details regarding the practices in place, potential roadblocks, and innovative approaches to use ITS to enhance traffic safety.

Table 2. Participant experience levels

Years of Transport Experience	Number of Participants
0-5 years	6
6-10 years	11
11-15 years	8
16+ years	5
Total	30

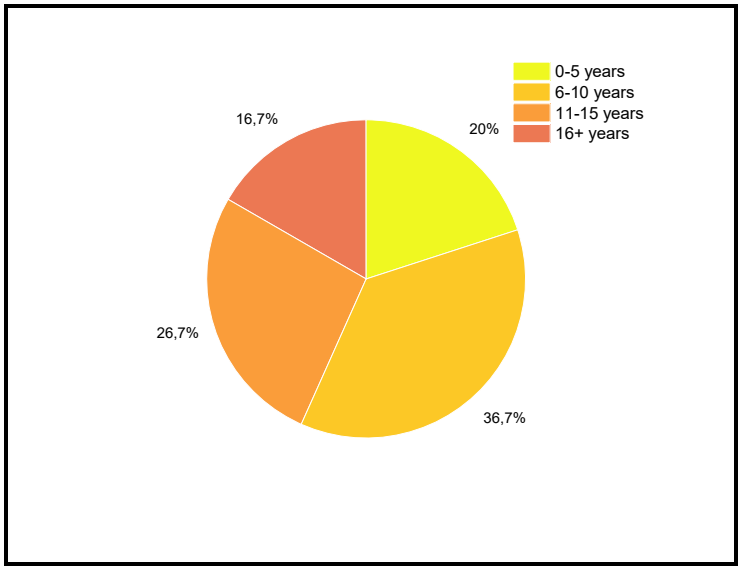

Figure 2. Frequency distribution of participant's years of experience in transport

As seen in Figure 2, of those present, six 20.0% were members of the younger generation of transportation experts, having between 0 and 5 years of experience. Eleven participants 36.66%, who had six to ten years of experience, offered a mid-career perspective on the requirements of transportation management. Eight participants 26.66% had a large amount of experience—between 11 and 15 years. Excellent ideas from both potential areas for innovation and well-established processes were brought with them. Finally, five participants

16.68% said that they had more than 16 years of experience, which enabled them to contribute their wealth of knowledge and enduring perspectives on the topics surrounding transportation safety. This combination of knowledge ensured a deep understanding of the state of the transportation industry and sparked discussions on innovative strategies for enhancing highway safety with ITS. Obtaining the views of stakeholders from a range of government agencies and experience levels, this research was able to gain a comprehensive understanding of the existing state of the transportation industry and its potential for development through the implementation of Intelligent Transportation Systems (ITS).

Data Import and Organization

Interview transcripts from the 30 key participants in North Cyprus were imported and arranged using NVivo software version 14. Significant patterns and trends in the perspectives of the stakeholders about the implementation of ITS and its effects on road safety in North Cyprus were found by looking at the links between various subjects. The results were shown in Table 3 and Table 4.

Table 3. Thematic analysis summary table using Nvivo 14. North Cyprus government transport officials and, stakeholders

Theme	Description	Potential Sub-Themes	Data Source (Codes)
Benefits of ITS for-Highway Safety	This theme explored the perceived advantages of implementing Intelligent Transportation Systems (ITS) for improving highway safety in North Cyprus.	Traffic Flow Optimization, Enhanced Driver Awareness, Improved Emergency Response Times, Data-Driven Safety Strategies	Traffic Management, Driver Assistance Systems, Incident Response, Data Analytics for Safety
Challenges of ITS Implementation	This theme examined the potential obstacles and complexities associated with integrating ITS into the existing transportation infrastructure in North Cyprus.	Infrastructure Upgrade Needs, Data Security and Privacy Concerns, Interoperability between Systems, User Adoption and Public Perception	Infrastructure Modernization, Data Security Measures, System Compatibility, Public Education and Outreach
Strategies for Effective ITS Integration	This theme explored key considerations and recommendations for successfully implementing ITS in North Cyprus.	Public-Private Partnerships, Stakeholder Collaboration, Capacity Building and Training Programs, Long-Term Planning and Investment	Partnership Models, Stakeholder Engagement, Workforce Development, Strategic Planning and Funding
Impact of ITS on-Transportation Stakeholders	This theme investigated the potential impact of ITS on various transportation stakeholders in North Cyprus, including government agencies, transportation authorities, and users.	Improved Efficiency for Transportation Departments, Enhanced Communication and Collaboration, User Benefits and Potential Challenges	Operational Efficiency, Information Sharing, User Convenience, Privacy Concerns

Table 3 above illustrates the thematic analysis summary for the interviewed transport officials of North Cyprus government, stakeholders and responsible sectors in the transport system of the government. The officials are in charge with the Intelligent Transportation Systems (ITS) in North Cyprus and are outlined in the NVivo 14 thematic analysis summary table that follows. Though it will consider all departments, this analysis concentrated on what the participants contributed during the interviews which were made. "Benefits of ITS for-Highway Safety," the first topic of the Intelligent Transportation Systems, highlights the potential advantages such as faster emergency response times, increased driver awareness thanks to enhanced warning systems, and more efficient traffic flow.

Table 4. Coding queries and visualization in Nvivo. North Cyprus government transport officials and, stakeholders

Objective	Coding Query	Expected Visualization
Investigate Benefits of ITS for-Highway Safety	Codes: Traffic Flow Optimization, Enhanced Driver Awareness, Improved Emergency Response Times	Word Cloud
Explore Challenges of ITS Implementation	Codes: Infrastructure Upgrade Needs, Data Security and Privacy Concerns, Interoperability between Systems	Cluster Analysis
Examine Strategies for Effective ITS Integration	Codes: Public-Private Partnerships, Stakeholder Collaboration, Capacity Building and Training Programs	Crosstabulation

Analyzing Stakeholder Opinions Regarding ITS Implementation

The NVivo software coding queries and visualizations shown in this table are designed to elicit more specific information regarding the Intelligent Transportation Systems (ITS) installation from North Cyprus transport officials' interviews. These questions and visualizations, which especially highlight the perspectives of government leaders who are closely involved in traffic safety, will provide a more thorough understanding of the main ITS themes.

Revealing the Presumed Benefits of ITS

Analyzing the "Benefits of ITS for-Highway Safety," the first search query examines codes pertaining to "Traffic Flow Optimization," "Enhanced Driver Awareness," and "Improved Emergency Response Times." The next step will be to create a Word Cloud representation. The most notable advantages that the respondents' thought was connected to ITS will be highlighted through a visual representation of the frequency of these coded terms. By means of an extensive examination of the Word Cloud, we are able to ascertain the particular advantages that are most important to the transportation officials.

Identifying Challenges and Potential Relationships

The second inquiry focuses on the "Challenges of ITS Implementation" by looking at codes such as "Infrastructure Upgrade Needs," "Data Security and Privacy Concerns," and "Interoperability between Systems." In this instance, a cluster analysis will be carried out. This analysis's goal is to identify potential pairings for these challenges. The visualization may point up areas where issues might be connected to one another or, by highlighting underlying patterns or connections between the coded situations, require a multidisciplinary approach to be solved. For example, the Cluster Analysis may identify a cluster between data security concerns and infrastructure enhancements, suggesting that certain infrastructure modifications may also address data security threats.

Analyzing Methods for Successful Integration

The study using categories like "Public-Private Partnerships," "Stakeholder Collaboration," and "Capacity Building and Training Programs," the third question is all about "Strategies for Effective ITS Integration." Subsequently, a crosstabulation will be executed to examine potential correlations between these strategies. The sectors highlighted in this picture stand to gain the most from collaboration or a combination of approaches. For instance, the Crosstabulation may reveal a strong correlation between public-private partnerships and stakeholder participation, suggesting that combining these approaches may be the most effective course of action.

With the help of these coding searches and visualizations, we may be able to discover a great deal about the opinions of North Cyprus transport officials regarding the implementation of ITS. By illuminating the perceived benefits of Intelligent Transportation Systems (ITS), as well as the primary challenges and potential solutions for a cooperative and successful integration process, the study seeks to increase highway safety in North Cyprus.

Table 5. Transcript analysis table using NVivo (North Cyprus ITS stakeholder ınterviews) transcript analysis table using NVivo (North Cyprus ITS stakeholder interviews

Theme	Participant Quotes	Sub-themes
Benefits of ITS for-Highway Safety	Participant 1: "Optimizing traffic flow through intelligent systems can significantly reduce congestion and accidents." (Traffic Flow Optimization)	Traffic Management
	Participant 18: "Advanced driver-assistance systems can warn drivers of potential hazards, improving overall awareness and reaction times." (Enhanced Driver Awareness)	Driver Assistance Systems
	Participant 23: "Real-time data from ITS can be used to streamline emergency response, potentially saving lives." (Improved Emergency Response Times)	Data-Driven Safety Strategies
	Participant 7: "Integration with weather forecasting systems can allow for proactive measures to address hazardous road conditions." (Weather Integration and Safety)	Advanced Safety Applications
Challenges of ITS Implementation	Participant 10: "Upgrading our existing infrastructure may be necessary to accommodate new technologies." (Infrastructure Upgrade Needs)	Infrastructure Modernization
	Participant 15: "Data security and privacy concerns require robust safeguards to ensure public trust." (Data Security and Privacy Concerns)	Data Security Measures
	Participant 28: "Ensuring compatibility between different ITS systems from various vendors is crucial for seamless operation." (Interoperability between Systems)	System Compatibility
	Participant 4: "Public education and outreach programs are essential to promote user adoption and address potential concerns." (User Adoption and Public Perception)	User Education and Awareness
Strategies for Effective ITS Integration	Participant 12: "Public-private partnerships can leverage expertise and resources for a successful implementation." (Public-Private Partnerships)	Partnership Models
	Participant 25: "Collaboration among stakeholders, including government agencies and transportation authorities, is vital." (Stakeholder Collaboration)	Stakeholder Engagement
	Participant 2: "Investing in capacity building and training programs will equip our workforce with the necessary skills." (Capacity Building and Training Programs)	Workforce Development
	Participant 20: "Long-term planning and dedicated funding are essential for sustained ITS development." (Strategic Planning and Funding)	Strategic Implementation Approach
Impact of ITS on-Transportation Stakeholders	Participant 9: "Improved efficiency through data-driven insights on traffic patterns can optimize resource allocation." (Improved Efficiency for Transportation Departments)	Operational Efficiency
	Participant 17: "Real-time information sharing between agencies can enhance communication and collaboration on incident response." (Enhanced Communication and Collaboration)	Information Sharing and Coordination
	Participant 27: "ITS can offer user benefits like reduced travel times and improved navigation, but privacy concerns need to be addressed." (User Benefits and Potential Challenges)	User Convenience and Privacy Considerations
	Participant 3: "Transparency and clear communication about data usage are crucial to maintain public trust." (Public Trust and Transparency)	Public Engagement and Transparency

Table 5 above summarizes the research key findings from an examination of thirty transportation stakeholders in North Cyprus who participated in interviews regarding Intelligent Transportation Systems (ITS). The "Benefits of ITS for-Highway Safety" section lists potential advantages such improved traffic flow, quicker emergency response times due to real-time data, and increased driver awareness thanks to advanced warning systems.

The data analysis chapter examined the potential benefits of Intelligent Transportation Systems (ITS) for enhancing traffic safety in North Cyprus. The qualitative methodology included semi-structured interviews and focus groups with thirty key stakeholders, the majority of whom were from the Ministry of Transportation. Thematic analysis was used to identify recurring themes in the qualitative data, and it was made possible via the NVivo program.

According to data-driven goals for highway safety, the investigation revealed that ITS should be used to enhance traffic flow, raise driver awareness via AWS, and shorten emergency reaction times. However, there were also reported challenges with ITS implementation. Upgrading the current infrastructure, ensuring that robust data security and privacy protections are in place, and guaranteeing that various ITS systems are interoperable with one another were the three main challenges to solve.

Another important element that was recognized was raising user adoption through outreach and public education programs. Key recommendations for an effective integration of ITS were looked at in the analysis. Stakeholder cooperation was seen as crucial for a coherent plan, and public-private partnerships were acknowledged as a means of optimizing knowledge and resources. It was found that in order to provide the workforce with the knowledge and skills necessary to effectively manage and deploy ITS, funding was needed for capacity building and training efforts. It was mentioned that committed funding and long-term planning were required for greatest impact and continuous expansion.

Finally, an examination of the potential effects of ITS on various transportation stakeholders was conducted. Through better resource allocation, data-driven insights on traffic patterns can support the operations of government organizations such as the Ministry of Transport. Agency-to-agency coordination and communication during incident response can be enhanced via ITS-enabled real-time information sharing. Benefits like quicker travel times and improved navigation are anticipated by customers, but preserving public confidence in the face of privacy issues requires careful consideration and honest dialogue. In conclusion, our data analysis demonstrates how ITS might raise traffic safety in North Cyprus. By identifying the challenges and implementing successful integration strategies, stakeholders may use ITS to make transportation safer and more efficient for everyone

Discussion

The data analysis that comes before it demonstrates a complex interplay of opportunities and challenges related to the application of Intelligent Transportation Systems (ITS) for improving road safety. It is based on qualitative research with significant stakeholders in North Cyprus through semi-structured interviews and focus groups. One important finding that is consistent with previous study on ITS installation (Alam et al., 2016) is the identification of ITS as a potential catalyst for improved traffic flow, greater driver awareness (Arena et al., 2020), and quicker emergency response (Guerrero-Ibáñez et al., 2018). These benefits align with the larger goal of lowering crashes and traffic fatalities in North Cyprus. However, the analysis also points out the critical problems that must be fixed for ITS integration to be successful. The primary obstacles include upholding robust privacy and data security measures (Ibáñez et al., 2015) modernizing the existing infrastructure (Ibáñez et al., 2015), and guaranteeing seamless interoperability between different ITS systems (Lin et al., 2017).

These findings corroborate earlier research on the challenges associated with ITS implementation. The importance of public-private partnerships, capacity building initiatives, and stakeholder cooperation is emphasized in the report. These strategies are essential for addressing the identified problems and ensuring a seamless upgrade to a more advanced transportation system. This is in line with earlier research that emphasizes the value of stakeholder cooperation and participation in the deployment of ITS (Ibáñez et al., 2015).

The paper also stresses how crucial it is to have committed funding and long-term planning in order to promote the advancement and application of ITS. This result is consistent with a greater number of studies on how ITS policies and infrastructure have changed over time (Alam et al., 2016; Ibáñez et al., 2015). Even though ITS has a lot of potential benefits, it's vital to think about how it can affect various stakeholders. Previous studies (Alam et al., 2016) have demonstrated that government organizations can benefit from enhanced efficiency and data-

driven decision-making. Strong data privacy laws must, however, be implemented in tandem with ITS deployment in order to maintain public confidence. This is consistent with the concerns raised in another research (Ibáñez et al., 2015).

According to earlier studies on the implications of ITS users, consumers should anticipate advantages including better navigation and faster journey times as end users of ITS (Arena et al., 2020). The study provides unique insights into the context of North Cyprus, which broadens the body of knowledge currently known in the field of ITS. The findings highlight the potential for Intelligent Transportation Systems (ITS) to increase traffic safety, but they also highlight significant challenges and potential solutions for ITS's broad implementation. This study contributes to the growing body of literature on ITS by providing empirical data on the benefits and challenges of adopting ITS in a specific institutional and geographic situation.

Focusing on five main objectives, this study aimed to determine how Intelligent Transportation Systems (ITS) could improve highway safety in North Cyprus: strengthening data security and privacy; improving infrastructure integration, assessing interoperability; finding deep learning applications, and, lastly, evaluating the total potential of ITS for increased safety. The research's conclusions greatly advance our understanding of these fields. The study emphasized the vital necessity for strong protocols to safeguard sensitive data while enabling ITS functionality in terms of data security and privacy. This immediately tackles the first goal and emphasizes how crucial it is to strike a balance between innovation and consumer trust. In line with the second goal, the examination of infrastructure integration showed that strategic planning and investment were required. Interoperability issues were also noted, highlighting the necessity of cooperation and standards to guarantee smooth system integration.

In addition, the investigation looked into the possibilities for deep learning uses, which helped with the fourth goal. Examining the views of important stakeholders, the study directly addressed the main goal of determining if ITS could improve highway safety by offering insightful information about the possible advantages, difficulties, and solutions related to ITS deployment. The stated goals and objectives of this research have been significantly met. The report provides insightful information for policymakers, transportation authorities, and technology developers looking to maximize the use of ITS for increased highway safety by analyzing the challenges of ITS adoption in the North Cyprus setting.

The discussion chapter examined a qualitative examination of information gathered from thirty important North Cyprus transportation sector players through interviews. The study aimed to investigate the potential of Intelligent Transportation Systems (ITS) in improving highway safety through the application of thematic analysis. Results show that ITS has potential for enhancing driver awareness, streamlining traffic flow, and enabling effective emergency response. But interoperability problems, data security worries, and infrastructural constraints turned out to be major roadblocks to the widespread use of ITS. The study highlights the necessity of strategic planning, stakeholder participation, and significant investments in infrastructure and human resources in order to fully exploit the promise of ITS.

Conclusion

The previous data study examined the intricacies of implementing Intelligent Transportation Systems (ITS) in North Cyprus, with a particular emphasis on the viewpoints of stakeholders and the possible effects on traffic safety. Key findings show that ITS shows promise in improving traffic flow, raising driver awareness (Arena et al., 2020), and enabling effective emergency response. These findings are consistent with earlier studies (Alam et al., 2016). Nonetheless, key barriers included in (Lin et al., 2017), data security (Ibáñez et al., 2015), and infrastructure updates (Ibáñez et al., 2015). In line with suggestions from earlier research, the study emphasizes the significance of stakeholder collaboration, public-private partnerships, and capacity building to optimize the potential of ITS (Ibáñez et al., 2015).

Although there are clear potential advantages of ITS, it is imperative to address issues like data protection and user acceptance (Ibáñez et al., 2015). By presenting actual data on the challenges and opportunities involved in ITS adoption in the North Cyprus environment, this study adds to the expanding corpus of information on ITS deployment. Future studies should examine the long-term effects of ITS, taking into account both its social and environmental ramifications. It would also be advantageous to look into how cutting-edge technologies like artificial intelligence and the Internet of Things may improve ITS capabilities.

Recommendations

To fully exploit the potential of ITS, further research is necessary due to its dynamic nature and complexity. Subsequent research endeavours may investigate the enduring consequences of information technology integration on diverse facets of the community, such as financial progress, ecological durability, and fairness in society. It's also critical to look into how new technologies like artificial intelligence and the Internet of Things might improve ITS capabilities. Additionally, carrying out comparative analyses among various nations or areas may offer insightful information regarding the applicability of ITS best practices. Policymakers and practitioners could learn a lot from studying the experiences of early ITS users. The field of ITS can advance and aid in the creation of safer and more effective transportation systems by pursuing various research avenues.

Scientific Ethics Declaration

* The authors declare that the scientific ethical and legal responsibility of this article published in EPSTEM Journal belongs to the authors.

* Hereby declare that all information, documents, analysis and results in this article have been collected and presented according to the academic rules and ethical guidelines of Institute of Graduate Studies, Near East University. I also declare that as required by these rules and conduct, I have fully cited and referenced information and data that are not original to this study.

Conflict of Interest

* The authors declare that they have no conflicts of interest

Funding

* This research received no specific grant from any funding agency in the public, commercial, or not-for-profit sectors

Acknowledgements or Notes

* This article was presented as an oral presentation at the International Conference on Basic Sciences, Engineering and Technology (www.icbaset.net) held in Trabzon/Türkiye on May 01-04, 2025.

References

Alam, M., Ferreira, J., & Fonseca, J. (2016). Introduction to ıntelligent transportation systems. *Studies in Systems, Decision and Control*, *52*, 1–17.

Alanazi, F., & Alenezi, M. (2024). Interoperability for intelligent traffic management systems in smart cities. *International Journal of Electrical and Computer Engineering (IJECE)*, *14*(2), 1864–1874.

Arena, F., Pau, G., & Severino, A. (2020). A review on IEEE 802.11p for ıntelligent transportation systems. *Journal of Sensor and Actuator Networks, 9*(2), 22.

Guerrero-Ibáñez, J., Zeadally, S., & Contreras-Castillo, J. (2018). Sensor technologies for ıntelligent transportation systems. *Sensors,* (4), 1212.

Hahn, D., Munir, A., & Behzadan, V. (2021). Security and privacy issues in intelligent transportation systems: Classification and challenges. *IEEE Intelligent Transportation Systems Magazine*, *13*(1), 181–196.

Hammi, B., Khatoun, R., Zeadally, S., Fayad, A., & Khoukhi, L. (2018). IoT technologiesfor smart cities. *IET Networks*, *7*(1), 1–13.

Ibáñez, J. A. G., Zeadally, S., & Contreras-Castillo, J. (2015). Integration challenges of intelligent transportation systems with connected vehicle, cloud computing, and Internet of Things technologies. *IEEE Wireless Communications*, *22*(6), 122–128.

Lin, Y., Wang, P., & Ma, M. (2017). Intelligent transportation system(ITS): Concept, challenge and opportunity. *2017 IEEE 3rd International Conference on Big Data Security on Cloud*

(BigDataSecurity), IEEE International Conference on High Performance and Smart Computing, (HPSC).

Author(s) Information

Hillary Makonise
Near East University
Faculty of Civil Engineering Department
Nicosia, North Cyprus
Contact e-mail: *hilmack@icloud.com*

Mustafa Alas
Near East University
Faculty of Civil Engineering Department
Nicosia, North Cyprus

To cite this article:

Makonise, H., & Alas, M. (2025). Enhancing highway safety through intelligent transportation system. *The Eurasia Proceedings of Science, Technology, Engineering and Mathematics (EPSTEM), 34,* 286-295.

The Eurasia Proceedings of Science, Technology, Engineering & Mathematics (EPSTEM)
ISSN: 2602-3199

The Eurasia Proceedings of Science, Technology, Engineering and Mathematics (EPSTEM), 2025

Volume 34, Pages 296-303

ICBASET 2025: International Conference on Basic Sciences, Engineering and Technology

Preparation, Identification, and Antioxidant Activity of Some New Transition Metal Complexes of Curcumin with Mono-and Bidentate Ligands

Omar Berradj
Mouloud Mammeri University of Tizi-Ouzou

Hadda Bougherra
Mouloud Mammeri University of Tizi-Ouzou

Abstract: Eight ternary copper (II) and nickel (II) complexes of curcumin (Cur) [1,7-bis(4-hydroxy-3-methoxyphenyl)-1,6-heptadiene-3,5-dione] as a primary ligand, o-phenylenediamine (OPD), dimethylglyoxime (H_2dmg), tryptophan (Tryp), bromoaniline (Br-Ani) or thymine (Thy) as a secondary ligand have been prepared and characterized by melting point, conductivity, infrared and electronic spectra. The complexes obtained are stable powders at room temperature, soluble in DMSO and are non-electrolyte. The IR and UV-vis spectroscopic analysis revealed that the complexes adopt either octahedral, tetrahedral or square planar geometry. All the ligands are bound to the cations Cu(II) and Ni(II) via the nitrogen and oxygen atoms. The synthesized compounds were screened for their in-vitro antioxidant activities using 2,2-diphenyl-1-picrylhydrazyl radical (DPPH·) free radical scavenging. The results obtained show that these complexes have a good antioxidant activity in comparison with ascorbic acid as positive control. These observations suggest the possibility of using the complexes as antioxidant agents to solve the problems linked to the presence of free radicals in living organisms.

Keywords: Complex, Curcumin, Ligand, Spectroscopic analysis, Antioxidant activity

Introduction

Metal bound organic compounds are known to possess potential activities in the areas of biological, clinical, analytical, catalytic, microbial, insecticidal, antibiotic, growth factors, food additive, tumor inhibitor, cell division etc. This is due to either the unused coordination sites present on the metal and ligand systems, or due to the selective oxidation state of the complexed metal ions in the coordination sphere (Cotton &Wilkinson, 1996). Scientific researches spanning over more than four decades have confirmed the diverse pharmacological effects of curcumin and established its ability to act as a therapeutic agent for several diseases (Gubendran, 2016).

The chemistry for oxime metal complexes has been investigated actively since the first synthesis of nickel (II) dimethylglyoximate and recognition of the chelate (Erdem-Tuncmen & Karipcin, 2012). Copper (II) complexes with dimethylglyoxime are known for their high stability, but their biological activity has been very scarcely studied (Bougherra et al., 2018). Metal-based antioxidants have captured outlook recently for their receptivity to concerve organisms and cells from harm induced by oxidative stress or scavenge free radicals (Mahadi- Hasan et al., 2021).

This paper describes the synthesis and the charcterization of eight new metal transition complexes of curcumin as a primary ligand and some mono-and bidentate organic compounds as secondary ligands. The antioxidant

activity is evaluated by DPPH radical scavenging activity using ascorbic acid as positive control. The aim of this studies is to examine in vitro the capacity of these complexes to inhibit free radicals present in living organism.

Method

Curcumin (Cur) and all the secondary ligands (o-phenylenediamine (OPD), dimethylglyoxime (H_2dmg), tryptophan (Tryp), bromoaniline (Br-Ani) and thymine (Thy)) were purchased from commercial sources and used as received. Other chemical reagents of reagent grade were used without purification. Melting points were measured using a melting point SMP30. The conductivity measurements are determined using a CONSORT C3030 standard at room temperature in 10^{-3} M solutions of the complexes in DMSO. IR spectra were recorded in the pure, undispersed solid state in a SHIMADZU IRAffinity-1S spectrometer at room temperature holder in the range 4000-400 cm^{-1}. The electronic absorption spectra in DMSO solution were recorded on a thermo-scientific, Evolution 220 UV-visible spectrophotometer in the 900-200 nm range.

Synthesis of Complexes

The solvent used in all reactions is ethanol. The experimental equipment consists of a heating tank topped with a column with cold water circulation to prevent the loss of matter. The reagents are kept under constant stirring at a temperature of 60°C until a solid precipitate was obtained, collected by filtration through a sintered glass filter and washed. Successively with water and ethanol to remove all traces of metal or ligand, then with ethyl ether and left to dry. Three complexes were synthesized by substitution method, whereas five have been prepared by addition method.

Copper(II) Complexes

$[Cu(Cur)_2Br_2] + H_2dmg \rightarrow [Cu(Cur)_2(H_2dmg)]$ **Complex 1**
$[Cu(Trp)_2] + Cur \rightarrow [Cu(Cur)(Trp)]$ **Complex 2**
$Cu(NO_3)_2, 3H_2O + Br\text{-}Ani + Cur \rightarrow [Cu(Cur)(Br\text{-}Ani)_2]$ **Complex 3**
$Cu(NO_3)_2, 3H_2O + OPD + Cur \rightarrow [Cu(Cur)(OPD)]$ **Complex 4**

Nickel(II) Complexes

$[Ni(Hdmg)_2] + Cur \rightarrow [Ni(Cur)(Hdmg)_2]$ **Complex 5**
$Ni(NO_3)_2, 6H_2O + Trp + Cur \rightarrow [Ni(Cur)_2(Trp)]$ **Complex 6**
$Ni(NO_3)_2, 6H_2O + Br\text{-}Ani + Cur \rightarrow [Ni(Cur)(Br\text{-}Ani)_2]$ **Complex 7**
$Ni(NO_3)_2, 6H_2O + Thy + Cur \rightarrow [Ni(Cur)(Thy)]$ **Complex 8**

Antioxidant Activity

Antioxidant activity of the synthesised compounds was evaluated by DPPH (Figure 1) radical scavenging effect. The 2,2-diphenyl-1-picrylhydrazyl radical (DPPH) is a stable free radical, which has been widely accepted as a tool for estimating the free radical scavenging activities of potential antioxidants (Brand-Williams & Cuvelier, 1995). The antioxidant capacity of the complexes was evaluated by the method of Wang et al. (Wang & Rangarajan, 1998). The diluted working solutions of the test compounds were prepared in DMSO. Ascorbic acid was used as positive control in 0.5-100 mmol/l solution. 0.002% of DPPH was prepared in ethanol and 2 ml of this solution was mixed with 40 ml of test compounds at different concentrations. The reaction mixture was incubated in the dark at room temperature for 30 min. The DPPH radical scavenging activity was determined by measuring the absorbance at 517 nm using the UV-vis spectrophotometer. The DPPH radical scavenging activity of ascorbic acid was also assayed for comparison. The absorbance was recorded and radical scavenging activity was expressed as percentage inhibition of DPPH radical and was calculated by the following equation (Embarek, 2005):

% Inhibition = $[A_0\text{-}A/A_0] \times 100$, where A_0 is the absorbance of the negative control; and A is the absorbance of the test compounds.

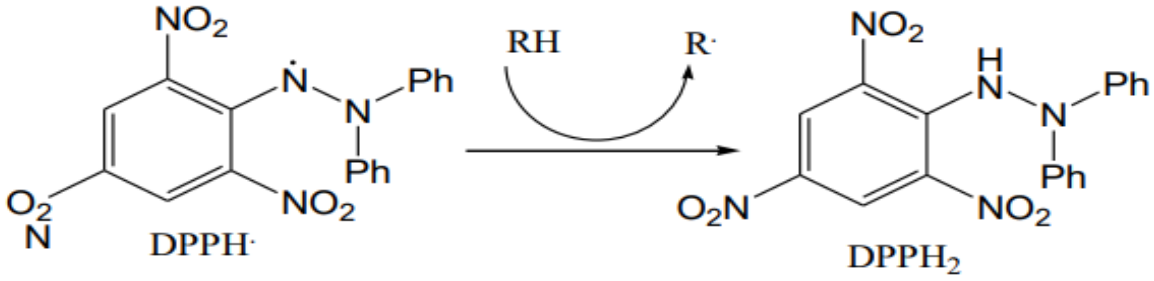

Figure 1. Reduction of the DPPH radical• (DPPH• + RH→ DPPH-H + R)

Results and Discussion

Physical Properties and Analytical Data

The physical properties and analytical data of the synthesized complexes are summarized in Table 1. The compounds are obtained in solid state; they are stable in air and at room temperature. Their melting points are above 165°C. All the complexes are insoluble in water, ethanol, and methanol, slightly soluble in the mixture water-ethanol, and soluble in dimethylsulfoxide. The nonelectrolyte nature of the complexes was confirmed by the low molar conductance values measured at 25°C (10^{-3} M) in DMSO solution.

Table 1. Characteristic and analytical data of complexes

Complex	Mol. Wt (g/mol)	Color	Yield (%)	M.P. (°C)	Λm (Ω^{-1}.cm ².mol^{-1})
[Cu(Cur)$_2$ (H_2dmg)]	916,42	Black	46,67	>350	14,50
[Cu(Cur)(Trp]	636,15	Black	66,7	>350	20,3
[Cu(Cur)(Br-Ani)$_2$]	663,95	Dark gray	14	>350	6,60
[Cu (Cur)(OPD)]	540,06	Light brown	62	254	3,31
[Ni(Cur)(Hdmg)$_2$]	659,31	Dark pink	42	318	2,50
[Ni (Cur)$_2$(Trp)]	999,68	Brown	94	>350	40,2
[Ni(Cur)(Br-Ani)$_2$]	771,13	Grayish white	52	>350	3,24
[Ni(Cur)(Thy)]	553,18	Orange	47	165	5,90

Spectroscopic Studies

FT-IR Spectra

The spectral data of the free ligands are given in Table 2. In the IR spectrum of free Curcumin, the absorption bands at 3505, 1629, 1504 and 1425 cm^{-1} are assigned respectively to ν(O-H)$_{enol}$, ν$_{as}$(C=O), ν(C=C) and δ(C-O)$_{enol}$ (Refat, 2013). The IR spectrum of free H_2dmg shows a broad band at 3196 cm^{-1} assigned to OH group of oxime, a medium intense band at 1436 cm^{-1} characteristic of C=N streching vibration, and a deformation band at 1135 cm^{-1} of N-O (Adkhis et al., 2017; Bougherra et al., 2018).

The infrared spectrum of tryptophan exhibits a band at 3404 cm^{-1} which is attributed to the ν (N-H) stretching vibration frequency of the indole heterocycle. The symmetric and asymmetric ν(NH_3^+) vibration bands appeared, respectively, at 3037 and 3081 cm^{-1} (Rabindra & Mohan, 2000). The IR spectrum of Br-Ani shows two absorption bands at 3473 and 3381 cm^{-1} assigned to the asymmetric and symmetric vibrations of the NH_2 group, respectively (Adkhis et al., 2017). Two other peaks are also observed at 1274 and 1607 cm^{-1} which correspond, respectively, to the ν(C-NH_2) frequency and the ν(C=C) frequency (Afraa, 2017).

In the OPD spectrum, the bands observed at 3185-3373 cm^{-1} are due to NH_2 and N-H vibrations, respectively. On the other hand, the band corresponding to the frequency of ν(C=C) is located at 1626 cm^{-1} (Bougherra et al., 2018). The spectrum of thymine shows two bands at 1672 cm^{-1} and 1752 cm^{-1} which are assigned to streching vibration of C=O group (Adkhis et al., 2017).

Table 2. IR spectra data of ligands (cm^{-1})

Ligand	Cur	H_2dmg	Tryp	Br-An	OPD	Thy
ν(O-H)	3505	3196	-	-	-	-
ν(N-H)	-	-	3404	-	3373	-
ν(NH_2)	-	-	-	3473, 3381	3185	-
ν(NH_3^+)	-	-	3037, 3081	-	-	-
ν(C=O)	1629	-	-	-	-	1725, 1672
ν(C=N)	-	1463	-	-	-	-
ν(C=C)	1504	-	-	1607	1626	-
δ(CH)	1271	-	-	-	-	1384
$\delta(C\text{-}O)_{phe}$	1425	-	-	-	-	-
δ(C-NH_2)	-	-	-	1274	1262	-
δ(NO)	-	1135	-	-	-	-

The IR spectra of the complexes show a band in the region 3502-3520 cm^{-1}. This band exists at almost the same frequency in free curcumin, indicating that the OH group is not involved in the complexation. All the other characteristic bands of free curcumin ν(C=O), $\delta(C\text{-}O)_{enol}$, ν(C=C), are displaced in the IR spectra of their complexes. The band at 1436 cm^{-1} of dimethylglyoxime assigned to (C=N) of the oxime is shifted to a higher frequency at 1504 cm^{-1} in complex 1 and at 1567 cm^{-1} in complex 5. Whereas the band observed at 1135 cm^{-1} which due to δ(N-O) of the oxime group is shifted in complex 1 to 1152 cm^{-1} and to 1225 cm^{-1} in complex 5. New bands appear in the region 518-522 cm^{-1} and 432-454 cm^{-1} which can be attributed to ν(M-O) and ν(M-N) respectively. This means that the coordination of curcumin with Cu(II) and (Ni) is carried out with the oxygen of the carbonyl groups in the enol form and by the nitrogen atom of the oxime function for H_2dmg (Table 3).

The vibrational frequency band ν(NH) of free tryptophan observed at 3404 cm^{-1} was shifted to lower frequencies at 3366 and 3373 cm^{-1} in complexes 2 and 6. On the other hand, that of ν(NH_3^+) was shifted to higher wavenumbers in these complexes, 1149 and 1139 cm^{-1}. Two new bands appear at 564-565 cm^{-1} and 458-482 cm^{-1} which correspond, respectively, to the M-O and M-N bonds attests that the Cu(II) and Ni(II) are coordinated to the ligands via the oxygen and nitrogen atoms (Refat, 2013; Ismail et al., 2014).

The bands at 3464 and 3373 cm^{-1} assigned to the asymmetric and symmetric stretching vibration ν(NH_2) in complex 3 and the band at 3409 cm-1 corresponding to the frequency ν(NH_2) in complex 7 (Figure 2) indicate the presence of bromoaniline in these two complexes (Adkhis et al., 2017). Thus the appearance of new bands at 530-566 cm^{-1} and in the region 456-489 cm^{-1} corresponding respectively to the frequencies ν(M-O) and ν(M-N).

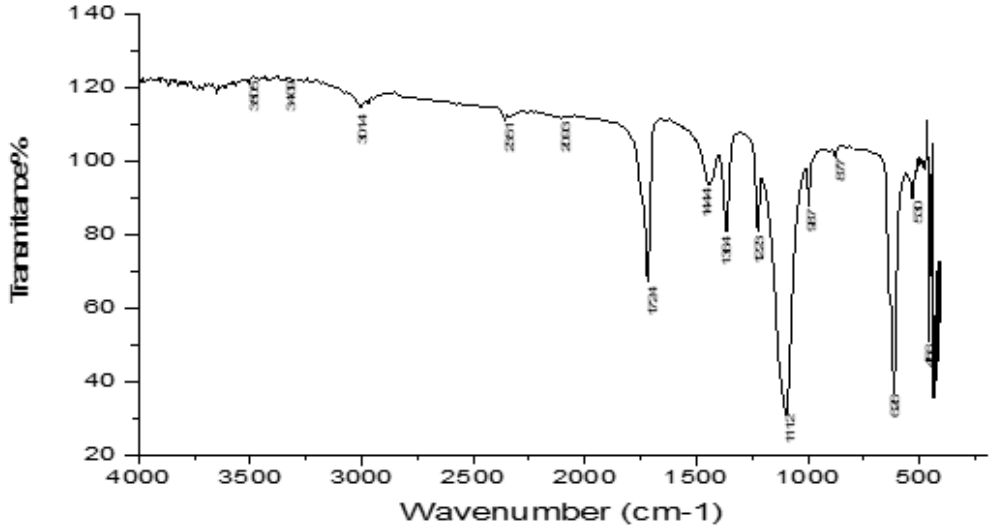

Figure 2. IR spectrum of [Ni(Cur)(Br-Ani)$_2$]

The IR spectrum of the complex 4 with OPD exhibits a characteristic band due to the N-H stretching vibration of the OPD ligand at 3352 cm^{-1}. On the other hand, the band corresponding to the ν(C=C) vibrational mode for complex 4 is clearly shifted to a lower frequency compared to that of free OPD which is located at 1494 cm-1. The bands in the region 1620-1578 cm^{-1} can be attributed to the C=O stretching vibration of curcumin and thymine coordinated in complex 8 (Adkhis et al., 2017). Two new bands appear at 545 and 462 cm^{-1} can be attributed to M-O and M-N vibrations, respectively.

Table 3. IR spectra data of Cu(II) and Ni(II) complexes (cm^{-1})

Complex	1	2	3	4	5	6	7	8
ν(O-H)	3514	3519	3514	3515	3519	3502	3505	3520
ν(N-H)	-	3366	-	3352	-	3452	-	-
ν(NH_2)	-	-	3464, 3373	-	-	-	3409	-
ν(NH_3^+)	-	3149	-	-	-	3139	-	-
ν(C=O)	1584	1613	-	1600	1567	1572	1724	1620, 1578
ν(C=N)	1453	-	-	-	1436	-	-	-
ν(C=C)	1504	1494	1578	1494	-	1488	-	1516
δ(CH)	1260	1285	-	-	-	-	1364	1362
$\delta(C\text{-}O)_{phe}$	1419	1397	1383	1411	1368	1417	1444	1411
δ(C-NH_2)	-	-	1278	1264	-	-	-	-
δ(NO)	1152	-	-	-	1225	-	-	-
ν(Cu-O)	522	567	566	573	-	-	-	-
ν(Cu-N)	454	482	489	482	-	-	-	-
ν(Ni-O)	-	-	-	-	518	567	530	545
ν(Ni-N)	-	-	-	-	432	458	456	462

UV-Visible Spectra

The spectrum of curcumin shows two bands, one in the ultraviolet region at 267 nm, attributed to the π → π * transition, and another in the visible region at 436 nm which is attributed to the n→π * transition. The spectrum of dimethylglyoxime contains one band in the ultraviolet at 269 nm corresponding to the π → π * transition (Bensiradj &Tidjani-Rahmouni, 2014). Electronic absorption data of all the ligands are given in the Table 4.

Table 4. Electronic spectra data of ligands

Ligand	Cur	H_2dmg	Tryp	Br-An	OPD	Thy
λ (nm)	267	269	291	283	269	273
	436			307	305	
Transition	π → π *	π → π *	π → π *	π → π *	π → π *	π → π *
	n → π *			π → π *	π → π *	

All complexes display a band in the 437-377 nm region (Table 5), this band is attributed to a charge transfer transition from the ligand to the metal (Amira et al., 2008). Copper (II) complexes 1, 2, and 3 exhibit two bands between 564 and 771 nm corresponding to the d-d transition; these transitions characterize a square-planar geometry. The electronic absorption spectrum of complex 4 exhibited two bands in the visible spectrum, the first at 556 nm and the second at 734 nm, attributed to the d-d transition.

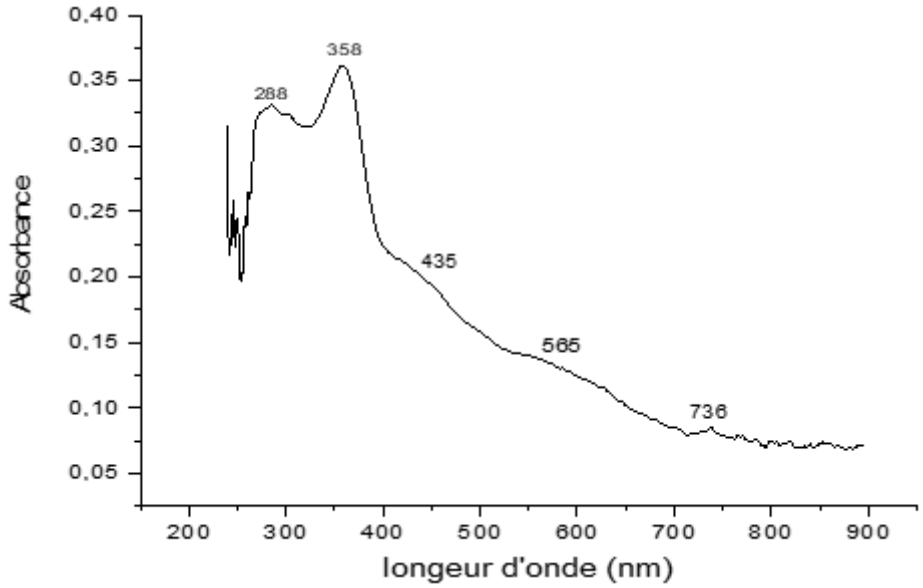

Figure 3. Electronic absorption spectrum of [Ni(Cur)(Br-Ani)$_2$]

Complexes 5 and 6 showed three bands in the visible range around 500 to 800 nm corresponding to the d-d transition. These transitions are characteristic of nickel complexes in an octahedral field (Refat, 2013). The complex 7 exhibits two bands, one at 565 nm and another at 736 nm (Figure 3) which correspond to the d-d transition, and conforms to a square-planar geometry. The electronic spectrum of complex 8 shows a broad band at 436 nm corresponding to the d-d transition which can be masked by the charge transfer transition, because they appear in the same area and whose geometry is tetrahedral.

Table 5. Electronic spectra data of complexes

Complex	1	2	3	4	5	6	7	8
λ (nm)	272	269	274	267	266	274	288	269
	320	361	363	310	320	364	358	303
	387	437	431	426	377	427	435	436
	564	585	505	556	582	569	565	
	641	730	771	734	681	740	736	
					796	819		
Transition	π → π *	π → π *	π → π *	π → π *	π → π *	π → π *	π → π *	π → π *
	π → π *	π → π *	π → π *	π → π *	π → π *	π → π *	π → π *	π → π *
	Tc (L-M)	Tc (L-M)	Tc (L-M)	Tc (L-M)	Tc (L-M)	Tc (L-M)	Tc (L-M)	Tc (L-M)
	d – d	d – d	d – d	d – d	d – d	d – d	d – d	d-d
	d – d	d – d	d – d	d – d	d – d	d – d	d – d	
					d – d	d – d		

Antioxidant Assay

The mixed metal complexes were estimated in various concentration of the compounds *in vitro* by 2,2-diphenyl-1-picrylhydrazyl radical (DPPH). In qualitative antioxidant assay, the matal complexes revealed free radical scavenging properties through ensuring the presence of yellow color on purple background on the TLC plate. Complexes also confirmed their antioxidant properties in quantitive DPPH free radical scavenging assay (Mubarak et al., 2017). The inhibition concentration of antioxidant was determined by mesearing the IC_{50} value. The antioxidant power of a compound is higher when its IC_{50} is small.

Five complexes showed antioxidant activity compared to the positive control ascorbic acid (AA) with IC_{50} values ranging from 0.05–0.5 mol/l (Figure 4), while ascorbic acid (positive control) showed a value of 0.0007 mol/l. The activity of all these complexes is mainly due to the presence of OH groups of non-deprotonated curcumin during complexation and which can easily release a hydrogen to reduce DPPH. The higher activity of complexes 1 and 5 which are complexes of dimethylgloxime and curcumin is due to the number of OH groups present in these two ligands.

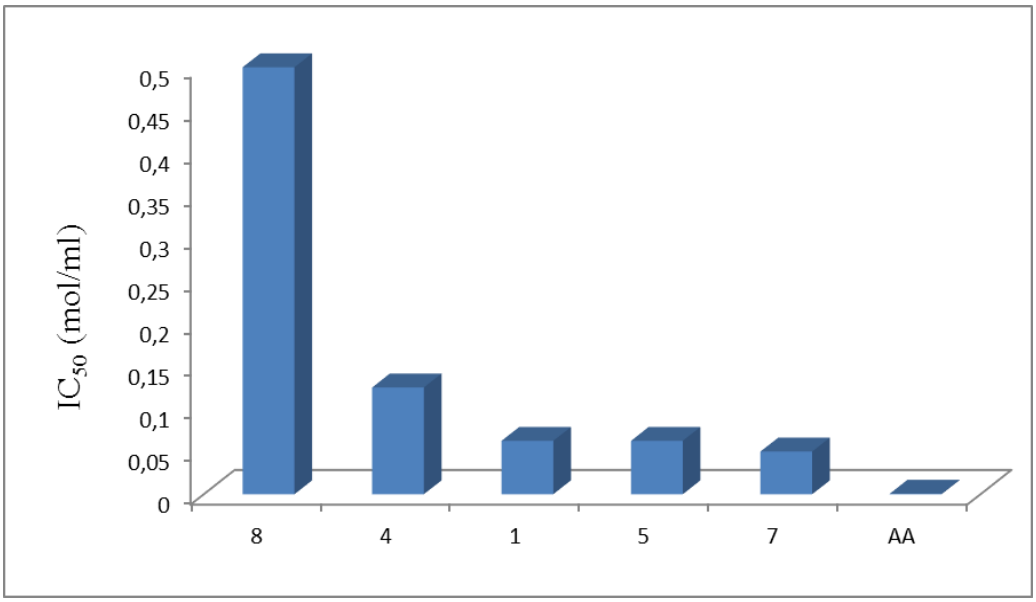

Figure 4. Antioxidant activity of complexes using DPPH assay

Conclusion

In this work, we report the preparation and characterization by different physicochemical and spectroscopic techniques eight ternary copper (II) and nickel (II) complexes of curcumin as a primary ligand, o-phenylenediamine, dimethylglyoxime, tryptophan, bromoaniline or thymine as a secondary ligand. Infrared spectroscopy studies comparing the spectra of the complexes with those of the corresponding ligands revealed the coordination of the ligands with the metals. Based on the UV-visible spectroscopy results we proposed tetrahedral and square planar geometries for Cu(II) complexes and octahedral, tetrahedral and square planar geometry for Ni(II) complexes.

Antioxidant assay revealed that complexes 1, 4, 5, 7 and 8 show an antioxidant effect compared to that of ascorbic acid (AA), due to the presence of protons from the phenols of curcumin. Complexes 1 and 5 show a strong activity due to the presence of OH groups of dimethylglyoxime, in addition to those of curcumin. These observations suggest the possibility of using complexes to solve the problem caused by the presence of free radicals in living organisms.

Scientific Ethics Declaration

* The authors declare that the scientific ethical and legal responsibility of this article published in EPSTEM journal belongs to the authors.

Conflict of Interest

* The authors declare that they have no conflicts of interest

Funding

* This research received no specific grant from any funding agency in the public, commercial, or not-for-profit sectors

Acknowledgements or Notes

* This article was presented as oral presentation at the International Conference on Basic Sciences, Engineering and Technology (www.icbaset.net) held in Trabzon/Türkiye on May 01-04, 2025.

References

Berradj, O., Adkhis, A., Bougherra, H., Bruno, G., & Michaud, F. (2017). Synthesis, spectroscopy, crystal structure and DFT studies of cobalt(III) complexes featuring dimethylglyoximate and aniline orp-bromoaniline ligands. *Journal of Molecular Structure, 1131*, 266-274.

Bougherra, H., Berradj, O., & Adkhis, A. (2018). Synthesis, characterization, electrochemical studies and antioxidant activity of some new dimethylglyoxime copper(II) complexes with purine bases and ortho-phenylenediamine. *Journal of Chemical and Pharmaceutical Research, 10*(4), 93-103.

Brand-Williams, W., Cuvelier, M., & Berset, C.1995). Use of a free radical method to evaluate antioxidant activity. *LWT-Food Science and Technology,28*(1),25-30.

Cotton, F. A., & Wilkinson, G. (1966). *Advanced ınorganic chemistry: A comprehensive text,* New York, NY: Interscience Publishers.

Erdem-Tuncmen, M., & Karipcin, F. (2012). Synthesis and characterization of new organocobaloxime derivatives with asymmetric dioxime ligands. *Journal of Inclusion Phenomena Macrocyclic Chemistry, 77,* 95-104.

Gubendran, A., Amutha, M., Dhanasekaran, P., Imayatharasi, A., & Vijayalakshmi, M. (2016). Synthesis,characterization and pharmaceutical applications of curcumin metal complex. *Journal of Pharmacy and Biological Sciences, 11*(6), 80-84.

Ismail, E. H., Sabry, D. Y., Mahdy, H., & Khalil, M. M. H. (2014). Synthesis and characterization of some ternary metal complexes of curcumin with 1, 10-phenanthroline and their anticancer applications. *Journal of Scientific Research*, *6*(3), 509-519.

Krishnaveni, G., Mubarak, M. S., Kiruthika, M., & Elayaperumal, R. (2017). Synthesis, spectral characterization, electrochemical behaviour, in vitro antimicrobial and DPPH radical scavenging activities of iron (II), cobalt (II) complexes with imidazolyl terpyridine. *Pelagia Research Library Der," Chemica Sinica*, *8*, 93-101.

Mahadi Hasan, M., Ahsan, H.M., Saha, P., Naime, J., Das, A.K., Asraf, M.A., & Nazmul Islam, A.B.M. (2021). Antioxidant, antibacterial and electrochemical activity of (E)-N-(4(dimethylamino)benzylidene)-4H-1,2,4-triazol-4-amine ligand and its transition metal complexes. *Results in Chemistry 3,* 100-115.

Mansouri, A., Embarek, G., Kokkalou, E., & Kefalas, P. (2005). Phenolic profile and antioxidant activity of the Algerian ripe date palm fruit (Phoenix dactylifera). *Food chemistry*, *89*(3), 411-420.

Masoud, M. S., Amira, M. F., Ramadan, A. M., & El-Ashry, G. M. (2008). Synthesis and characterization of some pyrimidine, purine, amino acid and mixed ligand complexes. *Spectrochimica Acta Part A: Molecular and Biomolecular Spectroscopy*, *69*(1), 230-238.

Mokhtari, R., Adkhis, A., Berradj, O., Francois, M., Yoann, R., & Michaud, F. (2017). Synthesis, spectroscopic, and x-ray structural study of aqua-bis(thymine-N^1, N^4)-ethylenediamine copper(II)dihydrate $[Cu(Thy)_2(en)(H_2O)].2H_2O$. *Inorganic and Nano-Metal Chemistry, 47*(6), 841-844.

Rabındra, P., Mohan, R.A. (2000). Synthesis and characterization of mixed ligand complexes of bio-metals with pyrimidine nucleoside (uridine) and amino acids. *Proceedings of the Indian Academy of Sciences:Chemical Sciences, 112*(6), 593–600.

Refat, M. S. (2013). Synthesis and characterization of ligational behavior of curcumin drug towards some transition metal ions: Chelation effect on their thermal stability and biological activity. *Spectrochimica Acta Part A: Molecular and Biomolecular Spectroscopy*, *105*, 326-337.

Shehab, A. S., Wahid, J. H. A., & Karee, J. H. (2017). Synthesis and characterization of some metal complexes with mannich basesderived from saccharin and study their biological activity. *Diyala Journal for Pure Science, 13*(2), 32-46.

Tidjani-Rahmouni, N., Bensiradj N. H., Djebbar S., Benali-Baitich O. (2014). Synthesis, characterization, electrochemical studies and DFT calculations of amino acids ternary complexes of copper (II) with isonitrosoacetophenone. Biological activity. *Journal of Molecular Structure, 1075*, 254-263.

Wang, M., Li, J., Rangarajan, M., Shao, Y., LaVoie, E. J., Huang, T. C., & Ho, C. T. (1998). Antioxidative phenolic compounds from sage (Salvia officinalis). *Journal of Agricultural and Food Chemistry*, *46*(12), 4869-4873.

Author(s) Information

Omar Berradj
Mouloud Mammeri University of Tizi-Ouzou
Nouvelle Ville BP 17 RP 15000 Tizi-Ouzou, Algeria
Contact e-mail: *omar.berradj@ummto.dz*

Hadda Bougherra
Mouloud Mammeri University of Tizi-Ouzou
Nouvelle Ville BP 17 RP 15000 Tizi-Ouzou, Algeria

To cite this article:

Berradj, O., & Bougherra, H. (2025). Preparation, identification, and antioxidant activity of some new transition metal complexes of curcumin with mono-and bidentate ligands. *The Eurasia Proceedings of Science, Technology, Engineering and Mathematics (EPSTEM), 34,* 296-303.

The Eurasia Proceedings of Science, Technology, Engineering & Mathematics (EPSTEM)
ISSN: 2602-3199

The Eurasia Proceedings of Science, Technology, Engineering and Mathematics (EPSTEM), 2025

Volume 34, Pages 304-309

ICBASET 2025: International Conference on Basic Sciences, Engineering and Technology

Chemical Composition of Municipal Sewage Sludge: A Tool for Risk Assessment of Agricultural Land Application

Rabia Cherfouh
Mouloud Mammeri University of Tizi-Ouzou

Samira Si Belkacem
Mouloud Mammeri University of Tizi-Ouzou

Fatima Sekai
Mouloud Mammeri University of Tizi-Ouzou

Si Ammar Kadi
Mouloud Mammeri University of Tizi-Ouzou

Azeddine Mouhous
Mouloud Mammeri University of Tizi-Ouzou

Ali Bouzourene
Mouloud Mammeri University of Tizi-Ouzou

Z. Dorbane
Mouloud Mammeri University of Tizi-Ouzou

N. Zirmi-Zembri
Mouloud Mammeri University of Tizi-Ouzou

Houci Guermah
Mohamed Boudiaf University

Farid Djellal
Ferhat Abbas University

Idir Moualek
Mouloud Mammeri University of Tizi-Ouzou

Abstract: A number of studies have shown that the application of sewage sludge to agricultural soils has a positive effect on plant nutrition. However, frequent application has been shown to result in soil contamination with potentially toxic metallic elements. The present research was conducted with the objective of establishing the chemical composition of sewage sludge from three urban wastewater treatment plants in Algerian's north region. We determined chemical parameters that account for their nutrient concentration and total content of Cr, Cu, N and Pb.The analysis revealed that the municipal sludge collected exhibited a high organic content, as well as significant concentrations of nitrogen, phosphorus, and potassium. This finding suggests that the use of sludge for agricultural purposes may be a beneficial application. The total contents of the five metals in the sludges were found to be significantly lower than the limit values that would be considered suitable for agricultural soil. However, it was observed that Ni concentration was already above the standards set by

AFNOR, while Cr was found to be equivalent to 50% of the limit. Furthermore, the results obtained by means of the sequential extraction protocol demonstrate that a significant proportion of the total content of Cu and Pb is associated with fractions (acid-soluble, carbonates, oxides, organic matter) exhibiting higher levels of bioavailability under soil conditions. In contrast, Ni and Cr have been found to be bound to the residual fraction in up to 80–90% of the total concentration, making it the least bioavailable form for environmental impact.The results indicated that regulatory guidelines require refinement to account for the bioavailability of heavy metals in relation to soil properties.

Keywords: Municipal sewage sludge, Nutrients, Heavy metals

Introduction

Increasing urbanisation, industrialisation and population pressures have resulted in growing challenges in wastewater management globally (Allaoui et al., 2015). In several countries, Sewage sludge generated from wastewater treatment plants are being usually reused in light of their potential for improving soil properties and for containing significant plant nutrients (Cherfouh et al., 2018; Peyton et al., 2016). It is now well recognized that, the disposal by landfills or by incineration are feasible options adept in many parts of the world, but both these strategies are expensive cost and able to lead environmental problems (Walter et al., 2006; Amir et al., 2005). The spreading on the agricultural lands of dewatered sludge has therefore become an attractive opportunity and disposal option. Sewage sludge is a good source of valuable components: organic matter, N, P and other plant secondary and micronutrients (Cherfouh et al., 2022; Martìnez et al., 2003, Zufiaurre, 1998).

The greater amounts of organic matter can improve the biological activity and the physical properties of the soil (Logan and Harrison, 1995). However, the presence of heavy metals in municipal sludge is probably the main obstacle to bear in mind, when sewage sludge its use as organic amendments for agricultural purposes (Zhang et al., 2017). Thus, it has been notified that applying sewage sludge to soil might provide metals in potentially toxic, labile forms (McBride, 1995). Although the determination of the total amount of heavy metals of a sludge as an important information and useful as overall contamination level of metals in sludge. However, such parameter it delivers no indication about the solubility of metals, which depends on their chemical ionic forms (Su & Wong, 2003). Sequential extraction protocol of heavy metals or their chemical speciation from soil and sediments is a useful technique for determining the mobility of heavy metals, their bioavailability, and leaching rates when sludges are applied to soils (Fluentes et al., 2004). These characteristics depend strongly on the metals specific chemical forms or positions of binding. It partitions elements into five operationally-defined geochemical fractions including: exchangeable; carbonates (acido-soluble); Fe and Mn oxides (reducible); organic matter (oxidisable); and residual (Merdy et al., 2024).

The objective of the present study was to evaluate the probable characteristics of sludge from sewage treatment plants by examining agronomical relevant parameters, concentrations, and the speciation of heavy metals. This investigation aimed to furnish a tool to assist in determining the most effective management of urban sewage sludge.

Material and Methods

The sludge samples materiel include sludge obtained from three treatment wastewater plant which are described in table1. The sludge produced from all treatment wastewater plant is obtained with using the biological wastewater process. A composite sample was collected after mixed of five primary samples and stored at 4°C. The samples were dried at 65°C, finely ground in an agate mortar, the material was sieved through a sieve with a mesh size of 160 µm and stored in polyethylene containers at 4°C until analysis.

The agronomical pertinent parameters of sludge such as pH and EC were measured in sludge extracts (sludge/water ratio 1:10 [w/v]) using a pH and conductivity meter, respectively. At last, three sample replicates and three analysis replicates for each sample were performed in order to meet statistical acceptance requirements. The organic matter was calculated from the total organic carbon (TOC) using the formula: OM (%) = TOC (%) x 1.724The sequential extraction scheme was performed using four step procedure inspired by Tessier et al. (1979). However, the hydrosoluble fraction was realized in the water extraction by using sludge/water ratio 1:10 (w/v). The concentration of metals was quantified by the inductively coupled plasma atomic emission spectrometry (ICP-AES).

Table 1. General characteristics of the wastewater treatment plants (DWTP) where sampling took place.

	Location	To be work	Treatment process (biological)	Capacity (eq/hab)	Natural outlet
PBT	Tizi-Ouzou	July 2000	medium discharge	120 000	Sébaou River
BLF	Boukhalf	November 2006	less discharge	2 5000	Sébaou River
TMT	Tadmaît	May 2007	less discharge	13 000	Sébaou River

Results and Discussion

Nutrients and Key Chemical Properties

The results of the analysis of sludge samples collected from the three wastewater treatment plants are presented in Table 2. The rate for N total were evaluated range 4.39% to 3.00%; equivalent to 44 to 30 kg/tons of sludge dread matter. The available phosphorous content is down in most of the sewage samples analysed having phosphorous contents be varied between 0.9 and 1.6 $g.kg^{-1}$. The sludge show important agronomic properties contained high major nutrients, and the values N, P and K are presented were increasing in the following order PBT > BLF > TMT.

The EC of the EST sludge was higher one, indicating a high salt content, it was some two at five times higher than others sludge. This indicates that the sludge can be lead important content of salts can be a source of soil salinization under poor soil leaching or low irrigation management. The organic matter content shows range of variation between 39% and 44%. The organic matter and nutrient contents were found mostly in high concentrations in the majority of sludge samples investigated irrespective of the type of wastewater treatment plant. The pH of sludge has been similar (7.65 to 7.73), slightly alkaline ranges. Sludge application may reduce the pH of soils due to humic acid release and may increase the electrical conductivity of soils. In another hand, the pH of soils may increase due to the exchangeable calcium and other cations present in sewage sludge. Agricultural crops grow well when soil pH is between 6 and 7 because nutrients are available more at pH of around 6.5 (Smith, 1994).

Table 2. Nutrients content and chemical properties of urban sludge

	pH	**CE** ($\mu s.cm^{-1}$)	**Nt** (%)	**$PO4^{---}$** ($g.kg^{-1}$)	**K^{+}** ($g.kg^{-1}$)	**CEC** $cmol.kg^{-1}$	**OM** (%)	**C/N**
BLF	7,65	946,5	3,69	0,90	2,49	38,5	39,3	6,2
PBT	7,70	1843,7	4,39	1,66	3,66	35,7	43,7	5,8
TMT	7,73	409,4	3,00	0,43	0,55	32,6	39,4	7,6

Total Concentration of Heavy Metals

The total content of the heavy metals copper (Cu), chromium (Cr), lead (Pb) and nickel (Ni) is presented, in addition to the threshold limits for these metals in sludge, as stipulated in the French AfNor standard (table 3). It was found that the total content of heavy metals in the sludge was generally low, and it was determined that there was a significant opportunity for its use as a fertiliser in agricultural soils. Nevertheless, TDM sludge poses a significant risk of potential pollution for Ni, Cr and Cu, given that their total contents are predominantly near the corresponding limit values. The highest metal content, attributable to the significant presence of chemical factories, which discharge their wastewater into the unban wastewater network. As indicated by the total content, the sludge resulting from BKH and EST could be utilised as effective organic fertilisers. Conversely, the TDM should not be used directly unless chemical remediation and bioremediation had been performed (Wong et al., 2000; Veeken & Hamelers, 1999).

The elevated concentrations of Ni (243 mg/kg) in the TDM sludge sample exceed the prescribed limits. The total content of Ni in all sludge samples ranged between a proportion of 54% and 120% of the set limit. The concentration of chromium (Cr) was found to be elevated (449 $mg.kg^{-1}$), attaining nearly 45% of the established limit value. This finding suggests the possibility of an ecological risk to agricultural land. Although the copper (Cu) concentration was below the limit value, the sludge from TMT poses a significant risk of contamination to agronomic soils.Despite their similar provenance, the three sludges exhibit distinct characteristics, including variations in heavy metal and organic matter content. It is imperative to employ the sludges in a manner that aligns with their unique characteristics. Consequently, the comprehensive analysis constitutes the foundation for the sustainable utilisation of sludge as a fertiliser within the agricultural land. The strict regulation and control of

wastewater discharges, coupled with the development of an industry that has minimal environmental impact, will facilitate the acceptance of these sludge for agricultural use.

Table 3. Total concentrations of heavy metals in sludge and permitted values of AFNor 44-041)

Metal	BLF	PBT	TMT	AFNor 44-041
Cr	246.7	294.3	448.6	1000
Cu	119.7	145.4	210.4	1000
Ni	107.1	137.9	242.9	200
Pb	91.7	108.9	90.0	800

The Speciation of Heavy Metals

The process of speciation in the context of metals signifies the distribution of the total quantity of metal present across the various metal-bearing fractions. Figure 2 provides a visual representation of the proportion of each of the five fractions in relation to the total content of the metals that have been investigated. The bioavailability and ecotoxicity effects of metals are contingent on their speciation in sludge. The quantity of heavy metal bound to the residual fraction (F-res) is frequently designated as the stable fraction and is considered to be unaffected by environmental processes. However, it is important to note that certain fractions, including the hydrosoluble (F-wat), acid soluble/exchangeable fraction (F-ac), reducible fraction (F-red), and oxidizable fraction (F-oxi), have the potential to become bioavailable under natural soil conditions.

The total copper concentration exhibited a partition of 59 to 77% in the F-wat, F-ac, F-red and F-oxi fractions. In the TMT sludge, F-oxi represents 45%, while F-red is dominant in EST and BKH with proportions of 32% and 37% respectively. The stability of Cu-organic matter complexes is a well-documented phenomenon (Walter et al., 2006; Walter & Cuevas, 1999). It can be hypothesised that the local environment, with its oxidising soil conditions, may facilitate the availability of the Cu bound to F-oxi. The total lead (Pb) concentration was predominantly present in the F-red fraction, accounting for 56 to 67%, while the F-res remained significant at 30 to 40%. Consequently, this Pb partitioning has the potential to predict the high potential bioavailability after sludge application the agricultural in soil.

The results obtained from this study indicate that Ni is predominantly bound to F-RES within the range of 80-85%, thereby suggesting its limited bioavailability in the environment. However, the Ni total concentration in TMT (243 $mg.kg^{-1}$) sludge exhibited a more significant increase according to limits values (200 $mg.kg^{-1}$) and may pose a greater environmental hazard. It is important to note that Ni is present as the soluble chemical form (15 at 20%), which is significant given its status as a toxic heavy metal and a potential contaminant. Conversely, the Ni content in BLF (107 $mg.kg^{-1}$) and EST (137 $mg.kg^{-1}$) is more suitable for agricultural use. Chromium (Cr) speciation has been found to be concentrated in the F-res, with a proportion of over 92%, indicating minimal direct environmental impact. With regard to Cr fractionation, the following order has been observed: F-res > F-oxi > F-red > F-wat > F-ac. Consequently, it is imperative to assess the quality of both soils and sludges prior to their utilisation in agriculture.

Conclusion

From an agronomic point of view, analysis of the physico-chemical parameters reveals sludge with similar chemical compositions. The results obtained from the analysis of the samples of sludge revealed that the pH level was most frequently between 6.4 and 8. This finding suggests that the process of sludge stabilisation may not be necessary when the sludge is applied to soil. The content of nitrogen, phosphorus and potassium were high in all three sludges, with the EST plant exhibiting the highest concentrations. The C/N ratios of the sludge samples were recorded as between 5 and 8, indicating that nitrogen mobilisation by incorporation into the cell mass may be less efficient. The elevated cation exchange capacity (CEC) of the sludge is advantageous for utilisation in agricultural contexts, as it indicates the material's potential for application as a fertiliser.In the case of the wastewater treatment plant at BLF and PBT, the total concentration of heavy metals in the sludge was found to be well below the thresholds stipulated by European and American regulations concerning the application of sludge on agricultural land.

Conversely, the sludge emanating from the TMT facility poses significant risks of contamination by heavy metals including nickel (Ni) and chromium (Cr). The cumulative Ni concentration in this instance exceeds the

established limit of 200mg/kg. Nonetheless, the analysis of speciation reveals that Ni and Cr are predominantly linked to the residual fraction, accounting for 83% and 93% of the total content, respectively. This finding suggests that the bioavailability of these metals in the soil environment may be low.

The current chemical composition of BLF and PBT municipal sludge has appreciable levels of nutrients, interesting properties for agricultural use and a low risk of heavy metal contamination of the soil. These results argue in favour of spreading the sludge on agricultural soils, with strict management in terms of doses and frequency of spreading. In order to ensure the sustainable utilisation of urban sludge, it is imperative that agricultural practices are appropriately regulated, on account of the fact that metals introduced into soil have the potential to accumulate over extended time periods.

Scientific Ethics Declaration

* The authors declare that the scientific ethical and legal responsibility of this article published in EPSTEM journal belongs to the authors.

Conflict of Interest

* The authors declare that they have no conflicts of interest

Funding

* This research received no specific grant from any funding agency in the public, commercial, or not-for-profit sectors

Acknowledgements

*This article was presented as poster presentation at the International Conference on Basic Sciences, Engineering and Technology (www.icbaset.net) held in Trabzon /Türkiye on May 01-04, 2025.

*We would like to thank the Algerian Ministry of Higher Education and Scientific Research (MESRS) and the Mouloud Mammeri University of Tizi-Ouzou for the facilities that made it possible to carry out this work and to present it as a poster at the International Conference on Basic Sciences and Technology (ICBASET2025).

References

Allaoui, M., Schmitz, T., Campbell, D., & de la Porte, A. C. (2015). *Good practices for regulating wastewater treatment: legislation, policies and standards. United Nations Environment Programme*. Retrieved from https://www.unep.org/

Amir, S., Hafidi, M., Merlina, G., Revel, J.C. (2005). Sequential extraction of heavy metals during composting of sewage sludge. *Chemosphere, 59,* 801-810.

Cherfouh, R., Lucas, Y., Derridj, A., & Merdy, P. (2018). Long term, low technicality sewage sludge amendment and irrigation with treated wastewater under Mediterranean climate: Impact on agronomical soil quality. *Environmental Science and Pollution Research, 25*, 35571–35581.

Cherfouh, R., Lucas, Y., Derridj, A., & Merdy, P. (2022). Metal speciation in sludges: A tool to evaluate risks of land application and to track heavy metal contamination in sewage network. *Environmental Science and Pollution Research, 29*(46), 70396– 70407.

Fuentes, A., Llorens, M., Saez, J., Aguilar, Ma Isabel, Ortuño, J.F., & Meseguer, V.F. (2004). Phytotoxicity and heavy metals speciation of stabilised sewage sludges. *Journal of Hazardous Materials, 108,* 161-169.

Kauthale, V.K., Takawale, P.S., Kulkarni, P.K., & Daniel, L.N. (2005). Influence of fly ash and sewage sludge application on growth and yield of annual crops. *International Journal of Tropical Agriculture, 23,*49-54.

Logan, T.J., Harrison, B.J. (1995). Physical characteristic of alkaline stabilized sewage sludge (N-Viro soil) and the effects of soil physical properties. *Journal of Environmental Quality, 24*(1), 153-164.

Martìnez, F., Cuevas, G., Calvo, R., & Walter, I. (2003). Biowaste effects on soil and native plants in a semiarid ecosystem. *Journal of Environmental Quality*, *32*(2), 472-479.

McBride, M.B. (1995). Toxic metal accumulation from agricultural use of sludge: are USEPA regulations protective? *Journal of Environmental Quality*, *24*(1), 5-18.

Merdy, P.Cherfouh, R., & Lucas, Y. (2024). Long-term agricultural reuse of treated wastewater and sewage sludge: Developing a time to critical content index for metal species. *Environmental Monitoring and Assessment ,196*(9), 836.

Peyton, D. P., Healy, M. G., Fleming, G. T. A., Grant, J., Wall, D., Morrison, L., ... & Fenton, O. (2016). Nutrient, metal and microbial loss in surface runoff following treated sludge and dairy cattle slurry application to an Irish grassland soil. *Science of the Total Environment*, *541*, 218-229

Su, D. C., & Wong, J. W. C. (2004). Chemical speciation and phytoavailability of Zn, Cu, Ni and Cd in soil amended with fly ash-stabilized sewage sludge. *Environment International*, *29*(7), 895-900.

Tessier, A., Campell, P., & Bisson, M. (1979). Sequential extractions procedure for the speciation of particulate trace metals. *Analytical Chemistry, 51*(7), 844-851.

Veeken, A. M. Hamelers, H.-M. (1999). Removal of heavy metals from sewage sludge by extraction with organic acids. *Water Science Technology, 40*(1), 129– 136.

Walter, I., Martínez, F., & Cala, V. (2006). Heavy metal speciation and phytotoxic effects of three representative sewage sludges for agricultural uses. *Environmental Pollution, 139,* 507-514.

Wong, W.C. Xiang, L. Chan, L.C. 2000. Removal of heavy metals from anaerobically digested sewage sludge by isolated indigenous iron oxidizing bacteria. *Chemosphere, 41*(1-2*)*, 283–287.

Zhang, X., Wang, X. Q., & Wang, D. F. (2017). Immobilization of heavy metals in sewage sludge during land application process in China: A review. *Sustainability*, *9*(11), 2020.

Zufiaurre, R., Olivar, A., Chamorro, P., & Callizo, A. (1998). Speciation of metals in sewage sludge for agricultural uses. *Analyst*, *123*(2), 255-259.

Author(s) Information

Rabia Cherfouh
Mouloud Mammeri University of Tizi-Ouzou
17 RP, Tizi-Ouzou Algeria
Contact e-mail: rabiacherfouh*@yahoo.fr*

Samira Si Belkacem
Mouloud Mammeri University of Tizi-Ouzou
17 RP, Tizi-Ouzou Algeria

Fatima Sekai
Mouloud Mammeri University of Tizi-Ouzou
17 RP, Tizi-Ouzou Algeria

Si Ammar Kadi
Mouloud Mammeri University of Tizi-Ouzou
17 RP, Tizi-Ouzou Algeria

Azeddine Mouhous
Mouloud Mammeri University of Tizi-Ouzou
17 RP, Tizi-Ouzou Algeria

Ali Bouzouren
Mouloud Mammeri University of Tizi-Ouzou
17 RP, Tizi-Ouzou Algeria

Zahia Dorbane
Mouloud Mammeri University of Tizi-Ouzou
17 RP, Tizi-Ouzou Algeria

Nacima Zimbri-Zirmi
Mouloud Mammeri University of Tizi-Ouzou
17 RP, Tizi-Ouzou Algeria

Houci Guermah
Mohamed Boudiaf University
M'sila, Algerie

Farid Djellal
Ferhat Abbas University
Setif, Algerie

Idir Moualek
Mouloud Mammeri University of Tizi-Ouzou
17 RP, Tizi-Ouzou Algeria

To cite this article:

Cherfouh R., Si Belkacem, S., Sekai, F., Kadi, S.A., Mouhous A., Bouzourene, A., Dorbane, Z., Zirmi-Zembri N., Guermah H., Djellal F., & Moualek, I. (2025). Chemical composition of municipal sewage sludge: A tool for risk assessment of agricultural land application. *The Eurasia Proceedings of Science, Technology, Engineering and Mathematics (EPSTEM), 34,* 304-309.

The Eurasia Proceedings of Science, Technology, Engineering & Mathematics (EPSTEM)
ISSN: 2602-3199

The Eurasia Proceedings of Science, Technology, Engineering and Mathematics (EPSTEM), 2025

Volume 34, Pages 310-319

ICBASET 2025: International Conference on Basic Sciences, Engineering and Technology

Optimal Control Problem and Integral Quality Criteria with a Special Gradient Term

Vugar Ibrahim Salmanov
Nakhchivan State University

Abstract: The paper deals with the optimal control problem with the full-range integral performance criterion for the nonlinear Schrödinger equation with the specific gradient summand and the complex potential when the performance criterion is the full-range integral. Concurrently, the first variation formula of the performance criterion under consideration and via which the necessary condition is established in the form of a variation inequality is found. This article investigates the differentiability of the optimal control problem for a three-dimensional nonlinear no stationary Schrödinger equation with a special gradient term and a real-valued potential, when the potential depending on both spatial and time dependence and is sought in the class of measurable bounded functions, and the coefficient in the nonlinear part of the equation is a complex number. Therefore, this work differs from previously studied problems nonlinear Schrödinger equation with a specific gradient term, complex potential and is relevant in its significance and also of scientific interest.

Keywords: Schrödinger equation, Optimal control problem, Complex potential

Introduction

Optimal control problems for various equations were previously studied in detail in Diveev et al., (2021), Emilio et al., (2022), Najafova, (2022), Salmanov (2020), Yagubov et al., (2017), etc. As is known, the Schrödinger equation with a special gradient term and initial-boundary value problems for this equation arise in quantum mechanics, nuclear physics, nonlinear optics and other areas of modern physics and technology (Iskenderov et al., 2019; Yagub et al., 2022). Especially in quantum mechanics and nonlinear optics, when studying the motion of charged particles in an inhomogeneous medium, the Schrödinger equation with a special gradient term arises, and the study of initial boundary value problems for this equation is of interest from both theoretical and practical points of view. It should be noted that the initial boundary value problems for the linear and nonlinear Schrödinger equations in various formulations were previously studied in detail in the works of others Yagub et al. (2015), Ibrahimov et al. (2022), Yakub et al. (2021), Zengin et al. (2021). However, the initial boundary value problems even for the linear Schrödinger equation with a special gradient term have been studied relatively little (Yagub et al., 2021). It should be noted that the work (Yagub et al., (2021)) study questions of the existence and uniqueness of solutions to initial boundary value problems for linear one-dimensional and two-dimensional Schrödinger equations with a special gradient term, when the coefficients are quadratically summable functions. Note that initial boundary value problems for the nonlinear Schrödinger equation with a special gradient term have been studied relatively little. In this direction, we can note the works Yagub et al. (2015), Ibrahimov et al. (2022), Yakub et al. (2021), Zengin et al. (2021) in which initial-boundary value problems for the nonlinear Schrodinger equation with a special gradient term are studied, when the coefficients of the equation depend only on a spatial variable or a time variable. Therefore, this paper is devoted to the study of the optimal control problem for a three-dimensional nonlinear Schrödinger equation with a specific gradient summand and with a complex potential, when the controls are real and imaginary parts of the complex potential and chosen from the class of measurable bounded functions depending on a time variable, and the quality criterion is the full-range integral, and it is of considerable scientific interest.

Method

Let's consider the functional minimizing problem:

$$J_\alpha(v) = \|\psi_1 - \psi_2\|^2_{L_2(\Omega)} + \alpha\|v-\omega\|^2_H \tag{1}$$

at the set:

$$V = \left\{ v = v(t) = \left(v_0(t), v_1(t)\right):\ v_m \in W_2^1(0,T), \left|v_m(t)\right| \le b_m, \left|\frac{dv_m(t)}{dt}\right| \le d_m, m = 0,1, \overset{0}{\forall} t \in (0,T) \right\}$$

subject to the conditions that:

$$i\frac{\partial \psi_p}{\partial t} + a_0\Delta\psi_p + ia_1(x,t)\nabla\psi_p - a(x)\psi_p + v_0(t)\psi_p + iv_1(t)\psi_p +$$

$$+a_2\left|\psi_p\right|^2\psi_p = f_p(x,t), p = 1,2,\ (x,t) \in \Omega, \tag{2}$$

$$\psi_p(x,0) = \varphi_p(x),\ \text{p=1,2}, x \in D, \tag{3}$$

$$\psi_1\big|_S = 0, \frac{\partial \psi_2}{\partial \nu}\bigg|_S = 0, \tag{4}$$

where, $i = \sqrt{-1}$; $T > 0,\ b_m > 0, d_m > 0,\ m = 0,1, a_0 > 0,\ \alpha \ge 0$ are the predetermined numbers, $\Delta = \frac{\partial^2}{\partial x_1^2} + \frac{\partial^2}{\partial x_2^2} + \frac{\partial^2}{\partial x_3^2}$ is the Laplace operator, $\nabla = \left(\frac{\partial}{\partial x_1}, \frac{\partial}{\partial x_2}, \frac{\partial}{\partial x_3}\right)$ – is the nabla operator; ν is the external normal of the boundary Γ of the area D; the complex number a_2 satisfies the condition:

$$a_2 = \operatorname{Re} a_2 + i \operatorname{Im} a_2, \operatorname{Re} a_2 < 0, \operatorname{Im} a_2 > 0, \operatorname{Im} a_2 \ge 2\left|\operatorname{Re} a_2\right|; \tag{5}$$

$a(x)$ is a measurable bounded function that satisfies the condition:

$$\mu_0 \le a(x) \le \mu_1,\ \overset{0}{\forall} x \in D,\ \mu_0, \mu_1 = const > 0; \tag{6}$$

$a_1(x,t) = \left(a_{11}(x,t), a_{12}(x,t), a_{13}(x,t)\right)$ is the specified function vector with the components that satisfy the conditions:

$$\left|a_{1j}(x,t)\right| \le \mu_2,\ \left|\frac{\partial a_{1j}(x,t)}{\partial x_k}\right| \le \mu_3, \left|\frac{\partial a_{1j}(x,t)}{\partial t}\right| \le \mu_4, j,k = \overline{1,3},$$
$$\overset{0}{\forall}(x,t) \in \Omega, a_{1j}\big|_S = 0, j = \overline{1,n},\ \mu_2, \mu_3, \mu_4 = const > 0; \tag{7}$$

$\varphi_p(x), f_p(x,t), p = 1,2$ are the complex-valued functions that satisfy the conditions:

$$\varphi_1 \in \overset{0}{W}{}_2^2(D), \varphi_2 \in W_2^2(D), \frac{\partial \varphi_2}{\partial \nu}\bigg|_\Gamma = 0; \tag{8}$$

$$f_p \in W_2^{0,1}(\Omega), p = 1,2; \tag{9}$$

$\omega \in H$ is a specified element, where $H \equiv W_2^1(0,T) \times W_2^1(0,T)$ and the symbol $\overset{0}{\forall}$ means "at almost all". The problem of determining functions $\psi_p = \psi_p(x,t) \equiv \psi_p(x,t;v), p = 1,2$ from the conditions (2)-(4) upon every $v \in V$ will be referred to as a reduced problem.

Definition 1. Under the solution of the reduced problems (2)-(4) for each $v \in V$, we mean a functions $\psi_1 \in B_1 \equiv C^0\left([0,T],\overset{0}{W}{}_2^2(D)\right) \cap C^1\left([0,T],L_2(D)\right)$, $\psi_2 \in B_2 \equiv C^0\left([0,T],W_2^2(D)\right) \cap C^1\left([0,T],L_2(D)\right)$, for almost all $x \in D$ and $t \in [0,T]$ satisfying equations (2), and the initial conditions (3) for almost all $x \in D$ and the boundary conditions (4) for almost $(\xi,t) \in S$.

It should be noted that the reduced problem type (2)-(4), that is, the first and second initial-boundary value problems (2)-(4) were previously studied in the paper Iskenderov et al. (2018). Based on the results of this paper the following statement can be formulated:

Theorem 1. Let's assume that the complex number a_2 satisfies the condition (5), and the functions $a(x)$, $a_1(x,t)$, $\varphi_p(x)$, $f_p(x,t), p=1,2$ satisfy the conditions (6)-(9). Then, the reduced problems (2)-(4) upon every $v \in V$ have the single solution $\psi_1 \in B_1, \psi_2 \in B_2$, and the following statements are valid for such solution:

$$\left\|\psi_1(\cdot,t)\right\|^2_{\overset{0}{W}{}_2^2(D)} + \left\|\frac{\partial \psi_1(\cdot,t)}{\partial t}\right\|^2_{L_2(D)} \le c_1\left(\left\|\varphi_1\right\|^2_{\overset{0}{W}{}_2^2(D)} + \left\|f_1\right\|^2_{W_2^{0,1}(\Omega)} + \left\|\varphi_1\right\|^6_{\overset{0}{W}{}_2^1(D)}\right), \forall t \in [0,T], \quad (10)$$

$$\left\|\psi_2(\cdot,t)\right\|^2_{\overset{0}{W}{}_2^2(D)} + \left\|\frac{\partial \psi_2(\cdot,t)}{\partial t}\right\|^2_{L_2(D)} \le c_2\left(\left\|\varphi_2\right\|^2_{W_2^2(D)} + \left\|f_2\right\|^2_{W_2^{0,1}(\Omega)} + \left\|\varphi_2\right\|^6_{W_2^1(D)}\right), \forall t \in [0,T], \quad (11)$$

where, $c_p > 0, p = 1,2$ are the constants not depending on t.

According to this theorem, the functional described in (1) makes sense for the problem under consideration. In work Salmanov (2020) the existence and uniqueness theorems for the solution of the optimal control problem we are considering for the nonlinear Schrödinger equation with a special gradient term and with a complex potential are proved, when the quality criterion is the integral over the entire domain.

The Functional Differentiability and the Necessary Condition for Solution of the Optimal Control Problems

Let us consider the necessary condition for solving problems (1)-(4) in the form of the variational inequality. Let's suppose that $\Phi_p = \Phi_p(x,t), p=1,2$ are the solution for the following conjugate problem:

$$i\frac{\partial \Phi_p}{\partial t} + a_0 \Delta \Phi_p + i\sum_{j=1}^{3} \frac{\partial}{\partial x_j}\left(a_{1j}(x,t)\Phi_p\right) - a(x)\Phi_p + v_0(t)\Phi_p - iv_1(t)\Phi_p +$$

$$+2\overline{a}_2\left|\psi_p\right|^2 \Phi_p + a_2\left(\psi_p\right)^2 \overline{\Phi}_p = (-1)^p 2\left(\psi_1(x,t) - \psi_2(x,t)\right), p=1,2, (x,t) \in \Omega, \quad (12)$$

$$\Phi_p(x,T) = 0, p=1,2, x \in D, \quad (13)$$

$$\Phi_1\big|_S = 0, \left.\frac{\partial \Phi_2}{\partial \nu}\right|_S = 0, \quad (14)$$

where $\psi_p = \psi_p(x,t) \equiv \psi_p(x,t;v), p=1,2$ is a solution to (2)-(4) provided that $v \in V$.

The solution of the conjugate problems (12)-(14) means the function $\Phi_p(x,t), p=1,2$ from the space $B_p, p=1,2$ meeting the equations (12) for $\forall t \in [0,T]$, the boundary conditions (13) and (14) for $\overset{\circ}{\forall} x \in D$ and $\overset{\circ}{\forall}(\xi,t) \in S$, respectively.

Theorem 2. Let's suppose that the number a_2 and functions $a(x), a_1(x,t)$, $\varphi_p(x)$, $f_p(x,t), p=1,2$ satisfy the conditions (5)-(9). Also, let's assume that $y \in \overset{0}{W}{}_2^2(D)$ is a specified function. Then, the conjugate problem (12)-(14) has the single solution from the space $\Phi_p \in B_p, p=1,2$ and the following estimates are valid for this solution:

$$\left\|\Phi_1(.,t)\right\|^2_{\overset{0}{W}{}_2^2(D)} + \left\|\frac{\partial \Phi_1(.,t)}{\partial t}\right\|^2_{L_2(D)} \le c_5 \left\|\psi_1 - \psi_2\right\|^2_{W_2^{0,1}(\Omega)}, \tag{15}$$

$$\left\|\Phi_2(.,t)\right\|^2_{W_2^2(D)} + \left\|\frac{\partial \Phi_2(.,t)}{\partial t}\right\|^2_{L_2(D)} \le c_6 \left\|\psi_1 - \psi_2\right\|^2_{W_2^{0,1}(\Omega)} \tag{16}$$

for $\forall t \in [0,T]$, where $c_5 > 0, c_6 > 0$ are the constant not depending on t.

This theorem is proved by the Galerkin method. To establish the necessary condition for the solution by specifying (1)-(4), we must show the differentiability of the functional $J_\alpha(v)$ onto the set V.

Theorem 3. Let's assume that the hypotheses of theorem 2 are satisfied and $\omega \in H$ is a specified element. Then, the functional $J_\alpha(v)$ for any function $w = w(t)$ from the space B has the first variation at the set V as follows:

$$\begin{aligned}
\delta J_\alpha(v,w) = {} & \int_\Omega \mathrm{Re}\left(\psi_1(x,t)\bar{\Phi}_1(x,t) + \psi_2(x,t)\bar{\Phi}_2(x,t)\right) w_0(t)\,dxdt - \\
& - \int_\Omega \mathrm{Im}\left(\psi_1(x,t)\bar{\Phi}_1(x,t) + \psi_2(x,t)\bar{\Phi}_2(x,t)\right) w_1(t)\,dxdt + \\
& + 2\alpha \int_0^T \left(v_0(t) - \omega_0(t)\right) w_0(t)\,dt + \int_0^T \left(\frac{dv_0(t)}{dt} - \frac{d\omega_0(t)}{dt}\right)\frac{dw_0(t)}{dt}dt + \\
& + 2\alpha \int_0^T \left(v_1(t) - \omega_1(t)\right) w_1(t)\,dt + \int_0^T \left(\frac{dv_1(t)}{dt} - \frac{d\omega_1(t)}{dt}\right)\frac{dw_1(t)}{dt}dt,
\end{aligned} \tag{17}$$

where $\psi_p(x,t) \equiv \psi_p(x,t;v), \Phi_p(x,t) \equiv \Phi_p(x,t;v), p=1,2$ are the solutions of the reduced problem (2)-(4), respectively, and the conjugate problem (12)-(14) provided that $v \in V$.

Proof. Let's consider the increment of the functional $J_\alpha(v)$ at any element $v \in V$. Based on the formulas (1) and (16) the following is obtained:

$$\begin{aligned}
\delta J_\alpha(v) = J_\alpha(v+\delta v) - J_\alpha(v) = {} & 2\int_\Omega \mathrm{Re}\left[\left(\psi_1(x,t) - \psi_2(x,t)\right)\left(\delta\bar{\psi}_1(x,t) - \delta\bar{\psi}_2(x,t)\right)\right]dx + \\
& + 2\alpha \int_0^T \left(v_0(t) - \omega_0(t)\right) v_0(t)\,dt + 2\alpha \int_0^T \left(\frac{dv_0(t)}{dt} - \frac{d\omega_0(t)}{dt}\right)\frac{dv_0(t)}{dt}dt + \\
& + 2\alpha \int_0^T \left(v_1(t) - \omega_1(t)\right) v_1(t)\,dt + 2\alpha \int_0^T \left(\frac{dv_1(t)}{dt} - \frac{d\omega_1(t)}{dt}\right)\frac{dv_1(t)}{dt}dt + \\
& + \left\|\delta\psi_1\right\|^2_{L_2(\Omega)} + \left\|\delta\psi_2\right\|^2_{L_2(\Omega)} - 2\int_\Omega \mathrm{Re}\left(\delta\psi_1(x,t)\delta\bar{\psi}_2(x,t)\right)dxdt + \alpha\left\|\delta v\right\|^2_H, \forall v \in V,
\end{aligned} \tag{18}$$

where $\delta\psi_p = \delta\psi_p(x,t), p=1,2$ is the solution of the system of the following initial boundary value problems:

$$i\frac{\partial\delta\psi_p}{\partial t} + a_0\Delta\psi_p + ia_1(x,t)\nabla\delta\psi_p - a(x)\delta\psi_p + \left(v_0(t)+\delta v_0(t)\right)\delta\psi_p + i\left(v_1(t)+\delta v_1(t)\right)\delta\psi_p =$$

$$= -\delta v_0(t)\psi_p - i\delta v_1(t)\psi_p - a_2\left(\left|\psi_{p\delta}\right|^2\psi_{p\delta} - \left|\psi_p\right|^2\psi_p\right), p=1,2\ (x,t)\in\Omega$$

$$\delta\psi_p(x,0)=0, p=1,2\ x\in D\ \delta\psi_1\big|_S = 0, \frac{\partial\delta\psi_2}{\partial\nu}\bigg|_S = 0$$

At first, the first summand from the right part of the formula is to be rearranged.

It is obvious that $\delta\psi_p \in B_p, p=1,2$ satisfy the following integral equalities:

$$\int_\Omega\left(i\frac{\partial\delta\psi_p}{\partial t} + a_0\Delta\delta\psi_p + ia_1(x,t)\nabla\delta\psi_p - a(x)\delta\psi_p + \left(v_0(t)+\delta v_0(t)\right)\delta\psi_p\right)\overline{\eta}_p(x,t)\,dxdt +$$

$$+i\int_\Omega\left(v_1(t)+\delta v_1(t)\right)\delta\psi_p\overline{\eta}_p(x,t)\,dxdt = -\int_\Omega\delta v_0(t)\psi_p\overline{\eta}_p(x,t)\,dxdt -$$

$$-i\int_\Omega\delta v_1(t)\psi_p\overline{\eta}_p(x,t)\,dxdt - \int_\Omega a_2\left[\left(\left|\psi_{p\delta}\right|^2+\left|\psi_p\right|^2\right)\delta\psi_p + \psi_{p\delta}\psi_p\delta\overline{\psi}_p\right]\overline{\eta}_p(x,t)\,dxdt, p=1,2 \quad (19)$$

for any functions $\eta_p\in L_2(\Omega), p=1,2$. Also, the solution of the conjugate problem $\Phi_p(x,t), p=1,2$ from $B_p, p=1,2$ satisfies the following integral equalities:

$$\int_\Omega\left(i\frac{\partial\Phi_p}{\partial t} + a_0\Delta\Phi_p + i\sum_{j=1}^{3}\frac{\partial}{\partial x_j}\left(a_{1j}(x,t)\Phi_p\right) - a(x)\Phi_p + v_0(t)\Phi_p - iv_1(t)\Phi_p +\right.$$

$$\left.+2\overline{a}_2\left|\psi_p\right|^2\Phi_p + a_2\left(\psi_p\right)^2\overline{\Phi}_p\right)\overline{\eta}_{1p}(x,t)\,dxdt = (-1)^p\,2\int_\Omega\left(\psi_1(x,t)-\psi_2(x,t)\right)\overline{\eta}_{1p}(x,t)\,dxdt \quad 20)$$

for any functions $\eta_{1p}\in L_2(\Omega), p=1,2$. In such integral equalities, the testing functions $\eta_{1p}(x,t), p=1,2$ are replaced with the functions $\delta\psi_p(x,t), p=1,2$ from $B_p, p=1,2$, respectively. Then, after applying integration by parts of the left side of the equality we obtained using conditions of the form (14) and (12), we obtain an equality whose complex conjugation has the form:

$$\int_\Omega\left(i\frac{\partial\delta\psi_p}{\partial t} + a_0\Delta\delta\psi_p + ia_1(x,t)\nabla\delta\psi_p - a(x)\delta\psi_p + v_0(t)\delta\psi_p + iv_1(t)\delta\psi_p\right)\overline{\Phi}_p\,dxdt +$$

$$+\int_\Omega 2a_2\left|\psi_p\right|^2\delta\psi_p\overline{\Phi}_p\,dxdt + \int_\Omega\overline{a}_2\left(\overline{\psi}_p\right)^2\delta\psi_p\Phi_p\,dxdt =$$

$$= (-1)^p\,2\int_D\left(\overline{\psi}_1(x,t)-\overline{\psi}_2(x,t)\right)\delta\psi_p(x,t)\,dxdt, p=1,2 \quad \ldots\ldots\ldots\ldots\ldots \quad (21)$$

In the integral equality (19), the testing functions $\eta_p(x,t), p=1,2$ are replaced with $\Phi_p(x,t), p=1,2$ from $B_p, p=1,2$, respectively. Then, the following is found:

$$\int_{\Omega}\left(i\frac{\partial\delta\psi_p}{\partial t}+a_0\Delta\delta\psi_p+ia_1(x,t)\nabla\delta\psi_p-a(x)\delta\psi_p+\left(v_0(t)+\delta v_0(t)\right)\delta\psi_p\right)\bar{\Phi}_p(x,t)\,dxdt+$$

$$+i\int_{\Omega}\left(v_1(t)+\delta v_1(t)\right)\delta\psi_p\bar{\Phi}_p(x,t)\,dxdt=-\int_{\Omega}\delta v_0(t)\psi_p\bar{\Phi}_p(x,t)\,dxdt-$$

$$-i\int_{\Omega}\delta v_1(t)\psi_p\bar{\Phi}_p(x,t)\,dxdt-\int_{\Omega}a_2\left[\left(\left|\psi_{p\delta}\right|^2+\left|\psi_p\right|^2\right)\delta\psi_p+\psi_{p\delta}\psi_p\delta\bar{\psi}_p\right]\bar{\Phi}_p(x,t)\,dxdt,\ p=1,2$$

Through deducting the equity (21), the validity if the equity is easily found:

$$2\int_{\Omega}\mathrm{Re}\left[\left(\psi_1(x,t)-\psi_2(x,t)\right)\left(\delta\bar{\psi}_1(x,t)-\delta\bar{\psi}_2(x,t)\right)\right]dxdt=\int_{\Omega}\delta v_0(t)\,\mathrm{Re}\left(\sum_{p=1}^{2}\psi_p\bar{\Phi}_p\right)dxdt-$$

$$-\int_{\Omega}\delta v_1(t)\,\mathrm{Im}\left(\sum_{p=1}^{2}\psi_p\bar{\Phi}_p\right)dxdt+\int_{\Omega}\delta v_0(t)\,\mathrm{Re}\left(\sum_{p=1}^{2}\delta\psi_p\bar{\Phi}_p\right)dxdt-$$

$$-\int_{\Omega}\delta v_1(t)\,\mathrm{Im}\left(\sum_{p=1}^{2}\delta\psi_p\bar{\Phi}_p\right)dxdt+\int_{\Omega}\mathrm{Re}\left(a_2\sum_{p=1}^{2}\psi_{p\delta}\bar{\Phi}_p\left|\delta\psi_p\right|^2\right)dxdt+$$

$$+\int_{\Omega}\mathrm{Re}\left(a_2\sum_{p=1}^{2}\psi_p\bar{\Phi}_p\left|\delta\psi_p\right|^2\right)dxdt+\int_{\Omega}\mathrm{Re}\left(a_2\sum_{p=1}^{2}\bar{\psi}_p\bar{\Phi}_p\left(\delta\psi_p\right)^2\right)dxdt\,. \tag{22}$$

Having considered the equity in the right part (18), the following is obtained:

$$\delta J_{\alpha}(v)=\int_{\Omega}\delta v_0(t)\,\mathrm{Re}\left(\sum_{p=1}^{2}\psi_p\bar{\Phi}_p\right)dxdt-\int_{\Omega}\delta v_1(t)\,\mathrm{Im}\left(\sum_{p=1}^{2}\psi_p\bar{\Phi}_p\right)dxdt+$$

$$+2\alpha\int_{0}^{T}\left(v_0(t)-\omega_0(t)\right)\delta v_0(t)\,dt+2\alpha\int_{0}^{T}\left(\frac{dv_0(t)}{dt}-\frac{d\omega_0(t)}{dt}\right)\frac{d\delta v_0(t)}{dt}\,dt+$$

$$+2\alpha\int_{0}^{T}\left(v_1(t)-\omega_1(t)\right)\delta v_1(t)\,dt+2\alpha\int_{0}^{T}\left(\frac{dv_1(t)}{dt}-\frac{d\omega_1(t)}{dt}\right)\frac{d\delta v_1(t)}{dt}\,dt+R(\delta v), \tag{23}$$

where $R(\delta v)$ is specified through the following formula:

$$R(\delta v)=\int_{\Omega}\delta v_0(t)\,\mathrm{Re}\left(\sum_{p=1}^{2}\delta\psi_p\bar{\Phi}_p\right)dxdt-\int_{\Omega}\delta v_1(t)\,\mathrm{Im}\left(\sum_{p=1}^{2}\delta\psi_p\bar{\Phi}_p\right)dxdt+$$

$$+\int_{\Omega}\mathrm{Re}\left(a_2\sum_{p=1}^{2}\psi_{p\delta}\bar{\Phi}_p\left|\delta\psi_p\right|^2\right)dxdt+\int_{\Omega}\mathrm{Re}\left(a_2\sum_{p=1}^{2}\psi_p\bar{\Phi}_p\left|\delta\psi_p\right|^2\right)dxdt+$$

$$+\int_{\Omega}\mathrm{Re}\left(a_2\sum_{p=1}^{2}\bar{\psi}_p\bar{\Phi}_p\left(\delta\psi_p\right)^2\right)dxdt+\alpha\left\|\delta v\right\|_H^2+$$

$$+\sum_{p=1}^{2}\left\|\delta\psi_p\right\|_{L_2(\Omega)}^2-2\int_{\Omega}\mathrm{Re}\left(\delta\psi_1\delta\bar{\psi}_2\right)dxdt,\forall v\in V \tag{24}$$

Upon the estimation of the rest summand $R(\delta v)$, then, through the Cauchy-Bunyakovsky inequality, the following is valid:

$$\left|R\left(\delta v\right)\right| \le \left(\left\|\delta v_0\right\|_{L_\infty(0,T)} + \left\|\delta v_1\right\|_{L_\infty(0,T)}\right)\sum_{p=1}^{2}\left\|\Phi_p\right\|_{L_2(\Omega)}\left\|\delta\psi_p\right\|_{L_2(\Omega)} +$$

$$+4\left|a_2\right|\sum_{p=1}^{2}\left(\left\|\psi_{p\delta}\right\|_{L_\infty(\Omega)} + \left\|\psi_p\right\|_{L_\infty(\Omega)}\right)\left\|\Phi_p\right\|_{L_\infty(\Omega)}\left\|\delta\psi_p\right\|^2_{L_2(\Omega)} +$$

$$+\alpha\left\|\delta v\right\|^2_H + 2\sum_{p=1}^{2}\left\|\delta\psi_p\right\|^2_{L_2(\Omega)}. \tag{25}$$

In view of inclusion of the space $W_2^2\left(D\right)$ into $L_\infty\left(D\right)$ [22] provided that $n=3$ the following are found:

$$\left\|\psi_{p\delta}\left(.,t\right)\right\|_{L_\infty(D)} \le c_7\left\|\psi_{p\delta}\left(.,t\right)\right\|_{W_2^2(D)}, p=1,2, \tag{26}$$

$$\left\|\psi_p\left(.,t\right)\right\|_{L_\infty(D)} \le c_8\left\|\psi_p\left(.,t\right)\right\|_{W_2^2(D)}, p=1,2, \tag{27}$$

$$\left\|\Phi_p\left(.,t\right)\right\|_{L_\infty(D)} \le c_9\left\|\Phi_p\left(.,t\right)\right\|_{W_2^2(D)}, p=1,2 \tag{28}$$

for any $t\in\left[0,T\right]$. Using the estimates (10), (11) for the functions $\psi_{p\delta}\left(x,t\right)$, $\psi_p\left(x,t\right), p=1,2$ and the estimates (15), (16) for the functions $\Phi_p\left(x,t\right), p=1,2$ the following inequality is valid:

$$\left\|\psi_{p\delta}\right\|_{L_\infty(\Omega)} \le c_{10},\ \left\|\psi_p\right\|_{L_\infty(\Omega)} \le c_{11},\ \left\|\Phi_p\right\|_{L_\infty(\Omega)} \le c_{12}, p=1,2. \tag{29}$$

Subject to such inequalities and the estimates (15), (15), (16) from (25), the following is found:

$$\left|R\left(\delta v\right)\right| \le c_{13}\left\|\delta v\right\|^2_B. \tag{30}$$

It means that

$$R\left(\delta v\right) = o\left(\left\|\delta v\right\|_B\right). \tag{31}$$

Then, in view of such correlation, the increment $J_\alpha\left(v\right)$ may be recorded as follows:

$$\delta J_\alpha\left(v\right) = J_\alpha\left(v+\delta v\right) - J_\alpha\left(v\right) = \int_\Omega \delta v_0\left(t\right)\mathrm{Re}\left(\psi_1\left(x,t\right)\bar{\Phi}_1\left(x,t\right) + \psi_2\left(x,t\right)\bar{\Phi}_2\left(x,t\right)\right)dxdt -$$

$$-\int_\Omega \delta v_1\left(t\right)\mathrm{Im}\left(\psi_1\left(x,t\right)\bar{\Phi}_1\left(x,t\right) + \psi_2\left(x,t\right)\bar{\Phi}_2\left(x,t\right)\right)dxdt +$$

$$+2\alpha\int_0^T\left(v_0\left(t\right)-\omega_0\left(t\right)\right)v_0\left(t\right)dt + 2\alpha\int_0^T\left(\frac{dv_0\left(t\right)}{dt} - \frac{d\omega_0\left(t\right)}{dt}\right)\frac{dv_0\left(t\right)}{dt}dt +$$

$$+2\alpha\int_0^T\left(v_1\left(t\right)-\omega_1\left(t\right)\right)v_1\left(t\right)dt + 2\alpha\int_0^T\left(\frac{dv_1\left(t\right)}{dt} - \frac{d\omega_1\left(t\right)}{dt}\right)\frac{dv_1\left(t\right)}{dt}dt + o\left(\left\|\delta v\right\|_B\right), \forall v\in V. \tag{32}$$

In this equity, $\delta v\in B$ is replaced with $\theta w\in B$, where $0<\theta<1$ and $w=w\left(t\right)$ are any function from the space B. Then, according to (32), the following is found:

$$\delta J_\alpha(v)=J_\alpha(v+\theta w)-J_\alpha(v)=\theta\int_\Omega \mathrm{Re}\left(\psi_1(x,t)\bar{\Phi}_1(x,t)+\psi_2(x,t)\bar{\Phi}_2(x,t)\right)w_0(t)\,dxdt-$$

$$-\theta\int_\Omega \mathrm{Im}\left(\psi_1(x,t)\bar{\Phi}_1(x,t)+\psi_2(x,t)\bar{\Phi}_2(x,t)\right)w_1(t)\,dxdt+$$

$$+2\alpha\theta\int_0^T\left(v_0(t)-\omega_0(t)\right)w_0(t)\,dt+2\alpha\theta\int_0^T\left(\frac{dv_0(t)}{dt}-\frac{d\omega_0(t)}{dt}\right)\frac{dw_0(t)}{dt}dt+$$

$$+2\alpha\theta\int_0^T\left(v_1(t)-\omega_1(t)\right)w_1(t)\,dt+2\alpha\theta\int_0^T\left(\frac{dv_1(t)}{dt}-\frac{d\omega_1(t)}{dt}\right)\frac{dw_1(t)}{dt}dt+\ o(\theta),\ \forall v\in V\ .\quad(33)$$

Deducting the first variation of the functional through this formula, the following formula is validated:

$$\delta J_\alpha(v,w)=\lim_{\theta\to 0}\frac{J_\alpha(v+\theta w)-J_\alpha(v)}{\theta}=\int_\Omega \mathrm{Re}\left(\psi_1(x,t)\bar{\Phi}_1(x,t)+\psi_2(x,t)\bar{\Phi}_2(x,t)\right)w_0(t)\,dxdt-$$

$$-\int_\Omega \mathrm{Im}\left(\psi_1(x,t)\bar{\Phi}_1(x,t)+\psi_2(x,t)\bar{\Phi}_2(x,t)\right)w_1(t)\,dxdt+$$

$$+2\alpha\int_0^T\left(v_0(t)-\omega_0(t)\right)w_0(t)\,dt+2\alpha\int_0^T\left(\frac{dv_0(t)}{dt}-\frac{d\omega_0(t)}{dt}\right)\frac{dw_0(t)}{dt}dt+$$

$$+2\alpha\int_0^T\left(v_1(t)-\omega_1(t)\right)w_1(t)\,dt+2\alpha\int_0^T\left(\frac{dv_1(t)}{dt}-\frac{d\omega_1(t)}{dt}\right)\frac{dw_1(t)}{dt}dt\ ,\ \forall v\in V\qquad(34)$$

for any function $w\in B$. Hence, the conclusion of the theorem is found. So, theorem 3 is proved. Using the theorem above, we now prove the necessary condition in the form of a variational inequality:

Theorem 4. Let us assume that all the conditions of theorem 3 are met. We assume that $v^*\in V$ -is any solution of the optimal control problem (1)-(3). Then, for any $v\in V$ the following inequality is valid:

$$\int_0^T\left[\int_D \mathrm{Re}\left(\psi_1^*(x,t)\bar{\Phi}_1^*(x,t)+\psi_2^*(x,t)\bar{\Phi}_2^*(x,t)\right)dx+2\alpha\left(v_0^*(t)-\omega_0(t)\right)\right]\left(v_0(t)-v_0^*(t)\right)dt+$$

$$\int_0^T\left[\int_D -\mathrm{Im}\left(\psi_1^*(x,t)\bar{\Phi}_1^*(x,t)+\psi_2^*(x,t)\bar{\Phi}_2^*(x,t)\right)dx+2\alpha\left(v_1^*(t)-\omega_1(t)\right)\right]\left(v_1(t)-v_1^*(t)\right)dt+$$

$$+2\alpha\int_0^T\left(\frac{dv_0^*(t)}{dt}-\frac{d\omega_0(t)}{dt}\right)\left(\frac{dv_0(t)}{dt}-\frac{dv_0^*(t)}{dt}\right)dt+$$

$$+2\alpha\int_0^T\left(\frac{dv_1^*(t)}{dt}-\frac{d\omega_1(t)}{dt}\right)\left(\frac{dv_1(t)}{dt}-\frac{dv_1^*(t)}{dt}\right)dt\ge 0,\qquad(35)$$

where $\psi_p^*(x,t)\equiv\psi_p(x,t;v^*)$, $\Phi_p^*(x,t)=\Phi_p(x,t;v^*),\ p=1,2$ - is the solution of reduced initial boundary (2)-(4) and conjugate problems (12)-(14) provided that $v^*\in V$.

Proof. Let's suppose that $v \in V$ is a certain element and $v^* \in V$ is an arbitrary solution for the optimal control problem (1)-(4). According to the structure of the set V, it is a convex set. So, for $v^* \in V$ and any $v \in V$ the following is found:

$$v^* + \theta\left(v - v^*\right) \in V, \forall\, \theta \in (0,1).$$

Therefore, to consider $v^* \in V$ as a minimal point of the functional $J_\alpha(v)$ at the set V, the satisfaction of the inequality for any $v \in V$ is necessary:

$$\frac{d}{d\theta} J_\alpha\left(v^* + \theta\left(v - v^*\right)\right)\Big|_{\theta=0} = \delta J_\alpha\left(v^*, v - v^*\right) \geq 0.$$

Hence, according to formula (17) provided that $w(t) = v(t) - v^*(t)$, the conclusion of the theorem is found. So, theorem 4 is proved.

Previously, initial boundary value problems for the nonlinear Schrödinger equation with a special gradient term were studied, when the coefficients of the equation depend only on a spatial variable or a time variable. In this paper, we study the problems of optimal control of a three-dimensional nonlinear Schrödinger equation with a specific gradient term and a complex potential, when the controls are the real and imaginary parts of the complex potential and are selected from the class of measurable bounded functions that depend on a time variable and the quality criterion is the full-range integral, which has not been previously studied.

Conclusion

The resolvability theorems as proved above, and the reported expression for the first variation of the quality criterion, as well as the displayed essential extremum condition enable to apply the numerical methods for solution of incorrect and inverse problems, including the optimal control problems with crude data arisen upon studying the movement process of charged particles in the constant uniform magnetic field where the complex potential is unknown and is to be determined.

Recommendations

The results of this paper can be used by researchers for the optimal control problem of a three-dimensional nonlinear Schrödinger equation with a specific gradient term and complex potential.

Scientific Ethics Declaration

* The author declares that the scientific ethical and legal responsibility of this article published in EPSTEM Journal belongs to the author.

Conflict of Interest

* The author declare that they have no conflicts of interest.

Funding

* The research described in this article was carried out with financial support from Nakhchivan State University.

Acknowledgments or Notes

* This article was presented as an oral presentation at the International Conference on Basic Sciences, Engineering and Technology (www.icbaset.net) held in Trabzon/Türkiye on May 01-04, 2025.

* For the assistance provided, special thanks are addressed to the rector of Nakhchivan State University Elbrus Isaev, my scientific supervisor A.D. Iskenderov and professor Gabil Yagub.

References

Diveev, A., Sofronova, E., & Konstantinov, S. (2021). Approaches to numerical solution of optimal control problem using evolutionary computations. *Applied Sciences, 11,* 7096.

Emilio, M., Alain, R., & Héctor, R. (2022). Equivalent formulations of optimal control problems with maximum cost and applications. *Journal of Optimization Theory and Applications, 195,* 953–975.

Ibrahimov, N.S., Yagub, G., & Farzaliyeva, U.M. (2022). The finite-difference method for solving the optimal control problem for the linear nonstationary quasi optics equation with a special gradient term. *XXXVII International Conference Problems of decision making under uncertainties (PDMU-2022),* 48-49.

Iskenderov, A.D., Yagub, G., Salmanov, V., Aktsoy, N.Y. (2019). Optimal control problem for the nonlinear Schrödinger equation with a special gradient term and with a complex potential. *Scientific works of Nakhchivan State University, Series of Physical, Mathematical and Technical Sciences, 4*(101), 32-44.

Iskenderov, A., Yagub, G., Salmanov, V. (2018). Solvability of the initial-boundary value problem for the nonlinear Schrodinger equation with a special gradient term and with a complex potential. *Scientific works of Nakhichevan State University, Series of Physical, Mathematical and Technical Sciences, 4*(93), 28-43

Najafova M.Y. (2022). Informatics and control problems. *Journal of Contemporary Applied Mathematics,12*(1), 51-82.

Salmanov, V.I. (2020). Existence and uniqueness of the solution to the problem optimal control problem with integral criterion qualities over the entire domain for a nonlinear Schrödinger equation with a special gradient. *Control and Cybernetics. Systems Research Institute, Polish Academy of Sciences,3,* 211-290.

Yagub, G., Ibrahimov, N., Suleymanov, N. (2022). The second initial boundary-boundary problem for equalization of a Schroedinger with a special gradient compound and with a measurement of a limited complex potential depending on time. *Scientific News:Lankaran State University. Mathematics and Natural Sciences Series, 1,* 13-30.

Yagub, G., Ibrahimov, N.S., Zengin, M. (2015). Solvability of the initialboundary value problems for the nonlinear Schrödinger equation with a spesial gradient terms. *XXV International Conference Problemsof Decision Making under Uncertainties (PDMU-2015),* 53-54.

Yagubov, G., Salmanov, V., Yagubov, V., Zengin, M. (2017). Solvability of initial-boundary value problems for the nonlinear two-dimensional Schrodinger equation. *Scientific Works of Nakhchivan State University, Series of physical, mathematical and Technical Sciences, 4*(85), 7-21.

Yagub, G., Ibrahimov, N.S., Zengin, M. (2021). Optimal control problem for the stationary quasi-optics equation with a special gradient term. *Advanced Mathematical Models & Applications, 6*(3), 252-265.

Zengin, M., Ibrahimov, N.S., & Yagub, G. (2021). Existence and uniqueness of the solution of the optimal control problem with boundary functional for nonlinear stationary quasi-optical equation with a special gradient term. *Scientific Proceedings Lankaran State University, Mathematical and Naturel Sciences Series, 1*, 27-42

Author Information

Vugar Ibrahim Salmanov
Nakhchivan State University
Nakhchivan city, University campus, AZ7012, Azerbaijan
Contact e-mail: *vugarsalmanov@ndu.edu.az*

To cite this article:

Salmanov, V.I. (2025). Optimal control problem and integral quality criteria with a special gradient term. *The Eurasia Proceedings of Science, Technology, Engineering and Mathematics (EPSTEM), 34,* 310-319.

The Eurasia Proceedings of Science, Technology, Engineering & Mathematics (EPSTEM)
ISSN: 2602-3199

The Eurasia Proceedings of Science, Technology, Engineering and Mathematics (EPSTEM), 2025

Volume 34, Pages 320-325

ICBASET 2025: International Conference on Basic Sciences, Engineering and Technology

Comparative Analysis of Measures to Reduce Wear on Ship Hull Structures in Areas Around Ballast System Suction Pipes

Yordan Denev
Technical University of Varna

Abstract: During the operation of a ship, it is necessary to take in and discharge ballast water. This is carried out with the help of the ship's ballast system. When the system is in operation, ulcers form in the areas beneath the suction pipes. This phenomenon is due to cavitation erosion, which is common in this type of system. The article examines measures to increase the wear resistance of the ship hull structure, most often the bottom plating of the ship hull in these areas. Criteria for evaluating two types of measures with the same purpose are proposed. It has been proven that by installing additional wear-resistant plates beneath the suction pipes of the ballast system, the wear problem is eliminated. On one hand, this measure helps reduce the time needed for hull repairs during docking and class repairs. On the other hand, it saves a significant amount of money for the shipowner, as additional activities related to providing repair conditions are not necessary.

Keywords: Wear, Suction pipes, Ship ballast system, Cost, Repair

Introduction

The wear and tear on ship structures around the suction and ballast tank pipes is a widely known and very common problem in ship repair practice. It occurs in relatively older ships of the world commercial fleet. In many cases, this wear leads to a breach in the watertight integrity of the ship's hull or the watertightness between ballast tanks.

Corrosion in ship ballast tanks is a phenomenon that cannot be completely restricted during the operation of the ship. It is caused by various factors such as microorganisms, among others, but fundamentally steel can interact with the environment when the corrosion protection is compromised. Intensive corrosion in these areas of the ship's hull causes serious damage to the ship's structural integrity. A study on the effects of microbiologically influenced corrosion as a serious problem in the shipping industry was conducted in Heyer et al. (2013). There, the authors thoroughly examine the construction and purpose of ballast tanks, summarize the mechanism of corrosion from an electrochemical perspective, and discuss surface treatment and coating applications. A significant aspect is the outlined measures to reduce microbiological corrosion. Some of these measures include excellent application of anti-corrosion coatings, structural changes to reduce sediment in the water, treating the water with nitrogen, and more. Part of these measures are already being implemented with the so-called ballast water treatment systems.

With the introduction of ballast water treatment systems, various installations and mechanisms for their treatment have also emerged. Some of them do not cause damage to the ship's hull structure in the areas around the suction pipes, while others do. One such method is the developed counter-rotating hydrodynamic device (Ren et al., 2023). Its purpose is to mechanically treat the ballast water on board the ship. It has been found that at a certain range of rotational speeds, cavitation bubbles form, which develop cavitation in later stages.

The accumulated sediments in ballast tanks lead to intense corrosion and wear in certain areas of the tanks. To reduce this undesirable phenomenon, a modification to the design of ships has been proposed in (Prange, 2013).

- Selection and peer-review under responsibility of the Organizing Committee of the Conference

The proposed modification involves the creation of scuppers on the floors and stringers, allowing easier passage of water to the suction points of the ballast system. This modification is also applicable to already constructed ships.

Non-ballast onboard (NOBOB) ships pose a significant environmental risk because even a small amount of residual ballast water can support the survival of benthic and planktonic organisms in the bottom of the tanks (Drake et al., 2005). These organisms were responsible for several invasive species outbreaks in both Chesapeake Bay and the Great Lakes during the 1980s, a time when regulations for residual sediments in tank bottoms were inadequate (Drake et al., 2007). With this type of ship, problems with wear under the suction and measuring pipes are absent, which somewhat facilitates their maintenance and repair.

For all types of corrosive and erosive wear, there are suitable methods for prevention and repair. Most commonly, these methods include welding and the installation of corrosion- and erosion-resistant plates. Additionally, it is important to analyze both methods in terms of the time required for making the improvement or repair.

Criteria for a Comparative Analysis Between the Measures for Wear Reduction

The proposed comparison criteria are adapted and fully comply with real ship repair practices. The two comparison options are as follows. Option one is when the erosion resistance plate is installed during the ship hull repair stages, and option two is when the erosion resistance plate is installed during the ship hull building stage.

The comparison and evaluation criteria are follows: opening and closing of the manhole, tank ventilation, cleaning before work, cleaning after work, and repair area preparation. As proposed, they are directly related to the technological time required for the ship's repair. Each one of them is described in the next paragraphs.

Figure 1. Option one without installed plate

Figure 2. Option two with installed plate

Manhole Opening/ Closing

The opening and closing of manholes on the ballast tanks of the hull is a routine procedure during repairs. They are not opened and closed if emergency repairs are being carried out and the respective tank is not affected. Besides providing easy access to the tank, they also play a role in its ventilation, however minimal that may be. It is unacceptable to enter a ballast tank without it being ventilated.

The manhole cover is closed using a threaded connection. During the opening process, the threads of some bolts become damaged, necessitating their re-threading or replacement with new ones. Replacing them with new bolts is a critical task because the welded joint must be watertight after the repair. If these activities are not accounted for in the ship's repair schedule, they can sometimes lead to an increase in the repair time. When closing the manholes, new gaskets must be installed. In most cases, these are rubber gaskets cut to the shape of the manhole.

Tank Ventilation

Ventilation of ballast tanks is a mandatory process before starting any work in them or gaining access for inspection. After opening the manholes of all ballast tanks, the quantity and composition of the air in them are determined. This is done using special devices called gas analyzers, after which specific protocols are filled out. Permission to work or inspect the tank is granted when the air is within the permissible limits. The main consideration is the minimum oxygen level, which must be no less than 21% (International Chamber of Shipping). If it is below the allowable limit, intensive ventilation of the tank is initiated. In practice, a pressure

ventilation system is often installed on one manhole of the tank, and a suction ventilation system, usually centrifugal fans, is installed on the other.

Cleaning Before Repair

The cleaning of the work areas begins after the tank is fully ventilated and a gas-free certificate is issued. Cleaning before starting repair activities is an important step. It can be carried out in two ways: partial cleaning for access or complete cleaning of the tank. Primarily, it involves cleaning out water that was not discharged overboard and mud settled during the ship's ballast operations. Proper cleaning ensures safe work and quick completion of repair activities in the ballast tank. The working time depends on the size of the tank, the type of construction, and the degree of contamination.

Cleaning After Repair

Cleaning after completing the repair is an important stage following the completion of the repair. It involves the removal of all technological waste generated during the repair process. Most often, these are remnants of electrodes, pieces of cut metal, electric bulbs, household waste such as water bottles, dust masks, and others. This process is mandatory because some of this waste can end up in the ballast system pipelines and disrupt their normal operation.

Repair Area Preparation

Preparing the area consists of a series of operations to ensure the smooth execution of the repair. The main operations performed are directly related to the cutting and welding processes. Their quality largely depends on the cleaning done before starting the repair and entering the tank in general.

The surface preparation for repair in option one consists of burning off the paint around and under the suction pipe, welding, grinding the welded areas, installing, and welding the anti-erosion plate. The peculiarity here is that all these activities cannot be performed by two people simultaneously. This is precisely why the repair takes a longer time to complete.

Evaluation Criteria Validation and Comparative Analysis

The preliminary developed criteria for evaluating the reduction of wear in the areas around the ballast pipeline suction pipes have to be validated. Validation consists of assigning each criterion to the corresponding option. In this case, whether a specific activity will be carried out in a particular option for reducing wear is defined by the number 1, and if it will not be done, by the number 0 Table1.

Table 1. Criteria validation

Criteria	Variant 1	Variant 2
Manhole opening/ closing	1	0
Tank ventilation	1	1
Cleaning before repair	1	0
Cleaning after repair	1	1
Repair area preparation	1	0

From the criteria presented in Table.1 and their validation for each of the two methods, it can be seen that all activities are applicable in option one. While in option two, only two of them are applicable. This is mainly due to the fact that such work to improve the wear resistance of these areas is much easier to perform when access to them is significantly easier and does not require much additional equipment.

In shipbuilding and ship repair practice, for easier quoting and pricing, it is customary to measure the work done in man-hours. For example, in Burler (2000), the number of man-hours for various types of activities related to the overall repair of the ship is presented. The required number of man-hours for the various activities related to the analysis and evaluation of two methods for reducing the wear of the hull structure around the ballast pipeline suction points is presented in Table 2.

Table 2. Man hours for different criteria

Criteria	Variant1, mh	Variant 2, mh
Manhole opening/ closing	2	0
Tank ventilation	10	10
Cleaning before working	5	0
Cleaning after working	2	2
Repair area preparation	6	0

The values of the man-hours presented in Table 2 for each criterion are based on experience from the ship repair practice of a small to medium-sized ship repair enterprise. The man-hour values include all activities from preparation to final completion, including working with crane equipment for activities related to tank cleaning. The cleaning work before and after the repair is carried out by several people, most often three or four. It should be noted that the specified values pertain to the repair in a single ballast tank. It is assumed that the cleaning covers 80% of the bottom area of the respective tank and there is 10 mm of water in the tank, which is the distance from the suction point to the bottom lining or the double bottom of the ship.

The comparative analysis shows that the total number of man-hours in option one is relatively higher than in option two, figure 3. This is partly due to not only the different types of additional work related to the repair but also to factors such as poor-quality materials, non-standard operating conditions of the ballast pumps, and other circumstances without which the ships would not be able to perform their functional purpose.

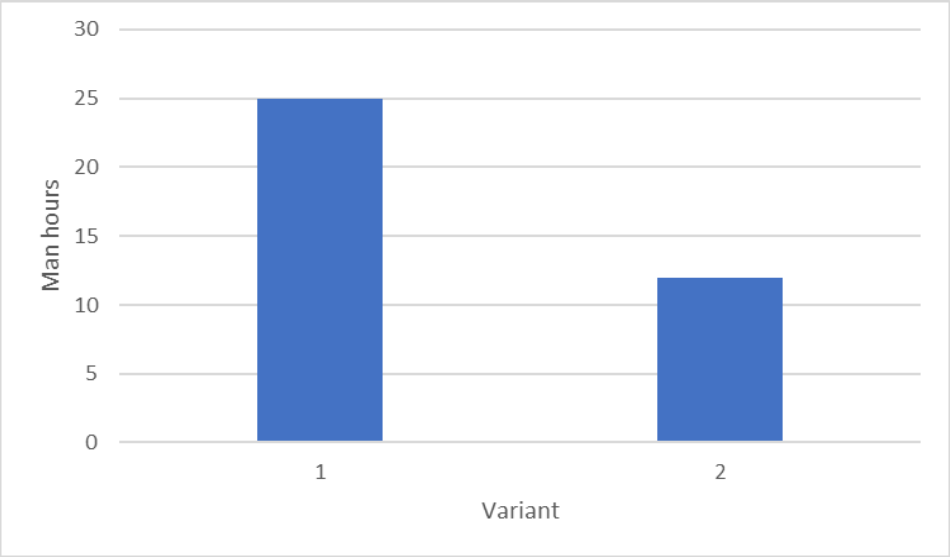

Figure 3. Comparative analysis between the variants

The results presented in fig.3 make it clear that with pre-installed wear-resistant plates under the ballast system suction points, significant savings are achieved in the ship repair time, and thus costs, which in most cases are not anticipated. The difference in man-hours, measured in percentages, is approximately 50% more time required to repair the worn areas around and under the suction pipes of the ship's ballast system when no wear-resistant plates were installed during the construction stages.

Conclusion

The wear of the ship's hull structure in the areas around the ballast system intakes is a common issue. In many cases, it is observed in relatively older ships and those with a non-stationary operating mode of elements (pumps) in the ballast system. Two possible solutions to this problem are presented. Option one is when the erosion resistance plate is installed during the ship hull repair stages, and option two is when the erosion resistance plate is installed during the ship hull building stage.

Criteria for evaluating each of the methods have been proposed. The proposed criteria are directly related to the time required for the construction or repair in these areas. The criteria include opening the manhole, tank ventilation cleaning before repair, cleaning after repair, and surface preparation in the area for performing hull work. The proposed criteria have been validated for each of the two methods. Average man-hours for the work

of each method have been presented. It has been found that the method based on installing a wear-resistant plate during the ship's construction stage takes about 50% less time for repairs compared to installing such a plate during dock repairs. The results obtained from the analysis provide a clear argument for implementing the installation of corrosion-resistant plates under the intakes of ballast systems on all ships in the global commercial fleet.

Scientific Ethics Declaration

* The author declares that the scientific ethical and legal responsibility of this article published in EPSTEM Journal belongs to the author.

Conflict of Interest

* The author declares no conflict of interest

Funding

* This research received no specific grant from any funding agency in the public, commercial, or not-for-profit sectors

Acknowledgements or Notes

* This article was presented as an oral presentation at the International Conference on Basic Sciences, Engineering and Technology (www.icbaset.net) held in Trabzon/Türkiye on May 01-04, 2025.

References

Bulter, G. (2000). *Guide to ship repair estimates (in man-hours).* Butterworth-Heinemann.

Drake, L. A., Jenkins, P. T., & Dobbs, F. C. (2005). Domestic and international arrivals of NOBOB (no ballast on board) vessels to lower Chesapeake Bay. *Marine Pollution Bulletin*, *50*(5), 560-565.

Heyer, A., D'Souza, F., Leon Morales, C.F., Ferrari, G., Mol, J.M.C., & de Wit, J.H.W. (2013). Ship ballast tanks a review from microbial corrosion and electrochemical point of view. *Ocean Engineering, 70*, 188-200.

Prange, G., & Pereira, N. (2013). Ship ballast tank sediment reduction methods. *Naval Engineers Journal, 125*(2), 127-134.

Ren, W., Bie, H., Liu, G., Guo, C., & Hao, Z. (2023). Research of a novel counter rotating hydrodynamic cavitation device applied for ballast water treatment. *Ocean Engineering, 288.*

Author Information

Yordan Denev
Technical University of Varna
Studentska 1 str., Varna, Bulgaria
Contact e-mail: *y.denev@tu-varna.bg*

To cite this article:

Denev, Y. (2025). Comparative analysis of measures to reduce wear on ship hull structures in areas around ballast system suction pipes. *The Eurasia Proceedings of Science, Technology, Engineering and Mathematics (EPSTEM), 34,* 320-325.

The Eurasia Proceedings of Science, Technology, Engineering & Mathematics (EPSTEM)
ISSN: 2602-3199

The Eurasia Proceedings of Science, Technology, Engineering and Mathematics (EPSTEM), 2025

Volume 34, Pages 326-332

ICBASET 2025: International Conference on Basic Sciences, Engineering and Technology

Investigation of DNA Protective Activities and Antimicrobial Effects of Spinach (*Spinacia oleracea L.)* Plant Extracts on *Stenotrophomonas maltophilia*

Suleyman Yilmaz
Gaziantep University

Ibrahim Halil Kilic
Gaziantep University

Maryam Mohammed-Ali
Gaziantep University

Mehmet Ozaslan
Gaziantep University

Abstract: Spinach *(Spinacia oleracea L.)* is a nutrient-dense leafy vegetable known for its rich phytochemical profile, including flavonoids, carotenoids, and phenolic compounds, which contribute to its significant antioxidant and antimicrobial potential. In this study, the DNA protective effects and antibacterial activities of spinach extracts were evaluated, particularly against the multidrug-resistant bacterium *Stenotrophomonas maltophilia*. Methanolic and aqueous extracts were prepared and analyzed for total phenolic and flavonoid contents, followed by antioxidant activity assessment through DPPH and FRAP assays. The ability of these extracts to protect plasmid DNA from oxidative damage was investigated using an in vitro hydroxyl radical-induced DNA fragmentation model. The antimicrobial activity was tested using the agar diffusion method and MIC determination. The findings indicated that spinach extracts exhibit high antioxidant activity, closely linked to their phytochemical richness, and significantly protect against DNA strand breaks caused by reactive oxygen species (Kaur & Kapoor, 2020; Patel et al., 2018). Furthermore, the methanolic extract showed inhibitory effects on *S. maltophilia,* suggesting the presence of antibacterial phytoconstituents (Ali et al., 2019; Lee et al., 2021). These results support the traditional use of spinach in health maintenance and its potential application in developing natural antimicrobial and DNA-protective agents, particularly relevant in the era of increasing antibiotic resistance (Singh & Verma, 2017).

Keywords: *Spinacia oleracea*, DNA protector, Antimicrobial effect, *Stenotrophomonas maltophilia,* antimicrobial activity

Introduction

Spinach *(Spinacia oleracea)* is a winter vegetable cultivated and consumed worldwide. Belonging to the Amaranthaceae family, it is native to Central Asia and is categorized among the leafy vegetables consumed for their edible leaves. Thanks to its rich content of minerals and vitamins, spinach holds high nutritional value and is considered a valuable and traditional component of many diets (Esiyok, 2012). Its annual global production is approximately 30 million tons, and its cultivation is widespread across the world. In terms of production, Turkey ranks fourth globally, following China, the United States, and Japan.

In Turkey, spinach can be grown in all regions except for the Eastern Black Sea Region. Spinach, a plant native to the Mediterranean region, is cultivated in three distinct growing seasons. In Europe and the United States, sowing techniques and cultivars have been developed to allow for year-round harvesting (Esiyok, 2012). In Turkey, spinach is a widely consumed vegetable during the winter months (Vural et al., 2000). As an important winter crop, spinach is highly nutritious due to its composition of essential minerals and vitamins. It is particularly rich in mineral salts, especially iron. Furthermore, spinach is an excellent source of vitamin A, vitamin K, vitamin C, vitamin B2, manganese, magnesium, folic acid, iron, and potassium. It also contains significant amounts of vitamin B6, vitamin E, omega-3 fatty acids, and dietary fiber (Patel et al.,2018).

Spinach consumption has been associated with numerous health benefits. It has been shown to possess lipid-lowering properties, cardiovascular protective effects, anti-obesity and anti-inflammatory activities, hypoglycemic action, anticancer potential, and neuroprotective functions (Lee et al., 2021). Plant-derived polyphenolic flavonoids found in spinach exhibit a range of biological and pharmacological properties and may help prevent chronic diseases.

Spinach flavonols have been specifically shown to exhibit antioxidant, anti-inflammatory, antimutagenic, and anticancer properties (Kaur & Kapoor, 2020). Spinach contains at least 13 different flavonoid compounds that function as antioxidants and anticancer agents. Phenolic compounds also serve as antifungal, antiviral, and antimicrobial agents (Esiyok, 2012). Fresh spinach is widely recognized for its antioxidant properties, largely attributed to the phenolic and flavonoid compounds concentrated in its leaves, including ferulic acid, quercetin, patuletin, spinacetin, and jaceidin (Vural et al., 2000).

The antimicrobial activity of plant-based foods like spinach is thought to result from their inhibitory effects on bacterial cells. These effects are associated with the formation of complexes with sulfhydryl groups of proteins, which act as enzyme cofactors, alter membrane permeability, and disrupt the respiratory chain. Antibiotics are classified according to their spectrum of activity, mechanisms of action, and chemical structure (Murcia et al., 2020). The development of microbial resistance as a result of antibiotic use dates back to the earliest days of antibiotic discovery. Initially a concern limited to hospital settings, resistant bacterial strains have now become a serious challenge in the treatment of community-acquired infections as well. *Stenotrophomonas maltophilia* is an aerobic, non-fermentative, Gram-negative bacillus. It is considered an opportunistic pathogen that can cause severe infections, particularly in hospitalized patients, especially those in intensive care units (Cho et al., 2008).

In recent years, there has been growing interest in studying the DNA-protective activity, antioxidant, antimicrobial, anticancer, and antifungal properties of products derived from medicinal and aromatic plants (Golla &Bhimathati, 2014). Spinach has been shown to exhibit antimicrobial effects against a variety of Gram-positive and Gram-negative bacteria. In this study, we investigated the bioactive potential of spinach water and methanol extracts, focusing on their effectiveness against *Stenotrophomonas maltophilia,* a pathogen increasingly associated with nosocomial (hospital-acquired) infections. Specifically, we evaluated the extracts' antioxidant potential and DNA-protective activity.

Materials and Methods

Spinach samples were obtained from local greengrocers and markets within the Gaziantep province. The collected spinach specimens were air-dried and then ground into a fine powder using a mechanical grinder. Subsequently, 40 grams of the spinach powder were subjected to extraction using methanol in a Soxhlet apparatus at approximately 75°C for 6 hours. The resulting extracts were then concentrated under reduced pressure using a rotary evaporator and stored at +4°C for further analysis.

Activity Analysis Against *Stenotrophomonas maltophilia*

To evaluate the antimicrobial activity of the spinach extracts, *Stenotrophomonas maltophilia* was used as the test organism. A standard strain of *S. maltophilia* was employed for the analyses. The Disk Diffusion Method was applied in accordance with the criteria established by the European Committee on Antimicrobial Susceptibility Testing (EUCAST).

Figure1. *S. maltophilia* strain cultured on Mueller-Hinton Agar (MHA) medium

DNA Protective Activity

The potential of the extracts to protect DNA from UV and oxidative damage was assessed using pBR322 plasmid DNA (Vivantis). DNA damage was induced by exposing the plasmid to hydrogen peroxide (H_2O_2) and ultraviolet (UV) light in the presence of the extracts. Visualization was performed on a 1.5% agarose gel in accordance with the method described by Russo et al. (2000). Each reaction tube contained 3.0 µl of pBR322 plasmid DNA (172 ng/µl) and 1.0 µl of 30% H_2O_2. The tube containing the spinach extract was then exposed to UV radiation for 5 minutes. After this exposure, 2.0 µl of loading dye was added, and the sample was loaded onto a 1.5% agarose gel.UV exposure was carried out using a UV transilluminator (DNR-IS) operating at a wavelength of 302 nm and an intensity of 8000 µW/cm² at room temperature. Following agarose gel electrophoresis, DNA bands were visualized and photographed using a gel documentation system (DNR-IS, MiniBIS Pro). In this test system, untreated pBR322 plasmid DNA (i.e., not exposed to UV or H_2O_2) served as the positive control.

Antioxidant Activity

Total Antioxidant Status (TAS) and Total Oxidant Status (TOS) analyses were performed using the Rel Assay Diagnostics kit, following the manufacturer's recommended protocols. To prepare the extract concentrations at 1.0%, 5.0%, and 10.0%, 10 mg of each water and methanol extract was weighed, and 100 µl of distilled water was added to each sample.

Results

To determine the antibacterial activity potential of the extracts against *Stenotrophomonas maltophilia*, the disk diffusion test was conducted in accordance with the criteria set by the European Committee on Antimicrobial Susceptibility Testing (EUCAST).

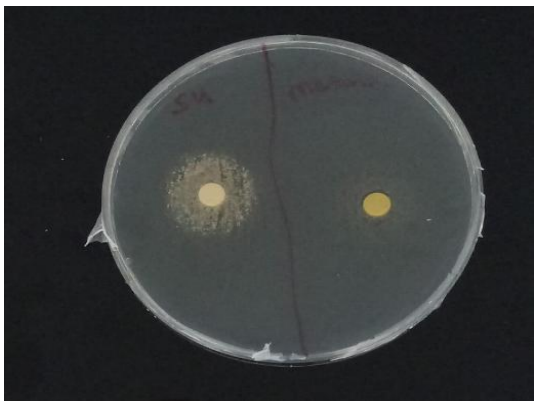

Figure 2. Activity test against *S. Maltophilia*

No inhibition zone was observed. It was determined that the spinach extract did not exhibit any antimicrobial effect against *Stenotrophomonas maltophilia.*

Findings on the DNA Protective Activity of Spinach Extracts

In agarose gel visualization of plasmid DNA, three distinct forms can typically be observed: nicked DNA, linear DNA, and supercoiled DNA. In control samples where only plasmid DNA is loaded without exposure to damaging agents, the supercoiled form predominates. This appears as a bright band near the lower region of the gel, often accompanied by a faint upper band corresponding to nicked DNA. The linear form is generally not observed in such cases.

When DNA is exposed to damaging agents, strand breaks result in the appearance of all three DNA forms on the agarose gel. The nicked DNA appears as the brightest band closest to the loading well, followed by decreasing brightness in the linear and supercoiled forms. In severely damaged DNA samples, only two bands are typically observed: a bright nicked DNA band near the well and a fading linear DNA band; the supercoiled band is absent, indicating complete structural deformation.In DNA protection assays, both the structural form and brightness of the bands are indicators of protective efficacy. A typical plasmid preparation usually exhibits both nicked and supercoiled DNA. Lane 1 reflects DNA damage, with predominance of nicked forms. Lane 2 shows complete DNA degradation. Lane 3 represents a good-quality plasmid preparation, with predominantly supercoiled DNA.

Figure 3. Gel electrophoresis image of spinach extracts

- **Positive Control (K1):** Plasmid DNA (3 µl) + dH_2O (6 µl)
- **Negative Control (K2):** Plasmid DNA (3 µl) + dH_2O (6 µl) + UV (5 min) + H_2O_2 (1 µl)
- **Sample 1:** Plasmid DNA (3 µl) + spinach water extract (5 µl) + UV (5 min) + H_2O_2 (1 µl)
- **Sample 2:** Plasmid DNA (3 µl) + spinach ethanol extract (5 µl) + UV (5 min) + H_2O_2 (1 µl)

As observed in the gel image, the DNA protective potentials of the samples prepared with spinach extracts were analyzed by comparing them with the control groups. The spinach extracts demonstrated partial protective activity against DNA damage.

Antioxidant Analysis

The antioxidant activities of spinach methanol and water extracts were determined using the Rel Assay antioxidant kit. The results obtained are presented in Table 1, as well as in Figures 1 and 2.

Table 1. Reference values for TAS and TOS

TAS(mmol Trolox Equiv/L)		TOS(mmol Trolox Equiv/L)	
> 2,00	Very Good	< 5,00	Very Good
1,45-2,00	Normal	8-5	Normal
1,20-1,45	Normal-Acceptable	12-8	High Oxidant Level
1,00-1,20	Low Antioxidant Level	> 12,00	Very High Oxidant Level
< 1,00	Very Low Antioxidant		

Table2. TAS, TOS ve osı , results

	TOS (µmol H2O2 Equiv/L)	TAS (mmol Trolox Equiv/L)	OSI
M1	1,784	2,827	0,6310577
M2	4,313	2,764	1,5604197
M3	3,222	2,209	1,4585785
W1	2,181	4,273	0,5104142
W2	2,776	4,262	0,6513374
W3	2,082	4,28	0,4864486

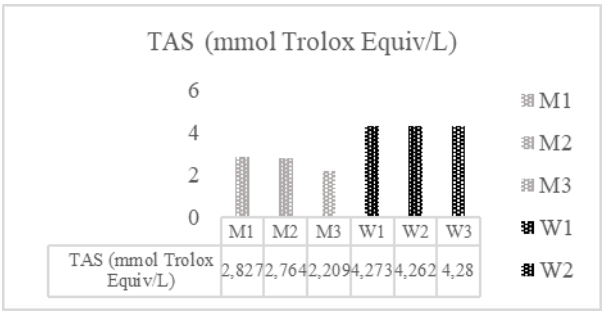

Graph1. TAS results of water and methanol extracts at different concentrations

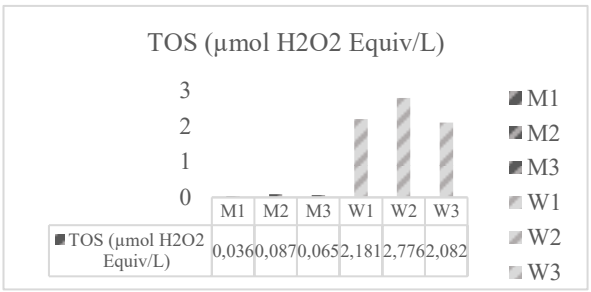

Graph 2. TOS results of water and methanol extracts at different concentrations

Discussion

Plants have been utilized since the dawn of humanity to support human health and enhance quality of life (Singh & Verma, 2017). Turkey holds a significant position among the richest countries in the world in terms of plant biodiversity. In addition to its botanical diversity and traditional plant usage, Turkey is also one of the leading countries in fruit and vegetable production.

Spinach flavonols have been shown to possess antioxidant, anti-inflammatory, antimutagenic, and anticancer properties (Kaur & Kapoor,2020). Spinach contains at least 13 different flavonoids that function as antioxidant and anticancer agents. Moreover, its phenolic compounds exhibit antifungal, antiviral, and antimicrobial activities (Esiyok, 2012). In our study, water extracts of spinach demonstrated strong antioxidant potential and did not display any oxidant activity.

The antimicrobial effect of plant-derived foods like spinach is believed to result from their inhibitory interactions with bacterial cells—through mechanisms such as disruption of membrane permeability, interference with enzyme cofactors, and complex formation with sulfhydryl groups of respiratory chain proteins. However, in our study, neither the water nor methanol extracts of spinach exhibited any detectable antimicrobial effect against *Stenotrophomonas maltophilia*.In recent years, extensive research has emerged on the DNA-protective properties of compounds derived from medicinal and aromatic plants. There is a growing interest, particularly in the cosmetics industry, in finding alternatives to synthetic UV-protective agents for use in sunscreens—especially those based on organic compounds. Our findings indicated that spinach water extract exhibited protective effects against both UV-induced and oxidative DNA damage.

This study aimed to evaluate the antioxidant, antimicrobial, and DNA-protective potential of water and methanol extracts of spinach. Literature review revealed that while numerous studies have examined the

biological activities of essential oils derived from spinach, there were no prior studies involving *Stenotrophomonas maltophilia* as a test organism. Additionally, no studies were found addressing the DNA-protective activity of spinach extracts. Therefore, this research represents a novel and significant contribution in terms of originality.

Recommendations

The analysis presented in this paper can be sophisticated by applying non-linear viscoelastic models of the beams. In this way, the effect of the cross-section shape on the longitudinal fracture behavior of non-linear viscoelastic inhomogeneous beams can be examined.

Scientific Ethics Declaration

* The author declares that the scientific ethical and legal responsibility of this article published in EPSTEM Journal belongs to the author.

Conflict of Interest

* The authors declare that they have no conflicts of interest.

Funding

* This research received no specific grant from any funding agency in the public, commercial, or not-for-profit sectors

Acknowledgements or Notes

* This article was presented as an oral presentation at the International Conference on Basic Sciences, Engineering and Technology (www.icbaset.net) held in Trabzon/Türkiye on May 01-04, 2025.

References

Acar, J.F., & Goldstein, F.W. 1996. Disk susceptibility test. In V. Lorian (Ed.), *Antibiotics in laboratory medicine* (4th ed.). Baltimore: Williams and Wilkins.

Ali, M., Khan, T., Fatima, K., Ali, Q. U., & Hussain, A. (2019). Antimicrobial activity of plant extracts against drug-resistant pathogens. *Saudi Journal of Biological Sciences, 26*(6), 1297–1304.

Cho, M. J., Howard, L. R., Prior, R. L., & Morelock, T. (2008). Flavonoid content and antioxidant capacity of spinach genotypes determined by high-performance liquid chromatography/mass spectrometry. *Journal of the Science of Food and Agriculture, 88*(6), 1099–1106.

Coenye, T., Vanlaere, E., LiPuma, J.J., & Vandamme, P. (2004). Identification of genomic groups in the genus *Stenotrophomonas* using gyrB RFLP analysis. *FEMS Immunology and Medical Microbiology, 40*(3), 181–85.

da Silva Dias, J.C., & Imai, S. (2017). Vegetables consumption and its benefits on diabetes. *Journal of Nutrition Therapy, 6*(1), 1-10.

Denton, M., & Kerr, K.G. (1998). Microbiological and Clinical Aspects of Infection Associated with *Stenotrophomonas maltophilia*. *Clinıcal Microbiology Reviews*,*11*(1), 57– 80

Esiyok, D. (2012). *Kıslık ve yazlık sebze yetistiriciligi.* Sidas Publishing.

Golla, U., & Bhimathati, S. S. R. (2014). Evaluation of antioxidant and DNA damage protection activity of the hydroalcoholic extract of *Desmostachya bipinnata L. Stapf. The Scientific World Journal, 2014*(1), 215084.

Gulay, Z. (2002). Antibiyotik duyarlılık testlerinin yorumu. *Toraks Dergisi, 3*(1), 75- 88.

Hermsdorff, H. H. M., Barbosa, K. B. F., Volp, A. C. P., Puchau, B., Bressan, J., Zulet, M. A., & Martinez, J. A. (2011). Vitamin C and fibre consumption from fruits and vegetables 124 improves oxidative stress markers in healthy young adults. *British Journal of Nutrition, 107*(8), 1119–1127.

Howard, L. R., Pandjaitan, N., Morelock, T., & Gil, M. I. (2002). Antioxidant capacity and phenolic content of spinach as affected by genetics and growing season. *Journal of Agricultural and Food Chemistry, 50*(21), 5891–5896.

Kaur, C., & Kapoor, H. C. (2020). Phytochemical and antioxidant properties of spinach extracts. *Food Chemistry, 323*, 126741.

Lee, H. S., Kim, Y. J., & Park, Y. S. (2021). Natural compounds from spinach and their antimicrobial potential. *Journal of Food Composition and Analysis, 98, 103975*.

Looney, WJ., Narita, M., & Muhlemann, K. (2009). *Stenotrophomonas maltophilia*: an emerging opportunist human pathogen. *Lancet Infectious Diseases. 9,* 312-23.

Maeda, N., Yoshida, H., & Mizushina, Y. (2010). Spinach and health. In *Bioactive foods in promoting health* (pp.393–405). Academic Press.

Murcia, M. A., Jimenez-Monreal, A. M., Gonzalez, J., & Martinez-Tome, M. (2020). Spinach. In *Nutritional composition and antioxidant properties of fruits and vegetables* (pp.181–195). Academic Press.

Patel, D., Goyal, R. K., & Bhatt, V. (2018). Spinach extract reduces DNA damage and exhibits anti-inflammatory properties. *Journal of Functional Foods, 45,* 176–183.

Roberts, J. L., & Moreau, R. (2016). Functional properties of spinach (*Spinacia oleracea L.)* phytochemicals and bioactives. *Food & Function, 7*(8), 3337–3353.

Schugerl, K. (2001). Progress in monitoring, modeling and control of bioprocesses during the last 20 years. *Journal of Biotechnology, 85*(2), 149-173.

Singh, N., & Verma, P. (2017). Oxidative stress and DNA damage protection by leafy vegetables. *Phytochemistry, 138*, 21–29.

Singh, N.D., Aquadro, C.F., & Clark, A.G. (2009). Estimation of fine-scale recombination intensity variation in the white-echinus interval of D. melanogaster. *Journal of Molecular Evoluation, 69*(1), 42--53.

Vural, H., Esiyok, D., & Duman, I. (2000). *Kultur sebzeleri.* Ege University.

Author(s) Information

Suleyman Yilmaz
Gaziantep University, Institute of Science/Molecular Biology Department
Gaziantep, Türkiye

Ibrahim Halil Kilic
Gaziantep University, Institute of Science/Molecular Biology Department
Gaziantep,Türkiye

Maryam Mohammed Ali
Gaziantep University, Institute of Science/Molecular Biology Department.
Gaziantep, Türkiye

Mehmet Ozaslan
Gaziantep University, Institute of Science/Molecular Biology Department
Gaziantep, Türkiye

To cite this article:

Yilmaz, S., Kilic, I. H., Mohammed-Ali, M., & Ozaslan, M. (2025). Investigation of DNA protective activites and antimicrobial effects of spinach (*Spinacia oleracea L.)* plant extracts on *Stenotrophomonas maltophilia. The Eurasia Proceedings of Science, Technology, Engineering and Mathematics (EPSTEM), 34,* 326-332.

The Eurasia Proceedings of Science, Technology, Engineering & Mathematics (EPSTEM)
ISSN: 2602-3199

The Eurasia Proceedings of Science, Technology, Engineering and Mathematics (EPSTEM), 2025

Volume 34, Pages 333-338

ICBASET 2025: International Conference on Basic Sciences, Engineering and Technology

Selective Transport of Bismuth from Heavy Metal Solution by Ionic Liquid-Based Polymer Inclusion Membrane IL-PIM

Mohamed Malki
University of Tizi Ouzou

Rabea Meziani
University of Tizi Ouzou

Lynda Mitiche
University of Tizi Ouzou

Amar Sahmoune
University of Tizi Ouzou

Claudia Fontas
University of Girona

Abstract: Bismuth is an important critical metal which is under risk of supply. It is mainly found and extracted at trace amounts in copper, lead, tin and gold mining by-product. In this work, we present the results of the selective transport of trace bismuth Bi(III) from a solution of heavy metals by an Ionic liquids-based Polymer Inclusion Membranes (PIM), using the task-specific ionic liquid: trihexyl(tetradecyl) phosphonium salicylate (THTDPS), as extractant and ion carrier. The TS-IL was first synthesized by exchanging the inorganic anion of trihexyl(tetradecyl) phosphonium chloride Cyphos IL 101 with the organic anion of sodium salycilate. Important parameters influencing extraction and transport have been examined and optimized. The studied PIM is composed of 50% CTA, and 50% THTDPS without any additional chemical (modifier or plasticizer). The performance and stability of the PIM was carried out in depth. The selective transport of Bi(III) from a solution containing the heavy metals: Pb(II), Cu(II), Cd(III), Ni(II) was carried out. The feed phase is composed of trace concentration of the metal ions (10 $mg.L^{-1}$) in 1M HCl. The optimal receiving phase conditions were studied and the best composition is EDTA 0.05M at pH 5. The PIM exhibits a good selectivity towards Bi(III), and the transport rates are reported to be 74.8 ± 9% for Bi(III), against 62.23%, 14.8 ± 9%, 3.15 ± 3.15%, and 2.5 ± 2.5% for Cd(II), Pb(II), Cu(II), and Ni(II), respectively. The study of the stability shows that the PIM can be used up to 5 cycles of extraction-back extraction without significant decrease in the efficiency.

Keywords: Ionic Liquids, Polymer inclusion membranes, Metal separation

Introduction

The extraction, separation, and recovery of strategic metal ions at trace amounts, either from ores in mines industry, or from end-of-life electronic materials in the recycling industry, or from different industrial wastewater recycling systems, constitute a very large domain of investigation. Bismuth (III) is rare and expensive, this latter attracts a lot of interest because it is the most harmless heavy metal, and has the status of a “green element”. It is widely used in various fields such as the manufacture of special alloys and in the pharmaceutical, cosmetic, and medicinal industry. The special properties of Bismuth (III) make it very interesting to study (Mohan, 2010).

The first work to report the use of polymer inclusion membranes in the extraction and separation of Bi was published by Kazemi et al. (2021). The optimal conditions were investigated. The PIM that demonstrated the most effective extraction is composed of 50% D2EHPA as ion carrier and PVC as base polymer. The PIM selectivity showed a minimal co-extraction of other metals, the stability and reusability demonstrated consistent extraction and back-extraction efficiency over 15 cycles.

Ghaderi et al.(2022), investigated the selective extraction and back extraction of Bi from chloride solution. The study of the optimal conditions led to the development of a PIM composed of 40% CTA as base polymer, 25% trioctylamine (TOA) as ion carrier, and 35% TBP as plasticizer. The speciation was also investigated and it is reported that Bi(III) is extracted under anionic complex $BiCl_5^{2-}$. The PIM showed high selectivity toward Bi(III) in the presence of other heavy metals and inorganic anions.

The first work that achieved direct transport of Bi(III) (Meziani et al., 2022), carried out a comparative study on the extraction, recovery and transport of Bi(III) using ionic liquids as ion carriers. The ionic liquids are the quaternary ammonium salt Aliquat 336, and quaternary phosphonium salt trihexyltetradecylphosphonium chloride THTDPCl, respectively. PIMs are composed of 30% CTA as base polymer, 45% NPOE as plasticizer, and 25% ionic liquid IL. In the reusability study both PIMs showed efficient extraction efficiency even after 7 cycles. THTDPCl-based PIM is showed to be the most stable.

The first application of PIM separation process for the recovery of Bi(III) from real industrial samples are reported by Kazemi and Yaftian, (2024). Kazemi investigated the application of a PVDF-HFP based PIM in the selective extraction and back extraction of Bi(III) from Zinc electrowinning sludge sample. The optimal PIM composition is 60% PVDF-HFP as base polymer and 40% D2EHPA as ion carrier. The PIM is used on the selective extraction of Bi(III) from real zinc electrowinning sludge sample, and the separation was highly efficient.

In this work, a new ionic liquid trihexyltetradecylphosphonium salicylate THTDPS was used as ion carrier in a polymer inclusion membrane for the extraction, and transport of Bi from a chloride medium. The PIM is composed of 50% cellulose triacetate CTA as polymer and 50%THTDPS.

Method

Reagents

All reagents were analytical grade. trihexyltetradecylphosphonium (Cyphos IL 101) and sodium salycilate $C_7H_5NaO_3$ were provided by Sigma-Aldrich. Bismuth (III) solutions were prepared from Bismuth Oxyde Bi_2O_3, provided by Sigma-Aldrich. Chloride acid (HCl), nitric acid (HNO_3), and sulfuric acid were respectively provided by Sigma-Aldrich, CHEMINOVA, and MERCK. Acetone and Chloroform are considered as industrial grade, and were respectively provided by Janssen Chimica, and CARLO ERBA

PIM Preparation

PIMs were prepared following the procedure already described by (Fontàs et al., 2007) . A chloroform solution of CTA (200 mg in 20 mL), and the ionic liquid with the same mass (200mg) were poured into a 9.0 cm diameter flat bottom glass Petri-dish. The dish was set horizontally and covered loosely. The solution was allowed to evaporate over 24 h at room temperature. The film was then carefully peeled out from the bottom of the Petri dish.

Apparatus

All metal samples were analysed using a flame atomic absorption spectrometer (AAS) (Schimadzu AA6800). Bi at λ= 223.1 nm, Pb at λ = 283.3 nm, Cd at λ =228.8 nm, Cu at λ = 324.8 nm.

Results and Discussion

Effect of Bi Concentration

The effect of Bi concentration and the maximum extraction capacity of the PIM is investigated by putting in contact different solutions of Bi at different concentrations from 5 mg L^{-1} to 150 mg L^{-1} with PIM1 (50%CTA-50%THTDPS). The results are shown in Figure 1.

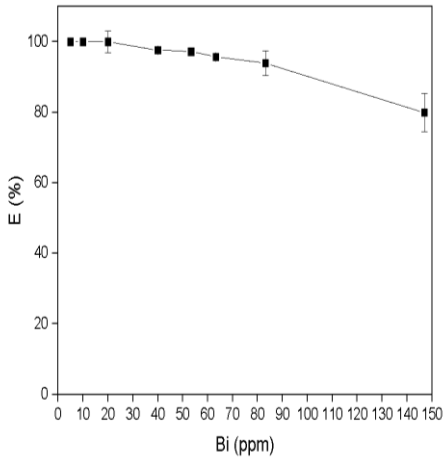

Figure 1. Extraction of Bi(III) at different concentrations. PIM1 = 50%CTA50%THTDPS. Feed phase: 1M HCl, V=10ml. time: 24h**.**

Figure 1 shows that from an initial concentration of 5 mg L^{-1} until 80 mg L^{-1} the extraction efficiencies don't go below 90%. And it decrease to 79.9% ±5.4% for an initial concentration of 150 mg. L^{-1}.

Recovery of Bi from Loaded PIM

PIMs loaded at different concentrations from previous experiments were put in contact with two different stripping solutions (1M HNO_3 and 0.05M EDTA at pH 5) at a volume V=10mL for 4 hours agitation time. The results are shown in figure 2. As can be observed, the chelating agent EDTA is the most suitable for the back-extraction of Bi from loaded PIM.

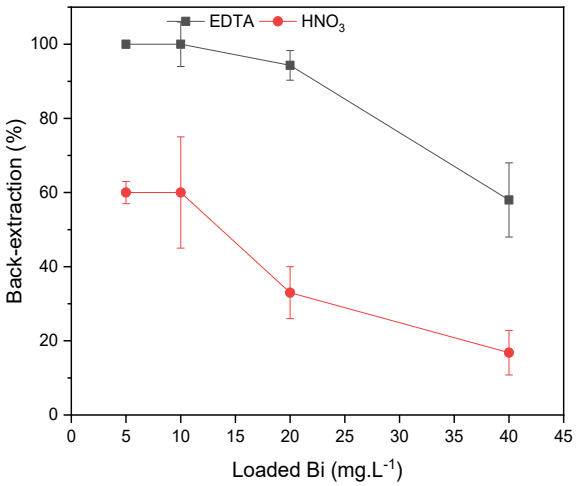

Figure 2. Back-extraction of Bi from different loaded-PIMs using EDTA (black) and HNO_3 (red) as stripping agents. [EDTA]=0.05M at pH 5. [HNO_3]=1M. Time: 4 h.

Reusability

The reusability of the PIM was studied by carrying out several cycles of extraction-back-extraction. Figure 3 highlights the results of the extraction and back-extraction. As can be observed, the extraction efficiency started

to decrease below 90% only at the 6th cycle (89.5% ±6.3%). In the case of the back-extraction efficiencies, the nearly complete recovery of the metal is performed for every cycle.

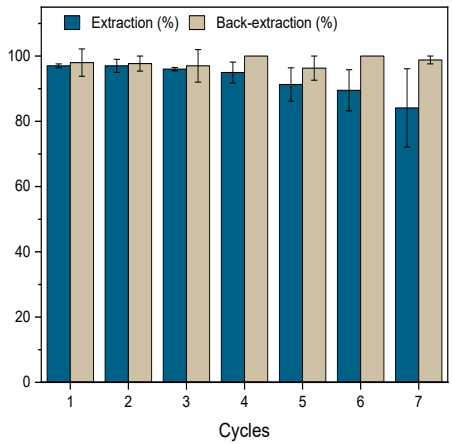

Figure 3. Reusability of PIM (50%CTA-50%THTDPS).

PIM made of 50% CTA+ 50%THTTPS is a promising membrane for the selective extraction and transport of Bi. It is of paramount importance to take into account the SL extraction performances, and the possible complete recovery via the chelating agent EDTA and the reusability for several cycles.

Transport Experiments

Transport experiments were carried out by putting the PIM in the middle of a transport cell separating two compartments: the feed phase, and the receiving phase. Each phase has a volume of V= 150ml and the diameter of the circular contact area of the PIMs is d= 1cm. HNO_3, EDTA, and NaCl were employed as stripping agents. Figure 2 shows that EDTA gives the highest transport rate of 70.6% ± 2%, after 24 hours, followed by HNO_3 which is slightly less efficient with a transport rate of 65% ± 2% and NaCl exhibited a very weak transport rate of 16.5%.

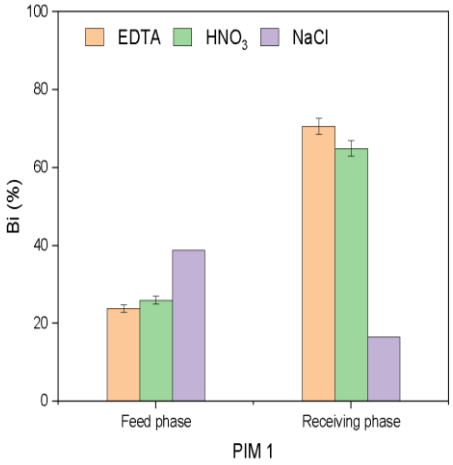

Figure 4. effect of different receiving phases on the transport rate of Bi. Feed phase: 20mg L^{-1} Bi in HCl 1M. V: 150ml. T= 24H. [HNO3] = 1M, [NaCl] =3M, [EDTA] = 0.05M at pH5. PIM= PIM 1.

Selective Transport of Bi from a Solution of Heavy Metals

Competitive transport of Bi (III) from mixture composed of the heavy metal ions Cd (II), Cu (II), Pb (II), and Ni (II) was carried out. The transport was carried out under the same optimal conditions previously determined for individual Bi (III) transport. The feed phase is composed of [Bi]= [Cd]= [Cu]= [Pb]= [Ni]= 10 mg L^{-1} in 1M HCl and the receiving phase is EDTA 0.05M at pH 5. Metals rate in the feed and receiving phases, and

separation factors Bi/ Metal are summarised in table 1. The best separation is obtained with Cu and Ni with a separation factor $SF_{Bi/Metal}$ >>>100 followed by Pb with a significant separation $SF_{Bi/Metal}$ = 42.7±42. Finally, Cd was the least separated with $SF_{Bi/Metal}$=2.1±0.98. The presence of other heavy metal ions didn't affect the transport efficiency of Bi which is reported to be 74.8%±9%. As can be observed, there is a co-transport of the element Cd with an efficiency of 62.2%.

Table 1. Separation of Bi from heavy metals. T= 24 hours. [M]= 10 mg L^{-1}. [EDTA]= 0.05 M. pH= 5.

Metals (M)	Feed phase (%)	Receiving phase (%)	D	$SF_{Bi/Metal}$
Bi	17.2 ± 8	74.8 ± 9	3.54 ± 1.9	
Cd	34.38	62.23	1.65	2.14 ± 0.98
Cu	95 ± 5	3.15 ± 3.15	0.033 ± 0.033	Quant
Ni	96.7 ± 3.3	2.5 ± 2.5	0.026 ± 0.026	Quant
Pb	85.2 ± 9	14.8 ± 9	0.1855 ± 0.1245	42.685 ± 42.065

Conclusion

The obtained results prove the great potential of this separation process and open up perspectives to further optimisations for specified applications. The complete extraction and back-extraction of Bi can be carried out at in a concentration rang that goes from 5 mg L^{-1} to 20 mg L^{-1}. Moreover, the reusability of the PIM exhibited a possible use of 5 cycles of extraction and back-extraction without significant decrease in the efficiency. The selective transport of bismuth from a heavy metal Pb, Cu, Cd, and Ni solution is successfully carried out by using the optimal conditions and Bi was separated from all the divalent metals. Only Cd was co-transported with Bi.

The results promise the conception of a PIM separation process for the practical use in the recovery of Bi from primary or secondary sources. Further works will be done, in the aim to optimize the PIM composition and reduce the intremembrane interactions, using other environmentally friendly chemical agents, and perform practical separations using real mineral/recycling samples.

Scientific Ethics Declaration

* The authors declare that the scientific ethical and legal responsibility of this article published in EPSTEM Journal belongs to the authors.

Conflict of Interest

* The authors declare that they have no conflicts of interest

Funding

* This work has been supported through the project PID2022-140312NB-C22 funded by MCIN/ AEI/10.13039/501100011033/ FEDER, UE

Acknowledgements or Notes

* This article was presented as an oral presentation at the International Conference on Basic Sciences, Engineering and Technology (www.icbaset.net) held in Trabzon/Türkiye on May 01-04, 2025.

References

Fontàs, C., Tayeb, R., Dhahbi, M., Gaudichet, E., Thominette, F., Roy, P., Steenkeste, K., Fontaine-Aupart, M. P., Tingry, S., Tronel-Peyroz, E., & Seta, P. (2007). Polymer inclusion membranes: The concept of

fixed sites membrane revised. *Journal of Membrane Science*, *290*(1–2), 62–72.

Ghaderi, N., Dolatyari, L., Kazemi, D., Sharafi, H. R., Shayani-Jam, H., & Yaftian, M. R. (2022). Application of a polymer inclusion membrane made of cellulose triacetate base polymer and trioctylamine for the selective extraction of bismuth(III) from chloride solutions. *Journal of Applied Polymer Science*, *139*(2), 1–13.

Kazemi, D., & Yaftian, M. R. (2024). PVDF-HFP-based polymer inclusion membrane functionalized with D2EHPA for the selective extraction of bismuth(III) from sulfate media. *Scientific Reports*, *14*(1), 11622.

Kazemi, D., Yaftian, M. R., & Kolev, S. D. (2021). Selective extraction of Bi(III) from sulfate solutions by a poly(vinyl chloride) based polymer inclusion membrane incorporating bis(2-ethylhexyl)phosphoric acid as the extractant. *Reactive and Functional Polymers*, *164*,104935.

Meziani, R., Mitiche, L., Fontàs, C., & Sahmoune, A. (2022). Polymer inclusion membranes with ionic liquids for the recovery of the technology-critical element Bi(III). *Chemical Engineering and Processing - Process Intensification*, *175*,108911.

Mohan, R. (2010). Green bismuth. *Nature Chemistry*, *2*(4), 336.

Author(s) Information

Mohamed Malki
Laboratory of physics and material chemistry.
University of Tizi Ouzou. 15000. Algeria.
Contact e-mail: *mohamed.malki@ummto.dz*

Rabea Meziani
Laboratory of physics and material chemistry.
University of Tizi Ouzou. 15000. Algeria.

Lynda Mitiche
Laboratory of physics and material chemistry.
University of Tizi Ouzou. 15000. Algeria.

Amar Sahmoune
Laboratory of physics and material chemistry.
University of Tizi Ouzou. 15000. Algeria.

Claudia Fontas
University of Girona, Department of chemistry.
Spain.

To cite this article:

Malki, M., Meziani R., Mitiche, L., Sahmoune, A., & Fontas C. (2025). Selective transport of bismuth from heavy metal solution by ionic liquid-based polymer inclusion membrane IL-PIM. *The Eurasia Proceedings of Science, Technology, Engineering and Mathematics (EPSTEM), 34,* 333-338.

The Eurasia Proceedings of Science, Technology, Engineering & Mathematics (EPSTEM)
ISSN: 2602-3199

The Eurasia Proceedings of Science, Technology, Engineering and Mathematics (EPSTEM), 2025

Volume 34, Pages 339-344

ICBASET 2025: International Conference on Basic Sciences, Engineering and Technology

Reliable Determination of Metabolic Syndrome Using Only One Biochemical Marker

Galya Atanasova
Pleven Medical University

Abstract: Objectives of this study were to evaluate opportunities of using of mean arterial pressure (MAP) as a component of the metabolic syndrome (MS) instead systolic and diastolic blood pressures (SBP and DBP) and to create a model, using logistic regression. Multiple logistic regressions were used to determine odds ratio (OR) of MS. The first model included the following components of MS - waist (WS), HDL cholesterol, blood glucose (GLU) and serum triglycerides (TG). The second model included WS and TG. MAP was used as the last variable in the both models. All dependent variables, except MAP, were dichotomous. Each dichotomous variable received value 1 if the criterion for corresponding component in definition was met. The p-values for overall models fit statistic was less than 0.00001. The values of regression coefficients and corresponding p-values were calculated. Thresholds for OR above which the decision about presence of MS should be made, were found. The results indicated strong relation between value of MAP and MS. The proposed model showed a reliable determination of MS, using only one biochemical marker. Reducing the number of used biochemical marker could improve the cost efficiency in the diagnostication of MS. MAP showed itself as a promising indicator, which after some broader studies could replace SBP and DBP in the MS definition.

Keywords: Metabolic syndrome, Biochemical marker, Healthcare engineering

Introduction

According to the definition of NCEP ATP III (National Cholesterol Education Program Third Adult Treatment Panel), the metabolic syndrome (MetS) is a manifestation of at least three of the following five clinical and laboratory risk factors: abdominal obesity (waist line >102 cm in males and >88 cm in females), hypertension (arterial pressure ≥ 130/85 mm Hg), hyperglycemia (fasting sugar ≥6 mmol/l), hypertriglyceridemia (serum glycerides ≥1.7 mmol/l) and lower levels of HDL-cholesterol (HDL < 1.03 mmol/l in males and < 1.3 mmol/l in females). WHO defines MetS as hyperinsulinemia or hyperglycemia in addition to two of the above risk factors – waist line ≥ 94cm, dyslipidemia (triglycerides ≥1.7 mmol/l or HDL<mmol/l), or AP ≥ 140/90 mm Hg (Schunemann et al., 2008).

At present, the International Diabetes Association defines MetS as “presence of central obesity (defined as waist line ≥ 94 cm in European males and ≥ 80 cm in European females, with ethnic specificity for both groups plus two of the following characteristics:

1. increased triglycerides (≥ 17 mmol/l) or specific treatment received for these lipid disorders;
2. reduced HDL-cholesterol level (< 1.03 mmol/l in males, < 1.29 in females) or specific treatment received for these lipid disorders;
3. increased AP (for systolic ≥ 130 mmHg or diastolic ≥ 85 mmHg), or treatment for previously diagnosed hypertension;
4. increased fasting blood sugar levels ≥ 5.6 mmol/l.

Because of these criteria, MetS varies between 10 and 25%. It increases with age and is more expressed in patients with DM. Individuals with MetS are at a risk twice as high for cardiovascular disease (CVD), as compared to those without MetS (Gocheva, 2009). In addition, the metabolic syndrome increases the risk for developing diabetes mellitus type II at least five times (Mirzaei et al., 2009).

Contemporary data show that in most countries it can be assumed that 20 to 30% of the adult population are with MetS (Chapman & Ginsberg 2011). The metabolic syndrome has reached the size of an epidemic in the USA. According to data obtained in the NHANES III (National Health and Nutrition Examination Survey), 48 million (23%) of adult Americans have MetS (European Heart Network. European Cardiovascular Disease Statistics. 2008). The incidence of MetS is comparable to that of hypertension, the latter being 24% (Tzekova, 2002, 2012). With ageing of the US population, the incidence of MetS increases among males and females of nearly all age groups. The spread of MetS among the older population groups may reach 50%. At age 70 and after, the spread of the syndrome reaches a plateau in women and decreases in men.

New biomarkers have a limited benefit, when added to the evaluation of the cardiovascular risk when using the SCORE algorithm. Highly sensitive CRP (hsCRP) and homocysteine can be used in patients at moderate cardiovascular risk (Gocheva, 2009). New biomarkers can be tested as alternative or can be considered as leading ones together with classical risk factors, using their capability to predict a 10-year cardiovascular morbidity or mortality. In view of this, the circulating biomarkers only are discussed here, i.e. those evaluated by standardized and validated methods, and are considered risk factors in clinical practice (Tzekova, 2012). Two groups of biomarkers are differentiated for evaluation of cardiovascular risk:

- Inflammatory: hsCRP, fibrinogen
- Thrombopoietic: homocysteine, lipoprotein-associated phospholipase (LpPLA2).

The highly sensitive CPR is a risk factor, integrating a multitude of metabolic and low-grade inflammatory factors, which are crucial for the development unstable atherosclerotic plaques (Berger & Jordan, 2010). Few drawbacks of this biomarker are seen when assessing the risk:

- Dependence on basic classical risk factors
- Lack of precision: a narrow diagnostic range for the level of hsCRP and the risk for CVD.
- Lack of specificity: a risk level similar to that for non-cardiovascular causes for morbidity and mortality.
- Lack of cause-effect relationship between changes in hs-CPR level and the risk for CVD.
- Lack of specific therapeutic strategies or agents referring to circulating CPR and demonstrating decrease in the incidence of CVD.
- High cost of the tests as compared to that of traditional biological factors (e.g. blood sugar and lipids)

Homocysteine has a modest influence on cardiovascular risk (Clarke et al., 2010). Intervention studies on using B-group vitamins to decrease the level of plasma homocysteine have proved their inefficiency for reduction of risk for CVD (Kaptoge et al., 2007). Having in mind the cost of the test, homocysteine remains a marker of second choice in cardiovascular risk assessment.

Not long ago, LpPLA2 emerged as a marker of high sensitivity and an independent risk factor for plaque rupture and atherothrombotic events. However, LpPLA2 has a small effect on risk in the general population and remains a second-line marker in cardiovascular risk assessment because of the cost of the test (Garza & Montori, 2007). The new emerging validated biomarkers can be added to make evaluation of the risk for CVD in specific subgroups of patients with moderate, uncommon or undefined levels of risk, e.g. asymptomatic patients without multiple major risk factors but with metabolic, inflammatory, endocrine or social indicators, associated with atherosclerosis or manifest signs of atherosclerotic progression.

Method

A total of 104 persons without any apparent disease were selected. Among these people MS was found in 35, according to NCEP-ATP III definition. One way ANOVA test, multiple comparison tests of means and multiple logistic regression analyses were used. The MAP was obtained by the formula MAP=SBP/3+2*DBP/3.

Results and Discussion

The mean values andstandard deviations of the clinical characteristics of the investigated individuals were obtained (Table 1). There were clear differences between mean values of SBP, DBP and MAP for people with and without metabolic syndrome. The average value of mean arterial pressure for all personswas 95.17 [mm Hg] and the standard deviation was 10.65 [mm Hg].

Table 1. Clinical characteristics of the participants

Characteristics	**Group with MetS**		**Group without MetS**	
	Mean value	**SD**	**Mean value**	**SD**
Waist circumference [cm]	98.36	±8.38	82.81	±13.76
SBP [mm Hg]	136.57	±16.28	119.43	±11.82
DBP [mm Hg]	87.85	±8.19	77.39	±9.11
MAP [mm Hg]	103.90	±9.38	90.73	±8.29
APO B [mg/dl]	92.39	±29.63	103.88	±24.2
APO A1 [mg/dl]	172.19	±33.73	169.22	±34.04
LDL - cholesterol [mmol/l]	3.41	±1.27	3.73	±1.02
HDL - cholesterol [mmol/l]	1.37	±0.41	1.17	±0.3
Blood sugar [mmol/l]	4.83	±1.3	5.45	±1.69
Total cholesterol [mmol/l]	5.34	±1.5	5.79	±1.21
hs-CRP [mg/l]	2.52	±2.99	4.24	±3.95
Triglyceride levels [mmol/l]	1.85	±1.93	2.89	±2.86
HbA1C [%]	5.32	±0.3	5.51	±0.23
BMI [kg/m2]	27.06	±5.38	31.48	±4.37

The mean values of SBP, DBP and MAP in three age groups for men and women were shown on Figures from 1 to 6. The analysis of results indicated that the variation of values of the mean values were relatively small with the age for men. The mean values increased with the age for women, but the changing wasn't so great. The results showed that the age wasn't a major factor influencing on mean values of blood pressures.

The four groups used in ANOVA were men and women with and without MS. The ANOVA F-statistic is 17.71 with p-value less than 0.00001 (Table 2). The box plot of ANOVA was shown on Figure 1. The multiple comparison tests showed statistically significant differences between groups of people with and without MS and negligible differences between men and women (Table 3). Regarding MAP, the differences between the groups of men and women with MS, as well as between the groups of men and women without MS are small. There was a statistically significant difference between the persons with MS and the health ones, irrespective of the gender. For the women, the difference between the mean values of MAP for those with MS and those without MS was greater than the differences registered between the respective groups of men. These results confirmed that the mean arterial pressure is a major risk factor, and it is better expressed in females as compared to males.

Table 2. Data from ANOVA analysis of MAP.

Deviations	**Sum of squares**	**Degrees of freedom**	**Mean value**	**F-test statistic**	**p-value**
Between groups	4055.26	3	1351.75	17.71	<0.00001
Within groups	7633.407	101	76.33407		
Total	11688.67	104			

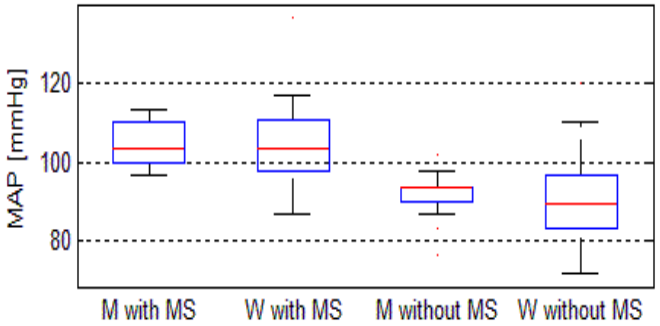

Figure 1. Men and women with and without MS

Table 3. Data from multiple component analysis of map by gender

Group One	**Group Two**	**Lowest value of CI [mm Hg]**	**Difference between means [mm Hg]**	**Highest value of CI [mm Hg]**
Menwith MS	Womenwith MS	-7.83656	0.039683	7.915929
Menwith MS	MenwithoutMS	4.892007	12.41005	19.9281
Womenwith MS	WomenwithoutMS	7.557816	13.65873	19.75964
MenwithoutMS	WomenwithoutMS	-4.34253	1.28836	6.919248

Multiple logistic regressions were used to determine odds ratio (OR) of MS. The first model includedthe following components of MS - waist (WS), HDL cholesterol, blood glucose (GLU) and serum triglycerides (TG).The second model included WS and TG. MAP was used as the last variable in the both models:

$$\text{Logit}(P) = \ln\left(\frac{P}{1-P}\right) = b_0 + b_1 * WS + b_2 * GLU + b_3 * TG + b_4 * HDL + b_5 * MAP\ ; \quad (1)$$

$$\text{Logit}(P) = \ln\left(\frac{P}{1-P}\right) = b_0 + b_1 * WS + b_2 * TG + b_3 * MAP\ . \quad (2)$$

All dependent variables, except MAP, were dichotomous. Each dichotomous variable received value 1 if the criterion for corresponding component in definition was met. The p-values for overall models fit statistic was less than 0.00001. The values of regression coefficients and corresponding p-values were calculated (Table 4). Thresholds for OR above which the decision about presence of MS should be made, were found (Table 4).There were two types of wrong decisions. The first was when a healthy person was determined as a one with metabolic syndrome. The second was when a person with metabolic syndrome was determined ashealthy one. When the first model was used with threshold for OR equal to 1 there were 1 wrong decision of first type and 2 wrong decisions of second type. The relative mistakes were respectively 1.45% and 5.71%. The model showedvery good results regarding the NCEP-ATP III definition of metabolic syndrome. When the second model was used with threshold for OR equal to 0.82 there were 3 wrong decision of first type and 2 wrong decisions of second type. The relative mistakes were respectively4.35% and 5.71%. This model also showed very good results regarding the NCEP-ATP III definition of metabolic syndrome. The basic advantage of the second model was the using only of one biochemical marker.

Table 4. Coefficientsof the two logistic regression models

Model 1							**Model 2**			
Coefficients	b0	b_1	b_2	b_3	b_4	b_5	b0	b_1	b_2	b_3
	-97.86	10.55	8.41	11.35	8.28	0.83	-49.16	6.42	8.24	0.42
p	0.015	0.025	0.035	0.021	0.047	0.016	0.0008	0.005	0.002	0.001
Thresholds	1						0.82			
Wrong decisions	with MS	1 (1.45%)					3 (4.35%)			
	without MS	2 (5.71%)					2 (5.71%)			

The analysis of the first model indicated that increasing of MAP with 1% (0.9517 mm Hg) of its mean value resulted in 2.2 times increase of OR. When the second model was used increasing of MAP with 1% of its mean value resulted in 1.5 times increase of OR. This indicated the significance of MAP as a component of metabolic syndrome. In previous work of author other logistic regression models were studied. One model used SBP, TG and HDL as components, until another one used DBP, TG and HDL. The results showed that increasing of SBP with 10% (13 mm Hg)of its mean value led to 1.78 times growth of OR for men and 2.16 times for women. The increasingof OR for the model with DBP (increasing with 8.2 mm Hg) were respectively1.13 times and 2.19 times. In these models the increasing of blood pressures with value around 10 times greater than increasing of MAP in proposed here models led to almost one and the same growth of OR. This comparison was another proof that MAP is much stronger marker of metabolic syndrome than SBP and DBP.

Conclusion

The results indicated strong relation between value of MAP and MS. The proposed model showed a reliable determination of MS, using only one biochemical marker. Reducing the number of used biochemical marker

could improve the cost efficiencyin the diagnostication of MS.MAP showed itself as a promising indicator, which after some broader studies could replace SBP and DBP in the MS definition.

Scientific Ethics Declaration

* The author declares that the scientific ethical and legal responsibility of this article published in EPSTEM Journal belongs to the author.

Conflict of Interest

* The author declares that there is no conflict of interest

Funding

* This research received no specific grant from any funding agency in the public, commercial, or not-for-profit sectors

Acknowledgements or Notes

* This article was presented as an oral presentation at the International Conference on Basic Sciences, Engineering and Technology (www.icbaset.net) held in Trabzon/Türkiye on May 01-04, 2025.

References

Berger, J. S., Jordan, C. O., Lloyd-Jones, D., & Blumenthal, R. S. (2010). Screening for cardiovascular risk in asymptomatic patients. *Journal of the American College of Cardiology*, *55*(12), 1169–1177.

Chapman, M. J., Ginsberg, H. N., Amarenco, P., Andreotti, F., Borén, J., Catapano, A. L., Descamps, O. S., Fisher, E., Kovanen, P. T., Kuivenhoven, J. A., Lesnik, P., Masana, L., Nordestgaard, B. G., Ray, K. K., Reiner, Z., Taskinen, M. R., …& Watts, G. F. (2011). Triglyceride-rich lipoproteins and high-density lipoprotein cholesterol in patients at high risk of cardiovascular disease: evidence and guidance for management. *European Heart Journal*, *32*(11), 1345–1361.

Chida, Y., & Steptoe, A. (2009). The association of anger and hostility with future coronary heart disease: a meta-analytic review of prospective evidence. *Journal of the American College of Cardiology*, *53*(11), 936–946.

Clarke, R., Halsey, J., Lewington, S., Lonn, E., Armitage, J., Manson, J. E., Bønaa, K. H., Spence, J. D., Nygård, O., Jamison, R., Gaziano, J. M., Guarino, P., Bennett, D., Mir, F., Peto, R., Collins, R., & B-Vitamin Treatment Trialists' Collaboration (2010). Effects of lowering homocysteine levels with B vitamins on cardiovascular disease, cancer, and cause-specific mortality: Meta-analysis of 8 randomized trials involving 37 485 individuals. *Archives of Internal Medicine*, *170*(18), 1622–1631.

Dyakova, M., Shipkovenska, E., Dyakov, P., Dimitrov, P., & Torbova, S. (2008). Cardiovascular risk assessment of Bulgarian urban population: cross-sectional study. *Croatian Medical Journal*, *49*(6),

European Heart Network. (2008). *European cardiovascular disease statistics.* Retrieved from https://coachmikeblogs.com. pdf

Fibrinogen Studies Collaboration, Kaptoge, S., White, I. R., Thompson, S. G., Wood, A. M., Lewington, S., Lowe, G. D., & Danesh, J. (2007). Associations of plasma fibrinogen levels with established cardiovascular disease risk factors, inflammatory markers, and other characteristics: individual participant meta-analysis of 154,211 adults in 31 prospective studies: the fibrinogen studies collaboration. *American Journal of Epidemiology*, *166*(8), 867–879.

Garza, C. A., Montori, V. M., McConnell, J. P., Somers, V. K., Kullo, I. J., & Lopez-Jimenez, F. (2007). Association between lipoprotein-associated phospholipase A2 and cardiovascular disease: a systematic review. *Mayo Clinic Proceedings*, *82*(2), 159–165.

Gocheva, N. (2009). Metabolic syndrome, inflammation (CRP) and cardiovascular risk. *Bulgarian Cardiology, 15*(4), 5-12.

Mirzaei, M., Truswell, A. S., Taylor, R., & Leeder, S. R. (2009). Coronary heart disease epidemics: not all the same. *Heart (British Cardiac Society)*, *95*(9), 740–746.

Perk, J., De Backer, G., Gohlke, H., Graham, I., Reiner, Z., Verschuren, M., Albus, C., Benlian, P., Boysen, G., Cifkova, R., Deaton, C., Ebrahim, S., Fisher, M., Germano, G., Hobbs, R., Hoes, A., Karadeniz, S., Mezzani, A., Prescott, E.,…& Ryden, L. (2012). European guidelines on cardiovascular disease prevention in clinical practice (version 2012). *European Heart Journal*, *33*(13), 1635–1701.

Schunemann, H. J., Oxman, A. D., Brozek, J., Glasziou, P., Jaeschke, R., Vist, G. E., Williams, J. W., Jr, Kunz, R., Craig, J., Montori, V. M., Bossuyt, P., Guyatt, G. H., & GRADE Working Group (2008). Grading quality of evidence and strength of recommendations for diagnostic tests and strategies. *BMJ (Clinical Research Ed.)*, *336*(7653), 1106–1110.

Tzekova, M. (2002). *Clinical and prognostic aspects in acute myocardial infarction without Q-wave*. (Doctoral dissertation).

Tzekova, M. (2012). *Prognostic value of biochemical markers of inflammation, fibrinilytic activity and cardiomyocytic necrosis in patients with acute coronary syndrom without ST-elevation.* (Doctoral dissertation).

World Health Organization. (1973). The prevention and control of major cardiovascular diseases. *Report of a Conference*, 8214.

Author Information

Galya Atanasova
Pleven Medical University, 1, Saint Kliment Ohridski Street,
5800, Bulgaria
Contact e-mail: *gal_na69@abv.bg*

To cite this article:

Atanasova, G. (2025). Reliable determination of metabolic syndrome using only one biochemical marker. *The Eurasia Proceedings of Science, Technology, Engineering and Mathematics (EPSTEM), 34,* 339-344.

The Eurasia Proceedings of Science, Technology, Engineering & Mathematics (EPSTEM)
ISSN: 2602-3199

The Eurasia Proceedings of Science, Technology, Engineering and Mathematics (EPSTEM), 2025

Volume 34, Pages 345-351

ICBASET 2025: International Conference on Basic Sciences, Engineering and Technology

Digital Analysis of Gravity Data of the Absheron Peninsula

Aynur Zamanova
Institute of Geology and Geophysics of the Ministry of Science and Education of Azerbaijan Republic

Azer Kadirov
Institute of Geology and Geophysics of the Ministry of Science and Education of Azerbaijan Republic

Gunel Sadigova
Institute of Geology and Geophysics of the Ministry of Science and Education of Azerbaijan Republic

Elnara Ahmadova
Baku State University

Abstract: The depth structure of the crust of the Absheron Peninsula was studied based on gravimetric data. Modern methods of mathematical processing and interpretation were used in the research work. Numerical analysis of gravity data of the research area was performed using Hartley transform and Butterworth filter. The Spector-Grant method was used to determine the average depth state of the masses causing the anomaly based on the values of the gravitational field power spectrum. The power spectrum of the gravitational field of the research area was analyzed to determine the cutoff frequency and the average depth of the density interface that form gravity anomalies. The average depth values of the density interface forming gravity anomalies were determined to be 6.8 and 36 km. As a result of applying the Parker-Oldenburg's method to the regional gravity anomalies of the Absheron Peninsula and adjacent areas, a model of the depth of the crust-lithosphere boundary (Moho) was created. Inversion estimation of the gravity field using the Parker-Oldenburg's method show that the depth of the Moho boundary on the Absheron Peninsula varies between 40-46 km. A gravity anomaly map of the Moho boundary was created applying the forward modeling algorithm. The main purpose of the research is to study the gravity anomalies of the Absheron Peninsula as a result of spectral analysis and to get the gravity model of the depth of the Moho boundary by applying the Parker-Oldenburg's method.

Keywords: Absheron peninsula, Gravity anomaly, Gravity model

Introduction

The Absheron Peninsula is located on the western shores of the Caspian Sea, at the southeastern end of the Greater Caucasus. The Absheron Peninsula is located in the western segment of the Absheron-Balkhan uplift zone of the Caspian mega-depression, and since it occupies a transitional position between the South-Eastern Caucasus and the Caspian basin, its internal structure belongs to the structures of the mountain-fold system. The main peculiarities of the Earth's crust have been studied by a number of researchers on the basis of gravity field data of the Absheron Peninsula (Hajiyev, 1965; Kadirov, 2000a). In recent years, many mathematical methods have been proposed based on numerical analysis of gravity field data to separate regional and local gravity anomalies, to estimate the depths of anomaly-causing sources, and to clarify the structure of the crystalline basement and sedimentary layer (Serkerov, 2000; Kadirov, 2000 b; Blakely, 1996).

The aim of the article is to carry out a numerical (spectral) analysis of the gravity field of the Absheron Peninsula and adjacent areas and to get a gravity model of the Moho boundary using the Parker-Oldenburg's method.

Gravity Anomalies of the Research Area

The research area is located in the area of minimum gravity on the map of Bouguer gravity anomaly compiled for the territory of Azerbaijan (Hajiyev, 1965; Tsimelzon, 1979; Kadirov, 2000a). The distribution of gravity anomalies in the Bouguer reduction of the research area is shown (Figure 1). A negative anomaly area is observed in the Absheron Peninsula and adjacent areas. The minimum area covering the Absheron Peninsula, Gobustan, Absheron Ridge, the Baku Archipelago and the seaward part of the Pre-Caspian-Guba zone is called the Azerbaijan minimum gravity.

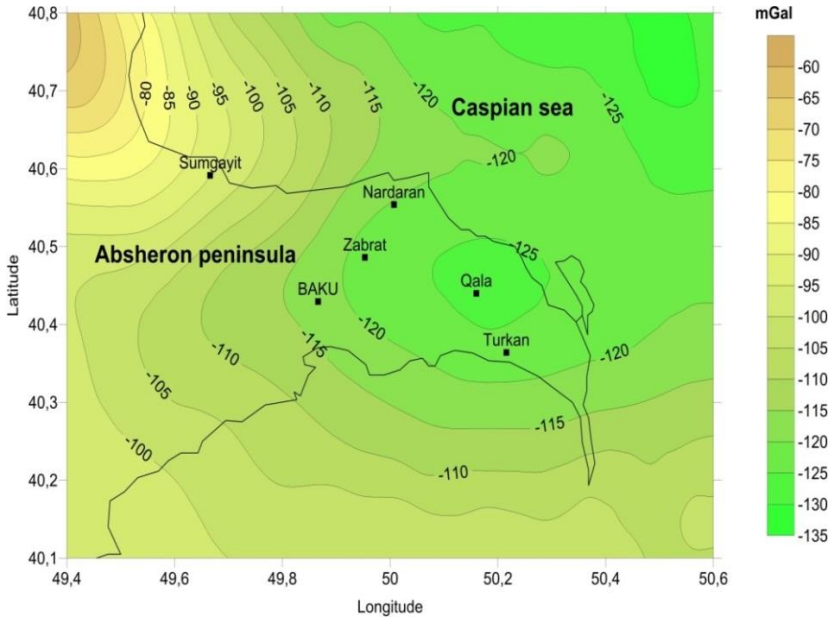

Figure 1. Bouguer gravity map of the Absheron Peninsula

The extremum value (-125 mGal) of the negative anomaly is located in the north of the Absheron Peninsula. This minimum area is bounded by the Azerbaijan maximum in the south-west part. The Dubrar relative maximum is located in the north-western part of the research area. Analysis of the gravity field shows that the average depth of the crystalline basement in the Absheron Peninsula is 18 km. The maximum depth of subsidence of the crystalline basement (23 km) is noted in the area of Yavany Mt.–Pirsaat–Gobustan and around Gala. In the zones of Dubrar Mt. and Yavany Mt.–Sangachal, the crystalline basements occurs at 6 and 12 km, respectively. The major part of the regional anomalies is caused by the topography of the pre-Mesozoic crystalline basement (Kadirov, 2000c).

The Power Spectrum of the Gravity Field of the Absheron Peninsula

Spectral analysis of gravity field data using the Spector-Grant method allows us to estimate the average depth of anomaly-causing density interface (Spector & Grant, 1970; Kamto et al., 2021; Kadirov, 2000a; Kadirov et al., 2024). A map of gravity anomalies in the Bouguer reduction was created of the research area to estimate the depth of the anomaly-creating sources in the frequency domain of the gravity field data in the research area (Figure 1). In order to interpret gravity anomalies, the coordinate origin is placed in the southwest corner of the Bouguer anomaly map, and the area is divided into a grid with a step of 5 km. The Bouguer anomaly value was determined at the intersection points. The X axis points the eastward and the Y axis points the northward. The number of elements on the X axis (N_x) and Y axis (N_y) was chosen as N_x=23 and N_y=17.

The Hartley transform was applied to gravimetric data at the intersection points of the 23x17 grid of the research area, divided by 5 km steps. The dependency graph of the logarithm of the power spectrum on spatial frequency was created to determine the depth of the anomaly-causing objects (Figure 2). The resulting graph consists of straight-line segments, the curves of which decrease as the frequency increases. Each line part corresponds to a discrete density interface.

The average depth of anomalous objects is determined by the following formula:

$$h = \frac{LnA(k_2) - LnA(k_1)}{2(k_2 - k_1)} \quad (1)$$

where k_1 and k_2 are the spatial frequencies at points 1 and 2, from which the value of - *LnA(k)* is taken. The *LnA(k)* values of the logarithm of the power spectrum are taken from the straight line drawn to these values.

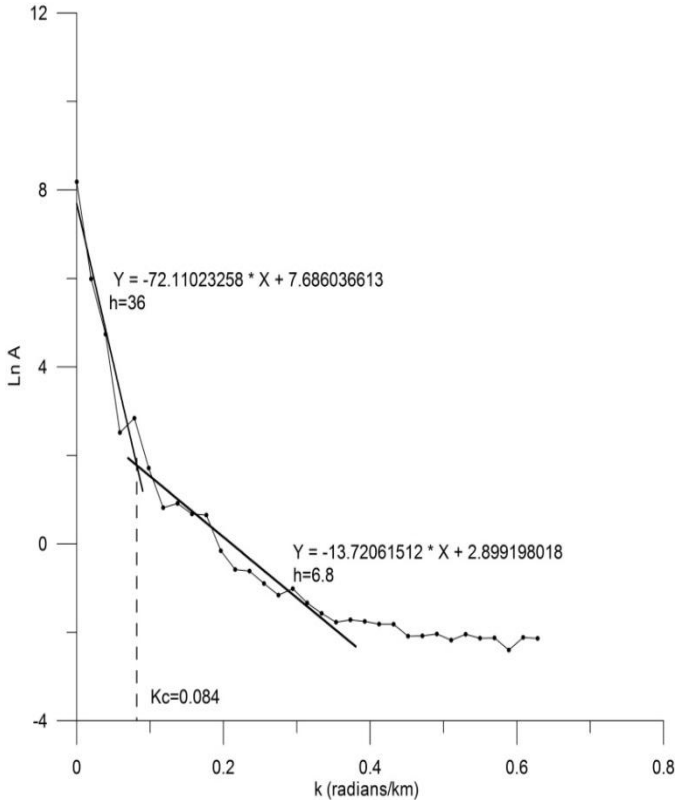

Figure 2. Logarithmic curve of the power spectrum of the Bouguer gravity field of the Absheron Peninsula and adjacent areas

Low-frequency and high-frequency fields associated with deep and shallow gravitational anomaly sources appear in the logarithmic curve of the power spectrum, respectively. Low-frequency and high-frequency areas are regional and local anomaly areas. The interface of the regional and local anomaly areas is determined by the intersection point of the straight lines built for these areas. The frequency corresponding to this point is called the cutoff frequency. It is possible to distinguish regional and local anomalies using a filtering operation and a cutoff frequency (Sadigova, 2018; Sadygova, 2020).

The cutoff (spatial) frequency (wave number) of the logarithm curve of power spectrum of the Bouguer gravity field was determined as k_c=0.084 rad.km^{-1} in the research area. According to the slope of the curve, the average depth of the density interface, intense anomaly-causing in the Earth's crust, was determined to be 36 km in the long-wave region and 6.8 km in the short-wave region.

According to the values of power spectrum of the gravity field, the anomaly-causing density interface with an average depth of 6.8 km is assumed to be related to the surface relief of Mesozoic sediments. The tectonic structure of the Absheron depression during the Mesozoic has been poorly studied by deep drilling and geophysical researches.

Method

The Parker-Oldenburg's method is an inversion method used for the analysis of gravimetric data in geophysics and the analysis of the structure of the Earth's crust. This method is used to identify underground structural alterations and to obtain information about its geological structure. This is mainly effective in the analysis of gravitational anomalies, especially in the researcg of the boundary between the Earth's crust and the lithosphere.

One of the main tasks of geophysical study is to determine the geometry of the interface from gravity anomaly, Parker-Oldenburg algorithm was used to obtain the 3D geometry of interface topography from the relationship between the Fourier transform of gravity data and the sum of the interface topography's Fourier transformation.

The Parker-Oldenburg inversion algorithm is defined as follows:

$$F[h(x)] = -\frac{F[\Delta g(x)]e^{(-kz_0)}}{2\pi G\rho} - \sum_{n=2}^{\infty} \frac{k^{n-1}}{n!} F[h^n(x)] \tag{2}$$

This algorithm is given as equation (2) iteratively from the given depth and density of an interface by (Parker, 1973), to calculate the gravity anomaly of uneven homogeneous layer by using the Fourier transform where, $F(\Delta g)$ is the Fourier transform of the gravity anomaly, G is the gravitational constant, ρ is the density contrast across the interface, K is the wave number, $h(x)$ is the depth to the interface (positive downwards) and z_0 is the mean depth of the horizontal interface. Oldenburg (1974) rearranged this equation to calculate the undulating interface depth.

The present equation (2) is a useful tool for calculation of density interface topography iteratively from Δg and z_0. From the beginning of the iteration, assignment of $h(x) = 0$ or an approximated value is assigned to the right part of the equation. Its inverse Fourier transform provides the first estimation of the topography. This topography value was used in calculation of the right hand sight of the equation to achieve the second topography approach. Until the convergence criterion is achieved; or until reaching the determined iteration number; or until the difference between successive steps is smaller than the convergence criterion, the iteration process continues. 3DINVER.M MATLAB program, developed by Gomez and Agarwal (2005) to compute 3D density geometry of the interface's from gridded gravity anomaly was used.

Results and Discussion

Estimation of the Depth of Moho Boundary in the Absheron Peninsula Using the Parker-Oldenburg's Method

Figure shows the results obtained from the application of the 3DINVER.M function. As a result of inversion estimation of the gravity field using the Parker-Oldenburg's method, a depth distribution model of the Moho boundary for the Absheron Peninsula was created (Figure 3). The depth of the surface varies between 40-46 km. The maximum valuesof the depth of the Moho surface are observed in the Gala and Turkan areas of the Absheron Peninsula and in the Caspian Sea (46 km). The depth decreases to 44 km in the northwest of the Absheron Peninsula (around Sumgayit and Baku).

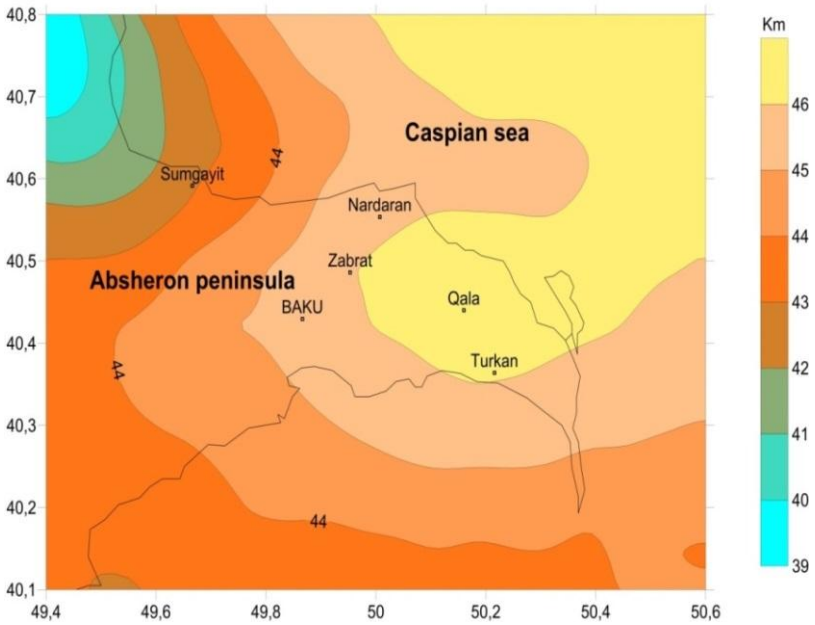

Figure 3. Depth distribution model of the Moho boundary in the Absheron Peninsula

Figure shows the gravity anomaly map obtained from the depth distribution model of the Moho boundary of the Absheron Peninsula using the forward modeling algorithm (Figure 4). The anomaly value is higher in the northeastern areas of the Absheron Peninsula (Nardaran, Caspian Sea).

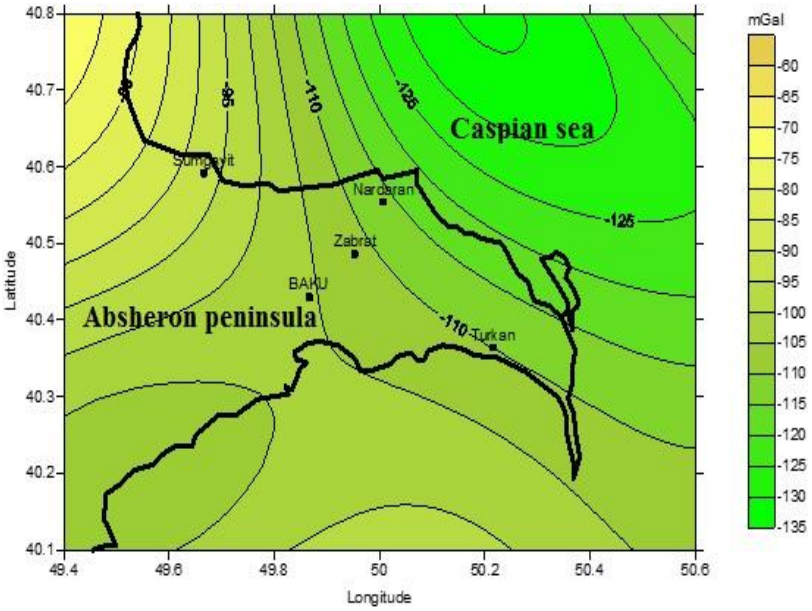

Figure 4. Gravity anomaly map obtained from the depth distribution model of the Moho boundary by inversion estimation

The difference map between the gravity anomalies obtained and observed from the estimated model of the Moho boundary is shown (Figure 5). The difference between the gravity anomalies estimated and observed from the Moho surface varies between -15 and 12 mGal. Negative differences of more than -10 mGal are observed in the territories of Baku, Turkan and Zabrat. Positive differences of up to +10 mGal are observed in the northeastern and southwestern parts of the map.

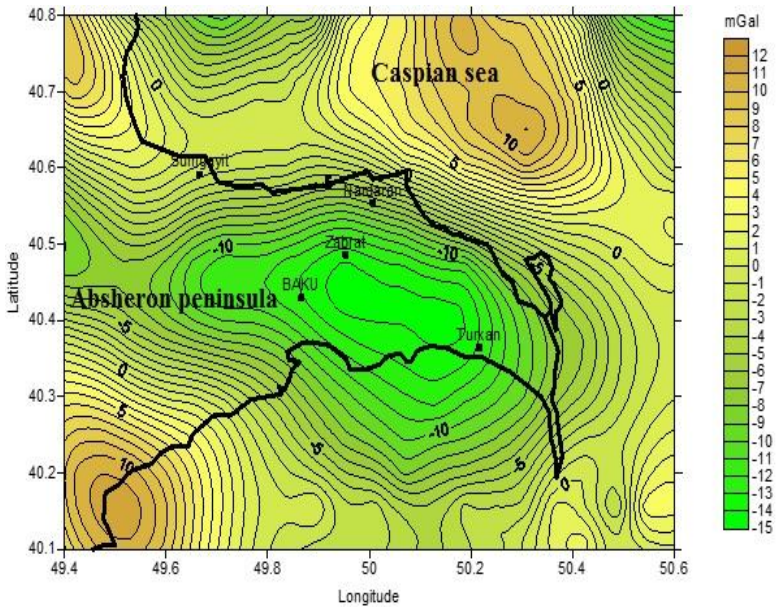

Figure 5. Difference map between gravity anomalies observed and obtained from the estimated model of Moho boundary

Conclusion

The depth of geological boundaries based on density alterations in the Earth's crust was estimated by using the spectral analysis method of the Bouguer gravity field. The spatial frequency in the logarithm curve of the power

spectrum is determined as k_c=0.084 rad.km^{-1}. The long-wave components reflect a deep density interface in the Earth's crust, and the average depth of this interface is estimated to be 36 km. The short-wave components show a shallower geological boundary with a density alteration at a depth of 6.8 km. As a result of inversion estimation using the Parker-Oldenburg's method, a depth distribution model of the Moho surface for the Absheron Peninsula was created. The model shows that the depth of the Moho boundary varies between 40-46 km, and the greatest depths are observed in the Turkan and Gala areas of the peninsula.

Recommendations

The results obtained can be used by scientific and industrial organizations to address various geological, geophysical, and geodynamic problems, and to investigate new geological structures.

Scientific Ethics Declaration

* The authors declare that the scientific ethical and legal responsibility of this article published in EPSTEM Journal belongs to the authors.

Conflict of Interest

* The authors declare that they have no conflicts of interest.

Funding

* The research was carried out at the expense of budgetary financing of the Institute of Geology and Geophysics of the Ministry of Science and Education of the Azerbaijan Republic.

Acknowledgements or Notes

* This article was presented as a poster presentation at the International Conference on Basic Sciences, Engineering and Technology (www.icbaset.net) held in Trabzon/Türkiye on May 01-04, 2025.

References

Blakely, R. J. (1996). *Potential theory in gravity and magnetic applications*. Cambridge: Cambridge University Press.

Gomez, O. D., & Agarwal, B. N. (2005). 3Dinver.M: A Matlab program to invert the gravity anomaly over a 3D horizontal density interface by Parker-Oldenburg's algorithm. *Computers & Geosciences*, *31*(4), 513-520.

Hajiev R. M. (1965). *Deep geological structure of Azerbaijan*. Baku: Azerneshr.

Kadirov, A. H., Zamanova, A. H., & Sadigova, G. R. (2024). The gravity field power spectrum and the deep structure of the Ajinour region (Azerbaijan). *Geophysical Research*, *25*(1), 57–68.

Kadirov, F. A. (2000a). *Gravity field and models of the deep structure of Azerbaijan*. Baku: Nafta-press. (In Russian).

Kadirov, F. A. (2000b). Gravity data filtering using the Hartley transform (on the example of the Kura intermountain trough). *Proceedings of the Russian Academy of Sciences, Physics of the Earth, 10*, 66-71.

Kadirov, F. A. (2000c). Application of the Hartley transform for interpretation of gravity anomalies in the Shamakhy–Gobustan and Absheron oil-and gas-bearing regions, Azerbaijan. *Journal of Applied Geophysics*, *45*, 49–61.

Kamto, P. G., Lemotio, W., Tokam, A. K., & Yap, L. (2021). Combination of terrestrial and satellite gravity data for the characterization of the southwestern coastal region of Cameroon: Appraisal for hydrocarbon exploration. *International Journal of Geophysics*, *2022*(1), 5554528.

Oldenburg, D. W. (1974). The inversion and interpretation of gravity anomalies. *Geophysics, 39*(4), 526–536.

Parker, R. L. (1973). The rapid calculation of potential anomalies. *Geophysical Journal of the Royal Astronomical Society, 31,* 447–455.

Sadigova, G. R. (2018). Inhomogeneity of the lithosphere, deep structure and modern geodynamic characteristics of the western coast of the Caspian Sea. *ANAS Transactions Earth Sciences*, *1,* 76-84.

Sadygova, G. R. (2020). Gravity anomalies of the Southeast Caucasus. *Geophysical Journal*, 42(2), 138-151.

Serkerov, S. A. (2000). *Potential theory in gravity prospecting and magnetic exploration*. Moscow: Nedra.

Spector, A., & Grant, F.S. (1970). Statistical models for interpreting aeromagnetic date, *Geophysics*, *35*(2), 293-302.

Tsimelzon, I. O., Amiraslanov T. S., & Mokhan, Ch. P. (1979). Methodology of use of multidimensional regression analysis for structural constructions using results of detailed gravity prospecting and schematic data of seismic exploration. *Izvestiya, Neft i Gaz*, (8), 9-14.

Author(s) Information

Aynur Zamanova
Institute of Geology and Geophysics of the Ministry of Science and Education of Azerbaijan Republic.
AZ1073, H.Javid av., 119, Baku, Azerbaijan Republic
Contact e-mail: *aynur-zamanova@rambler.ru*

Azer Kadirov
Institute of Geology and Geophysics of the Ministry of Science and Education of Azerbaijan Republic.
AZ1073, H.Javid av., 119, Baku, Azerbaijan Republic

Gunel Sadigova
Institute of Geology and Geophysics of the Ministry of Science and Education of Azerbaijan Republic.
AZ1073, H.Javid av., 119, Baku, Azerbaijan Republic

Elnara Ahmadova
Baku State University of the Ministry of Science and Education of the Azerbaijan Republic.
AZ1148 Z.Khalilov St.,33, Baku, Azerbaijan Republic

To cite this article:

Zamanova, A., Kadirov, A., Sadigova, G., & Ahmadova, E. (2025). Digital analysis of gravity data of the Absheron peninsula. *The Eurasia Proceedings of Science, Technology, Engineering and Mathematics (EPSTEM), 34,* 345-351.

The Eurasia Proceedings of Science, Technology, Engineering & Mathematics (EPSTEM)
ISSN: 2602-3199

The Eurasia Proceedings of Science, Technology, Engineering and Mathematics (EPSTEM), 2025

Volume 34, Pages 352-358

ICBASET 2025: International Conference on Basic Sciences, Engineering and Technology

An Analysis of a Numerical Solution of the Lotka-Volterra Predator-Prey Model

Mohammad H. Al-Towaiq
Jordan University of Science and Technology

Abstract: This paper explores numerical solutions of the Lotka-Volterra predator-prey model with specific initial conditions. We analysis the behavior of the model under different initial conditions to investigate the sensitivity of the solutions and their interdependence. This work demonstrates the application of numerical techniques in understanding ecological systems and the efficiency of the computational methods.

Keywords: Differential equations, Predator-prey system, Lotka-Volterra model, Ecological system

Introduction

No species can live in complete isolation. All species must eat to stay alive, hence they must interact. In this paper, we will consider a model where one population serves as food for another, which is called predator-prey model of two interacting species. Lotka-Volterra equations, (Volterra, 1926; Lotka, 1925), well recognized system presenting cyclical nature of such relationships.

For our purposes, we consider the following Lotka-Volterra predator-prey model

$$\acute{x_1}(t) = ax_1(1 - bx_2) \ , x_1(0) = x_{10}$$

$$\acute{x_2}(t) = cx_2(dx_1 - 1) \ , x_2(0) = x_{20} \tag{1}$$

where t: denote the time, $x_1(t)$: the size of the preys population at time t. $x_2(t)$: the size of the predators population at time t , x_{10} and x_{20} are the initial populations of x_1 and x_2, respectively, and a, b, c, d are positive constants describing the interaction of the two species. Solving (1) analytically is often infeasible because of their nonlinearity nature, so the use of numerical method to find an approximate solution to help us to understand the sensitivity of the model and the relationship between predator and prey populations, would be an excellent approach. Recently, several methods were proposed for the solution of (1), for example; He et al. (2024), proposed a new approach to solve the Lotka–Volterra predator–prey models approximately The method called Extreme Learning Machine. The method transformed the system of differential equations into a set of nonlinear equations. The authors show that their proposed method produced high-precision results compared with other numerical methods (Ripoll & Font,2023), discussed the impact of age-dependent interaction. They presented two approaches, the partial differential equation and the other is the renewal equation. They develop a numerical technique to analyze the instability of the steady-states and the time-evolution of the populations to test the efficiency of the proposed methods. Boulnois (2023), drove an exact, closed-form solution to the prey-predator model when the growth rate of the prey and decay rate of the predators are equal in magnitude. Cherniha and Davydovych (2022), reviewed a known methods of integrating Lotka–Volterra equations with diffusion and presented a range of exact solutions, the important of this summary, may serve as references for validating numerical approaches. In addition, for further readings, see the rest of references.

In this paper, we aim to see how numerical techniques and computational tools can provide deep insights into real-world problems. We consider three cases with different initial populations of the prey and predator sizes.

Numerical Demonstrations and Analysis

In this section, we consider the Lotka-Volterra predator-prey model (1) with the following different initial population sizes. Also, for calculations purposes, we assume constant interaction coefficients $\boldsymbol{a} = \mathbf{4}$: Growth rate of the prey, $\boldsymbol{b} = \mathbf{0.5}$: Rate at which predators consume prey, $\boldsymbol{c} = \mathbf{3}$: Growth rate of the predator due to predation, $\boldsymbol{d} = \mathbf{1/3}$: Efficiency of converting consumed prey into predator reproduction.

Case 1: First, we solve (1) with the initial populations $x_1(0) = 3\,, x_2(0) = 5$ over $0 \le t \le 2$ numerically using Mathematica. The following table and figures demonstrate the findings

Table 1. Shows the solution with$x_1(0) = 3\,, x_2(0) = 5$

t	Prey Population	Predator Population	t	Prey Population	Predator Population
0.0000	3.0000	5.0000	1.1000	1.8309	0.5990
0.1000	1.6900	4.6467	1.2000	2.4368	0.5485
0.2000	1.0664	3.9348	1.3000	3.2631	0.5392
0.3000	0.7808	3.1910	1.4000	4.3557	0.5833
0.4000	0.6580	2.5378	1.5000	5.7185	0.7137
0.5000	0.6246	2.0034	1.6000	7.2084	1.0095
0.6000	0.6522	1.5813	1.7000	8.3161	1.6362
0.7000	0.7337	1.2549	1.8000	8.0434	2.7891
0.8000	0.8740	1.0070	1.9000	5.9444	4.2050
0.9000	1.0869	0.8223	2.0000	3.4833	4.9690
1.0000	1.3951	0.6890			

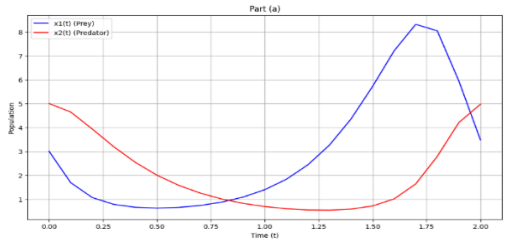

Figure 1. $x_1(t)$ and $x_2(t)$ vs. t with $x_1(0) = 3, x_2(0) = 5$

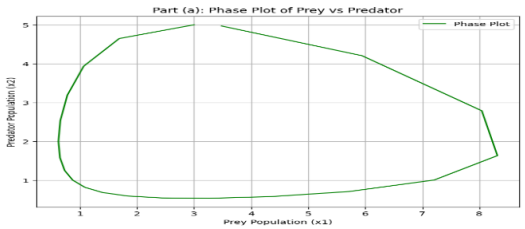

Figure 2. $x_1(t)$ vs. $x_2(t)$ with $x_1(0) = 3\,, x_2(0) = 5$

From Table 1 and Figures 1 and 2 we conclude that

1. the prey population starts at 3 but decreases rapidly due to the high number of predators, between t=0 and t=0.75, the prey population decreases steadily, reaching its minimum as predator pressure is strong, after t=0.75 , the prey population begins to recover as conditions likely improve (e.g., predator numbers decrease or prey reproduction exceeds predation), finally, the prey population reaches a maximum around t≈1.75 , before beginning to decline again
2. the predator population decreases steadily up to t =1.25 because the prey population deckine during this period which leads to food scarcity for predators, and may be due to the predator death rate which greater than its reproduction rate.

3. The closed curve , Fig. 2, indicates that the cyclic nature of the predator-prey relationship; As prey increases, predators increase shortly after and as predators peak, prey decreases due to higher predation rates. With fewer prey, predators decline, which allows prey to recover, restarting the cycle. Finally, the system oscillates around a central point (an unstable equilibrium), but it does not settle into a steady-state.

Case 2: in this case we consider the initial populations $x_1(0) = 3$ and $x_2(0) = 1$ over $0 \leq t \leq 2$. The following tables and figures demonstrate the findings:

Table 2. Shows the solution with $x_1(0) = 3\,, x_2(0) = 1$

t	Prey Population	Predator Population	t	Prey Population	Predator Population
0.0000	3.0000	1.0000	1.1000	1.4800	2.6464
0.1000	3.6565	1.0325	1.2000	1.3529	2.2565
0.2000	4.3948	1.1436	1.3000	1.3317	1.9103
0.3000	5.1132	1.3640	1.4000	1.3969	1.6210
0.4000	5.6120	1.7325	1.5000	1.5436	1.3901
0.5000	5.6281	2.2625	1.6000	1.7762	1.2149
0.6000	5.0247	2.8688	1.7000	2.1057	1.0918
0.7000	4.0105	3.3447	1.8000	2.5456	1.0197
0.8000	2.9969	3.5125	1.9000	3.1057	1.0011
0.9000	2.2366	3.3722	2.0000	3.7801	1.0455
1.0000	1.7531	3.0434			

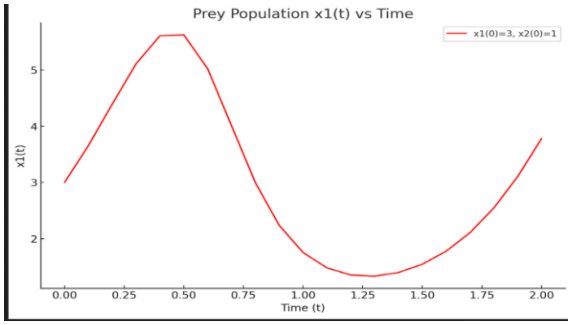

Figure 3. $x_1(t)$ vs. t with $x_1(0) = 3\,, x_2(0) = 1$

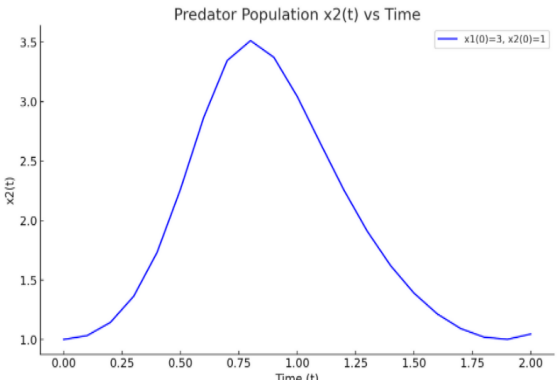

Figure 4. $x_2(t)$ vs. t with $x_1(0) = 3\,, x_2(0) = 1$

From Table 2 and Figures 3, 4, and 5, we conclude that

1. From t=0 , t≈0.5 the prey population increases due to the low initial number of predators, allowing the prey to reproduce without significant predation pressure. This leads to a peak in the prey population at t≈0.5. As time progresses, t≈0.5 to t≈1.25, the predator population likely grows in response to the earlier increase in prey, causing the prey population to decline. the decline continues until it reaches a minimum at t≈1.25, after that it starts to recover as the predator population potentially decreases or stabilizes, the prey population steadily rises.

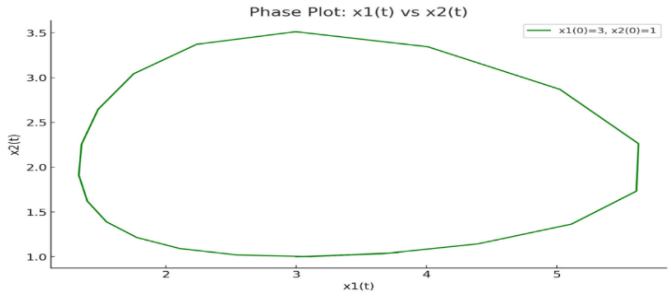

Figure 5. $x_1(t)$ vs. $x_2(t)$ with $x_1(0) = 3\,, x_2(0) = 1$

2. At the beginning, the predator population $x_2(t)$ is relatively low, while the prey population $x_1(t)$ is abundant. This abundance provides enough resources for predators to grow and reproduce, causing their numbers to increase rapidly over time. The predator population eventually reaches its maximum level when the prey population starts to decline due to overconsumption. At this point, resources for predators become scarcer, signaling the start of their decline. After the peak, the predator population $x_2(t)$ decreases as prey resources become insufficient to sustain their growth. Finally, over time, the system may stabilize as predator and prey populations balance each other, leading to cyclical patterns of rise and fall in population sizes.
3. The curve in Fig. 5 still forms a closed loop, indicating periodic oscillations between prey and predator populations. However, the trajectory is smaller and more compact compared to Fig. 2 reflecting the reduced initial predator population. Also, as you can see that the curve moves leftward, with both $x_1(t)$ and $x_2(t)$ decreasing.

Case 3: finally, in this case we consider the initial populations $x_1(0) = 3$ and $x_2(0) = 1.9$ over $0 \leq t \leq 2$. The following tables and figures demonstrate the findings

Table 3. The solution with $x_1(0) = 3\,, x_2(0) = 1.9$

t	Prey Population	Predator Population	t	Prey Population	Predator Population
0.0000	3.0000	1.9000	1.1000	2.8862	2.0779
0.1000	3.0594	1.9057	1.2000	2.8491	2.0503
0.2000	3.1130	1.223	1.3000	2.8297	2.0174
0.3000	3.1540	1.9484	1.4000	2.8297	1.9830
0.4000	3.1765	1.9812	1.5000	2.8486	1.9510
0.5000	3.1771	2.0169	1.6000	2.8845	1.9249
0.6000	3.1553	2.0511	1.7000	2.9338	1.9074
0.7000	3.1141	2.0792	1.8000	2.9913	1.9001
0.8000	3.0589	2.0975	1.9000	3.0510	1.9042
0.9000	2.9975	2.1034	2.0000	3.1058	1.9193
1.0000	2.9375	2.0965			

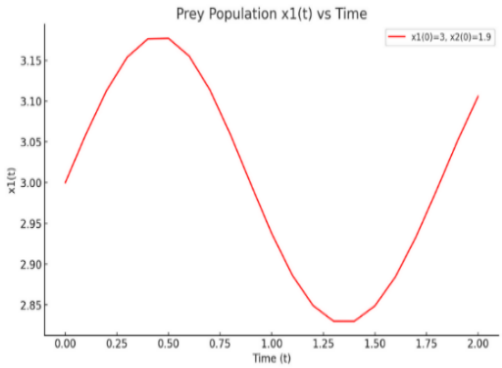

Figure 6. $x_1(t)$ vs. t with $x_1(0) = 3\,, x_2(0) = 1.9$

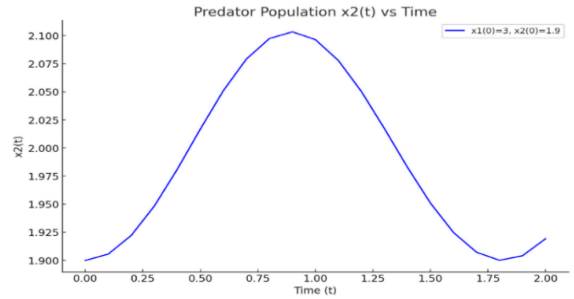

Figure 7. $x_2(t)$ vs. t with $x_1(0) = 3\,, x_2(0) = 1.9$

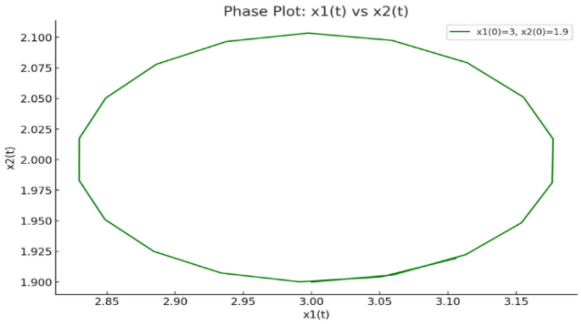

Figure 8. $x_1(t)$ vs. $x_2(t)$ with $x_1(0) = 3\,, x_2(0) = 1.9$

From Table 3 and Figures 6, 7, and 8, we conclude that

1- Initially, the predator population is moderate, allowing a slight increase in the prey population. So, the prey population reaches a peak of approximately 3.15 within a short period. After the peak, the population gradually decreases due to an increase in predator numbers. The prey population decreases to its lowest point of around 2.8 near t=1.5. After reaching the minimum, the prey population begins to recover as predator numbers decline. The predator numbers are insufficient to limit the growth of the prey population, allowing a slight increase. As predator numbers rise, the prey population declines.
2- The predator population reaches a peak at around 2.1, which is lower than in the earlier cases. This smaller peak indicates that the higher initial predator population reduces the overall growth potential. After reaching the peak, the predator population declines and stabilizes at a lower level, similar to previous behaviors but starting from a higher baseline. With $x_2(0)$=1.9, the predator population starts closer to its peak, leaving less room for growth. The higher initial predator count increases competition for prey, reducing the predators' ability to sustain higher population growth.
3- The closed loop indicates that the populations of prey (x_1) and predators (x_2) follow a periodic cycle. This behavior is typical of predator-prey systems modeled by the Lotka-Volterra equations. Finally, neither population grows unbounded nor collapses to zero, maintaining an oscillatory balance in the ecosystem.

Conclusion

In this paper, we aim to see how numerical techniques and computational tools can provide deep insights into real-world problems. Hence, we use Mathematica to examine the system's oscillatory and the relationship between the two populations by varying initial population sizes. The results illustrate the balance between predator and prey populations by revealing their cyclical nature and how the system is sensitive to the initial conditions. In addition, the solutions we obtained guaranteed accuracy and stability during the simulation over a period, $0 \leq t \leq 2$ with step size $h = 0.1$.

Future work

- To make the model more realistic for future research, include external variables such as environmental variability migration, or disease or include new species.

- For increased accuracy over longer simulation timeframes, smaller step sizes or adaptive techniques can be investigated.

Scientific Ethics Declaration

* The author declares that the scientific ethical and legal responsibility of this article published in EPSTEM journal belongs to the author.

Conflict of Interest

* The author declares no conflict of interest

Funding

* This research received no specific grant from any funding agency in the public, commercial, or not-for-profit sectors

Acknowledgments or Notes

* This article was presented as an oral presentation at the International Conference on Basic Sciences, Engineering, and Technology (www.icbaset.net) held in Trabzon/Türkiye on May 01-04, 2025.

References

Aida, M. (2022). Fourth-order runge-kutta method for solving applications of system of first-order ordinary differential equations. *Enhanced Knowledge in Sciences and Technology, 2*(1), 517-526.

Boulnois, J. L (2023), An exact closed-form solution of the lotka- volterra equations, *arXiv:2303.09317v1*.

Cassani, A., Monteverde, A., & Piumetti, M. (2021). Belousov-Zhabotinsky type reactions: The non-linear behavior of chemical systems. *Journal of Mathematical Chemistry, 59*, 792-826.

Cherniha, R. and Davydovych, V. (2022), Construction and application of exact solutions of the diffusive Lotka-Volterra system: a review and new results, *arXiv:2209.08863v1*.

Ghasemabadi, A., & Rahmani Doust, M. H. (2021). Investigating the dynamics of Lotka -Volterra model with disease in the prey and predator species. *International Journal of Nonlinear Analysis and Applications*, *12*(1), 633-648.

He, J., Zheng, Z., & Ye, Z. (2024), A new numerical approach method to solve the Lotka–Volterra predator–prey models with discrete delays, *Physica A: Statistical Mechanics and its Applications*, *635*, 129524.

Kovács, Z., & József, L. (2016). Numerical Solutions for the Lotka-Volterra equations. *Applied Mathematical Sciences*, *10*(35), 1711-1722.

Lotka, A.J**.** (1925). *Elements of physical biology.* Williams and Wilkins

Ripoll, J., & Font, J. (2023), Numerical approach to an age-structured Lotka-Volterra model, *Mathematical Biosciences and Engineering*, *20*(9), 15603- 15622.

Romanov, V. P., Agafonova, H. A., Sandybaeva, S. S., & Mullin, N. S. (2015). Innovation process simulation on the base predator and prey. *International Journal of Innovation, Management and Technology*, 6(1), 30.

Singh, A. (2021). Stochastic dynamics of predator-prey interactions. *Plos One*, *16*(8), e0255880.

Venturino, E. (2016). Ecoepidemiology: A more comprehensive view of population interactions. *Mathematical Modelling of Natural Phenomena*, *11*(1), 49-90.

Volterra, V**.** (1926). Fluctuations in the abundance of a species considered mathematically. *Nature, 118*(2972), 558- 560.

Voroshilova, A., & Wafubwa, J. (2020). Discrete competitive Lotka–Volterra model with controllable phase volume. *Systems*, *8*(2), 17.

Zawadzki, R. S., Gong, C. L., Cho, S. K., Schnitzer, J. E., Zawadzki, N. K., Hay, J. W., & Drabo, E. F. (2021). Where do we go from here? A framework for using susceptible-infectious-recovered models for policy making in emerging infectious diseases. *Value in Health*, *24*(7), 917-924.

Author Information

Mohammad H. Al-Towaiq
Jordan University of Science and Technology,
Department of Mathematics and Statistics
P. O. BOX 3030, Irbid 22110, Jordan
Contact e -mail: *towaiq@just.edu.jo*

To cite this article:

Al-Towaiq, M. H. (2025). An analysis of a numerical solution of the Lotka-Volterra predator-prey model. *The Eurasia Proceedings of Science, Technology, Engineering and Mathematics (EPSTEM), 34,* 352-358.

The Eurasia Proceedings of Science, Technology, Engineering & Mathematics (EPSTEM)
ISSN: 2602-3199

The Eurasia Proceedings of Science, Technology, Engineering and Mathematics (EPSTEM), 2025

Volume 34, Pages 359-368

ICBASET 2025: International Conference on Basic Sciences, Engineering and Technology

Incorporating Worker Heterogeneity in Flexible Flow Shop Environment

Kubra Ozpacaci
Abdullah Gul University

Seyma Bekli
Abdullah Gul University

Betul Kayisoglu
Abdullah Gul University

Abstract We study the flexible flow shop scheduling problem with the heterogeneous worker assignment. In many real-life manufacturing systems with flow shop environments, one of the fundamental scheduling challenges that needs to be addressed is job sequences across multiple workers. In addition, the manufacturing system may require workers to have different skills at various stages during their assignment. Therefore, worker availability at each stage may vary during the scheduling horizon. Unlike traditional flexible flow shop scheduling problem, where homogeneous workers are assumed, we consider workers with different skill levels, capabilities, and capacities. We present a mixed integer linear programming model to find the optimal sequence of job assignments, guaranteeing that jobs follow their predefined operation sequence while assigning workers with various skill sets in a flexible flow shop environment. The proposed model is tested at a battery manufacturing company. By analyzing the solution, we confirm its capability to represent the problem accurately. The proposed model offers a systematic scheduling approach for a flexible flow shop environment with a heterogeneous workforce and can be implemented in other industries.

Keywords: Production scheduling, Flexible workforce, Mixed integer linear programming, Sustainability

Introduction

In today's fast-paced business environments and fierce market conditions, companies try to enhance their competitiveness by meeting customer requirements, including product delivery times. Efficient delivery can be achieved through production scheduling. Production scheduling is the decision of timing and sequence of the tasks over available resources.

Production scheduling is a challenging task, especially considering complex manufacturing systems. Production systems often involve additional resources, including human- and robot-assisted operations, tools, and software (Benkalai et al., 2019; Mraihi et al., 2024). Many aspects need to be addressed while producing a schedule, such as human-related factors and varying processing times. Leaving out human factors and human-related operations notably limits the classical scheduling theory (Ostermeier, 2020). Even with Industry 4.0's significant role in production, human involvement will remain vital in operational systems (Neumann et al., 2021). The extent of an individual's involvement in a workspace depends on various factors, such as the capabilities and capacity of the worker. Workers' varying skills, qualifications, experience, and worker-specific characteristics affect where they can work and the speed at which they complete tasks. Multi-skilled workers or worker flexibility may decrease the bottlenecks in a production system and provide more efficient systems (Daniels et al., 2004). However, the heterogeneity of the skills makes the production scheduling problem difficult for the decision-makers. It brings about a "suboptimal" solution due to using worst-case scenarios or other measures

(Benavides et al., 2014). Therefore, the heterogeneity of the workers' qualifications must be considered when scheduling production.

The flexible flow shop problem (FFSP)(sometimes referred to as hybrid flow shop) is widely applicable to real-world systems and therefore got the attention of many researchers over the years (Burcin- Ozsoydan & Sagir, 2021; Naderi et al., 2009). FFSP can be considered a combination of parallel machine and flow shop scheduling. In FFSP, there are jobs that require sequential processing at stages, with at least one stage involving more than one machine providing a parallel machine environment (Pinedo, 2022; Tosun et al., 2020).

In this study, motivated by a battery production facility, we focus on an FFSP with the consideration of worker flexibility. It should be noted that worker/workforce flexibility terms cover flexible working hours, floaters, cross-training, teamwork, and temporary labor (Qin et al., 2015). In this context, we consider worker flexibility as cross-training and varying processing times. This study provides a mathematical model that explores the practical characteristics of labor multiskilling and heterogeneity of workers' processing times in a flexible flow shop environment, one of the commonly observed manufacturing environments, and helps managers to eliminate or decrease the bottlenecks in their systems through the optimal job assignments of multiskilled workers.

The remainder of the paper is organized as follows. First, we provide a background and related work on worker flexibility in flexible flow shop (FFS) environments. Second, we present the problem and a mixed integer linear programming model for the heterogeneous worker assignment problem in FFS environments. Thirdly, we introduce a real-life case representing the problem. Using real-world data from a battery manufacturing facility, we discuss the results in the Computational Experiments sections. Finally, we provide concluding remarks and highlight future directions.

Related Literature

This section briefly reviews production scheduling in FFS environments with a focus on flexible workers. However, interested readers are referred to Maccarthy and Liu (1993) for a more general analysis of production scheduling. For different aspects of scheduling, readers are referred to Davis et al. (2016) for job priorities, Danping and Lee (2011), Kayisoglu et al. (2024) for re-entrant jobs, Schmidt (2000) for limited machine availability, and Madenoglu (2021) for solution methods in FFSP.

Here, we review the related literature on flexible workers in FFSP for multi-skilled workers and varying processing times. Daniels et al. (2004) presented a MILP model for a flow shop scheduling problem where processing times depend on how many workers are assigned to the same machine given the workers' skill matrix. The computational results show that a significant share of the potential benefits of labor flexibility can be achieved with a modest increment in the skill matrix. Benavides et al. (2014) also examined a flow shop environment where workers could be assigned to jobs based on their skills. Unlike Daniels et al. (2004), only one worker could be assigned to a machine. They proposed a MILP model to solve the worker assignment problem in the flow shop environment and provided a heuristic algorithm based on scatter search and path relinking. Fekri et al. (2024) worked in an FFS environment with multiple skilled workers. The proposed MILP model minimizes the total weighted completion time and total weighted idle time of the workers by assigning sets of workers to the machines required for the jobs. A genetic algorithm and a simulated annealing algorithm are provided as solution methods.

Next, we examine the related literature on varying processing time, including the learning (and forgetting effects) in FFS environments. Gong et al. (2020) explored a novel FFSP, considering factors such as machine/worker flexibility, varying processing times, and energy consumption. A MILP model and a hybrid evolutionary algorithm are proposed as solution algorithms. We should also mention learning effects when presenting studies with varying processing times. Several researchers examined the learning effects of mass production, suggesting that a worker might produce the same product in a shorter time when producing the same item/job consecutively (Biskup, 2008). Fichera et al. (2017), Pargar et al. (2018) and Seidgar et al. (2015) examined the learning effect in FFS environments, assuming that the learning effect occurs through the reduction of setup times. Seidgar et al. (2015) provided a mixed integer linear programming (MILP) model to solve the FFSP with the learning and forgetting effects of the workers setting up the machines.

Pargar et al. (2018) also investigated the effects of worker learning in a bi-objective FFSP environment. A MILP is provided for the bi-objective model, and two new hybrid metaheuristic algorithms, hybridizing water

flow-like algorithms with non-dominated sorting and ranking concepts, are provided. Fichera et al. (2017) also provided a MILP model to minimize the makespan of a flow shop group scheduling problem with heterogeneous workers. For large-sized instances, an evolutionary algorithm was presented. Unlike the mentioned studies, Marichelvam et al. (2020) considered the learning effect over the processing times, setting the processing times of each worker to be equal to the multiplication of the skill factor, learning factor, forgetting factor, age factor of the worker, and processing time of the job. A MILP model and particle swarm optimization-based heuristic algorithms are proposed as solution algorithms.

Our study investigates FFSP with multiskilled workers as its primary focus. This problem is designed to represent a real-world scheduling challenge frequently encountered when different types of competencies are required for various operations in manufacturing. This study contributes to the literature by presenting a MILP model that considers multiskilled workers with various processing times in an FFSP setting.

Problem Definition and Proposed Mathematical Model

We focus on an extension of the traditional flexible flow shop scheduling problem (FFSSP). Unlike FFSSP, where worker capabilities are either ignored or assumed homogeneous, we consider workers with different skill levels, efficiencies, or processing speeds. Therefore, we study the flexible flow shop scheduling problem with heterogeneous worker assignment (FFSSP_HWA). Let J represent the set of jobs where $j, j' \in J$. Each job may have different order quantities that need to be processed. We define n_j as the number of orders of job j. Every job consists of a sequence of consecutive operations. Let I denote the set of operations, where $i, i' \in I$. There is a precedence relation between the operations ensuring that each job follows the specified sequence of operations in a predefined order as indicated by the operation numbers. In addition, if an operation of a job has started, the subsequent operations of that job cannot begin until the current operation is completed for the required order quantity of that job, denoted by n_j.

In FFSSP_HWA, there are workers with different skills. Let W denote the set of workers. We define a binary parameter a_{iw}, which equals 1 if worker w is capable of performing operation i, and 0 otherwise. Furthermore, due to differences in experience and efficiency, workers may have varying processing speeds. To represent this, we define the parameter p_{ijw}, which denotes the processing time for a single order of job j at operation i when performed by worker w.

The objective of FFSSP_HWA is to minimize the makespan, which represents the total completion time of the schedule, i.e., the time at which the last job finishes processing. We denote the makespan as . We develop a mathematical model for FSSP_HWA. The model determines the start and completion time of each operation for each job, denoted by the decision variables and , respectively. is a binary decision variable that equals 1 if worker is assigned to operation of job , and 0 otherwise.

Sets, parameters, and decision variables for FFSSP_HWA

Sets

I	*Set of operations where* $i, i' \in I$
J	*Set of jobs* where $j, j' \in J$
W	*Set of workers*

Parameters

a_{iw}	1 *if worker* w *is capable of performing operation* $i, 0$ *otherwise*
p_{ijw}	*Processing time of job* j *for operation* i *done by worker* w
n_j	*Number of orders of job* j
M	*Arbitrary large number*

Decision Variables

C_{max}	*Makespan (the time at which the last job finishes processing)*
X_{ij}	*Start time of operation* i *for job* j
C_{ij}	*Completion time of operation* i *for job* j
P_{ij}	*Processing time of operation* i *for job* j
O_{ijw}	$1,$ *if worker* w *is assigned to operation* i *of job* $j,$ 0 *otherwise.*
$Y_{ii'jj'}$	$1,$ *if operation* i *of job* j *starts before operation* i' *of job* $j',$ 0 *otherwise.*

Since assigned workers can influence the processing time of an operation, P_{ij} is introduced as a decision variable representing the processing time of operation i for job j. Lastly, the precedence decision variable $Y_{ii'jj'}$ takes the value 1 if operation i of job j starts before operation i' of job j', and 0 otherwise. With these definitions, the proposed model for FFSSP_HWA is given below:

$$Z = \text{Min } C_{max} \quad (1)$$

s.t.

$$C_{ij} \leq C_{max} \qquad \forall i \in I, \forall j \in J \quad (2)$$

$$C_{ij} = X_{ij} + P_{ij} \qquad \forall i \in I, \forall j \in J \quad (3)$$

$$\sum_{w} O_{ijw} = 1 \qquad \forall i \in I, \forall j \in J \quad (4)$$

$$X_{ij} + P_{ij} \leq X_{i+1,j} \qquad \forall i \in I \text{ and } i \neq |I|, \forall j \in J \quad (5)$$

$$X_{ij} + P_{ij} \leq X_{i'j} + M(1 - Y_{ii'jj}) \qquad \forall i, i' \in I, \forall j \in J \quad (6)$$

$$X_{ij} \leq X_{i'j'} + M(1 - Y_{ii'jj'}) \qquad \forall i, i' \in I, \forall j, j' \in J \quad (7)$$

$$X_{ij} + P_{ij} \leq X_{i'j'} + M(3 - Y_{ii'jj'} - O_{ijw} - O_{ij'w}) \qquad \forall i, i' \in I, \forall j, j' \in J, \forall w \in W \quad (8)$$

$$O_{ijw} \leq a_{iw} \qquad \forall i \in I, \forall j \in J, \forall w \in W \quad (9)$$

$$Y_{ii'jj'} + Y_{i'ij'j} = 1 \qquad \forall i, i' \in I \text{ and } i \neq i', \forall j, j' \in J \text{ and } j \neq j' \quad (10)$$

$$P_{ij} = \sum_{w} p_{ijw}\, n_j\, O_{ijw} \qquad \forall i \in I, \forall j \in J \quad (11)$$

$$P_{ij}, X_{ij}, C_{ij} \geq 0 \qquad \forall i \in I, \forall j \in J \quad (12)$$

$$Y_{ii'jj'} \in \{0,1\} \qquad \forall i, i' \in I, \forall j, j' \in J \quad (13)$$

$$O_{ijw} \in \{0,1\} \qquad \forall i \in I, \forall j \in J, \forall w \in W \quad (14)$$

The proposed model aims to minimize the time at which the last job completes processing, i.e., makespan, as defined in the objective function (1). Constraints (2) establish the makespan by ensuring that it is greater than or equal to all completion times. Constraints (3) define the completion time of each job as its starting time plus the processing duration. Constraints (4) guarantee that each operation is assigned to exactly one worker. Constraints (5) guarantee that, for the same job, the start time of an operation is greater than the completion time of the previous operation, as required by the precedence constraints. Constraints (6) establish the sequence of operations for the same job and accordingly define the values of the $Y_{ii'jj}$ variable. Constraints (7) ensure that operation i for job j must start before the operation i' for job j' if $Y_{ii'jj'}$ variable gets the value 1. Constraints (8) determine the sequence of operations for all jobs and ensure that workers are assigned accordingly, preventing them from being allocated to multiple jobs simultaneously. Constraints (9) ensure that workers are assigned to operations based on their capabilities. Constraints (10) guarantee that either operation i of job j starts before operation i' of job j' or vice versa. Constraints (11) determine the processing time of operation i of job j when executed by worker w. Finally, Constraints (12), (13), and (14) define the domains of the decision variables.

Case Study for FSSP_HWA

For the FFSSP_HWA, we consider a real-world case study from a manufacturing company specializing in the production of batteries. The production process involves four different types of batteries, each requiring the completion of sequential operations. There are a total of 19 operations. The precedence relationships among these operations are illustrated in Figure 1.

The workforce consists of eight workers, each possessing different skill sets and experience levels. As a result, processing times vary across workers, depending on their individual capabilities and familiarity with the specific operations. Out of the 19 operations, 18 require a worker, while Operation 1 (Cell Classification) is fully automated and performed by a machine. This operation does not require a worker. To incorporate this automated step into the model consistently, we introduce a dummy worker who is only assigned to Operation 1 and is not capable of performing any other task. This approach brings the total number of workers in the case to nine, including the dummy worker. Table 2 presents the worker skill matrix, which illustrates the operations each worker is capable of performing.

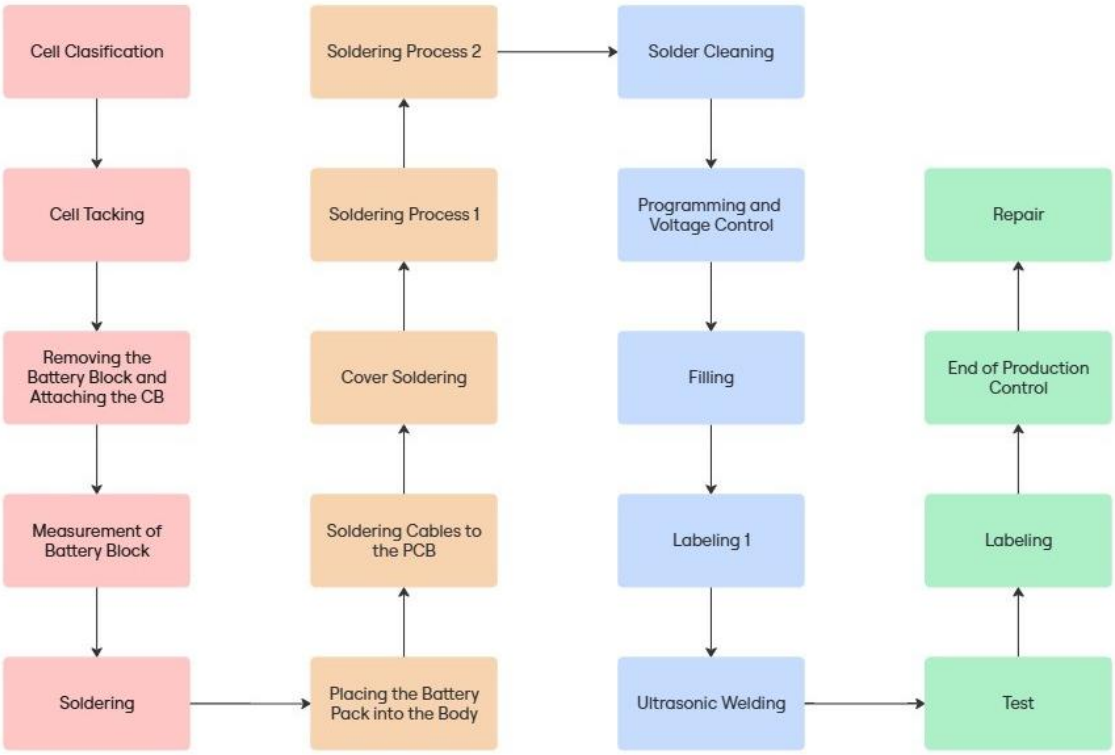

Figure 1. Precedence of operations

Table 2. Worker skill matrix

Operations	W1	W2	W3	W4	W5	W6	W7	W8	W9
1									✓
2				✓	✓	✓	✓	✓	
3	✓	✓	✓	✓	✓	✓	✓	✓	
4	✓	✓	✓	✓	✓	✓	✓	✓	
5					✓	✓	✓	✓	
6	✓	✓	✓	✓	✓	✓	✓	✓	
7					✓	✓	✓	✓	
8					✓	✓	✓	✓	
9					✓	✓	✓	✓	
10					✓	✓	✓	✓	
11	✓	✓	✓	✓	✓	✓	✓	✓	
12	✓	✓	✓	✓	✓	✓			
13	✓	✓	✓	✓	✓	✓	✓	✓	
14	✓	✓	✓	✓	✓	✓	✓	✓	
15	✓	✓	✓	✓					
16							✓	✓	
17	✓	✓	✓	✓	✓	✓	✓	✓	
18							✓	✓	
19	✓	✓	✓	✓	✓	✓	✓	✓	

In a single planning horizon, the company may receive varying order quantities for different jobs. A key scheduling constraint is that once an operation of a job has started, its subsequent operations cannot begin until the current operation is fully completed for the entire order quantity.

Computational Experiments with the Mathematical Model for FSSP_HWA

To test the proposed model for FFSSP_HWA through computational experiments, we utilized a production plan obtained from the company where we got our real-world case. The plan involves four different batteries, i.e., jobs, that will be scheduled within a single planning horizon. Specifically, it includes the production of 75 units of Job 1, 50 units of Job 2, 90 units of Job 3, and 100 units of Job 4. Our aim is to find the schedule that

minimizes makespan while assigning workers to operations based on their skill sets. We solved this case using CPLEX and successfully obtained the optimal solution. The objective function value, representing the makespan, is 135,200 minutes. Our analysis of the solution confirms that the model accurately represents the problem and fulfills all predefined requirements.

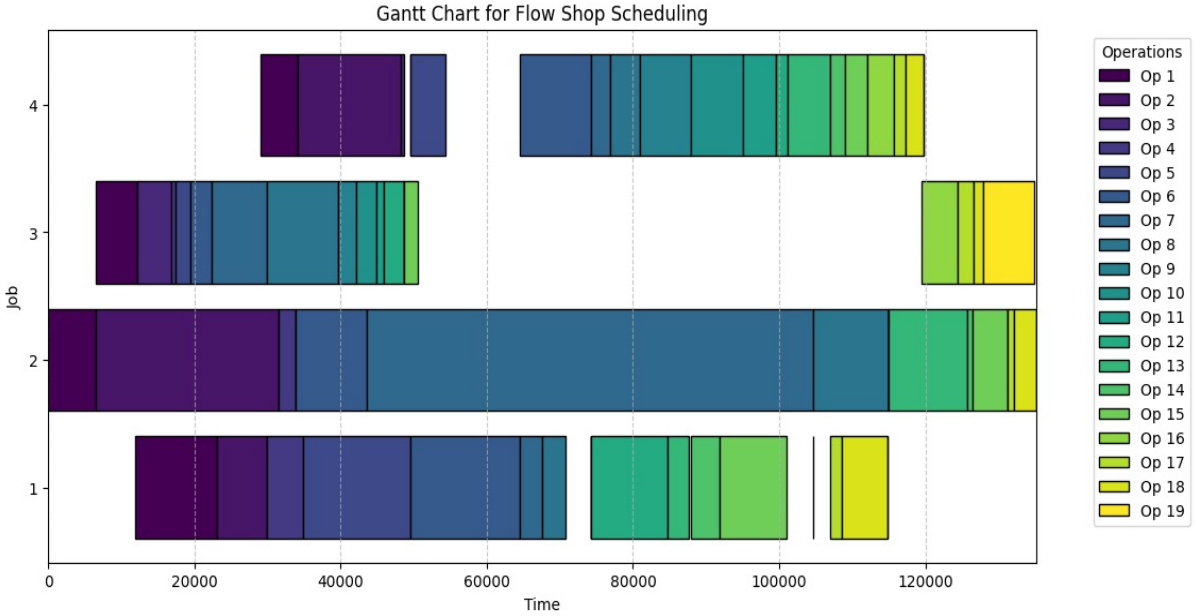

Figure 2. Gantt chart representing the schedule for each job

Figure 2 presents the Gantt chart illustrating the schedule for each job. Upon examining the chart, it is evident that the precedence constraints of the operations are satisfied. Makespan is equal to the completion time of the last operation of Job 2. In Job 2, each operation starts immediately after the preceding one, ensuring that no further improvement in makespan is possible for this production plan.

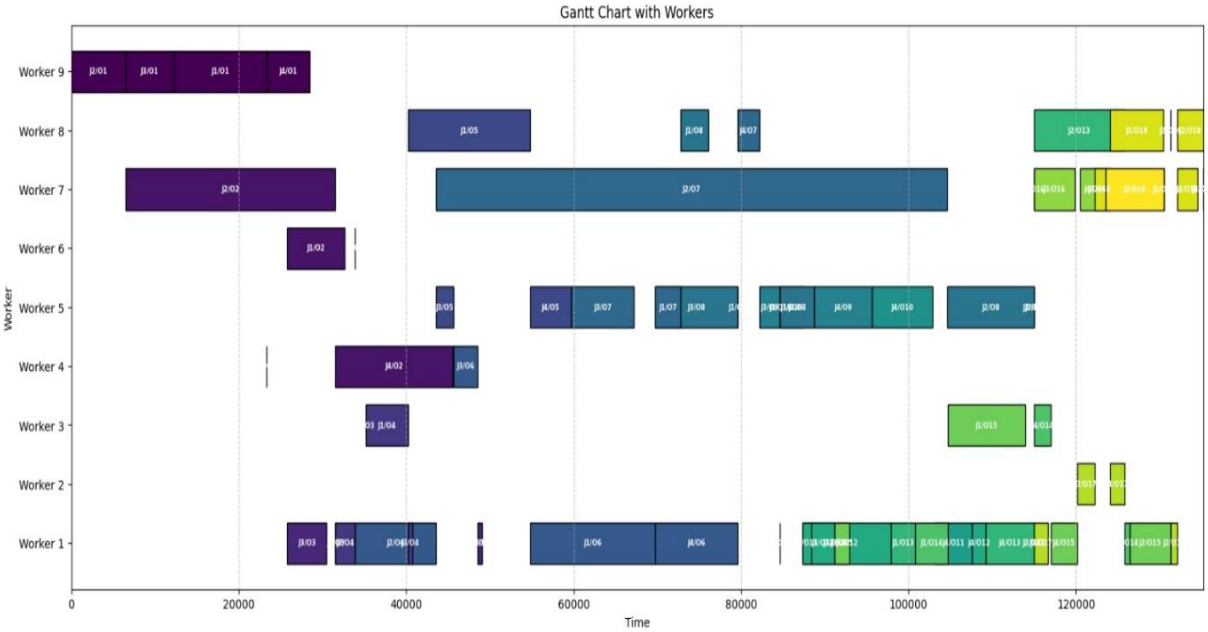

Figure 3. Gantt chart representing the schedule for each worker

Figure 3 presents the Gantt chart illustrating the schedule for each worker. As expected, workers are assigned to a new operation after completing their previous operation, as they cannot be assigned to multiple operations simultaneously. Upon analyzing the chart, we observed that some workers remain idle for a significant portion of the planning horizon. This observation prompted further analysis. To improve workforce utilization, we examined the possibility of assigning some workers to other tasks within the company instead of battery

production. Specifically, we identified that Workers 2, 3, 4, and 6 had considerably lower workloads compared to others. To assess the impact of reducing the number of workers, we re-ran the proposed model, sequentially excluding Worker 2, then Worker 3, followed by Worker 4, and finally Worker 6. The results indicated that the objective function value remained unchanged, confirming that these four workers could be reallocated to other tasks without affecting the makespan value. Figure 4 presents the Gantt chart illustrating the job schedule with only four workers, while Figure 5 displays the corresponding worker schedule. Figure 4 also shows that the makespan remains unchanged in this revised schedule. A closer examination of Figure 5 reveals that Workers 1, 5, 7, and 8 are mostly utilized, with closely aligned working hours where Worker 9 serves as a dummy worker representing the first operation, which is performed automatically without a worker.

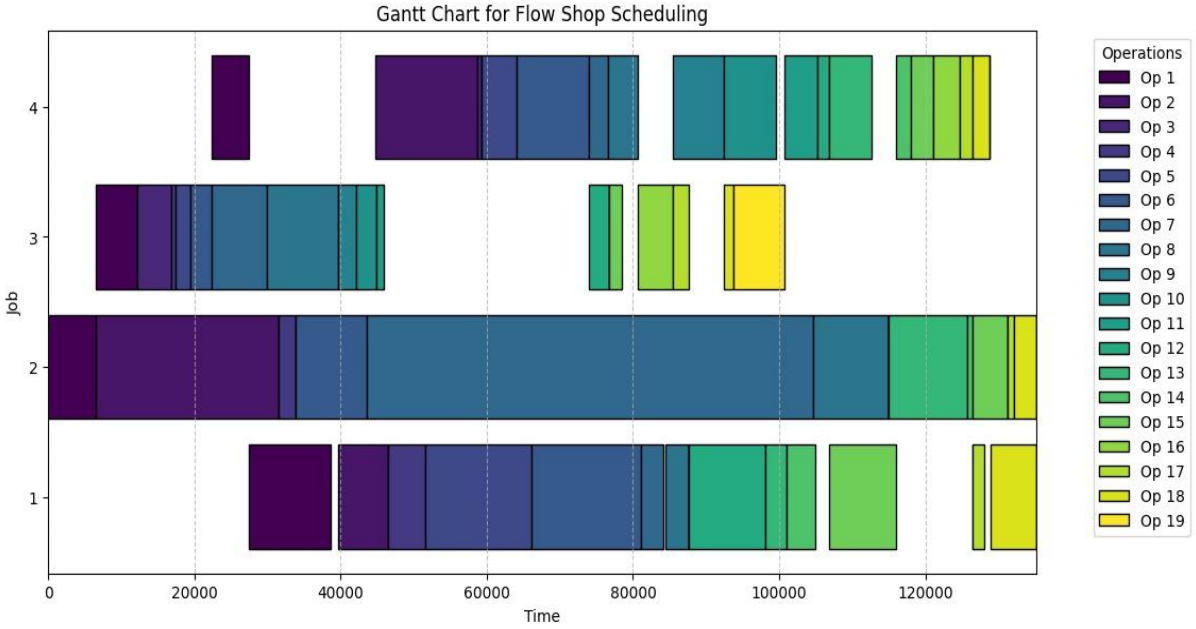

Figure 4. Gantt chart representing the schedule for each job with workers 1, 5, 7, 8 and 9

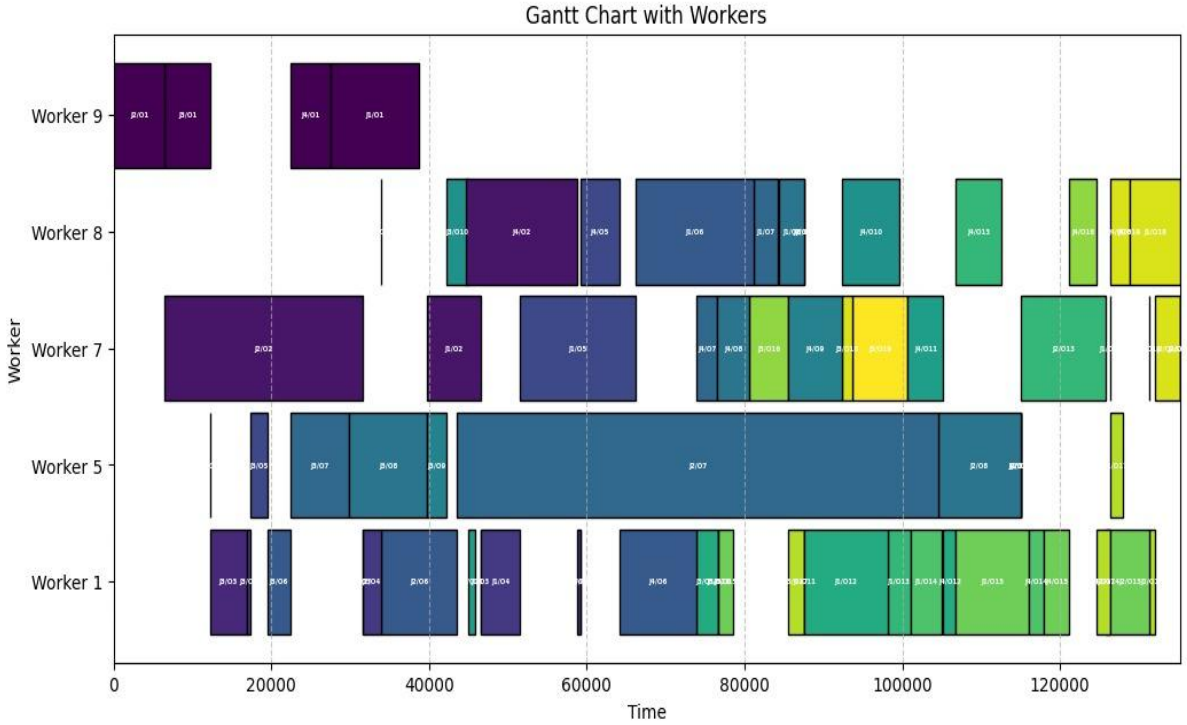

Figure 5. Gantt chart representing the revised schedule for each worker

Concluding Remarks and Future Research Directions

This study focuses on FFSSP_HWA, a flexible flow shop scheduling problem with heterogeneous worker assignment, inspired by a real-world company manufacturing batteries. Traditional flow shop scheduling models often ignore worker-related factors, assuming the processing capabilities of workers are the same. However, in real-life settings, workers possess different skills and experience levels that influence their suitability for specific operations and their processing speeds. To address this gap, our study incorporates both worker skills and worker efficiency variations in the scheduling process. By considering worker flexibility through cross-training and heterogeneous processing times, our model represents a more realistic production environment.

An integer programming model is developed for FFSSP_HWA. This model takes into account the precedence of the operations for the jobs, assigns workers to operations according to their skills, and minimizes the makespan. To test the proposed model, we conducted computational experiments using real-world production data. This case involves scheduling four different batteries, i.e., jobs with varying quantities, aiming to minimize the makespan while assigning workers based on their skill sets. The model was solved optimally using CPLEX. Examing the solution confirms its capability to represent the problem accurately. Additionally, we performed a sensitivity analysis on workforce utilization by analyzing worker assignments and identifying underutilized workers. Through iterative reduction of workers, we re-ran the model to assess its impact. The results proved that the makespan remained unchanged despite reducing the number of workers, indicating that some workers could be reassigned to other tasks. This analysis emphasizes the model's ability to support workforce planning decisions besides scheduling the jobs to minimize makespan in a flexible flow shop environment with heterogeneous workers.

To sum up, this study addresses the flexible flow shop scheduling problem with heterogeneous worker assignments, incorporating worker skills and varying processing speeds. By incorporating real-world constraints and solving the problem optimally using CPLEX, we show the model's effectiveness in accurately representing workforce flexibility in production scheduling. A case study from a company manufacturing battery validates the applicability of the proposed model. Moreover, sensitivity analyses on workforce utilization provide opportunities for optimizing labor allocation. While we were able to solve our case optimally using CPLEX, larger real-life problems with more jobs, operations, and workers may create computational challenges, making it difficult to reach optimality. As a future direction, we plan to test the model on larger instances. In cases where optimal solutions cannot be obtained, we aim to develop heuristic solution algorithms to solve the problem efficiently. Future studies could also extend this model by integrating additional constraints required for different industrial areas.

Scientific Ethics Declaration

* The authors declare that the scientific ethical and legal responsibility of this article published in EPSTEM Journal belongs to the authors.

Conflict of Interest

* The authors declare that they have no conflicts of interest

Funding

* This research received no specific grant from any funding agency in the public, commercial, or not-for-profit sectors

Acknowledgments or Notes

* This article was presented as an oral presentation at the International Conference on Basic Sciences, Engineering, and Technology (www.icbaset.net) held in Trabzon/Türkiye on May 01-04, 2025.

References

Benavides, A. J., Ritt, M., & Miralles, C. (2014). Flow shop scheduling with heterogeneous workers. *European Journal of Operational Research*, *237*(2), 713–720.

Benkalai, I., Rebaine, D., & Baptiste, P. (2019). Scheduling flow shops with operators. *International Journal of Production Research*, *57*(2), 338–356.

Biskup, D. (2008). A state-of-the-art review on scheduling with learning effects. *European Journal of Operational Research*, *188*(2), 315–329.

Burcin- Ozsoydan, F., & Sagir, M. (2021). Iterated greedy algorithms enhanced by hyper-heuristic based learning for hybrid flexible flowshop scheduling problem with sequence dependent setup times: A case study at a manufacturing plant. *Computers and Operations Research*, *125*, 105044.

Daniels, R. L., Mazzola, J. B., & Shi, D. (2004). Flow shop scheduling with partial resource flexibility. *Management Science*, *50*(5), 658–669.

Danping, L., & Lee, C. K. M. (2011). A review of the research methodology for the re-entrant scheduling problem. In *International Journal of Production Research*,*49*(8), 2221–2242.

Davis, R. I., Cucu-Grosjean, L., Bertogna, M., & Burns, A. (2016). A review of priority assignment in real-time systems. *Journal of Systems Architecture,65*, 64–82.

Fekri, M., Heydari, M., & Mahdavi Mazdeh, M. (2024). Bi-objective optimization of flexible flow shop scheduling problem with multi-skilled human resources. *Engineering Applications of Artificial Intelligence*, *133*, 108094.

Fichera, S., Costa, A., & Cappadonna, F. A. (2017). Heterogeneous workers with learning ability assignment in a cellular manufacturing system. *International Journal of Industrial Engineering Computations*, *8*(4), 427–440.

Gong, G., Chiong, R., Deng, Q., Han, W., Zhang, L., Lin, W., & Li, K. (2020). Energy-efficient flexible flow shop scheduling with worker flexibility. *Expert Systems with Applications*, *141*, 112902.

Kayisoglu, B., Bekli, S., Sahin, A. S., Akyurek, G. G., Aydinli, R., Copur, S. N., & Ekinci, T. (2024). Parallel machine scheduling with re-entrant jobs with consideration of set up times. *Technology, Engineering & Mathematics (EPSTEM)*, *32*, 311–319.

Maccarthy, B. L., & Liu, J. (1993). Addressing the gap in scheduling research: A review of optimization and heuristic methods in production scheduling. *International Journal of Production Research*, *31*(1), 59–79.

Madenoglu, F. S. (2021). Solving optimization problem with particle swarm optimization: Solving hybrid flow shop scheduling problem with particle swarm optimization algorithm. In B. A. Mercangoz (Ed.), *Applying particle swarm optimization*. Cham: Springer.

Marichelvam, M. K., Geetha, M., & Tosun, O. (2020). An improved particle swarm optimization algorithm to solve hybrid flowshop scheduling problems with the effect of human factors – A case study. *Computers and Operations Research*, *114*, 104812.

Mraihi, T., Driss, O. B., & EL-Haouzi, H. B. (2024). Distributed permutation flow shop scheduling problem with worker flexibility: Review, trends and model proposition. In *Expert systems with applications* (Vol. 238). Elsevier Ltd.

Naderi, B., Zandieh, M., & Roshanaei, V. (2009). Scheduling hybrid flowshops with sequence dependent setup times to minimize makespan and maximum tardiness. *International Journal of Advanced Manufacturing Technology*, *41*(11–12), 1186–1198.

Neumann, W. P., Winkelhaus, S., Grosse, E. H., & Glock, C. H. (2021). Industry 4.0 and the human factor – A systems framework and analysis methodology for successful development. *International Journal of Production Economics*, *233*, 107992.

Ostermeier, F. F. (2020). The impact of human consideration, schedule types and product mix on scheduling objectives for unpaced mixed-model assembly lines. *International Journal of Production Research*, *58*(14), 4386–4405.

Pargar, F., Zandieh, M., Kauppila, O., & Kujala, J. (2018). The effect of worker learning on scheduling jobs in a hybrid flow shop: A bi-objective approach. *Journal of Systems Science and Systems Engineering*, *27*(3), 265–291.

Pinedo, M. L. (2022). *Scheduling: Theory, algorithms, and systems* (6th ed.). Springer.

Qin, R., Nembhard, D. A., & Barnes, W. L. (2015). Workforce flexibility in operations management. *Surveys in Operations Research and Management Science*, 20(1), 19–33

Schmidt, G. (2000). Scheduling with limited machine availability. *European Journal of Operational Research*, *121*(1), 1-15

Seidgar, H., Abedi, M., & Rad, S. T. (2015). A new mathematical model for scheduling flexible flow shop problem with learning and forgetting effects of workers. *International Journal of Industrial and Systems Engineering*, *21*(4), 534–549.

Tosun, O., Marichelvam, M. K., & Tosun, N. (2020). A literature review on hybrid flow shop scheduling. In *Int. Journal of Advanced Operations Management*,*12*(2),156-194.

Author(s) Information

Kubra Ozpacaci
Abdullah Gul University
Kayseri, Turkiye
Contact e-mail: *kubraozpcaci@gmail.com*

Seyma Bekli
Abdullah Gul University
Kayseri,Turkiye

Betul Kayisoglu
Abdullah Gul University
Kayseri, Turkiye

To cite this article:

Ozpacaci, K., Bekli, S. & Kayisoglu, B., (2025). Incorporating worker heterogeneity in flexible flow shop environment. *The Eurasia Proceedings of Science, Technology, Engineering and Mathematics (EPSTEM), 34,* 359-368.

The Eurasia Proceedings of Science, Technology, Engineering & Mathematics (EPSTEM)
ISSN: 2602-3199

The Eurasia Proceedings of Science, Technology, Engineering and Mathematics (EPSTEM), 2025

Volume 34, Pages 369-376

ICBASET 2025: International Conference on Basic Sciences, Engineering and Technology

Experimental Comparison of Planar and Parabolic Reflectors for Improved Photovoltaic Output

Benlaria Ismail
Ahmed Draya University
Laboratoire de Developpement Durable et Informatique (LDDI),

Laidi Abdallah
Ahmed Draya University
Laboratoire de Developpement Durable et Informatique (LDDI),

Kouddad Elhachemi
Telecommunication and Digital Signal Processing Laboratory

Abstract: The global demand for renewable energy sources has propelled advancements in photovoltaic (PV) technology, aiming to enhance the efficiency and cost-effectiveness of solar power generation. This study empirically examines how reflector geometry affects photovoltaic (PV) system performance by contrasting flat and parabolic reflector designs. The two reflector types were tested in a controlled outdoor area with the same ambient factors and solar irradiation. Over 30 days, important performance indicators such as power output, current-voltage characteristics, and temperature impacts were measured. Because parabolic reflectors are better at concentrating diffuse and directing sunlight, the results show that they can increase PV output by up to 28% compared to planar reflectors. Planar reflectors, on the other hand, showed less vulnerability to hotspot development and more uniformity in light distribution. The results provide useful insights for developing reflector-integrated PV systems in a variety of climatic settings by highlighting the trade-offs between operational stability and efficiency benefits.

Keywords: Photovoltaic system, Reflector geometry, Parabolic reflectors, Planar reflectors, Power output

Introduction

Photovoltaic (PV) systems play a pivotal role in the transition to renewable energy due to their numerous advantages and wide range of applications. Solar energy is a reliable and sustainable resource that contributes to reducing environmental pollution and carbon dioxide emissions (Sarayu et al., 2023). PV systems facilitate the development of zero-energy buildings and enable households to function as small-scale energy producers (Islam, 2023). Their low maintenance requirements and affordability make them particularly suitable for decentralized electricity generation in urban environments (Vlad & Lungu, 2022). Recent advancements in PV technology, including material innovations and real-time monitoring algorithms, have further enhanced system efficiency and overall performance (Schilling, 2023). Additionally, PV systems offer a viable solution for electrification in remote areas, eliminating the need for costly grid infrastructure (Farooq & Talib, 2022). As a result, PV technology plays a crucial role in sustainable development by reducing energy consumption and mitigating greenhouse gas emissions.

Enhancing PV panel efficiency remains a key research focus. Several studies have emphasized the importance of maintaining optimal surface temperatures, utilizing dissipated heat, and capturing unused infrared photons to maximize electricity generation and efficiency (Kumari et al., 2023). The adverse effects of elevated module

temperatures on power conversion efficiency have also been highlighted, with solutions such as multi-pipe copper cooling frames integrated with phase change materials (PCM) proposed to mitigate thermal losses and improve electrical performance (Saeed & Fazal, 2023). Furthermore, artificial intelligence (AI) techniques have been introduced to analyze efficiency degradation patterns and optimize the performance of PV modules and large-scale solar plants (Manimegalai et al., 2023). Additionally, the indirect benefits of rooftop PV panels have been explored, revealing their potential to reduce reliance on the electrical grid and facilitate net-zero energy consumption in buildings.

The integration of parabolic and planar reflectors has been widely investigated as a method to enhance PV panel performance. Research indicates that reflectors can significantly increase solar irradiance, short-circuit current (Isc), and maximum output power (Pmax), while having minimal impact on open-circuit voltage (Voc) (Ismail et al., 2023). Reflectors effectively capture additional solar radiation compared to non-reflector PV systems, leading to power output improvements ranging from 5% to 37%, depending on factors such as PV module type, reflector geometry, and reflector inclination angle (Tsing, 2023). Studies have also examined the optimal reflector angles to maximize power generation, demonstrating variations in efficiency based on the orientation and positioning of the reflectors (F., 2023; Pradhan et al., 2022). Overall, both planar and parabolic reflectors have proven to be effective in enhancing PV system performance (Pradhan et al., 2022).

This study presents a real-time experimental comparison of two PV panels subjected to different reflector configurations under varying solar radiation and temperature conditions. One panel is equipped with planar reflectors, while the other utilizes parabolic reflectors. To ensure cost-effectiveness and maximize solar reflection, aluminum foil was selected as the reflector material. Aluminum foil is an economical and widely available reflective material, with a thickness ranging from 0.006 mm to an upper limit of 0.2 mm, as defined by the International Organization for Standardization (ISO). The findings of this study aim to provide insights into the practical implementation of reflector-integrated PV systems to improve energy yield and overall system efficiency.

Experimental Setup

The experiment was conducted in September 2024 at the Laboratory of Sustainable Development and Informatics (LDDI) in Adrar, Algeria, located at a latitude of 31.38° and a longitude of -2.15°. Two photovoltaic (PV) modules, each with a rated power of 150 W, were used to assess the impact of planar and parabolic reflectors on PV panel performance. The modules were installed at an inclination angle of $\alpha_2 = 31.63°$ relative to the horizontal plane and oriented southward. The first PV module was mounted on a fixed metal support and equipped with two mobile planar reflectors (Belhadj et al., n.d.), allowing an inclination adjustment relative to the horizontal plane at $\alpha_1 = 25°$, as illustrated in Figure 2 (Belhadj et al., n.d.).

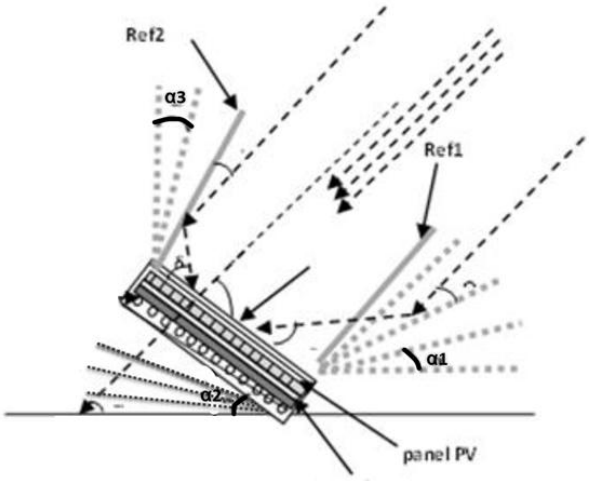

Figure 1. Diagram of PV panel with planar reflectors

The second PV module was also mounted on a fixed metal support but was paired with movable parabolic reflectors, which enabled inclination adjustments in relation to the vertical plane at $\alpha_3 = 25°$ (Benlaria et al., n.d.), as depicted in Figure 2. The reflectors were covered with aluminized foil, a cost-effective material known

for its ability to reflect diffuse solar radiation. Each reflector had a length of 1480 mm and a width of 600 mm and was installed in a movable configuration to optimize sunlight redirection.

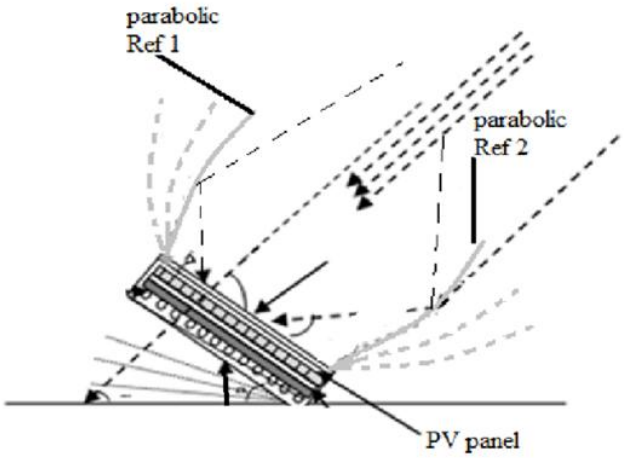

Figure 2. Diagram of PV panel with parabolic Bi-reflectors

The PV module specifications are given in Table 1 (at Standard Test Conditions 1.5 25 °C , 1000 W/m²).

Table 1. PV module specification

	Characteristic	**Value**
Current Characteristics	Maximum Current (Imax)	8.34 A
	Short Circuit Current (Ish)	8.98 A
Voltage Characteristics	Maximum Voltage (Vmax)	18 V
	Open Circuit Voltage (Voc)	22.54 V
Output Power	Maximum Power (Pmax)	150 W
	Standard Test Conditions	AM 1.5, 25°C, 1000 W/m²

The output voltage and current were measured with a multimeter under various irradiance and temperature conditions. According to the solar panel specifications that we use, with the equation we can calculate the output power of solar panel that is (Khanna et al., 2013):

$$P_{OUT} = V_{OC} \times I_{SC} \times FF$$
$$P_{OUT} = 22.54 \times 8.98 \times 0.74$$
$$P_{OUT} = 149.78W$$

we can calculate the solar panel's maximum efficiency output, which is defined by the percentage of optimum output power (Wong et al., 2010),

$$\eta = \frac{P_{OUT}}{P_{IN}} \times 100\%$$

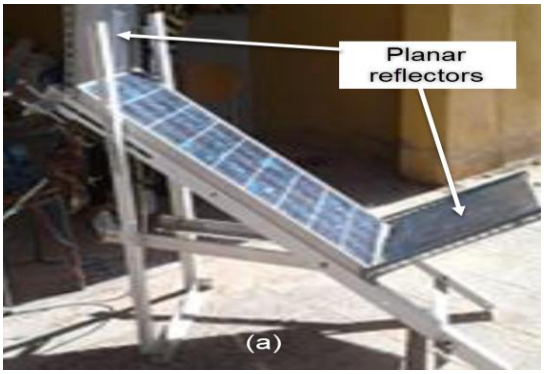

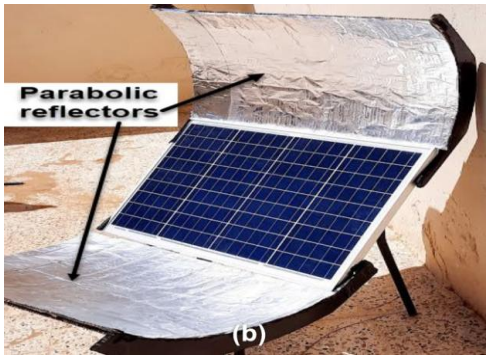

Figure 3. Experimental setup of PV modules with reflectors (a)with planar Reflectors - (b) with Parabolic Reflectors

The working principle of solar panel with optical reflectors is to obtain the maximum amount of sun radiation , Figure 3 illustrates the pv panels with optical (planar and parabolic) reflectors. Table 2 and table 3 illustrate the measurement of voltage, currant and power of the pv panels with planar and parabolic reflectors, the measurement was taken between 08:00 AM to 12:00 AM.

Table 2. Measurement results of PV panels with planar reflectors

Time	Voltage (V)	Current (A)	Power (W)	Optical Output
08:00	10	1.5	15	0.5
08:10	10.2	1.6	16.32	0.49
08:20	10.7	1.5	16.05	0.47
08:30	10.3	1.9	19.57	0.45
08:40	14	2	28	0.41
08:50	14.6	2.3	33.58	0.39
09:50	15	2.5	37.5	0.37
10:00	15.4	2.9	44.66	0.34
10:10	16	3	48	0.33
10:20	16.2	3.2	51.84	0.32
10:30	16.4	3.3	54.12	0.3
10:40	16.6	3.5	58.1	0.28

Table 3. Measurement results of PV panels with parabolic reflectors

Time	Voltage (V)	Current (A)	Power (W)	Optical Output
08:00	10	1.5	15	0.5
08:10	10.2	1.6	16.32	0.49
08:20	10.7	1.5	16.05	0.47
08:30	10.3	1.9	19.57	0.45
08:40	14	2	28	0.41
08:50	14.6	2.3	33.58	0.39
09:50	15	2.5	37.5	0.37
10:00	15.4	2.9	44.66	0.34
10:10	16	3	48	0.33
10:20	16.2	3.2	51.84	0.32
10:30	16.4	3.3	54.12	0.3
10:40	16.6	3.5	58.1	0.28

Results and Discussion

We conducted a comparative analysis of the experimental results by evaluating key performance parameters, including short-circuit current (Isc), open-circuit voltage (Voc), output power, and surface temperature of the PV modules equipped with planar and parabolic reflectors. The test results are presented in the corresponding figures.

For temperature measurements, data were recorded between 08:00 AM and 03:00 PM to assess the impact of temperature variations on PV panel performance. This time range was selected to capture the effects of solar irradiance and ambient temperature fluctuations throughout the peak sunlight hours.

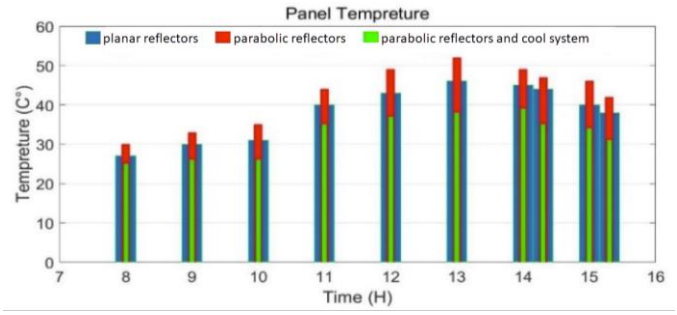

Figure 4. Solar panels temperature

The use of parabolic reflectors resulted in a steady increase in the surface temperature of the PV module, rising from 30°C at 08:00 AM to 52°C at 01:00 PM. In contrast, the surface temperature of the PV module equipped with planar reflectors increased from 27°C at 08:00 AM to 45°C at 01:00 PM, as illustrated in Figure 4. This difference indicates that parabolic reflectors, due to their enhanced concentration of sunlight, lead to higher thermal accumulation on the PV surface compared to planar reflectors.

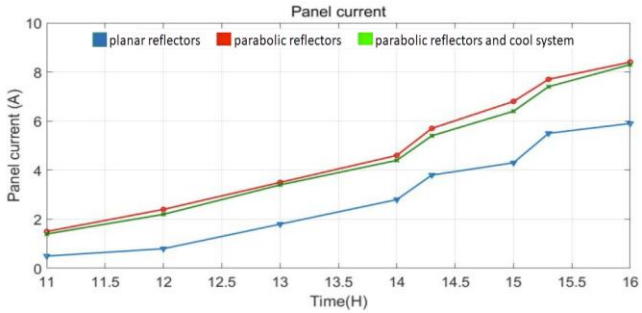

Figure 5. Panels output current.

Figure 5 presents the comparison of PV module current measurements between the panel equipped with parabolic reflectors and the panel with planar reflectors. The results indicate that the current PV panel with planar reflectors remained within the range of 0.5 A to 5.5 A, whereas the PV panel with parabolic reflectors exhibited a higher current range of 1.5 A to 8 A. This increase in current for the panel with parabolic reflectors can be attributed to the enhanced solar irradiation concentration provided by the reflector geometry, which effectively directs more sunlight onto the PV surface, thereby improving electrical performance.

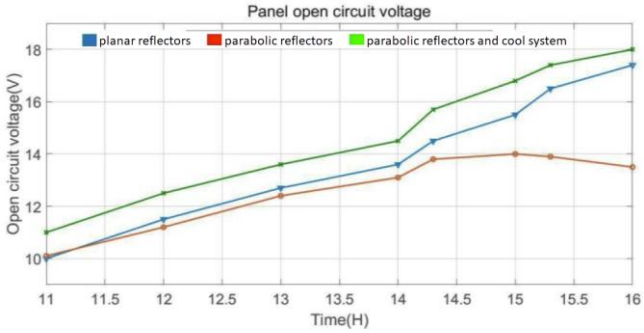

Figure 6. Panels Voc open circuit voltage

Figure 6 illustrates the open-circuit voltage (Voc) variation of the PV modules equipped with parabolic and planar reflectors. The results show that the Voc of the PV module with parabolic reflectors remained within the range of 10 V to 13 V, whereas the Voc of the PV module with planar reflectors was maintained between 11 V and 18 V. This reduction in Voc for the parabolic reflector configuration is primarily due to the higher surface temperature of the PV module, which negatively impacts the voltage output as temperature increases.

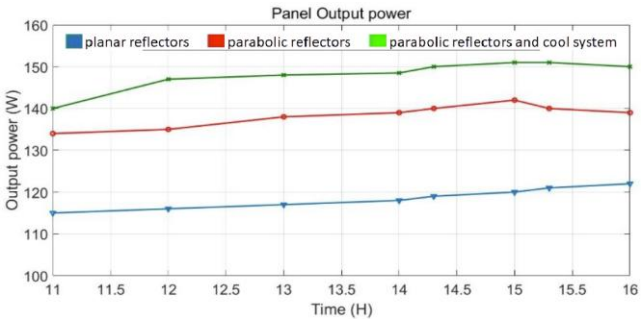

Figure 7. Panels output power

Figure 7 presents the output power measurements of PV panels equipped with planar and parabolic reflectors. The results indicate that the output power of the PV panel with planar reflectors ranged between 105 W and 117 W, whereas the PV panel with parabolic reflectors exhibited a higher output power range of 125 W to 139 W. This increase in power output for the parabolic reflector configuration is primarily attributed to the higher current generation, resulting from the enhanced solar irradiation concentration provided by the reflectors.

Conclusion

This study investigated the impact of solar irradiation enhancement on PV system performance through the integration of planar and parabolic reflectors. The experimental findings demonstrate that the use of reflectors significantly increases the output current and power of PV panels by redirecting additional sunlight onto the module surface. However, this technique also results in a temperature rise, with the parabolic reflector configuration causing surface temperatures to reach up to 55°C, which may negatively affect module efficiency and longevity.

The results indicate that parabolic reflectors outperform planar reflectors in enhancing PV panel output performance, as they enable a greater concentration of solar irradiation, leading to a higher increase in output power. Nevertheless, this advantage comes with a major drawback, as the excessive heat accumulation on the PV module surface can lead to thermal stress and potential panel degradation over time. To address this limitation, the integration of cooling systems is recommended to regulate surface temperature and maintain optimal operating conditions.

Overall, the use of reflectors presents a cost-effective and practical solution for improving PV system efficiency, particularly in high solar radiation regions. Further research is needed to explore hybrid reflector-cooling systems to mitigate thermal effects while maximizing energy yield.

Recommendations

To improve the performance of PV systems with reflectors, it is recommended to integrate cooling solutions, especially with parabolic reflectors, to reduce the risk of overheating and damage. Future studies should focus on optimizing reflector angles and materials to balance efficiency and thermal impact. The use of hybrid systems combining reflectors with smart control and monitoring can enhance performance. Finally, an economic analysis is suggested to evaluate the cost-effectiveness of using reflectors, particularly in hot climates.

Scientific Ethics Declaration

* The authors declare that the scientific ethical and legal responsibility of this article published in EPSTEM Journal belongs to the authors.

Conflict of Interest

* The authors declare that they have no conflicts of interest

Funding

* The authors received no financial support for the research, authorship, and/or publication of this article.

Acknowledgements or Notes

* The authors wish to acknowledge that this work was presented as a poster presentation at the International Conference on Basic Sciences, Engineering and Technology (www.icbaset.net) held in Trabzon, Türkiye. They also extend their gratitude to the Sustainable Development and IT Laboratory (LDDI) at Ahmed Draya University, Adrar, for providing the facilities and support necessary to conduct the experiments for this study.

References

Belhadj, M., Boufeldja, K., & Nasri, A. (2010). Estimation de la puissance maximale produite par un générateur photovoltaïque [Estimation of the maximum power produced by a photovoltaic generator]. *Revue des Énergies Renouvelables, 13*(2), 257–264.

Belhadj, M., Boufeldja, K., Nasri, A., & Benlaria, I. (2019). Design and modeling of optical reflectors for a PV panel adapted by MPPT control. *Indonesian Journal of Electrical Engineering and Computer Science, 16*(2), 653-660.

Benlaria, I., Belhadj, M., Othmane, A., & Sabouni, E. (2021). An experimental study of PV/T system using parabolic reflectors and heat exchanger]. *Indonesian Journal of Electrical Engineering and Computer Science, 24*(3), 1297-1306.

Farooq, I., & Talib, T. (2022). PV system multiple source single inverter. *International Journal of Innovative Research in Computer Science & Technology, 10*(4), 62–65. https://doi.org/10.55524/ijircst.2022.10.4.13

Islam, M. R. (Ed.). (2023). *Solar photovoltaic energy system*. IntechOpen. https://doi.org/10.5772/intechopen.108958

Ismail, T., Aminu, F., Alhassan, A. Y. J., Abdullahi, B., Aliyu, A., & Tsoho, A. (2023). Performance evaluation of reflectors and cooling system on photovoltaic system in Kano Northwest Nigeria. *FUDMA Journal of Sciences, 7*(3), 290–296. https://doi.org/10.33003/fjs-2023-0703-1776

Khan, M. A., Ko, B., Nyari, E. A., Park, S. E., & Kim, H.-J. (2017). Performance evaluation of photovoltaic solar system with different cooling methods and a bi-reflector PV system (BRPVS): An experimental study and comparative analysis. *Energies, 10*(6), Article 826. https://doi.org/10.3390/en10060826

Khanna, A., Mueller, T., Stangl, R. A., Hoex, B., Basu, P. K., & Aberle, A. G. (2013). A fill factor loss analysis method for silicon wafer solar cells. *IEEE Journal of Photovoltaics, 3*(4), 1170–1177. https://doi.org/10.1109/JPHOTOV.2013.2270348

Kumari, S., Bhende, A., Pandit, A. B., & Rayalu, S. (2023). Efficiency enhancement of photovoltaic panel by heat harvesting techniques. *Energy for Sustainable Development, 72,* 333–353. https://doi.org/10.1016/j.esd.2023.02.007

Manimegalai, D., Agastiya, S. W., Chandrasekhar, P., & Sivakumar, S. S. (2023, March). Efficiency enhancement of solar panel using IoT and artificial intelligence [Paper presentation]. *2023 International Conference on System, Computation, Automation and Networking (ICSSIT),* Puducherry, India. https://doi.org/10.1109/ICSSIT55814.2023.10060893

Pradhan, A., Panda, B., Nanda, L., Jena, C., & Sahoo, S. S. (2022, April). Analysis of various types of reflectors on the performance of PV panel [Paper presentation]. *2022 International Conference on Advancements in Technology (ICONAT),* Nashik, India. https://doi.org/10.1109/ICONAT53423.2022.9725825

Saeed, R., & Fazal, M. A. (2023). Efficiency enhancement of photovoltaic solar system by integrating multi-pipe copper frame filled with ZnO-doped phase change material. *MRS Energy & Sustainability, 10, Article e63*. https://doi.org/10.1557/s43581-023-00063-1

Sarayu, V., Vunnam, M., Vanithasri, & Rao, A. R. (2023). An outline of solar photovoltaic systems impact on environment. *Bulletin of Electrical Engineering and Informatics, 12*(5), 2835–2843. https://doi.org/10.11591/eei.v12i5.5584

Schilling, H. (2023). Chasing the sun: A journey in monitoring solar panels. *The Hague University of Applied Sciences*. https://doi.org/10.33540/1855

Tsing, A. L. (2023). Application of reflectors for improving the output performance of solar photovoltaic (PV) modules. In S. V. G. V. A. Prasad, M. V. S. S. S. M. Prasad, P. B. G. S. N. Murthy, & S. S. Rao (Eds.), *Advances in energy research*, Vol. 3 (pp. 209–222). Springer. https://doi.org/10.1007/978-3-031-26636-2_19

Vlad, C., & Lungu, P. C. (2022). Considerations regarding PV systems. *Annals of "Dunarea de Jos" University of Galati. Fascicle II Mathematics, Physics, Theoretical Mechanics, 45*(2), 103–108. https://doi.org/10.35219/ann-ugal-math-phys-mec.2022.2.14

Wong, S. M., Yu, H. Y., Li, J. S., Zhang, G., Lo, P. G. Q., & Kwong, D. L. (2010). Design high-efficiency si nanopillar-array-textured thin-film solar cell. *IEEE Electron Device Letters, 31(*4), 335–337. https://doi.org/10.1109/LED.2010.2040062

Author(s) Information

Benlaria Ismail
Ahmed Draya University - Adrar, Algeria.
Laboratoire de Développement Durable et Informatique (LDDI), Algeria
Contact: benlariaismail@univ-adrar.edu.dz

Laidi Abdallah
Ahmed Draya University - Adrar, Algeria.
Laboratoire de Développement Durable et Informatique (LDDI), Algeria

Kouddad Elhachemi
University of Sidi Bel Abbes
Telecommunication and Digital Signal Processing Laboratory, Algeria

To cite this article:

Ismail, B., Abdallah, L. & Elhachemi K. (2025). Experimental comparison of planar and parabolic reflectors for improved photovoltaic output. *The Eurasia Proceedings of Science, Technology, Engineering and Mathematics (EPSTEM), 34,* 369-376.

The Eurasia Proceedings of Science, Technology, Engineering & Mathematics (EPSTEM)
ISSN: 2602-3199

The Eurasia Proceedings of Science, Technology, Engineering and Mathematics (EPSTEM), 2025

Volume 34, Pages 377-387

ICBASET 2025: International Conference on Basic Sciences, Engineering and Technology

Synthesis of Biocomposite of Kappa Carrageenan and Polyvinyl Alcohol for Bioplastic

Nonni Soraya Sambudi
Universitas Pertamina

Chaterine Lovy Sarah Nova
Universitas Pertamina

Fitri Ayu Radini
National Research and Inovation Agency

Abstract: This research investigates the effect of incorporating kappa carrageenan and chitosan into biocomposites composed made from kappa carrageenan and polyvinyl alcohol, crosslinked with glutaraldehyde. The objective is to characterize the resulting biocomposites films and determine the optimal formulation based on mechanical properties and swelling behavior. The film were fabricated using the solution casting method, with varying concentrations of kappa carrageenan (3%, 4%, and 5% w/v) and chitosan (1.32%, 1.76%, and 2.2% w/v). Characterization was performed using Fourier Transform Infrared Spectroscopy (FTIR), water absorption testing, tensile strength analysis, and elongation measurements. The results showed that the addition of kappa carrageenan improved water resistance and tensile strength. Most biocomposite film samples met the National Standard for tensile strength in bioplastic applications, except for the formulations containing 3% kappa carrageenan with 1.76% chitosan and 5% kappa carrageenan with 2.2% chitosan, which did not meet the standard.

Keywords: Biocomposites, Kappa carrageenan, Solution casting, Chitosan

Introduction

Plastic is a synthetic material produced through the polymerization of various chemical compounds, typically derived from petroleum, natural gas, or other natural resources. Its widespread use is attributed to favorable properties such as strength, durability, formability, and relatively low production costs. Commonly used plastics include polyethylene, polypropylene (PP), polyvinyl chloride (PVC), polystyrene, and polyethylene terephthalate (PET). In Indonesia, the average annual plastic consumption per person is approximately 22.5 kg, which is lower compared to neighboring countries like Thailand, Malaysia, and Singapore, where consumption exceeds 60 kg per person. Most plastics are utilized in the packaging industry, particularly for food, beverages, and household products. According to the Directorate of Downstream Chemical and Pharmaceutical Industry, Indonesia produces 2.31 million tons of plastic annually, while national demand reaches 5.63 million tons (Ministry of Environment and Forestry, 2020).

Plastic waste, particularly from non-biodegradable materials, poses a significant environmental challenge. Some plastics take more than 400 years to decompose, breaking down into persistent microplastics. Indonesia generates an estimated 3.2 million tons of unmanaged plastic waste annually (Jambeck et al., 2015). This leads to soil and water contamination, with microplastics disrupting ecosystems and reducing soil fertility. One approach to managing this issue is through open-air waste processing facilities, such as the Integrated Waste Treatment Site (TPST) in Bantar Gebang, which processes up to 7,000 tons of waste per day. This samples from

this facility have been found to contain 6,061 microplastic particles per kilogram, underscoring the environmental urgency of reducing plastic pollution (Tun et al., 2022).

In response to these concerns, research has increasingly focused on developing biodegradable alternatives, such as bioplastics. Biocomposites—combinations of two or more natural materials—offer improved functional properties by leveraging the synergistic strengths of their components. In this study, PVA is used as the matrix polymer due to its thermoplastic behavior and hydrophilic characteristics resulting from a high content of hydroxyl groups. Kappa carrageenan is incorporated to enhance mechanical strength and water interaction properties. Chitosan is added as a natural filler with antimicrobial activity, while glutaraldehyde is used as a crosslinking agent to improve structural integrity by facilitating hydrogen bonding between the polymers. This combination aims to produce a biodegradable plastic film with balanced mechanical strength, water resistance, and environmental compatibility.

Methods

This research was conducted through several key stages, including the determination of kappa carrageenan and chitosan concentration variations, film preparation via solution casting, and comprehensive film characterization. The characterization involved Fourier Transform Infrared Spectroscopy (FTIR), swelling behavior analysis, mechanical strength testing (tensile strength and elongation), and a biodegradability assessment in soil.

Variations of Kappa Carrageenan and Chitosan Concentrations

The compositions of kappa carrageenan and chitosan used in the biocomposite films are listed in Table 1. Polyvinyl alcohol (PVA) was maintained at a constant concentration of 11% (w/v) across all samples, while the concentrations of kappa carrageenan and chitosan were varied. A 0.5% (w/v) glutaraldehyde solution was included as a crosslinking agent in selected formulations.

Table 1. Variation of concentration used in biocomposite film

Code	Kappa Carrageenan (%w/v)	PVA (%w/v)	Chitosan (%w/v)	Glutaraldehyde (%w/v)
A	-	11	1.32	
B	-	11	1.76	0.5
C	-	11	2.2	
D	3	11	1.32	
E	3	11	1.76	0.5
F	3	11	2.2	
G	4	11	1.32	
H	4	11	1.76	0.5
I	4	11	2.2	
J	5	11	1.32	
K	5	11	1.76	0.5
L	5	11	2.2	

Biocomposite Film Preparation via Solution Casting

To prepare the biocomposite film, 3 grams of PVA powder were dissolved in 27.3 mL of distilled water and stirred at 90°C for 1 hour. Chitosan (0.3 grams, 0.4 grams, and 0.5 grams) was separately dissolved in 22.7 mL of a 2% (v/v) acetic acid solution at room temperature for 2 hours. The PVA and chitosan solutions were then combined and stirred at 60°C for 1 hour. A 0.5% Glutaraldehyde (GA) solution was prepared by diluting 0.4 mL of a 25% (w/v) GA solution with 19.6 mL of distilled water and stirred at room temperature for 1 hour. This GA solution was added to the PVA-chitosan mixture and stirred at room temperature.

Kappa Carrageenan (KC) powder was sieved using a 100-mesh sieve. Weighed amounth (3 grams, 4 grams, and 5 grams) of KC powder were dissolved in 100 mL of distilled water at room temperature for 1 hour. Then, the KC solution was heated to 50°C to dissolve the KC completely dissolved. The KC solution was mixed with the

PVA/Chitosan/Glutaraldehyde solution at 50°C for 1.5 hour to obtain a homogeneous blend. The PVA/Chitosan/GA/KC solution (25 mL) was poured into petri dishes (100 mm diameter, 15 mm in height) and dried in an oven at 60°C for 12–24 hours to form biocomposite films.

FT-IR Characterization Test

The Fourier Transform Infrared (FTIR) technique is used as one of the characterizations for testing Kappa Carrageenan biocomposite samples with the aim of qualitatively identifying functional groups within the synthesized samples. FTIR measures the absorption of infrared radiation by each molecule in the sample, resulting in an infrared spectrum pattern that can be analysed based on the types of chemical bonds formed between atoms at unique vibrational frequencies. The FTIR instrument used for this testing is the Thermo Scientific Nicolet iS5 FTIR Spectrometer, employing the Attenuated Total Reflectance (ATR) method. A sample mass of 0.1 grams of the biocomposite film is prepared. This testing instrument is conducted using equipment located in the Integrated Chemistry Laboratory at the University of Pertamina.

Swelling Test

The swelling test on the biocomposite film samples is conducted using distilled water with a neutral pH of 7. Each film sample was cut into strips with dimensions of 3 cm × 1 cm. The initial dry mass (W_0) of each sample was measured prior to immersion. The samples were then placed in 25 mL of distilled water within sealed glass bottles and soaked for 7 hours. The swollen samples were removed at hourly intervals, blotted to remove surface water, and weighed to obtain the wet mass (W_s). The swelling degree was calculated using the following formula: (Costa-Júniora et al., 2009)

$$Swelling\ Degree\ (\%) = \frac{W_s - W_d}{W_d} \times 100\% \qquad (2.1)$$

Where:
Swelling Degree = Percentage of swelling film
Ws = mass of the sample at a specific time when it has swollen
Wd = mass of the sample in its dry or unswollen condition

Mechanical Strength Test

The Mechanical strength test is conducted to analyse the mechanical strength of the polymer biocomposite in response to external forces or loads applied. Tensile strength, strain at break, and Young's modulus are tested using the Universal Testing Machine AGS-G instrument, which is performed at the National Research and Innovation Agency (BRIN) for Plastics Tensile Test. The testing is carried out once and operates at a crosshead speed of 50 mm/min, a relative humidity of 54.40%, a temperature of 22.7 °C, and a gripped length of 25 mm. The film samples adhere to ASTM D882 standards. This testing method is used to determine how thin plastic sheets or films (with a thickness of less than 1.0 mm) can be stretched. The width should be at least 5.0 mm but not more than 25.4 mm, with a length that is 8 times longer than the width of the sample. Therefore, the sample size for this test is 8 cm in length and 1 cm in width (Markets, 2017).

Results and Discussion

Morphology

In this study, the polymers Polyvinyl Alcohol (PVA) and Kappa Carrageenan (KC) functioned as the primary matrices for biocomposite film synthesis using the solution casting method. Polyvinyl Alcohol (PVA) is a polymer material that acts as the continuous phase, or matrix, in the composite. PVA is hydrophilic, meaning it is water-absorbent, but it has good flexibility due to its high degree of hydrolysis, indicating a high content of O-H groups (Soeda, Yamagata, & Ishikawa, 2009). Kappa Carrageenan (KC) acts as a matrix to improve the hydrophilic properties of PVA and enhance the stiffness of the film (Ramadas, Rhim, & Roy, 2024). Chitosan was incorporated as a natural filler to improve antimicrobial properties and structural strength (Ke et al., 2021). Glutaraldehyde (GA) was employed as a crosslinking agent to strengthen intermolecular interactions between

PVA, KC, and chitosan (Migneault, Dartiguenave, Bertrand, & Waldron, 2004). Acetic acid (2% v/v) was used to dissolve chitosan, while distilled water served as the solvent for PVA, KC, and GA. The main experimental variables were the concentrations of Kappa Carageenan and chitosan.

The synthesis began with the mixing of 11% (w/v) solution of PVA with a 1.32% (w/v) chitosan solution, stirred at 60°C for 1 hour using a magnetic stirrer until a homogeneous mixture was obtained. Hydrogen bonding occurred between the hydroxyl groups of PVA and the functional groups of chitosan show in Fogure 1. The mixture was cast into petri dishes and dried in an oven at 60°C for 8 hours to form clear, elastic films with smooth surfaces.

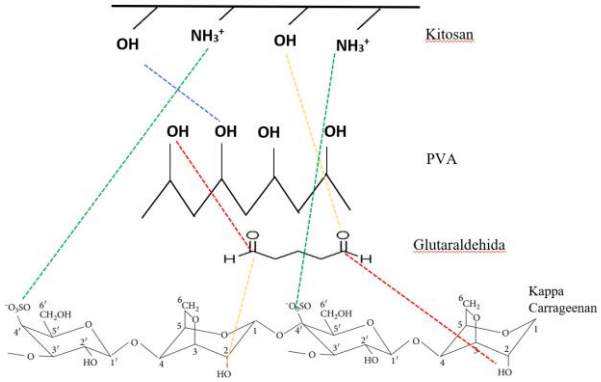

Figure 1. The functional group interactions between PVA kappa carrageenan, chitosan and GA

Subsequently, a 0.5% v/v glutaraldehyde (GA) solution was added to the PVA/chitosan mixture at room temperature and stirred for 1 hour. The GA served as a crosslinking agent to strengthen the bonds between the Kappa Carrageenan matrix and the PVA matrix, as well as the chitosan filler. A crosslinking agent is a chemical compound with two or more active functional groups that can crosslink two or more different chemical compounds, altering the chemical and physical properties of polymer networks. In this case, the hydroxyl groups in glutaraldehyde crosslink with the hydroxyl groups in PVA, Kappa Carrageenan, and chitosan, as depicted in Figure 1 below. The crosslinking agent GA forms a more complex polymer structure, thereby enhancing the mechanical properties of the film sample (Distantina, Noviyanti, Sutriyani, Fadilah, & Kaavessina, 2017; Li et al., 2020; Rojas, 2015). The drying process for the biocomposite film samples from the mixture of PVA/Chitosan/GA/KC is carried out at 60°C for a duration of 8-24 hours until the samples have a dry texture and can be peeled off. Based on observations, biocomposite film samples with an increased composition of Kappa Carrageenan exhibit a stiffer, harder, and yellowish-white appearance compared to control film samples with PVA and chitosan composition, which are flexible and clear in colour.

(a) (b)

Figure 2. The synthesis results of biocomposite film samples (a) PVA/chitosan (b) KC/PVA/chitosan/GA

Functional Groups Analysis

The kappa carrageenan biocomposite samples were analysed using FTIR spectra to determine the structural changes in the biocomposite film before and after the addition of the crosslinking agent. Figure 3 shows the FTIR spectra of the control film samples with the matrix composition of Polyvinyl Alcohol and the chitosan filler, compared to the film samples filled with Kappa Carrageenan matrix and the crosslinking agent

glutaraldehyde. The FTIR spectrum of the control sample containing PVA/Chitosan displays strong O-H stretch functional groups that broaden in the range between 3550-3200 cm^{-1} and N-H stretch functional groups for intramolecular and intermolecular structures of hydroxyl and primary amine groups in Polyvinyl Alcohol compounds. The FTIR spectrum of the PVA/Chitosan blend at a peak around 1640 cm^{-1} exhibits symmetric deformation of N-H bending functional groups as NH_3^+ groups, generated from the ionization of primary amino groups in an acidic medium. Furthermore, in the range of 1421-1440 cm^{-1}, O-H bend functional groups are identified, characteristic of carboxylic acid functional groups. Therefore, it can be concluded that Polyvinyl Alcohol reacts and combines with chitosan (Abdeen, 2011; Chopra et al., 2022; El-Hefian, Nasef, & Yahaya, 2010).

At peaks around 2850-3000 cm^{-1}, C-H stretch functional groups in aldehydes are shown, and the doublet absorption is identified to alkyl chains. At peaks around 1210-1260 cm cm^{-1}, sulphate S=O functional groups are present, and in the range of 1005-1080 cm^{-1}, glycosidic bonds are identified, which originate from the content of Kappa Carrageenan. The appearance of other peaks, specifically at 843-805 cm^{-1}, is characteristic of 3,6-anhydrogalactose-2-sulfate, a galactose unit bound by glycoside and a distinctive feature of Kappa Carrageenan. In Kappa Carrageenan, 3,6-anhydrogalactose-2-sulfate is a type of galactose unit that contains sulphate groups ($SO3^-$) and plays an essential role in forming a three-dimensional structure and a strong gel when this compound is hydrated (Hilliou et al., 2006; Mendoza et al., 2006; Pereira et al., 2009; Webber et al., 2012).

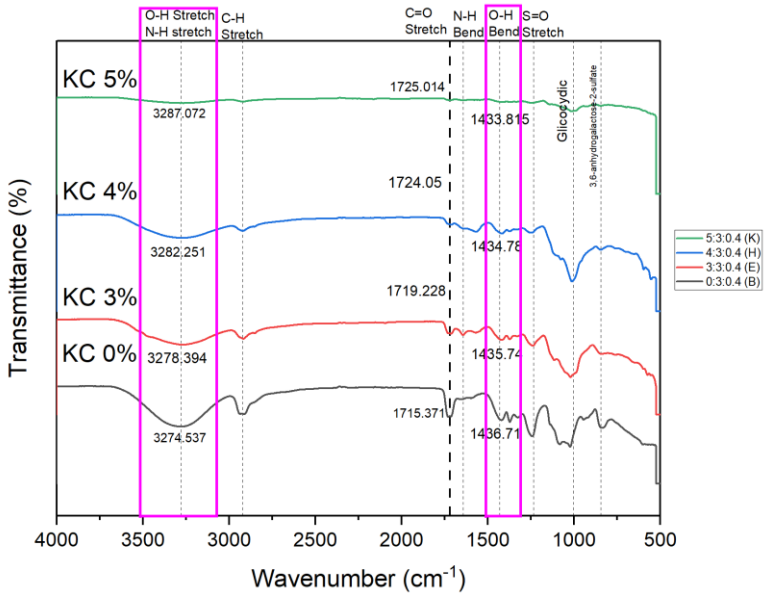

Figure 3. FTIR spectra of the kappa carrageenan addition in biocomposite PVA and chitosan

In the spectrum of samples containing Kappa Carrageenan (KC) at 3-5% w/v, structural changes in the biocomposite due to the addition of the crosslinking agent Glutaraldehyde (GA) are observed. Crosslinking reactions between glutaraldehyde, Kappa Carrageenan, and PVA occur through interactions of hydroxyl (OH) groups in each compound, as shown in Figure 3. Interactions between these compounds increase the intensity of O-H group absorption in the range of 3500-3200 cm^{-1}. However, based on the FTIR results, a reduction in the intensity of the O-H stretch peak is observed at compositions of Kappa Carrageenan 0%, 3%, 4%, and 5% in the absorption range of 3274.5 cm^{-1}, 3278.4 cm^{-1}, 3282.2 cm^{-1}, and 3287.1 cm^{-1}, respectively. On the other hand, in the fingerprint region for free hydroxyl (OH) groups, the intensity of the peak is reduced in compositions of Kappa Carrageenan 0%, 3%, 4%, and 5% in the absorption range of 1436.7 cm^{-1}, 1435.7 cm^{-1}, 1434.7 cm^{-1}, and 1433.7 cm^{-1}. Therefore, it can be concluded that the hydroxyl groups from Kappa Carrageenan, PVA, and chitosan are bound to the hydroxyl (OH) groups. This is also consistent with research conducted by (Tan et al., 2021), where the hydroxyl groups of PVA at 3251 cm^{-1} weaken after modification with Chitosan, Nanocrystalline cellulose, and tannic acid, which simultaneously interact with free hydroxyl (-OH) groups in the absorption range of 1411-1500 cm^{-1}, resulting in reduced peak intensity.

In the study by Distantina et al. (2017), Glutaraldehyde crosslinks OH groups from PVA with OH groups from Kappa Carrageenan through aldehyde groups (H-CH=O), leading to the appearance of peaks for new functional groups resulting from chemical crosslinking (CH_3CO^-). However, based on the FTIR results in Figure 3, the new functional groups formed due to the crosslinking agent glutaraldehyde cannot be identified. Therefore, the

addition of Kappa Carrageenan and chitosan to Polyvinyl Alcohol with the crosslinking agent glutaraldehyde results from physical mixing by combining functional groups from each component.

Swelling

Swelling Test in Kappa Carrageenan biocomposite film to analyse the interactions and absorption capacity between the film and a specific liquid or solvent. In this study, the film samples were immersed in distilled water at pH 7 for 7 hours, and the mass of the film samples was regularly checked every hour. Figure 4 and Figure 5 shows the results of water absorption tests on biocomposite film samples with variations in the addition of chitosan composition and Kappa Carrageenan composition.

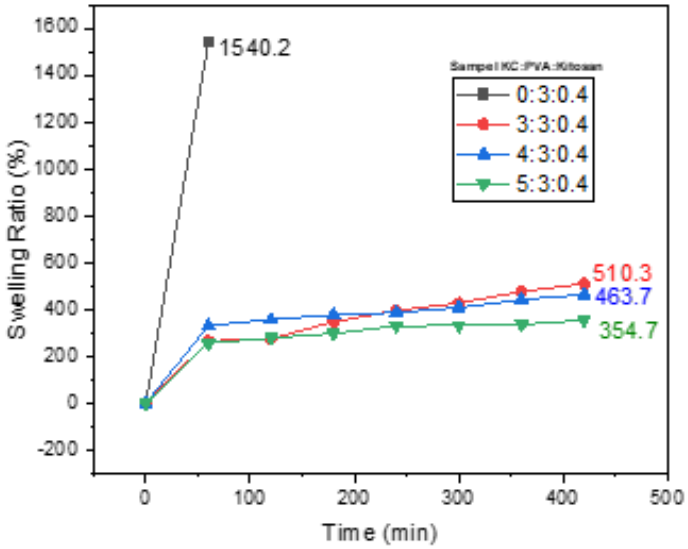

Figure 4. Swelling degree result after addition of kappa carrageenan in biocomposite film composition

Based on the graphs in Figure 4 the swelling degree of biocomposite films containing varying concentrations of kappa carrageenan. The control sample (PVA/chitosan, 0% KC) showed the highest swelling percentage, reaching 1540.2% within the first hour. All samples without KC fully disintegrated in water after 1 hour of immersion. This behavior is attributed to the hydrophilic nature of PVA, which possesses abundant free hydroxyl groups that readily form hydrogen bonds with water molecules. This is also consistent with FTIR results, where the control film exhibited a broad O–H peak between 3500–3200 cm^{-1}, indicating a high concentration of free hydroxyl groups.In contrast, films containing KC exhibited significantly lower swelling percentages and maintained their structural integrity throughout the test duration. This reduction in water absorption is due to the formation of hydrogen bonds between the hydroxyl groups of KC and PVA, which were further strengthened by glutaraldehyde crosslinking. The resulting crosslinked network limited water penetration and created a more compact film matrix.

Figure 5 shows the swelling behavior of samples with a constant KC concentration (5% w/v) and varying chitosan contents. The sample with 0.3% chitosan had the highest swelling among the three, while increasing chitosan to 0.4% and 0.5% reduced the swelling degree. This trend is explained by the additional hydrogen bonding introduced by chitosan, which further reinforces the network and restricts water diffusion. Furthermore, FTIR data support this conclusion, as the intensity of free O–H bending vibrations around 1430–1440 cm^{-1} decreased with the addition of KC and chitosan, indicating reduced availability of free hydroxyl groups and enhanced intermolecular bonding (Shahbazi et al., 2016). These findings suggest that both KC and chitosan play crucial roles in controlling water absorption. KC contributes to structural rigidity and reduced swelling, while chitosan enhances internal cohesion through hydrogen bonding, leading to improved film stability in aqueous environments

Furthermore, Kappa Carrageenan, as a matrix with hydroxyl groups, will interact more with the hydroxyl groups of PVA through crosslinking with glutaraldehyde, reducing the interaction between PVA polar groups and water molecules. The crosslinking between PVA and Kappa Carrageenan chains with the crosslinking agent glutaraldehyde results in a relatively rigid structure that restricts water's access to hydrophilic groups. This is also visually evident after 7 hours of swelling, samples with KC content swelled but still retained their film strip

shape. Additionally, the reduction in swelling percentage is also due to chitosan's role as a filler in the Kappa Carrageenan biocomposite, creating full hydrogen bonds within its constituent components, reducing the penetration of water molecules into the biocomposite film. This is also identified in the FTIR results with the addition of Kappa Carrageenan, resulting in a reduction in the peak intensity of free O-H groups in the range between 1430-1440 cm^{-1}, indicating the formation of bonds between the free hydroxyl (-OH) groups of PVA and the hydroxyl groups in Kappa Carrageenan and chitosan with the assistance of the aldehyde groups in glutaraldehyde as the crosslinker agent.

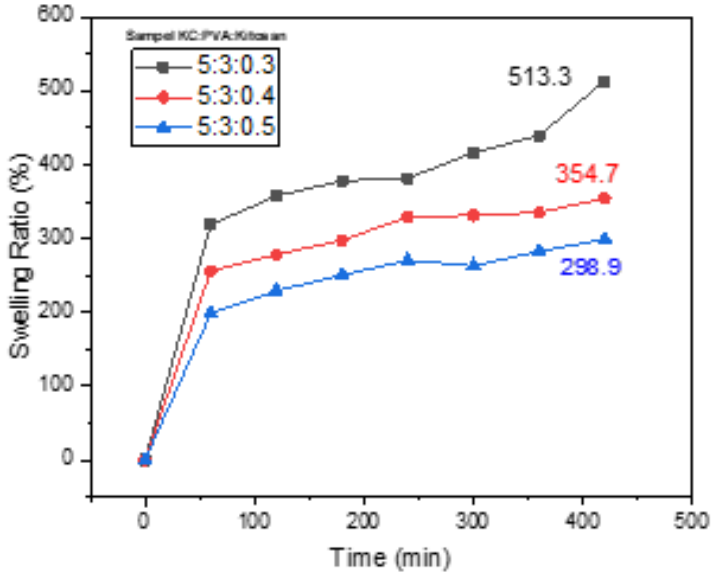

Figure 5. Swelling degree result after addition of chitosan in biocomposite film composition

Mechanical Strength

The mechanical strength test of Kappa Carrageenan biocomposite film samples includes tensile strength, elongation at break, and Young's modulus. Figure 6 and figure 7 shows the differences in material tensile strength and elongation values in samples with variations in chitosan composition and Kappa Carrageenan composition.

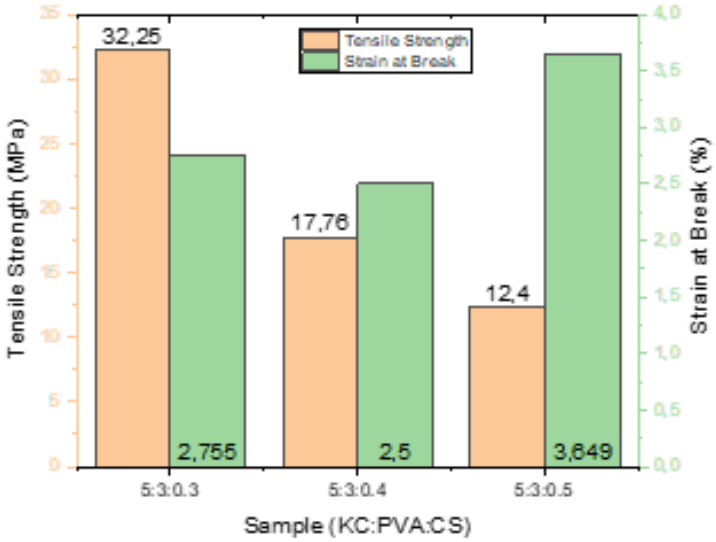

Figure 6. Tensile strength and elongation (strain at break) result after addition of chitosan in biocomposite film composition

Based on the graphs in Figure 6, the addition of chitosan composition to Kappa Carrageenan biocomposite film samples will increase the Strain at Break, which is the maximum length value of the film sample when subjected

to a load before breaking during the tensile test. The test results indicate that flexibility increases with the addition of chitosan. This is contrary to the intended purpose of adding chitosan to the biocomposite film as a filler to improve tensile strength and stiffness in the blending process of the Polyvinyl Alcohol matrix with the natural Kappa Carrageenan matrix. This is also consistent with the results of research conducted by (Shahbazi, Rajabzadeh, Rafe, Ettelaie, & Ahmadi, 2017), where the addition of Kappa Carrageenan and chitosan increased the stiffness of the blended film due to hydrogen bonding between the hydroxyl groups of PVA, Kappa Carrageenan, and chitosan. The inconsistency between tensile strength and elongation test results in this study is influenced by excessive crosslinking between the hydroxyl groups of each component. Excess chitosan molecules will localize in different phases than the polymer phase. Chitosan molecules that are not crosslinked between glutaraldehyde, Kappa Carrageenan, and PVA will inhibit the formation of intermolecular bonds in the polymer due to the steric hindrance of free hydroxyl groups of chitosan with the hydroxyl groups of PVA, Kappa Carrageenan, and interacting glutaraldehyde. This is the cause of decreased bond strength and increased elongation percentage (Alias & Ismail, 2020; Maghfiroh et al., 2013).

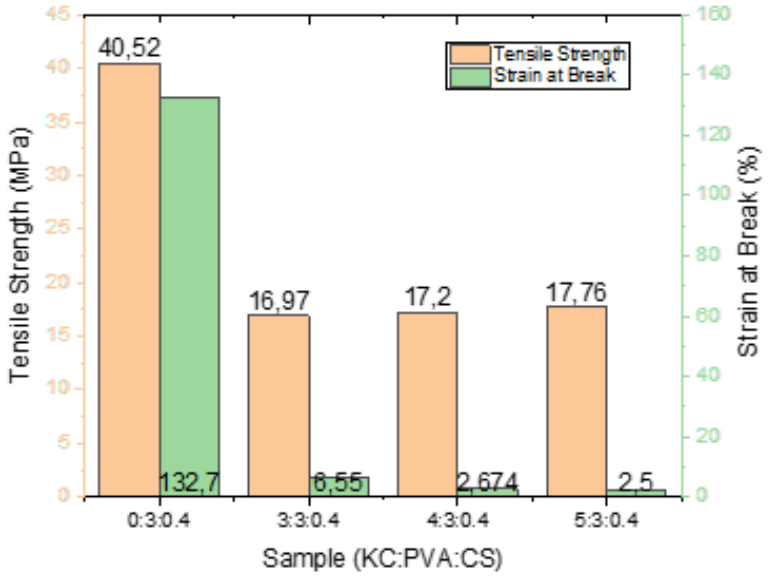

Figure 7. Tensile strength and elongation (strain at break) result after addition of kappa carageenan in biocomposite film composition

Based on figure 7, the effect of increasing KC concentrations in films with a fixed chitosan level (0.4% w/v). The addition of KC generally led to improved tensile strength, with a peak value of 40.52 MPa observed in the sample without KC (0% KC), followed by a moderate decrease in strength as the KC content increased to 5%. However, a notable decline in elongation at break was observed across all samples containing KC, with values falling below 10%. This trend suggests that the presence of KC contributes to the stiffness and rigidity of the films due to its ability to form dense hydrogen-bonded networks with PVA, enhanced further by crosslinking with glutaraldehyde. The reduced flexibility is attributed to a more compact and less mobile polymer structure. The PVA used in this study has a high degree of hydrolysis (88–89%), which provides more hydroxyl groups for hydrogen bonding. At elevated temperatures (60–80°C), the PVA-KC chains form a randomly entangled structure that transforms into a denser, coil-like configuration upon cooling, resulting in a stronger and stiffer film matrix. This is also identified in the FTIR results with the addition of Kappa Carrageenan, showing reduced peak intensity iin the O-H bending region (1430-1440 cm^{-1}), which indicates the formation between the free hydroxyl (-OH) groups of PVA reacting with the hydroxyl groups in chitosan and also Kappa Carrageenan crosslinked with the aldehyde groups in glutaraldehyde (Shahbazi et al., 2016; Tan et al., 2021). Based on the results of the mechanical strength test for biocomposites, the test results can be compared with the Indonesian National Standard (National; 2014) for bioplastic degradation category as follows:

Table 2. Indonesia national standard of biocomposite

SNI **No. 7818:2014**	Tensile Strength (Mpa)	Elongation (%)
Bioplastic	Min 13.7	400-1120%

However, the biocomposite film samples without the addition of kappa carrageenan exhibited the highest tensile strength compared to those containing kappa carrageenan. This observation is attributed to differences in the film formation process. Specifically, the extended drying time employed in the control sample preparation

ranging from 72-120 hours at 25°C and 24 hours at 40°C likely facilitated molecular rearrangement within the polymer matrix. This prolonged drying period promoted the development of a more ordered structure, increased crystallinity, and ultimately enhanced the film's mechanical strength (Costa-Júniora et al., 2009).

According to the Indonesian National Standard (SNI No. 7818:2014), bioplastic films must exhibit a minimum tensile strength of 13.7 MPa and an elongation percentage between 400–1120% to be classified under the degradable plastic category. Based on the mechanical test results (Table 3), most biocomposite films met the tensile strength requirement, except for the formulations containing 3% KC with 1.76% chitosan and 5% KC with 2.2% chitosan. However, none of the samples satisfied the elongation criteria, indicating that while the films are strong, they lack the flexibility required by the standard. All biocomposite film samples have not met the national standard for the elongation percentage of bioplastic.

Table 3. Results of the mechanical strength test for biocomposites

Sample (KC:PVA:CS)	Thickness (mm)	Tensile Strength (Mpa)	Elongation (%)
0:3:0:3	0.15	38.27	106.8
0:3:0:4	0.144	40.52	132.7
0:3:0.5	0.138	40.28	82.83
3:3:0.3	0.156	40.17	2.333
3:3:0.4	0.31	16.97	6.55
3:3:0.5	0.398	11.93	2.467
4:3:0.3	0.214	19.69	1.698
4:3:0.4	0.334	17.2	2.674
4:3:0.5	0.352	24.55	3.114
5:3:0.3	0.188	32.25	2.755
5:3:0.4	0.318	17.76	2.5
5:3:0.5	0.402	12.4	3.649

Conclusion

Based on the results of the research conducted, the synthesis of Kappa Carrageenan biocomposite was successfully carried out using the solution casting method. The addition of Kappa Carrageenan and chitosan concentrations to polyvinyl alcohol with the crosslinker agent glutaraldehyde resulted from physical mixing by combining the hydroxyl functional groups of each constituent component. This led to the formation of hydrogen bonds between the components of the Kappa Carrageenan, PVA, chitosan, and glutaraldehyde. In this process, new functional groups were not formed, but the intensity of absorption of free hydroxyl groups (-OH) in the fingerprint region of 1430-1440 cm^{-1} weakened due to bonding with hydroxyl groups among the biocomposite components. The characterization test results indicate that an increase in Kappa Carrageenan concentration improves the film's resistance to water absorption adn enhances tensile strength. Thus, the concentration of Kappa Carrageenan can be a crucial factor in enhancing the performance of the biocomposite film.

Scientific Ethics Declaration

* The authors declare that the scientific ethical and legal responsibility of this article published in EPSTEM Journal belongs to the authors.

Funding

* This research received no specific grant from any funding agency in the public, commercial, or not-for-profit sectors

Acknowledgements or Notes

* This article was presented as an oral presentation at the International Conference on Basic Sciences, Engineering and Technology (www.icbaset.net) held in Trabzon/Türkiye on May 01-04, 2025.

References

Abdeen, Z. (2011). Swelling and reswelling characteristics of cross-linked poly(vinyl alcohol)/chitosan hydrogel film. *Journal of Dispersion Science and Technology, 32*(9), 1337-1344.

Alias, N. F., & Ismail, H. (2020). Glutaraldehyde crosslinked polyvinyl alcohol/eggshell powder biocomposite films: properties and biodegradability. *Journal of Physical Science, 31*(2), 45-60.

Chopra, H., Bibi, S., Kumar, S., Khan, M. S., Kumar, P., & Singh, I. (2022). Preparation and evaluation of chitosan/PVA based hydrogel films loaded with honey for wound healing application. *Gels, 8*(2), 8020111.

Costa-Júniora, E. S., Barbosa-Stanciolib, E. F., Mansurc, A. A. P., Vasconcelosc, W. L., & Mansurc, H. S. (2009). Preparation and characterization of chitosan/poly(vinyl alcohol) chemically crosslinked blends for biomedical applications. *Carbohydrate Polymers, 76*, 472-481.

Distantina, S., Noviyanti, R. U., Sutriyani, S., Fadilah, F., & Kaavessina, M. (2017). Mass transfer of paracetamol from the crosslinked carrageenan-polyvinyl alcohol film. *International Scholarly and Scientific Research & Innovation, 11*(9), 619-623.

El-Hefian, E. A., Nasef, M. M., & Yahaya, A. H. (2010). The preparation and characterization of chitosan / poly (vinyl alcohol) blended films. *E-Journal of Chemistry, 7*(4), 1212-1219.

Hilliou, L., Larotonda, F. D. S., Abreu, P., Ramos, A. M., Sereno, A. M., & Gonc¸alves, M. P. (2006). Effect of extraction parameters on the chemical structure and gel properties of k/i-hybrid carrageenans obtained from Mastocarpus stellatus. *Biomolecular Engineering, 23*(4), 201-208.

Jambeck, J. R., Geyer, R., Wilcox, C., Siegler, T. R., Perryman, M., Andrady, A.,…& Law, K. L. (2015). Marine pollution. plastic waste inputs from land into the ocean. *Science, 347*(6223), 768-771.

Ke, C. L., Deng, F. S., Chuang, C. Y., & Lin, C. H. (2021). Antimicrobial actions and applications of chitosan. *Polymers (Basel), 13*(6), 13060904.

Li, Y., Li, J., Shi, Z., Wang, Y., Song, X., Wang, L., . . .& Zhao, C. (2020). Anticoagulant chitosan-kappa-carrageenan composite hydrogel sorbent for simultaneous endotoxin and bacteria cleansing in septic blood. *Carbohydr Polym, 243*, 116470.

Maghfiroh, Sumarni, W., & Susatyo, E. B. (2013). Sıntesıs dan karakterısası edıblefılmkıtosan termodıfikası pva dan sorbıtol. *Indonesian Journal of Chemical Science, 2*(1).

Markets, A. S. T. (2017). Standard test method for tensile properties of thin plastic sheeting. *ASTM D882-12 8*(1).

Mendoza, W. G., Ganzon-Fortes, E. T., Villanueva, R. D., Romero, J. B., & Montan˜o, M. N. E. (2006). Tissue age as a factor affecting carrageenan quantity and quality in farmed Kappaphycus striatum (Schmitz) Doty ex Silva. *Botanica Marina, 49*(1), 57-64.

Migneault, I., Dartiguenave, C., Bertrand, M. J., & Waldron, K. C. (2004). Glutaraldehyde: behavior in aqueous solution, reaction with proteins, and application to enzyme crosslinking. *Biotechniques, 37*(5), 790-796,

Ministry of Environment and Forestry, R. O. I. (2020). *National plastic waste reduction strategic actions for Indonesia*. Indonesia :Ministry of Environment and Forestry.

Pereira, L., Amado, A. M., Critchley, A. T., Velde, F. v. d., & Ribeiro-Claro, P. J. A. (2009). Identification of selected seaweed polysaccharides (phycocolloids) by vibrational spectroscopy (FTIR-ATR and FT-Raman). *Food Hydrocolloids, 23*(7), 1903-1909.

Ramadas, B. K., Rhim, J.-W., & Roy, a. S. (2024). Recent progress of carrageenan-based composite films in active and ıntelligent food packaging applications. *Polymers, 16*(7), 1-26.

Rojas, J. (2015). Improved polymer functionality by cross-linking with glutaraldehyde to achieve controlled drug release. In S. H. S. B. Ajit S. Narang (Ed.), *Excipient Applications in Formulation Design and Drug Delivery* (pp. 569-588): Springer, Cham.

Shahbazi, M., Rajabzadeh, G., Ettelaie, R., & Rafe, A. (2016). Kinetic study of κ-carrageenan degradation and its impact on mechanical and structural properties of chitosan/κ-carrageenan film. *Carbohydrate Polymers, 142*, 167-176.

Shahbazi, M., Rajabzadeh, G., Rafe, A., Ettelaie, R., & Ahmadi, S. J. (2017). Physico-mechanical and structural characteristics of blend film of poly (vinyl alcohol) with biodegradable polymers as affected by disorder-to-order conformational transition. *Food Hydrocolloids, 71*, 259-269.

Soeda, K., Yamagata, M., & Ishikawa, M. (2009). Preparation and characterization of chitosan/poly(vinyl alcohol) chemically crosslinked blends for biomedical applications. *Carbohydrate Polymers, 76*, 472-481.

Tan, R., Li, F., Zhang, Y., Yuan, Z., Feng, X., Zhang, W.,…& Huang, X. (2021). High-performance biocomposite polyvinyl alcohol (PVA) filmsmodified with cellulose nanocrystals (CNCs), tannic acid (TA),and chitosan (CS) for food packaging. *Journal of Nanomaterials, 2021*, 9.

Tun, T. Z., Kunisue, T., Tanabe, S., Prudente, M., Subramanian, A., Sudaryanto, A.,…& Nakata, H. (2022). Microplastics in dumping site soils from six Asian countries as a source of plastic additives. *Sci Total Environ, 806*(Pt 4), 150912.

Webber, V., Crvalho, S. M. d., Ogliari, P. J., Hayashi, L., & Barreto, P. L. M. (2012). Optimization of the extraction of carrageenan from Kappaphycus alvarezii using response surface methodology. *Food Science and Technology, 32*(4), 812-818.

Author(s) Information

Nonni Soraya Sambudi
Chemical Engineering Departement, Universitas Pertamina
Teuku Nyak Arief Street, Simprug, Kebayoran Lama,
Jakarta 12220, Indonesia
Contact e-mail: *nonni.ss@universitaspertamina.ac.id*

Chaterine Lovy Sarah Nova
Chemical Engineering Departement, Universitas Pertamina
Teuku Nyak Arief Street, Simprug, Kebayoran Lama,
Jakarta 12220, Indonesia

Fitri Ayu Radini
Research Centre for Polymer Technology, National
Research and Inovation Agency
Gedung 460 Kawasan Sains dan Teknologi (KST) B.J.
Habibie Setu, Tangerang Selatan, Banten, 15314, Indonesia

To cite this article:

Sambudi, N.S., Nova, C.L.S., & Radini, F.A., (2025). Synthesis of biocomposite of kappa carragenan and polyvinyl alcohol for bioplastic. *The Eurasia Proceedings of Science, Technology, Engineering and Mathematics (EPSTEM), 34,* 377-387.

The Eurasia Proceedings of Science, Technology, Engineering & Mathematics (EPSTEM)
ISSN: 2602-3199

The Eurasia Proceedings of Science, Technology, Engineering and Mathematics (EPSTEM), 2025

Volume 34, Pages 388-393

ICBASET 2025: International Conference on Basic Sciences, Engineering and Technology

A Novel All-Optical Photonic Crystal Sensor for Petrochemical Liquid Detection

Elhachemi Kouddad
University of Adrar
University Djillali Liabes

Sououdi Boumediene Chabani
University of Adrar

Islam Hassani
University of Adrar

Abstract: In this study, we introduce a novel and innovative optical sensor based on photonic crystals designed for the detection of petrochemical liquids. This device leverages the unique properties of photonic crystals to provide exceptional sensitivity and measurement accuracy. The sensor comprises a square lattice of gallium arsenide (GaAs) rods suspended in air and coupled to an optimized ring resonator. This compact architecture, measuring only 274 μm², enables the sensor to be easily integrated into miniaturized systems. The interaction of petrochemical liquids such as petrol, kerosene, or diesel with the sensor induces changes in its optical properties. These variations, measured by analyzing the transmitted light, allow for the precise identification and quantification of the substances present in the sample. This approach offers rapid and reliable detection, opening up new prospects in industrial quality control, environmental monitoring, and safety. The strengths of this sensor lie in its high sensitivity, enabling the detection of trace amounts of contaminants, and its extremely short response time, ideal for real-time monitoring. Moreover, its fabrication relies on well-established processes, promising large-scale production at a competitive cost. The potential applications of this sensor are numerous and could revolutionize detection methods in the petrochemical industry.

Keywords: Petrochemical, Photonic crystal resonator, Sensors, Optical circuits.

Introduction

The rise of the automotive industry has led to increased consumption of petrochemical products, such as diesel and gasoline. Consequently, the quality of fuel used in a motor vehicle affects its longevity. Inferior, or impure, fuel not only impairs engine performance but also poses a significant environmental risk. The use of inferior quality fuels in automobiles significantly contributes to the increase in carbon dioxide (CO_2) emissions, a major air pollutant that exacerbates global warming (Chiang et al., 1996; Florides & Christodoulides, 2009). Therefore, it is imperative that the scientific community develop an effective mechanism for the detection of pure petrochemical products. Although several technologies have been identified in this area, including techniques based on the evaluation of physico-chemical properties: density, viscosity, odor, color, etc. and analytical methods such as chromatography, titration and ultrasonic techniques (Shahru Bahari et al., 1992; Gupta & Sharma, 2010; Sadat, 2014), the latter present limitations in terms of complexity, cost, speed, sensitivity and accuracy.

Interest in photonic crystal (PhC)-based sensors has grown significantly over the past decade due to their exceptional potential for detecting a wide range of parameters, including temperature (Elhachemi et al., 2022), pressure (Elhachemi & Leila, 2023), electromagnetic fields (Chabani et al., 2024), glucose (Iman et al., 2022),

- Selection and peer-review under responsibility of the Organizing Committee of the Conference

cancer cells (Panda et al., 2023), liquids and chemical compounds (Yang et al., 2024). Unlike conventional sensors, photonic crystal devices are distinguished by their easily tunable optical properties, which gives them increased adaptability for specific detection applications. In addition, the possibility of selectively introducing liquids or chemical compounds into the structure of photonic crystals induces efficient light-matter interactions, a considerable advantage for the detection of liquids and chemical compounds (Yang et al., 2024). In order to meet the critical need for the detection of petrochemical products, we propose a novel design of optical sensor based on the use of two-dimensional photonic crystals. This innovative approach aims to optimize the sensitivity of the detection of liquid samples of petrochemical products by focusing on the miniaturization of the device, the improvement of the response time and the simplification of its manufacture.

Detection Principles for Petrochemical Sensors

In the petrochemical sector, sensors play a crucial role in the precise analysis of the composition of fluids used. These sensors are based on the principle of photonic resonance in ring resonator structures. The objective of this text is to provide an in-depth analysis of the principle of photonic resonance, explaining the fundamental concepts and mechanisms that govern it. Photonic resonance occurs when a light wave is confined within a ring resonator whose dimensions are on the order of its wavelength. This phenomenon generates distinct resonance modes, each defined by a specific wavelength and quality factor (Q).

The resonance wavelength is strongly influenced by the refractive index of the material constituting the structure, as well as its geometric configuration. The refractive index (RI) is a dimensionless quantity that characterizes the ability of a medium to deviate light. It is defined as the ratio between the speed of light in a vacuum and its speed in the medium under consideration. Liquid hydrocarbons derived from petroleum, such as petrol, kerosene, and diesel, exhibit distinct refractive indices that allow their identification. Each liquid hydrocarbon possesses a unique RI, which constitutes a reliable method of identification, as illustrated in the table below (Kumar et al., 2024; Hossain et al., 2023).

Table 1. Refractive index for petrol, kerosene and diesel

Petrochemical liquid	Refractive index (RI)
Petrol	1.418
Kerosene	1.44
Diesel	1.46

Basic Structure and Analysis of Photonic Properties

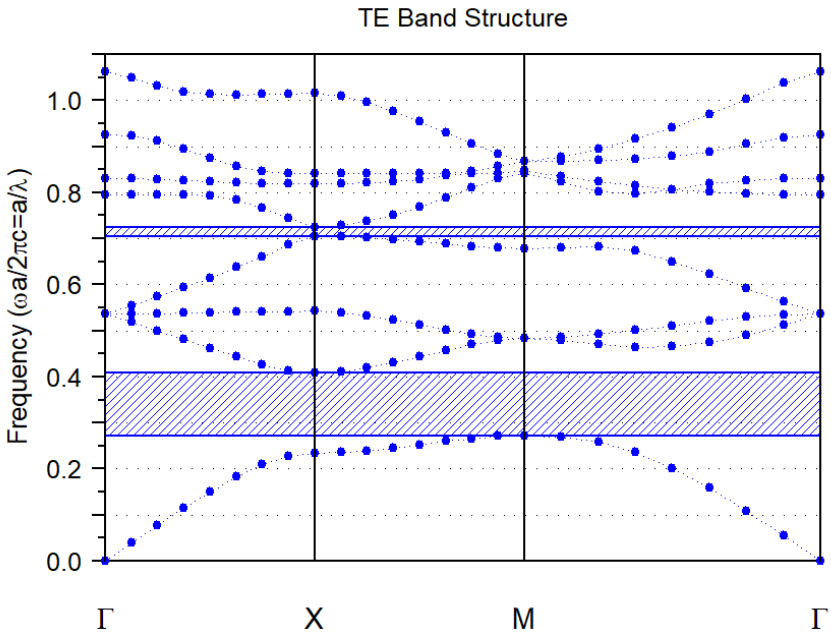

Figure1. The fundamental PhC band structure

This photonic device is fundamentally comprised of a two-dimensional, square lattice of free-standing Gallium Arsenide (GaAs) rods within an air matrix (refractive index n = 1). The array consists of 29 rows and 29 columns of rods. The inter-rod spacing, or period (a), is 0.5635 μm, measured along the X and Z axes. Each rod possesses a radius (r) equal to 0.2a.

The optical properties of the structure, specifically light propagation and confinement were investigated using the plane wave expansion (PWE) method. This numerical analysis, employing optimized structural parameters, facilitated the calculation of the structure's photonic bandgaps (PBGs) and propagation modes. The results of this analysis are presented in Figure 1.

The structure demonstrates two distinct photonic band gaps (PBGs) for transverse electric (TE) polarized modes. The first PBG spans from 0.268 to 0.414 a/λ, equivalent to wavelengths of 1361.11 nm to 2102.61 nm. The second PBG ranges from 0.7 to 0.728 a/λ, corresponding to wavelengths of 774 nm to 805 nm. Notably, the first TE-mode PBG (1361.11 nm to 2102.61 nm) coincides precisely with the low-loss third optical window of Gallium Arsenide (GaAs). This spectral alignment renders the proposed structure highly advantageous for its intended application in petrochemical sensing.

Petrochemical Liquid Sensor Design

A Gaussian optical signal with a central wavelength of 1550 nm is initially injected into the input port of an optimized ring resonator. The device is designed to favor the exclusive transmission of this specific wavelength while attenuating others. The signal passes through the resonator in an air medium, in the absence of petrochemical liquids, and is collected at the output port. The output spectrum analysis is performed by applying the Fast Fourier Transform (FFT) to the Gaussian signal recorded and stored by a sampling oscilloscope (represented in green) (Figure 2a and 2b). The Finite-Difference Time-Domain (FDTD) method is employed to simulate the normalized transmission spectrum at the resonator output in the presence of various petrochemical liquids introduced on the sensor (Rsoft Design Group, 2014). This approach allows evaluating the influence of these substances on the transmission properties of the resonator and characterizing its sensitivity to the detection of petrochemical liquids.

Evaluation of the performance of petrochemical liquid sensors is crucial to ensure their reliability and efficiency in various industrial applications. A key parameter in this evaluation is the quality factor Q, which reflects the sensor's ability to discriminate between different wavelengths of the light spectrum. This quality factor is defined as the ratio of the resonance wavelength (λ) to the full width at half maximum (FWHM) of the wavelength spectrum (Δλ). The quality factor Q can be calculated using the following equation:

$$Q = \lambda / \Delta\lambda \tag{1}$$

Where: λ represents the resonance wavelength of the sensor

Δλ corresponds to the full width at half maximum of the wavelength spectrum

This equation allows the quantification of the sensor's ability to detect subtle variations in the composition of petrochemical liquids, based on their refractive index. Measurement of the quality factor Q is essential to evaluate the sensor's sensitivity and accuracy in the detection of petrochemical liquids. A high-quality factor indicates better spectral resolution, thus enabling more precise identification of the components present in the samples analyzed.

Furthermore, the quality factor provides a reliable indication of the sensor's performance in specific applications, such as quality control of petroleum products or contaminant detection in fuels. The quality factor Q is frequently used to evaluate energy storage and losses within a ring resonator. An increase in the value of Q is manifested by a sharply pronounced peak at the resonance wavelength, thus illustrating a direct proportional and inversely proportional relationship with energy storage and losses, respectively. Therefore, the acquisition of the quality factor from the proposed petrochemical liquid sensor is important in this field.

Our study demonstrates that the resonance wavelength of each petrochemical liquid (petrol, kerosene, and diesel) exhibits a shift towards higher values, indicating an enhanced sensitivity for each liquid. The performance of the microstructure-based optical sensor is quantitatively evaluated by the sensitivity to the

refractive index of each liquid. This sensitivity is defined as the ratio of the resonance wavelength shift to the refractive index variation of the injected liquid (Mallika et al., 2015):

$$S = \Delta\lambda / \Delta n \quad (2)$$

Where $\Delta\lambda$ represents the resonance wavelength shift, and Δn corresponds to the refractive index variation for each petrochemical product.

In general, an increase in the sensitivity to the refractive index of each petrochemical liquid induces significant shifts in the resonance wavelength as a function of these index variations. Within the scope of this study, the ring resonator micro-sensor exhibits a particularly high sensitivity to the refractive index of petrochemical liquids, reaching approximately 1334 nm/RIU (Refractive Index Unit). For each petrochemical liquid analyzed, Figure 3 and Table 2 summarize the performance parameters of our petrochemical sensor, including resonance wavelength, normalized transmission efficiency, quality factor, and sensitivity.

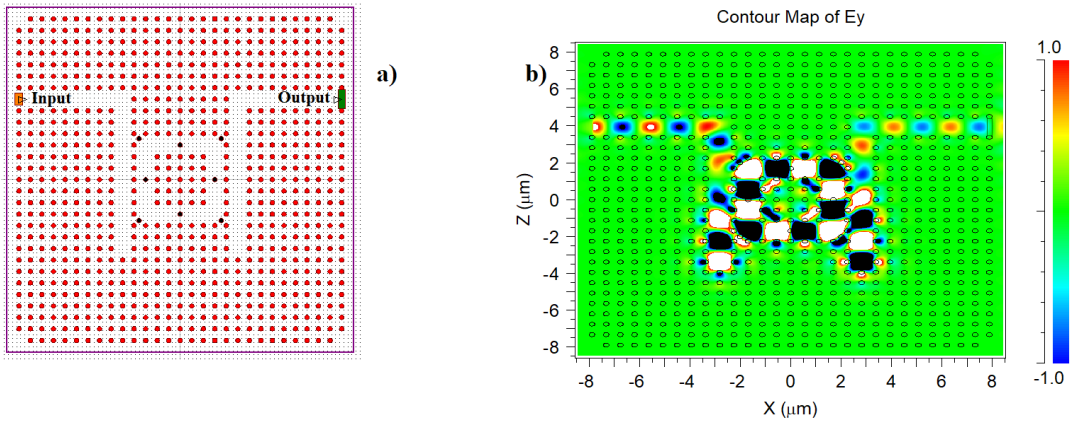

Figure 2. Proposed layout of the petrochemical liquid sensor

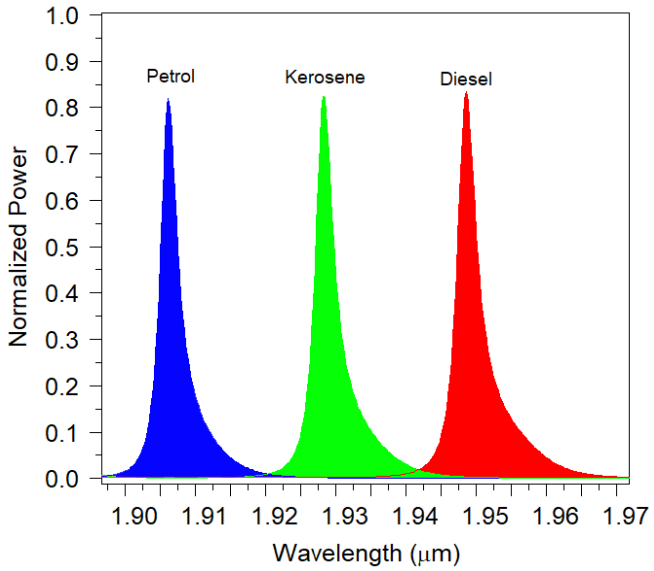

Figure 3. Study of the normalized resonance spectrum of a petrochemical liquid sensor

Table 2. Functional characterization of a petrochemical sensor

Petrochemical liquid	Refractive Index (RIU)	Resonant Wavelength (nm)	Transmission Efficiency (%)	Quality factor	Sensitivity (nm/ RIU)
Petrol	1.418	1906.1	82	705	1344
Kerosene	1.44	1928.3	82.4	664	1339
Diesel	1.46	1948.6	83.4	608	1334

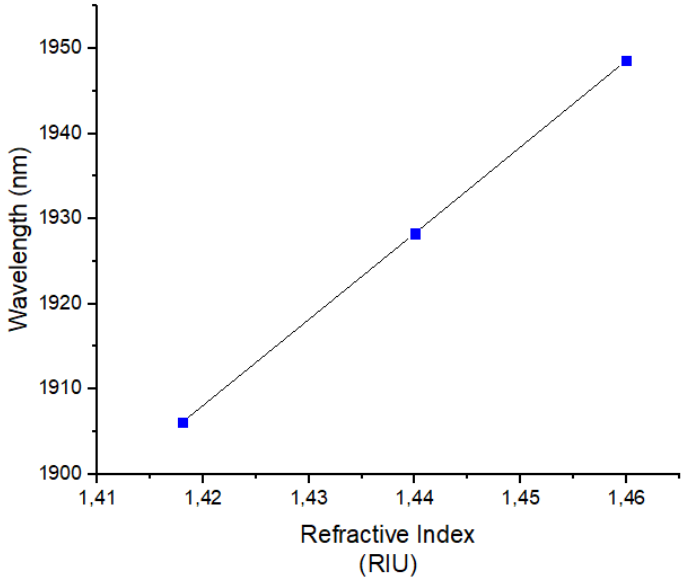

Figure 4. Interaction between the resonant wavelength and the refractive index of petrochemical

Consequently, the illustration provided in Figure 4 highlights the linear correlation between resonance wavelengths and the refractive index of petrochemical compounds. The collected data confirms the enhanced effectiveness of our petrochemical sensors using a ring resonator compared to conventional sensors currently available.

Conclusion

In the framework of our work, we propose a novel all-optical photonic crystal-based sensor for the detection of petrochemical liquids. The operating principle relies on the injection of various petrochemical products, such as petrol, kerosene, and diesel, into the sensor. The sensor's performance was numerically evaluated using two methods: Plane Wave Expansion (PWE) and Finite Difference Time Domain (FDTD). This sensor exhibits high sensitivity, an ultra-compact size of 274 μm^2, and a response time on the order of the picosecond, which corresponds to a very high data rate, on the order of the terahertz. The proposed sensor, adaptable to integrated optics, industry, and nanotechnology-based sensing applications, offers several advantages.

Scientific Ethics Declaration

* The authors declare that the scientific ethical and legal responsibility of this article published in EPSTEM Journal belongs to the authors.

Funding

* This work was supported by the Directorate General for Scientific Research and Technological Development (DGRSDT).

Conflict of Interest

* The authors declare that they have no conflicts of interest

Acknowledgements or Notes

* This article was presented as an oral presentation at the International Conference on Basic Sciences, Engineering and Technology (www.icbaset.net) held in Trabzon/Türkiye on May 01-04, 2025.

References

Chiang, P. C., Chiang, Y. C., Chang, E. E., & Chang, S. C. (1996). Characterizations of hazardous air pollutants emitted from motor vehicles. *Toxicological & Environmental Chemistry, 56*(1-4), 85-104.

Chabani, S. B., Dekkiche, L., Kouddad, E., & Hassani, I. (2024). A novel proposal of an electro-optical sensor to measure various levels of an electric field using pockels effect photonic crystals. *Journal of Nanoelectronics and Optoelectronics, 19*(6), 665-668.

Elhachemi, K., & Leila, D. (2023). High-sensitivity all-optical pressure sensor based on photonic-crystal nanotechnology. *Journal of Russian Laser Research, 44*(3), 284-288.

Elhachemi, K., Leila, D., & Rafah, N. (2022). High sensitivity and ultra-high-quality factor for an all-optical temperature sensor based on photonic crystal technology. *Nano Tech Nano Sci Ind J, 16*(6), 174.

Florides, G. A., & Christodoulides, P. (2009). Global warming and carbon dioxide through sciences. *Environment International, 35*(2), 390-401.

Gupta, A. K., & Sharma, R. K. (2010). A new method for estimation of automobile fuel adulteration. *Air Pollution, 10*, 10054.

Hossain, M. B., Kříž, J., Dhasarathan, V., & Rahaman, M. E. (2023). Photonic crystal fiber (PhCF) for petrochemical sensing. *Frontiers in Physics, 10*, 1097841.

Iman, O., Samia, D., & Benattou, F. (2022, May). All optical biosensors for glucose and urea detection based on photonic crystal nano-technology. In *2022 7th International Conference on Image and Signal Processing and their Applications (ISPA)* (pp. 1-5). IEEE.

Kumar, V., Raghuwanshi, S. K., & Kumar, S. (2024). Nanocomposite thin film-based surface plasmon sensor for detection of ethanol in petrochemical industries. *IEEE Transactions on Plasma Science*.

Mallika, C. S., Bahaddur, I., Srikanth, P. C., & Sharan, P. (2015). Photonic crystal ring resonator structure for temperature measurement. *Optik, 126*(20), 2252-2255.

Panda, A., Van Nguyen, C., Pukhrambam, P. D., & Dhasarathan, V. (2023). Employing metamaterial and Ti3C2Tx (MXene) material for cancer cells detection using defective 1D photonic crystal. *Optical and Quantum Electronics, 55*(5), 480.

Sadat, A. (2014). Determining the adulteration of diesel by an optical method. *International Journal of Computer Applications, 100*(13).

Shahru Bahari, M., Criddle, W. J., & Thomas, J. R. (1992). Fuel cell methodology for determining petrol adulteration with kerosene. In *Analytical Proceedings* (Vol. 29, No. 1, pp. 30-31).

Yang, Y., Yu, L., Jiang, X., Li, Y., He, X. W., Chen, L., & Zhang, Y. (2024). Recent advances in photonic crystal-based chemical sensors. *Chemical Communications*, *69*: 9177-9193.

Author(s) Information

Elhachemi Kouddad
Department of Electrical Engineering, Faculty of Science and Technology, University of Adrar 01000, Algeria.
Telecommunication and Digital Signal Processing Laboratory, Faculty of Electrical Engineering, Department of Telecommunications, University Djillali Liabes, Sidi-Bel-Abbes 22000, Algeria.
Email: elh.kouddad@univ-adrar.edu.dz

Sououdi Boumediene Chabani
Department of Electrical Engineering, Faculty of Science and Technology, University of Adrar 01000, Algeria.
Laboratory of Energy, Environment and Information Systems, University of Adrar 01000, Algeria.

Islam Hassani
Department of Electrical Engineering, Faculty of Science and Technology, University of Adrar 01000, Algeria
Sustainable Development and Informatics Laboratory (LDDI), University of Adrar, Algeria

To cite this article:

Kouddad, E., Chabani, S.B., & Hassani, I., (2025). A novel all-optical photonic crystal sensor for petrochemical liquid detection. *The Eurasia Proceedings of Science, Technology, Engineering and Mathematics (EPSTEM), 34,* 388-393.

The Eurasia Proceedings of Science, Technology, Engineering & Mathematics (EPSTEM)
ISSN: 2602-3199

The Eurasia Proceedings of Science, Technology, Engineering and Mathematics (EPSTEM), 2025

Volume 34, Pages 394-401

ICBASET 2025: International Conference on Basic Sciences, Engineering and Technology

Study *in-Vitro* Digestibility of Vicia Narbonensis L. and Vicia Sativa L. Seeds Cultivated for Ruminants

Farid Djellal
Ferhat Abbas University

Selma Mahmah
Ferhat Abbas University

Si Ammar Kadi
Mouloud Mammeri University of Tizi-Ouzou

Azeddine Mouhous
Mouloud Mammeri University of Tizi-Ouzou

Rabia Cherfouh
Mouloud Mammeri University of Tizi-Ouzou

Ali Bouzourene
Mouloud Mammeri University of Tizi-Ouzou

Idir Moualek
Mouloud Mammeri University of Tizi-Ouzou

Amar Mebarkia
Ferhat Abbas University

Abstract: Vicia narbonensis L. and Vicia sativa L. seeds are legumes rich in protein and energy, commonly used for ruminant feeding. Their integration into feed rations requires an assessment of their digestibility, a crucial factor for their nutritional value. This study aims to determine the *in-vitro* organic matter digestibility of these seeds, obviously while taking into account the influence of the semi-arid climatic conditions of Sétif on their chemical composition. The experiment involved two species of the genus Vicia, with ten ecotypes of Vicia narbonensis L. from ICARDA and two ecotypes of Vicia sativa L. from Algeria, the latter serving as controls due to their wide use by Algerian farmers. The data were subjected to variance analysis followed by a Fisher test (LSD) at significance threshold at 5%. The results show a significant variability ($P < 0.05$) in digestibility between the ecotypes of the two species. The most digestible ecotypes are for Vicia narbonensis L.; ecotypes N-2392 (dMO = 77%) and N-2464 (dMO = 75%), and for Vicia sativa L.; ecotype S-BBA (dMO = 74%). Thus, the Vicia narbonensis and Vicia sativa seeds grown in Sétif can be an excellent source feed for ruminants. Their digestibility is generally high but can be optimized by technological processes such as soaking or cooking. It is important to take into account local specificities to determine the best way to incorporate these seeds into animal rations.

Keywords: Vetch, Digestibility, Ruminants, Nutritive value, Agricultural engineering

Introduction

Although fodder legumes are less demanding than many other crops and play a key role in production systems, especially by contributing to crop rotation through their cleansing effect and by enriching the soil with nitrogen and organic matter while serving as a food source for livestock, they have not always received the attention they deserve in Algeria. In particular, research on species of the *Vicia* genus, specifically *Vicia narbonensis* L., remains scarce in our country.

Forage legumes occupy a significant economic position in the animal feed market and deserve particular attention in arid and semi-arid Mediterranean areas (Kokten et al., 2009), and due to the diversity of breeding conditions and the nature, level and composition of products, a targeted protein diet for ruminants must be mastered (Andrieu & Demarquilly, 1992).

It would therefore be beneficial to further encourage the cultivation of fodder legumes. Development strategies should be tailored to the specific characteristics and potential of the semi-arid agro-ecological zone, ensuring a balance between the availability of fodder resources and the nutritional needs of livestock. In other words, it is essential to establish a compromise between fodder supply and herd requirements in this region to achieve food self-sufficiency and, ultimately, to implement a strategy that fosters complementarity between different zones.

Method

Objectif

This study aims to determine the organic matter (OM) content and assess the *in vitro* digestibility of ten ecotypes of *Vicia narbonensis* L., compared to two ecotypes of *Vicia sativa* L., under the characteristic rainfed conditions of the semi-arid region of Sétif. The goal is to estimate their nutritional value for ruminant feeding. The pepsin-cellulase enzymatic method, developed by Aufrère (1982), is widely used to predict organic matter digestibility in forages. This method provides a significantly more accurate *in vivo* digestibility prediction than crude fiber measurement alone. In fact, incorporating nitrogenous matter content alongside crude fiber does not enhance prediction accuracy compared to using crude fiber alone.

Presentation of the Study Region

The trials were conducted on plots located at the FERHAT Abbas-Sétif1 University Campus (36°12’ N; 5°21’ E) in the Sétif region under rainfed conditions. This region experiences a continental climate, characterized by significant annual and daily temperature variations, along with two major constraints: frost and the sirocco. Situated in the semi-arid bioclimatic zone at an altitude of 1,025 meters, winter temperatures can drop below 0 °C, while summer temperatures occasionally exceed 40 °C. Additionally, the temperature differences between day and night—reaching up to 20 °C in winter and spring, promote frost episodes that pose significant challenges to plant growth (Bouzerzour & Benmahammed, 1994).

The soils in the experimental area belong to the steppe soil group (Perrier & Soyer, 1970) and are characterized by a silty-clayey texture, a lumpy structure, a basic pH (7.81), a total limestone content of 17.7%, and an organic matter content ranging between 2.0% and 3.0%. The region receives an average annual rainfall of approximately 450 mm (Seltzer, 1947), with an average of 373.8 mm recorded between 2006 and 2017 (ONM, 2017), although significant intra- and inter-annual variations have been observed. The experiment was conducted over three consecutive growing seasons (2017-2018, 2018-2019 and 2019-2020). Rainfall showed significant variation from one year to the next, with 469.05 mm recorded during the first season, 321.20 mm during the second, and 384.56 mm during the third. On the other hand, maximum and minimum temperatures remained relatively stable throughout the three growing seasons.

Presentation of Plant Material

The study focused on two species of the *Vicia* genus, including ten ecotypes of *Vicia narbonensis* L. from various origins (provided by ICARDA) and two ecotypes of *Vicia sativa* L. from Algeria. The latter were chosen as controls, as they are well known to Algerian farmers (Table 1).

Table 1. Origins of the Vicia narbonensis ecotypes and Vicia sativa L. studied

Species	Ecotypes	Code	Origin
Vicia narbonensis L.	1	N-2380	Libanon
	2	N-2383	Libanon
	3	N-2390	Libanon
	4	N-2392	Libanon
	5	N-2393	Syria
	6	N-2461	Turqey
	7	N-2464	Turqey
	8	N-2466	Turqey
	9	N-2468	Libanon
	10	N-2561	Syria
Vicia sativa L.	11	S-174	Algéria (Sétif)
	12	S-BBA	Algéria (BBA)

Presentation of the Test

Sowing was performed using a single seed lot over three growing seasons (January 2018, December 2019, and December 2020). The ecotypes were manually sown in randomized blocks on plots previously cultivated with durum wheat. Each plot consisted of four rows, each 4 meters long and spaced 30 cm apart, with approximately 336 seeds sown (70 seeds/m²). The cultivation process included deep plowing, two cover crop passes to control weeds and prepare the seedbed, and continuous manual weeding without fertilizer application. Harvesting was conducted manually at specific times for each season.

In Vitro Digestibility of Organic Matter (dOM)

The pepsin-cellulase enzymatic method, also known as the Aufrère method (1982), is used to estimate the digestibility of organic matter in feed for ruminants. It replicates ruminal digestion by first exposing the sample to pepsin, followed by cellulase. The amount of undigested organic matter is then measured through gravimetric weighing.

Procedure **:**

- Weigh 0.5 g of the sample (denoted as *Ps*) and place it in a porous bag (porosity 2).
- Place the bag in an Erlenmeyer flask and add 40 mL of preheated (40 °C) pepsin-HCl 0.1 solution.
- Cover the Erlenmeyer flask with parafilm and place it in a water bath at 40 °C for 24 hours, ensuring the water level fully submerges the reagent (mechanical agitation is maintained).
- After 24 hours, rinse the residue and the bottom of the Erlenmeyer flask with hot distilled water.
- Add 40 mL of preheated (40 °C) cellulase solution, cover again with parafilm, and return to the water bath at 40 °C for another 24 hours.
- Rinse the residue and the bottom of the Erlenmeyer flask again with hot distilled water.
- Place the bag in a porcelain crucible and dry it at 105 °C for 24 hours.
- Weigh the cooled crucible after placing it in a desiccator (P_0).
- Ash the crucible at 550 °C for 5 hours, then weigh it again after cooling in a desiccator (*Pa*).

Calculations **:**

- E(OM) = (Ps × % OM) / 100
- % DcellOM = [E(OM) – ((P0 – Pa) / E(OM))] × 100 (Aufrère et al., 2005)
- % dOM = 0.699 × DcellOM + 22.6 (Baumont et al., 2007)

E(OM) corresponds to the test intake and DcellOM represents the cellulosic digestibility of the organic matter

Statistical Processing

The data were analyzed using SPSS 20 software, applying a one-way analysis of variance (ANOVA) to evaluate differences among the ten ecotypes of *Vicia narbonensis* L. Mean comparisons were subsequently conducted using Tukey's test (homogeneous groups) with a significance threshold of 5%.

Results and Discussion

Chemical Composition and In Vitro Digestibility of Organic Matter

Significant differences (P <0.05) were observed in the chemical composition and *in vitro* digestibility of seed organic matter, highlighting variability both between and within species (Table 2).

Table 2. Variance in chemical composition and in vitro digestibility of seed organic matter from 12 vetch ecotypes

Sources of variation	df	DM (%)	TA (g/kg DM)	OM (g/kg DM)	CP (g/kg MS)	Fat (g/kg MS)	CF (g/kg MS)	dOM (%)
Total	35	0.31	11.87	11.87	3738.17	51.15	1215.26	85.87
Ecotype	11	0.27*	10.28*	10.28*	3726.22*	46.47*	1020.41*	80.65*
Average		89.27	37.21	962.79	386.37	37.41	124.79	69.46
Standarddeviation		0.33	2.08	2.08	34.34	4.22	21.31	5.38
CV (%)		0.37	5.58	0.22	8.89	11.28	17.08	7.74

* : significant à 5% ; df : degree of freedom ; DM : dry matter ; TA : Totales ashes ; OM : Organic matter ; CP : Crudes Proteins ; MG : Fat ; CF : Crude fiber ; dOM : Digestibility *in vitro* of organic matter ; CV : Coefficient of variation.

Total Ash and Organic Matter Contents

Significant differences (P <0.05) were found among vetch ecotypes in total ash and organic matter contents (Table 3). On average, *Vicia sativa* L. exhibited a slightly higher total ash content (37.57 g/kg DM) compared to *Vicia narbonensis* L. (37.14 g/kg DM). Among the *Vicia narbonensis* L. ecotypes, the highest total ash contents were observed in N-2380 (41.48 g/kg DM), N-2466 (38.82 g/kg DM), and N-2392 (38.33 g/kg DM). Conversely, ecotype N-2461 had the lowest total ash content, measuring 34.28 g/kg DM (Figure 1).

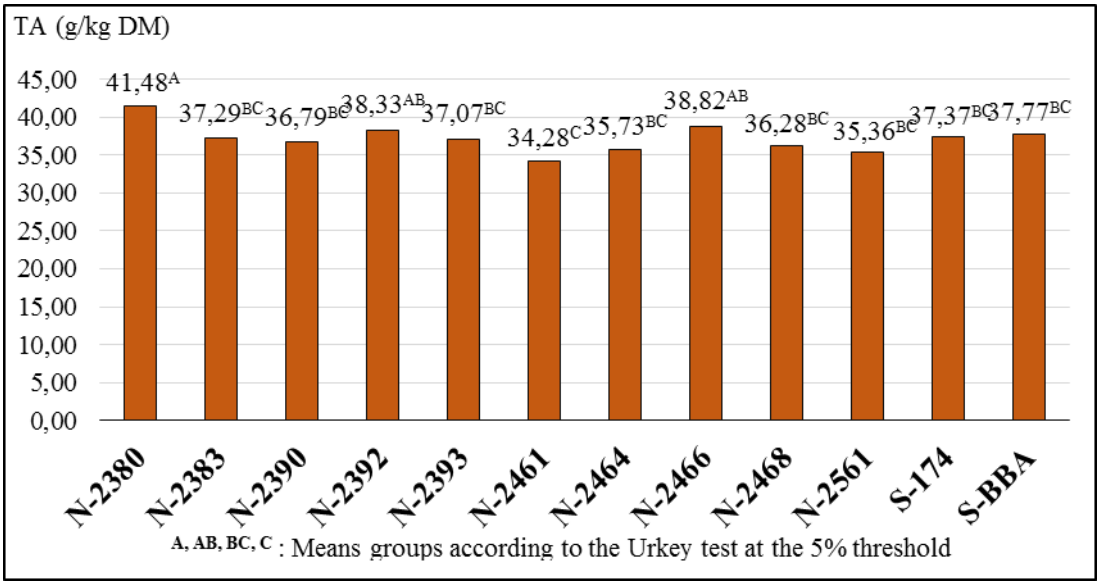

Figure 1. Total ash content of ecotypes Vicia narbonensis L. and Vicia sativa L.

In terms of organic matter content, *Vicia narbonensis* L. averages 962.86 g/kg DM, closely followed by *Vicia sativa* L. with 962.43 g/kg DM. The highest organic matter contents were recorded in ecotypes N-2461 (965.72

g/kg DM), N-2561 (964.64 g/kg DM), and N-2464 (964.27 g/kg DM). In contrast, ecotype N-2380 exhibited the lowest organic matter content, at 958.52 g/kg DM (Figure 2).

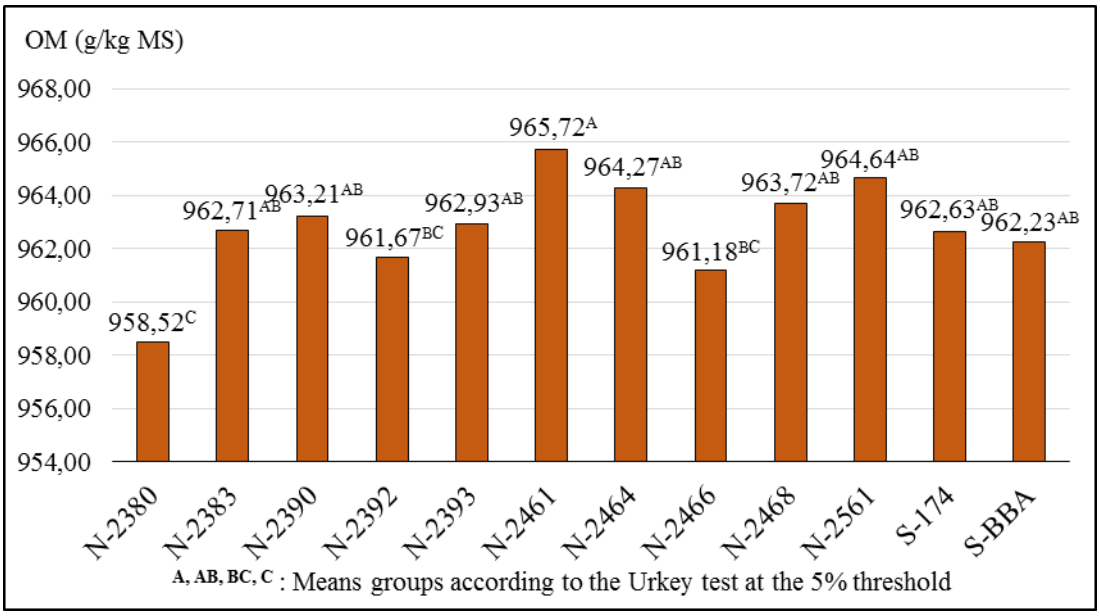

Figure 2. Organic matter content of Vicia narbonensis L. and Vicia sativa ecotypes

Guedes and Dias da Silva (1996) reported total ash contents in *Vicia narbonensis* and *Vicia sativa* seeds that align with our findings. According to Hadjipanayiotou (2000), *Vicia narbonensis* seeds contain 45.0 g/kg DM of total ash and 955.0 g/kg DM of organic matter. In contrast, soybeans have approximately 54 g/kg DM of total ash, a higher value than those observed in our study (Batterham & Egan, 1986). As noted by Jarrige et al. (1995) and Tobia et al. (2008), factors such as soil quality, climatic conditions, and root system development play a key role in determining mineral matter content.

In Vitro Digestibility of Organic Matter

Significant differences ($P < 0.05$) were found in the *in vitro* digestibility of organic matter (dOM) among *Vicia narbonensis* L. and *Vicia sativa* L. ecotypes. On average, *Vicia narbonensis* L. had a slightly higher dOM (69.56%) compared to *Vicia sativa* L. (68.97%). Among the ecotypes studied, N-2392 exhibited the highest digestibility at 76.65%, followed by N-2464 at 74.81% (both from *Vicia narbonensis* L.), and S-BBA at 73.76% (*Vicia sativa* L.). Conversely, ecotype N-2390 had the lowest digestibility, at 61.37% (Figure 3).

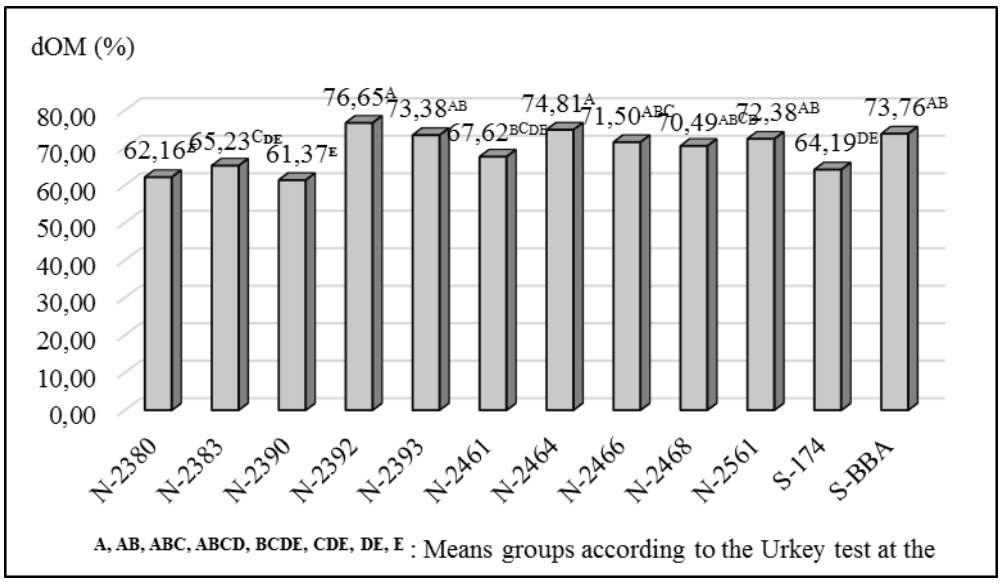

Figure 3. In vitro digestibility of organic matter of Vicia narbonensis L. and Vicia sativa L. ecotypes

In this study, Narbonne vetch (*Vicia narbonensis* L.) demonstrated slightly higher *in vitro* digestibility of organic matter compared to common vetch (*Vicia sativa* L.). This difference was attributed to the lower crude fiber content in *Vicia narbonensis* L. relative to *Vicia sativa* L. The *in vitro* digestibility values observed for *Vicia narbonensis* L. and *Vicia sativa* L. seeds were lower than those reported by Hadjipanayiotou (2000), who recorded a digestibility of 79.9% for *Vicia narbonensis* seeds. This result is in contradiction with those reported by Khériji (1999). In addition, the digestibility values for common vetch hay reported by Cheng et al. (2024) are also higher than current results. It was established that the variety significantly influenced the in vitro digestibility of common vetch, Narbonne vetch, and pea (Larbi et al., 2010).

According to Baumont et al. (2008), the digestibility of organic matter in forage plants is primarily determined by their cell wall content and its digestibility. While intracellular components such as sugars and fructans are almost entirely digestible, cell wall digestibility ranges from 40% to 90%, depending on lignin content. For a given sample, the pepsin-cellulase enzymatic method provides a more accurate estimation of *in vivo* digestibility than crude fiber measurement alone. Moreover, incorporating nitrogenous matter content into crude fiber analysis does not significantly enhance the precision of digestibility prediction compared to crude fiber alone (Aufrère, 1982). Whereas more optimal growth conditions were linked to increased fiber content and reduced digestibility (Piltz et al., 2021).

Certain plant species, particularly woody plants, exhibit lower digestibility, with enzymatic digestibility values ranging from 20% to 36% of dry matter. This reduction is primarily due to the presence of anti-nutritional compounds such as tannins, lignins, and polyphenols, which can bind to proteins and digestive enzymes, thereby hindering the digestion process.

Moreover, a study by Kahlaoui et al. (2021) found that *Vicia narbonensis* and *Vicia sativa* exhibit higher *in vitro* digestibility of organic matter compared to *Vicia villosa*, making them more nutritionally valuable for animal feed. Finally, as forage mature, there is a point at which the accumulation of digestible DM declines despite increasing forage DM yields (Gezahagn et al., 2014). in the same perspective, significant differences ($p < 0.001$) were also observed among the four common vetch in rapidly degradable DMfraction and effective DM degradability of straw; however, no difference was observed in other DMdegradation parameters and neutral detergent fiber degradation parameters (Yafeng et al., 2019).

Conclusion

The findings of this study enhance our understanding of the nutritional potential of *Vicia narbonensis* L. as a ruminant feed, offering essential insights for optimizing their diet.

Recommendations

Encouraging the integration of *Vicia narbonensis* L. into ruminant feeding systems would be beneficial, with larger-scale trials needed to assess its performance under real farming conditions. Additionally, further research on optimizing its cultivation and evaluating its overall impact on animal productivity could facilitate its adoption by livestock farmers.

Scientific Ethics Declaration

* The authors declare that the scientific ethical and legal responsibility of this article published in EPSTEM Journal belongs to the authors.

Conflict of Interest

* The authors declare that they have no conflicts of interest

Funding

* This research received no specific grant from any funding agency in the public, commercial, or not-for-profit sectors

Acknowledgements or Notes

* This article was presented as an oral presentation at the International Conference on Basic Sciences, Engineering and Technology (www.icbaset.net) held in Trabzon/Türkiye on May 1-4, 2025.

* We would like to thank all the technical staff at the farm and the laboratory at Ferhat ABBAS University Sétif-1.

References

Aufrère, J. (1982). Etude de la prévision de la digestibilité des fourrages par une méthode enzymatique. *Annales de Zootechnie*, *31*, 111-130.

Aufrère, J., Andrieu, J., Baumont, R., Dulphy, J. P., Delaby, L., & Peccatte, J. R. (2005). Analyse d'une banque de données de digestibilités mesurées in vivo et par la technique pepsine-cellulase: Perspective pour la prévision de la valeur énergétique des fourrages. *Rencontres autour des Recherches sur les Ruminants*, *12*, 109.

Batterham, E. S. & Egan, A. R. (1986). Utilization of food legumes as feed. In E. S. Wallis & D. E. Byth (Eds.), *Food legume improvement for Asian farming systems* (pp.193-200). Canberra: ACIAR.

Baumont, R., Aufrère, J., Niderkorn, V., Anduza, D., Surault, F., Peccatte, J.R., delaby, L., & Pelletier, P. (2008). La diversité spécifique dans le fourrage : Conséquence sur la valeur alimentaire. *Fourrages*, *194*,189-206.

Baumont, R., Dulphy, J. P., Sauvant, D., Meschy, F., Aufrère, J., & Peyraud, J. L. (2007). Valeur alimentaire des fourrages et des matières premières: Tables et prévision. In *Alimentation des bovins, ovins et caprins. Besoins des animaux et valeurs des aliments* (p.307). TVersailles, France.

Bouzerzour, H., & Benmahammed, A. (1994). Environmental factors limiting barley grain yield in the high plateaus of eastern Algeria. *Rachis*, *12*, 11-14.

Cheng, X., Wang, S., Zhang, K., Jiang, T., Ye, Y., Lu, Y., Yu, Y., Wei, H., Zhang, Z., & Huang, Y. (2024). Hay yield, chemical composition, and in vitro digestibility of five varieties of common vetch. *Agriculture*, *14*, 1538.

Demarquilly, C., & Andrieu, J. (1992). Composition chimique, digestibilité et ingestibilité des fourrages européens exploités en vert. *INRA Productions Animales, 5*(3), 213-221.

Gezahagn, K., Getnet, A., Alemayehu, M. & Fekede, F. (2014). Forage nutritive values of vetch species and their accessions grown under nitosol and vertisol conditions in the central highlands of Ethiopia. *Livestock Research for Rural Development, 26*(1),1-14.

Guedes, C. M. & Dias da Silva, A. (1996). Cinétique de la dégradation dans le rumen de la matière sèche et de l'azote de graines de légumineuses méditerranéennes. *Annales de Zootechnie*, *45* (5), 423-435.

Hadjipanayiotou, M., & Economides, S. (2001). Chemical composition, *in situ* degradibility and amino acid composition of protein supplements fed to livestock and poultry in Cyprus. *Livestock Research for Rural Development, 13*(6), 2001.

Jarrige, R., Grenet, E., Demarquilly, C., & Besle, M. J. (1995). Les constituants de l'appareil végétatif des plantes fourragères. In R. Jarrige, Y. Ruckebusch & C. Dermarquilly (Eds.), *Nutrition des ruminants domestiques, ingestion et digestion* (pp.25-82). Paris: INRA.

Kahlaoui, S., Hassan, H., Bouzid, S., & Stambouli-Essassi, S. (2021). Évaluation de la valeur nutritive de trois espèces de vesces Tunisiennes: *Vicia sativa* L., *Vicia villosa* Roth. et *Vicia narbonensis* L. (Fabaceae, Faboïdeae). *Journal of Animal and Plant Sciences*, *47*(3), 8527-8541.

Kokten K., Toklu F., Atis I. & Hatipoglu R. (2009). Effects of seeding rate on forage yield and quality of vetch (Vicia sativa L.) - triticale (Triticosecale Wittm.) mixtures under east mediterranean rainfed conditions. *African Journal of Biotechnology*, *8* (20), 5367-5372.

Larbi, A., Hassan, S., Kattash, G., Abd El-Moneim, A.M., Jammal, B., Nabil, H., Nakkul, H. (2010). Annual feed legume yield and quality in dryland environments in north-west Syria: 1. Herbage yield and quality. *Animal Feed Sciences and Technology*, *160*(3-4), 81–89.

Office National de la Météorologie. (2017). *Données climatiques annuelles*. Algeria: ONM.

Piltz, J. W., Rodham, C. A., Wilkins, J. F., & Hackney, B. F. (2021). A comparison of cereal and cereal/vetch crops for fodder conservation. *Agriculture*, *11*(5), 459.

Seltzer, P. (1947). *Le climat de l'Algérie*. Université Alger, Institut de Météorologie et de Physique du globe de l'Algérie

Tobía, C., Villalobos, E., Rojas, A., Soto, H., & Moore, K. J. (2008). Nutritional value of soybean (*Glycine max* L. Merr.) silage fermented with molasses and inoculated with Lactobacillus brevis 3. *Livestock Research for Rural Development, 20*(7), 1-9.

Author(s) Information

Farid Djellal
Département d'agronomie, FSNV, Ferhat Abbas University-UFAS-1- 19000, Sétif, Algeria. Campus El Bez. Sétif 19137, Algeria.
Contact e-mail : *fariddjellal@yahoo.fr*

Selma Mahmah
Département d'agronomie, FSNV, Ferhat Abbas University-UFAS-1- 19000, Sétif, Algeria. Campus El Bez. Sétif 19137, Algeria.

Si Ammar Kadi
Faculté des Sciences Biologiques et des Sciences Agronomiques, Mouloud Mammeri University of Tizi-Ouzou, UN1501, Tizi-Ouzou, Alegria. UMMTO. Nouvelle ville BP 17 RP. 15000 Tizi Ouzou. Algeria

Azeddine Mouhous
Faculté des Sciences Biologiques et des Sciences Agronomiques, Mouloud Mammeri University of Tizi-Ouzou, UN1501, Tizi-Ouzou, Alegria. UMMTO. Nouvelle ville BP 17 RP. 15000 Tizi Ouzou. Algeria

Rabia Cherfouh
Faculté des Sciences Biologiques et des Sciences Agronomiques, Mouloud Mammeri University of Tizi-Ouzou, UN1501, Tizi-Ouzou, Algeria. UMMTO. Nouvelle ville BP 17 RP. 15000 Tizi Ouzou. Algeria

Ali Bouzourene
Faculté des Sciences Biologiques et des Sciences Agronomiques, Mouloud Mammeri University of Tizi-Ouzou, Tizi-Ouzou, Algeria. UMMTO. Nouvelle ville *BP 17 RP. 15000 Tizi Ouzou*. Algeria

Idir Moualek
Faculté des Sciences Biologiques et des Sciences Agronomiques, Mouloud Mammeri University of Tizi-Ouzou, UN1501, Tizi-Ouzou, Algeria. UMMTO. Nouvelle ville BP 17 RP. 15000 Tizi Ouzou, Algéria

Amar Mebarkia
Département d'agronomie, FSNV, Ferhat Abbas University-UFAS-1- 19000, Sétif, Algeria.
Campus El Bez. Sétif 19137, Algeria.

To cite this article:

Djellal, F., Mahmah, S., Kadi, S.A., Mouhous, A., Cherfouh, R., Bouzourene, A., Moualek, I., & Mebarkia, A. (2025). Study in-vitro digestibility of Vicia narbonensis L. and Vicia sativa L. seeds cultivated for ruminants. *The Eurasia Proceedings of Science, Technology, Engineering and Mathematics (EPSTEM), 34,* 394-401.